



## Improvement of Corrosion Resistance for Brass in 3.5% NaCl Media by Using 4-fluorophenyl-2,5-dithiohydrazodicarbonamide

Mothana Ghazi Kadhim AlFalah <sup>a,b\*</sup> , Ahmed Elid <sup>c</sup> , Amgad Ahmed Abdo Ali <sup>c</sup> , Ersin Kamberli <sup>c</sup> , Bahar Nazlı <sup>c</sup> , Sevilay Koyun <sup>c</sup> , Alihan Tosun <sup>c</sup> , Muhammed Kadirlioglu <sup>c</sup> , Fatma Elkassum <sup>c</sup> , Saleh Quddus Saleh <sup>c</sup> , Abdulrahman Obied <sup>c</sup> , Fatma Kandemirli <sup>c</sup> 

<sup>a</sup> Metallurgy and Materials Engineering Department, Faculty of Engineering and Architecture, Kastamonu University, 37150, Kastamonu, Turkey.

<sup>b</sup> Materials of Engineering Department, College of Engineering, University of Al-Qadisiyah, 58002, Al-Qadisiyah, Iraq.

<sup>c</sup> Biomedical Engineering Department, Faculty of Engineering and Architecture, Kastamonu University, 37150, Kastamonu, Turkey.

**Abstract:** Corrosion poses a significant challenge for numerous industries. The use of corrosion inhibitors is essential within these industries. The efficacy of environmentally friendly corrosion inhibitors should remain high even when used at low concentrations. In the present study, the compound 4-fluorophenyl-2,5-dithiohydrazodicarbonamide (FTSC) was used as a corrosion inhibitor for brass in 3.5% NaCl solution. The inhibitor efficiency was determined by using a series of electrochemical techniques such as open circuit potential (OCP), potential dynamic polarisation (PDP), linear polarisation resistance (LPR), and electrochemical impedance spectroscopy (EIS). All experimental tests have been done in stagnant conditions. The findings of the experiments revealed that the compound FTSC looked to be of the cathodic type. Furthermore, the maximum inhibitor efficiency was reached at 98.28% at  $1 \times 10^{-3}$  and at an immersion time of 1 h. The current density was reduced from 16.5 to 0.284  $\mu\text{A}\cdot\text{cm}^{-2}$ . The adsorption of compound on the brass surface in 3.5% NaCl solution obeyed the Langmuir isotherm with a low negative value of the standard Gibbs free energy of adsorption ( $-33.8 \text{ kJ/mol } \Delta G_{\text{ads}}$  (chemisorption and physisorption). The results confirmed that the compound FTSC can be used as a corrosion inhibitor for brass in 3.5% NaCl.

**Keywords:** Corrosion Inhibition; Electrochemistry; Brass.

**Submitted:** March 21, 2023. **Accepted:** July 12, 2023.

**Cite this:** AlFalah MGK, Elid A, Ali AAA, Kamberli E, Nazlı B, Koyun, S et al. Improvement of corrosion resistance for brass in 3.5% NaCl media by using 4-fluorophenyl-2, 5-dithiohydrazodicarbonamide. JOTCSA. 2023;10(4):869-76.

**DOI:** <https://doi.org/10.18596/jotcsa.1268115>.

**\*Corresponding author. E-mail:** [ersinkamberli@gmail.com](mailto:ersinkamberli@gmail.com).

### 1. INTRODUCTION

Brass, a Cu-Zn alloy, is ubiquitous due to its practical and aesthetic use across a wide range

of sectors. Due to its resistance to corrosion, brass is often used in heat exchangers, construction, and maritime engineering. Brass is susceptible to dissolving in solutions with

high oxygen concentrations as well as chloride, sulfate, and nitrate ions, in spite of the corrosion resistance provided by the oxide layers that have developed on its surface (1). In general, corrosion may be minimized by regulating pH levels or using inhibitors (2). Theoretically, heterocyclic organic molecules do what they do by combining with the inhibitor to make an insoluble polymeric complex. This complex then forms a protective layer on the surface of the metal. Brass corrosion inhibitors in chloride media have been researched for many kinds of compounds (3,4).

Inhibitors have been found to be the most effective approach for protecting metals from alkaline corrosion in recent years, outperforming other widely used techniques including cathodic and anodic protection, alloying, and coating (5). On metal surfaces, organic inhibitors are often used to provide a light barrier. Organic compounds containing highly electronic heteroatoms (P, S, N, and O) or heteroatoms with an aromatic ring are the most effective (6,7). Furthermore, pi electron-containing compounds with functional groups such as -N=N, -C=N, and  $\gamma$ NH often exhibit corrosion properties (8,9). N- and S-heterocyclic compounds are the best corrosion inhibitors for copper in alkaline environments (10-12). Organic chemicals have a long history and are by far the most advanced and economical tool employed by manufacturers. The majority, however, are toxic and detrimental to the ecology. Global attempts have been made to find a cheap, non-hazardous corrosion inhibitor that is also effective (13-15).

The compound 4-fluorophenyl-2,5-dithiohydrazodicarbonamide (FTSC) was synthesized and investigated in our previous work as a corrosion inhibitor for mild steel (or copper) in acidic (or alkaline) solution with excellent results (10,12). Therefore, in this work, we used a corrosion inhibitor for brass in a 3.5% NaCl solution. The evaluation of inhibitors has been measured by electrochemical techniques such as open circuit potential (OCP), linear polarization resistance, potentiodynamic polarisation, and electrochemical impedance spectroscopy (EIS).

## 2. MATERIALS AND METHODS

Brass rod has been bought from a local market with the following chemical composition (%Wt): 58% Cu, 40% Zn, and 2% Pb. Cylindrical specimens having a diameter of 0.8 cm and a length of 3 cm were prepared from brass rod. The brass has been used to investigate the

corrosion resistance of 3.5% NaCl without and with the presence of the corrosion inhibitor FTSC. The sample was connected from the back by copper wire, and after that, it was put in epoxy resin with an exposed surface area of 0.502 cm<sup>2</sup>. Specimens were polished using silicon carbide papers, starting from 600 up to 2500 grits, to acquire a mirror-like finish. After polishing, specimens were thoroughly washed with double-distilled water and dried in the air.

All electrochemical measurements were performed using an electrochemical analyzer of type COMPACTSTAT (IVIUM). Potential dynamic polarization (PDP), linear polarization resistance (LPR) measurements of brass samples immersed in 1 M HCl solution without and within corrosion inhibitors were made at a scan rate of 60 mV/min at room temperature. The potentials were starting from a cathodic potential (-0.5 V) against a corrosion potential ( $E_{corr}$ ) and being allowed to sweep in the anodic direction till (0.1 V) above the  $E_{corr}$  and the potential scan was reversed down to a potential equal to  $E_{corr}$ . LPR tests were carried out at a range  $\pm 10$  mV with respect to OCP. The electrochemical impedance spectroscopy (EIS) technique was used to evaluate the corrosion behavior of brass samples with and without corrosion inhibitors. The experiments were performed at room temperature over the frequency range between 100 kHz and 0.01 Hz at open circuit potential. The amplitude of the voltage signal was 5 mV. The system corrosion cell was made from beaker glass of size 100 mL, the brass sample with 0.502 cm<sup>2</sup> was used as a working electrode, a platinum wire was used as a counter electrode; and silver chloride (Ag/AgCl) was used as a reference electrode. All plots were fitted to 1 cm<sup>2</sup>.

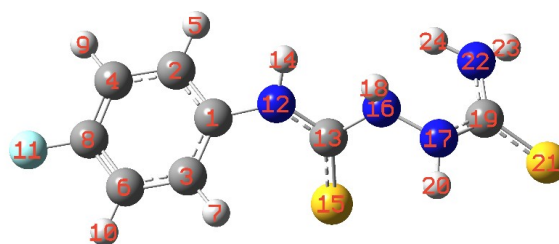


**Figure 1:** 4- Fluorophenyl-2,5-dithiohydrazodicarbonamide (FTSC) structure (10).

### 3. RESULTS AND DISCUSSION

#### 3.1. OCP, PDP and LPR Studies

First, the open circuit potential (OCP) of brass was measured for 60 minutes in both a blank solution and in the presence of an inhibitor. The obtained results are shown in Fig. (2) for compound FTSC. At the start of immersion in the inhibitor-free solution, the OCP value swings in the negative direction, which might be related to the creation of an oxide film on the

brass surface. The OCP values get increasingly positive as the immersion duration increases, suggesting that the oxide film is dissolving and a Cu/Zn chloride layer is forming (16-18). When an inhibitor is present, the potential at the end of the test moves in a more negative direction. This phenomenon might be due to the inhibitor molecules adsorbing on the active sites of brass and forming a protective layer (19-21).

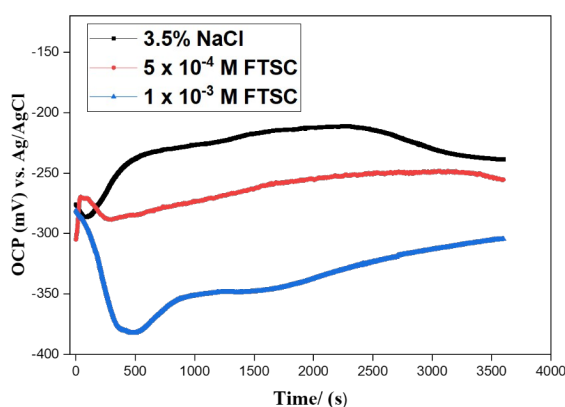


**Figure 2:** Open circuit potential for brass in 3.5% NaCl solution with and without the presence of FTSC.

The potentiodynamics polarization and linear polarization resistance measurements were used to explore corrosion inhibitor. Corrosion potential ( $E_{corr}$ ), anodic ( $\beta_a$ ) and cathodic ( $-\beta_c$ ) Tafel slopes, corrosion current density ( $i_{corr}$ ), surface coverage ( $\theta$ ), Resistance polarization ( $R_p$ ) and inhibition efficiency (IE%) all kinetic corrosion values were calculated and listed in Table (1) for FTSC. The  $IE_{PDP}$  % and  $IE_{LPR}$  % values were calculated by using the following equations (22,23):

$$IE_{PDP}(\%) = \frac{i_{corr}^{\circ} - i_{corr}^{\circ}(inh)}{i_{corr}^{\circ}} \times 100 \quad (1)$$

$$IE_{LPR}(\%) = \frac{R_{p(inh)} - R_p^{\circ}}{R_{p(inh)}} \times 100 \quad (2)$$

Figure (3) shows Tafel curves for uninhibited brass and inhibited brass with the presence of different concentrations of FTSC in 3.5% NaCl at immersion time of 1 h. It can be seen that both anodic and cathodic curves changed remarkably leading to reduce the corrosion current with increase the concentration of corrosion inhibitor due to adsorption molecules

on the active part of brass that lead to protect brass surface to ingress of  $Cl^-$  ions. Moreover, it can be seen from Figure 3 for FTSC, Corrosion potential ( $E_{corr}$ ) was significantly shifted from -0.221 V without corrosion inhibitor to -0.329, and -0.251 V with the presence of corrosion inhibitor FTSC at concentration  $5 \times 10^{-4}$  M, and  $1 \times 10^{-3}$  M, respectively due to adsorb the molecules of inhibitor on the surface as results of increasing amount of inhibitors FTSC. Furthermore, the current density was reduced from  $16.5 \mu A \cdot cm^{-2}$  without corrosion inhibitor to  $0.284 \mu A \cdot cm^{-2}$  with presence of corrosion inhibitor FTSC at concentration  $1 \times 10^{-3}$  M due to increase the area of adsorption for inhibitor compound on the surface of brass and prevent the surface from aggressive ions. In other words, the corrosion inhibitor efficiency was increased systematically from 97.51% at low concentration of inhibitor to 98.28% at high concentration of inhibitor FTSC. The resistance polarization for compounds was approved the Tafel results. The corrosion inhibitor can be classified as cathodic type inhibitor due to move  $E_{corr}$  to higher than 0.085 V. The maximum displacement in the  $E_{corr}$  with presence inhibitors was 0.108 V (23).

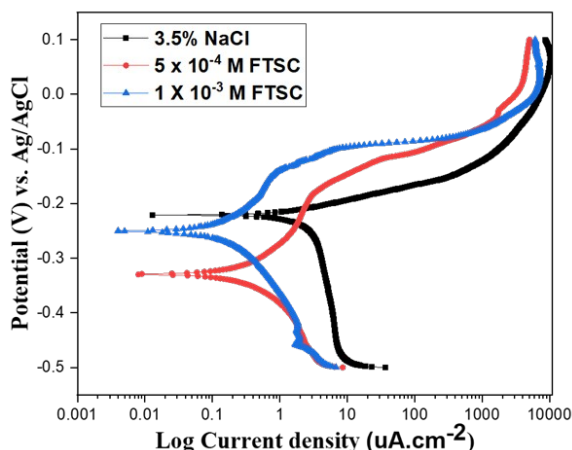


**Figure 3:** PDP for brass in 3.55% NaCl solution with and without the presence of FTSC.

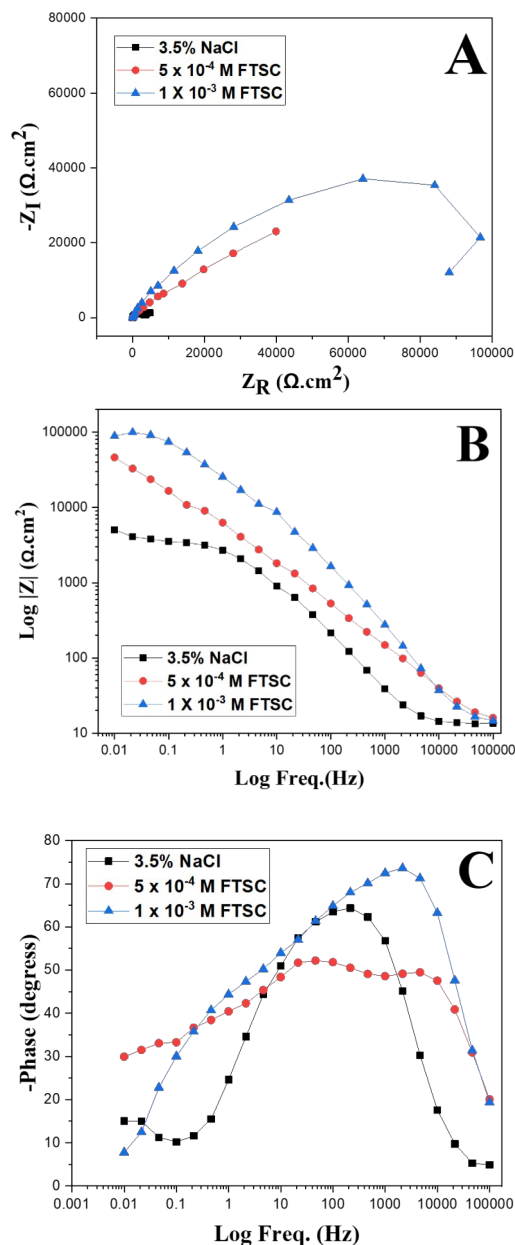
**3.2. Electrochemical impedance studies (EIS)**

All parameters for electrochemical impedance spectroscopy calculated from equivalent circuit as shown in Figure.5 fitting and listed in Table.2 for compound FTSC. The corrosion inhibitor efficiency was calculated by using equation as shown below (24):

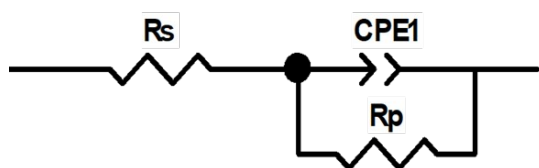
$$IE_{EIS}(\%) = \frac{R_{P(inh)} - R_P^\circ}{R_{P(inh)}} \times 100 \quad (3)$$

Figure 4 (A-C) illustrate Nyquist and Bode curves for compound FTSC. It can be noticed that from Figure (4), Nyquist curve for brass without inhibitor contain fading semicircle in the high frequency which is referred to the roughness and inhomogeneity of electrode , while at low frequency the shape of plot is changed to straight line due to the diffusion of soluble brass species from brass surface to bulk solution. In addition, Figure 4 also depicts that it can be noticed that the diameter of semicircle turns into bigger with presence of corrosion inhibitor due to protect the surface by molecules of corrosion inhibitor (25). It is well known that the impedance |Z| at lower frequencies the parameter utilized for evaluating the inhibitor's corrosion resistance. Figure (B-C) shows that in comparison to uninhibited brass, the impedance |Z| has increased as the inhibitor concentration has increased, indicating the robustness of inhibitor barriers to corrosive media. With FTSC present, the curve of the phase angle becomes significantly higher and it reached 75°, as seen in Figure 4 (C ).The cause for this behavior

might be attributed to the adsorption of the FTSC molecule relaxing effect (12). The EIS results are in agreement with OCP, LPR, and PDP measurements. Figure 5 shows equivalent circuit for brass without inhibitor FTSC and with the presence of inhibitor FTSC. Rs is resistance of solution, CPE is constant phase element, and Rp is resistance polarization.



**Figure 4:** Electrochemical impedance spectroscopy (EIS) for brass in 3.5% NaCl without and with the presence of FTSC, Nyquist curve (A), and Bode curves (B-C).



**Figure 5:** Equivalent Circuit for brass without inhibitor and with presence of inhibitor FTSC.

### Adsorption isotherm

The most significant advance in the consumption restraint process is the adsorption of an inhibitor on the metal surface. Distinctive adsorption isotherms, including Langmuir, Frumkin, and Freundlich, are frequently used to portray the adsorption component of inhibitors.

In this work the Langmuir adsorption isotherm, exhibited by equation as shown below, was observed to be the most reasonable to fit.

$$\frac{C_{inh}}{\theta} = \frac{1}{K_{ads}} + C_{inh} \quad (4)$$

Where  $C_{inh}$  is the concentration of inhibitor,  $\theta$  is the level of surface inclusion by inhibitor and  $K$  is the equilibrium constant of adsorption.

The plot of  $C_{inh}/\theta$  versus inhibitor fixation ( $C_{inh}$ ), (Figure 5) is straight, showing that the Langmuir adsorption isotherms material to portray the adsorption of FTSC. The estimation of the relationship coefficient ( $R^2$ ) affirms that the adsorption of FTSC pursues the Langmuir

isotherm. Additionally, this estimation of  $R^2$  demonstrates that the compound atoms formed a monomolecular layer on the terminal surface (26). Further, the Gibbs free vitality of adsorption ( $-\Delta G_{ads}$ ) is determined by equation as shown below:

$$\Delta G_{ads} = -RT \times \ln(55.5 \times K_{ads}) \quad (5)$$

The values of  $\Delta G_{ads}$  around  $-20 \text{ kJ mol}^{-1}$  imply complete electrostatic association (physisorption) while those with  $-40 \text{ kJ mol}^{-1}$  or more negative represents chemical interaction (27,28). So, the present investigation involves the estimations of which was found  $-33.8 \text{ kJ mol}^{-1}$  for FTSC which recommended the  $\Delta G_{ads}$  association of the inhibitor with the brass surface via mixed (chemisorption and physisorption) (10).

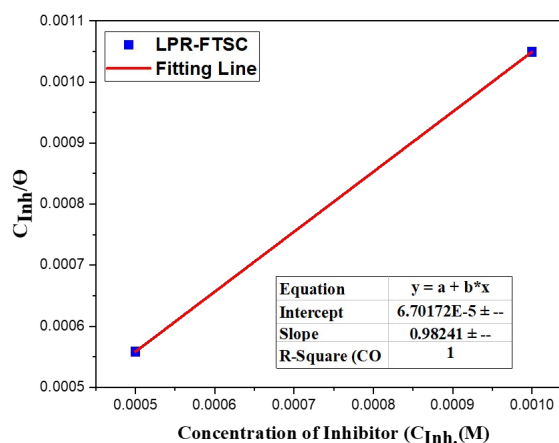


**Figure 5:** Langmuir adsorption isotherm of FTSC on the brass surface for 1 h.

**Table 1:** PDP and LPR for brass in 3.5% NaCl solution with and without the presence of FTSC.

Compound	Concentration (M)	$E_{corr}$ (V)	$i_{corr}$ ( $\mu A.cm^{-2}$ )	$-\beta_c$ (V/dec)	$\beta_a$ (V/dec)	$\theta$	% IE	$R_p$ ( $\Omega.cm^2$ )	$\theta$	% IE
FTSC	3.5%NaCl	-0.221	16.5	0.641	0.165	-----	-----	3058.7	-----	-----
	$5 \times 10^{-4}$	-0.329	0.470	0.14	0.052	0.9715	97.51	29326.8	0.8957	89.57
	$1 \times 10^{-3}$	-0.251	0.284	0.223	0.034	0.9828	98.28	64908.6	0.9529	95.29

**Table 2:** EIS for brass in 3.5% NaCl solution without and with the presence of FTSC

Sample	Conc. (M)	$R_s$ ( $\Omega.cm^2$ )	$R_{p1}$ ( $\Omega.cm^2$ )	$CPE_1$ ( $\mu F.cm^{-2}$ )	$n_1$	$R_{pT}$ ( $\Omega.cm^2$ )	% IE
FTSC	Blank	5.94	2024.1	82.2	0.75	2024.1	-----
	$5 \times 10^{-4}$	3.86	43298	41.3	0.78	43298	95.32
	$1 \times 10^{-3}$	4.33	45673	32.2	0.83	45673	95.60

#### 4. CONCLUSION

The following conclusion may be drawn according to the collected data:

- The compound FTSC appeared to be an excellent corrosion inhibitor for brass in 3.5%NaCl solution and maximum efficiency reached 98.28% at  $1 \times 10^{-3}$  M and immersion time 1 h.
- Tafel curve showed that the corrosion potential shifted to a more negative value with the presence of FTSC and it can be classified as a cathodic type inhibitor.
- For EIS graphs with and without FTSC, there is a single equivalent circuit. The polarizing resistance rises when FTSC is present in a 3.5% NaCl solution, which lowers the double layer capacitance.
- A Langmuir adsorption model is the best match for the adsorption of FTSC molecules on the brass surface.

#### 5. ACKNOWLEDGEMENT

This study was financed by Kastamonu University Scientific Research Coordination Unit. Project Number KÜ-BAP01/2021-44.

#### 6. REFERENCES

1. Fan H., Li S., Zhao Z., Wang H., Shi Z., Zhang L., Inhibition of brass corrosion in sodium chloride solutions by self-assembled silane films. *Corrosion Science* [Internet]. 2011 Dec [cited 2022 Sep 4];53:4273-4281. Available from: <URL>.
2. Ravichandran R., Nanjundan S., Rajendran N., Effect of benzotriazole derivatives on the corrosion and dezincification of brass in neutral chloride solution. *Journal of Applied Electrochemistry* [Internet]. 2004 Mar 3 [cited 2022 Sep 4];34:1171-1176. Available from: <URL>.
3. Radovanović M.B., Tasić Ž.Z., Mihajlović M.B.P., Simonović A.T., Antonijević M.M., Electrochemical and DFT studies of brass corrosion inhibition in 3% NaCl in the presence of environmentally friendly compounds [Internet]. *Scientific Reports* [Internet]. 2019 Nov 6 [cited 2022 Sep 4];9:1-16. Available from: <URL>.
4. Ebrahimzadeh M., Gholami M., Momeni M., Kosari A., Moayed M.H., Davoodi A., Theoretical and experimental investigations on corrosion control of 65Cu-35Zn brass in nitric acid by two thiophenol derivatives. *Applied Surface Science* [Internet]. 2015 Mar 30 [cited 2022 Sep 4];332:384-392. Available from: <URL>.
5. Rbaa M., Ouakki M., Galai M., Berisha A., Lakhrissi B., Jama C., Warad I., Zarrouk A., Simple preparation and characterization of novel 8-Hydroxyquinoline derivatives as effective acid corrosion inhibitor for mild steel: Experimental and theoretical studies. *Colloids and Surfaces A: Physicochemical and Engineering Aspects* [Internet]. 2020 Oct 5 [cited 2022 Sep 4];602:125094. Available from: <URL>.
6. Şahin E.A., Solmaz R., Gecibesler İ.H., Kardaş G., Adsorption ability, stability and corrosion inhibition mechanism of phoenix dactylifera extract on mild steel. *Materials Research Express* [Internet]. 2020 Jan 27 [cited 2022 Sep 4];7:016585. Available from: <URL>.
7. Xu Y., Zhou Q., Liu L., Zhang Q., Song S., Huang Y., Exploring the corrosion performances of carbon steel in flowing natural sea water and synthetic sea waters. *Corrosion Engineering, Science and Technology* [Internet]. 2020 May 3 [cited 2022 Sep 4];55:579-588. Available from: <URL>.
8. Olasunkanmi L.O., Ebenso E.E., Experimental and computational studies on propanone derivatives of quinoxalin-6-yl-4,5-dihydropyrazole as inhibitors of mild steel corrosion in hydrochloric acid. *Journal of Colloid and Interface Science* [Internet]. 2020 Mar 1 [cited 2022 Sep 4];561:104-116. Available from: <URL>.
9. Guo L., Obot I.B., Zheng X., Shen X., Qiang Y., Kaya S., Kaya C., Theoretical insight into an empirical rule about organic corrosion inhibitors containing nitrogen, oxygen, and sulfur atoms. *Applied Surface Science* [Internet]. 2017 Jun 1 [cited 2022 Sep 4];406:301-306. Available from: <URL>.
10. AlFalah M.G.K., Kandemirli F., Corrosion Inhibition Potential of Dithiohydrazodicarbonamide Derivatives for Mild Steel in Acid Media: Synthesis, Experimental, DFT, and Monte Carlo Studies. *Arabian Journal for Science and Engineering* [Internet]. 2021 Dec 3 [cited 2022 Sep 4];47:6395-6424. Available from: <URL>.
11. AlFalah M.G.K., Abdulrazzaq M., Saracoglu M., Kandemirli F., 4-Naphthyl-3-Thiosemicarbazide as Corrosion Inhibitor for Copper in Sea Water (3.5% Sodium Chloride). *Eurasian Journal of Science Engineering and Technology* [Internet]. 2020 Sep 1 [cited 2022 Sep 4];1:27-34. Available from: <URL>.
12. AlFalah M.G.K., Guo L., Saracoglu M., Kandemirli F., Corrosion inhibition performance of 2-ethyl phenyl-2, 5-dithiohydrazodicarbonamide on Fe (110)/Cu (111) in acidic/alkaline solutions: Synthesis, experimental, theoretical, and molecular dynamic studies. *Journal of the Indian Chemical Society* [Internet]. 2022 Sep [cited 2022 Sep 4]; 99:100656. Available from: <URL>.
13. Fernandes C.M., Faro L. V., Pina V.G.S.S., Souza M.C.B.V., Boechat F.C.S., Souza M.C., Briganti M., Totti F., Ponzio E.A., Study of three new halogenated oxoquinolinecarbohydrazide N-phosphonate derivatives as corrosion inhibitor for mild steel in acid environment. *Surfaces and Interfaces* [Internet]. 2020 Dec [cited 2022 Sep 4];21: 100773. Available from: <URL>.
14. Chaouiki A., Chafiq M., Lgaz H., Al-Hadeethi M.R., Ali I.H., Masroor S., Chung I.-M., Green Corrosion

Inhibition of Mild Steel by Hydrazone Derivatives in 1.0 M HCl, Coatings [Internet]. 2020 Jun 29 [cited 2022 Sep 4];10:640. Available from: <URL>.

15. Tan B., Xiang B., Zhang S., Qiang Y., Xu L., Chen S., He J., Papaya leaves extract as a novel eco-friendly corrosion inhibitor for Cu in H<sub>2</sub>SO<sub>4</sub> medium. *Journal of Colloid and Interface Science* [Internet]. 2021 Jan 15 [cited 2022 Sep 4];582:918-931. Available from: <URL>.

16. Tasić Ž.Z., Mihajlović M.B.P., Radovanović M.B., Simonović A.T., Antonijević M.M., Cephadrine as corrosion inhibitor for copper in 0.9% NaCl solution. *Journal of Molecular Structure* [Internet]. 2018 May 5 [cited 2022 Sep 4];1159:46-54. Available from: <URL>.

17. Amin M.A., Abd El-Rehim S.S., El-Sherbini E.E.F., Bayoumi R.S., The inhibition of low carbon steel corrosion in hydrochloric acid solutions by succinic acid. *Electrochimica Acta* [Internet]. 2007 Sep [cited 2022 Sep 4];52:3588-3600. Available from: <URL>.

18. AlFalah M.G.K., Kamberli E., Abbar A.H., Kandemirli F., Saracoglu M., Corrosion performance of electrospinning nanofiber ZnO-NiO-CuO/polycaprolactone coated on mild steel in acid solution. *Surfaces and Interfaces* [Internet]. 2020 Dec [cited 2022 Sep 4];21: 100760. Available from: <URL>.

19. Verma C., Obot I.B., Bahadur I., Sherif E.-S.M., Ebenso E.E., Choline based ionic liquids as sustainable corrosion inhibitors on mild steel surface in acidic medium: Gravimetric, electrochemical, surface morphology, DFT and Monte Carlo simulation studies. *Applied Surface Science* [Internet]. 2018 Nov 1 [cited 2022 Sep 4];457:134-149. Available from: <URL>.

20. AlFalah M.G.K., Abdulrazzaq M., Saracoglu M., Kandemirli F., 4-Naphthyl-3-Thiosemicarbazide as Corrosion Inhibitor for Copper in Sea Water (3.5% Sodium Chloride). *Eurasian Journal of Science Engineering and Technology* [Internet]. 2020 Sep 1 [cited 2022 Sep 4];1:27-34. Available from: <URL>.

21. Abd El-Lateef H.M., Mohamed I.M.A., Zhu J.-H., Khalaf M.M., An efficient synthesis of electrospun TiO<sub>2</sub>-nanofibers/Schiff base phenylalanine composite and its inhibition behavior for C-steel corrosion in acidic chloride environments. *Journal of the Taiwan Institute of Chemical Engineers* [Internet]. 2020 June [cited 2022 Sep 4];112:306-321. Available from: <URL>.

22. Tiwari N., Mitra R.K., Yadav M., Corrosion protection of petroleum oil well/tubing steel using thiadiazolines as efficient corrosion inhibitor: Experimental and theoretical investigation. *Surfaces and Interfaces* [Internet]. 2021 Feb [cited 2022 Sep 4];22:100770. Available from: <URL>.

23. Kadhim M.G., Ali D.M.T., A Critical Review on Corrosion and its Prevention in the Oilfield Equipment. *Journal of Petroleum Research and Studies* [Internet]. 2017 [cited 2022 Sep 4];7:162-189. Available from: <URL>.

24. Murmu M., Saha S.K., Bhaumick P., Murmu N.C., Hirani H., Banerjee P., Corrosion inhibition property of azomethine functionalized triazole derivatives in 1 mol L<sup>-1</sup> HCl medium for mild steel: Experimental and theoretical exploration. *Journal of Molecular Liquids* [Internet]. 2020 Sep 1 [cited 2022 Sep 4];313:113508. Available from: <URL>.





25. Tabti L., Khelladi R.M., Chafai N., Lecointre A., Nonat A.M., Charbonnière L.J., Bentouhami E., Corrosion Protection of Mild Steel by a New Phosphonated Pyridines Inhibitor System in HCl Solution. *Advanced Engineering Forum* [Internet]. 2020 Jun [cited 2022 Sep 4];36:59-75. Available from: <URL>.

26. Ferigita K.S.M., AlFalah M.G.K., Saracoglu M., Kokbudak Z., Kaya S., Alaghani M.O.A., Kandemirli F., Corrosion behaviour of new oxo-pyrimidine derivatives on mild steel in acidic media: Experimental, surface characterization, theoretical, and Monte Carlo studies. *Applied Surface Science Advances* [Internet]. 2022 Feb [cited 2022 Sep 4];7:100200. Available from: <URL>.





## Biosynthetic Gold Nanoparticles as Sensitive and Selective Colorimetric Method for Mercury Ions

Maryam A. Ahmed<sup>1</sup> , Safana A. Farhan<sup>2</sup> , Rasha M. Dadoosh<sup>2</sup> ,  
Abdulkadir M. N. Jassim<sup>3\*</sup> 

<sup>1</sup> Renewable Energy Science Department, College of Energy & Environmental Sciences, Alkarkh University of Science, Baghdad-Iraq

<sup>2</sup> Polymer research unit, College of Science, Mustansiriyah University, Baghdad-Iraq

<sup>3</sup> Department of Chemistry, College of Science, Mustansiriyah University, Baghdad-Iraq

**Abstract:** Gold nanoparticles (AuNPs) are widely studied materials that have intense applications in various fields. Different methods use to synthesize the AuNPs, one of them is eco-friendly biological method, known as "green synthesis" a simple and inexpensive method. The Synthesis of AuNPs, using ginger extract is described here. The components found in ginger work as a stabilizing and reducing agent. Hydrogen tetrachloroaurate (HAuCl<sub>4</sub>) are mixed with the ginger extract to produce AuNPs. The Surface Plasmon Resonance (SPR) measured at  $\lambda_{max} = 540$  nm. UV-Vis, FTIR and Zeta potential are used to identify AuNPs, as well as AFM and SEM. Data indicate that AuNPs has a spherical structure. The results demonstrate that AuNPs stabilized by ascorbic acid were used as a colorimetric probe for Hg<sup>2+</sup> ions, based on the production of (Au-Hg) amalgamate which made changes in their absorbance, due to its ability to reduce Hg<sup>2+</sup> to Hg<sup>0</sup>, to enhance amalgamation. Practically, this procedure has successfully worked to detect Hg<sup>2+</sup> in tap water as a sensitive and selective probe with upper limit of detection equal to 120  $\mu$ M as well as the limit of detection (LOD) equal to 0.65  $\mu$ M, so the method proved to be sensitive and selective probe.

**Keywords:** Gold Nanoparticles, Ginger extract, Phytochemicals, Mercury detection, Selective sensing.

**Submitted:** May 23, 2023. **Accepted:** July 12, 2023.

**Cite this:** Ahmed MA, Farhan SA, Dadoosh RM, Jassim AMN. Biosynthetic Gold Nanoparticles as Sensitive and Selective Colorimetric Method for Mercury Ions. JOTCSA. 2023;10(4):877-86.

**DOI:** <https://doi.org/10.18596/jotcsa.1300270>

\* **Corresponding author. E-mail:** [kadirchem@yahoo.com](mailto:kadirchem@yahoo.com), [kadirchem@uomustansiriyah.edu.iq](mailto:kadirchem@uomustansiriyah.edu.iq)

### 1. INTRODUCTION

Gold nanoparticles (AuNPs) are widely studied materials that have intense applications in various fields. Recently, the need to nanomaterials that are used in many industries has increased, because they have much better properties than other large-sized molecules and materials due to they have a larger surface area than large molecules(1). Several methods including physical, chemical and biological approaches have been described for preparation of NPs. The wide range of uses for metal nanoparticles in sensing, catalysis, electronics, and photonics has a huge interest (2, 3). These NPs are in colloidal forms suitable for biological applications as they do not contain any harmful chemicals (4, 5). On the other hand, suitable selection is appropriate in this case, to find out which parts of the plant have

excellent reducing or stabilizing components (6, 7). Biological methods are among the best, cheapest, safest and easiest methods of preparation(8-10). Therefore, ginger extract contains many compounds that act as antioxidants which are able to reducing gold ions as Au<sup>+3</sup> and converting them to AuNPs as Au<sup>0</sup> (11, 12).

It is well known that mercury (II) ion has been one of the most common heavy metals that induced human poisoning , as well as for the global environment. The accumulation of this metal, and other metals, leads to a diversity of toxic effects on a variety of body tissues and organs (13, 14). According to the World Health Organization (WHO) and the US Environmental&Protection Agency (EPA), the permissible limit of mercury (II) ion in drinking water is approximately low 30 and 10 nanometres,

respectively(15). So, it is necessary to design a potent selective and sensitive way that can accurately identify and detect the presence of environmentally mercury ion. Therefore, scientists have developed different techniques for detecting mercury ions attributed on various mechanisms and materials, as atomic emission spectroscopy(16), Surface enhanced Raman scattering(17), Electrochemical methods(18), Fluorescent methods(19) and colorimetric methods(20, 21). Presently, different techniques used for quantitation of  $Hg^{2+}$  involve atomic absorption spectrometry(22), inductively coupled plasma mass spectrometry(23) and cold vapour selective fluorescent atomic spectrometry(24). Due to their elevated toxicity, safety contents in food and the environment of mercury had been set to be exceedingly low. These techniques include commercial tools and are so complicated, time-consuming, expensive, as well as not suitable for onsite applications. In the past time, colorimetric methods using AuNPs have been an alternative technique for  $Hg^{2+}$  detection because of their characteristic as simplicity, speediness, selectivity and sensitivity (25-30).

So, this study aimed to biosynthesis of AuNPs using ginger extract and study of its efficiency to detect  $Hg^{2+}$  by colorimetric change, as well as, a proved if this procedure helpful and efficient for  $Hg^{2+}$  detection in different real aqueous samples.

## 2. EXPERIMENTAL SECTION

### 2.1. Materials

Hydrogen tetrachloroaurate(III) ( $H AuCl_4$ ); ascorbic acid (AA, 99%); mercury chloride and all the metal salts from Merck. ginger was taken from local market in Baghdad, Iraq. Double distilled water (D.D.) was used throughout the study. All other reagents are of analytical grade.

#### 2.1.1. Preparation of ginger extract

All dirt and contaminants were removed from ginger by washing it well with distilled water, after that plant (ginger) was peeled, then cut it into a little part and converted into juice using the mixer, later it was filtered through gauze to remove the residues (fibers) and get a clear juice then filtered throughout filter paper No.1 to obtained the ginger extract, set aside at  $4^{\circ}C$  until used (31).

#### 2.1.2. Preparation of AuNPs

The ginger extract 5 mL was added to 13 mL of 2 mM aqueous solution of  $H AuCl_4$  in a beaker in order to reduction of  $Au^{+3}$  to  $Au^0$ . The bio-reduction for gold ions was observed periodically by measuring the solution by UV-Vis spectroscopy. The reduction of gold chloride to gold ions was observed by changing the color from light yellow to purple, later to dark purple. The obtained solutions were stored at  $4^{\circ}C$  in dark container (32).

### 2.2. Characterization of AuNPs

#### 2.2.1. UV-Vis spectra

The UV-Vis spectrum was performed through spectrophotometer model (PG-Instruments Limited,

T80, Germany). The reduction of AuNPs was made by spectroscopy assay at regular intervals in the range of (300 - 800)nm. Three milliliter of the sample was added into a test tube and thereafter analyzed at room temperature (33).

#### 2.2.2. Zeta potential

Zeta potential assay was performed in order to identifying both of Nano-material and the ginger extract. Zeta potential was determined the light dispersion using the Zeta Plus tool. The data were being around with 5 measurements. Measurement of NPs Size were done using Electrophoretic light scattering (ELS) and dynamic light scattering (DLS), while characterizing of nano-materials surfaces and estimated their surface charge through the determination of the zeta potential (34).

#### 2.2.3. Scanning electron microscopy

Scanning electron microscope (SEM) analysis performed to characterize the shape, size, and morphologies of NPs formed. The SEM provides high-resolution images of the sample surface, which makes this technique helpful to characterizing the size distribution of NPs. Energy dispersive spectrometer (EDS) analysis for the confirmation of gold was carried out to detection of elemental gold(5).

#### 2.2.4. Atomic force microscopy

The Atomic Force Microscope (AFM) analysis performed to determining the topography of NPs formed. The AFM generally measure the height of AuNPs. A drop of liquid sample was drained on a glass cover slide ( $2 \times 6 \text{ cm}^2$ ), and dehydrated the sample prior to scan (35).

#### 2.2.5. Fourier transmission infrared spectroscopy

Fourier Transmission infrared (FTIR) is an analytical method used to measure the intensity of infrared radiation against its wave number or wavelength light of possible bio molecule in the samples. After complete reduction of  $AuCl_4^-$  ions by the ginger extract, the AuNPs dried and ginger extract were analyzed by FTIR (Shimadzu) using potassium bromide (KBr) discs in the range  $400-4000 \text{ cm}^{-1}$ . The AuNPs were centrifuging for 15 minutes at 5000 rpm. This method was repeated 3-5 times, then proceeds the precipitate and dry it in oven at  $40^{\circ}C$  for 4 hours (36).

### 2.3. Detection of Mercury

Standard stock solution of  $Hg^{+2}$  ions ( $120 \mu M$ ) was prepared by serial of dilution. The selectivity and sensitivity of this procedure to the  $Hg^{2+}$  ions, pH of the reaction, time of incubation, LSPR of AuNPs and ascorbic acid content were adjusted preliminarily. To detect  $Hg^{2+}$  ions, approximately 1.5 mL AuNPs solution at pH 5.0 and  $32 \mu L$  from 0.1 M of ascorbic acid was added into 2mL centrifuge tube. After gently shaking, aliquots  $320 \mu L$  of  $Hg^{2+}$  ions solution (final concentrations: 5, 10, 15, 20, 25, 30, 35, 40, 45,50, 55,60)  $\mu M$  were added, one at a time, into all tube. After a while the solutions were mixed and later, placed for 50 min at room temperature, the photos and UV-Vis spectra were taken.

The selectivity of this method was investigated toward  $\text{Hg}^{2+}$  by repeated the method mentioned above, but  $\text{Hg}^{2+}$  ions was replaced with 720  $\mu\text{M}$  of other metallic ions, including ( $\text{Co}^{+3}$ ,  $\text{Cr}^{+3}$ ,  $\text{Cu}^{+2}$ ,  $\text{Mg}^{+2}$ ,  $\text{Fe}^{+3}$ ,  $\text{Ni}^{+2}$ ,  $\text{Mn}^{+2}$ ,  $\text{Sn}^{+2}$ ,  $\text{Ca}^{+2}$  and  $\text{Zn}^{+2}$ ).

#### 2.4. Analysis of Real Samples

Before starting the assay, each one of water samples used in this study was filtered through membrane with a thickness of 0.2  $\mu\text{m}$ . The  $\text{Hg}^{2+}$  standard solution of different concentrations was added to the spiked water samples. or  $\text{Hg}^{2+}$  standard solutions of different concentrations were added to the spiked water samples.. Later, all of the tubes

with water samples were mixed with 1.5 mL of AuNPs at pH 5 and 32  $\mu\text{L}$  of ascorbic acid 0.1M for assay.

### 3. RESULTS AND DISCUSSION

#### 3.1. Biosynthesis of AuNPs

In this study, the biosynthesis of AuNPs was carried out using ginger extract as a reducing agents to aqueous gold solution of  $\text{HAuCl}_4$ , and the results indicated a clear change in solution color from yellow into reddish-purple, and this indicate to producing of AuNPs. As shown in (Figure 1) the change in color obtained, which is in agreement with a number of other studies (37, 38) .



**Figure 1:** The color change during the synthesis of AuNPs.

#### 3.2. Characterization of AgNPs

##### 3.2.1. UV-Vis Study

The features of AuNPs were known via UV-Vis spectra. The data indicated that there was no clear band for the ginger extract, while when  $\text{HAuCl}_4$

was added; a broad peak appears in the range 530-540 nm as illustrated in (Figure 2). As a further definite by other characterizations, this band appoints the formation of mono-dispersed spherical form of AuNPs(39). This reaction occurs in a period of (50 minutes) with the obvious color change.

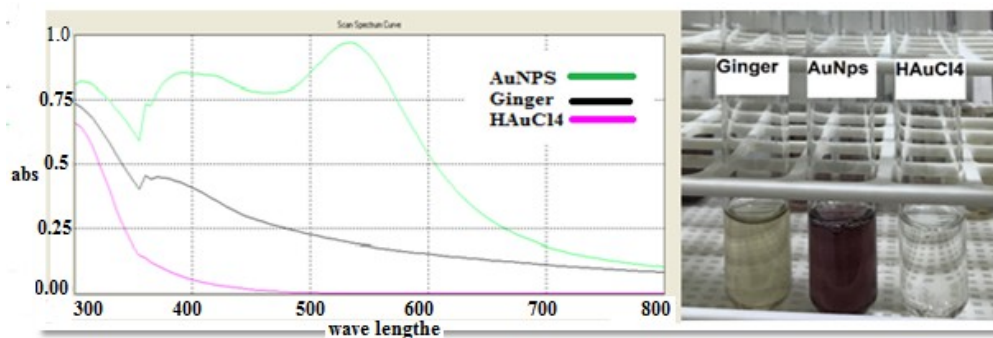


**Figure 2:** UV-VIS spectra and change in color of  $\text{HAuCl}_4$ , ginger extract and AuNPs.

##### 3.2.2. FTIR study

The FTIR spectra was using for the identifying the probable bio-reducing components in the ginger

extract and in the prepared AuNPs following reaction with  $\text{HAuCl}_4$ , (Figures 3).

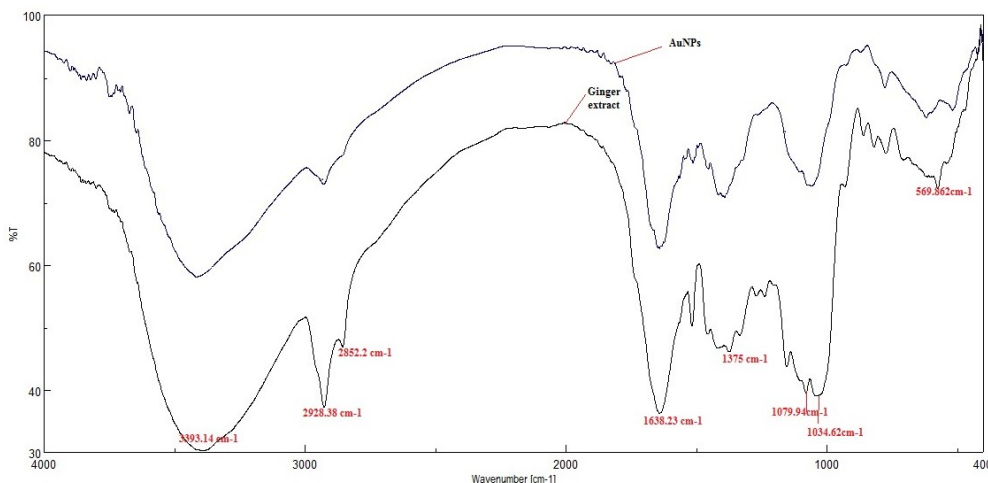


**Figure 3:** The FTIR for ginger extract and synthesized AuNPs.

The spectra of the used ginger extract and AuNPs were showed bands nearby 569 and 540 $\text{cm}^{-1}$  which is refer to  $-\text{CH}$  bend vibrations of substituted ethylene  $-\text{CH}=\text{CH}-$ , while the band at 1034 to 1149  $\text{cm}^{-1}$  belong to vibration of C-O stretching. The band of 1409 - 1454  $\text{cm}^{-1}$  relates to stretching C-C aromatic group, the main band in 3393.14  $\text{cm}^{-1}$  is specified to stretching of  $-\text{NH}$  and  $-\text{OH}$  for the phyto-components obtained in ginger extract. The band in 2928.38  $\text{cm}^{-1}$  is belonging to stretching of C-H. Bands appear to C=O stretching as well as bending  $-\text{NH}$  are join together as one and show a broad peak at range of 1863-1516  $\text{cm}^{-1}$  with a focus at 1638  $\text{cm}^{-1}$ . The peak at 1375  $\text{cm}^{-1}$  is equivalent to the side chain vibrations bands which can clarify the ginger extract proteins also carbohydrates. The AuNPs spectra indicated every one of the ginger extract vibrations bands, which recommended that NPs were become stable by the phyto-constituents(39-

41). Previous works illustrate that the constituents of phyto-proteins has a tendency to produce a photo-induced electron transfer for reduce metal ions(42), therefore, this study advise that the bio-constituents obtained in this extract referee the photo-induced preparation of AuNPs as well as the stability of NPs in the aqueous media.

### 3.2.3. AFM Study

The AFM was used to distinguish the surface morphology and to define topography which provides 2D and 3D of NPs surface images at an atomic level with the conforming size distribution of AuNPs. The average particle diameter size is 31.35 nm which was calculated in nano-scale size as indicated in Figure 4. Surface analysis by AFM needs good care because the agents that might be effect on the results like tip or contaminations(43).

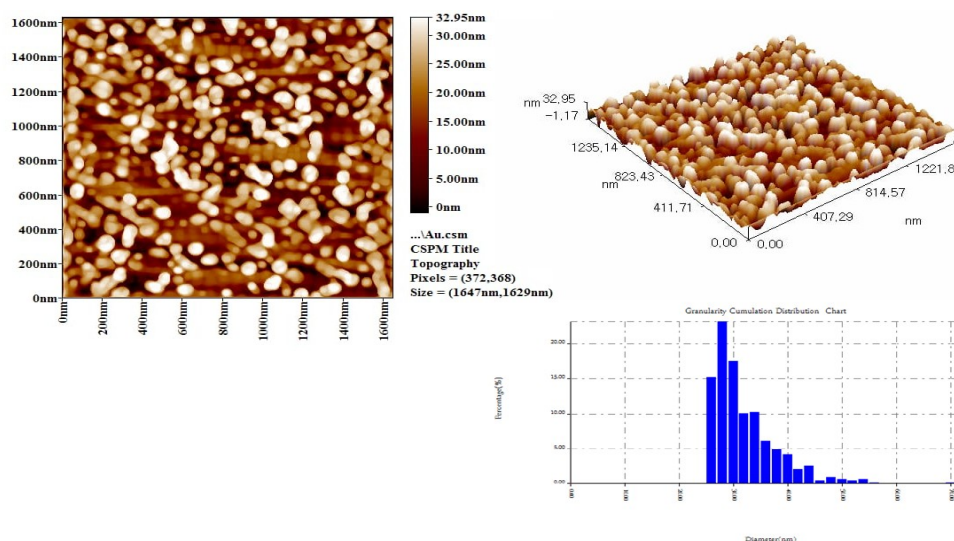


**Figure 4:** AFM images and size distributions of prepared AuNPs.

### 3.2.4. SEM Study

The SEM was applied to study the NPs structure and morphology (44), as well as obtained further

knowledge of the AuNPs gained from the suggested biosynthesis process using ginger extract. The SEM results explained different shapes, such as linear

and spherical, but the chief shape or the largest quantity of the NPs shape is the spherical (Figure 5).

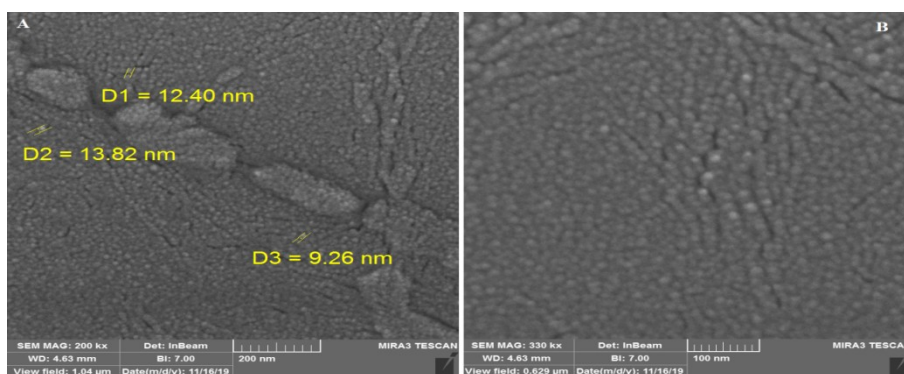


**Figure 5:** SEM images of AuNPs (A=200 nm, B=100 nm).

The average particles size and distribution are firm arbitrarily using SEM technique. The surface of NPs is smooth with good crystallinity, in agreement with other study(45). The chief particles size of the AuNPs between 9.26 to 13.82 nm. Notable, this size gotten from SEM measurements is meaningfully lesser than.

Existence of elemental gold in formation of AuNPs was definite by EDS micro-analysis, (Figure 6). The

spectrum shows an indication of gold area. Metallic gold nano crystal presentation an absorption peak near 3 keV belongs to SPR(46, 47). Another signs for other metals C, N, O, Na, Mg, P, S, Cl, K and Ca existing during reaction media established that the additional cellular organic components from ginger extract were initiate on the AuNPs surface or the nearness.

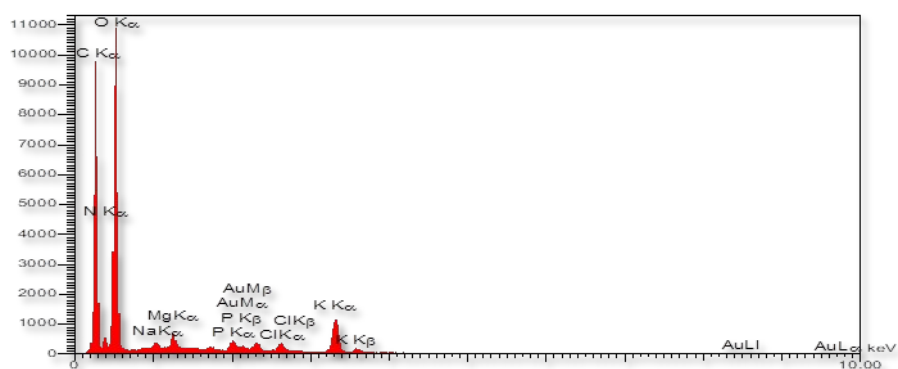


**Figure 6:** The EDS pattern of spherical synthesized AuNPs using ginger extract.

### 3.2.5. Zeta potential study

Zeta potential measured the stability of NPs in the suspension material (colloidal solution). Its achieved by ELS to ginger equal to -17.88 mV and the mobility value equal to -1.40 ( $\mu/s$ ) / (V/cm) as illustrated in (Figure 7 A), while the reading for AuNPs was -26.89 mV and -2.10 ( $\mu/s$ ) / (V/cm), respectively, (Figure 7 B). These suggest that the electrical boundary of the AuNPs is comparatively separate from each other and reduced the

aggregation of NPs. Also, ELS is initially applied to measure the charges belong to the colloidal particles found on the surface or other macromolecules in an electric field of fluid media(48). So, the value showed that the particles present in fluid media has less stable because the value of zeta potential has less than  $\pm 30$  mV and it has further stable as colloidal materials (found as NPs) than it has initiated in ginger extract one.

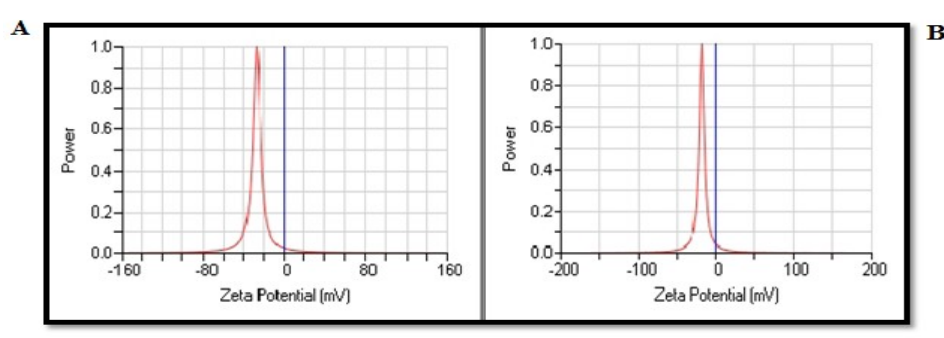


**Figure 7:** Zeta potential distribution of AuNPs (A) and ginger extract (B).

**3.3. Selectivity of the Detection Probe**

The selectivity for AA-AuNPs was tested in concentration 720 μM of Hg<sup>2+</sup>, as well as various concentrations 120 μM of different metal cations (Zn<sup>2+</sup>, Cu<sup>2+</sup>, Cr<sup>3+</sup>, Mg<sup>2+</sup>, Co<sup>3+</sup>, Mn<sup>2+</sup>, Sn<sup>2+</sup>, Fe<sup>3+</sup>, Ni<sup>2+</sup>,

and Ca<sup>2+</sup>), were also measured. Each one of the metal cations didn't show any changes in color except the mercury ions Hg<sup>2+</sup>, as shown in (Figure 8).

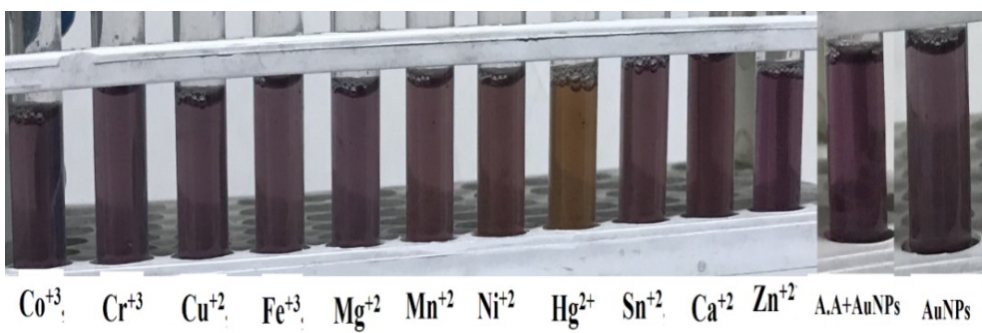


**Figure 8:** Photo-image of selectivity test to AuNPs after the addition of different metal cations.

The UV-Vis absorption of AA-AuNPs solutions in pH 5 and 50 °C, were measured in different metal cations as illustrated in (Figure 9). The high peak appeared near 540 nm belong to Hg<sup>2+</sup>, this allows easy distinction between different metal cations. Ratio of absorbance (ΔAbs/Abs 540) for the liquid component of AA-AuNPs through addition of each one of cation was recorded to study the selectivity test for Hg<sup>2+</sup> ion. The elevation in ratio of absorbance for Hg<sup>2+</sup>-AA-AuNPs was attributed to the aggregation of component AA-AuNPs, while a decreasing in ratio of absorbance for AA-AuNPs in existence of different

metal cations illustrated the keeping of well-dispersed forms in AA-AuNPs component, so that, the selectively coordinated of Hg<sup>2+</sup> ion must be done with a specific site of AA-AuNPs. The interaction effect in existence of different metal cations was tested in AA-AuNP component through addition of Hg<sup>2+</sup> ions which mixed with other ions. These ions didn't interfere with Hg<sup>2+</sup> ions detection, despite of their concentrations were ten times higher than that of Hg<sup>2+</sup> ions.

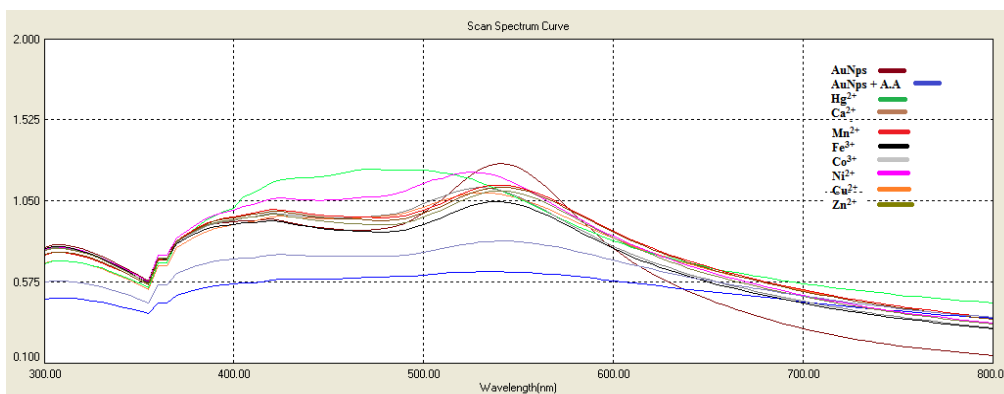


**Figure 9:** UV-VIS spectrum of selectivity test to AA-AuNPs after the addition of different metal cations.

### 3.4. Sensitivity of the Detection Probe

The sensitivity study was conducted by interacting between different concentrations of  $\text{Hg}^{2+}$  with AA-AuNPs solution. The color of  $\text{Hg}^{2+}$  ion solution with concentration 120  $\mu\text{M}$ , work as a control solution. The purple color of AA-AuNPs solution changed to brown color with elevating in concentration of  $\text{Hg}^{2+}$

ions as shown in (Figure 10). This visible color changing in M-AA-AuNPs solution refer to interaction of potential and effective components present on the surface of NPs with  $\text{Hg}^{2+}$  ions through metal-ligand interactions. These interactions together with  $\text{Hg}^{2+}$  ions in solution might be responsible for M-AuNPs aggregation.

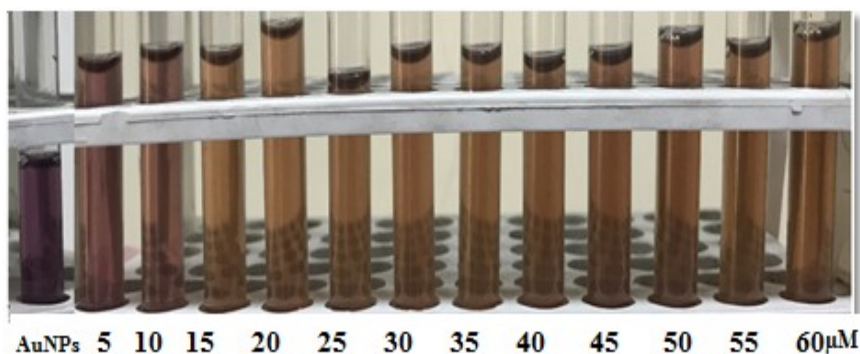


**Figure 10:** Changing in visible color of AA-AuNPs with different concentrations of  $\text{Hg}^{2+}$  ions.

Furthermore, the alterations in band intensity, position as well as width were studied through UV-Vis analysis. Various concentrations were prepared

to study SPR spectra. The band intensity at 450 nm will reduce related to  $\text{Hg}^{2+}$  ion concentrations (Figure 11).

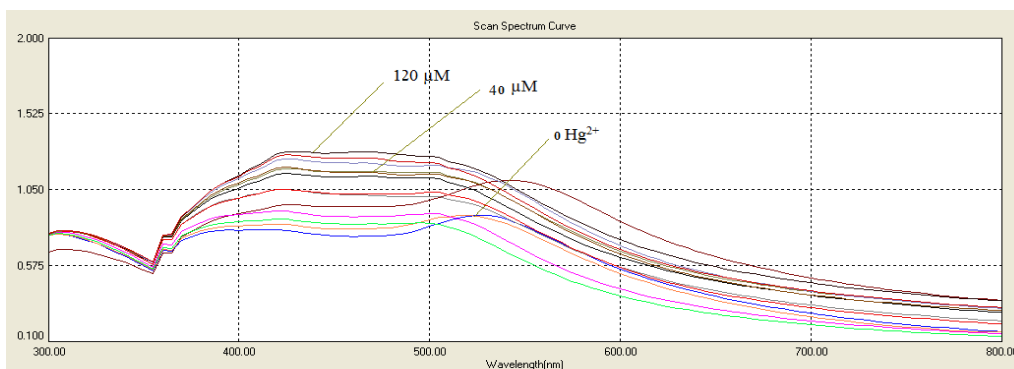


**Figure 11:** UV-Vis spectrum of AA-AuNPs through addition of different concentrations of  $\text{Hg}^{2+}$  ions.

The color changes obvious and could be seen with the unaided eye as the concentration of  $\text{Hg}^{2+}$  is increase more than 15  $\mu\text{M}$ . A linear relationship was established between  $\Delta A/A_0$  and the concentration of  $\text{Hg}^{2+}$   $A(\text{AU}) = 0.0035-0.007c$  ( $\mu\text{M}$ ) as well as the coefficient value  $R^2 = 0.9919$ . The upper limit of detection for this procedure equal to 120  $\mu\text{M}$  as well

as the limit of detection (LOD) equal to 0.65  $\mu\text{M}$  determined by  $3S$ , the limit of quantification equal to 2.14 lowering than the limit set by both WHO and EPA. As compared to the probe using gold nanorods, the data found in this study is more sensitive for  $\text{Hg}^{2+}$  estimation, these results plotted in (Figure 12).

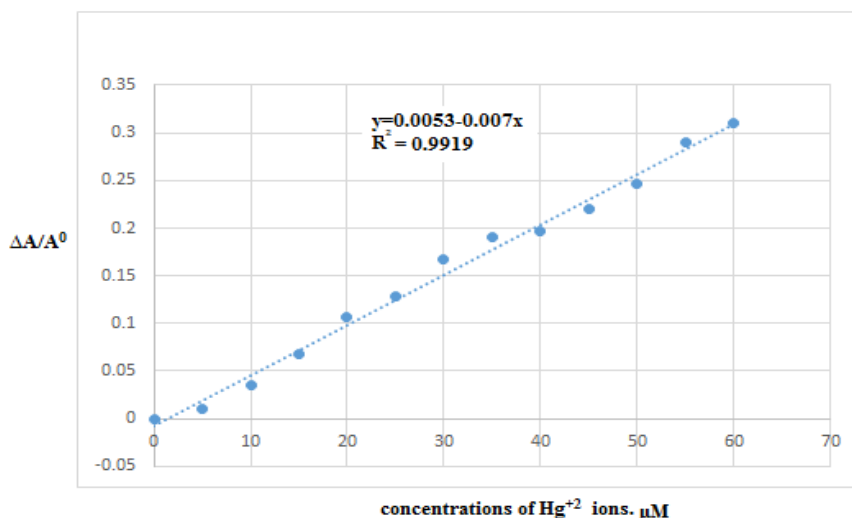


**Figure 12:** Plot of  $\Delta A/A^0$  at 540 nm versus different concentrations of  $Hg^{2+}$  ions.

In contrast to most other reported NPs-based methods that depend on disaggregation or aggregation, the assay in this study is depend on  $Hg^{2+}$  induced morphological transformation of AuNPs. Also, the data found in this study is further sensitive than atomic absorption spectroscopy (AAS) (22), as well as fluorescence methods(49). As compar to other study, the data indicated that LOD equal to (0.53  $\mu M$ ) and linear range equal to (0-398  $\mu M$ ) for Au-Ag Bimetallic NPs(50). Furthermore, our assay has an extremely good selectivity for  $Hg^{2+}$  equal to 5 $\mu M$ , over the measured metal ions (20  $\mu M$ ), including (  $Zn^{2+}$ ,  $Cu^{2+}$ ,  $Cr^{3+}$ ,  $Mg^{2+}$ ,  $Co^{+3}$ ,  $Mn^{2+}$ ,  $Sn^{2+}$ ,  $Fe^{3+}$ ,  $Ni^{2+}$ , and  $Ca^{2+}$ ) as shown above.

### 3.5. Detection of $Hg^{2+}$ in Water Samples

To examine the colorimetric method for environmental systems, different samples of tap water were chosen and  $Hg^{2+}$  ions were added with known concentration. The spiked samples had been tagged with the proposed detection system. The results indicated that none of the tap water samples caused a change in visible color change of AA-AuNPs probe, pointing to the quantity of  $Hg^{2+}$  ions of these samples are below 180  $\mu M$ . Conversely, when the tap water samples spiked with  $Hg^{2+}$  with concentration 120  $\mu M$ , change to brown color of water was shown. The data assure that the detection assay established here can be used to detection of  $Hg^{2+}$  ions in real environmental and water samples.

So, by taking a benefits and advantage of the colorimetric method using AuNPs toward  $Hg^{2+}$  ion, a very simple colorimetric probe was developed to detect  $Hg^{2+}$  ion depending on ascorbic acid with AuNPs. This proposed method has many remarkable advantages, as compared to other known sensors or probe to  $Hg^{2+}$  ion, like: simplicity to use AuNPs, easily to synthesis its complex; short detection period with suitable condition (room temperature, aqueous solution); the method proved to be sensitive and selective probe toward  $Hg^{2+}$  ion in presence of other metal ions; easily monitoring the

end point of reaction by color change; and finally low cost(51, 52).

## 4. CONCLUSION

In this work, we describe a simple, fast and reproducible method of environment. Our data revealed that the novel colorimetric AuNPs sensor was successfully developed. Easy synthesis of AuNPs without the need for expensive reducing agents. Gold ions Chemically reduced to NPs by ginger extracts. AuNPs stabilized by ascorbic acid can be used as a colorimetric probe for  $Hg^{2+}$  ions with detection limit equal to 0.65  $\mu M$ . Other countered metal ions exist in the solution didn't interact or effect in detection of  $Hg^{2+}$  ions. Practical applicability of AuNPs stabilized by ascorbic acid exhibits successfully using to detection of  $Hg^{2+}$  ions as highly sensitive and selective probe in different water samples like tap, and river water. The method also provided to be highly sensitive and selective probe to detection of  $Hg^{2+}$  ions, so other samples should be used in the future to indicated that our newly developed assay might open a new approach to detect  $Hg^{2+}$  levels .

## 5. CONFLICT OF INTEREST

The authors have no conflicts of interest regarding this investigation.

## 6. ACKNOWLEDGMENTS

The authors would like to thank Mustansiriyah University (www.uomustansiriyah.edu.iq) Baghdad-Iraq for its support in the present work.

## 7. REFERENCES

1. Kaehler T. Nanotechnology: basic concepts and definitions. Clinical Chemistry. 1994 Sep 1;40(9):1797-9. Available from: <URL>.



2. Eman TS, Amjed MO. Gold nanoparticle capped citrate as a ligand for chromium (III) ion: optimization and its application in contaminated tap water. *Indonesian Journal of Chemistry (Indones J Chem)*. 2022;22(4):1025-34. Available from: [<URL>](#).
3. Patil KB, Patil NB, Patil SV, Patil VK, Shirsath PC. Metal based Nanomaterial's (Silver and Gold): Synthesis and Biomedical application. *Asian Jour Pharm and Technol*. 2020;10(2):97. Available from: [<URL>](#).
4. Farhan S, Dadoosh R, Jassim A. Evaluation of Phytochemical, Total phenolic and Antioxidant Activity of Carica Papaya Seed for Its Use in Biosynthesis of Gold Nanoparticles. *Egypt J Chem*. 2021 Apr 19;0(0):0-0. Available from: [<URL>](#).
5. Nallagouni CSR, Gangapuram BR, Karnati PR. Green synthesis of Gold nanoparticles using leaf extract of *Caesalpinia bonducella* and its biological applications. *Research journal of pharmacy and technology*. 2021;14(2):1037-40. Available from: [<URL>](#).
6. Sivasankari G, Boobalan S, Deepa D. Dopamine sensor by Gold Nanoparticles Absorbed Redox behaving metal Complex. *Asian Jour Pharm and Technol*. 2018;8(2):83. Available from: [<URL>](#).
7. Renugadevi K, Kumar N, Nachiyar CV. Phytosynthesis of Silver Nanoparticle using Ginger extract as a Reducing agent by Microwave Irradiation method and invitro Evaluation of its Antibacterial activity and Cytotoxicity. *Rese Jour of Pharm and Technol*. 2017;10(12):4142. Available from: [<URL>](#).
8. Prathyusha P, Sundararajan R. UV spectrophotometric method for determination of Bilastine in bulk and pharmaceutical formulation. *Rese Jour of Pharm and Technol*. 2020;13(2):933. Available from: [<URL>](#).
9. Senthilnathan B, Vivekanandan K, Bhavya E, Masilamani, Priya BS. Impact of Nanoparticulate Drug Delivery System of Herbal Drug in Control of Diabetes Mellitus. *Rese Jour of Pharm and Technol*. 2019;12(4):1688. Available from: [<URL>](#).
10. Ghosh NS, Pandey E, Gillhotra RM, Singh R. Biosynthesis of Gold Nanoparticles using Leaf Extract of *Desmodium gangeticum* and their Antioxidant Activity. *Rese Jour of Pharm and Technol*. 2020;13(6):2685. Available from: [<URL>](#).
11. Daniel MC, Astruc D. Gold Nanoparticles: Assembly, Supramolecular Chemistry, Quantum-Size-Related Properties, and Applications toward Biology, Catalysis, and Nanotechnology. *Chem Rev*. 2004 Jan 1;104(1):293-346. Available from: [<URL>](#).
12. Rao CNR, Cheetham AK. Science and technology of nanomaterials: current status and future prospects. *J Mater Chem*. 2001 Nov 23;11(12):2887-94. Available from: [<URL>](#).
13. Selin NE. Global Biogeochemical Cycling of Mercury: A Review. *Annu Rev Environ Resour*. 2009 Nov 1;34(1):43-63. Available from: [<URL>](#).
14. Balali-Mood M, Naseri K, Tahergorabi Z, Khazdair MR, Sadeghi M. Toxic Mechanisms of Five Heavy Metals: Mercury, Lead, Chromium, Cadmium, and Arsenic. *Front Pharmacol*. 2021 Apr 13;12:643972. Available from: [<URL>](#).
15. Xu D, Yu S, Yin Y, Wang S, Lin Q, Yuan Z. Sensitive Colorimetric Hg<sup>2+</sup> Detection via Amalgamation-Mediated Shape Transition of Gold Nanostars. *Front Chem*. 2018 Nov 27;6:566. Available from: [<URL>](#).
16. Li Q, Zhang Z, Wang Z. Determination of Hg<sup>2+</sup> by on-line separation and pre-concentration with atmospheric-pressure solution-cathode glow discharge atomic emission spectrometry. *Analytica Chimica Acta*. 2014 Oct;845:7-14. Available from: [<URL>](#).
17. Wang X, Liu F, Shao Q, Yin Z, Wang L, Fu Z. A novel chemiluminescent immunochromatographic assay strip for rapid detection of mercury ions. *Anal Methods*. 2017;9(16):2401-6. Available from: [<URL>](#).
18. Sharma VV, Tonelli D, Guadagnini L, Gazzano M. Copper-cobalt hexacyanoferrate modified glassy carbon electrode for an indirect electrochemical determination of mercury. *Sensors and Actuators B: Chemical*. 2017 Jan;238:9-15. Available from: [<URL>](#).
19. Li D, Li CY, Li YF, Li Z, Xu F. Rhodamine-based chemodosimeter for fluorescent determination of Hg<sup>2+</sup> in 100% aqueous solution and in living cells. *Analytica Chimica Acta*. 2016 Aug;934:218-25. Available from: [<URL>](#).
20. Zhao Y, Gui L, Chen Z. Colorimetric detection of Hg<sup>2+</sup> based on target-mediated growth of gold nanoparticles. *Sensors and Actuators B: Chemical*. 2017 Mar;241:262-7. Available from: [<URL>](#).
21. Rasheed T, Bilal M, Nabeel F, Iqbal HMN, Li C, Zhou Y. Fluorescent sensor based models for the detection of environmentally-related toxic heavy metals. *Science of The Total Environment*. 2018 Feb;615:476-85. Available from: [<URL>](#).
22. Hatch WR, Ott WL. Determination of submicrogram quantities of mercury by atomic absorption spectrophotometry. *Analytical Chemistry*. 1968;40(14):2085-7. Available from: [<URL>](#).
23. Wu X, Yang W, Liu M, Hou X, Zheng C. Vapor generation in dielectric barrier discharge for sensitive detection of mercury by inductively coupled plasma optical emission spectrometry. *J Anal At Spectrom*. 2011;26(6):1204. Available from: [<URL>](#).
24. Bendl R, Madden J, Regan A, Fitzgerald N. Mercury determination by cold vapor atomic absorption spectrometry utilizing UV photoreduction. *Talanta*. 2006 Feb 15;68(4):1366-70. Available from: [<URL>](#).
25. Du J, Jiang L, Shao Q, Liu X, Marks RS, Ma J, et al. Colorimetric Detection of Mercury Ions Based on Plasmonic Nanoparticles. *Small*. 2013 May 27;9(9-10):1467-81. Available from: [<URL>](#).
26. Chansuvarn W, Tuntulani T, Imyim A. Colorimetric detection of mercury(II) based on gold nanoparticles, fluorescent gold nanoclusters and other gold-based nanomaterials. *TrAC Trends in Analytical Chemistry*. 2015 Feb;65:83-96. Available from: [<URL>](#).
27. Chen G, Guo Z, Zeng G, Tang L. Fluorescent and colorimetric sensors for environmental mercury detection. *Analyst*. 2015;140(16):5400-43. Available from: [<URL>](#).
28. Xu X, Li YF, Zhao J, Li Y, Lin J, Li B, et al. Nanomaterial-based approaches for the detection and speciation of mercury. *Analyst*. 2015;140(23):7841-53. Available from: [<URL>](#).

29. Ding Y, Wang S, Li J, Chen L. Nanomaterial-based optical sensors for mercury ions. *TrAC Trends in Analytical Chemistry*. 2016 Sep;82:175-90. Available from: [<URL>](#).
30. Lee JS, Han MS, Mirkin CA. Colorimetric Detection of Mercuric Ion (Hg<sup>2+</sup>) in Aqueous Media using DNA-Functionalized Gold Nanoparticles. *Angew Chem Int Ed*. 2007 May 25;46(22):4093-6. Available from: [<URL>](#).
31. Priyaa GH, Satyan KB. Biological synthesis of silver nanoparticles using ginger (*Zingiber officinale*) extract. *J Environ Nanotechnol*. 2014;3(4):32-40. Available from: [<URL>](#).
32. Xin Lee K, Shameli K, Miyake M, Kuwano N, Bt Ahmad Khairudin NB, Bt Mohamad SE, et al. Green Synthesis of Gold Nanoparticles Using Aqueous Extract of *Garcinia mangostana* Fruit Peels. *Journal of Nanomaterials*. 2016;2016:1-7. Available from: [<URL>](#).
33. Kumar SS, Venkateswarlu P, Rao VR, Rao GN. Synthesis, characterization and optical properties of zinc oxide nanoparticles. *Int Nano Lett*. 2013 Dec;3(1):30. Available from: [<URL>](#).
34. Weiss M, Fan J, Claudel M, Sonntag T, Didier P, Ronzani C, et al. Density of surface charge is a more predictive factor of the toxicity of cationic carbon nanoparticles than zeta potential. *J Nanobiotechnol*. 2021 Jan 6;19(1):5. Available from: [<URL>](#).
35. Nirmala S, Ravichandiran V, Vijayalakshmi A, Nadasabapathi P. Protective effect of Gymnemic acid isolated from *Gymnema sylvestris* leaves coated Chitosan reduced gold nanoparticles in hyperlipidemia and Diabetes Induced vascular tissue damage in Rats. *Rese Jour of Pharm and Technol*. 2018;11(3):1193. Available from: [<URL>](#).
36. Luo LB, Yu SH, Qian HS, Zhou T. Large-Scale Fabrication of Flexible Silver/Cross-Linked Poly(vinyl alcohol) Coaxial Nanocables by a Facile Solution Approach. *J Am Chem Soc*. 2005 Mar 9;127(9):2822-3. Available from: [<URL>](#).
37. Ahmed MA, Jassim A, AL-Ameri SA. Selective Colorimetric Mercury Ions Sensing in Different Samples Using Silver Nanoparticles Prepared from Ginger Extract. *Plant Archives*. 2020;20(2):5505-15. Available from: [<URL>](#).
38. Jassim AMN, Mohammed MT, Farhan SA, Dadoosh RM, Majeed ZN, Abdula AM. Green synthesis of silver nanoparticles using *Carica papaya* juice and study of their biochemical application. *Journal of Pharmaceutical Sciences and Research*. 2019;11(3):1025-34. Available from: [<URL>](#).
39. Mukundan D, Mohankumar R, Vasanthakumari R. Green Synthesis of Silver Nanoparticles Using Leaves Extract of *Bauhinia tomentosa* Linn and its *In Vitro* Anticancer Potential. *Materials Today: Proceedings*. 2015;2(9):4309-16. Available from: [<URL>](#).
40. Lal SS, Nayak P. Green synthesis of gold nanoparticles using various extract of plants and spices. *International journal of science innovations and discoveries*. 2012;2(23):325-50.
41. Hadi MY, Hameed IH. Uses of Gas Chromatography-Mass Spectrometry (GC-MS) Technique for Analysis of Bioactive Chemical Compounds of *Lepidium sativum*: A Review. *Rese Jour of Pharm and Technol*. 2017;10(11):4039. Available from: [<URL>](#).
42. Hussein HJ, Hameed IH, Hadi MY. Using Gas Chromatography-Mass Spectrometry (GC-MS) Technique for Analysis of Bioactive Compounds of Methanolic Leaves extract of *Lepidium sativum*. *Rese Jour of Pharm and Technol*. 2017;10(11):3981. Available from: [<URL>](#).
43. Balakumaran MD, Ramachandran R, Balashanmugam P, Mukeshkumar DJ, Kalaichelvan PT. Mycosynthesis of silver and gold nanoparticles: Optimization, characterization and antimicrobial activity against human pathogens. *Microbiological Research*. 2016 Jan;182:8-20. Available from: [<URL>](#).
44. Irvani S. Green synthesis of metal nanoparticles using plants. *Green Chem*. 2011;13(10):2638. Available from: [<URL>](#).
45. Krishnaraj C, Ramachandran R, Mohan K, Kalaichelvan PT. Optimization for rapid synthesis of silver nanoparticles and its effect on phytopathogenic fungi. *Spectrochimica Acta Part A: Molecular and Biomolecular Spectroscopy*. 2012 Jul;93:95-9. Available from: [<URL>](#).
46. Jagtap UB, Bapat VA. Green synthesis of silver nanoparticles using *Artocarpus heterophyllus* Lam. seed extract and its antibacterial activity. *Industrial Crops and Products*. 2013 Apr;46:132-7. Available from: [<URL>](#).
47. Manal AA, Awatif AH, Khalid MOO, Dalia FAE, Nada EE, Lamia. AA lahib, et al. Silver nanoparticles biogenic synthesized using an orange peel extract and their use as an anti-bacterial agent. *Int J Phys Sci*. 2014 Feb 9;9(3):34-40. Available from: [<URL>](#).
48. Sadeghi B, Gholamhoseinpoor F. A study on the stability and green synthesis of silver nanoparticles using *Ziziphora tenuior* (Zt) extract at room temperature. *Spectrochimica Acta Part A: Molecular and Biomolecular Spectroscopy*. 2015 Jan;134:310-5. Available from: [<URL>](#).
49. Nirmalraj PN, Lutz T, Kumar S, Duesberg GS, Boland JJ. Nanoscale Mapping of Electrical Resistivity and Connectivity in Graphene Strips and Networks. *Nano Lett*. 2011 Jan 12;11(1):16-22. Available from: [<URL>](#).
50. Mathaweesansurn A, Vittayakorn N, Detsri E. Highly Sensitive and Selective Colorimetric Sensor of Mercury (II) Based on Layer-by-Layer Deposition of Gold/Silver Bimetallic Nanoparticles. *Molecules*. 2020 Sep 27;25(19):4443. Available from: [<URL>](#).
51. Zhou Y, Dong H, Liu L, Li M, Xiao K, Xu M. Selective and sensitive colorimetric sensor of mercury (II) based on gold nanoparticles and 4-mercaptophenylboronic acid. *Sensors and Actuators B: Chemical*. 2014 Jun;196:106-11. Available from: [<URL>](#).
52. Deshpande K, Thekkedath A. Selective determination of mercury (II) in coastal water using bio-functionalized gold nanoparticles. *J Water Environ Nanotechnol [Internet]*. 2022 Dec [cited 2023 Sep 10];7(4). Available from: [<URL>](#).



## Hydration Processes in HCl and Aqueous Salt Solutions

Shahbazova Gunel Mugaddas<sup>\*</sup> , Masimov Eldar Ali

<sup>1</sup>Baku state University, Department of Physics, Baku, AZ1148, Azerbaijan

**Abstract:** In this work, the number of hydration of ions ( $K^+$  and  $Cl^-$ ,  $K^+$  and  $Br^-$ ,  $K^+$  and  $I^-$ ,  $H^+$  and  $Cl^-$ ,  $Li^+$  and  $Cl^-$ ,  $Cs^+$  and  $Cl^-$ ,  $Na^+$  and  $Cl^-$ ) in dilute aqueous solutions of some electrolytes of KCl, KBr, KI, HCl, LiCl, CsCl, and NaCl was studied by the proposed refractometric method. Further, the effect of polyethylene glycol (PEG-6000) on the hydration processes for ions in aqueous solutions of KCl and KBr was studied. It turned out that when the polymer is introduced into the solution, the hydration numbers of ions decrease, which is apparently due to the role of the PEG oxygen atom competing with ions in interaction with water molecules.

**Keywords:** Hydration, hydration number, solution, salts, polyethylene glycol

**Submitted:** November 8, 2022. **Accepted:** July 21, 2023.

**Cite this:** Mugaddas SG, Ali ME. Hydration Processes in HCl and Aqueous Salt Solutions. JOTCSA. 2023;10(4):887-92.

**DOI:** <https://doi.org/10.18596/jotcsa.1201298>.

**\*Corresponding author. E-mail:** [shahbazova.gunel@mail.ru](mailto:shahbazova.gunel@mail.ru)

### 1 INTRODUCTION

As is known, all the properties of substances, including solutions, are related to their energy state and structure. Therefore, studying the interaction between all components of the solution leading to the formation of a certain structure is important. One of the important processes occurring in the solution is solvation (hydration, if the solvent is water).

When salts are dissolved in water, the salt dissociates into ions, and these ions do not interact with each other in dilute solutions. The hydration number of a compound is defined as the average number of molecules bound to the compound more strongly than they are bound to other water molecules (1).

As is known, hydration is the process of interaction of water molecules with ions, atoms, and molecules introduced into it. The process of hydration characterizes practically all structural and energetic changes occurring in the solution.

The degree of hydration is characterized by the number of hydrates ( $h$ ) and the thickness of the hydrate shell of the particles of the dissolved substance.

There are multiple methods of determining the number of hydrations based on the differences in the properties of water in the general and hydrated shell (NMR, IK) (2-7). Therefore, the obtained values of the hydration number, determined by different methods, do not, as a rule, coincide (8). In the present research paper, hydration numbers of ions were found by the refractometric method described in the work (9-11).

### 2 EXPERIMENTAL SECTION

In the work, we used PEG with a molecular weight of  $M_n=6000$  produced by the company "Panreac" (Spain), as well as salts of the "chemically clean" type, KCl, KBr, KI, HCl, LiCl, CsCl, and NaCl. All experiments were carried out using bidistilled water.

As known, polyethylene glycol (PEG) of different molecular masses is widely used in various biotechnological processes.

Mixtures of aqueous solutions of PEG and various polymers and a number of organic and inorganic salts form two-phase systems that are widely used for the separation and purification of biological materials (proteins, viruses, cells, etc.), for the fractionation of some high-molecular-weight compounds, for the early diagnosis of some diseases, etc. Therefore, the study of the effect of polyethylene glycol on the process of hydration of ions is important when studying the mechanisms of phase formation in water two-phase systems.

It is known that the formation of water-two-phase systems is connected with the interactions of phase-forming components (hydrophobic and hydrophilic hydration) with water. Different local microstructures arise around each component, and upon reaching a certain size, each of these structures turns into a separate stable thermodynamic phase, and the system becomes two-phase.

With the aim of achieving this goal, we conducted a study on the process of hydration of salts used to obtain different two-phase systems in diluted aqueous solutions. Additionally, we investigated the impact of PEG on this process. PEG serves as a polymer component of the two-phase system PEG-sodium citrate-water.

### 3. RESULTS AND DISCUSSION

A very simple and experimentally convenient method for determining the hydration number of salts was proposed based on the study of the concentration dependence of the refractive index of a salt solution.

In the works indicated in the introduction, an analytical formula was obtained that relates the slope of the concentration dependence of the refractive index of the solution to the number of hydrations (9-11):

$$h_1 + h_2 = \frac{3 M t g \Phi}{\rho N_A \alpha_{H_2O}} - i \frac{r_{K^+}^3}{r_{H_2O}^3} - j \frac{r_{R^-}^3}{r_{H_2O}^3} \quad (1)$$

where  $\rho$  is the density of the solution;  $N_A$  — Avogadro's number;  $M$  — molar mass KR;  $h_1, h_2$  — number of hydration ions  $K^+$  and  $R^-$ ; and  $c$  — mass concentration of KR in the solution.

We applied this method to determine the hydration number of ions in dilute aqueous solutions of HCl and the salts NaCl, CsCl, LiCl, KCl, KBr, and KI. The concentration dependence of the refractive index of dilute aqueous solutions of salts was carried out on a refractometer FR0429.

In dilute solutions, when the ions do not interact with each other, the value  $(n^2-1)/(n^2+2)$  depends linearly on the concentration. When reaching certain threshold concentrations, the linear dependence is broken  $(n^2-1)/(n^2+2) - c$ . We worked in areas of such concentrations where this dependence does not deviate from linearity.

The obtained data in coordinates  $(n^2-1)/(n^2+2) - c$  for various salts are presented in Figures 1 and 2.

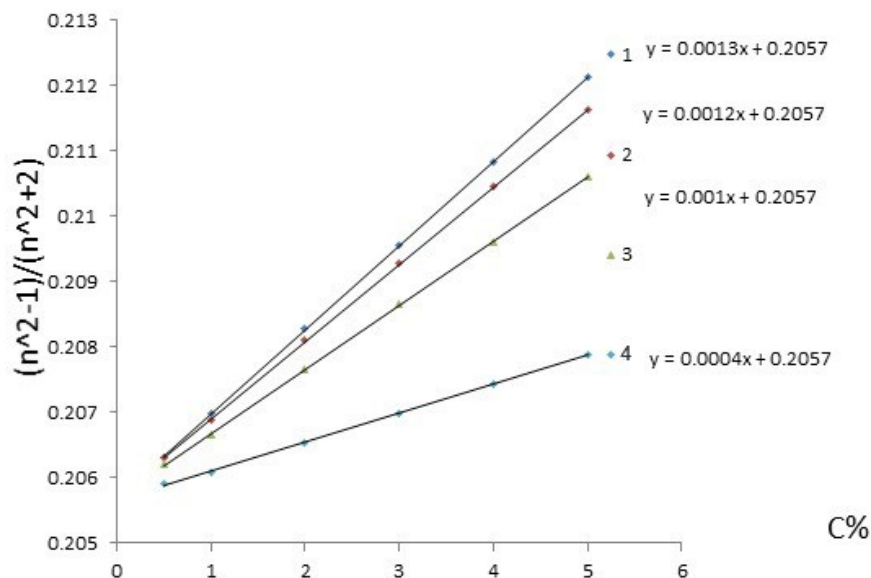


**Figure. 1.** Concentration relationship  $(n^2-1) / (n^2+2)$  for aqueous solutions 1.HCl, 2.LiCl, 3.NaCl, 4.CsCl

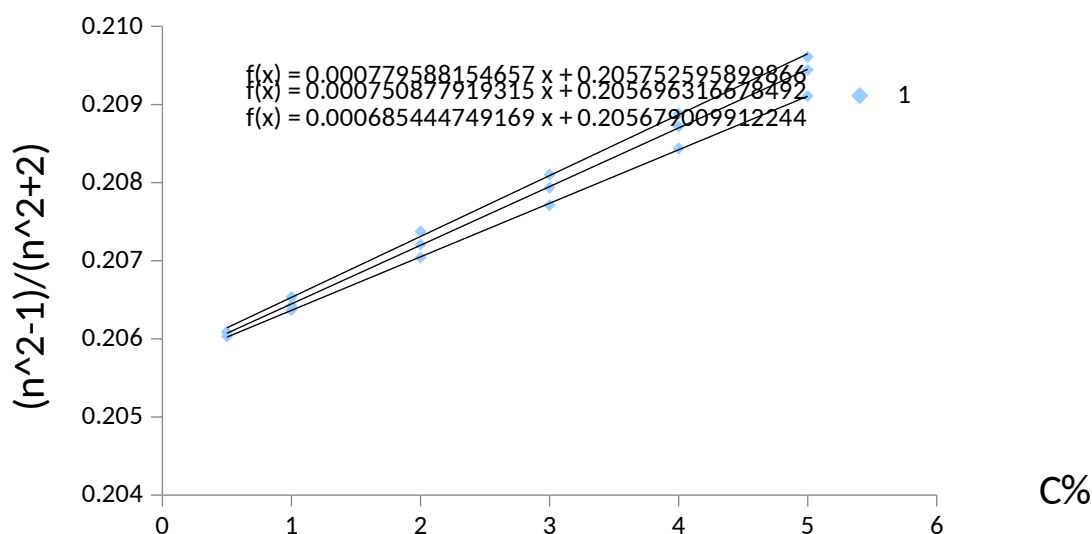


**Figure.2.** Dependence of the ratio on the concentration  $(n^2-1) / (n^2+2)$  of KCl, KBr, KI in the system 1. KCl+ water, 2. KBr+ water, 3. KI+ water

As follows from the figures, these dependences have a linear character. Substituting parameters taken from literature (12-14), ( $r_{H^+}=33 \text{ pm}$ ,  $r_{Cs^+}=167 \text{ pm}$ ,  $r_{H_2O}=140 \text{ pm}$ ,  $\alpha_{H_2O}=1.45 \times 10^{-30} \text{ m}$ ,  $\rho \approx 10^3 \text{ kg/m}^3$ ,  $r_{Cl^-}=200 \text{ pm}$ ,  $r_{K^+}=138 \text{ pm}$ ,  $r_{Er^-}=196 \text{ pm}$ ) included in formula [1], we determined the sum of the hydration numbers of  $H^+$  and  $Cl^-$ ,  $Li^+$  and  $Cl^-$ ,  $Na^+$  and  $Cl^-$ ,  $Cs^+$  and  $Cl^-$ ,  $K^+$  and  $Cl^-$  ions based on the angular coefficient of the graph presented in

Figures 1 and 2,  $K^+$  and  $Br^-$ ,  $K^+$  and  $I^-$ , in aqueous solutions of HCl, LiCl, NaCl, CsCl, KCl, KBr, and KI.

Refractive indices of dilute aqueous solutions of potassium salts KCl, KBr and KI were measured by the refractometric method in the concentration interval  $0 \leq c \leq 5\%$ . As can be seen from Table 1. the relationship is a linear function of salt concentration: The values of the parameters obtained from the experiment and for the aqueous solutions studied at a temperature of  $25^\circ \text{C}$  were as follows: for all solutions,

$A=0.02057$ , and values for KCl  $B=0.001$ , for KBr  $B=0.0008$ , for KI  $B=0.0007$ , etc.

**Table 1.** The sum of numbers of hydration of potassium ions  $K^+$  and anions  $Cl^-$ ,  $Br^-$ ,  $I^-$  at temperature  $25^\circ C$

	$r_1+r_2$	$h_1+h_2$
KCl	319	23.7
KBr	334	24.2
KI	358	37.3

Through  $h_1$ , the number of hydration of potassium ions is indicated, and through  $h_2$  - the number of hydration of  $Cl^-$ ,  $Br^-$ , and  $I^-$  anions, respectively. It can be seen that with the growth of the radii of the anions, the sum of the hydration numbers of the ions increases. If the number of hydrations of cation (anion) ions is assumed to be the same in all cases, then the increase in the amount can be explained by the growth of the surface area of anions (cations) with the growth of their radii.

Despite the identical charges of all anions (cations) in this case, the main role is played by

the steric factor: with the growth of the radii of anions (cations), new positions for the placement of water molecules on the surface of the anion (cation) arise, and the number of hydration of anions (cations) increases in the following sequence:  $Cl^-$ ,  $Br^-$  and  $I^-$ . ( $H^+$ ,  $Li^+$ ,  $Na^+$ ,  $Cs^+$ , Table 2.)

**Table 2.** The sum of the numbers of hydration ions  $Cl^-$  and cations  $H^+$ ,  $Li^+$ ,  $Na^+$ ,  $K^+$ ,  $Cs^+$  at temperature  $25^\circ C$

	$r_1+r_2$	$h_1+h_2$
HCl	233	13.3
LiCl	276	14
NaCl	295	16.3
CsCl	348	20

Figure 3 shows the graph of the dependence of the sum of the hydration numbers of the cations  $H^+$ ,  $Li^+$ ,  $Na^+$ ,  $Cs^+$ , and anion  $Cl^-$  on the sum of the radii of the  $Cl^-$  and the corresponding cations constructed according to Table 2.

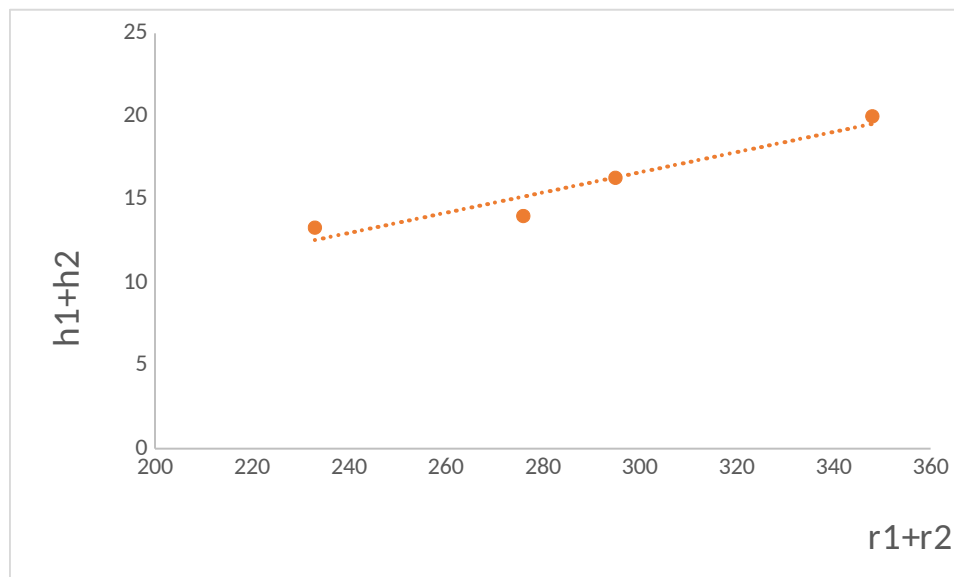


**Figure 3.** Dependence of the hydration numbers of anion  $Cl^-$  and cations  $H^+$ ,  $Li^+$ ,  $Na^+$ ,  $Cs^+$  on the radius of the corresponding ions

The influence of polyethylene glycol (PEG-6000) on the value ( $h_1+h_2$ ) for ions  $K^+$  and  $Cl^-$ ,  $K^+$  and  $Br^-$  is studied further. The obtained results are shown in tables 3 and 4.

**Table 3.** The sum of the numbers of hydration of anion  $Cl^-$  and cation  $K^+$  at temperature  $25^\circ C$

Solvents	$h_1+h_2$
KCl+ $H_2O$	23.7
KCl+PEG(0.04 g 39%)+ $H_2O$	13.5
KCl+PEG(1.1g 39%)+ $H_2O$	5.8

**Table 4.** The sum of the hydration numbers of anion Br<sup>-</sup> and cation K<sup>+</sup> at temperature 25°C

Solvents	$h_1+h_2$
KBr+H <sub>2</sub> O	24.2
KBr+PEG(0.3g)+ H <sub>2</sub> O	16.7
KBr+PEG(0.5g)+ H <sub>2</sub> O	12.6

As follows from the table, when the polymer is introduced into the solution, the number of hydration ions decreases, which is apparently connected with the competing role of the PEG oxygen atom in the interaction with water molecules.

#### 4. CONCLUSION

In this work, we studied the number of hydration of ions (K<sup>+</sup> and Cl<sup>-</sup>, K<sup>+</sup> and Br<sup>-</sup>, K<sup>+</sup> and I<sup>-</sup>, H<sup>+</sup> and Cl<sup>-</sup>, Li<sup>+</sup> and Cl<sup>-</sup>, Cs<sup>+</sup> and Cl<sup>-</sup>, Na<sup>+</sup> and Cl<sup>-</sup>) in aqueous solutions of HCl, KCl, KBr, KI, HCl, LiCl, CsCl, and NaCl. An analysis of the hydration numbers of ions suggests that the hydration number increases with increasing ion radius. This result can be explained by the increase in the surface area of the ions as their radii increases.

As it follows from the obtained data, when polyethylene glycol is introduced into the studied solution due to the structuring of water under the influence of PEG, the number of free water molecules and the possibility of salt ion hydration decrease, which is accompanied by a decrease in the number of hydration of ions.

#### 5. CONFLICT OF INTEREST

The authors declare no conflict of interest.

#### 6. REFERENCES

- Zavitsas AA. Some opinions of an innocent bystander regarding the Hofmeister series. *Current Opinion in Colloid & Interface Science*. 2016;23:72-81. Available from: [<URL>](#).
- Mahler J, Persson I. A study of the hydration of the alkali metal ions in aqueous solution. *Inorganic chemistry*. 2012;51(1):425-38. Available from: [<URL>](#).
- Uchida T, Hirano T, Ebinuma T, Narita H, Gohara K, Mae S, et al. Raman spectroscopic determination of hydration number of methane hydrates. *AIChE journal*. 1999;45(12):2641-5. Available from: [<URL>](#).
- Rempe SB, Pratt LR, Hummer G, Kress JD, Martin RL, Redondo A. The hydration number of Li<sup>+</sup> in liquid water. *Journal of the American Chemical Society*. 2000;122(5):966-7. Available from: [<URL>](#).

5. Werner EJ, Avedano S, Botta M, Hay BP, Moore EG, Aime S, et al. Highly soluble tris-hydroxypyridonate Gd (III) complexes with increased hydration number, fast water exchange, slow electronic relaxation, and high relaxivity. *Journal of the American Chemical Society*. 2007;129(7):1870-1. Available from: [<URL>](#).

6. Dec SF, Bowler KE, Stadterman LL, Koh CA, Sloan ED. Direct measure of the hydration number of aqueous methane. *Journal of the American Chemical Society*. 2006;128(2):414-5. Available from: [<URL>](#).

7. Smirnov P, Trostin V. Structures of the nearest surroundings of the K<sup>+</sup>, Rb<sup>+</sup>, and Cs<sup>+</sup> ions in aqueous solutions of their salts. *Russian Journal of General Chemistry*. 2007;77:2101-7. Available from: [<URL>](#).

8. Mahler J, Persson I. A study of the hydration of the alkali metal ions in aqueous solution. *Inorganic chemistry*. 2012;51(1):425-38. Available from: [<URL>](#).

9. Masimov EA, Abbasov KhF. *Journal of Qafqaz University N23*, 2008, str.59.

10. Masimov E, Abbasov H. Refractometry determination of the hydration number of ions in diluted aqueous solutions of magnesium sulfate. *Russian Journal of Physical Chemistry A*. 2012;86:399-401. Available from: [<URL>](#).

11. Masimov EA, Abbasov HF. in *Proceedings of the Conference on Chemical Thermodynamics*, June 20 – July 6, 2007, p. 35239.

12. Campbell J. *Chemical Systems* (Freeman, New York, 1970; Mir, Moscow, 1975), Vol. 1.

13. Bokii, GB. *Crystallochemistry* (Khimiya, Moscow, 1971) [in Russian].

14. Amirhanov AKh. Some questions of chemical technology and physical and chemical analysis. Tashkent, izd. AN Uz. USSR, 1963, p. 76-86.







## Characterization of Active Food Packaging Films Based on Poly(vinyl alcohol)/Boric acid/Montmorillonite Nanocomposite Incorporated with Polyphenol

Serap MUTLU YANIC <sup>1\*</sup> , Esen Gul ATES <sup>2</sup> 

<sup>1</sup> Istanbul Gedik University, Chemistry Technology Program, Istanbul, 34906, Turkey

<sup>2</sup> Turkish Energy, Nuclear and Mineral Research Agency, Ankara, Turkey

**Abstract:** Biopolymer-based nanocomposites are a new type of material that exhibits significantly improved properties, such as barrier, mechanical, and thermal characteristics. They are considered non-toxic and alternative food packaging materials. Therefore, the production of biopolymer-based active films has been initiated to reduce the environmental problems caused by non-biodegradable plastic waste and eliminate their negative effects on human health. In this study active food packaging films based on poly(vinyl alcohol)/boric acid/montmorillonite (PVA/BA/MMT) nanocomposite incorporated with ferulic acid (FA) were synthesized using solution casting method. The structural, thermal, transmittance, antimicrobial, and antifungal properties of nanocomposite films have been investigated. The fourier transforms infrared (FTIR) spectroscopy used to demonstrate the chemical structure of films and interaction between boric acid (BA) and PVA. X-Ray diffraction analysis (XRD) was performed to determine the dispersion and exfoliated of the montmorillonite in the PVA matrix. Thermal stability of PVA/BA/MMT films incorporated with FA were evaluated by using TG/DTA analyzer. Optical properties of films and PVA determined using by UV/VIS spectrophotometer in the range of 400-700 nm wavelength at scanning percent transmittance. The transmittance of PVA exhibited UV light 89.2% of T<sub>700</sub> and 86.7% of T<sub>400</sub>, indicating the high transparency of PVA. The antimicrobial activity of PVA membranes samples was carried out test method AATCC 100. According to the antimicrobial activity test, more than 300 colonies were detected for all microorganisms in the samples belonging to the PVA group. But the antimicrobial and antifungal activity of the films incorporated with FA could inhibit bacterial growth. It has been determined that the nanocomposite films have antibacterial properties against *Escherichia coli* (*E.coli*, ATCC 25922), *Staphylococcus aureus* (*S. aureus*, ATCC6538), and antifungal properties against *Candida albicans*.

**Keywords:** Polyvinyl alcohol, boric acid, montmorillonite, polyphenol, packaging film.

**Submitted:** April 30, 2023. **Accepted:** July 12, 2023.

**Cite this:** Mutlu Yanic S, Ates EG. Characterization of Active Food Packaging Films Based on Poly(vinyl alcohol)/Boric acid/Montmorillonite Nanocomposite Incorporated with Polyphenol. JOTCSA. 2023;10(4): 893-902.

**DOI:** <https://doi.org/10.18596/jotcsa.1290365>.

**\*Corresponding author. E-mail:** [serap.mutlu@gedik.edu.tr](mailto:serap.mutlu@gedik.edu.tr).

### 1. INTRODUCTION

Plastic is one of the most widely used materials due to its excellent mechanical and barrier properties. However, many plastic materials are petroleum-based, biologically non-degradable, and cause significant environmental problems. Therefore, in recent years, research has increased on alternative biodegradable plastics that will reduce waste disposal problems, while also not

posing a threat to consumer health (1-3). Biopolymer-based food packaging films, which exhibit significantly improved properties such as barrier, mechanical, thermal, and antimicrobial characteristics, are considered as alternative food packaging films.

As a type of synthetic linear polymer material,

poly(vinyl alcohol) (PVA) have several advantages such as film-forming ability, high oxygen resistance, biodegradability, and water solubility (4). These advantageous properties have led to applications in a wide range of resins, and coatings in various fields such as papermaking, medicine, and food packaging. However, due to the hydroxyl groups present in the polyvinyl alcohol molecular chain, it is moisture-sensitive, which limits its applications in various fields. Therefore, improvement in their hydrophilic property of PVA is great of importance to investigate its applications (5-9).

Several studies have explored to advance the hydrophilic properties of synthetic PVA by many physical methods such as ultraviolet radiation, electron beam irradiation and heat treatment. Many studies have used boric acid as a chemical crosslinking agent (10-12). Specifically, extensive research has been conducted on cross-linking polyvinyl alcohol (PVA) with boric acid (BA), resulting in enhanced water resistance, barrier properties, thermal stability, and mechanical properties. These advancements have led to the development of various water-soluble food packaging materials. (13-14).

On the other hand, using clay to improve the thermal and mechanical properties of PVA is a very interesting method. Montmorillonite (MMT) is a type of clay nanofiller that is commonly used due to its low cost and ability to good dispersed in a polymer matrix. Many studies have showed that incorporating an appropriate amount of MMT or modified MMT into PVA can result in the formation of intercalated or exfoliated composite materials (30-36). These composites exhibit improved mechanical strength, water resistance, gas barrier properties, and thermal stability when compared to pure PVA. (15-16).

Active food packaging can be categorized based on the specific additive it incorporates, with a primary focus on those that possess antioxidant properties and antimicrobial activity. Particularly, antimicrobial additives inhibit the growth and activity of microorganisms responsible for product contamination and deterioration (active 3-4-5). In recent years, polyphenols, which are compounds in which multiple phenol groups are present in a single molecule, have been utilized for their antimicrobial activity (1-3). Ferulic acid (FA) is a natural phenolic compound that belongs to the hydroxycinnamic acid family and is known for its various beneficial properties. Ferulic acid has been found to have antimicrobial properties, which means it can help to inhibit the growth of microorganisms such as bacteria and fungi. The incorporation of ferulic acid into active packaging films has demonstrated to improve their tensile strength, swelling performance, and antifungal activity which can make them more durable and effective in various applications (17-20).

In this study, polyvinyl alcohol based PVA/Boric Acid/Montmorillonite (PVA/BA/MMT) active food packaging film incorporated with FA were synthesized using solution casting method. Then, ferulic acid polyphenol compound at certain weight ratios (0,1,2,3) was added to PVA/BA/MMT nanocomposites to improve their antimicrobial and antifungal properties.

## 2. EXPERIMENTAL SECTION

### 2.1. Materials

PVA with a degree of hydrolysis: 99% was obtained from Sigma Aldrich. Montmorillonite clay was provided by Acros Organics, surface area = 240 m<sup>2</sup>/g. Glycerol and BA were purchased Merck. Ferulic acid (FA, C<sub>10</sub>H<sub>10</sub>O<sub>4</sub>) was purchased was purchased Wuhan ChemFaces Biochemical Co., Ltd.

### 2.2. Active Packaging Films Preparation

The PVA/BA/MMT active packaging films were prepared using the solution-casting method (1). PVA polymer (5 g), MMT (0.1 g) (2% w/w), and boric acid (0.25 g) were added to 100 mL of distilled water. The PVA mixture was heated to 90 °C and stirred continuously until the PVA/BA mixture was homogeneous. 1 g of glycerol was used as a plasticizer and added to the mixture, which was stirred continuously for 2 hours. Various amounts of FA (0%, 1%, 2%, 3%, w/w) were dissolved in 5 mL of distilled water at room temperature. The FA solutions were added to the PVA solution FA solutions were added to PVA solutions and then stirred for 2 hours at 40 °C on a magnetic stirrer. The prepared nanocomposite mixtures were then placed in a glass petri dish and dried at 45 °C for 1 day. The nanocomposite films containing 0%, 1%, 2%, and 3% FA were marked as PVA0, PVA1, PVA2, and PVA3 respectively.

### 2.3. Characterization

#### 2.3.1 X-ray Diffraction (XRD) Analysis

The structural analysis of all samples was performed using a PANalytical/Empyrean X-ray diffractometer with a scanning rate of 0.4/minute, 40 kV, and 40 mA, using Cu K radiation at a wavelength of 0.1546 nm. The d-spacing value (d001) of the samples was made a calculated using the (20), Bragg's equation as following:

$$d = \frac{\lambda}{2 \sin \theta}$$

Where d is the interplanar distance, λ is the wavelength of X-ray beam and θ is the diffraction angle.

#### 2.3.2 Fourier transform infrared (FTIR) spectroscopic analysis

FTIR measurements were characterized the crosslinked PVA and the chemical structure of the PVA/BA/MMT films and by using a Varian/660-IR spectrometer in the range of 4000 cm<sup>-1</sup> to 400 cm<sup>-1</sup> (FTIR).

#### 2.3.4 Transmittance

Optical property of the films, was determined by scanning the percent transmittance in whole visible light region (400-700 nm) using UV-VIS-NIR Spectrophotometer Shimadzu/UV 3600 Plusat at a scanning rate of 60 nm/min (32)..

### 2.3.5 Thermogravimetric Analysis (TGA)

The thermal stability of the pure PVA and nanocomposite films was determined using a Netzsch/STA 449 F3 Jupiter thermal analyzer. The mass of the active food packaging films used was in the range of 6-8 mg in aluminum oxide crucible. The film samples were cut and thermal analysis was performed by heating them up to 600 °C at a heating rate of 10 °C/minute under a nitrogen atmosphere with a purge flow of 20 mL/min (33).

### 2.3.6 Antimicrobial and antifungal activities

The antimicrobial activity of PVA membrane samples was carried out according to the test method (34) AATCC 100 with some modifications. For this purpose, samples sterilized by 25 kG  $\gamma$  irradiation were used and inoculum concentrations of  $1 \times 10^5$  cfu/mL of *Escherichia coli* (*E.coli*, ATCC 25922), *Staphylococcus aureus* (*S. aureus*, ATCC6538), and *Candida albicans* (*C. albicans*) were used. Samples with a surface area of 2 cm<sup>2</sup> were inoculated with 86.8  $\mu$ L of *E. coli* or *C. albicans* inoculum of  $1 \times 10^5$  cfu/mL and incubated at 37 °C for *E. coli* and *S. aureus*, and 25 °C for *Candida albicans* for 24 hours. After incubation, the samples were washed by vortexing with 8.68 mL of phosphate buffer for 1 minute, which was 100 times the volume of the inoculum, and 100  $\mu$ L of the solution obtained after washing was spread on agar petri dishes. Colonies were counted 24 hours after incubation. As experimental control groups, the inoculum concentration of each microorganism was diluted 100-fold and spread on agar petri dishes.

## 3. RESULTS AND DISCUSSION

### 3.1 XRD Analysis

The X-ray diffraction analyses were carried out the morphology of the PVA/BA/MMT incorporated with FA in the region  $2\theta=5-50^\circ$ , as shown in Figure 1. The pattern of pure PVA exhibits three characteristic diffraction peak at  $2\theta = 19,87^\circ$ ,  $22,73^\circ$ , and  $40,99^\circ$ , corresponding peaks of PVA (xrd pva). The peak intensity at  $2\theta = 19,87^\circ$  in the based on PVA films decreased and a new at peak  $2\theta = 20,61^\circ$ .

The XRD pattern of naturel MMT appeared a strong diffraction peak at around  $2\theta = 8,920^\circ$ , corresponding to the d-spacing of 9.91 Å. No diffraction peaks of PVA0, PVA1, PVA2 nanocomposite films were found ranging  $2\theta=5-$

$50^\circ$ . This could be primarily attributed to the MMT silicate layers being in an exfoliated state, where the layers are considerably spaced apart ( $>5$  nm), and the parallel stacking is disrupted (2). But PVA3 nanocomposite film showed that characteristic diffraction peak of clay MMT at  $2\theta = 9,02^\circ$ . These results demonstrate that MMT is exfoliated in the PVA0, PVA1, and PVA2 nanocomposite films, but not in the PVA3 nanocomposite film. The finding suggests that the MMT layers might be predominantly exfoliated or disordered intercalated arrangements in the PVA matrix (1,xrd)

### 3.2 FTIR Analysis

The FTIR spectra of interactions and crosslinking reactions between PVA and BA are showed in Figure 2. The greatest evidence of crosslinking interaction of boric acid with PVA is the covalent bonds established two slight indications O-B-O and B-O-C. The spectra of O-B-O linkage are observed at a frequency of  $665\text{ cm}^{-1}$  in the PVA0 film. The PVA0 film exhibited a new broad peak at  $1286\text{ cm}^{-1}$  corresponding to the B-O-C bond. Looking at the results, it can be seen in Figure 2 that crosslinking occurs between BA, which is used as a crosslinking agent to improve the hydrophobic property of PVA (37).

Figure 3 displays the FTIR spectra of PVA/BA/MMT active nanocomposite films with different weight ratios and FA contents. Pure PVA exhibited characteristic peaks at  $3230\text{ cm}^{-1}$  was assigned -OH stretching, which includes the groups that participate in intramolecular and intermolecular hydrogen bonding. The bands at about  $2923\text{ cm}^{-1}$ ,  $1423\text{ cm}^{-1}$ , and  $1330\text{ cm}^{-1}$  were determined to -CH<sub>2</sub> asymmetric stretching and symmetrical bonding the bands at about  $1145\text{ cm}^{-1}$  and  $1080\text{ cm}^{-1}$  were similar to C-O stretching of the crystalline and amorphous regions of PVA (10,17). The intensity of peaks at  $1145\text{ cm}^{-1}$  and  $1080\text{ cm}^{-1}$  decreased due to the interaction between boric acid and the crystalline regions of PVA. The peak at  $1648\text{ cm}^{-1}$  was assigned C=O stretching of acetate groups remaining in partly hydrolyzed pure PVA. In addition, the characteristic peaks of PVA are given in Table 1. The peak at  $1020\text{ cm}^{-1}$  in MMT added PVA/BA packaging films were assigned to Si-O stretching vibration (38). This peak is observed in all films, but with an increased amount of FA, it has shifted to  $1035\text{ cm}^{-1}$  in the PVA2 film. The characteristic peaks at  $3423\text{ cm}^{-1}$ ,  $1683\text{ cm}^{-1}$ , and  $1280\text{ cm}^{-1}$  in the FTIR spectra of FA correspond to the stretching vibrations of carboxylic acid O-H, carboxylic acid C=O, and carboxylic acid C-O, at  $1502\text{ cm}^{-1}$ ,  $1604\text{ cm}^{-1}$  for aromatic C=C bonds, respectively. (Figure 3) (39).

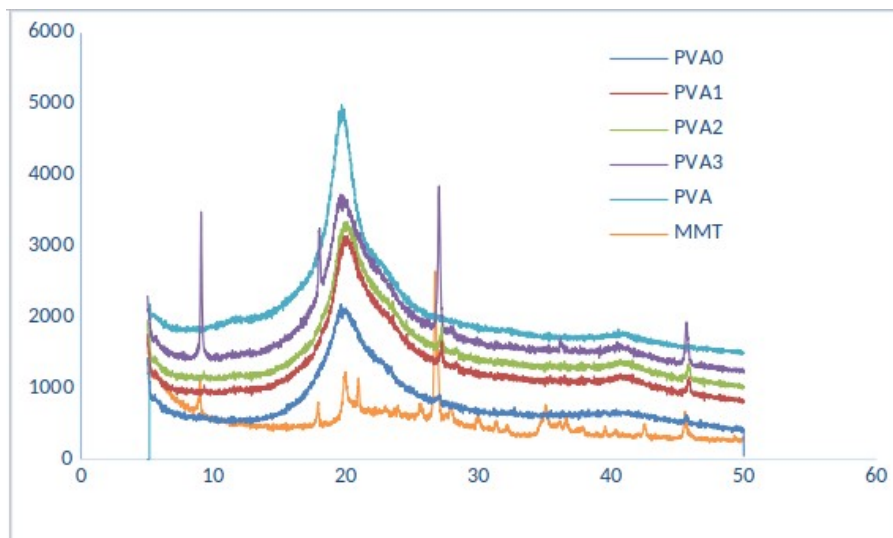


**Figure 1:** XRD patterns of the pure PVA and nanocomposite films incorporated with FA.

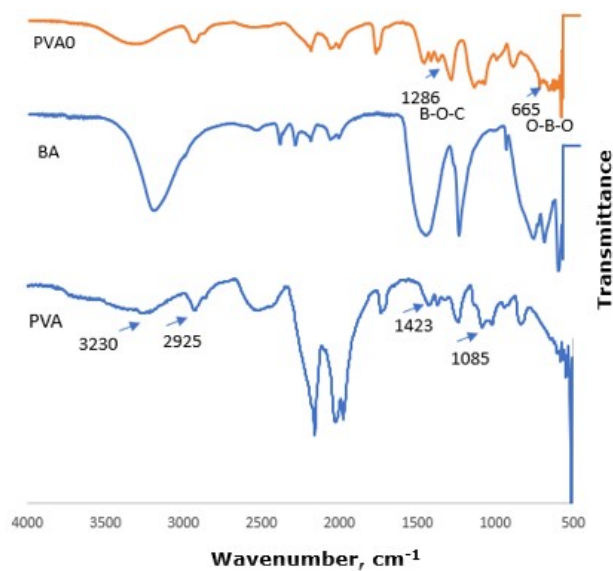


**Figure 2:** FTIR spectra of pure PVA, BA, and PVA0 nanocomposite films.

**Table 1:** The FTIR spectra of pure PVA and its band assignments.

Peaks, $\text{cm}^{-1}$	Assignments
3100-3500	-OH stretching band
2940-2906	-CH <sub>2</sub> asymmetric stretching and symmetric bending
1648	Symmetric stretching vibration of C-O-C band
1425	-CH wagging vibration band
1138-1085	C-O stretching of the crystalline

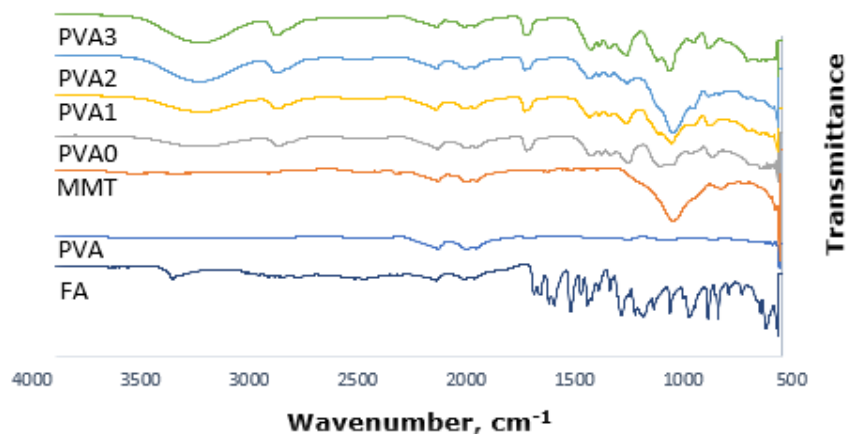


**Figure 3:** FTIR spectra of Pure PVA and nanocomposite films.

### 3.3 Effects of FA on Film Transmittance

Transparency is an important parameter for active packaging films. Films are generally desired to be transparent in order to observe changes such as mold, fungus, and discoloration that may occur in food materials (40,24). The transparent graph of the active packaging films measured with UV-Vis in the range of 400-700 nm wavelength is given in Figure 4. The transmittance of PVA exhibited UV light 89,2% of T700 and 86,7% of T400, indicating the high transparency of PVA. With an increasing amount of ferulic acid, the transmittance values are observed to decrease. In the case of PVA0 nanocomposite film, the T700 transmittance value is 74.2, whereas in the PVA3 film, this value decreased to 62.5. The results have shown that pure PVA has high transmittance properties but decreased transmittance due to the ferulic acid added to enhance and improve the properties of PVA.

### 3.4 Thermogravimetric Analysis

Thermal stability is important in nanocomposite films because high temperature, mechanical stress, or other environmental factors can deteriorate the structural and functional properties of the film. Therefore, thermal stability is a significant factor in maintaining the durability and long-term performance of the film. Additionally,

since high temperature conditions are frequently used in industrial applications, thermal stability is a critical feature for the food industrial production and use of composite films (41). The thermal stabilities of pure PVA and different nanocomposite films were investigated by TGA and the results are given in Figure 5.

According to TGA results, all the nanocomposite films exhibited one minor and two major thermal degradation from room temperature to 600 °C. The onset temperature for thermal degradation of PVA was 297 °C. The first slight weight loss located at around 100-180 °C was attributed to the evaporation of adsorbed moisture and/or water. The second significant weight loss observed at 200-295 °C and 388-395 °C for the PVA and PVA-based active packaging films. The maximum degradation temperature of PVA,  $T_{max}$ , is approximately 460 °C. The  $T_{max}$  value of PVA0 is 470 °C, and it can be observed from the thermogram that the thermal stability slightly increases with the addition of MMT and BA to pure PVA. However, the  $T_{max}$  values of PVA1, PVA2, PVA3 had no significant difference with pure PVA. In this study, it was observed that the addition of ferulic acid to PVA/BA/MMT nanocomposite films did not lead to a significant increase in thermal stability compared to pure PVA.

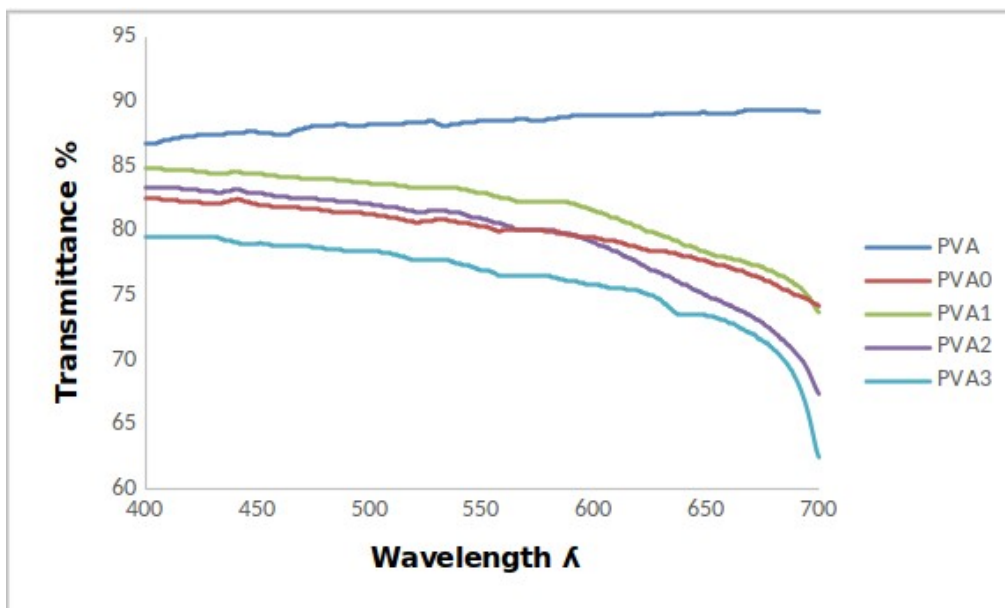


Figure 4: Transmittance spectra of pure PVA and nanocomposite films.

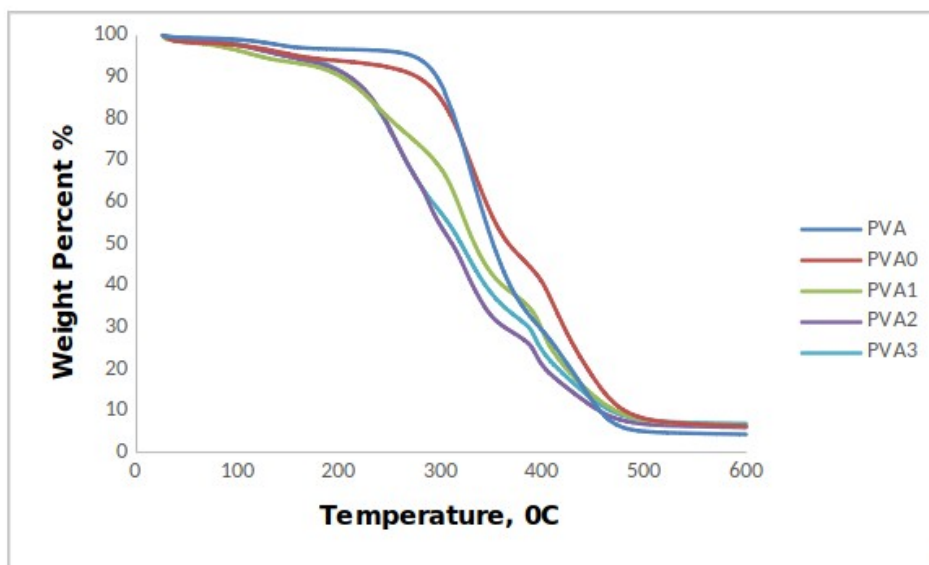


Figure 5: Thermogravimetric analysis (TGA) curve of pure PVA and nanocomposite films.

### 3.5 Antimicrobial and Antifungal Activities

Antimicrobial packaging is a new technology product that protects packaged food products from spoilage that can occur through the contamination of foodborne pathogens (bacteria, parasites, and viruses) and lead to foodborne illness (42). The antimicrobial and antifungal activities of pure PVA and PVA/BA/MMT nanocomposite films incorporated with different content FA were shown in the Tablo 2. After 24 hours of incubation, the average colony counts in the control group were found to be 252 for *E. coli*, 296 for *S. aureus*, and 240 for *C. albicans*.

According to the antimicrobial activity test, more than 300 colonies were detected for all microorganisms in the samples belonging to the PVA group, which was the control group for the samples. This indicates that the PVA group did not have any antibacterial or antifungal effect. When the test results of the PVA0 group were examined, it was determined that it did not have an antibacterial effect against *E. coli* and *S. aureus* but had an antifungal effect against *C. albicans*. The PVA1, PVA2 and PVA5 groups, on the other hand, exhibited antibacterial and antifungal properties against all

microorganisms tested. The results indicate that the addition of a polyphenol compound called ferulic acid to PVA-based nanocomposite films creates antimicrobial activity.

**Table 2.** The cfu (colony forming unit) averages (n=3) of the sample groups inoculated with *E. coli*, *S. aureus*, and *C. albicans*

	E. coli (cfu)	S. aureus (cfu)	C. albicans (cfu)
PVA	>300	>300	>300
PVA0	>300	76,67±11,59	0
PVA1	0	0	0
PVA2	0	0	0
PVA3	0	0	0

#### 4. CONCLUSION

Polyvinyl alcohol-based and ferulic acid added active food packaging films were successfully prepared by solution casting method. The MMT was used as a nanofiller material to improve the mechanical and barrier properties of the nanocomposite films, and it was observed to be exfoliated in the XRD analysis of PVA0, PVA1, and PVA2 nanocomposites. It was demonstrated by FTIR analysis that boric acid added to the nanocomposites improved of PVA hydrophilic properties by forming a crosslink with PVA. The UV-VIS analysis revealed that the transmittance percentage of the nanocomposite films decreased with the increasing amount of FA. According to the TGA results of the nanocomposite films, thermal stability has not significantly changed. However, it was observed that the addition of montmorillonite and boric acid to pure PVA resulted in an increase in the degradation temperature. It was found that active packaging films showed antibacterial activity against *E. coli* and *S. aureus* microorganisms and antifungal activity against *C. albicans* microorganism.

In summary, the sensitivity of the hydroxyl groups in the molecular chain of PVA to water molecules has been eliminated by crosslinking with boric acid. Thus, by alleviating the moisture sensitivity of PVA, it has become suitable for utilization in active packaging films. The addition of ferulic acid to the nanocomposite films synthesized for active packaging films has resulted in gaining antibacterial and antifungal properties.

#### 5. ACKNOWLEDGMENTS

The authors wish to thank Istanbul Gedik University, where nanocomposite film synthesis was carried out in this study, and Sema Akbaba for their useful cooperation.

#### 6. REFERENCES

1. Chen C, Tang Z, Ma Y, Qui W, Yang F, Mei J. Physicochemical, microstructural, antioxidant and antimicrobial properties of active packaging films based

on poly(vinyl alcohol)/clay nanocomposite incorporated with tea polyphenols. *Progress in Organic Coatings*. 2018;123:176-184. Available from: <DOI>.

2. Liu G, Song Y, Wang J, Zhuang H, Ma L, Li C, et al. Effects of nanoclay type on the physical and antimicrobial properties of PVOH-based nanocomposite films. *LWT - Food Science and Technology*. 2014;57:562-568. Available from: <DOI>.

3. Park K, Oh Y, Panda PK, Seo J. Effects of an acidic catalyst on the barrier and water resistance properties of crosslinked poly (vinyl alcohol) and boric acid films. *Progress in Organic Coatings*. 2022;173:107186. Available from: <DOI>.

4. Chen C, Chen Y, ie J, u Z, Tang Z, Yang F, Fu K. Effects of montmorillonite on the properties of cross-linked poly(vinyl alcohol)/boric acid films. *Progress in Organic Coatings*. 2017;112:66-74. Available from: <DOI>.

5. Lim M, Kwon H, Kim D, Seo J, Han H, Khan SB. Highly-enhanced water resistant and oxygen barrier properties of cross-linked poly(vinyl alcohol) hybrid films for packaging applications. *Progress in Organic Coatings*. 2015;85:68-75. Available from: <DOI>.

6. Miyazaki T, Takeda Y, Akane S, Itou T, Hoshiko A, En K. Role of boric acid for a poly (vinyl alcohol) film as a cross-linking agent: Melting behaviors of the films with boric acid. *Polymer*. 2010;51:5539-5549. Available from: <DOI>.

7. Balasubramaniam MP, Murugan P, Chenthamara D, et al. Synthesis of chitosan-ferulic acid conjugated poly(vinyl alcohol) polymer film for an improved wound healing. *Materials Today Communications*. 2020;25:101510. Available from: <DOI>.

8. Kokabi M, Sirousazar M, Hassan ZM. PVA-clay nanocomposite hydrogels for wound dressing. *Macromolecular Nanotechnology*. 2007;43:773-781. Available from: <DOI>.

9. Ochiai H, Fukushima S, Fujikawa M, Yamamura H. Mechanical and Thermal Properties of Poly(vinyl alcohol) Crosslinked by Borax. *Polymer Journal*. 1976;1(8):131-133. Available from: <DOI>.

10. Das Mi Ghatak S. Synthesis of boron nitride from boron containing poly(vinyl alcohol) as ceramic precursor. *Bulletin of Materials Science*. 2012 Feb;35:99-102. Available from: <DOI>.

11. Ochiai H, Fujino Y, Tadokoro Y, Murakami I. Polyelectrolyte behavior of poly(vinyl alcohol) in aqueous borax solution. *Polymer Journal*. 1982;14:423-426. Available from: <DOI>.
12. Lin, HL, Liu WH, Shen KS, Yu TL, Cheng CH. Weak Gel Behaviour of Poly(vinyl alcohol)-Borax Aqueous Solutions. *Journal of Polymerr Research*. 2003;10:171-179. Available from: <DOI>.
13. Lim M,Kwon H, Kim D, Seo J, Han H, Khan SB. Highly-enhanced water resistant and oxygen barrier properties of cross-linked poly(viynl alcohol) hybrid films for packaging applications. *Progress in Organic Coatings*. 2015;85;68-75. Available from: <DOI>.
14. Woo JH, Kim NH, Kim S, Park OK, Lee JH. Effects of the addition of boric acid on the physical properties of Mene/polyvinyl alcohol (PVA) nanocomposites. *Composites Part B: Engineering*. 2020 Oct;199:108205. Available from: <DOI>.
15. Strawhecker KE, Manias E. Structure and properties of poly(vinyl alcohol)/ Na<sup>+</sup> montmorillonite nanocomposites. *Chem. Mater*. 2000;12 (no. 10):2943-2949. Available from: <DOI>.
16. Li C, Hou T, Vongsvivut J, Li Y, She X, She F, Gao W, Kong L. Simultaneous crystallization and decomposition of PVA/MMT composites during non-isothermal process. *Thermochim*. 2015;618:26-35. Available from: <DOI>.
17. Li C, Li Y, She X, Vongsvivut J, Li J, She F, Gao W, Kong L. Reinforcement and deformation behaviors of polyvinyl alcohol/graphene/montmorillonite clay composites. *Sci. Technol*. 2015;118:1-8. Available from: <DOI>.
18. Yang Y, Liu C, Wu H. Preparation and properties of poly(vinyl alcohol)/exfoliated  $\alpha$ -zirconium phosphate nanocomposite films, *Polym. Test*. 2009;28: 371-377. Available from: <DOI>.
19. Johansson C, Clegg F. Effect of clay type on dispersion and barrier properties of hydrophobically modified poly(vinyl alcohol)-bentonite nanocomposites. *Journal of Applied Polymer Science*. 2015;132(28). Available from: <DOI>.
20. Andrade J, Martinez CG, Chiralt A. Physical and active properties of poly (vinyl alcohol) films with phenolic acids as affected by the processing method. *Food Packaging and Shelf Life*. 2022;33:100855. Available from: <DOI>.
21. Rodriguez-Felix F, Corte-Tarazon JA, Rochin-Wong S, et. al. Physicochemical, structural, mechanical and antioxidant properties of zein films incorporated with no-ultrafiltered and ultrafiltered betalains extract from the beetroot (*Beta vulgaris*) bagasse with potential application as active food packaging. *Journal of Food Engineering*. 2022;334:111153. Available from: <DOI>.
22. Bhowmik S, Agyei D, Ali A. Bioactive chitosan and essential oils in sustainable active food packaging: Recent trends, mechanisms, and applications. *Food Packaging and Shelf Life*. 2022;34:100962. Available from: <DOI>.
23. Ahmed W, Haque A, Mohibullah Md, et. al. A review on active packaging for quality and safety of foods: Current trends, applications, prospects and challenges. 2022;33:100913. Available from: <DOI>.
24. Abbas M, Saeed F, Anjun FM, Afzaal M, Tufail T, Bashir MS. Natural polyphenols: An overview. *International Journal of Food Properties*. 2017;20(8):332-338. Available from: <DOI>.
25. Scalbert A, Johnson IJ, Saltmarsh M. Polyphenols: antioxidants and beyond. *The American Journal of Clinical Nutrition*. 2005;81(1):215-217. Available from: <DOI>.
26. Othman L, Slemien A. Antimicrobial Activity of Polyphenols and Alkaloids in Middle Eastern Plants. *Frontiers*. 2019; 10:293-298. Available from: <DOI>.
27. Mallakpour S, Madani M. Transparent and thermally stable improved poly (vinyl alcohol)/Cloisite Na /ZnO hybrid nanocomposite films: Fabrication, morphology and surface properties. *Progress in Organic Coatings*. 2012;74(3):520-525. Available from: <DOI>.
28. Cepeda MV.P, Nastasiienko NS, Kulik TV, Palianytsia BB , Alonso E, Aspromonte SG. Adsorption and thermal transformation of lignin model compound (ferulic acid) over HY zeolite surface studied by temperature programmed desorption mass-spectrometry, FTIR and UV-Vis spectroscopy. *Microporous and Mesoporous Materials*. 2023 Jan; 348:112394. Available from: <DOI>.
29. Qian K, Shen Z Zhang L, iang , Feng T, Zhang L. Preparation of MgF<sub>2</sub>-CaF<sub>2</sub> nanocomposite ceramics with high infrared transmittance. *Journal of the European Ceramic Society*. 2022 Dec; 42(15):7203-7208. Available from: <DOI>.
30. Feng Z, Xu D, Shao Z, Zhu P, Qiu J, Zhu L. Rice straw cellulose microfiber reinforcing PVA composite film of ultraviolet blocking through pre-cross-linking. *Carbohydrate Polymers*. 2022 Nov;296:119886. Available from: <DOI>.
31. Karimi A, Daud WM. Comparison the properties of PVA/Na<sup>+</sup>-MMT nanocomposites hydrogels prepared by physical and physicochemical crossling. *Polymer Composites*. 2014;37(3):897-906. Available from: <DOI>.
32. Gaume J, Gueho CT, Cros S, et.al. Optimization of PVA clay nanocomposites for ultra-barrier multilayer encapsulation of organic solar cells. *Solar Energy Materials and Solar Cells*. 2012;99:240-249. Available from: <DOI>.
33. Krumova M, Lopez P, Benavente R, Mijangos C, Perena M. Effect of crosslinking on the mechanical and thermal properties of poly(vinyl alcohol). *Polymer*. 2000;41(26):9265-9272. Available from: <DOI>.
34. Fei Y, Wang H, Gao W, Wan Y, Fu J, Yang R. Antimicrobial activity and mechanism of PLA/TP composite nanofibrous films. 2014;105:196-202. Available from: <DOI>.
35. El-Gama S, El sayed AM, Abdel-Hady EE. Effect of cobalt oxide nanoparticles on the nano-scale free volume and optical properties of biodegradable CMC/PVA films. *Journal of Polymer and the Environment*. 2017;26:2536-2545. Available from: <DOI>.
36. Strawhecker KE,, Manias E. Structure and Properties of Poly(vinyl alcohol)/Na<sup>+</sup> Montmorillonite Nanocomposites. *Chem. Matter*. 2000;12:2943-2949. Available from: <DOI>.



37. Gao X, Li R, Hu L, Lin J, Wang Z, Yu C, Fang Y, Liu Z, Tang C, Huang Y. Preparation of boron nitride nanofibers/PVA composite foam for environmental remediation. *Colloids and Surfaces A: Physicochemical and Engineering Aspects*. 2020 Nov;604:125287. Available from: [<DOI>](#).

38. Mohamed MB, Heiba ZK, Imam NG. Optical and thermogravimetric analysis of  $Zn_{1-x}Cu_xS$ /PVA nanocomposite films. *Journal of Molecular Structure*. 2018 July; 1163:442-448. Available from: [<DOI>](#).

39. Mroz P, Bialas S, Mucha M, Kaczmarek H. Thermogravimetric and DSC testing of poly(lactic acid) nanocomposites. *Thermochimica Acta*. 2013 Dec;573:186-192. Available from: [<DOI>](#).

40. Zhao W, Xu H, Yanxia L, Xu J, Luan R, Feng. Temperature-dependent transmittance nanocomposite hydrogel with high mechanical strength and controllable swelling memory behavior. *European Polymer Journal*. 2019 March;112:328-333. Available from: [<DOI>](#).

41. Chen X, Wang M, Cheng J, Zhao C, Tang Z. High thermal conductivity, good electrical insulation, and excellent flexibility of FGN/PVA films based on a large sheet and narrow diameter distribution of fluorographene. *Materials Today Chemistry*. 2023 Ap; 29:101422. Available from: [<DOI>](#).

42. Gou J, Lu Y, Xie M, Tang X, Chen L, Zhao J, Li G, Wang H. Antimicrobial activity in Asterceae: The selected genera characterization and against multidrug resistance bacteria. *Heliyon*. 2023 Ap;9(4):e14985. Available from: [<DOI>](#).





## Experimentally and Computational Studies of Nitric Acid Treated Natural Sargassum Algae for Efficient Removal of Crystal-Violet Dye

Hussein S. Mohamed<sup>1</sup> , Zeinab S. Hamza<sup>1</sup>, Wael Z. Tawfik<sup>2</sup>, Nada A. Mohammed<sup>1</sup>, H. R. Abd El-Mageed<sup>3</sup>, N. K. Soliman<sup>4</sup>, Amany H. El-Zairy<sup>1</sup>, and Momtaz Y. Hegab<sup>5,6</sup> 

<sup>1</sup>Chemistry of medicinal and aromatic plants department, Research Institute of Medicinal and Aromatic plants (RIMAB), Beni-Suef University, Beni-Suef 62511, Egypt

<sup>2</sup>Department of Physics, Faculty of Science, Beni-Suef University, Beni-Suef 62511, Egypt

<sup>3</sup>Micro-Analysis and Environmental Research and Community Services Center, Faculty of Science, Beni-Suef University, Beni-Suef City, Egypt

<sup>4</sup>Basic Science Department, Nahda University, Beni-Suef University, Beni-Suef 62511, Egypt

<sup>5</sup>Department of Botany, Faculty of Science, Beni-Suef University, Beni-Suef 62511, Egypt

<sup>6</sup>Research Institute of Medicinal and Aromatic plants (RIMAB), Beni-Suef University, Beni-Suef 62511, Egypt

**Abstract:** In this work, crystal-violet (CV) dye was removed using a chemical carbonization process to create carbonized sargassum algae (CSA), which poses less environmental danger. The produced CSA is examined using a scanning electron microscope and a Fourier-Transform Infrared spectrometer. The following parameters were measured: pH, contact duration, temperature, adsorbent concentration, and starting CV dye concentration. The highest removal % was recorded as 91.17%. at pH 7, 3 hours, 25 °C, 0.01 g of adsorbent dosage, and 100 mg/L initial dye concentration. The kinetic testing indicated that pseudo-second-order was the most effective kinetic model for CV adsorption. According to the isotherms for the adsorption of CV dye, the Langmuir constant (K) was used to measure thermodynamic properties like free enthalpy (H), entropy (S), and energy (G). The Freundlich model, followed by Temkin models, best described the data. The earlier research is supported by computational studies like molecular dynamics (MD) simulation and Monte Carlo (MC) simulation.

**Keywords:** Sargassum, crystal violet, adsorption, kinetics, MD simulation.

**Submitted:** April 26, 2023. **Accepted:** July 13, 2023.

**Cite this:** Mohamed HS, Hamza ZS, Tawfik WZ, Mohammed NA, Abd El-Mageed HR, Soliman NK, El-Zairy HA, Hegab MY. Experimentally and Computational Studies of Nitric Acid Treated Natural Sargassum Algae for Efficient Removal of Crystal-Violet Dye. JOTCSA.2023;10(4):903-18.

**DOI:** <https://doi.org/10.18596/jotcsa.1287989>.

**\*Corresponding author. E-mail:** [h\\_gendy\\_2010@yahoo.com](mailto:h_gendy_2010@yahoo.com), Phone: +201000800296.

### 1. INTRODUCTION

Life and survival depend on access to enough clean water. Dyes, phenols, detergents, pesticides, heavy metals, and other air pollutants that are found in water sources come from domestic, industrial, and agricultural pollution sources.(1, 2). Today, a wide range of companies, including those in the paper,

printing, pharmaceutical, and cosmetics sectors, employ dyes in essential ways to color their goods. Over 20% of the coloring is discharged into the aquatic environment during the coloring process.(3). the crystal violet dye's chemical composition  $C_{25}N_3H_{30}Cl$  is one of these cationic dyes, and it is employed for coating, coloring, and dyeing among other things. Environmental contaminants like CV,

although having a wide range of applications, have been referred to as biohazard dyes and refractory dye molecules that stay in the environment for a long time and have a harmful influence on the ecosystem. (4-6). Industries related to dyes use vast volumes of dyes, which are particularly harmful to aquatic life and even relatively harmless in the aquatic environment (7, 8). The ecological equilibrium of the water and aquatic life is disturbed by dyes because they prevent light from flowing through, absorb it, and reflect it back, triggering a process that prevents photosynthesis (9-11). Effects from the dye release may be felt by those who use water for drinking, washing, bathing, and other activities. Certain teeth can result in allergies, skin problems, and mutagenesis consequences in living organisms(12-15). Numerous methods, including oxidation, clotting, photo-degradation, precipitation, membrane filtration, electric flotations, and ion exchange, have been created as a result of the threat that dyes bring to marine life(16-18) and other physical/chemical techniques have been employed. It also talks about oxidation. However, due to their high prices and various disadvantages, small and medium-sized firms are unable to employ these approaches to manage bulk. The adsorption technique seems to be the most efficient way to treat wastewater due to its simplicity, low cost, reduced energy consumption, ease of operation, negligible effects of highly toxic materials, and the primary quality of emission handled for well-engineered sorption systems.(19). One of the wastewater chemical contaminants unit activities is adsorption (6, 20-27). Activated carbon (AC) is the most widely used adsorbent for treating wastewater or removing contaminants from wastewater(25, 28-33). Flax fiber, sugarcane bagasse, and pine tree wood are just a few of the raw ingredients utilized to create AC(15, 21, 23, 34, 35). Without any surface modification, activated carbon has a very poor adsorption capacity due to its small specific area. In some cases, it becomes crucial to treat the activated carbon to increase its capacity for bonds, which in turn raises its capacity for adsorption. Numerous methods, including physical, chemical, and biological ones, are employed for the surface treatment of activated carbon(35). Treatment of activated carbon, also known as surfactant modification, is essential. Activated carbon is treated with surfactants to create a strong bond with water, increasing the dispersion and solubility of AC in water(6). The period of adsorption depends on how well the thermodynamic and adsorbent mass transfer work (36-38). Marine algae known as seabed have large metal binding capabilities because they feature polysaccharides, proteins, or lipids on the surface of the cell wall that contain functional groups like amino, hydroxyl, carboxy, and sulphate that can serve as binding sites for metals (39-41). The thallus structures that resemble sheets and have a thickness of two cells are created by a

broad region of uniform and active cells in sargassum(23, 42). In this study, experimental factors for the adsorption process, such as mass, pH, temperature, duration of contact, and concentration, were looked at. The Freundlich and Langmuir adsorption isotherm equations were fitted to the equilibrium biosorption data. In order to understand the nature of the system, measurements of thermodynamic parameters were also made. Monte Carlo (MC) simulation and molecular dynamic (MD) simulation studies were carried out to examine the adsorption of crystal violet dye on the carbonized sargassum algae and to determine the desorption sites of crystal violet dye on the surface.

## 2. EXPERIMENTAL METHOD

### 2.1. Collection of Sargassum

Ras Sudr Was Used To Collect Sargassum Algae. Ras Sudr Is Located On The Red Sea Shore Of The Gulf Of Suez At A Longitude Of 32° 43' East And A Latitude Of 29° 35' North. It Is Included In The South Sinai Governorate. Ras Sudr Is Located On The Sinai Peninsula's Western Side, Around 200 Kilometers From Cairo And 60 Kilometers From The Ahmed Hamdi Tunnel Crossing In Suez. Ayn El Sokhna, A Resort On The Opposite Red Shore, Is Also Literally Across The Street. Ras Sudr Has A Coastline Of 95 Kilometers.

### 2.2. Preparation of Carbonized Sargassum Algae

Sargassum was cleaned with water to remove any remaining soil before being dried for 48 hours at room temperature (25 °C). Sargassum was then crushed into little pieces. After soaking in nitric acid (Sigma, 99.99%) for 24 hours, it was dried for another 24 hours at 100 °C. The solid mass was then immersed in filtered water for 24 hours before being dried for 6 hours at 40 degrees Celsius. It was then soaked in sulfuric acid for 6 hours before being dried for 12 hours at 100 °C. The completed product was carbonized for 3 hours at 500 °C.

### 2.3. Characterization

To characterize the CSA derived from sargassum algae, various approaches were applied. FTIR was utilized to examine the chemical structure. An X-ray diffractometer (XRD; type Ultima-IV; Rigaku, Japan) was used to measure CSA. At room temperature, FTIR spectrometer (VERTEX 70 FT-IR) spectra were recorded on ATR discs in the wave number range 4000-600 cm<sup>-1</sup>. A scanning electron microscope (SEM) model JSM-6510LA was used to characterize surface morphology. Samples were made by placing a tiny film on a carbon tube on a stub covered with a thin layer of gold.

### 2.4. Adsorption Experiments

To characterize the CSA derived from sargassum algae, various approaches were applied. FTIR was utilized to examine the chemical structure. An X-ray diffractometer (XRD; type Ultima-IV; Rigaku, A set of dye solutions of varied concentrations is created. A series of adsorption tests were performed on CSA

adsorbent under varied reaction circumstances, including beginning dye concentration (10, 25, 50, and 100 mg/L), temperature ranging from 25 to 60 °C, CSA dosage of 0.01-0.04 g per 50 mL of solution, and solution initial pH (2-10). The contacting time in both tests was 180 minutes, and the solution volume was 50 mL. The shifts in the tested CV dye concentration were determined using a UV-vis spectrophotometer and its characteristic absorption peaks (max= 592 nm). The first set of experiments were conducted with the adsorbent dosage remaining constant at 0.01 g per 50 mL of solution, the pH remaining constant at 7, the temperature remaining constant at 25 °C, and the dye concentration varying between 10, 25, 50, and 100 mg/L. The purpose of this experiment was to determine the effect of starting dye concentration on the percentage of CV removal over CSA adsorbents. In the second series, the dye starting concentration remained constant at 100 mg/L, the pH was set to 7, the temperature was set to 25°C, and the adsorbent dosage was varied from 0.01 to 0.04 g per 50 ml of solution. The purpose of this test was to determine the influence of adsorbent dosage on the percentage of CV dye removal over CSA adsorbents. The third series of studies involved adjusting the temperature from 25 °C to 60 °C while keeping the dye starting concentration at 100 mg/L, pH at 7, and adsorbent dosage at 0.01 g per 50 mL of solution constant. The purpose of this experiment was to determine the effect of temperature on the percentage of CV removed by CSA adsorbents. The third set of trials entailed adjusting the solution's starting pH from 2 to 10, while keeping the dye initial concentration constant at 100 mg/L, at a temperature of 25 °C, and with an adsorbent dosage of 0.01 g per 50 mL of solution. The purpose of this experiment was to examine the effect of pH on the percentage of CV dye removal over CSA adsorbents. By adding dilute HCl and NaOH dropwise, the pH was adjusted to the right amounts. Equations (1) through (3) can be used to calculate the amount of dye extracted by sargassum adsorbents at equilibrium ( $q_e$ (mg/g)), the amount of dye removed by sargassum adsorbents at any time ( $q_t$ ), and the dye removal percentage. (43, 44).

$$q_e = (C_0 - C_e) \frac{V}{m} \tag{1}$$

$$q_t = (C_0 - C_t) \frac{V}{m} \tag{2}$$

$$\text{Dye removal \%} = \frac{(C_0 - C_t)}{C} \times 100 \tag{3}$$

where  $C_0$  denotes the initial dye concentration in mg/L,  $C_t$  denotes the dye concentration in mg/L over time  $t$ ,  $C_e$  denotes the dye concentration in mg/L at equilibration, and  $m$  denotes the CAB  $V$  is the solution volume in milliliters, and  $m$  is the mass in milligrams.

### 2.5. Kinetic Studies

The kinetics of CV adsorption studies on CSA were carried out using 0.01 g of adsorbent at CV concentrations of 10, 25, 50, and 100 mg/L, adsorption periods ranging from 10 to 180 minutes, temperatures of 25 °C, and pH of 7. Adsorption kinetics were evaluated using models such as pseudo first order, pseudo second order, Elovich, and intra-particle adsorption.

#### 2.5.1. Pseudo-first-order model

The Lagergren's pseudo-first-order equation (45)

$$\log(q_e - q_t) = \log(q_e) - K_1 t / 2.303 \tag{4}$$

Where  $q_e$  and  $q_t$  are the amounts of dye absorbed on the CSA at equilibrium and the amount of dye absorbed at any time  $t$ , respectively.  $K_1$  the constant rate of the pseudo first order.

#### 2.5.2. Pseudo-second-order Model

Pseudo-second-order model is represented by following equation formulated by (46)

$$\frac{t}{q_t} = \frac{1}{K_2} q_e^2 + \frac{t}{q_e} \tag{5}$$

where  $K_2$  is the constant rate of the pseudo second order. The parameters of kinetic model with  $R_2$  are compared in the Table 2.  $R^2$  values show that the pseudo second order is better than the other.

#### 2.5.3. Intraparticle diffusion model

It is represented by using the following equation(47)

$$q_t = K_{int} t^{1/2} + C \tag{6}$$

where  $K_{int}$  is the intraparticle diffusion constant and  $C$  is the intercept.

#### 2.5.4. Elovich kinetic model

The equation of it has the following form(48)

$$\frac{q}{q_e} = \frac{1}{\beta q_e} \ln(\alpha \beta) + \frac{1}{\beta q_e} \ln t \tag{7}$$

where,  $\alpha$  is the initial adsorption rate and  $\beta$  is the relationship between the degree of surface coverage and the activation energy involved in the chemisorption.

### 2.6. Adsorption isotherm

It depicts the distribution of the solute in two phases (liquid and adsorbed). The Langmuir, Freundlich, and Temkin isotherms were used to research adsorption isotherms.(49)

#### 2.6.1. The Langmuir isotherm

It is used, for homogeneous adsorption, and its linearized form can be defined by the equation below (50).

$$\frac{C_e}{q_e} = \frac{1}{K_a Q_0} + \frac{C_e}{Q_0} \quad (8)$$

where  $q_e$  (mg/g) and  $C_e$  (mg/L) are the amounts of dye adsorbed per unit mass of adsorbent and unadsorbed dye concentration in the solution,  $Q_0$  is the maximum amount of dye adsorbed per unit mass of adsorbent on the entire monolayer surface, and  $K_a$  is a constant related to the affinity of the binding sites.

### 2.6.2. Freundlich isotherm model

This is used for heterogeneous surface at different temperatures. It has the following form (51):

$$\log q_e = \log k_f + \log \frac{C_e}{n} \quad (9)$$

where  $k_f$  is the Freundlich constant, and  $1/n$  is the heterogeneity factor.

### 2.6.3. Temkin isotherm

It has the following form:

$$Q_e = BT \ln KT + BT \ln C_e \quad (10)$$

where,  $B T$  is a temperature dependent constant related to the heat of adsorption  $K T$  and is the equilibrium constant. The degree of favorability of the Langmuir isotherms for the equilibrium data could be predicted from the value of ( $R_L$ ) the dimensionless separation factor constant that can be determined from Equation 11 (52).

$$R_L = \frac{1}{1 + K_L C_{max}} \quad (11)$$

where  $C_{max}$  represents the maximum initial DR concentration.

### 2.7. Thermodynamic Parameters

Thermodynamic parameters such as standard free energy, enthalpy, and entropy are used (53). The following calculations were used to assess the effect of heat on the adsorption period at various dye concentrations.

$$K_{id} = \frac{q_e}{C_e} \quad (12)$$

$$\Delta G^0 = -RT \ln K_{id} \quad (13)$$

$$\ln K_{id} = \frac{\Delta S^0}{R} - \frac{\Delta H^0}{RT} \quad (14)$$

Where  $K = b$  is the adsorption equilibrium constant,  $R$  is the gas constant (8.314 J/K mol),  $T$  is the absolute temperature,  $\Delta H^0$  enthalpy,  $\Delta S^0$  entropy  $\Delta S$  and  $\Delta G^0$  free energy.

### 2.8. Computational Details

#### 2.8.1. Monte Carlo (MC) simulation

MC simulation was conducted in this work to study the adsorption of crystal violet dye on the carbonized sargassum algae and to find the desorption sites of crystal violet dye on the carbonized sargassum algae surface. MC simulation was carried out by Adsorption Locator module as shown in this study(54, 55) using The COMPASS force field (Condensed-phase Optimized Molecular Potentials for Atomistic Simulation Studies) as a force field and use current in the charges section. The basic principles of MC simulation used in this work have been described by Frenkel and Smit (56).

#### 2.8.2. Molecular dynamics (MD) simulation

In the MD simulations, the electrostatic and van der Waals terms were treated with Ewald and group-based methods, respectively. The MD was simulated under NPT ensemble for 1 ns, followed by isothermal-isobaric (NPT) conditions at 1 atm and 300 K for 4 ns, with time step of 1 fs. The temperature and pressure were controlled by Nose thermostat and Berendsen barostat, respectively. The velocity Verlet algorithm was used in the integration of the equations of motion (57). The theoretical background of MD simulation is done according to this study (55).

## 3. RESULTS AND DISCUSSION

### 3.1. Analysis of Carbonized Sargassum Algae

FTIR and SEM were performed to analyze the chemical composition.

#### 3.1.1. FTIR spectrum

After loading the crude powder of Nitric acid-treated natural sargassum algae into the FT-IR, the primary functional group of the components was separated based on the peak ratio. The functional groups of bioactive components are denoted by the peak values of the FTIR spectrum (Figure 1 and Table 1). In the FT-IR spectrum of Nitric acid-treated natural sargassum algae, peaks at 3722, 3375, 2954, 2412, 2470, 2353, 2206, 1494, 1363, 1222, 1078, 871, 732, 628 and 559  $\text{cm}^{-1}$  were discovered. The stretching vibrations of CH, C-C, and C-O in solid band, as well as C-O stretch mode in signals at 3375-559  $\text{cm}^{-1}$ , mirrored the axial position stretching vibrations of OH. According to research, the absorption bands between 1100 and 1000  $\text{cm}^{-1}$  are crucial for carbohydrates and polysaccharides, pointing to a variety of mechanisms such as C-H deformation, C-O or C-C stretching (58, 59). The toxic interaction sites of algae's carboxyl, amino acid, and hydroxyl groups were investigated using FT-IR spectra of seaweed extracts (60, 61). A new survey found the bands in diverse materials at significantly different frequencies, with peaks of 1222 and 1078  $\text{cm}^{-1}$ . Carbohydrates were found to be the most effective absorbers between 1200 and 1000  $\text{cm}^{-1}$  in those samples (62). In nucleic acids, as in a variety of other molecules, identical absorption bands in the same spectral area of similar functional groups were found.

3.1.2. SEM analysis

Scanning electron micrographs (SEM) of carbonized sargassum algae at low and high magnification are shown in Figure 2. When the sargassum algae was treated with nitric acid at high temperatures, it disintegrated dramatically and the surface of the sample began to shrink, possibly due to nitric acid's partial loss of hemicellulose. Furthermore, the high temperature may have caused the cellulose fibers to be liberated from their initial clusters.

3.2. Optimization of Parameters

3.2.1. Dye's initial concentration

Figure 3 shows how dye starting concentrations and contact time affect removal percentages and adsorption capacities when CSA is used as an adsorbent. Figure 3 demonstrates that with an initial concentration of 100 mg/L, the adsorption percentage for diffuse CV dye achieved 91.17 %.

**Table 1:** FTIR peak value of Nitric acid-treated natural sargassum algae.

S. No.	Peak Value	Spectroscopic Assignments	Functional Groups
1.	2375	O-H stretch, H-bonded	Alcohols, Phenols
2.	2353	O-H stretch	Carboxylic acids
3.	2954	-C≡C- stretch	Alkynes
4.	1631.080	C-C stretch (in-ring)	Aromatics
5.	1363,1494,1222	C-H bend	Alkanes
6.	1078	C-O stretch	Alcohols, Carboxylic acids, Esters, Ethers
7.	871,732,628,559	-C≡C-H: C-H bend	Alkynes

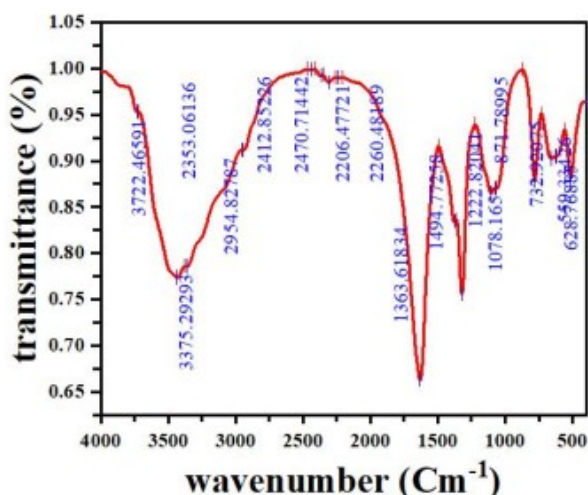


**Figure 1:** FT-IR of the crude powder of Nitric acid-treated natural sargassum algae.

The presence of a large number of free adsorption sites on the adsorbent surface can explain the quick adsorption rate observed during the primary stage of adsorption processes. The adsorbed dye molecules fill the exposed areas over time, generating in a repulsive force between the adsorbate scatter CV dye molecules on the CSA surface and those in the bulk liquid form. When it comes to CSA, the percentage of diffuse CV dye removal normally increases as the dye level

increases. Figure 3 shows that when the original diffuse CV dye concentration increases, so does the sum of adsorbed dyes. This could be attributable to an increase in concentration gradient as diffuse CV dye starting concentration increases. As a result, the driving power increases and is required to overcome the resistance to mass transfer between adsorbate and adsorbent (43, 63).

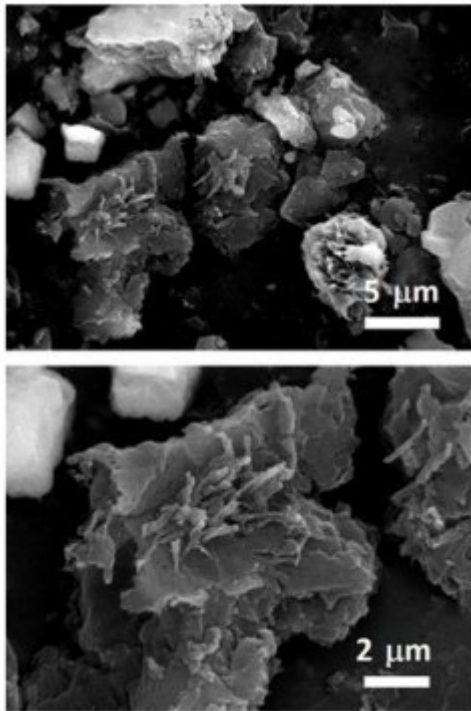


**Figure 2:** SEM images of carbonized sargassum algae.

**3.2.2. Effect of adsorbent weight mass**

We researched the effect of CSA adsorbent doses on the removal percent of disperse crystal violet dye to establish the optimal adsorbent weight that gives the highest performance in order to calculate the wastewater treatment cost per unit of disperse crystal violet dye using CSA adsorbent. Figure 4(a) depicts the influence of CSA weight on the scatter crystal violet dye removal percent. The dye removal % increases as the CSA weight increases from 0.01 to 0.04 g per 50 mL of disperse crystal violet dye solution at an initial concentration of 100 mg/L at 25°C and pH 7. The dye removal percentage improved to 91.17 %, which may be attributed to increased surface area and the number of surface-active sites accessible for adsorption as adsorbent dosage was raised. (64). The best adsorption at dose 0.01 g.

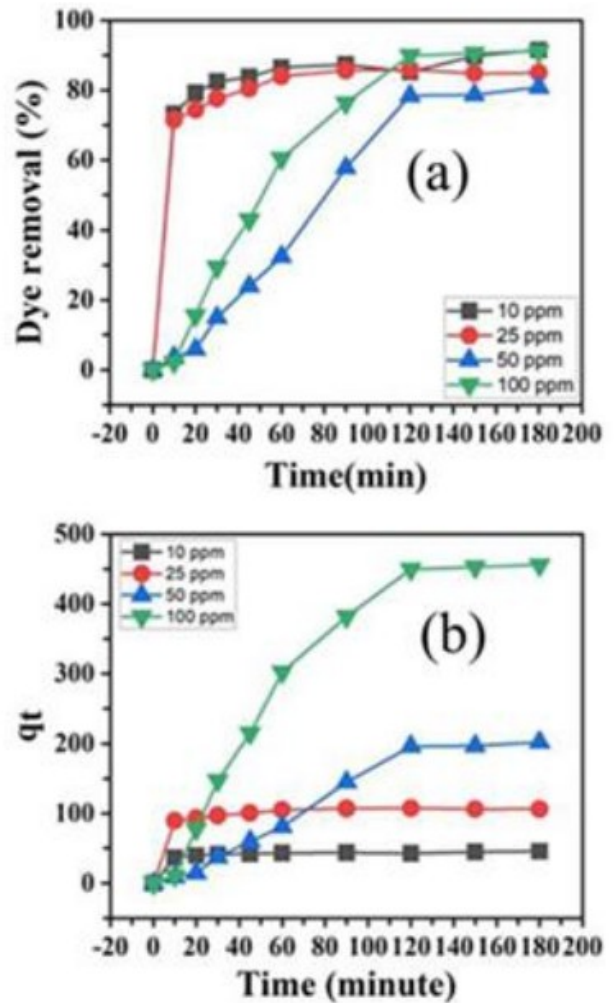


**Figure 3:** Effect of CV dye concentrations and contact time on (a) the removal % of dye adsorbed and (b) the amount of dye adsorbed at 25 °C and pH 7 by 10 mg of adsorbent.



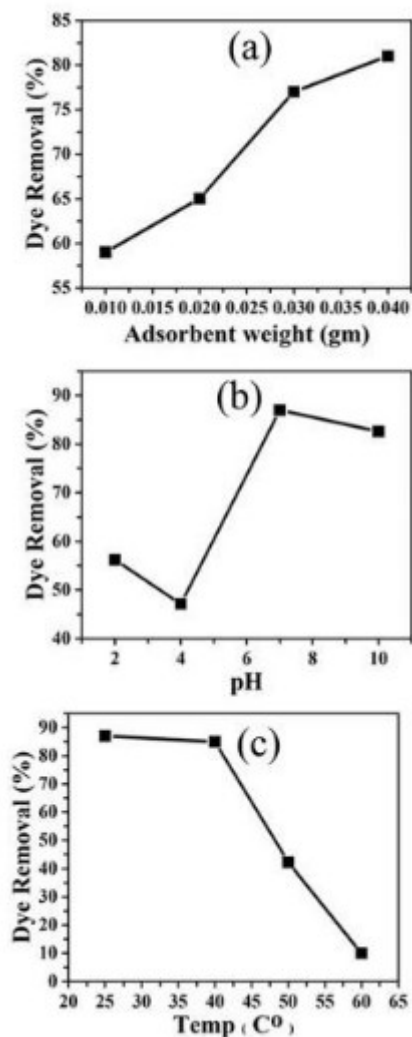


**Figure 4:** Effect of adsorption conditions on the removal % of CV dye by carbonized sargassum algae. Where (a) represent the effect of adsorbent weight. (b) represent the effect of Initial pH of the solution. (c) represent the effect of adsorption temperature.

**3.2.3. Initial pH of the solution**

The pH regulates the amount of electrostatic charge on the sorbent and sorbate. Because of their effect on ionization/dissociation of the sorbent molecules and their effect on the adsorbent surface, pH of the solution plays an important role in adsorption power (65). The effect of the initial pH values of the aqueous dye solutions on the removal percent of diffuse CV dye using CSA sorbent is seen in Figure 4(b). Because of the high concentration of hydrogen (H+) ions and the protonation of the adsorbent base, the elimination percentage generally increases as the pH value increases from 2 to 7 (66). The dye anions are drawn strongly to the positively charged adsorbent surface (67, 68). In other words, as the pH of the CSA increases, the surface becomes negatively charged, causing the polarization of the electric double layers to reverse. As a result, as seen in Figure 2, the adsorption percentage of diffuse CV

dye decreases (b)(69). The maximum amount of adsorbed at pH 7.

**3.2.4. Effect of adsorption temperature**

The temperature effect on the adsorption of industrial disperse CV dye over CSA was studied at four different reaction temperatures (25 °C, 40 °C, 50 °C, and 60 °C), and the results are shown in Figure 4. (c). The dye removal percentage for CSA falls significantly as the temperature rises from 25 °C to 60 °C. The negative value H (see section (3-5) thermodynamic study) confirms that the adsorption of disperse CV dye onto CSA was an exothermic phase. The higher temperature stability of CSA adsorbent demonstrated that temperature had little effect on the adsorption forces between the adsorbent (CSA active sites) and adsorbate (disperse CV dye molecules)(70). The higher attraction between adsorbate active sites and ions of dye molecules resulted in the beneficial adsorption of CV at a relatively low temperature. The percentage of diffuse crystal violet dye removal decreased as the temperature increased from 25°C to 60°C. 25°C is the optimal temperature for diffuse crystal violet dye adsorption over CSA adsorbent.

**3.3. Adsorption Isotherm**

The statistical significance of R<sup>2</sup> (the correlation coefficient) for the linear plots of Ce/qe versus Ce, log qe against log Ce and qe against Ln Ce was the criteria by which the data fitting to the Langmuir, Freundlich, and Temkin isotherms was checked (Figure 5). The estimated values of Q<sub>0</sub>, K<sub>L</sub>, K<sub>F</sub>, and 1/n, K<sub>T</sub>, and B, and R<sup>2</sup> were determined from the linear plots and reported in Table 2. CV adsorption on CSA adsorbent does not follow the Temkin and Langmuir isotherm models (Table 2). The Freundlich isotherm model has the maximum R<sup>2</sup> value; the adsorption mechanism almost follows the Freundlich isothermal model. As a result, the dye is eliminated at the active sites of the CSA adsorbent on a single surface plate, and the adsorbed CV molecules do not react with one another. The R<sup>2</sup> value determined by the Langmuir isotherms at 25 °C was 0.2092. The value of R<sub>L</sub> is 1, meaning that the adsorption of CV in the study case is beneficial (2). The overall adsorption potential of CSA according to the Langmuir adsorption isotherm is 666 mg/g.

**3.4. Adsorption Kinetics**

To study the most suitable adsorption kinetics model, the adsorption process of CV on CSA under various initial dye concentrations was followed. The first-order, second order, intraparticle diffusion and Elovich kinetics linear graphs were represented by plotting ln (qe - qt) versus t, versus t, against and qt versus ln t, respectively, as shown in Figure 6(a-d), in order. The adsorption kinetics parameters k<sub>1</sub>, k<sub>2</sub>, k<sub>3</sub>, q<sub>e</sub>, I, β, and α of the evaluation model in addition to R<sup>2</sup> were calculated from the linear graph and depicted in Table 3. The linear fit and regression coefficient values (Table 3) for all the investigated kinetic models verified that the pseudo-second-order model adequately manages CV adsorption into CSA. Similarly, the values of q<sub>e</sub> Exp. (measured q<sub>e</sub>)

and  $q_e$  (calculated  $q_e$ ) obtained from a pseudo-second order plot of all CV concentrations agree well (Table 3). The  $k_1$  value (pseudo-secondary rate constant) and the CV concentration tested have an inverse relationship.

**Table 2:** Isotherm constants for CV adsorption onto 10 mg algae at 25 °C and pH 7.

Langmuir isotherm			
$Q_o$ (mg/g)	$K_L$ (L/mg)	$R_L$	$R^2$
666	0.71	0.013	0.2092
Freundlich isotherm			
1/n	$K_F$	$R^2$	
0.79	47.8	0.8368	
Temkin isotherm			
B (J/mol)	$K_T$ (L/mol)	$R^2$	
118.5	1.35	0.5456	

**Table 3:** Parameters of the kinetic models for CV dye adsorption onto 0.01 g of algae at 25°C and pH 7.

First order kinetic model					
Dye concentration (ppm)	10	25	50	100	
K	0.007	0.010	0.011	0.015	
$Q_e$	2.9	4.2	12.1	18.1	
$R^2$	0.5458	0.7250	0.8908	0.9345	
$q_{eexp}$	45.7	106.2	202.1	455.8	
Second order kinetic model					
K	$5.6 \times 10^{-3}$	$3.5 \times 10^{-3}$	$3.6 \times 10^{-6}$	$1.2 \times 10^{-6}$	
$q_e$	45.8	108.3	-525	-1428	
$R^2$	0.9985	0.9996	0.2193	0.0347	
$q_e$ exp	45.7	106.2	202.1	455.8	
Elovich kinetic model					
$\beta$ (g/mg)	0.366	0.152	0.012	0.005	
$\alpha$ (mg/min)	$2.5 \times 10^5$	$5.8 \times 10^5$	6	15.5	
$R^2$	0.9166	0.9112	0.9078	0.9769	
Intraparticle diffusion kinetic model					
K	2.3	5.6	18.6	42	
I	20.5	49.5	-43.5	-60.1	
$R^2$	0.5449	0.5410	0.9128	0.9391	

A straight line in the graph of  $q_t$  versus  $t^{1/2}$  suggests that the intraparticle diffusion model is applicable. The slope and intercept of the plot can be used to calculate  $k_2$  and I, and the results are seen in Table 3. The  $R^2$  values (correlation coefficients) obtained from the model are relatively

small and unsatisfactory; additionally, the value of the intercept  $I$  is not zero, indicating that the intraparticle diffusion model may not be the only rate-controlling factor in deciding the kinetics of the adsorption mechanism. In comparison to the pseudo-first order, Elovich kinetics model, and intraparticle diffusion kinetic models, the pseudo-second-order kinetic model obtained a respectable correlation coefficient, indicating that CV adsorption on the CSA follows the pseudo-second-order rate model.

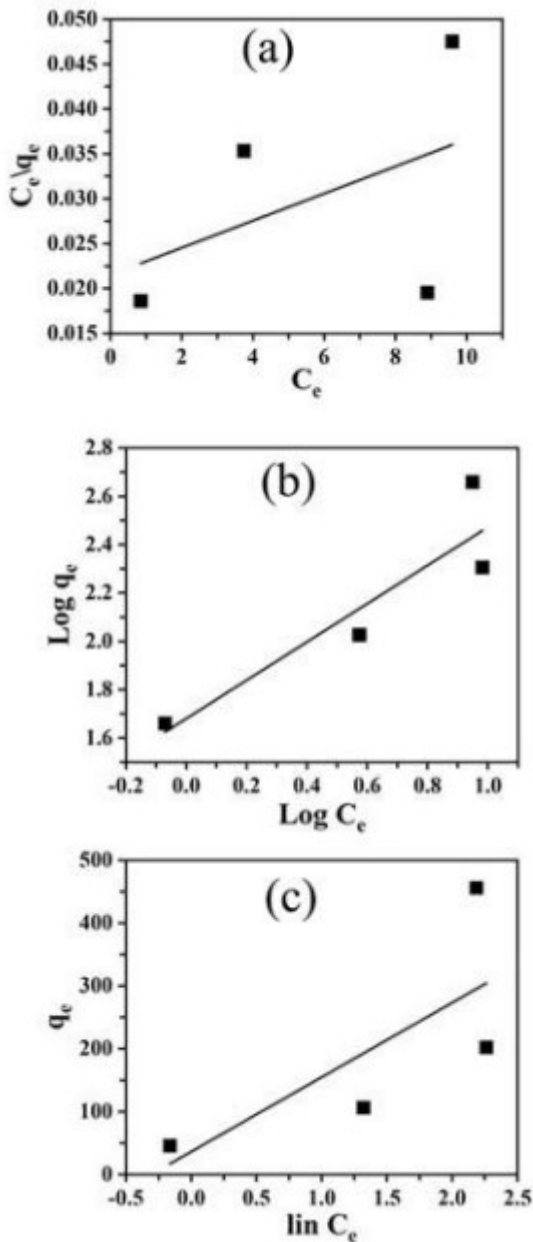


**Figure 5:** Plots of adsorption isotherm for the adsorption of CV dye by 10 mg of adsorbent at 25 °C and initial pH of the solution 7 where (a) represents Langmuir isotherms model, (b) Freundlich isotherms model and (c) Temkin isotherms model.

According to the data in Table 3, the pseudo-second-order paradigm is dominant. The pseudo-second-order adsorption process has two steps. The first step is an outward diffusion stage, in which CV molecules migrate from both sides of the solution to the CSA's outer surfaces. This is followed by a second stage in which CV molecules adsorb and adhere to the surfaces of CSA.

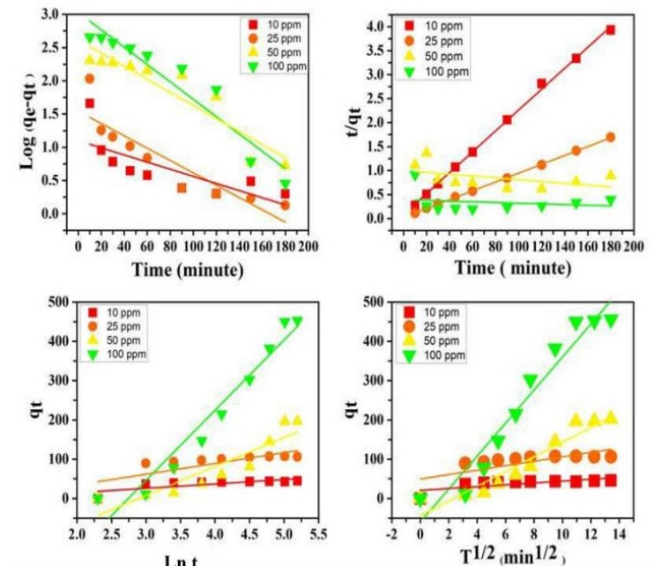


**Figure 6:** Sorption kinetics of CV dye at 25 °C and pH 7 by 10 mg of adsorbent where a) Represent Pseudo-first order, (b) Pseudo-second order, (c) Elovich kinetic model and (d) Intra-particle sorption.

### 3.5. Thermodynamic Study

Table 4 shows the thermodynamic parameters derived from CV adsorption on CSA adsorption thermodynamics. The negative  $\Delta G$  value in Table 4 indicates that CV adsorption is a random operation. The change of the value of  $\Delta G$  to a more correct value at higher temperatures shows that the adsorption mechanism is unfavorable at higher temperatures. The  $\Delta G$  value ranges from -9.7 to 1.9 kJ/mol. These values are also within the physical adsorption range of  $\Delta G$  (the physical adsorption range of  $\Delta G$  is -20-0 kJ/ mol range), indicating that the adsorption mechanism on CSA is physical. The "n" value calculated by the Freundlich isotherm measurement model also confirms this finding, with a value greater than unity, representing a physical adsorption mechanism (71). Similarly, the RL value ranges between 0 and 1, indicating that CV adsorption is favorable under experimental conditions (72). The fact that the H value is negative indicates that the CV adsorption on CSA is an exothermic operation. The -ve value of S indicates a reduction in randomness at the solid/liquid interface as a result of CV adsorption on the surface of CSA (73).

### 3.6. MC Simulation

The lowest configuration obtained due to the adsorption of crystal violet dye on the carbonized sargassum algae surface in dry system (no solvent) is summarized in Figures 7. The aim of MC simulation is studying the adsorption of crystal violet dye on the carbonized sargassum algae and to find the desorption sites of crystal violet dye on the carbonized sargassum algae surface. The adsorption ( $\Delta E_{ads}$ ), interaction ( $E_{int}$ ), and deformation ( $E_{def}$ ) energies as well as substrate-adsorbate configurations ( $dE_{ads}/dNi$ ), in which one of the adsorbate components has been removed, of crystal violet dye absorbed on the carbonized sargassum algae surface is displayed in Table 5. The crystal violet dye molecule has different hydrogen bond (HB) donor and acceptor sites. Thus, the oxygen atom of the cellulose carbonized sargassum algae has formed hydrogen bond with the hydrogen atom of crystal violet dye molecule with distance (1.70 Å) as shown in Figure 7.  $\Delta E_{ads}$  crystal violet dye absorbed on the carbonized sargassum algae surface is negative which revealed that the adsorption of crystal violet dye absorbed on the carbonized sargassum algae surface is exothermic, energetically favorable and spontaneous, due to the existence of the intermolecular interactions. Also, it can be observed that the crystal violet dye absorbed on the carbonized sargassum algae surface following a parallel mode, which confirms the strong interactions between the crystal violet dye and the carbonized sargassum algae surface atoms. Analysis of the molecular structures of the crystal violet dye and the carbonized sargassum algae surface shows that the adsorption of the crystal violet dye onto the carbonized sargassum algae surface may be related to the contribution of the electrons of nitrogen, and oxygen (chemical adsorption). Furthermore, the Van Der Waals dispersion forces can also contribute to catch the crystal violet dye towards the carbonized sargassum algae (physical adsorption) which confirm the results obtained in the experimental part.

**Table 4:** Thermodynamic parameters for adsorption of CV dye onto algae.

Temperature (K)	$\Delta G$ (kJ/mol)	$\Delta H$ (kJ/mol)	$\Delta S$ (kJ/mol. K)
298	-9.7		
313	8.4		
323	-3.2	-108.9	-0.328
333	1.9		

**Table 5:** Adsorption energies (kcal/mol), Rigid adsorption energy, and Deformation energy, and substrate-adsorbate configurations ( $dE_{ads}/dNi$ ) for the adsorption configuration of crystal violet dye on the algae doped activated carbon surface.

Adsorption energy	Rigid adsorption energy	Deformation energy	DR: $dE_{ads}/dNi$
-94.70	-34.39	-93.76	-651.21

### 3.7 MD Simulation

The MD simulation was used to investigate the influence of the presence of water solvent molecules on the adsorption of crystal violet dye on the carbonized sargassum algae surface, in which the configuration of crystal violet dye absorbed on the carbonized sargassum algae surface obtained from MC simulation was simulated in explicit water using MD. The ultimate simulation conformation of crystal violet dye carbonized sargassum algae was shown in Figure 8. The water molecules of aqueous solution moved freely to interact with the crystal violet dye and the carbonized sargassum algae during the simulations. MD snapshot at 5000 PS of the adsorption of crystal violet dye absorbed on the carbonized sargassum algae is shown in Figure 8. The crystal violet dye has different hydrogen bond (HB) donor and acceptor sites, and thus, it has formed several hydrogen bonds with the carbonized sargassum algae atoms. Also, the oxygen atoms of the carbonized sargassum algae were formed HBs with the hydroxyl hydrogen atoms of the crystal violet dye molecule. Figure 9 display that crystal violet dye molecule formed coordination bonds with carbonized sargassum algae atoms in water. In water system, intramolecular HBs between the functional groups of the crystal violet dye molecule, as well as HBs between crystal violet dye with water molecules, were observed. Thus, the MD simulation confirms that crystal violet dye is still interacts with the carbonized sargassum algae atoms even in presence of water molecules. Radial distribution function (RDF) was computed from the MD simulation to gain more insights into the stability of crystal violet dye- carbonized sargassum algae surface complex in water explicitly. This RDF can help us to understand the interaction between crystal violet molecule dye and the carbonized sargassum algae surface. RDF explained as the probability of locating particle "B" within the range ( $r+dr$ ) of a particle A, and usually expressed as  $g(r)$ . It was used to investigate the interaction between crystal violet molecule dye and the carbonized sargassum algae surface, as well as describe the formation of hydrogen bonds with water. Figure 10 shows the RDF obtained due to the adsorption of crystal violet molecule on the carbonized sargassum algae surface atoms. As it can be seen from Figure 10 that the bonds RDF obtained due to the adsorption of crystal violet molecule on the carbonized sargassum algae surface atoms has a bond length= 2.3 Å. RDFs reveal that crystal violet

still interacts with the carbonized sargassum algae surface in the presence of water molecules.

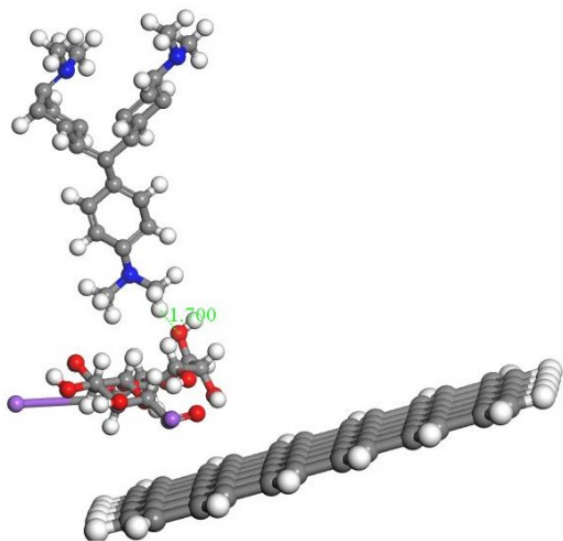


**Figure 7:** The adsorption configurations of the crystal violet dye onto the carbonized sargassum algal surface, obtained from MC simulation.

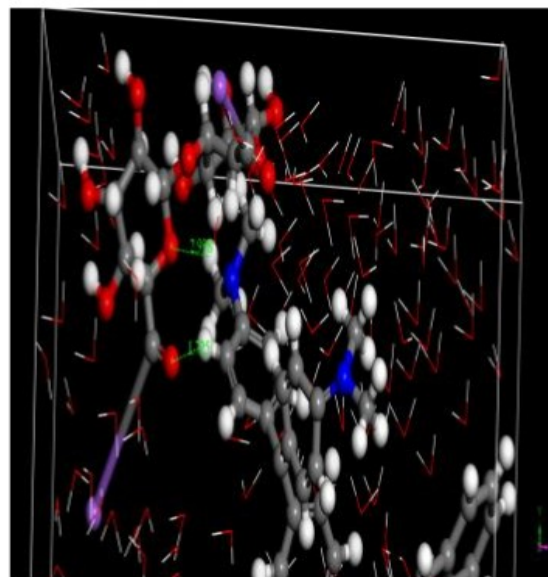


**Figure 9:** MD snapshots at 5000 ps of the adsorption of crystal violet dye on the carbonized sargassum algae surface, the bond length is in Ångströms.

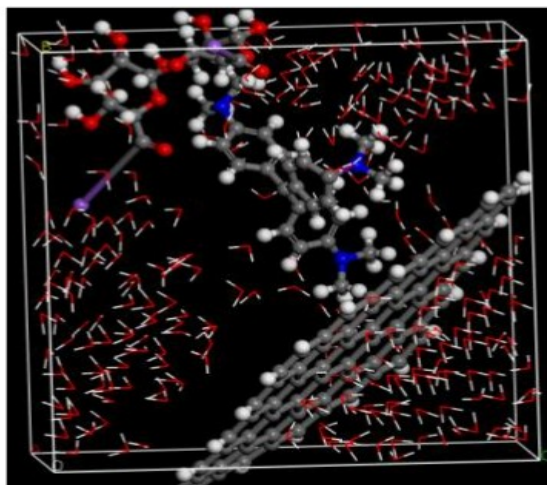


**Figure 8:** Simulation conformation of crystal violet dye absorbed on the carbonized sargassum algae.

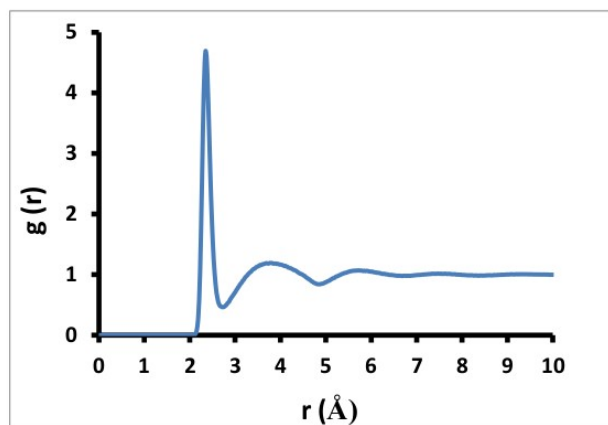


**Figure 10:** The RDFs for the adsorption of crystal violet dye on the carbonized sargassum algae surface atoms in the presence of water at 5 ns.

**Table 6:** Comparison among adsorption capacities of Crystal violet dye onto different adsorbents.

Seaweed Species	Sorption capacity (mg g <sup>-1</sup> )	Refs.
Activated carbons derived from male flowers of coconut tree	60.42	(74)
Kaolinite-supported nanoscale zero-valent iron	129	(75)
Merck activated carbon	67.09	(76)
Grapefruit peel	259.91	(77)
Zeolite from bottom ash	17.6	(78)
Raw <i>S. latifolium</i>	4.926	(41)
carbonized sargassum algae	666	This work

### 3.8. Comparison Between Our Study and Other Studies

Carbonized Sargassum seaweed (CSA) used in the study is a low cost adsorbent with high removal capacity (Table 6).

### 4. CONCLUSION

This paper looked into the adsorption of CV on an algae (Sargassum sp.) CSA preparation. The findings of this work support the notion that CSA is an effective low-cost adsorbent for extracting CV from aqueous solutions. CV adsorption is influenced by the initial dye concentration, contact time, adsorbent weight density, pH, and temperature. Maximum CV removal on CSA occurs when the starting dye concentration is 100 mg/L, the contact time is 3 hours, the adsorbent weight mass is 0.01 g, the pH is 7, and the temperature is 25°C (room temperature), the highest removal % was recorded as 91.17 % (666 mg/g). Freundlich's isothermal adsorption is depicted, and kinetics analysis results are correlated using a pseudo-second-order model. Monte Carlo (MC) and molecular dynamic (MD) simulation studies were performed to investigate the adsorption of crystal violet dye on the carbonized sargassum algae surface and to identify crystal violet dye desorption sites on the carbonized sargassum algae surface. The MC simulation reveals that the adsorption of Eads crystal violet dye on the carbonized sargassum algae surface is negative, indicating that the adsorption of crystal violet dye on the algae doped activated carbon surface is exothermic, energetically favorable, and spontaneous, owing to the presence of intermolecular interactions. The MD simulation reveals that even in the presence of water molecules, crystal violet dye interacts with the carbonized sargassum algae atoms. RDFs reveal that crystal violet still interacts with the carbonized sargassum algae surface in the presence of water molecules.

### 5. CONFLICT OF INTEREST

The authors declare no conflict of interest.

### 6. REFERENCES

- 1 Nemerow N. Liquid waste of industry: theories, practices and treatment. Addison-Wesley Publishing Company; 1971.
- 2 Nemerow NL. Liquid waste of industry. Theories, practices, and treatment. Addison-Wesley Publishing Company Inc, 8. 1971:590.
- 3 Al-Degs YS, El-Barghouthi MI, El-Sheikh AH, Walker GM. Effect of solution pH, ionic strength, and temperature on adsorption behavior of reactive dyes on activated carbon. Dyes and pigments. 2008;77(1):16-23. Available from: [<URL>](#).
- 4 Ju Y, Fang J, Liu X, Xu Z, Ren X, Sun C, et al. Photodegradation of crystal violet in TiO<sub>2</sub> suspensions using UV-vis irradiation from two microwave-powered electrodeless discharge lamps (EDL-2): Products, mechanism and feasibility. Journal of Hazardous Materials. 2011;185(2-3):1489-98. Available from: [<URL>](#).
- 5 Miyah Y, Lahrchi A, Idrissi M, Boujraf S, Taouda H, Zerrouq F. Assessment of adsorption kinetics for removal potential of Crystal Violet dye from aqueous solutions using Moroccan pyrophyllite. Journal of the Association of Arab Universities for Basic and Applied Sciences. 2017;23:20-8. Available from: [<URL>](#).
- 6 Goswami R, Dey AKJAS, Technology. Use of anionic surfactant-modified activated carbon for efficient adsorptive removal of crystal violet dye. 2022;2022. Available from: [<URL>](#).
- 7 Zare K, Sadegh H, Shahryari-Ghoshekandi R, Maazinejad B, Ali V, Tyagi I, et al. Enhanced removal of toxic Congo red dye using multi walled carbon nanotubes: kinetic, equilibrium studies and its comparison with other adsorbents. Journal of Molecular Liquids. 2015;212:266-71. Available from: [<URL>](#).
- 8 Sebeia N, Jabli M, Ghith A, Elghoul Y, Alminderej FM. Production of cellulose from Aegagropila Linnaei macro-algae: Chemical modification, characterization and application for the bio-sorption of cationic and anionic dyes from water. International journal of biological macromolecules. 2019;135:152-62. Available from: [<URL>](#).
- 9 Allen S, Mckay G, Porter JF. Adsorption isotherm models for basic dye adsorption by peat in single and binary component systems. Journal of colloid and interface science. 2004;280(2):322-33. Available from: [<URL>](#).
- 10 Sebeia N, Jabli M, Ghith A, El Ghoul Y, Alminderej FM. Populus tremula, Nerium oleander and Pergularia tomentosa seed fibers as sources of cellulose and lignin for the bio-sorption of methylene blue. International journal of biological macromolecules. 2019;121:655-65. Available from: [<URL>](#).
- 11 Jabli M. Synthesis, characterization, and assessment of cationic and anionic dye adsorption performance of functionalized silica immobilized chitosan bio-polymer. International journal of biological macromolecules. 2020;153:305-16. Available from: [<URL>](#).
- 12 Bhatnagar A, Jain A. A comparative adsorption study with different industrial wastes as adsorbents for the removal of cationic dyes from water. Journal of Colloid and Interface Science. 2005;281(1):49-55. Available from: [<URL>](#).
- 13 Jabli M, Gamha E, Sebeia N, Hamdaoui M. Almond shell waste (Prunus dulcis): Functionalization with [dimethyl-diallyl-ammonium-chloride-diallylamin-co-polymer] and chitosan polymer and its investigation in dye adsorption. Journal of Molecular Liquids. 2017;240:35-44. Available from: [<URL>](#).
- 14 Mohamed HS, Soliman N, Abdelrheem DA, Ramadan AA, Elghandour AH, Ahmed SA. Adsorption of Cd<sup>2+</sup> and Cr<sup>3+</sup> ions from aqueous solutions by using residue of Padina gymnospora waste as promising low-cost adsorbent. Heliyon. 2019;5(3). Available from: [<URL>](#).
- 15 Rabie AM, Abukhadra MR, Rady AM, Ahmed SA, Labena A, Mohamed HS, et al. Instantaneous

- photocatalytic degradation of malachite green dye under visible light using novel green Co-ZnO/algae composites. *Research on Chemical Intermediates*. 2020;46:1955-73. Available from: [<URL>](#).
16. Naim MM, El Abd YM. Removal and recovery of dyestuffs from dyeing wastewaters. *Separation and Purification Methods*. 2002;31(1):171-228. Available from: [<URL>](#).
  17. Ul-Islam S. *Advanced Materials for Wastewater Treatment*: John Wiley & Sons; 2017.
  18. Kiran S, Nosheen S, Abrar S, Javed S, Aslam N, Afzal G, et al. Remediation of textile effluents via physical and chemical methods for a safe environment. *Textiles and Clothing*. 2019:191-234. Available from: [<URL>](#).
  19. Rathi A, Puranik S. Treatment of wastewater pollutants from direct dyes. *American dyestuff reporter*. 1999;88(7-8):42-50.
  20. Chakraborty S, De S, DasGupta S, Basu JK. Adsorption study for the removal of a basic dye: experimental and modeling. *Chemosphere*. 2005;58(8):1079-86. Available from: [<URL>](#).
  21. Mohamed HS, Soliman N, Abdelrheem DA, Ramadan AA, Elghandour AH, Ahmed SA. Adsorption of Cd<sup>2+</sup> and Cr<sup>3+</sup> ions from aqueous solutions by using residue of *Padina gymnospora* waste as promising low-cost adsorbent. *Heliyon*. 2019;5(3):e01287. Available from: [<URL>](#).
  22. Rabie AM, Abukhadra MR, Rady AM, Ahmed SA, Labena A, Mohamed HS, et al. Instantaneous photocatalytic degradation of malachite green dye under visible light using novel green Co-ZnO/algae composites. *Research on Chemical Intermediates*. 2020;46(3):1955-73. Available from: [<URL>](#).
  23. Soliman N, Mohamed HS, Ahmed SA, Sayed FH, Elghandour AH, Ahmed SA. Cd<sup>2+</sup> and Cu<sup>2+</sup> removal by the waste of the marine brown macroalga *Hydroclathrus clathratus*. *Environmental Technology & Innovation*. 2019;15:100365. Available from: [<URL>](#).
  24. Dey AK, Dey A, Goswami RJAWS. Adsorption characteristics of methyl red dye by Na<sub>2</sub>CO<sub>3</sub>-treated jute fibre using multi-criteria decision making approach. 2022;12(8):1-22.
  25. Goswami R, Dey AKJAJoC. Synthesis and application of treated activated carbon for cationic dye removal from modelled aqueous solution. 2022;15(11):104290. Available from: [<URL>](#).
  26. Dey AK, Dey AJGfSD. Selection of optimal processing condition during removal of Reactive Red 195 by NaOH treated jute fibre using adsorption. 2021;12:100522.
  27. Khan MM, Dey AJMC, Physics. Hybrid MCDM approach for examining the high-stress abrasive wear behaviour of in situ ZA-27/TiCp MMCs. 2022;277:125319. Available from: [<URL>](#).
  28. Bichave MS, Kature AY, Koranne SV, Shinde RS, Gongle AS, Choudhari VP, et al. Nano-metal oxides-activated carbons for dyes removal: A review. 2022. Available from: [<URL>](#).
  29. Yang X, Zhu W, Song Y, Zhuang H, Tang HJJoML. Removal of cationic dye BR46 by biochar prepared from *Chrysanthemum morifolium* Ramat straw: A study on adsorption equilibrium, kinetics and isotherm. 2021;340:116617. Available from: [<URL>](#).
  30. Faccenda HB, Melara F, Damini G, Godinho M, Manera C, Piccin JSJES, et al. Graywater treatment of emerging pollutant linear alkylbenzene sulfonate by adsorption with leather shave waste activated carbon. 2022;29(53):79830-40. Available from: [<URL>](#).
  31. Zhang M, Li W, Jin ZJJoHM. Structural properties of deprotonated naphthenic acids immersed in water in pristine and hydroxylated carbon nanopores from molecular perspectives. 2021;415:125660. Available from: [<URL>](#).
  32. Verma AK, Dash AK, Bhunia P, Dash RRJS, Interfaces. Removal of surfactants in greywater using low-cost natural adsorbents: A review. 2021;27:101532. Available from: [<URL>](#).
  33. Sharaf A, Liu YJC. Mechanisms and kinetics of greywater treatment using biologically active granular activated carbon. 2021;263:128113. Available from: [<URL>](#).
  34. Mohamed HS, Soliman N, Moustafa A, Abdel-Gawad OF, Taha RR, Ahmed SA. Nano metal oxide impregnated Chitosan-4-nitroacetophenone for industrial dye removal. *International Journal of Environmental Analytical Chemistry*. 2021;101(13):1850-77. Available from: [<URL>](#).
  35. Mohamed HS, Tawfik WZ, Hamza ZS, Kfayf YR, El-Bassuony AA, Ahmed SA, et al. Removal of dye by adsorption on nitric acid treated sugar bagasse wastes, an experimentally, theoretically, and computational studies. *Russian Journal of Physical Chemistry A*. 2022;96(14):3232-43. Available from: [<URL>](#).
  36. Ahsaine HA, Zbair M, El Haouti R. Mesoporous treated sewage sludge as outstanding low-cost adsorbent for cadmium removal. *Desalin Water Treat*. 2017;85:330-8. Available from: [<URL>](#).
  37. Parra Parra A, Márquez Aguilar PA, Semjonova J, Serrano Nava ME, Vlasova M. Adsorption properties of carbonized Sargassum algae. *MRS Advances*. 2022:1-6. Available from: [<URL>](#).
  38. Liranzo-Gómez RE, García-Cortés D, Jáuregui-Haza U. Adaptation and sustainable management of massive influx of Sargassum in the Caribbean. *Procedia Environ Sci Eng Manag*. 2021;8:543-53. Available from: [<URL>](#).
  39. Turner A, Lewis MS, Shams L, Brown MT. Uptake of platinum group elements by the marine macroalga, *Ulva lactuca*. *Marine Chemistry*. 2007;105(3-4):271-80. Available from: [<URL>](#).
  40. Jabli MJJobm. Synthesis, characterization, and assessment of cationic and anionic dye adsorption performance of functionalized silica immobilized chitosan bio-polymer. 2020;153:305-16. Available from: [<URL>](#).
  41. Abd El-Hamid HT, AlProl AE, Hafiz MA. The efficiency of adsorption modelling and Plackett-Burman design for remediation of crystal violet by *Sargassum latifolium*. *Biocatalysis and Agricultural Biotechnology*. 2022;44:102459. Available from: [<URL>](#).
  42. Tka N, Jabli M, Saleh TA, Salman GA. Amines modified fibers obtained from natural *Populus tremula* and

their rapid biosorption of Acid Blue 25. *Journal of Molecular Liquids*. 2018;250:423-32. Available from: [<URL>](#).

43. khamis Soliman N, Moustafa AF, Aboud AA, Halim KSA. Effective utilization of Moringa seeds waste as a new green environmental adsorbent for removal of industrial toxic dyes. *Journal of Materials Research and Technology*. 2019;8(2):1798-808. Available from: [<URL>](#).

44. Khedr M, Halim KA, Soliman N. Synthesis and photocatalytic activity of nano-sized iron oxides. *Materials Letters*. 2009;63(6-7):598-601 Available from: [<URL>](#).

45. Lagergren SK. About the theory of so-called adsorption of soluble substances. *Sven Vetenskapsakad Handlingar*. 1898;24:1-39.

46. Kang YL, Toh SKS, Monash P, Ibrahim S, Saravanan P. Adsorption isotherm, kinetic and thermodynamic studies of activated carbon prepared from *Garcinia mangostana* shell. *Asia-Pacific Journal of Chemical Engineering*. 2013;8(6):811-8.

47. Azizian S. Kinetic models of sorption: a theoretical analysis. *Journal of colloid and Interface Science*. 2004;276(1):47-52. Available from: [<URL>](#).

48. Çoruh S, Geyikçi F, Nuri Ergun O. Adsorption of basic dye from wastewater using raw and activated red mud. *Environmental technology*. 2011;32(11):1183-93. Available from: [<URL>](#).

49. Depci T, Kul AR, Onal Y, Disli E, Alkan S, Turkmenoglu ZF. ADSORPTION OF CRYSTAL VIOLET FROM AQUEOUS SOLUTION ON ACTIVATED CARBON DERIVED FROM GÖLBAŞI LIGNITE. *Physicochemical Problems of Mineral Processing*. 2012;48(1). Available from: [<URL>](#).

50. Langmuir I. The adsorption of gases on plane surfaces of glass, mica and platinum. *Journal of the American Chemical society*. 1918;40(9):1361-403.

51. Freundlich H. Over the adsorption in solution. *J Phys Chem*. 1906;57(385471):1100-7.

52. Ozdemir O, Armagan B, Turan M, Celik MS. Comparison of the adsorption characteristics of azo-reactive dyes on mesoporous minerals. *Dyes and pigments*. 2004;62(1):49-60. Available from: [<URL>](#).

53. Demirbas E, Nas M. Batch kinetic and equilibrium studies of adsorption of Reactive Blue 21 by fly ash and sepiolite. *Desalination*. 2009;243(1-3):8-21. Available from: [<URL>](#).

54. Serna-Carrizales JC, Collins-Martínez VH, Flórez E, Gomez-Duran CF, Palestino G, Ocampo-Pérez R. Adsorption of sulfamethoxazole, sulfadiazine and sulfametazine in single and ternary systems on activated carbon. Experimental and DFT computations. *Journal of Molecular Liquids*. 2021;324:114740. Available from: [<URL>](#).

55. Abd El-Mageed H, Taha M. Exploring the intermolecular interaction of serine and threonine dipeptides with gold nanoclusters and nanoparticles of different shapes and sizes by quantum mechanics and molecular simulations. *Journal of Molecular Liquids*. 2019;296:111903. Available from: [<URL>](#).

56. Sun H, Ren P, Fried J. The COMPASS force field: parameterization and validation for phosphazenes. *Computational and Theoretical Polymer Science*. 1998;8(1-2):229-46. Available from: [<URL>](#).

57. Mohamed N, Sabaa M, El-Ghandour A, Abel-Aziz M, Abdel-Gawad O. Preparation, characterization and antimicrobial activity of carboxymethyl chitosan Schiff bases with different benzaldehyde derivatives. *Journal of American Science*. 2013;9(3):247-64.

58. Li Y-M, Sun S-Q, Zhou Q, Qin Z, Tao J-X, Wang J, et al. Identification of American ginseng from different regions using FT-IR and two-dimensional correlation IR spectroscopy. *Vibrational spectroscopy*. 2004;36(2):227-32. Available from: [<URL>](#).

59. Gliemann G. K. Nakamoto: *Infrared and Raman Spectra of Inorganic and Coordination Compounds*. John Wiley and Sons, New York, Chichester, Brisbane, Toronto 1978. 3. Aufl., XV, 448 Seiten mit 109 Abbildungen und 95 Tabellen. Preis: \$31, 15. Wiley Online Library; 1978.

60. Mishra A, Jha B. Isolation and characterization of extracellular polymeric substances from micro-algae *Dunaliella salina* under salt stress. *Bioresource technology*. 2009;100(13):3382-6. Available from: [<URL>](#).

61. Marimuthu J, Essakimuthu P, Narayanan J, Anantham B, Tharmaraj RJJM, Arumugam S. Phytochemical characterization of brown seaweed *Sargassum wightii*. *Asian Pacific Journal of Tropical Disease*. 2012;2:5109-513. Available from: [<URL>](#).

62. Diem M, Chiriboga L, Yee H. Infrared spectroscopy of human cells and tissue. VIII. Strategies for analysis of infrared tissue mapping data and applications to liver tissue. *Biopolymers: Original Research on Biomolecules*. 2000;57(5):282-90. Available from: [<URL>](#).

63. Sharma YC. Optimization of parameters for adsorption of methylene blue on a low-cost activated carbon. *Journal of Chemical & Engineering Data*. 2010;55(1):435-9. Available from: [<URL>](#).

64. Raval NP, Shah PU, Shah NK. Nanoparticles loaded biopolymer as effective adsorbent for adsorptive removal of malachite green from aqueous solution. *Water Conservation Science and Engineering*. 2016;1(1):69-81. Available from: [<URL>](#).

65. Mohan SV, Rao NC, Karthikeyan J. Adsorptive removal of direct azo dye from aqueous phase onto coal based sorbents: a kinetic and mechanistic study. *Journal of hazardous materials*. 2002;90(2):189-204. Available from: [<URL>](#).

66. Foo K, Hameed B. Preparation, characterization and evaluation of adsorptive properties of orange peel based activated carbon via microwave induced K<sub>2</sub>CO<sub>3</sub> activation. *Bioresource technology*. 2012;104:679-86. Available from: [<URL>](#).

67. Ansari R, Mosayebzadeh Z. Removal of Eosin Y, an anionic dye, from aqueous solutions using conducting electroactive polymers. 2010.

68. Heibati B, Rodriguez-Couto S, Al-Ghouti MA, Asif M, Tyagi I, Agarwal S, et al. Kinetics and thermodynamics of enhanced adsorption of the dye AR 18 using activated carbons prepared from walnut and poplar woods. *Journal of Molecular Liquids*. 2015;208:99-105. Available from: [<URL>](#).

69. Elkady M, Hussein M, Salama M. Synthesis and characterization of nano-activated carbon from El Maghara Coal, Sinai, Egypt to be utilized for wastewater purification. *American Journal of Applied Chemistry*. 2015;3(3):1-7.



70. Ho Y-S, Chiu W-T, Wang C-C. Regression analysis for the sorption isotherms of basic dyes on sugarcane dust. *Bioresource technology*. 2005;96(11):1285-91. Available from: [<URL>](#).
71. Özcan AS, Erdem B, Özcan A. Adsorption of Acid Blue 193 from aqueous solutions onto BTMA-bentonite. *Colloids and Surfaces A: Physicochemical and Engineering Aspects*. 2005;266(1-3):73-81. Available from: [<URL>](#).
72. Hall KR, Eagleton LC, Acrivos A, Vermeulen T. Pore- and solid-diffusion kinetics in fixed-bed adsorption under constant-pattern conditions. *Industrial & Engineering Chemistry Fundamentals*. 1966;5(2):212-23. Available from: [<URL>](#).
73. Yadav S, Srivastava V, Banerjee S, Weng C-H, Sharma YC. Adsorption characteristics of modified sand for the removal of hexavalent chromium ions from aqueous solutions: Kinetic, thermodynamic and equilibrium studies. *Catena*. 2013;100:120-7. Available from: [<URL>](#).
74. Lin Y, He X, Han G, Tian Q, Hu W. Removal of Crystal Violet from aqueous solution using powdered mycelial biomass of *Ceriporia lacerata* P2. *Journal of Environmental Sciences*. 2011;23(12):2055-62. Available from: [<URL>](#).
75. Chen Z, Wang T, Jin X, Chen Z, Megharaj M, Naidu R. Multifunctional kaolinite-supported nanoscale zero-valent iron used for the adsorption and degradation of crystal violet in aqueous solution. *Journal of colloid and interface science*. 2013;398:59-66. Available from: [<URL>](#).
76. Sarabadian M, Bashiri H, Mousavi SM. Removal of crystal violet dye by an efficient and low cost adsorbent: modeling, kinetic, equilibrium and thermodynamic studies. *Korean Journal of Chemical Engineering*. 2019;36(10):1575-86. Available from: [<URL>](#).
77. Saeed A, Sharif M, Iqbal M. Application potential of grapefruit peel as dye sorbent: kinetics, equilibrium and mechanism of crystal violet adsorption. *Journal of hazardous materials*. 2010;179(1-3):564-72. Available from: [<URL>](#).
78. Amodu OS, Ojumu TV, Ntwampe SK, Ayanda OS. Rapid adsorption of crystal violet onto magnetic zeolite synthesized from fly ash and magnetite nanoparticles. *Journal of Encapsulation and Adsorption Sciences*. 2015;5(04):191. Available from: [<URL>](#).





## Thermal Degradation Kinetics of Modified Fe<sub>3</sub>O<sub>4</sub> With Poly(Vinyl Chloride) via Click Chemistry

Abdulrahman Tukur<sup>1</sup> , Mustafa Ersin Pekdemir<sup>2\*</sup> , Abdullahi Musa Abubakar<sup>3</sup> 

<sup>1</sup> Federal University Dutse, Faculty of Science, Department of Chemistry, Dutse, Jigawa State, 7156, Nigeria

<sup>2</sup> Firat University, Faculty of Science, Department of Chemistry, Elazığ, 23119, Turkey

<sup>3</sup> Kano University of Science and Technology, Faculty of Science, Department of Chemistry, Wudil, Kano State, 3244, Nigeria.

**Abstract:** The PVC-g-poly(POHMAC-co-VTM)-g-Fe<sub>3</sub>O<sub>4</sub> and its precursors were characterized based on thermal properties comprising the initial decomposition and final decomposition temperatures and the maximum decomposition rate temperature were studied by TG/DTG and the decomposition steps were investigated. Then, the thermal characteristics of the final product formed via click chemistry, PVC-g-poly(POHMAC-co-VTM)-g-Fe<sub>3</sub>O<sub>4</sub> were evaluated through thermogravimetric analysis (TGA) under argon atmosphere at 5, 10, and 15 °C/min. The studied temperature selection is 0 to 800 °C. Centered on the iso-conversional method, the thermal degradation kinetic parameter of the energy of activation was computed by the free model methods of the Flynn-Wall-Ozawa method (FWO) and Kissinger-Akahira-Sinuse method (KAS). The predicted activation energy values ranged from 41.40 to 117.83 KJ/mol meanwhile the average energy of activation values were computed as 85.75 KJ/mol and 72.31 KJ/mol respectively for the FWO method and KAS method. In addition, a saturation magnetization of 33.7 emu/g was recorded using vibration sample magnetometer (VSM).

**Keywords:** Click chemistry, Fe<sub>3</sub>O<sub>4</sub>, Kinetics, PVC, Thermal degradation.

**Submitted:** January 25, 2023. **Accepted:** July 14, 2023.

**Cite this:** Tukur A, Pekdemir ME, Abubakar AM. Thermal Degradation Kinetics of Modified Fe<sub>3</sub>O<sub>4</sub> with Poly(Vinyl Chloride) via Click Chemistry. JOTCSA. 2023;10(3):919-28.

**DOI:** <https://doi.org/10.18596/jotcsa.1241976>

**\*Corresponding author's E-mail:** ersinpkdmr58@gmail.com

### 1. INTRODUCTION

The property known as the ability of a polymeric material to resist the action of heat and to maintain properties such as strength and elasticity at a given temperature is defined as the thermal stability of polymers (1, 2). The thermal stability of polymers is usually done by thermogravimetric analysis (TGA). In recent years, researchers have attempted to analyze polymeric materials by combining TGA with FTIR or mass spectrometry (3). In the case of polymeric materials, changes in mass can involve multiple steps. In general, the incorporation of the doping material into a polymer matrix increases the thermal stability of the pure polymer (4). The thermal stability of polymers varies depending on the degree of crystallinity, molecular weight, and chemical structure. While it is known that effects such as aromatic structures and cross-linking of polymers in the polymer chain improve the thermal stability of polymers, the presence of oxygen or double bonds in the main chain reduces the thermal stability (5, 6).

Currently, immense importance is being paid to the stability of the polymeric material with precise qualities of resistance to the high temperature called thermal stability. The thermal stability of polymeric materials can be determined based on initial, half, and final temperatures of decomposition via several thermal methods. Additionally, the stability of polymeric materials by thermal means can be substantiated by some kinetic parameters. Thermal degradation behavior of different types of polymeric materials has been extensively studied by thermo-gravimetric analysis (TGA), differential scanning calorimetry (DSC), differential thermal gravimetry (DTG), differential thermal analysis (DTA), thermo-mechanical analysis (TMA), and other techniques. Currently, thermal and thermo-oxidative degradation of polymeric materials, composites, and modified polymer materials has been studied by thermo-analytical methods (7-10). Moreover, methods of thermal analysis were applied to a great extent in analyzing the thermal aspect of polymers, composites, and polymers modified with nanoparticles and also, arrangements of complexes

and polymer chelate compounds of transition metal ions (10-12).

It is accustomed to studying the thermal degradation of this modified polymer compound to get hold of valuable data on the polymer-magnetic nanoparticle bonds and stability course. TGA is the utmost prevalent technique for computing thermal decomposition owing to the speedy and remarkable facts which allow the thorough analysis of the mass fragments and the determination of the kinetic parameters (13, 14). Thermal degradation and kinetics of PVC have been discussed in detail (15-18). Thermal degradation and kinetics of PVC modified with different nanoparticles have been argued thoroughly. The degradation kinetics behavior of PVC and its blend with ZnO leads to the decline in activation energy of the PVC due to the physical impact of volatilization on the whole mass loss (19). Other works of literature include (20-22). In this communication, we focused on thermal characteristics and kinetic studies of  $\text{Fe}_3\text{O}_4$  modified with poly(vinyl chloride) via click chemistry and compared the thermal properties of the modified polymer and its precursors under the flow of argon at a heating rate of  $10\text{ }^\circ\text{C}/\text{min}$ . The kinetics from the results of the acquired TGA data at diverse heating rates under non-isothermal conditions were ascertained by the model-free methods, FWO and KAS. The activation energy values were computed via the aforementioned methods. The current work evaluated the kinetic parameter such as activation energy ( $E_a$ ) and thermal characteristics from TGA/DTG data obtained. The results allowed us to study the thermal stability values for the modified polymer and its precursors (Figure 1).

## 2. METHODS

### 2.1. Synthesis and Technique

The novel PVC-modified  $\text{Fe}_3\text{O}_4$  (PVC-*g*-poly(POHMAC-*co*-VTM)-*g*- $\text{Fe}_3\text{O}_4$ ) and its precursors were synthesized, characterized, and published elsewhere (23). The pathway of the synthesis is shown in Figure 1. Thermal analysis was put through by TGA/DTG at a heating rate of  $10^\circ\text{C}/\text{min}$  under argon flow and the magnetic property was measured using the vibration sample magnetometer (VSM) at 300 K.

### 2.2. Kinetics Method

Non-Isothermal thermogravimetry analysis (TGA) of novel modified  $\text{Fe}_3\text{O}_4$  was carried out by PerkinElmer instruments Pyris Diamond. TGA experiments were conducted from 0 to  $800\text{ }^\circ\text{C}$  at diverse heating rates of 5, 10, and  $15\text{ }^\circ\text{C}/\text{min}$  under an argon atmosphere. About 5 mg of samples were used for all the TG measurements. Figure 2 depicts the non-isothermal

TG curves of novel PVC-*g*-poly(POHMAC-*co*-VTM)-*g*- $\text{Fe}_3\text{O}_4$ .

## 3. RESULTS AND DISCUSSION

### 3.1. Thermal Stability of Modified Magnetic Nanoparticle

The thermal degradation behavior of the modified magnetic nanoparticle was deduced and deliberated. The thermal degradation (TGA/DTG) curves of modified  $\text{Fe}_3\text{O}_4$  were shown in Figure 2 and evaluated in Table 1. The initial decomposition temperature, percentage mass losses, and residue in the thermal decomposition of modified  $\text{Fe}_3\text{O}_4$  have been examined through TG analysis at a heating rate of  $10\text{ }^\circ\text{C}/\text{min}$  under an atmosphere of argon. TG analyses were performed for weight loss in milligrams of modified  $\text{Fe}_3\text{O}_4$  for raising the temperature. Peak, initial, and final decomposition temperatures of modified  $\text{Fe}_3\text{O}_4$  were pinpointed by DTG investigation. The thermographs are depicted in Figure 2. The thermal stability properties of modified  $\text{Fe}_3\text{O}_4$  were assessed by using TGA/DTG data over the temperature range  $0\text{--}800\text{ }^\circ\text{C}$  and outcomes obtained showed good thermal stabilities for the whole modified  $\text{Fe}_3\text{O}_4$  compounds.

As seen from Figure 3, the thermograms of poly(POHMAC-*co*-VTM) show a single-step weight loss at a peak ( $T_{max}$ ) of  $424\text{ }^\circ\text{C}$  while for poly(POHMAC-*co*-VTM)-*g*- $\text{Fe}_3\text{O}_4$  and PVC-*g*-poly(POHMAC-*co*-VTM)-*g*- $\text{Fe}_3\text{O}_4$ , both show two steps weight loss over a wide temperature range of  $334\text{ }^\circ\text{C}\text{--}413\text{ }^\circ\text{C}$  and  $334\text{ }^\circ\text{C}\text{--}787\text{ }^\circ\text{C}$ , respectively. The initial temperatures of decomposition ( $T_i$ ) of poly(POHMAC-*co*-VTM), poly(POHMAC-*co*-VTM)-*g*- $\text{Fe}_3\text{O}_4$ , and PVC-*g*-poly(POHMAC-*co*-VTM)-*g*- $\text{Fe}_3\text{O}_4$  recorded from the thermograms are 266, 280 and  $275\text{ }^\circ\text{C}$  correspondingly which infers that adding of  $\text{Fe}_3\text{O}_4$  to the copolymer augment the thermal stability of the copolymer meaningfully. Afterward the click reaction of azide PVC with the copolymer having  $\text{Fe}_3\text{O}_4$ , there was an infinitesimal drop in thermal stability which was foreseen to be an outcome of the materialization of a 1,2,3-triazole ring. At  $330\text{ }^\circ\text{C}$ , 20% of poly(POHMAC-*co*-VTM) have undergone thermal decomposition but poly(POHMAC-*co*-VTM)-*g*- $\text{Fe}_3\text{O}_4$  and PVC-*g*-Poly(POHMAC-*co*-VTM)-*g*- $\text{Fe}_3\text{O}_4$  reaches the same percentage decomposition respectively at a temperature of  $770\text{ }^\circ\text{C}$  and  $795\text{ }^\circ\text{C}$ . This implies that at a 20% decomposition state, PVC-*g*-Poly(POHMAC-*co*-VTM)-*g*- $\text{Fe}_3\text{O}_4$  is more stable than it is precursors. The % residue at  $T_f$  for poly(POHMAC-*co*-VTM) recorded is 21 which was lesser than that of poly(POHMAC-*co*-VTM)-*g*- $\text{Fe}_3\text{O}_4$ , indicating the bonding of the  $\text{Fe}_3\text{O}_4$  to the copolymer. The 20% for PVC-*g*-poly(POHMAC-*co*-VTM)-*g*- $\text{Fe}_3\text{O}_4$  was most likely a result of a click reaction with azide PVC.

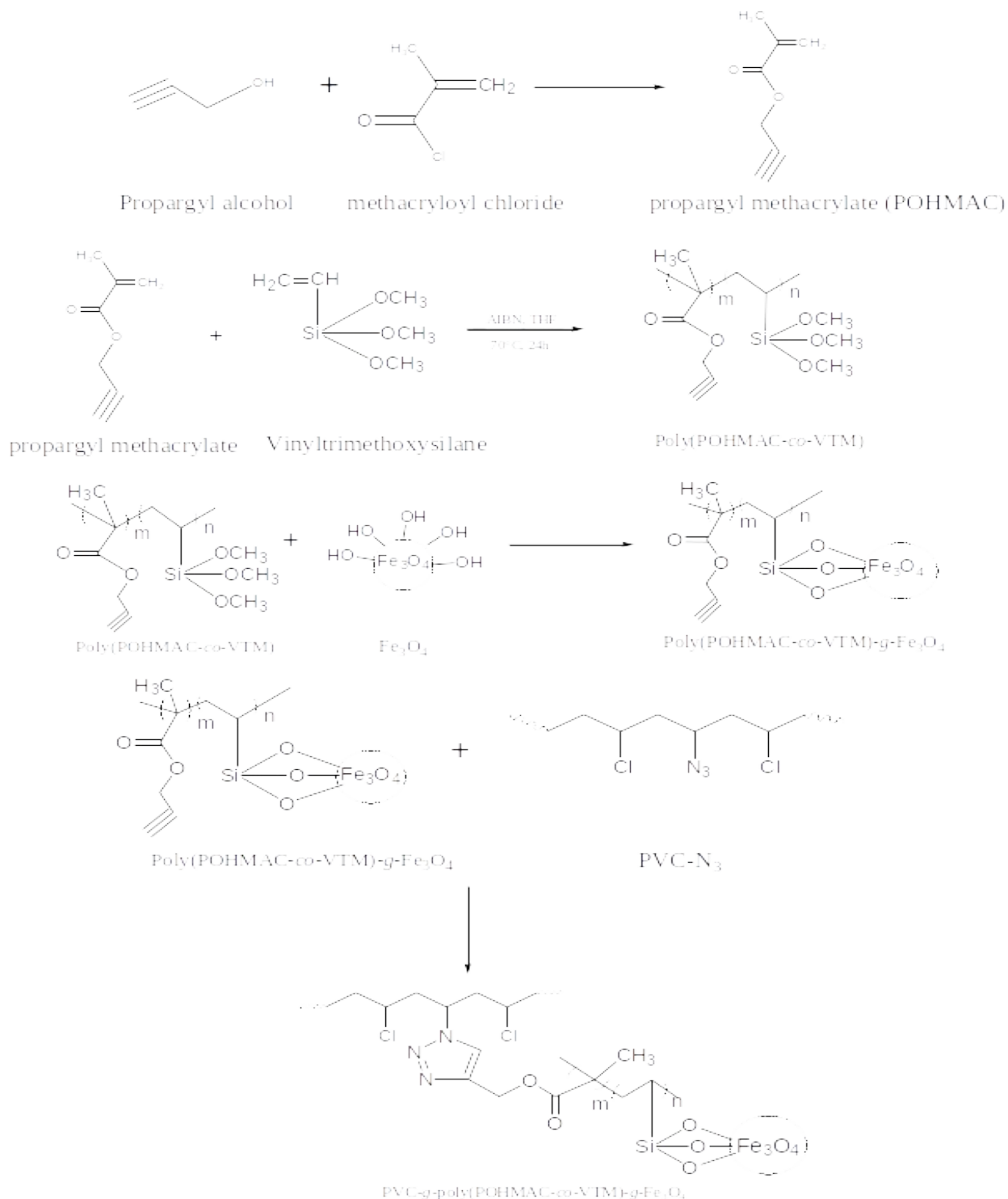


**Figure 1:** Synthetic pathway and structure of PVC-g-poly(POHMAC-co-VTM)-g- $\text{Fe}_3\text{O}_4$ .

## 2. METHODS

### 2.1. Synthesis and Technique

The novel PVC-modified  $\text{Fe}_3\text{O}_4$  (PVC-g-poly(POHMAC-co-VTM)-g- $\text{Fe}_3\text{O}_4$ ) and its precursors were synthesized, characterized, and published elsewhere (23). The pathway of the synthesis is shown in Figure 1. Thermal analysis was put through by TGA/DTG at a heating rate of  $10^\circ\text{C}/\text{min}$  under argon flow and the magnetic property was measured using the vibration sample magnetometer (VSM) at 300 K.

### 2.2. Kinetics Method

Non-Isothermal thermogravimetry analysis (TGA) of novel modified  $\text{Fe}_3\text{O}_4$  was carried out by PerkinElmer instruments Pyris Diamond. TGA experiments were conducted from 0 to  $800^\circ\text{C}$  at diverse heating rates of 5, 10, and  $15^\circ\text{C}/\text{min}$  under an argon atmosphere. About 5 mg of samples were used for all the TG measurements. Figure 2 depicts the non-isothermal TG curves of novel PVC-g-poly(POHMAC-co-VTM)-g- $\text{Fe}_3\text{O}_4$ .

## 3. RESULTS AND DISCUSSION

### 3.1. Thermal Stability of Modified Magnetic Nanoparticle

The thermal degradation behavior of the modified magnetic nanoparticle was deduced and deliberated. The thermal degradation (TGA/DTG) curves of modified  $\text{Fe}_3\text{O}_4$  were shown in Figure 2 and evaluated in Table 1. The initial decomposition temperature, percentage mass losses, and residue in the thermal decomposition of modified  $\text{Fe}_3\text{O}_4$  have been examined through TG analysis at a heating rate of  $10\text{ }^\circ\text{C}/\text{min}$  under an atmosphere of argon. TG analyses were performed for weight loss in milligrams of modified  $\text{Fe}_3\text{O}_4$  for raising the temperature. Peak, initial, and final decomposition temperatures of modified  $\text{Fe}_3\text{O}_4$  were pinpointed by DTG investigation. The thermographs are depicted in Figure 2. The thermal stability properties of modified  $\text{Fe}_3\text{O}_4$  were assessed by using TGA/DTG data over the temperature range  $0\text{-}800\text{ }^\circ\text{C}$  and outcomes obtained showed good thermal stabilities for the whole modified  $\text{Fe}_3\text{O}_4$  compounds.

As seen from Figure 3, the thermograms of poly(POHMAC-co-VTM) show a single-step weight loss at a peak ( $T_{max}$ ) of  $424\text{ }^\circ\text{C}$  while for poly(POHMAC-co-VTM)- $g\text{-Fe}_3\text{O}_4$  and PVC- $g\text{-poly(POHMAC-co-VTM)-}g\text{-Fe}_3\text{O}_4$ , both show two steps weight loss over a wide temperature range of  $334$

$^\circ\text{C}$ - $413\text{ }^\circ\text{C}$  and  $334\text{ }^\circ\text{C}$ - $787\text{ }^\circ\text{C}$ , respectively. The initial temperatures of decomposition ( $T_i$ ) of poly(POHMAC-co-VTM), poly(POHMAC-co-VTM)- $g\text{-Fe}_3\text{O}_4$ , and PVC- $g\text{-poly(POHMAC-co-VTM)-}g\text{-Fe}_3\text{O}_4$  recorded from the thermograms are  $266$ ,  $280$  and  $275\text{ }^\circ\text{C}$  correspondingly which infers that adding of  $\text{Fe}_3\text{O}_4$  to the copolymer augment the thermal stability of the copolymer meaningfully. Afterward the click reaction of azide PVC with the copolymer having  $\text{Fe}_3\text{O}_4$ , there was an infinitesimal drop in thermal stability which was foreseen to be an outcome of the materialization of a 1,2,3-triazole ring. At  $330\text{ }^\circ\text{C}$ , 20% of poly(POHMAC-co-VTM) have undergone thermal decomposition but poly(POHMAC-co-VTM)- $g\text{-Fe}_3\text{O}_4$  and PVC- $g\text{-Poly(POHMAC-co-VTM)-}g\text{-Fe}_3\text{O}_4$  reaches the same percentage decomposition respectively at a temperature of  $770\text{ }^\circ\text{C}$  and  $795\text{ }^\circ\text{C}$ . This implies that at a 20% decomposition state, PVC- $g\text{-Poly(POHMAC-co-VTM)-}g\text{-Fe}_3\text{O}_4$  is more stable than it is precursors. The % residue at  $T_f$  for poly(POHMAC-co-VTM) recorded is 21 which was lesser than that of poly(POHMAC-co-VTM)- $g\text{-Fe}_3\text{O}_4$ , indicating the bonding of the  $\text{Fe}_3\text{O}_4$  to the copolymer. The 20% for PVC- $g\text{-poly(POHMAC-co-VTM)-}g\text{-Fe}_3\text{O}_4$  was most likely a result of a click reaction with azide PVC.

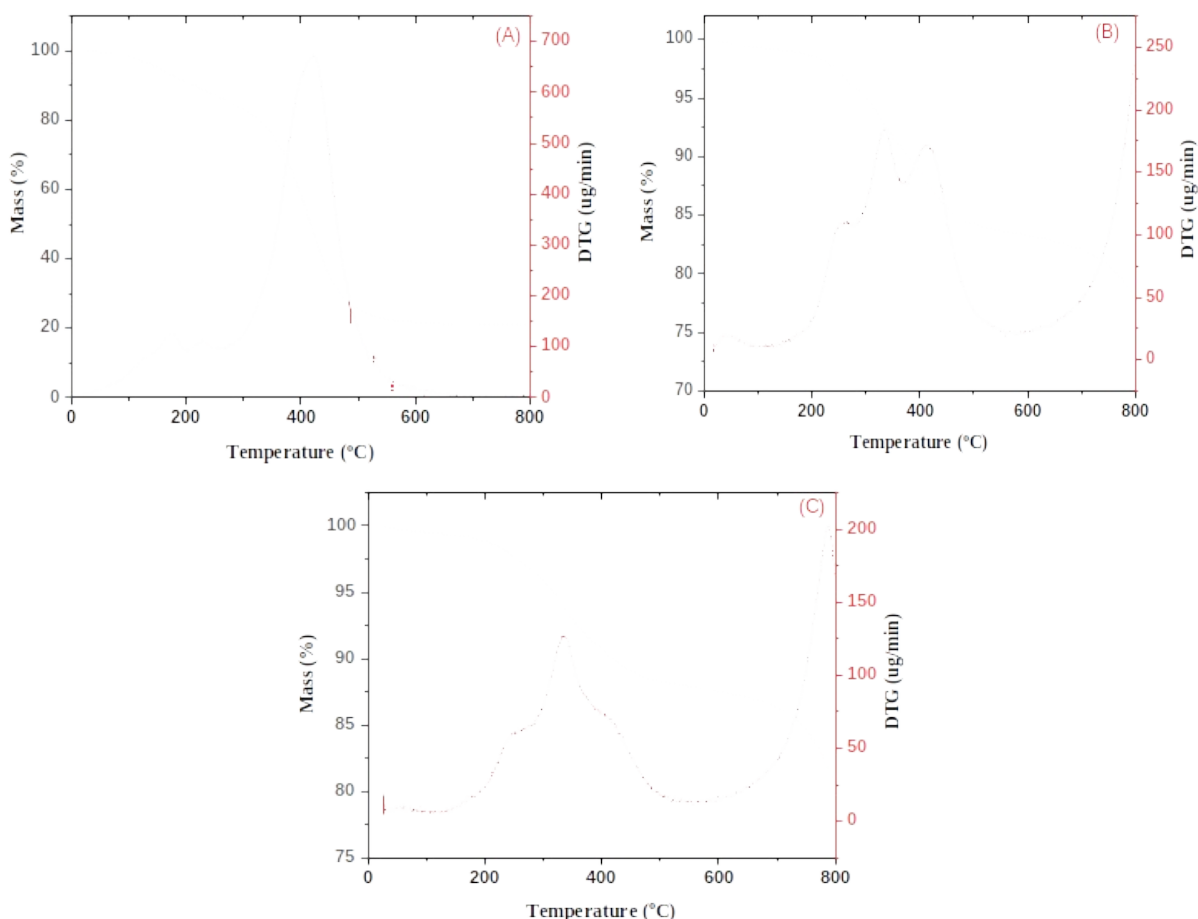


**Figure 2:** TGA/DTG of (A) poly(POHMAC-co-VTM) (B) poly(POHMAC-co-VTM)- $g\text{-Fe}_3\text{O}_4$  and (C) PVC- $g\text{-poly(POHMAC-co-VTM)-}g\text{-Fe}_3\text{O}_4$ .

**Table 1:** TGA/DTG evaluation of PVC-*g*-poly(POHMAC-*co*-VTM)-*g*-Fe<sub>3</sub>O<sub>4</sub>.

Polymer	$T_i$ (°C)	$T_{\%20}$	Residue (%) at $T_f$	Decomposition Stage	$T_{max}$ (°C)
Poly(POHMAC- <i>co</i> -VTM)	266	330	21	1	424
Poly(POHMAC- <i>co</i> -VTM)- <i>g</i> -Fe <sub>3</sub> O <sub>4</sub>	280	770	23	2	334, 413
PVC- <i>g</i> -Poly(POHMAC- <i>co</i> -VTM)- <i>g</i> -Fe <sub>3</sub> O <sub>4</sub>	275	795	20	2	334,787

$T_i$  Initial decomposition temperature

$T_{\%20}$  Temperature at 20% of decomposition

$T_{max}$  Temperature at a maximum rate of decomposition

$T_f$  final decomposition temperature

### 3.2. Thermal Decomposition Kinetics Based on Thermo-gravimetric Measurements

Non-isothermal thermo-gravimetric (TG) analyses of novel PVC-*g*-poly(POHMAC-*co*-VTM)-*g*-Fe<sub>3</sub>O<sub>4</sub> formed as a result of click reaction were carried out by PerkinElmer instruments Pyris Diamond. The modified Fe<sub>3</sub>O<sub>4</sub> was subjected to heating from 0 to 800 °C at a diverse heating rate of 5, 10, and 15 °C/min under an argon atmosphere. All the TG assessments were followed through with approximately 5 mg of the sample.

There exist methods, which can be detached into two various ways such as model-fitting and model-free for evaluating non-isothermal solid-state kinetic information from TGA analysis that has been effectively used for researching the kinetics of various substances (24). The model-free methods originated through the belief of reaction rate reliance on temperature and conversion degree simply devoid of creating whichever premise about the reaction function and reaction order evading the

possibility of finding erroneous kinetic parameters. In other to examine the consequence of thermal activation on non-isothermal decomposition kinetics of novel PVC-*g*-poly(POHMAC-*co*-VTM)-*g*-Fe<sub>3</sub>O<sub>4</sub> depending on thermo-gravimetric analysis, thirteen conversion values from 1 to 13% by way of an addition of 1% are practiced for the kinetic studies. Mainly, FWO and KAS analysis methods are extensively proven to be appropriate for model-free methods (25-28).

Various collections of kinetic information founded on thermal analysis and calorimetry (ICTAC) commendations have been documented in the literary works. One of the commendations was the report of  $\alpha$ -temperature curves at diverse heating rates under an inert gas atmosphere (29). For this purpose, the TGA curve of novel PVC-*g*-poly(POHMAC-*co*-VTM)-*g*-Fe<sub>3</sub>O<sub>4</sub> obtained under argon flow at diverse heating rates (5, 10, and 15 °C/min) was shown in Figure 3.

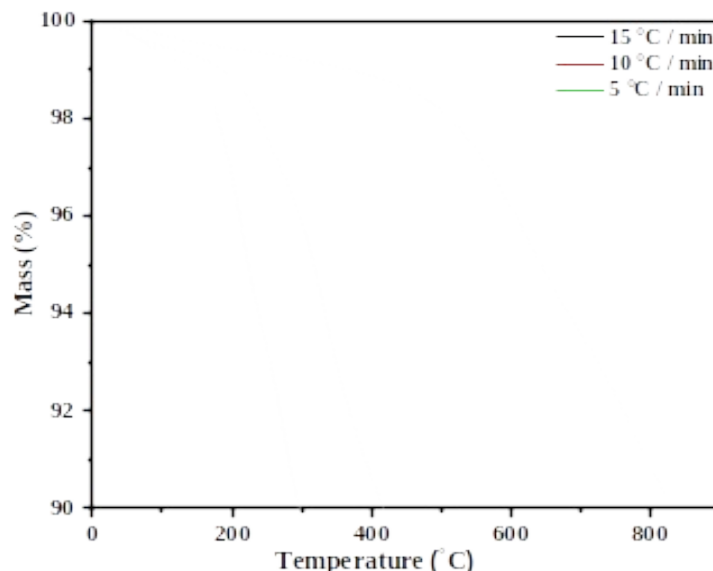


**Figure 3:** TGA curves of novel PVC-*g*-poly(POHMAC-*co*-VTM)-*g*-Fe<sub>3</sub>O<sub>4</sub> obtained under argon flow at different heating rates (5, 10, and 15 °C/min).

The Flynn-Wall-Ozawa (FWO) method is gotten from the integral isoconversional way that Flynn, Wall (30), and Ozawa (31) suggested for the computation of the energy of activation by Doyle's approximation of the temperature integral (32) as shown in Equation (1). As for Kissinger-Akahira-Sunose (KAS) method, the Coats-Redfern approximation is used for the temperature integration (26) as presented in Equation (2).

$$\ln(\beta) = \ln\left(\frac{AEa}{Rg(\alpha)}\right) - 5.331 - 1.052 \frac{Ea}{RT} \quad (1)$$

$$\ln\left(\frac{\beta}{T^2}\right) = \ln\left[\frac{AEa}{Rg(\alpha)}\right] - \frac{Ea}{RT} \quad (2)$$

The lines of best fit of  $\ln(\beta)$  against  $1/T$  for the FWO method and  $\ln(\beta/T^2)$  against  $1/T$  for the KAS method which is achieved conditional on thermograms determined at different heating rates, should be a linear graph whose slope can be practiced to calculate the energy of activation. In this research, the TGA was controlled under the temperature heating rates of 5, 10, and 15 °C/min, and the lines

of best fit centered on the FWO and KAS methods are presented in Figure 4(a)(b) correspondingly. It can be noticed from these figures that the lines of best fit have a linear relationship designating the activation energy at the varied conversions following a distinct mechanism or unification of multiple reaction mechanisms. The slope, activation energy ( $E_a$ ), and average  $E_a$  are listed in Table 2.

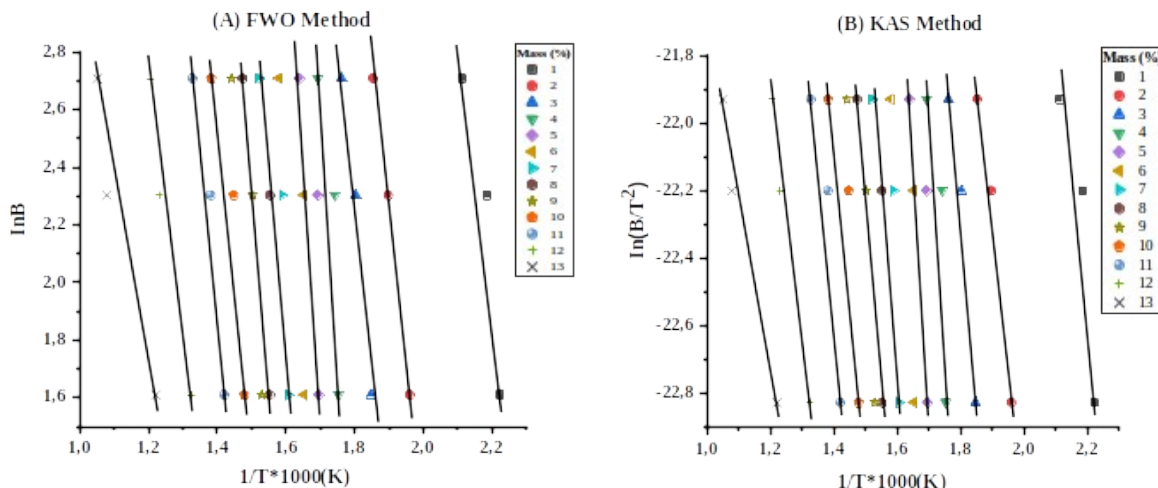


**Figure 4:** Regression lines to thermal decomposition of PVC-g-poly(POHMAC-co-VTM)-g-Fe<sub>3</sub>O<sub>4</sub> based on (A) FWO method and (B) KAS method at 5, 10, and 15 °C/min.

As data demonstrated in Table 2, it is remarkable to notice there is not much major change in the activation energy achieved amid the two varied methods. It is verified that not only one mathematical method could be applied to evaluate the activation energy in as much as they are accurately chosen, and yet the value may differ to an assertive degree. It can be accessed that the activation energy for PVC-g-poly(POHMAC-co-VTM)-g-Fe<sub>3</sub>O<sub>4</sub> thermal degradation is in the range of 41.40-117.83 KJ/mol with changeable conversion (1% ≤ α ≤ 13%). The average value is ascertained as 85.72 KJ/mol and 72.31 KJ/mol for FWO and KAS respectively. With the thermal degradation proceeding, the activation energy gets increased

moderately and reaches its peak at 4% conversion for both methods. Thus far, as the conversion is repositioned from 3% to 4%, the equivalent activation energy is altered from 101.63 KJ/mol to 117.83 KJ/mol for the FWO method and 87.38 KJ/mol to 97.94 KJ/mol for KAS method, which is increased by 15.94% and 12.09% respectively. An increase in activation energy is noticed as the conversion is shifted from 6% to 7%, 8% to 9%, and 10% to 11%. All at once, the activation energy starts to drop when the conversion value surpasses 11%. At the conversion of 13%, the activation energies distinctly decline to 46.87 KJ/mol for FWO and 41.40 KJ/mol for the KAS method.

**Table 2:** Slope,  $E_a$ , and average  $E_a$  deduced from FWO and KAS methods.

$\alpha/\%$	FWO method		KAS method	
	Slope	$E_a/\text{KJ/mol}$	Slope	$E_a/\text{KJ/mol}$
1	9.41	74.37	7.58	63.02
2	10.32	81.56	8.48	70.50
3	12.86	101.63	10.51	87.38
4	14.91	117.83	11.78	97.94
5	14.11	111.51	11.01	91.54
6	10.49	82.90	8.16	67.84
7	11.04	87.25	8.75	72.75
8	9.64	76.19	7.48	62.19
9	11.49	90.81	9.21	76.57
10	10.58	83.61	8.49	70.59
11	11.56	91.36	9.36	77.82
12	8.71	68.84	7.27	60.44
13	5.93	46.87	4.98	41.40
Average		85.75		72.31



Furthermore,  $E_a$ - $\alpha$  curves of PVC-*g*-poly(POHMAC-*co*-VTM)-*g*-Fe<sub>3</sub>O<sub>4</sub> obtained at diverse heating rates of 5, 10, and 15 °C/min under argon atmosphere have been shown in Figure 5. In this condition, the activation energies are found to be 74.37 KJ/mol for FWO and 63.02 KJ/mol for KAS at a conversion of

1%. The highest activation energy value is on the FWO curve at a conversion of 4%. There is also a corresponding increase in the activation energy after a slight decrease at conversion values of 7%, 9%, and 11% for both the FWO and KAS curves.

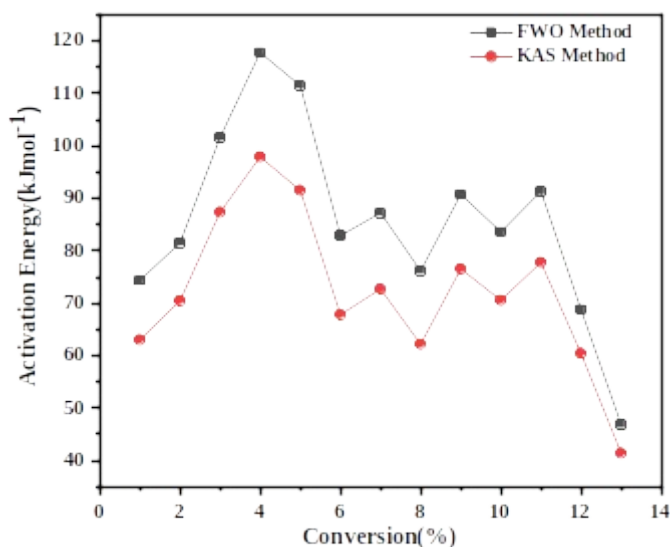


**Figure 5:**  $E_a$ - $\alpha$  curves of PVC-*g*-poly(POHMAC-*co*-VTM)-*g*-Fe<sub>3</sub>O<sub>4</sub> were obtained at different heating rates of 5, 10, and 15 °C/min.

### 3.3. Magnetic Property

Figure 6 depicts the magnetization curve acquired from the vibration sample magnetometry (VSM) of novel PVC-*g*-poly(POHMAC-*co*-VTM)-*g*-Fe<sub>3</sub>O<sub>4</sub> at 300 K for routine magnetic measurements (33). The VSM plot is vital evidence of the formation of PVC-poly(POHMAC-*co*-VTM)-*g*-Fe<sub>3</sub>O<sub>4</sub>. From the plot, the PVC-*g*-poly(POHMAC-*co*-VTM)-*g*-Fe<sub>3</sub>O<sub>4</sub> displayed a saturation magnetization ( $M_s$ ) of 33.72 emu/g which was less than saturation magnetization ( $M_s$ ) values

stated by various literature work of pure Fe<sub>3</sub>O<sub>4</sub> nanoparticle. Several literary works were 53.24 emu/g (23), 65.0 emu/g (34), and 75.30 emu/g (35). The lesser value acquired for PVC-*g*-poly(POHMAC-*co*-VTM)-*g*-Fe<sub>3</sub>O<sub>4</sub> than the given kinds of literature was purely due to the bonding of the PVC to the copolymer bearing Fe<sub>3</sub>O<sub>4</sub>. A study by Tukur et al. (36) has described that the modification of Fe<sub>3</sub>O<sub>4</sub> with polyvinyl chloride via click chemistry shows a saturation magnetization value of 41.55 emu/g.

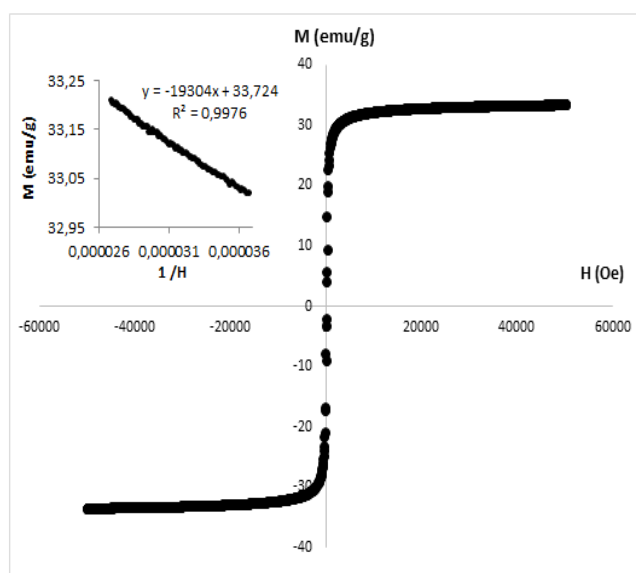


**Figure 6.** VSM plot of PVC-*g*-poly(POHMAC-*co*-VTM)-*g*-Fe<sub>3</sub>O<sub>4</sub>.

### 4. CONCLUSION

In this communication, a slight highlighting was put on the thermal characterization of novel PVC-

poly(POHMAC-*co*-VTM)-*g*-Fe<sub>3</sub>O<sub>4</sub> and its precursors at a heating rate of 10 °C/min under argon flow. Based on TGA-DTG data and kinetics calculations were computed at several heating rates of 5, 10, and 15

°C/min for PVC-poly(POHMAC-co-VTM)-g-Fe<sub>3</sub>O<sub>4</sub> under the study. Two descriptive model-free approaches, FWO and KAS methods were designated to compute the activation energy and the average values inferred from the two methods are respectively 85.75 KJ/mol and 72.31 KJ/mol. The utmost activation energy was realized at 4% conversion. A saturation magnetization (M<sub>s</sub>) value of 33.7 emu/g was recorded using vibration sample magnetometry (VSM). This research is anticipated to boost the basic data for industrial application of PVC-poly(POHMAC-co-VTM)-g-Fe<sub>3</sub>O<sub>4</sub> thermal degradation.

## 5. CONFLICT OF INTEREST

The authors declare no conflict of interest.

## 6. ACKNOWLEDGMENTS

This work was supported by the Management Unit of the Scientific Research Projects of Firat University (FUBAP) (Project Number: FF.23.01).

## 7. REFERENCES

- Charles J, Ramkumaar GR, Azhagiri S, Gunasekaran S. FTIR and Thermal Studies on Nylon-66 and 30% Glass Fibre Reinforced Nylon-66. *E-Journal Chem* [Internet]. 2009;6(1):23–33. Available from: <URL>.
- Stepito RFT, Work WJ. International Union of Pure and Applied Chemistry Commission on Macromolecular Nomenclature (IV. 1). *Polym news*. 1998;23(5).
- Ehrenstein GW, Riedel G, Trawiel P. Thermal analysis of plastics: theory and practice. Carl Hanser Verlag GmbH Co KG; 2012.
- Chrissafis K, Bikiaris D. Can nanoparticles really enhance thermal stability of polymers? Part I: An overview on thermal decomposition of addition polymers. *Thermochim Acta* [Internet]. 2011 Aug 20;523(1–2):1–24. Available from: <URL>.
- Hurley MJ, Gottuk D, Hall JR, Harada K, Kuligowski E, Puchovsky M, et al., editors. *SFPE Handbook of Fire Protection Engineering* [Internet]. New York, NY: Springer New York; 2016. Available from: <URL>.
- Król-Morkisz K, Pielichowska K. Thermal Decomposition of Polymer Nanocomposites With Functionalized Nanoparticles. In: *Polymer Composites with Functionalized Nanoparticles* [Internet]. Elsevier; 2019. p. 405–35. Available from: <URL>.
- Mano JF, Koniarova D, Reis RL. Thermal properties of thermoplastic starch/synthetic polymer blends with potential biomedical applicability. *J Mater Sci Mater Med* [Internet]. 2003 Feb 1;14(2):127–35. Available from: <URL>.
- Wang H, Tao X, Newton E. Thermal degradation kinetics and lifetime prediction of a luminescent conducting polymer. *Polym Int* [Internet]. 2004 Jan 1;53(1):20–6. Available from: <URL>.
- Chang TC, Yang CW, Wu KH, Wu TR, Chiu YS. Organic-inorganic hybrid materials3
- Characterization and degradation of poly(imide-silica) hybrids doped with LiCF<sub>3</sub>SO<sub>3</sub>. *Polym Degrad Stab* [Internet]. 2000 Apr;68(1):103–9. Available from: <URL>.
- Chaudhary RG, Juneja HD, Gandhare N V. Evaluation of kinetic parameters from TG/DTG data of chelate polymer compounds of isophthaoyl bis (paramethoxyphenylcarbamide). *J Chinese Adv Mater Soc* [Internet]. 2013 Dec;1(4):305–16. Available from: <URL>.
- Carvalho CT, Caires FJ, Lima LS, Ionashiro M. Thermal investigation of solid 2-methoxycinnamylidenepyruvate of some bivalent transition metal ions. *J Therm Anal Calorim* [Internet]. 2012 Mar 3;107(3):863–8. Available from: <URL>.
- Sekerci M, Yakuphanoglu F. Thermal analysis study of some transition metal complexes by TG and DSC methods. *J Therm Anal Calorim* [Internet]. 2004 Nov 2;75(1):189–95. Available from: <URL>.
- Chaudhary RG, Juneja HD, Gharpure MP. Thermal degradation behaviour of some metal chelate polymer compounds with bis(bidentate) ligand by TG/DTG/DTA. *J Therm Anal Calorim* [Internet]. 2013 May 21;112(2):637–47. Available from: <URL>.
- Padole Gaikwad GS, Juneja HD. Synthesis, thermal degradation, and kinetic parameters studies of some coordination polymers. *J Therm Anal Calorim* [Internet]. 2010 May 31;100(2):645–50. Available from: <URL>.
- Xu Z, Kolapkar SS, Zinchik S, Bar-Ziv E, McDonald AG. Comprehensive kinetic study of thermal degradation of polyvinylchloride (PVC). *Polym Degrad Stab*. 2020 Jun;176:109148. Available from: <URL>.
- Ephraim A, Pozzobon V, Lebonnois D, Peregrina C, Sharrock P, Nzihou A, et al. Pyrolysis of wood and PVC mixtures: thermal behaviour and kinetic modelling. *Biomass Convers Biorefinery* [Internet]. 2023 Jul 13;13(10):8669–83. Available from: <URL>.
- Wang Z, Xie T, Ning X, Liu Y, Wang J. Thermal degradation kinetics study of polyvinyl chloride (PVC) sheath for new and aged cables. *Waste Manag* [Internet]. 2019 Nov 1;99:146–53. Available from: <URL>.
- Zhou R, Huang B, Ding Y, Li W, Mu J. Thermal Decomposition Mechanism and Kinetics Study of Plastic Waste Chlorinated Polyvinyl Chloride. *Polymers (Basel)* [Internet]. 2019 Dec 12;11(12):2080. Available from: <URL>.
- Altarawneh S, Al-Harashsheh M, Dodds C, Buttress A, Kingman S. Thermal degradation kinetics of polyvinyl chloride in presence of zinc oxide. *Thermochim Acta* [Internet]. 2022 Jan 1;707:179105. Available from: <URL>.
- Ghaebi Mehmandoust S, Alizadeh R, Babaluo AA. Kinetic study of the poly(vinyl chloride)/titanium dioxide nanocomposites photodegradation under

- accelerated ultraviolet and visible light exposure. *Polym Adv Technol* [Internet]. 2014 Aug 1;25(8):799–808. Available from: <URL>.
21. Shi Z, Wang Y, Xiao T, Dong S, Lan T. Preparation and Thermal Decomposition Kinetics of a New Type of a Magnetic Targeting Drug Carrier. *ACS Omega* [Internet]. 2021 Feb 2;6(4):3427–33. Available from: <URL>.
22. AlFannakh H. Nonisothermal Kinetic Analysis and AC Conductivity for Polyvinyl Chloride (PVC)/Zinc Oxide (ZnO) Nanocomposite. *Adv Polym Technol* [Internet]. 2020 Aug 17;2020:1233401. Available from: <URL>.
23. Pekdemir ME, Tukur A, Coskun M. Thermal and dielectric investigation of magnetic nanoparticles functionalized with PVC via click chemistry. *Polym Bull* [Internet]. 2021 Oct 17;78(10):6047–57. Available from: <URL>.
24. Šimon P. Isoconversional methods. *J Therm Anal Calorim* [Internet]. 2004;76(1):123–32. Available from: <URL>.
25. Manikandan G, Jayabharathi J, Rajarajan G, Thanikachalam V. Kinetics and vaporization of anil in nitrogen atmosphere – Non-isothermal condition. *J King Saud Univ - Sci* [Internet]. 2012 Jul 1;24(3):265–70. Available from: <URL>.
26. Li H, Niu S, Lu C. Thermal Characteristics and Kinetic Calculation of Castor Oil Pyrolysis. *Procedia Eng* [Internet]. 2017 Jan 1;205:3711–6. Available from: <URL>.
27. Gundogar AS, Kok M V. Thermal characterization, combustion and kinetics of different origin crude oils. *Fuel* [Internet]. 2014 May 1;123:59–65. Available from: <URL>.
28. Lim ACR, Chin BLF, Jawad ZA, Hii KL. Kinetic Analysis of Rice Husk Pyrolysis Using Kissinger-Akahira-Sunose (KAS) Method. *Procedia Eng* [Internet]. 2016 Jan 1;148:1247–51. Available from: <URL>.
29. Biryán F, Demirelli K. Thermal decomposition, kinetics and electrical measurements of Poly(3-Acetamidopropyl Methacrylate)/graphite composites. *Ferroelectrics* [Internet]. 2019 Oct 3;550(1):51–75. Available from: <URL>.
30. Flynn JH, Wall LA. General treatment of the thermogravimetry of polymers. *J Res Natl Bur Stand Sect A Phys Chem* [Internet]. 1966 Nov;70A(6):487. Available from: <URL>.
31. Ozawa TB. *Chemical Society* [Ml. Japan. 1965;38:1881.
32. Doyle CD. Estimating isothermal life from thermogravimetric data. *J Appl Polym Sci* [Internet]. 1962 Nov 1;6(24):639–42. Available from: <URL>.
33. Foner S. Versatile and Sensitive Vibrating-Sample Magnetometer. *Rev Sci Instrum* [Internet]. 1959 Jul 1;30(7):548–57. Available from: <URL>.
34. Long Y, Chen Z, Duvail JL, Zhang Z, Wan M. Electrical and magnetic properties of polyaniline/Fe<sub>3</sub>O<sub>4</sub> nanostructures. *Phys B Condens Matter* [Internet]. 2005 Dec 15;370(1–4):121–30. Available from: <URL>.
35. Hu P, Kang L, Chang T, Yang F, Wang H, Zhang Y, et al. High saturation magnetization Fe<sub>3</sub>O<sub>4</sub> nanoparticles prepared by one-step reduction method in autoclave. *J Alloys Compd* [Internet]. 2017 Dec 25;728:88–92. Available from: <URL>.
36. Tukur A, Pekdemir ME, Haruna H, Coşkun M. Magnetic nanoparticle bonding to PVC with the help of click reaction: characterization, thermal and electrical investigation. *J Polym Res* [Internet]. 2020 Jun 18;27(6):161. Available from: <URL>.





## Tyramine Adsorption Using the Modification of Takari Natural Sand-Based Silica with Bovine Serum Albumin (BSA)

Johnson N. Naat<sup>1\*</sup>, Yantus A. B Neolaka<sup>1</sup>, Yosep Lawa<sup>1</sup>, Petrus M. Noning<sup>1</sup>, Ayu W. M. Menno<sup>1</sup>, Rosnita<sup>1</sup>, Fransiskus B.O. Weo<sup>1</sup>, Dewi Lestarani<sup>1</sup>, Sri Sugiarti<sup>2</sup>, Dyah Iswanti<sup>2\*</sup>

<sup>1</sup>University of Nusa Cendana, Kupang, Chemistry Education Department, Faculty of Education and Teachers Training, East Nusa Tenggara, 85001, Indonesia

<sup>2</sup>Bogor Agricultural University, Department of Chemistry, Bogor, 16144, Indonesia

**Abstract:** In this article, we use a batch method to convey tyramine adsorption by modifying Takari natural sand-based silica with BSA and tyramine adsorption. The research stages include the optimization of adsorbent mass, pH, temperature, determination of the isotherm model, and thermodynamic parameters of tyramine adsorption. The tyramine concentration was determined using UV-Vis. The characterizations carried out were functional groups using FT-IR and surface morphology using SEM. The results of FT-IR characterization demonstrated the success of BSA modification, as observed in the C-H, N-H, and C-N groups, which are the typical functional groups of BSA. The SEM image of SiO<sub>2</sub>@BSA before tyramine adsorption revealed unevenly sized particles, uneven distribution, and agglomeration, leading to larger particles. The morphology of SiO<sub>2</sub>@BSA-tyramine appeared to be more uniform, exhibiting a smoother shape with a slightly uneven surface. The optimum pH was 5 ( $q_e=11.74$  mg/g), and the optimum temperature was 303 K ( $q_e= 2.47$  mg/g). The isotherm study showed that the adsorption adhered to the Redlich-Peterson isotherm model with an  $R^2$  value of 0.987 ( $q_e=5.157$  mg/g and  $n =3.759$ ). The thermodynamic study demonstrated  $\Delta H^\circ = 49.08$  kJ/mol,  $\Delta G^\circ = -17.84; -20.05$  and  $-22.26$  kJ/mol, and  $\Delta S^\circ = 0.22$  kJ/mol.K. These results indicated that the tyramine adsorption process on SiO<sub>2</sub>@BSA adsorbent occurred endothermically and spontaneously at the temperature of 303 K, and the adsorption was of a physical-chemical adsorption type.

**Keywords:** Takari natural sand, adsorption, SiO<sub>2</sub>@BSA, kinetics, isotherm, thermodynamics, tyramine.

**Submitted:** January 31, 2023. **Accepted:** July 10, 2023.

**Cite this:** Naat JN, Neolaka YA, Lawa Y, Noning PM, Menno AWM, Rosnita, Weo FBOW, Lestarani D, Sugiarti S, Iswanti D. Tyramine Adsorption Using the Modification of Takari Natural Sand-Based Silica with Bovine Serum Albumin (BSA). JOTCSA. 2023;10(4):929-40.

**DOI:** <https://doi.org/10.18596/jotcsa.1244774>.

**\*Corresponding author.** E-mail: [johnson\\_naat@staf.undana.ac.id](mailto:johnson_naat@staf.undana.ac.id); [dyahprado@yahoo.co.id](mailto:dyahprado@yahoo.co.id)

### 1. INTRODUCTION

Tyramine is one of the biogenic amine compounds formed from the amino acid tyrosine through a decarboxylation process with the help of the aromatic amino acid decarboxylase enzyme (1). Tyramine can be found in several types of food and beverages, including cheese, fish, fresh meat, fermented meat and vegetables, tomatoes, bananas, prunes, and alcoholic beverages (2-4). Tyramine is essential in the human body in controlling blood pressure by raising blood pressure (3). However, consuming foods or

beverages containing high tyramine can cause adverse effects, namely causing high blood pressure (3, 4), gastric acid hypersecretion, migraine, increased blood sugar levels (5, 6), and toxicity. Higher than histamine, which can cause cell death (7). Therefore, it is necessary to overcome the adverse effects of tyramine. Standard methods used for the determination of tyramine include the extraction and purification of the analyte using acidic solvents such as hydrochloric acid or trichloroacetic acid (8), high-performance liquid chromatography (HPLC) (9), capillary electrophoresis (CE) (10), and thin-layer

chromatography/densitometry (TLC) (11). While these methods are effective, they require expensive equipment, reagent preparation and can be challenging to operate. One method that has been carried out is the adsorption method (12–14). The adsorption method's advantages include using low-cost reagents, simple operation, rapid action, high efficiency, and low cost (15). Adsorption is a mass transfer event on the surface of the adsorbent particles (16). Adsorption occurs because of the attractive force between the adsorbate molecules and the molecules or atoms that compose the surface of the adsorbent (17). The use of the adsorption method as a solution to reduce and remove tyramine has been carried out with several adsorbents, including carbon nanotubes (13), zirconium phosphate (18), Ca-montmorillonite (14), and silica (12).

Silica has an active site in the form of a silanol group ( $\equiv\text{SiOH}$ ) and a siloxane group ( $\equiv\text{Si-O-Si}\equiv$ ) on its surface, thus having polar and hydrophilic qualities (17, 19). Many uses of silica as an adsorbent are based on silica's advantages, which are stable in acidic conditions, not expandable, and high-temperatures resistant. Silica also has a high-mass exchange, good porosity, and a large surface area (19, 10). However, silica has the disadvantage of low surface selectivity and effectiveness. This is because the active sites of silica only have silanol and siloxane groups in which the silanol group consists of oxygen which has a weak ability as an electron pair donor (19–21). To overcome this weakness, the silica surface can be modified by adding organic functional groups to the silica surface (22). One of the ways is to use bovine serum albumin (BSA) (12).

BSA is a protein transporting various chemical compounds in bovine blood (12). The advantages of BSA as a modifying agent are biocompatibility, biodegradability, up to 60 °C for approximately 10 hours of heat resistance, stability at pH 4-9, and non-toxic. BSA also has high solubility at pH 7.4 and good ligand connection properties (23-25). These advantages make BSA a safe modifier of silica modification for tyramine adsorption.

The factors of mass, pH, temperature, and concentration influence the effectiveness of adsorption. Adsorption capacity by  $\text{SiO}_2\text{@BSA}$  adsorbent can vary depending on the mass composition and pH of the solution to determine the interaction of adsorbent and adsorbate (14). Adsorption isotherm studies were conducted to obtain information about the phenomena and interactions between adsorbate and adsorbent. Several adsorption isotherm models of tyramine can predict adsorption performance because adsorption isotherm models can provide information about adsorbent capacity, adsorption mechanism, and evaluation of adsorption process performance (26). In addition, the temperature of the solution affects the adsorbent's ability to adsorb, and thermodynamic studies determine what kind of adsorption process takes place.

Adsorption can exhibit spontaneous or non-spontaneous behavior and can be characterized as exothermic or endothermic. The adsorption properties can be physical, chemical, or a combination of both (27). Previous studies have not widely reported research and reports related to the adsorption and degradation of tyramine, so it is a novelty in this reported article. This article conveys the mass, optimum pH, temperature, eight isotherm models, and thermodynamic parameters of tyramine adsorption using the modification of Takari natural sand-based silica with BSA.

## 2. EXPERIMENTAL SECTION

### 2.1. Materials

Takari natural sand, histamine hydrochloride ( $\text{C}_8\text{H}_{11}\text{NO}\cdot\text{HCl}$ ), Bovine Serum Albumin (heat shock fraction,  $\geq 98\%$  Sigma-Aldrich, USA), distilled water, NaOH crystal pro analyze (Merck KgaA; Darmstadt, Germany), HCl pro analyzes 37%,  $\text{AgNO}_3$ ,  $\text{KH}_2\text{PO}_4$  (Merck KgaA; Darmstadt, Germany), sulfanilic acid pro analyzes (Merck KgaA; Darmstadt, Germany),  $\text{NaNO}_2$  extra pure for analysis (CIMS, Indonesia), and  $\text{Na}_2\text{CO}_3$  (Merck KgaA; Darmstadt, Germany).

### 2.2. Silica extraction and the making of $\text{SiO}_2\text{@BSA}$ adsorbent

The procedure for Silica Extraction from Takari natural sand was obtained from the one carried out by Naat et al. (2018) (20).  $\text{SiO}_2\text{@BSA}$  adsorbent was made as follows: 0.2 g of silica was dissolved in 20 mL of phosphate buffer and sonicated for 7 minutes with a power of 50 W. Next, each 10 mL of BSA solution containing 20, 40, 60, 80, and 100 mg/L was prepared separately in phosphate buffer. Then, each BSA solution was interacted with silica suspension, stirred using a magnetic stirrer for 80 minutes, and sonicated for 7 min. The suspension result was centrifuged for 10 minutes at 300 rpm and washed using phosphate buffer and distilled water. Then, the precipitate was filtered and dried at room temperature to produce  $\text{SiO}_2\text{@BSA}$  powder (23). Characterization was carried out using FT-IR and SEM.

### 2.3. Optimization of Tyramine Adsorption

The optimization of the adsorbent mass was carried out at mass variations of 0.02; 0.04; 0.06; 0.08; 0.1; 0.15, and 0.2 g with pH 7. The optimization of pH was carried out with variations of 4; 5; 6; 7, and 8. Temperature optimization was conducted at 30, 40, and 50 °C variations. All treatments were carried out by interacting 25 mL of tyramine solution with  $\text{SiO}_2\text{@BSA}$  adsorbent, which was stirred using a magnetic stirrer and, centrifuged for 10 minutes, then filtered. The obtained filtrate was added with Pauly reagent and tested using a UV-Vis spectrophotometer at a wavelength of 470 nm (optimum). The adsorption efficiency represents the tyramine percentage removed during the adsorption process. Mathematically, the tyramine adsorption efficiency can be calculated using the equation (28, 29):

$$\%EP = \frac{(C_0 - C_e)}{C_0} \times 100\% \quad (1)$$

$C_0$  represents the initial concentration of the solution (mg/L), while  $C_e$  represents the residual concentration (mg/L). Adsorption capacity states the amount of adsorbate absorbed in the adsorbent at a specific time (mg/L); mathematically, it can be written as follows (30–32):

$$q_e = \frac{(C_0 - C_e)V}{m} \quad (2)$$

Where  $V$  is the volume of the solution (L), and  $m$  is the mass of the adsorbent (g).

#### 2.4. Tyramine Adsorption Isotherm Model

25 mL of tyramine solution with various concentrations of 10, 20, 30, 40, and 50 mg/L were put into beakers with pH 5 solution. In each beaker, 0.1 g of  $\text{SiO}_2\text{@BSA}$  adsorbent was added. Adsorption was carried out in a batch method for 60 minutes while stirring at a temperature of 303 K. After the adsorption, the solution was centrifuged for 10 minutes. The filtrate was then analyzed using a UV-Vis spectrophotometer at a wavenumber of 470 nm to determine the remaining tyramine concentration (12). The data obtained were used to determine the appropriate adsorption isotherm model for the tyramine adsorption process. The isotherm models used for tyramine adsorption are shown in Table 1.

**Table 1:** Mathematical model of adsorption isotherm of tyramine using  $\text{SiO}_2\text{@BSA}$ .

Isotherm Model	Equation	Plotting	Parameter	Reference
Langmuir	$\frac{1}{q_e} = \frac{1}{q_m K_L} \frac{1}{C_e} + \frac{1}{q_m}$	$\frac{1}{C_e}$ vs $\frac{1}{q_e}$	$\frac{1}{q_m}$ = Intercept $q_m = \frac{1}{\text{intercept}}$ $K_L = \frac{1}{q_m \times \text{slope}}$	(26,33)
Freundlich	$\ln q_e = \ln k_f + \frac{1}{n} \ln C_e$	$\ln C_e$ vs $\ln q_e$	$n = \frac{1}{\text{slope}}$ $k_f = e^{\text{intercept}}$	(34)
Temkin	$q_e = B(\ln A) + B(\ln C_e)$	$\ln C_e$ vs $q_e$	$A = e^{\text{intercept}/B}$ $B = \text{slope}$	(26, 34)
Brunauer-Emmett-Teller (BET)	$\frac{C_e}{[(C_0 - C_e)q_e]} = \frac{1}{B q_m} + \frac{(B-1) C_e}{B q_m C_0}$	$\frac{C_e}{[(C_0 - C_e)q_e]}$ vs $\frac{C_e}{C_0}$	$q_m = \text{intercept}$ $\frac{(B-1)}{q_m} = \text{slope}$	(28)
Redlich-Peterson	$\ln \frac{C_e}{q_e} = \beta \ln C_e - \ln K_R$	$\ln C_e$ vs $\ln \frac{C_e}{q_e}$	$K_R = \text{intercept}$ $\beta = \text{slope}$	(28)
Halsey	$\ln q_e = \frac{1}{n_H} \ln k_H - \frac{1}{n_H} \ln C_e$	$\ln C_e$ vs $\ln q_e$	$n_H = \frac{1}{\text{slope}}$ $k_H = e^{\text{intercept}}$	(26)
Jovanovic	$\ln q_e = \ln q_{\max} - k_J C_e$	$C_e$ vs $\ln q_e$	$q_{\max} = e^{\text{intercept}}$ $k_J = \text{slope}$	(33,36)
Dubinin-Radushkevich	$\ln q_e = \ln Q_s - \beta \epsilon^2$	$\epsilon^2$ vs $\ln q_e$	$\beta = K_{DR} = \text{slope}$ $\ln Q_s = \text{intercept}$	(26)

\*Note: The symbol descriptions in Table 1 can be seen in the abbreviations

#### 2.5. Study of Adsorption Thermodynamic of Tyramine

The adsorption thermodynamics was determined by preparing tyramine solutions with 10, 20, 30, 40, and 50 mg/L concentrations at pH 5 of 25 mL each. The solution was then put into vials, and 0.1 grams of  $\text{SiO}_2\text{@BSA}$  was added to each vial.

Adsorption was carried out in a batch method while slowly stirring at 303 K for 60 minutes. After the adsorption, each solution was centrifuged at 300 rpm for 10 minutes and filtered. The filtrate was analyzed using a UV-Vis spectrophotometer to determine the residual tyramine concentration. The same procedure was carried out with

temperatures of 313 K and 323 K. For each temperature variation, the respective K values will be obtained. The K value is then plotted between  $\ln K$  vs  $1/T$ , and from this plot, the values of  $\Delta H^\circ$  and  $\Delta S^\circ$  can be determined, while  $\Delta G^\circ$  can be calculated using equation (37):

$$\Delta G^\circ = \Delta H^\circ - T\Delta S^\circ \quad (3)$$

The enthalpy and entropy changes were calculated using Van't Hoff linear equation (37):

$$\ln K_d = \frac{\Delta S^\circ}{R} - \frac{\Delta H^\circ}{RT} \quad (4)$$

$K_d$  represents the equilibrium constant ( $K_d = q_e/C_e$ ), which depends on the tyramine concentration and temperature. R denotes the ideal gas constant ( $8.314 \text{ JK}^{-1}\text{mol}^{-1}$ ), and T represents the absolute temperature (K). The  $\ln K_d$  vs.  $1/T$  plot data is shown in Figure 6. The value of  $K_d$  can be determined from the intercept of the plot of  $\ln q_e/C_e$  versus  $q_e$ . By plotting  $\ln K_d$  versus  $1/T$ , the values of  $\Delta S^\circ$  and  $\Delta H^\circ$  can be determined from the slope and intercept.

### 3. RESULTS AND DISCUSSION

#### 3.1. Characterization using FT-IR and SEM

$\text{SiO}_2$  and  $\text{SiO}_2@\text{BSA}$  characterization using FT-IR showed a stretching vibration of the -OH functional group from the silanol at a wavenumber of

$3442.97 \text{ cm}^{-1}$ , which decreased in  $\text{SiO}_2@\text{BSA}$  to  $3294.27 \text{ cm}^{-1}$ . A new functional group originating from BSA was shown to be formed at a wavenumber of  $2956.13 \text{ cm}^{-1}$ , which is the C-H stretching vibration from BSA. In  $\text{SiO}_2@\text{BSA}$ , there were 2 wave numbers of  $1651.61 \text{ cm}^{-1}$  and  $1535.34 \text{ cm}^{-1}$ , respectively, which are the stretching of N-H amide and C-N group on the silica surface due to the adsorption of C-N originating from BSA. The results of FT-IR characterization presented the success of BSA modification seen in the C-H, N-H, and C-N groups which are the typical groups of BSA. This result is consistent with previous research reported by Naat et al. (2021) (37). The results of FT-IR for  $\text{SiO}_2@\text{BSA}$  after adsorption showed a stretching vibration originating from the active silica Si-OH group shown on the wave number of  $3442.54 \text{ cm}^{-1}$  and confirmed by the peak on the adsorption at a wavenumber of  $1060.45 \text{ cm}^{-1}$ . Asymmetrical bending vibration of the  $-\text{NH}_3^+$  group from tyramine at a wavenumber of  $1642.54 \text{ cm}^{-1}$  underwent an overlap with the stretching vibration of the N-H group from BSA; this result is also in line with the report by Kulik et al. (2010) and Makara et al., (2008) (38, 39). The FT-IR spectra for  $\text{SiO}_2$  show peaks at a wavenumber of  $1093.27 \text{ cm}^{-1}$  and  $795.75 \text{ cm}^{-1}$ , indicating the asymmetrical and symmetrical stretching vibrations of Si-O in the siloxane (Si-O-Si) structure of  $\text{SiO}_2$ . Wavenumbers of  $791.05 \text{ cm}^{-1}$  and  $447.76 \text{ cm}^{-1}$  displayed symmetrical stretching vibration from Si-O and the bending vibration from the siloxane group (14, 37, 40).

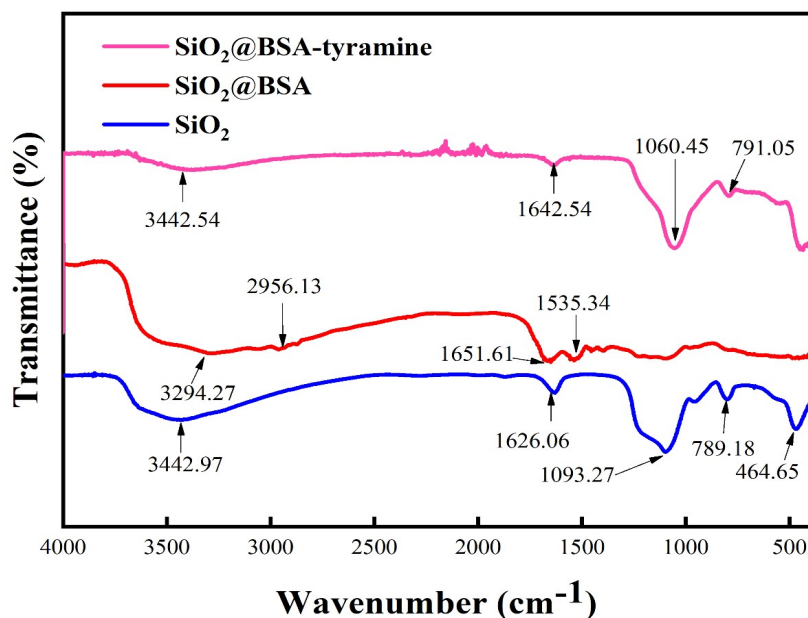


**Figure 1:** FT-IR spectra of  $\text{SiO}_2$ ,  $\text{SiO}_2@\text{BSA}$ , and  $\text{SiO}_2@\text{BSA}$ -Tyramine.

Image result of morphology SEM of the  $\text{SiO}_2@\text{BSA}$  surface (Figure 2.a) and  $\text{SiO}_2@\text{BSA}$ -Tyramine (Figure 2.b) is shown in Figure 2. SEM image of  $\text{SiO}_2@\text{BSA}$  before tyramine adsorption showed particles in non-uniform size, unevenly distributed, and agglomerated, creating bigger particles.

$\text{SiO}_2@\text{BSA}$  after tyramine adsorption demonstrated a more apparent difference. The initially clear particle shape turned unseen after adsorption. Surface morphology after adsorption appeared to be more uniformly distributed, with finer shapes and a slightly uneven surface. SEM image showed



that the SiO<sub>2</sub>@BSA adsorbent surface had ensnared the tyramine molecule, and the tyramine

molecule itself covered most of the SiO<sub>2</sub>@BSA adsorbent surface.

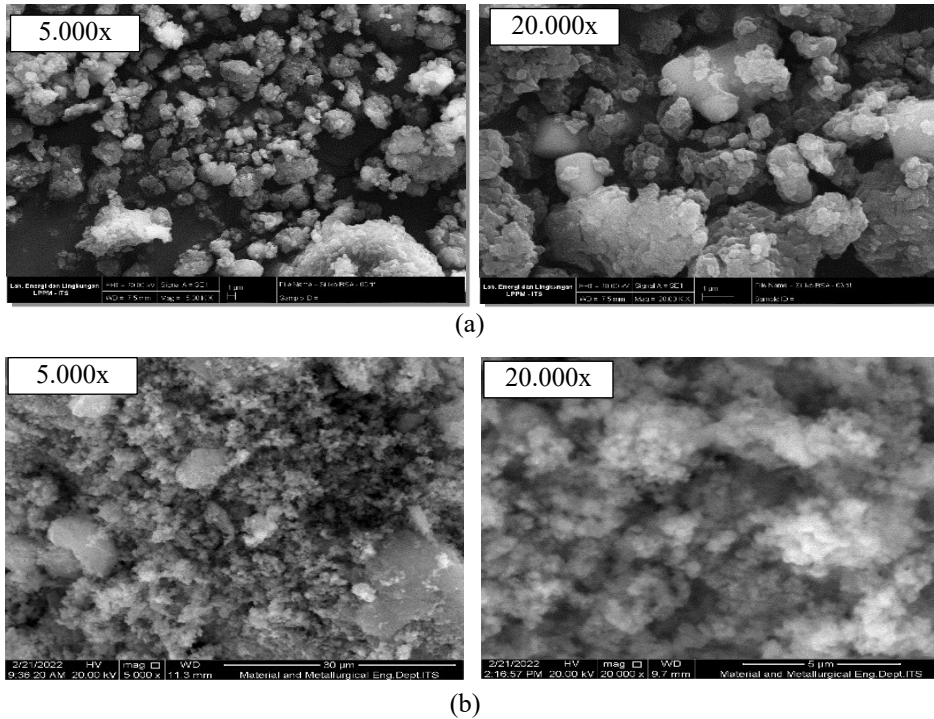


Figure 2: SEM images of SiO<sub>2</sub>@BSA specimen (a) before and (b) after tyramine adsorption.

### 3.2. Optimization of Tyramine adsorption

#### 3.2.1. Optimization of Adsorbent Mass

The result analysis of the tyramine adsorption capacity in each of the SiO<sub>2</sub>@BSA adsorbent mass variations is presented in Figure 3.

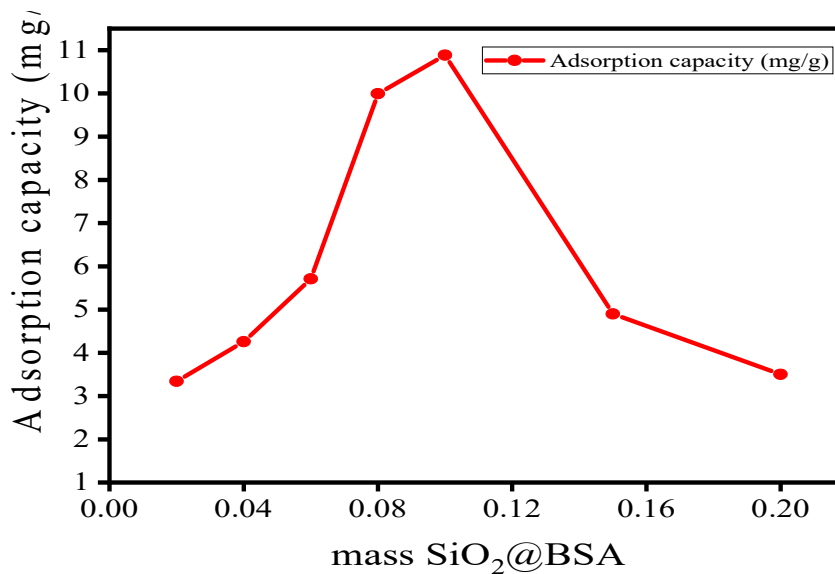


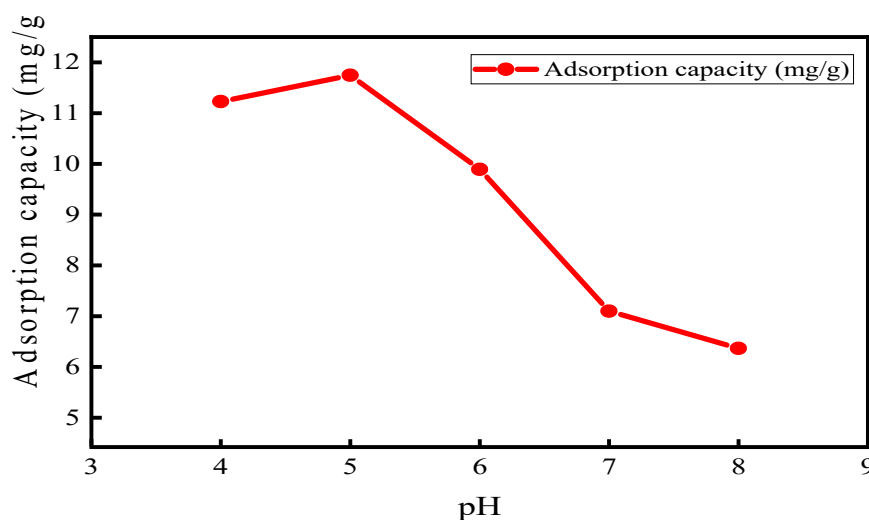
Figure 3: Tyramine adsorption capacity curve according to SiO<sub>2</sub>@BSA mass variation.

Figure 3 shows that tyramine adsorption capacity increased to 0.1 grams of SiO<sub>2</sub>@BSA mass. This increase resulted from adding an active group (-COOH from BSA) on the SiO<sub>2</sub> surface until reaching the optimum ratio to adsorb tyramine. Meanwhile, there was a regular decrease in tyramine adsorption capacity on 0.15-0.2 grams of SiO<sub>2</sub>@BSA mass variation. The decrease in adsorption capacity is due to the BSA polymer overlapping silica surface that further causes interprotein interaction between the electropositive amino group and the electronegative carboxylate

group. The incurred interaction causes the reduction of active adsorbent groups that can interact with tyramine. Therefore, the increased amount of BSA causes the reduced amount of active adsorbent group, thus decreasing tyramine adsorption capacity.

### 3.2.2. pH Optimization of Tyramine Adsorption

The optimum pH of tyramine adsorption in every pH solution variation of 4-8 is presented in Figure 4.



**Figure 4:** Tyramine adsorption capacity curve according to variation of pH solution.

Figure 4 shows an increased adsorption capacity at pH 4-5. This increase resulted from the hydrogen bond between BSA and tyramine. Adsorption capacity occurred at pH 5 ( $q_e=11.74$  mg/g) because BSA tends to be positively charged, which prompts repulsion against tyramine and thus may disrupt the forming of hydrogen bonds between the carboxylate group with tyramine. At pH 5, BSA was in a neutral state; therefore, the forming of hydrogen bonds between BSA and tyramine can proceed well; this is also consistent with a report by Chang et al. (2018) that tyramine bonds with hydrogen through the nitrogen group from amino with oxygen group from the water molecule (41-43). In addition, it is assumed that in this state, there is an H<sub>3</sub>O<sup>+</sup> group that tends to reject tyramine cation and causes the lack of competition between the hydroxide ion of water and the BSA functional group to adsorb tyramine. On the other hand, there was a decrease in adsorption capacity at pH 6 to 8.

**Table 2:** Data of the Optimization of Tyramine Adsorption using SiO<sub>2</sub>@BSA Adsorbent.

Optimized Parameter	Optimum Value	Adsorption Capacity (mg/g)
Adsorbent mass (g)	0.1	10.88
pH	5	11.74
Temperature (K)	303	2.47

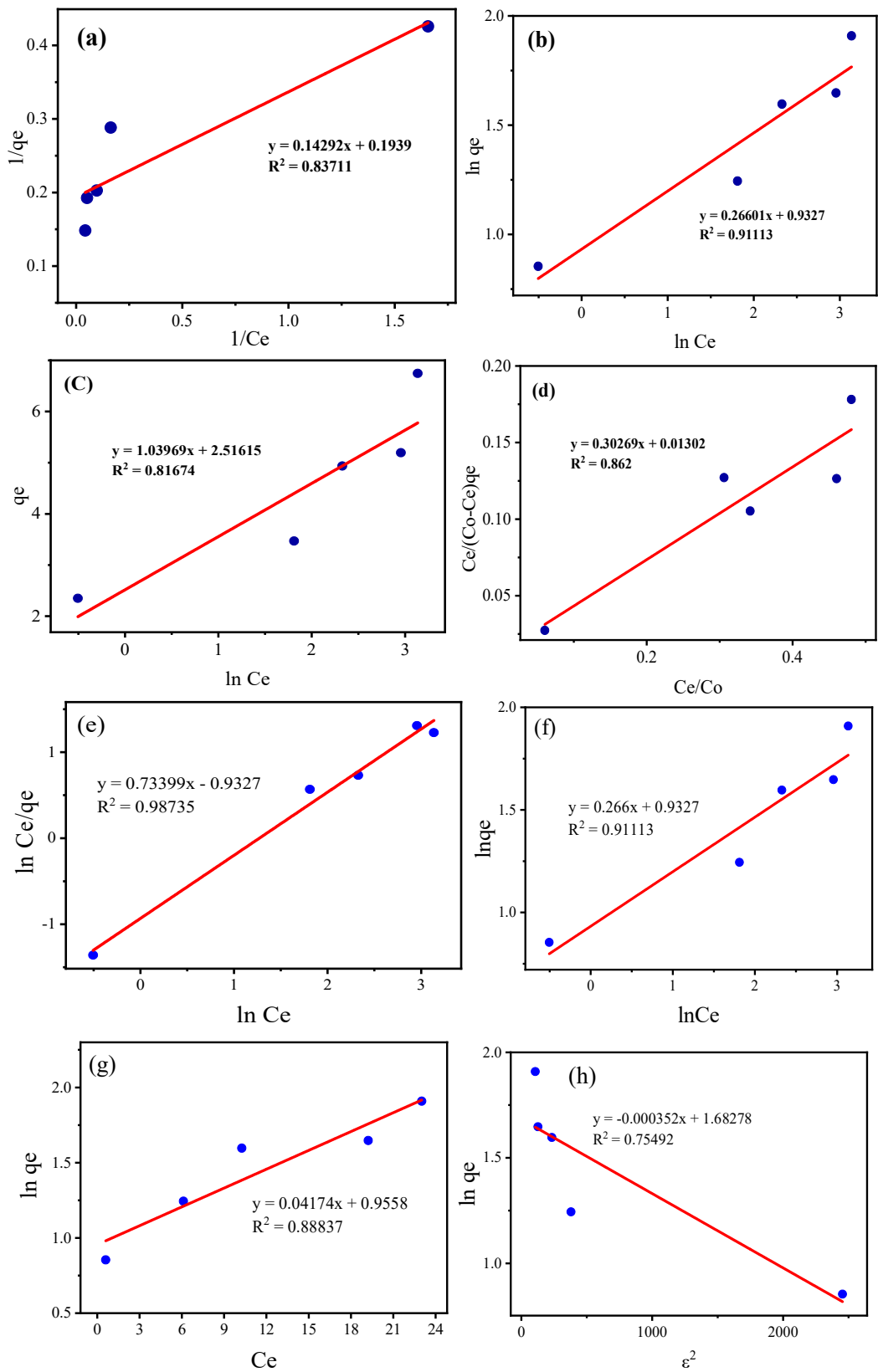
Notes: V=25 mL, T=25 °C, C<sub>0</sub> = 50 mg/L, t = 60 min, and stirred with a shaker at 300 rpm

### 3.3. Tyramine Adsorption Isotherm using SiO<sub>2</sub>@BSA adsorbent

Isotherm determination is carried out by varying initial tyramine concentration from 10-50 mg/L. Adsorption efficiency and capacity are calculated using equations 1 and 2, then proceed to make Langmuir, Freundlich, Temkin, Brunauer-Emmett-Teller (BET), Redlich-Peterson, Halsey, and Jovanovic isotherm model graphs as shown in Figure 5.

**Table 3:** Data of Tyramine Adsorption Isotherm Model Parameter by [SiO<sub>2</sub>@BSA](#).

<b>Isotherm Model</b>	<b>Parameter</b>	<b>Value</b>
Langmuir	$q_m$ (mg/g)	5.157
	$K_L$ (L/mg)	1.357
	$R^2$	0.837
Freundlich	$n$	3.759
	$K_f K_f$ (L/mg)	2.541
	$R^2$	0,911
Temkin	$B$ (J/mol)	1.040
	$A$ (L/mg)	11.250
	$R^2$	0.817
BET	$q_m$	76.805
	$B$	24.248
	$R^2$	0.862
Redlich-Peterson	$K_R$ (L/g)	0.394
	$\beta$	0.734
	$R^2$	0.987
Halsey	$n_H$	3.759
	$k_H$	2.541
	$R^2$	0.911
Jovanovic	$Q_{max}$ (mg/g)	2.601
	$k_J$ (L/mg)	0.042
	$R^2$	0.888
Dubinin-Radushkevich	$\beta = K_{DR}$	-0.0004
	$Q_s$	5.381
	$R^2$	0.755



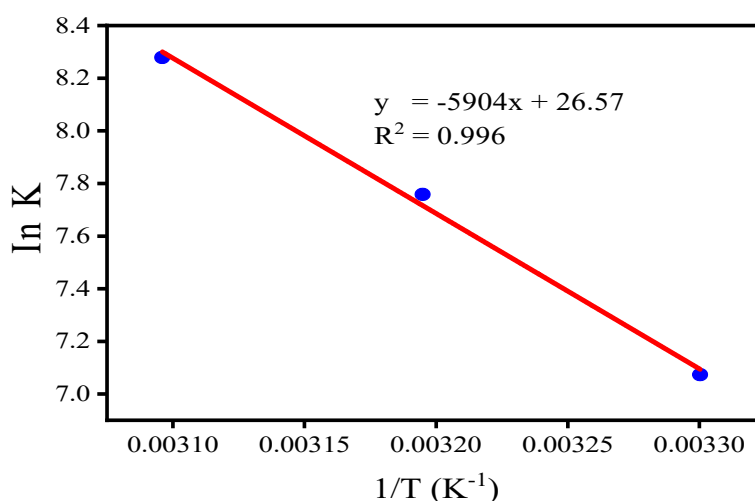
**Figure 5:** 8 Graphs of tyramine adsorption isotherm model by SiO<sub>2</sub>@BSA: (a). Langmuir, (b). Freundlich, (c). Temkin, (d). BET, (e). Redlich-Peterson, (f). Hasley, (g). Jovanovic, (h). Dubinin- Radushkevich.

Figure 5 shows eight isotherm models that have been studied to understand the tyramine adsorption isotherm model using SiO<sub>2</sub>@BSA with silica sourced from Takari natural sand. The tyramine adsorption isotherm model by SiO<sub>2</sub>@BSA adsorbent adheres to the Redlich-Peterson isotherm model as it possesses a coefficient correlation closer to one ( $R^2=0.987$ ) than another isotherm model. This model is the hybrid model of the Langmuir and Freundlich model that can be applied both in a heterogeneous and homogeneous system. In other words, both models are applicable during this adsorption process (44). This isotherm model shows adsorption equilibrium in a wide range (45). Langmuir isotherm model is referred to in low concentration of tyramine, while

the Freundlich isotherm model in a high concentration of tyramine (44, 46). According to the Langmuir isotherm model, the maximum capacity is at 5.157 mg/g, and the  $n$  value in the Freundlich model is obtained as 3.759, which means that the interaction occurred between tyramine and SiO<sub>2</sub>@BSA has involved a chemical reaction and formed monolayer coating.

### 3.4. Adsorption Thermodynamic of Tyramine using SiO<sub>2</sub>@BSA

The result analysis of the adsorption thermodynamic of the tyramine parameter by SiO<sub>2</sub>@BSA adsorbent is presented in Figure 6 and Table 4.



**Figure 6:** Van't Hoff Adsorption Curve on SiO<sub>2</sub>@BSA adsorbent.

**Table 4:** Thermodynamic parameter values of tyramine adsorption on SiO<sub>2</sub>@BSA.

Temperature (K)	$\Delta G^\circ$ (kJ/mol)	$\Delta H^\circ$ (kJ/mol)	$\Delta S^\circ$ (kJ/mol.K)
303	-17.84		
313	-20.05	49.08	0.22
323	-22.26		

Figure 6 and Table 4 indicate that the thermodynamic parameter value presented is  $\Delta H^\circ$  49.08 kJ/mol. A positive value shows that the tyramine adsorption process occurred endothermically, which means the reaction absorbed heat and adsorption capacity increased along with the temperature increase (36, 47, 48). From the enthalpy data, it can be stated that the

BSA adsorption process followed a physical-chemical mechanism with a small entropy change  $\Delta S^\circ$  value of 0.22 kJ/mol which indicates a decrease in randomness or irregularity on the silica surface during the adsorption process.  $\Delta S^\circ$  value also shows conformity between tyramine adsorbate with the active site of SiO<sub>2</sub>@BSA adsorbent and good adsorption reversibility (47-48). The negative Gibbs free energy ( $\Delta G^\circ$ ) values at -17.84; -20.05; -22.26 kJ/mol are at 30, 40, and 50°C, respectively, showing that the adsorption process occurred spontaneously (33). According to the resulting study, it can be concluded that the BSA adsorption process on silica adsorbent occurred endothermically and spontaneously at the temperature of 303 K, and the adsorption occurred as a physical-chemical adsorption type.

**Table 5:** Comparison of the isotherm and thermodynamic studies of adsorption with several types of SiO<sub>2</sub>@BSA and histamine adsorbates.

Adsorbent	Adsorbate	Isotherm models	Thermodynamic (Adsorption Model)	References
Ca-montmorillonite (SAz-2)	Tyramine (TY)	Langmuir	a physical-chemical adsorption type	(14)
Na modified zirconium phosphate Na-ZrP	Tyramine (TY)	Langmuir	-	(18)
SiO <sub>2</sub> @BSA	Tyramine (TY)	Redlich-Peterson	A physical-chemical adsorption	This study

#### 4. CONCLUSION

Silica extracted from Takari natural sand and modified with BSA has been successfully used to adsorb tyramine. FT-IR and SEM characterization results showed that tyramine adsorbed on the SiO<sub>2</sub>@BSA surface. The optimum mass of tyramine adsorption in SiO<sub>2</sub>@BSA adsorbent was 0.1 g, with an adsorption capacity of 10.88 mg/g. The optimum pH was at 5 with an adsorption capacity of 11.74 mg/g and an optimum temperature of 303 K with an adsorption power of 2.47 mg/g. Isotherm study showed that adsorption adheres to the Redlich-Peterson isotherm model with an R<sup>2</sup>=0.987 value with an adsorption capacity equilibrium of 5.157 mg/g and n value of 3.759. The thermodynamic study demonstrated thermodynamic parameter  $\Delta H^\circ = 49.08$  kJ/mol,  $\Delta G^\circ = -17.84; -20.05$  and  $-22.26$  kJ/mol, also  $\Delta S^\circ = 0.22$  kJ/mol.K which showed that tyramine adsorption process on SiO<sub>2</sub>@BSA adsorbent occurred endothermically and spontaneously at the temperature of 303 K and the adsorption occurred as a physical-chemical adsorption type.

#### 5. CONFLICT OF INTEREST

The explicit declaration of whether the conflict of interest does or does not exist.

#### 6. ACKNOWLEDGMENTS

The authors are grateful to the "Ministry of Education, Culture, Research, and Technology" for its financial support through the "Cooperation Research between Universities/PKPT" scheme with a master contract number: 041/E5/PG.02.00.PT/2022 and derivative contract number: 55/UN15.19/SP2H/LT/2022.

#### 7. ABBREVIATIONS

q<sub>e</sub>: adsorbate concentration at equilibrium time (mg/g); q<sub>t</sub>: adsorbate concentration at time t (minutes) (mg/g); k: adsorption rate constant; C<sub>0</sub>: initial concentration of adsorbate in solution (mg/L); C<sub>t</sub>: Concentration of tyramine in solution at time t (mg/L); V: volume of solution (mL); EP:

Absorption Efficiency (%); m: adsorbent mass (g); a: (<1); β: desorption constant related to surface area and chemisorption activation energy (mg/g); t: time. q<sub>max</sub>: the capacity of the adsorbent monolayer (mg/g); K<sub>L</sub>: the Langmuir adsorption constant; C<sub>e</sub>: the adsorbate equilibrium concentration (mg/L); K<sub>f</sub>: Freundlich constant; K<sub>L</sub>: the Langmuir adsorption constant; n: the value indicating the degree of linearity between adsorbate solution and the adsorption process; A: the binding equilibrium constant; B: exponent that lies between 0 and 1; K<sub>H</sub> dan n: the Halsey model constants; K<sub>J</sub>: the Jovanovic constant; B: the Dubinin-Radushkevich isotherm constant; Q<sub>s</sub>: refers to the saturation capacity of theoretical isotherms; ε: the Polanyi potential (J/mol); K<sub>R</sub>: the Redlich-Peterson constants; C<sub>BET</sub>: Isotherm constant which explains the interaction energy with the surface (L/mg); q<sub>m-BET</sub>: Isotherm constant which explains theoretical isotherm saturation capacity (mg/g); B<sub>T</sub>: the adsorption heat constant; A<sub>T</sub>: the binding equilibrium constant; T: the absolute temperature.

#### 8. REFERENCES

1. Finberg JPM & Gillman K. Selective inhibitors of monoamine oxidase type B and the cheese effect. International review of neurobiology. 2011(100):169–190. Available from: <URL>.
2. McCabe-Sellers BJ, Staggs CG & Bogle ML. Tyramine in foods and monoamine oxidase inhibitor drugs: A crossroad where medicine, nutrition, pharmacy, and food industry converge. Journal of Food Composition and Analysis. 2006(19). Available from: <URL>.
3. Halász A, Baráth Á, Simon-Sarkadi L, & Holzapfel W. Biogenic amines and their production by microorganisms in food. Trends Food Sci. Technol. 1994(5):42–49. Available from: <URL>.
4. Santos MHS. Biogenic amines: their importance in foods. 1996 (29):213–231. Available from: <URL>.

5. Andersen G, Marcinek P, Sulzinger N, Schieberle P, and Krautwurst D. Food sources and biomolecular targets of tyramine. *Nutrition reviews*. 2019(77): 107–115. Available from: [<URL>](#).
6. Spano G, Russo P, Lonfau F. Biogenic amines in fermented foods. *Eur J Clin Nutr* 64 (Suppl 3), 2010: S95–S100. Available from: [<URL>](#).
7. Linares DM, del Rio B, Redruello B, Ladero V, Martín MC, Fernández M. Comparative analysis of the in vitro cytotoxicity of the dietary biogenic amines tyramine and histamine. *Food chemistry*, 2016(197):658–663. Available from: [<URL>](#).
8. Loizzo MR, Menichini F, Picci N, Puoci F, Spizzirri UG, Restuccia D. Technological aspects and analytical determination of biogenic amines in cheese. *Trends Food Sci. Technol.*, 2013(30): 38-55. Available from: [<URL>](#).
9. Redruello B, Ladero V, Cuesta I, Álvarez-Buylla JR, Martín MC, Fernández M, Alvarez MA. A fast, reliable, ultra high performance liquid chromatography method for the simultaneous determination of amino acids, biogenic amines and ammonium ions in cheese, using diethyl ethoxymethylenemalonate as a derivatising agent. *Food Chem.* 2013(13): 1029-1035. Available from: [<URL>](#).
10. Jastrzębska, A. A comparative study for determination of biogenic amines in meat samples by capillary isotachopheresis with two electrolyte systems. *Eur Food Res Technol* 2012(235): 563–572. Available from: [<URL>](#).
11. Romano A, Klebanowski H, Guerche SL, Beneduce L, Spano G, Murat ML, Lucas P. Determination of biogenic amines in wine by thin-layer chromatography/densitometry, *Food Chem.* 2012(135): 1392-1396. Available from: [<URL>](#).
12. Vlasova NN, Markitan OV, and Golovkova LP. Adsorption of biogenic amines on albumin-modified silica surface. *Colloid J.* 2011(73): 24–27. Available from: [<URL>](#).
13. Sidorenko IG, Markitan OV, Vlasova NN, Zagorovskii GM, and Lobanov VV. The Adsorption of Biogenic Amines on Carbon Nanotubes. 2009(83): 1139–1142. Available from: [<URL>](#).
14. Chang PH, Jiang WT, and Li Z. Mechanism of tyramine adsorption on Ca-montmorillonite. *Sci. Total Environ.* 2018(642):198–207. Available from: [<URL>](#).
15. Naat J. Pb(II) Adsorption using Silica from Natural Sand of Takari-NTT. *KOVALEN: Jurnal Riset Kimia.* 2022(8): 266-279. Available from: [<URL>](#).
16. Asip F, Mardhiah R, and Husna. Eggshell Effectiveness Test in Adsorbing Fe Ions with Batch Process. *J. Tek. Kim.* 2008(15): 22–26.
17. Suzuki M. [Adsorption Engineering. Tokyo: Kodansha Ltd., 1990.](#)
18. Amghouz Z, Ancín-Azpilicueta C, Burusco KK, García JR, Khainakov SA, Luquin A, Nieto R, & Garrido JJ. Biogenic amines in wine: Individual and competitive adsorption on a modified zirconium phosphate. *Microporous Mesoporous Mater.* 2014(197): 130–139. Available from: [<URL>](#).
19. Buhani and Suharso. Modifikasi silika dengan 3-aminopropiltrimetoksisilan melalui proses sol gel untuk adsorpsi ion Cd(II) dari larutan. *J.Sains MIPA.* 2010(16):177–183.
20. Naat JN, Lapailaka T, Sabarudin A, and Tjahjanto RT. Synthesis And Characterization of Chitosan-Silica Hybrid Adsorbent From The Extraction Of Timor-East Nusa Tenggara Island Silica and its App. *Rasayan J. Chem.* 2018(11):1467–1476.
21. Nurhajawarsi N, Rafi M, Syafitri UD, and Rohaeti E. L-Histidine-Modified Silica from Rice Husk and Optimization of Adsorption Condition for Extractive Concentration of Pb(II). *J. Pure Appl. Chem. Res.* 2018(7):198–208.
22. Alswieleh AM, Modification of Mesoporous Silica Surface by Immobilization of Functional Groups for Controlled Drug Release (2020). Available from: [<URL>](#).
23. Mallakpour S and Nazari HY. The influence of bovine serum albumin-modified silica on the physical-chemical properties of poly(vinyl alcohol) nanocomposites synthesized by ultrasonication technique. *Ultrason. Sonochem.* 2017(41):1–10. Available from: [<URL>](#).
24. Elzoghby AO, Samy WM, and Elgindy NA. Protein-based nanocarriers as promising drug and gene delivery systems. *J. Control. Release.* 2012(161):38–49. Available from: [<URL>](#).
25. Choi JS, and Meghani N. Impact of surface modification in BSA nanoparticles for uptake in cancer cells. *Colloids Surfaces B Biointerfaces.* 2016(145): 653–661. Available from: [<URL>](#).
26. Ragadhita R, Bayu A, and Nandiyanto D. Indonesian Journal of Science & Technology How to Calculate Adsorption Isotherms of Particles Using Two-Parameter Monolayer Adsorption Models and Equations. 2021(6): 205–234. Available from: [<URL>](#).
27. Xu J, Zhen C, Yilin Z, Lou. J. A review of functionalized carbon nanotubes and graphene for heavy metal adsorption from water: Preparation, application, and mechanism. *Chemosphere.* 2018(195):351–364. Available from: [<URL>](#).

28. Naat JN, Neolaka YAB, Lapailaka T, Triandi R, Sabarudin A, Darmokoesoemo H, Kusuma HS. Adsorption of Cu(II) and Pb(II) using Silica@Mercapto(HS@M) hybrid Adsorbent Synthesized from Silica of Takari Sand: Optimization of Parameters and Kinetics, *Rasayan J Chem.* 2021(14):550–560. Available from: [<URL>](#).
29. Aderonke AO, Abimbola BA, Ifeanyi E, Omotayo SA, Oluwagbemiga SA, and Oladotun WM. Adsorption of heavy metal ions onto chitosan grafted cocoa husk char. *African J. Pure Appl. Chem.* 2014(8):147–161. Available from: [<URL>](#).
30. Neolaka YAB, Lawa Y, Naat JN, Riwu AAP, Iqbal M, Darmokoesoemo H, Kusuma HS. The adsorption of Cr(VI) from water samples using graphene oxide-magnetic (GO-Fe<sub>3</sub>O<sub>4</sub>) synthesized from natural cellulose-based graphite (kusambi wood or *Schleichera oleosa*): Study of kinetics, isotherms and thermodynamics *J. Mater. Res. Technol.* 2020(9):6544–6556. Available from: [<URL>](#).
31. Neolaka YAB, Lawa Y, Naat JN, Riwu AAP, Mango AW, Iqbal M, Darmokoesoemo H, B. Widyaningrum WA, Kusuma HS. Efficiency of activated natural zeolite-based magnetic composite (ANZ-Fe<sub>3</sub>O<sub>4</sub>) as a novel adsorbent for removal of Cr(VI) from wastewater. *J. Mater. Res. Technol.* 2022(9): 2896–2909. Available from: [<URL>](#).
32. Kali A, Dehmani Y, and Loulidi I. Study of the adsorption properties of an almond shell in the elimination of methylene blue in an aquatic. 2022(3): 509–522. Available from: [<URL>](#).
33. Ayawei N, Ebelegi AN, and Wankasi D. Modelling and Interpretation of Adsorption Isotherms. *J. Chem.* 2017: 1-11. Available from: [<URL>](#).
34. Binaeian E, Mottaghizad M, Hoseinpour AK, and Babae AS. Bovine serum albumin adsorption by Bi-functionalized HMS, nitrilotriacetic acid-amine modified hexagonal mesoporous silicate. *Solid State Sci.* 2020(103): 106194. Available from: [<URL>](#).
35. Al-Ghouti MA and Da'ana DA. Guidelines for the use and interpretation of adsorption isotherm models: A review. *J. Hazard. Mater.* 2020(393):122383. Available from: [<URL>](#).
36. Kouar J, Bellahcen TO, El Amrani A, and Cherif A. Removal of Eriochrome Black T dye from aqueous solutions by using nano- crystalline calcium phosphate tricalcic apatitic. 2021(4):715–727. Available from: [<URL>](#).
37. Naat JN, Neolaka YAB, Lawa Y, Wolu CL, Lestarani D, Sugiarti S, Iswantini D. Modification of Takari natural sand based silica with BSA (SiO<sub>2</sub>@BSA) for biogenic amines compound adsorbent. *AIMS Materials Science.* 2022(9): 36-55. Available from: [<URL>](#).
38. Kulik TV, Vlasova NN, Palyanytsya BB, Markitan OV, and Golovkova LP. Spectroscopic study of biogenic amine complexes formed at fumed silica surface. *J. Colloid Interface Sci.* 2010(351): 515–522. Available from: [<URL>](#).
39. Makara K, Misawa K, Miyazaki M, Mitsuda H, Ishiuchi S, and Fujii M. Vibrational Signature of the Conformers in Tyramine Studied by IR Dip and Dispersed Fluorescence Spectroscopies. *J. Phys. Chem.* 2008(112):13463–13469. Available from: [<URL>](#).
40. Timin A, Rummyantsev E, and Solomonov A. Synthesis and application of amino-modified silicas containing albumin as hemoadsorbents for bilirubin adsorption. *J. Non. Cryst. Solids.* 2014(385): 81–88. Available from: [<URL>](#).
41. Yoon I, Seo K, Lee S, Lee Y, and Kim B. Conformational Study of Tyramine and Its Water Clusters by Laser Spectroscopy. *J. Phys. Chem.* 2007(111):1800–1807. Available from: [<URL>](#).
42. Chang P, Jiang W, and Li Z. Mechanism of tyramine adsorption on Ca-montmorillonite. *Sci. Total Environ.* 2018(642):198–207. Available from: [<URL>](#).
43. Malferrari D, Bernini F, Tavanti F, Tuccio L, and Pedone A. Experimental and Molecular Dynamics Investigation Proves That Montmorillonite Traps the Biogenic Amines Histamine and Tyramine. *J. Phys. Chem.* 2017(121). Available from: [<URL>](#).
44. Al-ghouti MA and Da DA. Guidelines for the use and interpretation of adsorption isotherm models: A review. *J. Hazard. Mater.* 2019(393): 122383. Available from: [<URL>](#).
45. Tsai C, Chang W, Saikia D, Wu C, and Kao H. Functionalization of cubic mesoporous silica SBA-16 with carboxylic acid via one-pot synthesis route for effective removal of cationic dyes. Elsevier B.V. 2015: 236-248. Available from: [<URL>](#).
46. Foo KY and Hameed BH. Insights into the modeling of adsorption isotherm systems. *Chem. Eng. J.* 2010(156):2–10. Available from: [<URL>](#).
47. Chaudhry SA, Khan TA, and Ali I. Equilibrium, kinetic and thermodynamic studies of Cr(VI) adsorption from aqueous solution onto manganese oxide coated sand grain (MOCSG). *J. Mol. Liq.,* 2017(236):320–330. Available from: [<URL>](#).
48. Maleki MS, Moradi O, and Tahmasebi S. Adsorption of albumin by gold nanoparticles: Equilibrium and thermodynamics studies. *Arab. J. Chem.* 2015(10):S491–S502. Available from: [<URL>](#).





## Carbon Paste Electrode Modified by Dibenzo 18-crown-6 for the Determination of Pb in Carrot Using Differential Pulse Voltammetry

Irdhawati Irdhawati , Ayu Jyostisya Yotirani Arya Wijana, Emmy Sahara, Manuntun Manurung

<sup>1</sup>Udayana University, Department of Magister Chemistry, Denpasar, 80112, Indonesia

**Abstract:** In this research, modification of carbon paste electrode (CPE) using dibenzo 18-crown-6 was carried out to detect Pb level in carrot. The purpose of this electrode modification is to increase the sensitivity of the measurement. The optimized parameters were scan rate, composition of dibenzo 18-crown-6 in carbon paste, and supporting electrolyte. Measurements were validated by determining the linear concentration range, detection limit (LoD), quantification limit (LoQ), repeatability, selectivity, and recovery. At the best measurement conditions, the modified CPE (CPE-Dbc) was applied to determine Pb in carrot. The optimum measurements conditions were obtained the optimum concentration of crown ether in carbon paste was 0.8%, the scan rate using CPE at 15 mV/s, increased to 20 mV/s, and H<sub>2</sub>SO<sub>4</sub> solution as supporting electrolyte. The linear concentration was found in the range of 5-100 µg/L using CPE and became wider to 5-2000 µg/L using CPE-Dbc. The values of LoD and LoQ measurement using CPE were 0.3575 µg/L and 0.3583 µg/L, and decreased to 0.1265 µg/L and 0.1266 µg/L using CPE-Dbc. CPE and CPE-Dbc had good precision with Horwitz ratio values were 0.2231 and 0.2183, which is smaller than two. The percentage of recovery of Pb in the mixture of standard and sample solutions was (88.97 ± 2.76)%. The presence of Cu, Cd and Na in the solution did not interfere the measurement of Pb. The concentration of Pb in carrot sample was (1.8423 ± 0.0002) mg/kg, which was higher than the acceptable concentration according to SNI No. 7387:2009, which is 0.5 mg/kg.

**Keywords:** Carbon paste electrode, carrot, dibenzo 18-crown-6, differential pulse voltammetry, lead (Pb), validation

**Submitted:** May 24, 2022. **Accepted:** August 17, 2023.

**Cite this:** Irdhawati I, Wijana AJYA, Sahara E, Manurung M. Carbon Paste Electrode Modified by Dibenzo 18-crown-6 for the Determination of Pb in Carrot Using Differential Pulse Voltammetry. JOTCSA. 2023;10(4):941-52.

**DOI:** <https://doi.org/10.18596/jotcsa.1120078>.

\*Corresponding author. E-mail: [rdhawati@unud.ac.id](mailto:rdhawati@unud.ac.id).

### 1. INTRODUCTION

Voltammetry is one of the techniques of chemical analysis that is often used to determine metal concentrations in trace levels. The method has advantages, namely it is efficient, highly sensitive, and inexpensive compared to other methods (1). Several previous studies using voltammetry method in the analysis of Pb have been carried out by researchers (2-4). Determination of Pb levels in plants using anodic stripping voltammetry obtained a detection limit value of bare electrode was found at 112.10 µg/L and activated carbon from coconut husk modified CPE was found at 0.72 µg/L in the linear range concentration of 0-1100 µg/L (5). The result of Pb detection using crosslinked

chitosan/carbon nanotubes thin film electrodes obtained at the concentration range of 0.63-3.70 mg/L with limit of detection 0.6 mg/L ( $R^2 = 0.972$ ) (6). LoD and LoQ of Pb using silver nanoparticle modified graphene paste electrode were 12 µg/L and 36 µg/L in linear range concentration of 100-900 µg/L ( $R^2 = 0.9928$ ) (7).

In voltammetry, the working electrode can be modified to improve the performance and lower the detection limit. Some of the modifier materials can be used to analyze Pb, such as activated clay, biopolymer lignin, and crown ether (8-10). Crown ether can bind metals and form stable complexes because they have a cavity in the middle so that able to trap metal ion in the appropriate size (11).

These properties of crown ether can increase the current response of Pb(II) measurement.

The previous studies of Pb(II) determination using modified carbon paste electrode were conducted by researchers, and found different LoD within certain linear range concentration. Measurement of Pb(II) ion using crown ether modified carbon paste electrodes (5% in graphite) had detection limit of 0.11  $\mu\text{g/L}$  at the range of 0.5-60  $\mu\text{g/kg}$  (12). 4-carboxybenzo-18-crown-6 graphite-epoxy composite electrodes for Pb(II) measurement had linear range concentration from 5.0- 186.5  $\mu\text{g/L}$  and LoD value was 1.5. 4-carboxybenzo-15-crown-5 graphite-epoxy composite electrodes had linear range concentration of 10.9-186.5  $\mu\text{g/L}$  and LoD at 3.3 (10). The voltammetric response of N-(2-hydroxypropyl)methacrylamide-co-N-acryloxysuccinimide with 2-aminomethyl-18-crown-6 (p(HPMA-NAS18C6))-modified electrode had linear response in the interval of 0.01-4.39 mg/L Pb(II), and LoD: 0.17  $\mu\text{g/L}$  (13). Screen-printed carbon paste modified with siloxane-crown ether polyamide was used for Pb measurement and had linear concentration range from 50-2760  $\mu\text{g/L}$  and LoD at 30  $\mu\text{g/L}$  (14).

Dibenzo 18-crown-6 (crown ether) is a group of macrocyclic compounds, can form stable complexes with alkali metals, and bind metals and organic ammonium cations (11). These properties indicate that dibenzo 18-crown-6 can be used as a chelating agent with Pb to form a complex. The development of crown ether-based molecular assemblies for the analysis of alkali and heavy metal ions is getting increase. Crown ethers are often used as ionophores for ion-selective electrodes. Electrodes modified with dibenzo-18-crown-6 (CPE-Dbc) are capable for measuring of Pb(II) ion at concentrations below 10 mg/L in the presence of other interfering metal ions, except for Al(III) and Hg(II) which can affect the peak current of Pb(II) measurement significantly (15).

In the development method, validation is very important to determine the performance of the modified working electrode. The validation parameters include a linear concentration range, limit of detection (LoD), limit of quantification (LoQ), precision, accuracy, and selectivity of measurements. Another factor in measuring the peak current of the analyte, is supporting electrolyte solution to reduce the migration current. The choice of a supporting electrolyte solution is very important because solution is a medium for ionization, reduction, and oxidation processes (1). The presence of ions with the same charge or similar atomic radius can produce current response, in addition to the response of the target analyte. The effect of interference ions can be observed by calculating the selectivity coefficient ( $K_{ij}$ ) (16). A modified carbon paste electrode with bigarreau burlat kernel shell (BBKS-CPE) was used for the simultaneous analysis of the same charge ions, i.e. Cd(II), Pb(II) and Cu(II) and obtained a good peak separation (17).

Pb can be produced from various human activities, such as forest fires, air pollution from fuel, industrial waste, and use of fertilizers and pesticides (18). If Pb accumulated in the human body, can cause acute and chronic health problems. Some of the effects of Pb to the human body are damage to the kidneys, testes, liver, nervous system, immune system, and blood (19). Therefore, the detection of Pb in the food and environment needs a selective and sensitive method.

In this study, dibenzo-18-crown-6 was use as a modifier in carbon paste electrode. The concentration of dibenzo-18-crown-6, scan rate, and supporting electrolyte were optimized. Linear concentration range, LoD, LoQ, precision, accuracy, and selectivity of measurement were observed to determine the performance of working electrode in Pb determination. Furthermore, working electrode modified with dibenzo 18-crown-6 were applied to determine the concentration of Pb in carrots from Bedugul vegetable plantation, Tabanan-Bali.

## 2. MATERIALS AND METHOD

### 2.1. Chemicals and Tools

The voltammograms were recorded by an Ingsens potentiostat 1030 (China), DC 12 V adaptor, Ag/AgCl electrode (KCl 0.1 M) as a reference electrode, platinum electrode as counter electrode (Nilaco), analytical balance (Ohaus PX224), magnetic stirrer (Thermoline), micro pipette (Socorex), copper wire  $\varnothing$  2,0 mm (Nilaco), Teflon tube, Metal block digester ZX, oven, and mortar agate.

$\text{HNO}_3$ , HCl,  $\text{Pb}(\text{NO}_3)_2$ ,  $3\text{CdSO}_4 \cdot 8\text{H}_2\text{O}$ ,  $\text{CuSO}_4 \cdot 5\text{H}_2\text{O}$ ,  $\text{K}_3\text{Fe}(\text{CN})_6$ ,  $\text{K}_4\text{Fe}(\text{CN})_6 \cdot 3\text{H}_2\text{O}$ ,  $\text{H}_2\text{SO}_4$ ,  $\text{H}_3\text{PO}_4$ ,  $\text{NaH}_2\text{PO}_4 \cdot 2\text{H}_2\text{O}$ ,  $\text{Na}_2\text{HPO}_4 \cdot 12\text{H}_2\text{O}$ ,  $\text{CH}_3\text{COONa} \cdot 3\text{H}_2\text{O}$ , and  $\text{CH}_3\text{COOH}$  were purchased from Merck, NaCl, KCl, graphite, liquid paraffin, and dibenzo-18-crown-6 were obtained from Wako, and carrot sample was taken from vegetable plantations in the Bedugul area, Tabanan, Bali.

### 2.2. Optimization of Dibenzo-18-crown-6 Concentration in Carbon Paste

The working electrode body was made by inserting a 1 mm Cu wire into a Teflon tube, and leaving an empty space at the bottom of about  $\pm 5$  mm for the carbon paste. 100 mg of graphite and 45  $\mu\text{L}$  of liquid paraffin were mixed until homogeneous in an agate mortar. The carbon paste was inserted into the empty space in the working electrode body. The surface of electrode was smoothed by polishing on the wax paper until shiny (CPE). A modified CPE was prepared by adding dibenzo 18-crown-6 to a carbon paste in concentration of 0.2; 0.4; 0.5; 0.6; 0.7; 0.8; 1.0; 1.2 and 1.4% of the total mass of graphite and dibenzo 18-crown-6, respectively, and continued with the same way with CPE. The working electrode, reference electrode, and counter electrode were immersed into a voltammetric cell containing 10.0 mL of Pb 500  $\mu\text{g/L}$ . Next, the three electrodes were connected to a potentiostat and current measurements were made by DPV, as parameters in

Table 1. The measurement replicated three times for each concentration of dibenzo-18-crown-6.

**Table 1:** Parameters of current measurement in various concentrations of dibenzo 18-crown-6 in carbon paste.

Parameter	Values
Potential Range (mV)	650 s/d -400
Pulse increment (mV)	2.5
Pulse amplitude (mV)	37.5
Scan rate (mV/s)	15

The optimum concentration of dibenzo 18-crown-6 in carbon paste is the composition that produces the highest peak current.

### 2.3. Optimization of Scan Rate

The CPE/modified CPE at the optimum concentration of dibenzo-18-crown-6 as working electrodes, into a voltammetric cell containing 10.0 mL of a 500 µg/L metal standard solution. The solution was measured with various scan rate of 5; 10; 15; 20; 25; and 30 mV/s. The optimum scan rate was determined from the highest peak current.

### 2.4. The Effect of Supporting Electrolyte

The solution Pb(II) 500 µg/L was made in several types of 0.1 M supporting electrolytes i.e. HCl, HNO<sub>3</sub>, H<sub>2</sub>SO<sub>4</sub>, H<sub>3</sub>PO<sub>4</sub>, acetic acid, NaCl, KCl, phosphate buffer, and acetate buffer. The peak current was measured for each supporting electrolyte and the current response was recorded by DPV technique. The supporting electrolyte with the highest peak current was used for the next experiment.

### 2.5. Linear Concentration Range, LoD, and LoQ

Linearity is a concentration range that has a correlation coefficient value close to 1.00 (20). In this work, the linearity was studied in the range of 5-2000 µg/L. The line equation obtained from the linear concentration range was used to calculate LoD and LoQ with the following equation.

$$\text{LoD} = y_B + 3 S_B \quad (1)$$

$$\text{LoQ} = y_B + 10 S_B \quad (2)$$

$$S_B = \frac{S_{y/x}}{\sqrt{\sum (x - \bar{x})^2}} \quad (3)$$

$$S_{y/x} = \sqrt{\frac{\sum (y_i - \hat{y}_i)^2}{n-2}} \quad (4)$$

$$\hat{y}_i = a + bx \quad (5)$$

Description:  $y_B$  is the intercept,  $S_B$  is the relative error of the slope,  $\hat{y}$  value obtained from the substitution of concentration value to the linear equation,  $y_i$  is the peak current measured, and  $n$  is the number of measurements (20).

### 2.6. Repeatability (Precision)

The repeatability of measurement was determined by measuring the concentration of Pb(II) 500 µg/L

ten times, the Horwitz ratio value was calculated. A precision is acceptable if the value of the Horwitz ratio is less than two (21). The Horwitz ratio is calculated by the following equation.

$$SD = \sqrt{\frac{\sum (x - \bar{x})^2}{(n-1)}} \quad (6)$$

$$RSD = \frac{SD}{\bar{x}} \quad (7)$$

$$CV_{\text{count}} = RSD \times 100\% \quad (8)$$

$$CV_{\text{Horwitz}} = 2^{1-(0.5 \log C)} \quad (9)$$

$$\text{Horwitz Ratio} = \frac{CV_{\text{count}}}{CV_{\text{Horwitz}}} \quad (10)$$

The variable of  $x$  is the peak current for each measurement,  $\bar{x}$  is the average of peak currents,  $n$  is the number of measurements, and  $C$  is the concentration fraction of the standard solution. One Way Analysis of Variance (ANOVA) test was used to determine the significance of the peak current, between and within of measurement results. The peak currents were measured using the same type of working electrodes with several measurements (within CPE or CPE-Dbc), and different electrode (between CPE and CPE-Dbc), then the  $F$  value is calculated and compared with the  $F$  table. The calculated  $F$  value is determined by the following equation (22).

$$MSB = \frac{SSB}{k-1} \quad (11)$$

$$MSW = \frac{SSW}{N-k} \quad (12)$$

$$SSB = \sum_{i=1}^k n_i (\bar{x}_i - \bar{x})^2 \quad (13)$$

$$SSW = \sum_{i=1}^k \sum_{j=1}^{n_j} (\bar{x}_{ij} - \bar{x}_i)^2 \quad (14)$$

$$F_{\text{count}} = \frac{MSB}{MSW} \quad (15)$$

$$F\alpha = F_{\text{table}} \text{ at } \frac{df \text{ MSB}}{df \text{ MSW}} \alpha = 0.05 \quad (16)$$

Description: MSB is the Mean Squares Between Variance, MSW is the Mean Squares Within Variance, SSB is the Sum of Squares Between, SSW is the Sum of Squares Within, N is the total sample of the entire population,  $n_i$  is the number of population samples  $i$ ,  $k$  is the total population or group,  $\bar{x}$  is the total mean, and  $\alpha$  is the error level. A good precision is

obtained if the  $F_{count}$  value is smaller than  $F_{table}$  (22).

### 2.7. Percentage of Recovery (Accuracy)

The percent recovery was calculated by comparing the measured and known of standard concentration in the presence of sample as a matrix in solution. An accuracy value is good if the percentage of recovery is in the range of 80-110% (23).

$$Recovery = \frac{(\text{concentration of sample+standard measured}) - (\text{concentration of sample})}{\text{concentration of known standard}} \times 100\% \quad (17)$$

### 2.8. Selectivity Coefficient

The selectivity of Pb(II) was determined by calculating the current response of Pb(II) in the presence of interference ions of Cu(II), Cd(II), and Na(I). The current response was measured in separated and mixed solution methods, as recommended by IUPAC (24). The main concentration of Pb(II), and the interfering ions Cd(II), Cu(II), and Na(I) were varied, i.e. 100; 300; 500; and 1000  $\mu\text{g/L}$ . In the separated solution method, the voltammograms of target and interference ions were recorded separately, but in mixed solution method, the target and interference ions were mixed before measurement. The selectivity coefficient ( $K_{ij}$ ) is calculated by:

$$\log K_{ij}^{pot} = \frac{E_i - E_j}{2,3030 RT / zF} \quad (17)$$

$$K_{ij}^{pot} = \frac{(e^{\Delta E z_i / RT} - 1) a_i}{a_j^{z_i / z_j}} \quad (18)$$

$K_{ij}^{pot}$  is selectivity coefficient of target to interference ions,  $E_i$  is peak potential of target ion,  $E_j$  is the peak potential of interference ion,  $z$  is charge of ion,  $a_i$  and  $a_j$  are the activity of target and interference ions,  $R$ : the gas constant ( $8.314 \text{ J mol}^{-1} \text{ K}^{-1}$ ),  $T$ : temperature (K), and  $F$ :  $96.5 \text{ KJ mol}^{-1}$ . A good selectivity or peak potential resolution is obtained if the value of  $K_{ij}$  is less than one (25).

### 2.9. Sample Analysis

The carrots sample was taken from a vegetable plantation in the Bedugul area, Baturiti District,

Tabanan, Bali, Indonesia, with coordinates location at  $8^{\circ}15'15.2''\text{S } 115^{\circ}09'27.7''\text{E}$ . The samples were washed and cut to a thickness of  $\pm 2 \text{ mm}$  and dried at room temperature for 24 hours. The samples were weighed and then dried in an oven at  $80^{\circ}\text{C}$  for 1 hour. The sample was cooled in a desiccator and weighed, dried and weighed again until a constant mass was obtained. Furthermore, the water content in the sample was calculated.

The dry sample was crushed and weighed around 2 gram and transferred into a digestion tube. 16 mL of aqua regia ( $\text{HNO}_3$ :  $\text{HCl}$ = 4:12) was pipetted into a digestion tube to dilute the sample and heated in a metal block digester at temperature of  $120^{\circ}\text{C}$  during  $\pm 60$  minutes. The digested sample solution was cooled, filtered, and the filtrate was moved into a 50.0 mL volumetric flask and diluted with double distilled water to the mark.

Sample solution was analyzed by standard addition method. 2.0 mL of sample solution was pipetted into 10.0 mL volumetric flask and added standard solution of Pb(II) 1 mg/L with various volume, then diluted up to the mark. The peak current for each solution were measured. The concentration of Pb(II) in the carrot sample was calculated by extrapolated the linear regression line to the axis. The analyte concentration in the sample is  $-C_s = C_x$ ,  $C_s$  is the standard concentration and  $C_x$  is the sample concentration after dilution.

## 3. RESULTS AND DISCUSSION

### 3.1. Optimization of Dibenzo-18-crown-6 Concentration in Carbon Paste

The optimum concentration of dibenzo-18-crown-6 in carbon paste is shown in Figure 1.

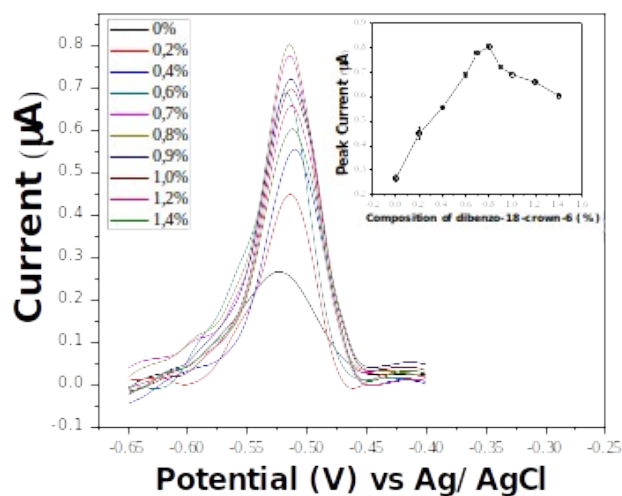


**Figure 1:** Voltammogram and plot between the concentration of the dibenzo 18-crown-6 in carbon paste, against the peak current.

Figure 1 showed the highest peak current was obtained at 0,8% dibenzo-18-crown-6 in carbon paste. The peak current increased from 0.2% up to 0.8% then decreased on the concentration higher than 0.8%. The peak current response using CPE-Dbc in various concentrations of dibenzo-18-crown-6

getting increased at the same potential around -0.50 V. It was indicated that the redox reaction of Pb(II) in presence of dibenzo-18-crown-6 in carbon paste was stable. The complex formation reaction of Pb(II) and dibenzo-18-crown 6 can be seen in Figure 2.

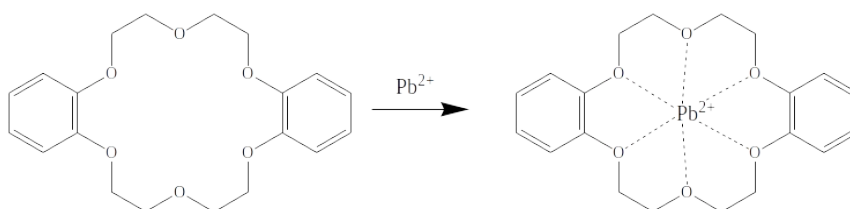
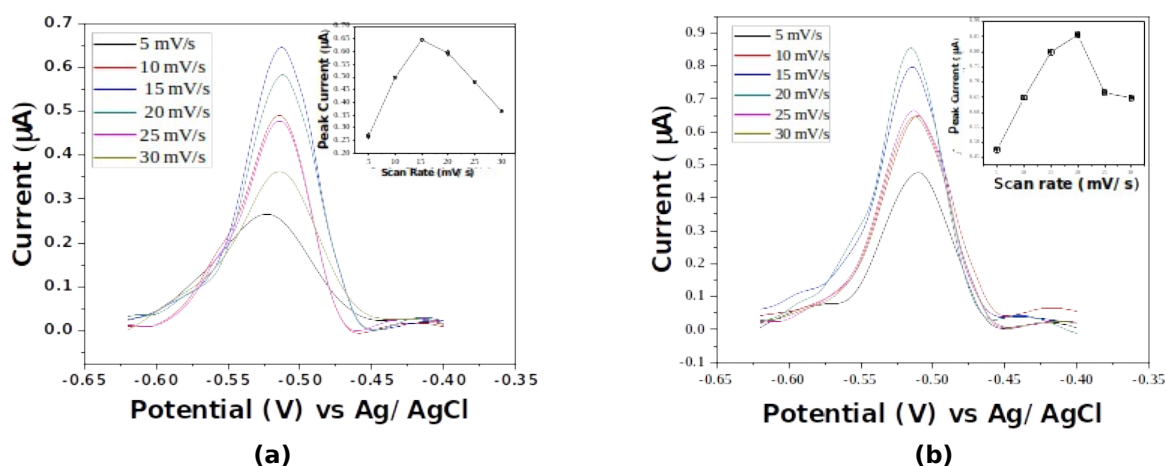


**Figure 2:** Complex formation reaction of dibenzo-18-crown-6 and Pb(II).

Dibenzo-18-crown-6 has an effect on the peak current in the voltammogram was caused by the presence of two benzene rings can reduce the polarity. Therefore dibenzo-18-crown-6 can be dissolved in paraffin (26). Dibenzo-18-crown-6 formed a stable complex compound with Pb(II) metal due to the cavity, which is able to trap appropriate size of metal ion (11) as shown in Figure 2.

### 3.2. Optimization of Scan Rate

Optimum scan rate was measured to determine the redox reaction rate which has highest current response. The voltammogram of Pb(II) at various scan rates was showed in Figure 3, using CPE and CPE-Dbc.



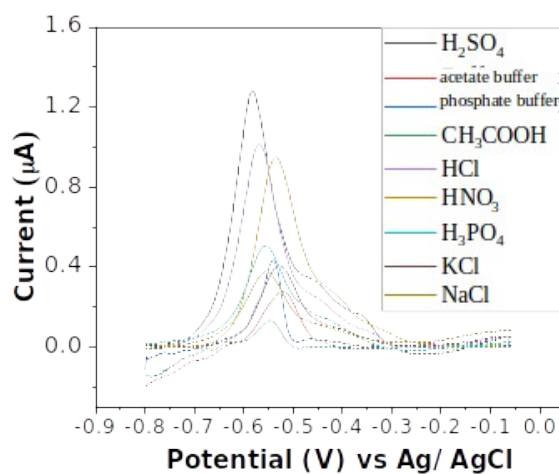
**Figure 3:** Voltammogram in the determination of optimum scan rate using CPE (a) and CPE-Dbc (b).

Figure 3 showed the optimum scan rate using CPE was found at 15 mV/s, with a peak current of 0.6470, and optimum scan rate become faster to be 20 mV/s with a higher peak current of 0.8561 using CPE-Dbc. The addition of dibenzo-18-crown-6 in

carbon paste can accelerate the transfer of electrons at the electrode surface.

### 3.3. The Effect of Supporting Electrolyte

The current response of Pb(II) measurement using different supporting electrolyte as shown in Figure 4.



**Figure 4:** Voltammogram of Pb(II) Measurement in Different Supporting Electrolytes.

The order of peak currents from the highest to the lowest were H<sub>2</sub>SO<sub>4</sub> > HCl > HNO<sub>3</sub> > H<sub>3</sub>PO<sub>4</sub> > phosphate buffer > KCl > NaCl > acetic buffer > acetic acid. The result showed the higher peak current response was found in strong acid electrolyte solutions, compared to the weak acids, inorganic salts, phosphate, and acetic buffer solutions. This is caused by Pb(II) completely dissociating in low pH, and strong acid solution has high conductivity as well. Sulfuric acid solution has

higher peak current than HCl and HNO<sub>3</sub> because H<sub>2</sub>SO<sub>4</sub> is a diprotic acid which can deliver the current more than others.

### 3.4. Linear Concentration Range, LoD, and LoQ

The significant current response and concentration can be determine from the linearity of regression line. The observation of linear concentration range can be seen in Figure 5.

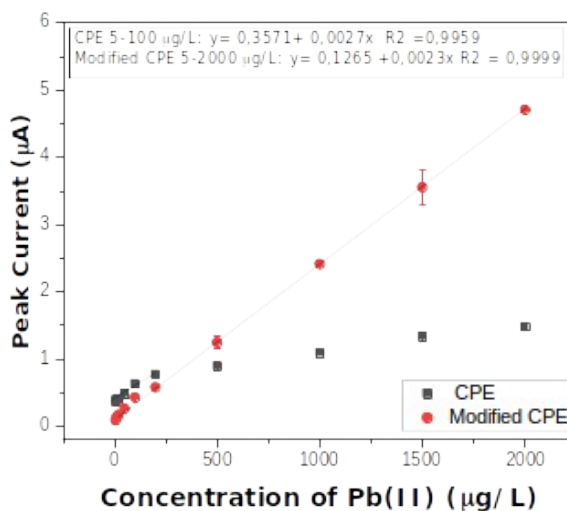


**Figure 5:** Linear Concentration Range of Pb(II) using CPE and modified CPE with dibenzo-18-crown-6.

Figure 4 shows that the linearity using CPE as working electrode was found in the range of 5-100 g/L with  $R^2 = 0.9959$  and increased to 5-2000 g/L using modified CPE by 18-crown-6 dibenzo, with  $R^2 = 0.9999$ . This shows that the addition of dibenzo 18-crown-6 in carbon paste can cause the peak current increase significantly with increasing of concentration. The values of determination coefficient ( $R^2$ ) showed excellent linearity of the calibration curve for the method.

The LoD and LoQ values were obtained using CPE at 0.3575 g/L and 0.3583 g/L, and down to 0.1265 g/L and 0.1266 g/L using CPE-Dbc, respectively. This shows that the modified CPE can be able to detect

Pb(II) at lower concentrations, compared with CPE without modification.

### 3.5. Repeatability (Precision)

The precision determination of Pb(II) measurement using CPE and CPE-Dbc was carried out by ten times peak current recording, performed in different days. The plot between peak current and measurement repeatability as shown in Figure 6.

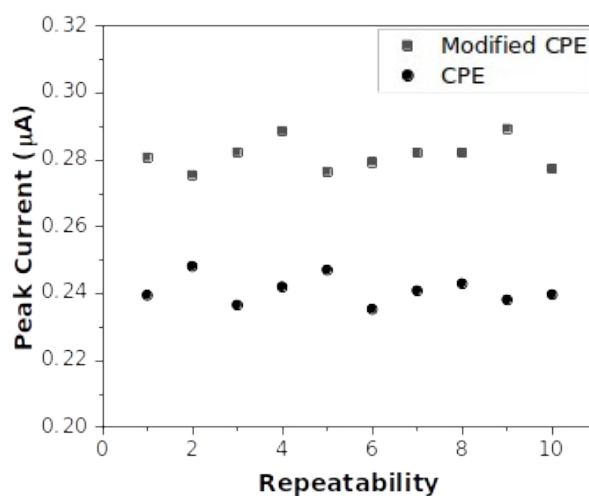


**Figure 6:** Repeatability measurements of Pb(II) using CPE and modified CPE.

Measurement repeatability is a measure of the spread of measurement data and can be expressed as variance (27). Measurement of the repeatability of CPE and modified CPE resulted in the Horwitz ratio of 0.2231 and 0.2183, respectively. A good repeatability value is obtained if the Horwitz Ratio

(HorRat) value is less than two (21). Both of CPE and modified CPE had good repeatability and met the specified requirements. The result of statistic calculation to determine the significant of peak current in ten times measurements is shown in Table 2.

**Table 2:** One Way ANOVA on Recurrence using CPE and CPE modified by dibenzo-18-crown-6.

MS Within Group	$5.98 \times 10^{-5}$
SS Within Group	0.0011
MS Between Group	0.21
SS Between Group	0.2084
$F_{\text{calculated}}$	3485.88
$F_{\text{Table}}$	4.41

The obtained result for  $F_{\text{calculated}}$  is greater than the  $F_{\text{table}}$  values. This means that the addition of a modifier in the working electrode has a significant different peak current.

### 3.6. Percentage of Recovery (Accuracy)

The accuracy of an analytical method is based on the closeness of the test results obtained using the proposed method and the true value (20). The accuracy was accessed from three replicate measurements of Pb(II) 50  $\mu\text{g/L}$ . The value of the recovery from standard solution of Pb(II) using CPE-Dbc was  $(88,97 \pm 2,76\%)$ . It is evident that the

proposed method is accurate within in acceptable range.

### 3.7. Selectivity Coefficient

Selectivity of measurement is determined by observing the current response of analyte in the presence of interference ions. The calculation of the selectivity coefficient ( $K_{ij}$ ) aims to show the level of selectivity of the method for measuring the analyte against the interfering ions. The voltammogram of Pb(II) measurements in the presence of Cu(II) and Cd(II) as interference ions were shown in Figure 7 (separated solution), Figure 8 and Figure 9 (mixed solution).

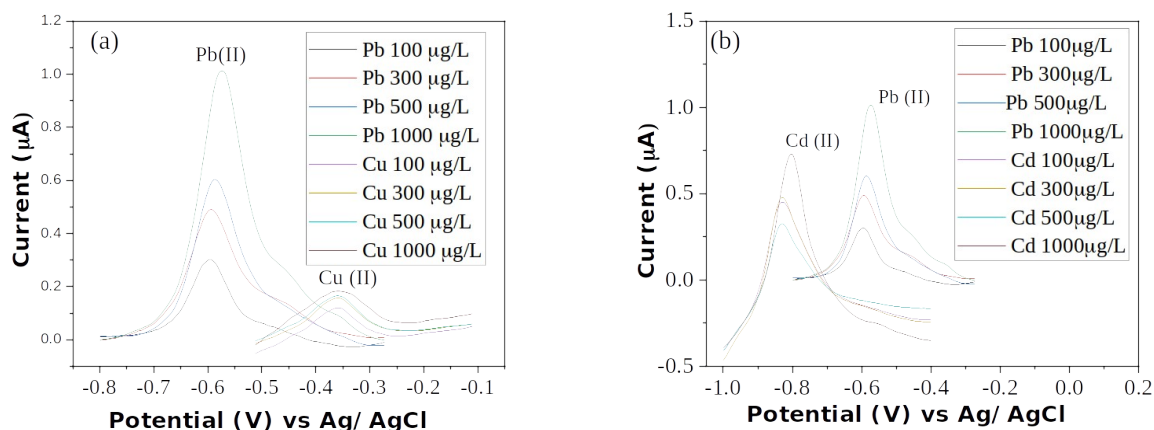


**Figure 7:** Voltammogram of Determination of Selectivity Coefficient of Pb (II) in the presence of Cu(II) (a) and Cd(II) (b) in Separated Solution.



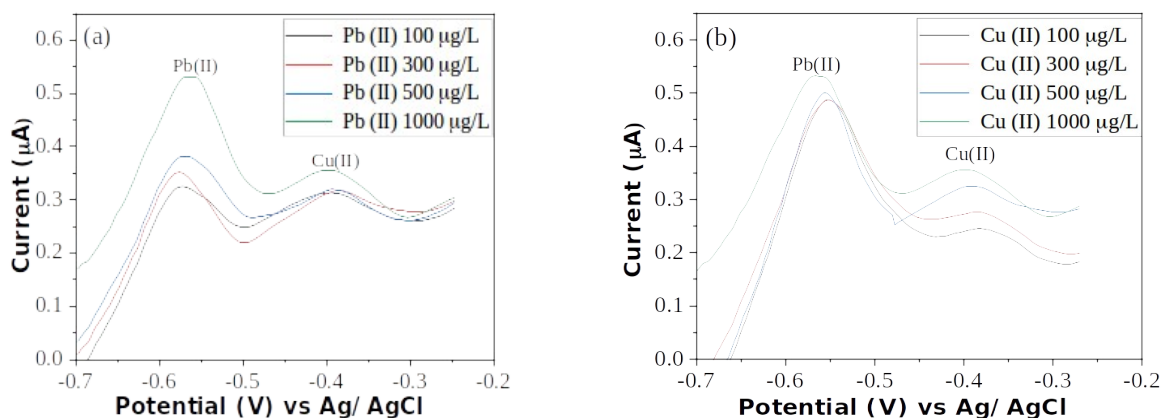


**Figure 8:** Voltammogram of Determination the Selectivity Coefficient of Pb (II) to Cu(II) with Various Concentration of Pb(II) (a), and Various Concentration of Cu(II) (b) in Mixed Solution

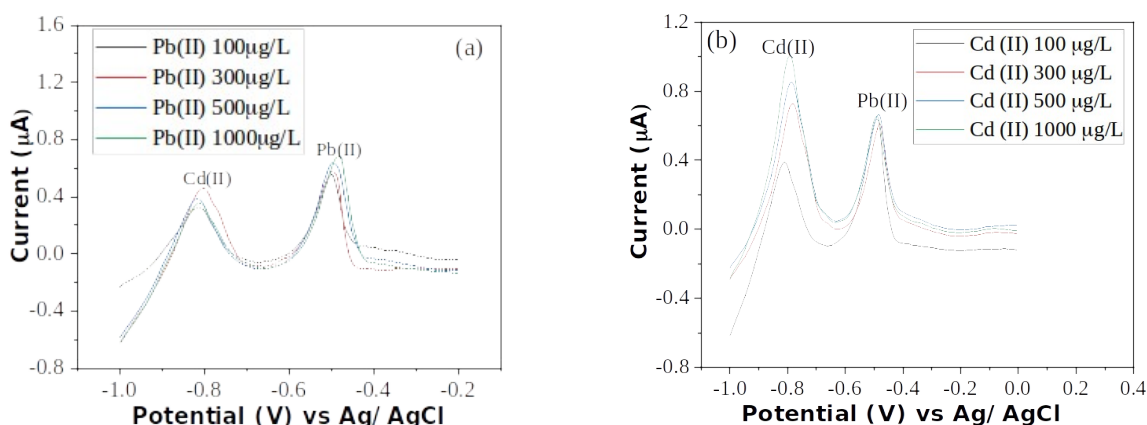


**Figure 9:** Voltammogram of Determination the Selectivity Coefficient of Pb (II) to Cd(II) with Various Concentration of Pb(II) (a), and Various Concentration of Cd(II) (b) in Mixed Solution

The peak potentials for measurements of Pb(II), Cd(II), and Cu(II) were obtained at -0.5879 V, -0.8288 V, and -0.3585 V, respectively. The peak potential values indicated that the measurement of ion Pb(II) in the presence of interfering ions of Cd(II) and Cu(II) using a dibenzo-18-crown-6 modified carbon paste electrode had good resolution. This is in accordance with the research of Hermouche et al (2021) which found that there was good separation peak potential for Cd(II), Pb(II) and Cu(II) ion simultaneously (17). There was no peak in Na(I) measurement at the potential range of Pb(II) because the standard reduction potential value ( $E^\circ$ ) of Na(I) ( $E^\circ = -2.73$  V) and Pb(II) ( $E^\circ = -0.13$  V) totally different. The standard reduction potential of Cd(II) ( $E^\circ = -0.40$  V) and Cu(II) ( $E^\circ = +0.34$  V) are close to  $E^\circ$  of Pb(II), and produce peaks in the potential range of measurements. This shows that the standard reduction potential values of ions is the important factor in determining selectivity. The results of

selectivity coefficient measurement Pb(II) in the presence of Cu(II) and Cd(II) can be seen in Table 3.

In the separated solution,  $K_{ij}$  values were found between  $10^{-8}$  -  $10^{-9}$  and in the mixed solution it is between  $10^{-5}$  -  $10^{-3}$  for the interfering ions of Cu(II) and Cd(II). The selectivity coefficient in separated solution is smaller than that of the mixed solution. In the mixed solution, there is interaction of analyte and interference in the measurement. In separated solution, no interaction of analyte and interference when measuring current. Theoretically, the electrode is declared selective for interfering ions if selectivity coefficient ( $K_{ij}$ ) value is less than one (25). The results obtained indicate that the  $K_{ij}$  values was less than one from both of separated and mixed solutions. Therefore, this method provides good selectivity for the measurement of Pb(II) in the presence of interfering ions of Cu(II) and Cd(II).

**Table 3:** Selectivity coefficient of Pb(II) measurement to Cu(II) and Cd(II) at various concentrations.

Concentration of Pb(II) ( $\mu\text{g/L}$ )	Concentration of Interference Ions ( $\mu\text{g/L}$ )		Selectivity Coefficient( $K_{ij}$ )	
	Cu(II)	Cd(II)	Separated Solution	Mixed Solution
100		500	$1.45 \times 10^{-8}$	$1.23 \times 10^{-3}$
300		500	$1.45 \times 10^{-8}$	$1.10 \times 10^{-3}$
500		500	$8.09 \times 10^{-9}$	$1.12 \times 10^{-3}$
1000		500	$3.08 \times 10^{-9}$	$1.14 \times 10^{-3}$
500	100		$1.87 \times 10^{-8}$	$2.23 \times 10^{-4}$
500	300		$2.00 \times 10^{-8}$	$2.23 \times 10^{-4}$
500	500		$2.27 \times 10^{-8}$	$2.20 \times 10^{-4}$
500	1000		$1.54 \times 10^{-8}$	$2.10 \times 10^{-4}$
500		100	$8.09 \times 10^{-9}$	$1.12 \times 10^{-3}$
500		300	$7.59 \times 10^{-9}$	$1.19 \times 10^{-3}$
500		500	$8.09 \times 10^{-9}$	$1.16 \times 10^{-3}$
500		1000	$7.59 \times 10^{-9}$	$1.24 \times 10^{-3}$
100	500		$1.27 \times 10^{-8}$	$1.04 \times 10^{-4}$
300	500		$1.64 \times 10^{-8}$	$1.03 \times 10^{-4}$
500	500		$2.27 \times 10^{-8}$	$9.66 \times 10^{-5}$
1000	500		$6.37 \times 10^{-8}$	$9.98 \times 10^{-5}$

### 3.8. Sample Analysis

To evaluate the analytical performance of the CPE-Dbc, the quantitative determination of Pb(II) was explored by DPV technique. Before measurement,

the water content of carrot sample was observed at  $(82.8 \pm 2.75)\%$ . The digested sample was measured by standard addition method, obtained the voltammogram as shown in Figure 10.

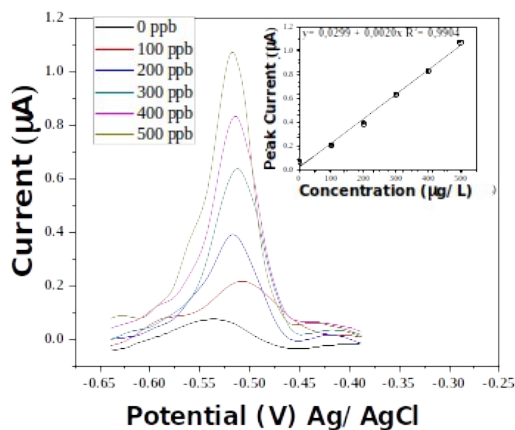


**Figure 10:** Differential Pulse Voltammogram of CPE-Dbc after the addition of Pb(II) into Sample Solution, and Calibration Plot of Oxidation Peak Currents against the Concentration of Pb(II).

The potential peak currents were increased with increase in the Pb(II) concentration. The peak current showed a good linear relationship with Pb(II) concentration over the range between 0 to 500  $\mu\text{g/L}$ . The regression line equation from calibration curve was found at  $y = 0.0299 + 0.0020x$  and  $R^2 = 0.9904$ . The obtained result was satisfactory with the recovery range at  $(88.97 \pm 2.76\%)$ . The content of Pb(II) in carrot sample was obtained at  $1.8423 \pm$

$0.0002 \text{ mg/kg}$ . The content of Pb(II) in this sample is due to the location of the plantation close to the highway, so the residual exhaust fumes from motor vehicles containing Pb(II) can be absorbed into the plants. Based on the Indonesian National Standard (SNI) No. 7387:2009, concerning the maximum limit for Pb contamination in fruits and vegetables and their processed products, the acceptable value is maximum 0.5 mg/kg. The concentration of Pb(II) in

the carrot sample exceeded the maximum specified limit.

#### 4. CONCLUSION

In summary, CPE modified by 0,8% dibenzo 18-crown-6 was prepared for the detection of Pb(II) in the solution as well as in the real sample of carrot. This working electrode is a highly sensitive, stable, and good electrochemical sensor for Pb(II). The excellent performance of CPE-Dbc is due to the properties of dibenzo-18-crown-6 for complex formation, and excellent conductivity for fast electron transport. Based on the results, CPE-Dbc as working electrode is suitable due to its low cost, high sensitivity, easy preparation, and short time measurement.

#### 5. CONFLICT OF INTEREST

All authors declared no conflicts of interest.

#### 6. ACKNOWLEDGMENT

The author would like to thank Mr. Made Atmika as the owner of the carrot plantation, and all of laboratory member in analytical chemistry group in Department of Chemistry, Udayana University.

#### 7. REFERENCES

- Wang J. Analytical electrochemistry. 2nd ed. New York: Wiley Publisher. 2000 ISBN: 0471-28272-3.
- Pizarro J, Segura R, Tapia D, Navarro F, Fuenzalida F, dan Aguirre MJ. Inexpensive and green electrochemical sensor for the determination of Cd (II) and Pb(II) by square wave anodic stripping voltammetry in bivalve mollusks. *Food Chemistry*. 2020 August 15; 321: 1-8. Available from: <DOI>.
- Dahaghin, Z, Kilmartin PA, dan Mousavi HZ. Simultaneous determination of lead(II) and cadmium(II) at a glassy carbon electrode modified with GO@Fe<sub>3</sub>O<sub>4</sub>@benzothiazole-2-carboxaldehyde using square wave anodic stripping voltammetry. *Journal of Molecular Liquids*. 2018 January; 249: 1125-1132. Available from: <DOI>.
- Guo Z, Li DD, Luo XK, Li YH, Zhao QN, LI MM, Zhao YT, Sun TS, dan Ma C. Simultaneous determination of trace Cd(II), Pb(II) and Cu(II) by differential pulse anodic stripping voltammetry using a reduced graphene oxide-chitosan/poly-L-lysine nanocomposite modified glassy carbon electrode. *Journal of Colloid and Interface Science*. 2017 March 15; 490: 11-12. Available from: <DOI>.
- Palisoc S, Estioko LCD, Naticidad M. Voltammetric determination of lead and cadmium in vegetables by graphene paste electrode modified with activated carbon from coconut husk. *Mater Res Express*. 2018 July 27; 5(8): 1-10. Available from: <DOI>.
- Wu KH, Lo HM, Wang JC, Yu SY, Yan BD. Electrochemical detection of heavy metal pollutant using crosslinked chitosan/carbon nanotubes thin film electrodes. *Materials Express*. 2017; 7(1): 15-24. Available from: <DOI>.
- Palisoc S, Lee ET, Natividad M, Racines L. Silver nanoparticle modified graphene paste electrode for the electrochemical detection of lead, cadmium and copper. *International Journal of Electrochemical Science*. 2018;13: 8854 - 8866. Available from: <DOI>.
- Blaise N, Vale'ry HG, Maallah R, Oubaouz M, Justin BTD, Ofudje EA, Chtaini A. Simultaneous electrochemical detection of pb and cd by carbon paste electrodes modified by activated clay. *Journal of Analytical Methods in Chemistry*. 2022 January 19;2022: 1-9. Available from: <DOI>.
- Ifguis O, Moutcine A, Laghlimi C, Ziat Y, Bouhdadi R, Chtaini A, Moubarik A, Mbarki M. Biopolymer-modified carbon paste electrode for the electrochemical detection of Pb(II) in water. *Journal of Analytical Methods in Chemistry*. 2022 January 31;2022: 1-9. Available from: <DOI>.
- Serrano N, Calabuig AG, Valle MD. Crown ether-modified electrodes for the simultaneous stripping voltammetric determination of Cd(II), Pb(II) and Cu(II). *Talanta*. 2015 January 31; 138:1-30. Available from: <DOI>.
- Bradshaw JS, Izzat RM. Crown Ethers: The search for selective ion ligating agents. *Account of Chemical Research*. 1997 August 13;30:338-345. Available from: <DOI>.
- Keawkim K, Chuanuwatanakul S, Chailapakul O. Determination of lead and cadmium in rice samples by sequential injection/anodic stripping voltammetry using a bismuth film/crown ether/nafton modified screen- printed carbon electrode. *Food Control*. 2013 May 1; 31(1):14-21. Available from: <DOI>.
- Simionca AA, Pinteala M. Crown ether-based structures for sensitive electrochemical detection Ion. *High Performance Polymers*. 2015 July 6;27(5): 669-675 2015. Available from: <DOI>.
- Simionca IM, Arvinte A, Ardeleanu R, et al. Siloxane-crown ether polyamide based electrode for electrochemical determination of lead(II) in aqueous solution. *Electroanalysis*. 2012; 24(10): 1995-2004. Available from: <DOI>.
- Jackson DT, Peter N, Nelson PT, Booyesen IN. Lead Ion Selective Electrodes from Dibenzo-18-crown-6 derivatives: An exploratory study. *Journal of Molecular Structure*. 2021 March 5;1227: 1-27. Available from: <DOI>.
- Iyabu H. Pengantar elektrode selektif ion (ESI). 1st ed. Gorontalo: UNG Press. 2014.
- Hermouche L, Aqil Y, Abbi K, Hamdouni YE, Ouanji F, Hajjaji SE, Mahi ME, Lotfi EM, Labjar N. Eco-friendly modified carbon paste electrode by bigarreau burlat kernel shells for simultaneous trace detection of cadmium, lead, and copper. *Chemical Data Collections*. 2021 April;32: 1-17. Available from: <DOI>
- Agustina T. Kontaminasi logam berat pada makanan dan dampaknya pada kesehatan. *Jurnal Teknobuga*. 2014; 1(1) 53-65. Available from: <DOI>.
- Vianne MSA, Hanani Y, Lanang H. Analisis risiko kesehatan lingkungan kandungan kadmium (cd) dalam

- ikan bandeng di kawasan tambak lorok semarang. Jurnal Kesehatan Masyarakat. 2017;5(5) 724-732. Available from: <URL>.
20. Miller JN, Miller JC. Statistics and chemometrics for analytical chemistry. 6th ed. Harlow: Pearson Education Limited. 2010. ISBN: 9780273730439 0273730436.
21. Horwitz, Albert. The Horwitz Ratio (HorRat): A Useful Index of Method Performance with Respect to Precision. Journal Of AOAC International. 2006; 89(4). Available from: <DOI>.
22. Seltman HJ. Experimental design for the behavioral and social sciences: ANOVA one way. 1st ed. Pittsburgh: Carnegie Mellon University. 2012.
23. Association of Official Analytical Chemist (AOAC). Official methods of analysis of AOAC international. 21st ed. MD Gaithersburg: AOAC International. 2019. ISBN: 0935584544 9780935584547.
24. Buck RP, Lindner E. Recommendation for nomenclature of ion selective electrodes, Pure and Application Chemistry. 2009 January 1;66: 2527-2536. Available from: <DOI>.
25. Umezawa Y, Bulhmann P, Umezawa K, Tohda K, Amemiya S. Potentiometric selectivity coefficients of ion-selective electrodes. Pure and Applied Chemistry. 2009 January 1; 72(10):1851-2082. Available from: <DOI>.
26. Balal K, Mohammad H, Baharer B, Ali B, Maryam H, Morgan Z. Zeolite nanoparticle modified carbon paste electrode as biosensor for determination of dopamine and tryptophan. Journal of the Chinese Chemical Society. 2013 September 25;56(4): 789-796. Available from: <DOI>.
27. Harvey D. Modern analytical chemistry 1th ed. New York: Mc Graw Hill.2000. ISBN: 0072375477.



## 3-Hydroxypyridine and 3-(Hydroxymethyl)pyridine in the Synthesis of Salts of Aryldithiophosphonic Acids on the Basis of Monoterpenyl Alcohols

Ilyas S. Nizamov<sup>1,2\*</sup> , Andrey A. Yakovlev<sup>1</sup> , Ilnar D. Nizamov<sup>1</sup> , Marina P. Shulaeva<sup>3</sup> 

<sup>1</sup>Kazan Federal University, A.M. Butlerov Chemical Institute, Kazan, 420008, Russia

<sup>2</sup>A.E. Arbuzov Institute of Organic and Physical Chemistry of Kazan Scientific Center of Russian Academy of Sciences, Laboratory of Organometallic and Coordination Compounds, Kazan, 420088, Russia

<sup>3</sup>Kazan State Medical Academy, Department of Microbiology, Kazan, 420012, Russia

**Abstract:** 3-Hydroxypyridinium and 3-(hydroxymethyl)pyridinium O-terpenyl aryldithiophosphonates were obtained by the reactions of 3-hydroxypyridine and 3-(hydroxymethyl)pyridine with O-terpenyl aryldithiophosphonic acids on the basis of (1*R*,2*S*,5*R*)-(-)-menthol, (1*S*)-endo(-)-borneol, racemic isborneol, and carvacrol. The obtained salts possess high antimicrobial activity against *Bacillus cereus* and *Candida albicans*.

**Keywords:** 3-Hydroxypyridine, 3-(hydroxymethyl)pyridine, dithiophosphonates, antimicrobial activity.

**Submitted:** May 5, 2023. **Accepted:** July 20, 2023.

**Cite this:** Nizamov IS, Yakovlev AA, Nizamov ID, Shulaeva MP. 3-Hydroxypyridine and 3-(Hydroxymethyl)pyridine in the Synthesis of Salts of Aryldithiophosphonic Acids on the Basis of Monoterpenyl Alcohols. JOTCSA. 2023;10(4):953-960.

**DOI:** <https://doi.org/10.18596/jotcsa.1290931>.

\*Corresponding author. E-mail: [isnizamov@mail.ru](mailto:isnizamov@mail.ru).

### 1. INTRODUCTION

Among the pharmacophoric pyridine derivatives, 3-hydroxypyridine was found as a natural product in *Paeonia lactiflora* and *Salvia divinorum* (1). 3-Hydroxypyridine and its derivatives possess therapeutic properties (1-3) (Figure 1). The antihypoxic effect of 3-hydroxypyridine and succinic acid derivatives was established (2). 2-Ethyl-6-methyl-3-hydroxypyridinium N-acetyl-L-glutamate has acute hypoxia and a neuroprotective effect on rats (3). The decreasing of the anxiolytic effect of mexidol as a mixture of 3-hydroxypyridine cation and succinate anion was detected (4). Mexidol (2-ethyl-6-methyl-3-hydroxypyridinium succinate) was used for the solubilization of magnetite nanoparticles in hydrophilic medium (5). 3-Hydroxypyridine and erythropoietin had positive neuroprotective effects on rats as hemorrhagic stroke models (6). As pharmacological agents for the correction of

ischemic brain injury after intracerebral hemorrhage, derivatives of 3-hydroxypyridine such as 3-hydroxy-2-ethyl-6-methylpyridinium, N-acetylaminohexanoate, 4-aminobenzoate, N-acetylaminooacetate, and hydroxybutanedioate were used on rats (7, 8). Bacterial purulent meningitis of rats caused by *Streptococcus pneumoniae* leads to edema of the brain, which is reduced when 2-ethyl-6-methyl-3-hydroxypyridinium 2,6-dichlorophenyl (amino)phenylethanoic acid and bis(2-ethyl-6-methyl-3-hydroxypyridinium) 2,6-dichlorophenyl (amino)phenylethanoic acid are administered to rats (9). 3-Hydroxy-2-methylpyridine, 3-hydroxy-6-methylpyridine and 3-hydroxy-2,6-dimethylpyridine abolish lysozyme fibril formation that is associated with protein-misfolding disorders, including prevalent neurodegenerative diseases (10). Thus, no antimicrobial effects of 3-hydroxypyridine were detected.

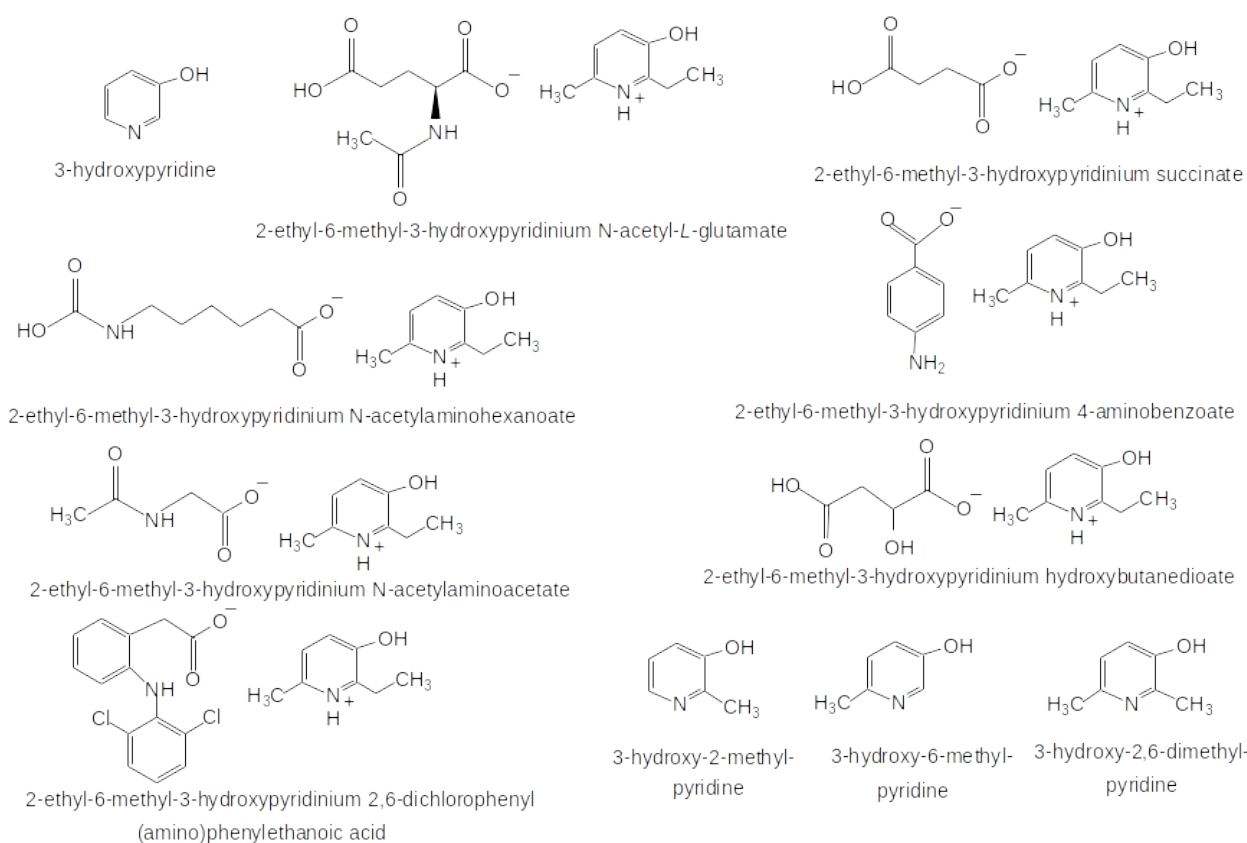


**Figure 1:** 3-Hydroxypyridine and its derivatives.

On the other hand, less attention has been paid to the antimicrobial properties of pyridinium derivatives. Among them, we have chosen phosphorus dithioacids, which have a relatively low toxicity to warm-blooded animals compared to insects (11, 12). The use of phosphorus dithioacids in the reactions with pyridine alkaloids is likely to lead to low toxicity organosulfurphosphorus derivatives possessing ionic structures and promising as antimicrobials. Thus, the antimicrobial activity of pyridinium salts of dithiophosphoric acids on the basis of 3-hydroxypyridine and 3-pyridinemethanol, as well as the corresponding 3-hydroxypyridinium bisdithiophosphonic acids, was recently established (13, 14). In the development of research on synthesis of antimicrobial pyridinium salts of phosphorus dithioacids, we turned to chiral dithiophosphonic acids on the basis of optically active monoterpene alcohols as well as racemic and aryl monoterpene alcohols. In this article, the reactions of O-terpene dithiophosphonic acids with 3-hydroxypyridine and 3-(hydroxymethyl)pyridine and their antimicrobial activity are presented.

## 2. EXPERIMENTAL SECTION

### 2.1. Materials

3-Hydroxypyridine (purity 98%), 3-(hydroxymethyl)pyridine (purity 98%), (1*R*,2*S*,5*R*)-(-)-menthol (purity 99.5%), (1*S*)-*endo*-(-)-borneol (purity 97%), racemic isoborneol (purity 95%), carvacrol (purity 99%), Lawesson's reagent (purity 97%), and tetraphosphorus decasulfide (purity

99%) were purchased from Sigma-Aldrich Co. (St. Louis, MO, USA). 2,6-Di-*tert*-butylphenol (purity 99%) was purchased from Acros Organics (New Jersey, USA). The organic solvents were dried prior to use. Test cultures of pathogenic and opportunistic microflora of museum strains of *Bacillus cereus* (ATCC 19637), *Staphylococcus aureus* (ATCC 29213) and *Candida albicans* (ATCC 885-653) were used from the Department of Microbiology of Kazan State Medical Academy.

### 2.2. Instrumentation

Fourier transform IR spectra were taken on a Bruker Tensor 27 infrared spectrophotometer (Bruker BioSpin AG, Fällanden, Switzerland) (400–4000  $\text{cm}^{-1}$ ) in liquid film or KBr pellet ( $\delta$  = the deformation vibration, *s* – symmetric and *as* – asymmetric vibrations, *gem* – geminal, *vst* = very strong, *st* = strong, *w* = weak, *vw* = very weak, *m* = medium, *vbr* = very broad, *br* = broad vibrations). The  $^1\text{H}$  NMR spectra were obtained on a Bruker Avance-400 (400 MHz) (Bruker BioSpin AG, Fällanden, Switzerland) (400 MHz) or a Bruker Avance-600 (600 MHz) (Bruker BioSpin AG, Fällanden, Switzerland) in in  $\text{CD}_3\text{OD}-\text{CCl}_4$  (1:1). The  $^{13}\text{C}\{^1\text{H}\}$  and  $^{13}\text{C}$  NMR spectra were registered on a Bruker Avance-400 (Bruker BioSpin AG, Fällanden, Switzerland) (100.6 MHz) at ambient temperature (*s* = singlet, *d* = doublet, *t* = triplet, *q* = quartet, *sept* = septet, *m* = multiplet). Chemical shifts ( $\delta$ ) are measured relative to the residual resonance of solvents and given in parts per million (ppm). The  $^{31}\text{P}$  NMR spectra were run on a Bruker Avance-400 (Bruker BioSpin AG, Fällanden, Switzerland)

(161.98 MHz) with 85% H<sub>3</sub>PO<sub>4</sub> as an external reference. The observed optical rotations were detected on a Perkin-Elmer 341 polarimeter at 20 °C (Norwalk, CT, USA) (*D*-line of sodium, 589 nm, a pathlength of 5.52 cm, concentration of 1%) and presented as specific rotations  $[\alpha]^{20}_D$ . The determination of the carbon, hydrogen, nitrogen, and sulfur compositions was carried out on a EuroEA3000 CHNS-O Analyzer (EuroVector S.p.A., Milano, Italy). Phosphorus content was measured by the pyrolysis method on a non-serial instrument.

## 2.3. Synthesis

### 2.3.1. Preparation of initial arylthiophosphonic acids 1a-d

**O-(1R,2S,5R)-(-)-2-Isopropyl-5-methylcyclohex-1-yl 3,5-di-tert-butylphenyldithiophosphonic acid (1d)** was prepared by the reaction of 2,4-bis(3,5-di-tert-butylphenyl) 1,3,2,4-dithiadiphosphetane-2,4-disulfide with (1R,2S,5R)-(-)-menthol in the molar ratio 1:2 in chloroform at 50 °C for 1 h according to the literary method (15).  $[\alpha]^{22}_D = -33.2$  (*c* = 1.00, C<sub>6</sub>H<sub>6</sub>). <sup>31</sup>P{<sup>1</sup>H} NMR (161.98 MHz, CHCl<sub>3</sub>,  $\delta$ , ppm): 86.1. 2,4-Bis(3,5-di-tert-butylphenyl) 1,3,2,4-dithiadiphosphetane-2,4-disulfide was prepared by the reaction of tetraphosphorus decasulfide with 2,6-di-tert-butylphenol according to the literary method (16).

**O-(1R,2S,5R)-(-)-2-Isopropyl-5-methylcyclohex-1-yl 4-methoxyphenyldithiophosphonic acid (1a)** was obtained similarly by the reaction of Lawesson's reagent with (1R,2S,5R)-(-)-menthol in benzene at 50 °C for 2 h according to the literary method (15).  $[\alpha]^{22}_D = -44.5$  (*c* = 1.00, C<sub>6</sub>H<sub>6</sub>). <sup>31</sup>P{<sup>1</sup>H} NMR (161.98 MHz, C<sub>6</sub>H<sub>6</sub>,  $\delta$ , ppm): 83.6.

**O-endo-(1S)-(-)-Trimethylbicyclo[2.2.1]hept-2-yl 4-methoxyphenyldithiophosphonic acid (1b)** was obtained similarly by the reaction of Lawesson's reagent with (1S)-endo-(-)-borneol in benzene at 50 °C for 3 h according to the literary method (17).  $[\alpha]^{22}_D = -25.4$  (*c* = 0.99, C<sub>6</sub>H<sub>6</sub>). <sup>31</sup>P{<sup>1</sup>H} NMR (161.98 MHz, C<sub>6</sub>H<sub>6</sub>,  $\delta$ , ppm): 84.7.

**O-(R,S)-( $\pm$ )-Trimethylbicyclo[2.2.1]hept-2-yl 4-methoxyphenyldithiophosphonic acid (1c)** was obtained similarly by the reaction of Lawesson's reagent with racemic borneol in benzene at 50 °C for 3.5 h. <sup>31</sup>P{<sup>1</sup>H} NMR (161.98 MHz, C<sub>6</sub>H<sub>6</sub>,  $\delta$ , ppm): 84.3.

**O-2-Isopropyl-5-methylcyclohex-6-yl-phenyl 4-methoxyphenyldithiophosphonic acid (1e)** was obtained similarly by the reaction of Lawesson's reagent with carvacrol in benzene at 50 °C for 5 h according to the literary method as likely thymol (18). <sup>31</sup>P{<sup>1</sup>H} NMR (161.98 MHz, CDCl<sub>3</sub>,  $\delta$ , ppm): 85.3.

### 2.3.2. Synthesis of 3-hydroxypyridinium arylthiophosphonates 3a-d and 3-(hydroxymethyl)pyridinium arylthiophosphonates 4a-c

#### 3-Hydroxypyridinium O-(1R,2S,5R)-(-)-2-isopropyl-5-methylcyclohex-yl 4-methoxyphenyldithiophosphonate (3a)

3-Hydroxypyridine **2** (0.1 g, 1.1 mmol) was added portionwise under dry argon with stirring at 20 °C to the solution of acid **1a** (0.4 g, 1.1 mmol) in anhydrous ethanol (10 mL). The mixture was stirred at 20 °C for 2 h, stored at 20 °C for 12 h, evaporated at reduced pressure (0.5 mm Hg) at 40 °C for 1 h, and then in vacuum (0.02 mm Hg) for 1 h to give **3a** (0.5 g, 80%) as a colorless semisolid that was isolated as crystalline solid when washed with acetone,  $[\alpha]^{20}_D = -29.5$  (*c* = 1.00, EtOH). <sup>31</sup>P{<sup>1</sup>H} NMR (161.98 MHz, EtOH,  $\delta$ , ppm): 108.7. Microelemental analysis: found C 58.56; H 7.03; N 2.76; P 6.64; S 14.43 %. C<sub>22</sub>H<sub>32</sub>NO<sub>3</sub>PS<sub>2</sub>. calcd. C 58.25; H 7.11; N 3.09; P 6.83; S 14.14 %. Salts **3b-d** and **4a-c** were obtained similarly as semisolids and then isolated as crystalline solids when washed with acetone. These salts melt below 30-40 °C.

**3-Hydroxypyridinium O-endo-(1S)-(-)-trimethylbicyclo[2.2.1]hept-2-yl 4-methoxyphenyldithiophosphonate (3b)**: yield 76 %,  $[\alpha]^{20}_D = -13.5$  (*c* = 1.00, EtOH). <sup>31</sup>P{<sup>1</sup>H} NMR (161.98 MHz, EtOH,  $\delta$ , ppm): 105.6. Microelemental analysis: found C 58.51; H 6.70; N 3.10; P 6.86; S 14.20 %. C<sub>22</sub>H<sub>30</sub>NO<sub>3</sub>PS<sub>2</sub>. calcd. C 58.51; H 6.70; N 3.10; P 6.86; S 14.20 %.

**3-Hydroxypyridinium O-(R,S)-( $\pm$ )-trimethylbicyclo[2.2.1]hept-2-yl 4-methoxyphenyldithiophosphonate (3c)**: yield 88%, <sup>31</sup>P{<sup>1</sup>H} NMR (161.98 MHz, EtOH,  $\delta$ , ppm): 104.7 and 106.8 (1:0.14). Microelemental analysis: found C 58.45; H 6.43; N 3.05; P 6.73; S 14.56 %. C<sub>22</sub>H<sub>30</sub>NO<sub>3</sub>PS<sub>2</sub>. calcd. C 58.51; H 6.70; N 3.10; P 6.86; S 14.20 %.

**3-Hydroxypyridinium O-(1R,2S,5R)-(-)-2-isopropyl-5-methylcyclohex-yl 3,5-di-tert-butylphenyldithiophosphonate (3d)**: yield 80%,  $[\alpha]^{20}_D = -13.2$  (*c* = 1.16, EtOH). <sup>31</sup>P{<sup>1</sup>H} NMR (161.98 MHz, EtOH,  $\delta$ , ppm): 109.1. Microelemental analysis: found C 63.34; H 8.22; N 2.43; P 5.34; S 11.89 %. C<sub>26</sub>H<sub>46</sub>NO<sub>3</sub>PS<sub>2</sub>. calcd. C 63.12; H 8.40; N 2.54; P 5.61; S 11.62 %.

**3-(Hydroxymethyl)pyridinium O-(1R,2S,5R)-(-)-2-isopropyl-5-methylcyclohex-yl 4-methoxyphenyldithiophosphonate (4a)**: yield 92%, <sup>31</sup>P{<sup>1</sup>H} NMR (161.98 MHz, EtOH,  $\delta$ , ppm): 103.8. Microelemental analysis: found C 59.34; H 7.01; N 2.79; P 6.32; S 13.98 %. C<sub>23</sub>H<sub>34</sub>NO<sub>3</sub>PS<sub>2</sub>. calcd. C 59.07; H 7.33; N 3.00; P 6.62; S 13.71 %.

**3-(Hydroxymethyl)pyridinium O-(R,S)-( $\pm$ )-trimethylbicyclo[2.2.1]hept-2-yl 4-methoxyphenyldithiophosphonate (4b)**: yield 85%, <sup>31</sup>P{<sup>1</sup>H} NMR (161.98 MHz, EtOH,  $\delta$ , ppm): 104.6 and 106.8 (7.3:2). Microelemental analysis: found C 59.12; H 6.78; N 3.32; P 6.39; S 13.94 %. C<sub>23</sub>H<sub>32</sub>NO<sub>3</sub>PS<sub>2</sub>. calcd. C 59.33; H 6.93; N 3.01; P 6.65; S 13.77 %.

**3-(Hydroxymethyl)pyridinium O-2-isopropyl-5-methylcyclohex-6-yl-phenyl 4-methoxyphenyldithiophosphonate (4c):** yield 96%,  $^{31}\text{P}\{^1\text{H}\}$  NMR (161.98 MHz, EtOH,  $\delta$ , ppm): 106.8. Microelemental analysis: found C 59.64; H 6.19; N 3.28; P 6.43; S 14.16 %.  $\text{C}_{23}\text{H}_{28}\text{NO}_3\text{PS}_2$ . calcd. C 59.85; H 6.11; N 3.03; P 6.71; S 13.89 %.

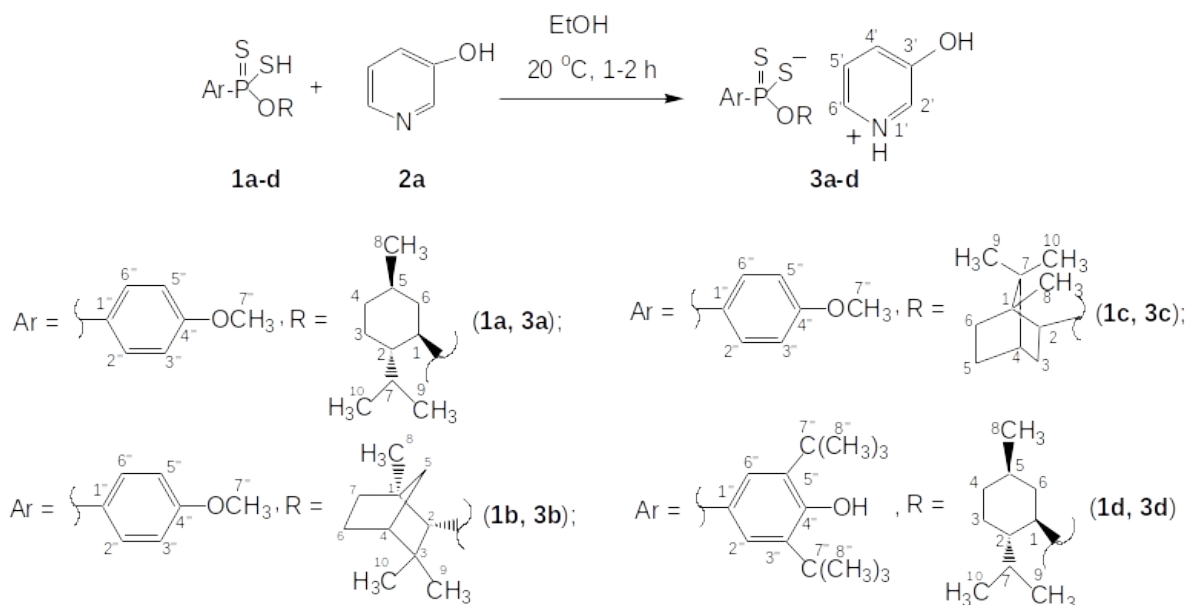
## 2.4. Bioactivity Tests

24 h cultures of bacteria and fungi were washed with physiological solution from beef nutrient agar and standardized according to the turbidity standard up to 0.5 by McFarland ( $1.5 \times 10^8$  CFU  $\text{mL}^{-1}$ ). Bacterial and fungal cultures (0.4 mL) were added to melted and then cooled (at 45 °C) Mueller-Hinton agar (10 mL). The mixture was stirred, poured on sterile Petri dishes (90 mm), and allowed to solidify. Agar plates were punched with a sterile borer with a 6 mm diameter, and holes were filled with the test compounds. Petri dishes were incubated at 35 °C for 24–48 h in an incubator. After the incubation period, the diameter of the growth inhibition zones was measured with an accuracy of 0.1 mm.

## 3. RESULTS AND DISCUSSION

### 3.1. Synthesis and characterization of 3-hydroxypyridinium aryldithiophosphonates

In general, aryldithiophosphonic acids possess a strong P-C bond and a prochiral tetracoordinated phosphorus atom. The presence of asymmetric carbon atoms in O-terpenyl substituents at the phosphorus atom in the aryldithiophosphonic acids can serve as the basis for the creation of new selective antimicrobial drugs. 3-Hydroxypyridine as well as other pyridine derivatives have an unshared electron pair and exhibit basic properties in reactions with strong acids to form pyridinium salts (19). As rather strong organic acids, O-terpenyl aryldithiophosphonic acids can be used in reactions with 3-hydroxypyridine. For these reactions, it was necessary to find a suitable organic solvent. 3-Hydroxypyridine is known to exist in a tautomeric equilibrium between the enol and zwitterion forms in neutral aqueous solution (16). The protonated form at the nitrogen atom of 3-hydroxypyridine cannot accept a proton from the sulfhydryl group of the aryldithiophosphonic acids. Ethanol, as a protic polar organic solvent, seems to shift equilibrium towards the hydroxy form of 3-hydroxypyridine. That is why we have managed to carry out the reactions of chiral O-terpenyl aryldithiophosphonic acids **1a-d** with 3-hydroxypyridine **2a** in ethanol under mild conditions (20 °C, 1–2 h) to give 3-hydroxypyridinium dithiophosphonates **3a-d** in 76–88% yields (Scheme 1).



**Scheme 1:** Synthesis of 3-hydroxypyridinium aryldithiophosphonates **3a-d**.

Thus, ethanol appears to be the most suitable organic solvent and promotes the formation of ionic compounds **3a-d**. In contrast to this, in nonpolar organic solvents, e.g., benzene, these reactions practically do not occur. Salts **3a-d** formed as colorless or yellow semisolids purified by reprecipitation from acetone. Compounds **3a**, **3b**, and **3d** on the basis of (1*R*,2*S*,5*R*)-(–)-menthol and (1*S*)-endo-(–)-borneol possess optical activity (see Experimental). In contrast, **3c** obtained from racemic borneol as well as **4c** obtained on the basis of carvacrol are optically inactive.

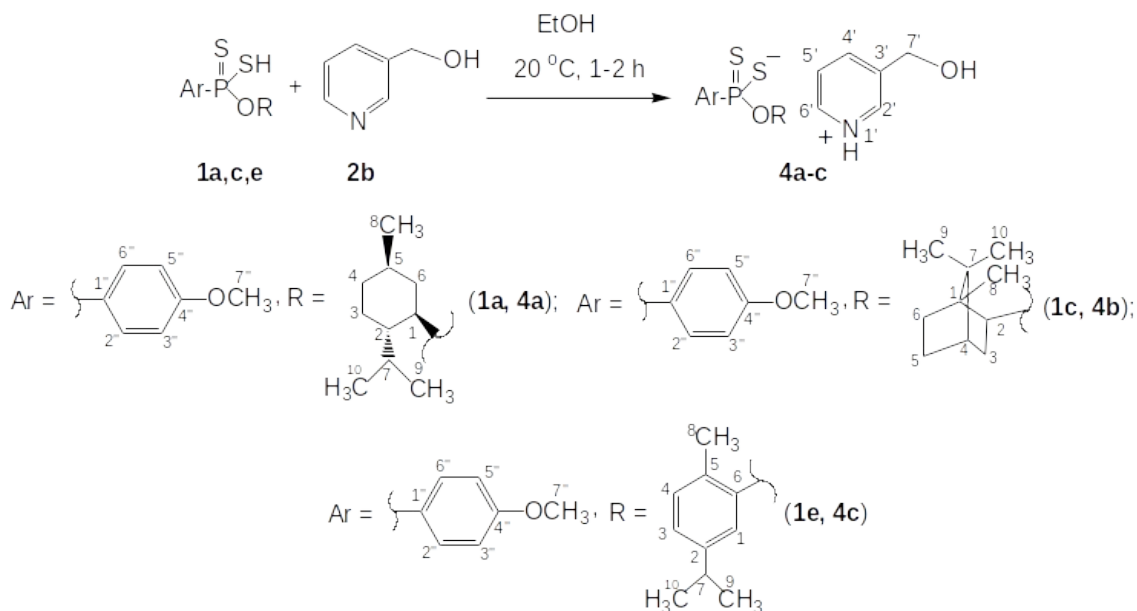
The  $^{31}\text{P}\{^1\text{H}\}$  NMR spectra of **3a-d** in ethanol reveal signals in the range of  $\delta = 104\text{--}109$  ppm like those of other salts of phosphorus dithioacids (20). These resonances are shifted toward low field in comparison with the  $^{31}\text{P}\{^1\text{H}\}$  data of the initial acids **1a-d** ( $\delta = 83\text{--}86$  ppm in benzene or chloroform). It is noteworthy that, as a mixture of isomers, **3c** reveals two signals at  $\delta = 104.7$  and 106.8 ppm in the ratio 1:0.14 in the  $^{31}\text{P}\{^1\text{H}\}$  NMR spectrum in ethanol. In the FTIR spectra of **3a-d**, a medium broad band in the range of  $\nu = 3279\text{--}3632$   $\text{cm}^{-1}$  is attributed to the O–H stretching vibrations of 3-hydroxypyridinium cation, similarly to monograph



(18). The FTIR spectra of **3a-d** confirmed the absence of the bands in the range of  $\nu = 2400\text{--}2550\text{ cm}^{-1}$  of the stretching vibrations of the S–H bonds attributed to acids **1a-b** (21). The  $^1\text{H}$  NMR spectrum of **3b** in  $\text{CD}_3\text{OD-CCl}_4$  solution (1:1) exhibits a doublet at  $\delta = 0.82\text{ ppm}$  ( $^3J_{\text{HH}} = 7.0\text{ Hz}$ ) due to the methyl protons of the fragment  $\text{C}^8\text{H}_3\text{CH}$  of O-menthyl substituent. A doublet at  $\delta = 8.21\text{ ppm}$  ( $^3J_{\text{HH}} = 4.0\text{ Hz}$ ) and a singlet at  $\delta = 8.27\text{ ppm}$  are assigned to the aromatic protons of the fragments  $\text{C}^6\text{H}$  and  $\text{C}^2\text{H}$  respectively, of the cation. In the  $^{13}\text{C}\{^1\text{H}\}$  NMR spectra in  $\text{CD}_3\text{OD-CCl}_4$  solution (1:1), **3b** and **3c** are characterized by a singlet in the low field region (154–155 ppm), that is attributed to the carbon atom of the  $\text{C}^3\text{-OH}$  group of cation. The proton of the  $\text{C}^3\text{-OH}$  fragment of racemic **3c** resonates as two singlets at 154.8 and 154.9 ppm. Thus, the aromatic hydroxyl group of 3-hydroxypyridine is not involved in reactions with arylthiophosphonic acids. The reactions proceed with the protonation of the pyridine nitrogen atom by the action of dithiophosphonic acids.

### 3.2. Synthesis and characterization of 3-(hydroxymethyl)pyridinium arylthiophosphonates

In continuation of a study of the reactivity of the pyridine derivatives towards phosphorus dithioacids, we have tried to extend the salt formation reactions to 3-(hydroxymethyl)pyridine. It should be emphasized that 3-(hydroxymethyl)pyridine contains a more active aliphatic hydroxyl group compared to the aromatic O–H bond of 3-hydroxypyridine. It could be expected that 3-(hydroxymethyl)pyridine would react with arylthiophosphonic acids with the participation of the O–H bond under severe conditions, which would lead to S-ester arylthiophosphonates. However, under mild conditions (20 °C, 1–2 h), the reaction of acids **1a,c,e** with 3-(hydroxymethyl)pyridine **2b** has been found to brought about the formation of 3-(hydroxymethyl)pyridinium dithiophosphonates **4a-c** in 85–96% yields (Scheme 2).



**Scheme 2:** Synthesis of 3-(hydroxymethyl)pyridinium arylthiophosphonates **4a-c**.

The  $^{31}\text{P}\{^1\text{H}\}$  NMR spectral signals of **4a-c** with 3-(hydroxymethyl)pyridinium cation ( $\delta = 104\text{--}109\text{ ppm}$  in ethanol) show no significant change compared to **3a-d**. In the case of racemic isborneol derivative **4b**, its  $^{31}\text{P}\{^1\text{H}\}$  NMR spectrum exhibits two singlets at  $\delta = 104.6$  and 106.8 ppm in the ratio 7,3:2 that is assigned to the formation of the mixture of isomers. The FTIR spectra of the hydroxymethyl containing salts **4a-c** reveal a strong broad band in the range of  $\nu = 3313\text{--}3329\text{ cm}^{-1}$  due to the stretching vibrations of the O–H bond of the cation. In the  $^1\text{H}$  NMR spectrum of **4a** in  $\text{CD}_3\text{OD-CCl}_4$  (1:1), the methylene protons of the  $\text{C}^7\text{H}_2\text{O}$  fragment of 3-(hydroxymethyl)pyridinium cation appear as a singlet at  $\delta = 4.77\text{ ppm}$ . Similar singlets are also observed in the  $^1\text{H}$  NMR spectra of **4b** and **4c** in  $\text{CD}_3\text{OD-CCl}_4$  (1:1) ( $\delta = 4.59\text{ ppm}$  for **4b** and 4.78 ppm for **4c**). In the  $^{13}\text{C}$  NMR spectrum of **4a** in  $\text{CD}_3\text{OD-CCl}_4$  (1:1), the carbon atom of the  $\text{C}^7\text{H}_2\text{OH}$  fragment of cation resonates as a triplet at  $\delta = 60.5\text{ ppm}$  ( $^1J_{\text{CH}} = 143.4\text{ Hz}$ ), whereas in the

$^{13}\text{C}\{^1\text{H}\}$  NMR spectrum the same carbon atom appears as a singlet. Thus, under mild conditions, 3-(hydroxymethyl)pyridine reacts with arylthiophosphonic acids with an increase in the coordination number of the pyridine nitrogen atom and the formation of 3-(hydroxymethyl)pyridinium arylthiophosphonates.

### 3.3. Biological evaluation

Bacteria and fungi cause significant damage by affecting food and feed, causing various diseases in humans and animals (22, 23). So, the creation of new bactericidal and fungicidal drugs is an urgent problem. To develop the scientific basis for novel selective antimicrobials, the synthesized pyridinium salts **3a-d** and **4a-c** were screened for bactericidal and fungicidal activities against *Bacillus cereus* (ATCC 19637), *Staphylococcus aureus* (ATCC 29213), and *Candida albicans* (ATCC 885-653) (Table 1) using gel diffusion test on

Mueller-Hinton agar in 1% solutions of test compounds in dimethyl sulfoxide (DMSO).

Antibiotic cefazolin (1% in DMSO) and fungicide triticonazole (1% in DMSO) were used as controls.

**Table 1:** The antimicrobial activity of products obtained.<sup>a</sup>

Compound	<i>B. cereus</i>	<i>S. aureus</i>	<i>C. albicans</i>
<b>3a</b>	17	17	16
<b>3b</b>	26	25	14
<b>3c</b>	29	28	-
<b>3d</b>	22	13	19
<b>4a</b>	19	20	12
<b>4b</b>	27	30	-
<b>4c</b>	14	12	20
<b>Cefazolin<sup>b</sup></b>	25	38	13
<b>Triticonazole<sup>b</sup></b>	-	-	22

<sup>a</sup>Inhibition zone in mm in DMSO

<sup>b</sup>1% in DMSO

Salts **3c** and **4b** containing a racemic O-isoborneolyl substituent show the most bactericidal activity against *B. cereus* (growth inhibition zone of 29–27 mm) as compared to cefazolin (25 mm). Salt **4c** bearing a pharmacophoric O-aryl substituent (on the basis of carvacrol) exhibits remarkable antifungal activity toward the tested *C. albicans* (20 mm) and approaches triticonazole (22 mm). Thus, substituted pyridinium salts of dithiophosphonic acids prepared from racemic monoterpenyl alcohols possess more antifungal activity as compared to salts on the basis of enantiomerically pure monoterpenyl alcohols.

#### 4. CONCLUSION

The synthesis of 3-hydroxypyridinium and 3-(hydroxymethyl)pyridinium O-terpenyl aryldithiophosphonates has been successfully carried out. These salts were obtained by reacting O-terpenyl aryldithiophosphonic acids with 3-hydroxypyridine and 3-(hydroxymethyl)pyridine under mild conditions. Ethanol is the best organic solvent for these reactions and promotes the formation of ionic products. Pyridinium aryldithiophosphonates on the basis of (1*R*,2*S*,5*R*)-(-)-menthol and (1*S*)-endo(-)-borneol possess optical activity. The reactions proceed with the protonation of the pyridine nitrogen atom by the action of dithiophosphonic acids. The synthesized salts have been tested for their antimicrobial activity. 3-Hydroxypyridinium and 3-(hydroxymethyl)pyridinium aryldithiophosphonates containing a racemic O-isoborneolyl substituent show the most bactericidal activity against *Bacillus cereus*. 3-(Hydroxymethyl)pyridinium aryldithiophosphonate bearing O-carvacrolyl substituent exhibits remarkable antifungal activity toward *Candida albicans*. The obtained results seem promising for carrying out the next steps in the antimicrobial activity study.

#### 5. CONFLICT OF INTEREST

The authors declare no conflicts of interest.

#### 6. ACKNOWLEDGMENTS

This paper has been supported by the Kazan Federal University Strategic Academic Leadership Program ("PRIORITY-2030"), and the Russian

Foundation for Basic Research (grants no. 18-415-160012-p\_Volga Region\_a). The authors are grateful to the staff of Distributed Spectral-Analytical Center of Shared Facilities for Study of Structure, Composition and Properties of Substances and Materials of Federal Research Center of Kazan Scientific Center of the Russian Academy of Sciences for their research and assistance in discussing the results. The researchers are thankful to Professor Oscar K. Pozdeev, Kazan State Medical Academy, Department of Microbiology, for biological evaluation.

#### 7. REFERENCES

1. Encyclopedia of Endocrine Diseases. I Huhtaniemi, L Martini Eds. 2th ed. Academic Press; 2018. Vol. 15. ISBN 978-0-12-812200-6
2. Volchegorskii IA, Rassokhina LM, Miroshnichenko Iu. Antihypoxic effect of 3-hydroxypyridine and succinic acid derivatives and their nootropic action in alloxan diabetes. Eksp Klin Farmakol. 2011;74(12):27–32.
3. Yasnetsov VV, Skachilova SYa, Sernov LN, Voronina TA. Synthesis and pharmacological properties of a new 3-hydroxypyridine derivative. Pharm Chem J. 2012;46:199–202. Available from: <URL>.
4. Volchegorskii IA, Miroshnichenko IY, Rassokhina LM, Faizullin RM, Malkin MP, Pryakhina KE, Kalugina AV. Comparative analysis of the anxiolytic effects of 3-hydroxypyridine and succinic acid derivatives. Bull Exp Biology Med. 2015;158(6)756–61. Available from: <URL>.
5. Vazhnichaya YeM, Mokliak YeV, Kurapov YuA, Zabozaev AA. Role of mexidol (2-ethyl-6-methyl-3-hydroxypyridine succinate) in the obtaining of stabilized magnetite nanoparticles for biomedical application. Biomeditsinskaya Khimiya. 2015;61(3)384–88. Available from: <URL>.
6. Kolesnichenko PD, Scheblykina OV, Nesterova NI, Scheblykin DV, Nesterov AV, Pokrovskiy MV, Zhuchenko MA, Tverskoy AV, Reznikov KM. Additive neuroprotective effect of 3-hydroxypyridine derivatives and human erythropoietin analogue on a hemorrhagic stroke model in rats. Pharmacy & Pharmacology. 2020;8(3):169–180. Available from: <URL>.
7. Shcheblykina OV, Shcheblykin DV, Trunov KS, Danilenko AP, Lipatov VS. Experimental study of new derivatives of 3-hydroxypyridine as pharmacological agents for the correction of ischemic brain injury after

- intracerebral hemorrhage. *Research Results in Pharmacology*. 2022;8(1):71–83. Available from: [<URL>](#).
8. Nesterova NI, Shcheblykina OV, Kolesnichenko PD, Nesterov AV, Shcheblykin DV, Popova IA, Yakovlev DV. Neuroprotective effects of taurine and 3-hydroxypyridine derivatives in the intracerebral hemorrhage model in rats. *Research Results in Pharmacology*. 2019;5(3):87–94. Available from: [<URL>](#).
9. Agarkova AA, Pokrovsky MV, Kolesnichenko PD, Nesterov AV. The effect of new derivatives of 3-hydroxypyridine on the development of brain edema in bacterial purulent meningitis in experimental conditions. *Siberian Sci Med J*. 2021;41(3):32–37. Available from: [<DOI>](#).
10. Mariño L, Pauwels K, Casasnovas R, Sanchis P, Vilanova B, Muñoz F, Donoso J, Adrover M. Orthomethylated 3-hydroxypyridines hinder hen egg-white lysozyme fibrillogenesis. *Sci Rep*. 2015;(5):12052. Available from: [<URL>](#).
11. Massoud A, SaadAllah M, Dahran NA, Nasr NE, El-Fkharany I, Ahmed MS, Alsharif KF, Elmahallawy EK, Derbalah A. Toxicological effects of malathion at low dose on wister male rats with respect to biochemical and histopathological alterations. *Front. Environ. Sci*. 2022;10:860359. Available from: [<URL>](#).
12. Razzaque MSh. Phosphate toxicity: new insights into an old problem. *Clin. Sci. (Lond.)* 2011;120(3):91–7. Available from: [<URL>](#).
13. Nizamov IS, Salikhov RZ, Timushev ID, Nikitin YeN, Nizamov ID, Yakimov VYu, Shulaeva MP, Pozdeev OK, Batyeva ES, Cherkasov RA, Ponomareva AS. Pyridinium salts of dithiophosphoric acids on the basis of nicotinic acids and their isomers, 3-hydroxypyridine, and 3-pyridinemethanol. *Phosphorus, Sulfur, and Silicon, and the Related Elements*. 2020;193(3): 226–230. Available from: [<URL>](#).
14. Nizamov IS, Belov TG, Nizamov ID, Mavrov EA, Davletshin RR, Cherkasov RA. Reactions of bis-dithiophosphonic acids with 3-hydroxypyridine and 3-(hydroxymethyl)pyridine. *Russ. J. Gen. Chem*. 2022;92(7):1–8. Available from: [<URL>](#).
15. Sofronov AV, Almetkina LA, Nikitin EN, Nizamov IS, Cherkasov RA. Optically active aryldithiophosphonic acids and their salts based on L-(–)-menthol and D-(+)-menthol. *Russ. J. Org. Chem*. 2010;46(2):300–301. Available from: [<URL>](#).
16. Lecher HZ, Greenwood RA, Whitehouse KC, Chao TH. The phosphonation of aromatic compounds with phosphorus pentasulfide. *J. Amer. Chem. Soc*. 1956;78:5018–5022. Available from: [<URL>](#).
17. Nizamov IS, Gabdullina GT, Al'metkina LA, Shamilov RR, Batyeva ES, Cherkasov RA. (1S)-endo-(–)-Borneol in the synthesis of optically active phosphorus dithioacids. *Russ. J. Gen. Chem*. 2012;82(10):1751–1752. Available from: [<URL>](#).
18. Nizamov IS, Gabdullina GT, Al'metkina LA, Shamilov RR, Cherkasov RA. Thiophosphorylation of thymol with phosphorus sulfides. *Russ J. Gen. Chem*. 2013;49(1):145–146. Available from: [<URL>](#).
19. Katritzky AR, Ramsden ChA, Joule JA, Zhdankin VV. *Handbook of Heterocyclic Chemistry*. 3d ed. Elsevier; 2010. Available from: [<URL>](#).
20. Crutchfield MM, Dungan CH, Letcher JH, Mark V, Van Wazer JR. *Topics in Phosphorus Chemistry*. Vol. 5 (M Grayson, EJ Griffith Eds.). New York: John Wiley & Sons. 1967. 492 p.
21. Colthup NB, Daly LH, Wiberley SE. *Introduction to Infrared and Raman Spectroscopy*, New York: Academic Press, Inc. 1964. 511 p.
22. Suner SS, Sahiner M, Ayyala RS, Sahiner N. Degradable and non-degradable chondroitin sulfate particles with the controlled antibiotic release for bacterial infections. *Pharmaceutics* 2022;14:1739. Available from: [<URL>](#).
23. Kohler JR, Casadevall A, Perfect J. The spectrum of fungi that infects humans. *Cold Spring Harb. Perspect. Med*. 2015;5:a019273. Available from: [<URL>](#).





## Investigation of Adsorptive Removal of Methylene Blue from Synthetic Wastewater Using Polymeric Composite

Monsuru Dauda<sup>1,2</sup>, Ayobami Ajani<sup>1,2</sup>, Abass Alade<sup>1,2,3\*</sup> , Tinuade Jolaade Afolabi<sup>1,2</sup>

<sup>1</sup>Ladoke Akintola University of Technology, Department of Chemical Engineering, Faculty of Engineering, Ogbomoso, Nigeria.

<sup>2</sup>Ladoke Akintola University of Technology, Bioenvironmental, Water and Engineering Research Group (BWERG), Ogbomoso, Nigeria.

<sup>3</sup>Ladoke Akintola University of Technology, Science and Engineering Research Group (SAERG), Ogbomoso, Nigeria.

**Abstract:** Recycling polymeric waste into another useful material is considered to be the preferred way of taking care of the issues of slow degradable plastic waste, particularly in anticipation of natural contamination. In this study, the adsorptive treatment of Methylene Blue (MB) using adsorbents from chemically recycled polymeric waste was investigated. Three polymeric materials were employed in this study: styrofoam waste (EPS1), intruded extended polystyrene (EPS2), and sunflower xylem (*Tithonia diversifolia* xylem) (TDX). The alterations in microscopic surface morphology before and after the adsorption process were examined using scanning electron microscopy (SEM) system to resolve the intercalation of MB with the adsorbent. The experimental batch data was collected and the effects of concentration and contact time on the removal of MB from synthetic wastewater were studied. Adsorption kinetics, equilibrium, and thermodynamics were studied and fitted by various models. According to the result, the uptake of adsorbate increased as contact time and concentration rose, with the pseudo-second-order model best depicting the adsorption kinetics.

**Keywords:** Adsorbent composite; Methylene blue; Polymeric adsorbents.

**Submitted:** July 26, 2022. **Accepted:** August 3, 2023.

**Cite this:** Dauda M, Ajani A, Alade A, Afolabi TJ. Investigation of Adsorptive Removal of Methylene Blue from Synthetic Wastewater Using Polymeric Composite. JOTCSA. 2023;10(4):961-74.

**DOI:** <https://doi.org/10.18596/jotcsa.1148910>

**\*Corresponding author's E-mail:** [aalade@lautech.edu.ng](mailto:aalade@lautech.edu.ng)

### 1. INTRODUCTION

The new lifestyle has pushed humanity towards the massive use of plastic materials for most edible, medical, and other personal care products (1). Tragically, the treatment of plastic waste is not remote from the expanded interest in plastic items. A basic and notable method for curing polymeric waste is burning, however, it creates potentially perilous discharges. In this manner, reusing is viewed as the preferred approach to tackling the issues of slow degradable plastic waste, particularly in anticipation of natural contamination. Notwithstanding, the interaction is expensive since the cost of the hydrocarbon and monomer is a lot lower than that recuperated by recycling (1). Thus, significant consideration has been paid to the compound

reusing of polymeric waste to yield different valuable materials like adsorbents (1, 2).

Polymeric adsorbents can trap a large number of the omnipresent organic contaminants, in particular colors, phenolic compounds, natural acids, fragrant or polyaromatic hydrocarbons, alkanes, and their derivatives. Polymeric materials appear to be more appealing than activated carbon, cellulose, alginate, diatomite, and sand, because of their superb mechanical strength and movable surface chemistry (2). These polymers as adsorbents display the following properties: vast surface area and wonderful skeleton strength, basic physicochemical properties like internal surface region and pore size dissemination that can be adjusted by fluctuating the polymerization conditions, high water

sanitization limit, colorless, scentless, and non-harmful, low expense, re-expanding limit, biodegradability, biocompatibility, good toughness, and stability in a swelling environment (3).

Removal of MB from industrial wastewater has been explored utilizing different techniques, for example, sedimentation, nanofiltration, filtration innovation, synthetic treatment with coagulating flocculating materials, oxidation by utilizing oxidizing agents, electrochemical techniques, high-level oxidation processes (AOPs), enzymatic interaction, photodegradation response, electrochemical evacuation, chemical coagulation, film filtration, and physical adsorption methods (4,5). Among them, the adsorption process is among the most researched methods for MB removal, and it has ended up being effective and economical in the removal of refractory pollutants (including dye) from wastewater due to its lower initial development cost, simple design, easy operation, and free from or less generation of poisonous substances (6).

## 2. MATERIALS AND METHODS

### 2.1. Sampling and Preparation of Polymeric Composite

Samples of polymeric materials, which are Styrofoam waste (EPS1), intruded extended polystyrene (EPS2), and "*Tithonia diversifolia xylem*" (TDX), were used. The samples were washed to remove the oil, dust, and sand particles from them. Washed materials were sun-dried till the materials became very dry and then underwent surface area reduction using milling processes at 8000 rpm. Phosphoric acid, H<sub>3</sub>PO<sub>4</sub> (Aldrich) (3 M) was used for chemical activation for 24 h. The adsorbents were neutralized to a pH range of 6.9 - 7.1 with sodium hydroxide (NaOH) (BDH), filtered immediately, and dried very well (7).

### 2.2. Preparation of Adsorbate Solution

Methylene Blue (C<sub>16</sub>H<sub>18</sub>N<sub>3</sub>SCI, BDH) was bought from Bond Chemicals, Ibadan, Oyo State. Methylene blue was used without further purification and was prepared with distilled water. A stock solution of 1000 mg/L was first prepared by dissolving 1.127 g of methylene blue in 1000 mL of distilled water. The experimental solution (50 mg/L) was prepared by diluting the stock solution with distilled water. The concentration of MB was then determined at 665 nm by a UV-visible spectrophotometer.

### 2.3. Characterization of the Adsorbent

The structural chemical functional groups of the adsorbents were determined utilizing the Fourier Transform Infrared Technique (FTIR, Nicolet IS5) and the before and after adsorption microscopic surface morphology changes of samples were determined using SEM images obtained using the scanning electron microscopy (SEM) system. The working voltage choice was within the scope of 10-20 kV (8).

### 2.4. Batch Adsorption Studies

A batch adsorption experiment was done to evaluate the adsorption behavior of the adsorbent. The MB parameters of concentration of adsorbate, contact time, and adsorbent dosage were studied. A solution (100 mL) of different concentrations from 40-100 mg/L was brought into contact with 1 g of the optimized polymeric composite adsorbent at a different time (10-110 min) to determine the effect of contact time and change in concentration. The adsorption capacity and removal efficiency were evaluated in Equations 1 and 2, respectively. The data obtained were used to estimate equilibrium relationships between sorbent and adsorbate at a constant temperature using adsorption isotherm techniques. Adsorption kinetics were also estimated to describe the rate of retention or release of MB from simulated waste water to a solid-phase polymeric adsorbent interface.

### 2.5. Optimization of Contact Time

The 100 mg/L prepared solution of MB was diluted with water to obtain 80 mg/L, 60 mg/L, 50 mg/L, and 40 mg/L. Polymeric adsorbent (1 g) composite with the optimized ratio of 20% of material Styrofoam to 20% of material intruded EPS to 60% of material TDS and 100 mL of each solution of MB synthesized wastewater into eleven different flasks of 250 mL capacity, varying contact time between 10 and 110 min. All the flasks were placed in a rotary shaker at 180 rpm. Then, flasks were withdrawn from the shaker in the range of 10-110 min, respectively, to optimize and relate the activeness of the adsorbent to the time, after keeping the rate of agitation and temperature constant. A plot of MB q<sub>e</sub> against time was used to optimize time for further study and a plot of MB removal against time was utilized to examine the contact time for the adsorption process.

### 2.6. Initial MB Concentration and Adsorption Capacity

MB solutions (100 mL) of concentrations between 40 and 100 mg/L each were placed into different flasks of 250 mL capacity and equilibrated with 1 g of the polymeric adsorbent composite with the optimized ratio of 20% of material Styrofoam, 20% of material Intruded EPS and 60% of material TDS. All the flasks were placed in a rotary shaker at 180 rpm. Then, flasks were withdrawn from the shaker at a constant time to relate the activeness of the adsorbent to the adsorbate concentration after keeping the rate of agitation and temperature constant. The data obtained were fitted to adsorption isotherm models.

### 2.7. Calculations

#### 2.7.1. Uptake and adsorption removal

The MB uptake per gram of sorbent and the percentage of adsorption removal were calculated using Equations 1 and 2:

$$q_e = \frac{C_0 - C_e}{m} V \quad (1)$$

$$\%RE = \frac{C_0 - C_e}{C_0} * 100 \% \quad (2)$$

where  $m$  is the mass of the composite (g).  $q_e$  was the equilibrium adsorption capacity (mg/g),  $C_0$  is the initial MB concentration (mg/L),  $C_e$  is the experimental concentration (mg/L) of MB solution,  $V$  was the volume of aqueous solution (L) and  $m$  was the dry weight of the adsorbent (g).

### 2.7.2. Langmuir isotherm model

The adsorption isotherm inferred by Langmuir for the adsorption of a solute from a fluid arrangement is given in Equation 3 (9).

$$q_e = \frac{q_m K_a C_e}{1 + K_a C_e} \quad (3)$$

where  $q_e$  is the amount of adsorbate adsorbed per unit amount of adsorbent at equilibrium (g/mg),  $q_m$  is the amount of adsorbate adsorbed per unit amount of adsorbent required for monolayer adsorption (limiting adsorbing capacity),  $K_a$  is the constant related to enthalpy of adsorption (L/ $\mu$ g)<sup>n</sup>, and  $C_e$  is the concentration of adsorbate solution at equilibrium (mg/L). The four linear forms of the Langmuir isotherm model considered are given in Equations 4-7.

### 2.7.3. Langmuir first isotherm model

$$\frac{C_e}{q_e} = \frac{1}{q_m K_a} + \frac{1}{q_m} C_e \quad (4)$$

Using a linear mathematical expression for the Langmuir model, a graph can be obtained by plotting  $C_e / q_e$  Vs  $C_e$ .

### 2.7.4. Langmuir second isotherm model

$$\frac{1}{q_e} = \frac{1}{q_m} + \frac{1}{k_a q_m C_e} \quad (5)$$

A plot of  $1 / q_e$  against  $1 / C_e$  gives an intercept of  $1 / q_m$  and a slope of  $1 / k_a q_m$  (10).

### 2.7.5. Langmuir third isotherm model

$$q_e = q_m - \frac{q_e}{k_a C_e} \quad (6)$$

A plot of  $q_e$  against  $q_e / C_e$  gives an intercept of  $q_m$  and a slope of  $-1 / K_a$  (10).

### 2.7.6. Langmuir fourth isotherm model

$$\frac{q_e}{C_e} = K_a q_m - q_e \quad (7)$$

A plot of  $q_e / C_e$  against  $q_e$  gives an intercept of  $K_a q_m$  and a slope of  $K_a$  (10). (11) introduced a dimensionless equilibrium term  $R$ , otherwise called the partition component to communicate the Langmuir consistency  $b$ . The essential characteristic of the Langmuir isotherm can be expressed in terms of dimensionless constant separation factor  $R_L$  (7). Langmuir isotherm is often investigated with dimensionless separation factor  $R$  according to Equation 8 (7)

$$R = \frac{1}{1 + K C_0} \quad (8)$$

where  $C_0$  is the initial concentration of adsorbate (mg/L) and  $K_L$  is Langmuir constant.

The value of the dimensionless separation factor  $R$  gives significant data about the idea of adsorption. The value of  $R$  is somewhere in the range of 0 and 1 for good adsorption, while  $R > 1$  addresses negative adsorption and  $R = 1$  addresses linear adsorption. The adsorption interaction is irreversible if  $R = 0$  (12).

### 2.7.7. Freundlich Isotherm model

The Freundlich model (13) is an empirical equation and may be the most broadly utilized nonlinear sorption model since it precisely depicts a lot of adsorption information for heterogeneous adsorbent surfaces. The model is introduced as Equation 9, while the linearized form can be represented as Equation 10:

$$q_e = K C_e^{1/n} \quad (9)$$

$$\log q_e = \log K + \frac{1}{n} \log C_e \quad (10)$$

where  $q_e$  is the MB uptake (mg/g) at equilibrium,  $K$  is the proportion of the sorption limit,  $1/n$  is the sorption intensity, and  $C_e$  is the equilibrium concentration (mg.L<sup>-1</sup>).  $K_f$  and  $n$  are Freundlich constants connected with the adsorption capacity and adsorption force, respectively. These boundaries can be determined from the capture and the slope of the linear plot of  $\log q_e$  against  $\log C_e$ . The slope, which ranges between 0 and 1 is a measure of adsorption force or surface heterogeneity, becoming more heterogeneous as its value gets closer to zero.

### 2.7.8. Temkin isotherm model

Temkin studied the adsorbate-adsorbate interactions in an adsorption process and the model is introduced as Equation 11, while the linear form is represented as Equation 12:

$$q_e = \frac{RT}{\Delta q} \in K_0 + \frac{RT}{\Delta q} \in C_e \quad (11)$$

$$q = B \ln A + B \ln C_e \quad (12)$$

Where  $B = RT / \Delta q$ ,  $T$  is the absolute temperature in K and  $R$  is the universal gas constant of 8.3143 J/mol K. The steady is connected with the intensity of adsorption  $q_e$  (mg/g) and  $C_e$  (mg/L) and the equilibrium concentration, respectively.  $A$  and  $B$  are constants connected with the adsorption limit and force of adsorption. A plot of  $q_e$  versus  $\ln C_e$  yields a slope of  $B$  and an intercept of  $B \ln A$  (14).

2.7.9. Harkin - Jura isotherm model

The Harkin-Jura isotherm model portrays the chance of multi-facet adsorption on the outer layer of the adsorbent having heterogeneous pore dissemination as illustrated in Equation 13:

$$\frac{1}{q_e^2} = \frac{B}{A} - \frac{1}{A} \log C_e \quad (13)$$

Where  $A$  and  $B$  are Harkin-Jura constants that can be gotten by plotting  $1 / q_e^2$  against  $\log C_e$  (14).

2.7.10. Hill-De Boer isotherm model

Hill-De Boer isotherm model portrays a situation where there is versatile adsorption as well as horizontal interaction among adsorbed particles. The linearized type of this isotherm model is expressed as follows (Equation 14):

$$\ln \left( \frac{C_e^2}{C_o - C_e} \right) - \frac{C_o - C_e}{C_e} = -\ln K_1 - \frac{K_2 (C_o - C_e)}{RT \cdot C_o} \quad (14)$$

Where  $K_1$  and  $K_2$  are the Hill-DeBoer constant in (L/mg) and the constant of the interaction between adsorbed molecules (KJ/mol) respectively. Experimental data from the adsorption process can

be analyzed by plotting  $\ln \left( \frac{C_e^2}{C_o - C_e} \right) - \frac{C_o - C_e}{C_e}$  against  $\frac{C_o - C_e}{C_o}$ , where the slope is  $-\frac{K_2}{RT}$  and the intercept is  $-\ln K_1$  (14).

2.7.11. Dubinin-Radushkevich isotherm (D-R) model

Dubinin-Radushkevich isotherm model is an adsorption model that is applied to impart the adsorption instrument with Gaussian energy dispersion onto heterogeneous surfaces. This isotherm is only fitting for an intermediate range of adsorbate focuses because it shows an absurd asymptotic way of behaving and doesn't predict Henry's laws at low pressure. It is expressed numerically as (Equation 15):

$$q = q_e e^{-\beta RT \ln \left( 1 + \frac{1}{C_e} \right)^2} \quad (15)$$

where,  $q$  = maximum adsorption capacity (mg/g),  $q_e$  = equilibrium adsorption capacity (mg/g),  $\beta$  = Free energy of adsorption per mole of adsorbate,  $C_e$

= equilibrium concentration (mg/L).

The Dubinin-Radushkevich isotherm model is expressed in linear logarithmic form (Equation 16)

$$\ln q_e = \ln q - \beta \epsilon^2 \quad (16)$$

$\epsilon$  = Polanyi potential which is given as (Equation 17)

$$\epsilon = RT \ln \left( 1 + \frac{1}{C_e} \right) \quad (17)$$

where  $R$  is the gas constant (8.34 J/mol/K) and  $T$  is the absolute temperature. A plot of  $\ln q_e$  versus  $\epsilon^2$  gives the slope  $\beta$  and intercept  $\ln q_e$  (14).

2.7.12. Jovanovich isotherm model

Assumptions contained in the Langmuir model were used in predicting the Jovanovich model, but in adding the possibility of some mechanical contact between the adsorbent and adsorbate (14). The linear form of the Jovanovich isotherm is expressed as (Equation 18):

$$\ln q_e = \ln q_{max} - K_f C_e \quad (18)$$

Where  $q_e$  is the amount of adsorbate in the adsorbent at equilibrium (mg/g),  $q_{max}$  is the maximum uptake of adsorbate (L/mg). The plot of  $\ln q_e$  against  $C_e$  gives a straight line, and Jovanovich constants  $K_f$  and  $q_{max}$  were evaluated using the slope and intercept of the plot, respectively (14).

2.8. Sorption Kinetics

2.8.1. Zeroth order kinetics

A Zeroth Order Kinetics equation is given as (Equation 19):

$$q_t^* = q_o^* + K_o t \quad (19)$$

Where  $q_t^*$  is the amount of solute sorbed on the surface of the sorbent at any time,  $t$ , (mg/g),  $q_o^*$  is the amount of solute sorbed at time  $t = 0$  (mg/g), and  $K_o$  zero-order reaction rate constant, (mg/g min). A plot of  $q_t^*$  against  $t$  gives a straight line, and  $K_o$  and  $q_o^*$  can be calculated using the slope and intercept, respectively (10).

2.8.2. First-order model

The first-order condition for sorption in the fluid system depends on the solid limit. The Lagergren rate condition is the most generally involved rate condition for the sorption of a solute from a fluid arrangement (Equation 20).

$$\frac{d q_t}{d t} = K_1 (q_m - q_t) \quad (20)$$

Integrating this for the initial ( $t = 0$  and  $q_t = 0$ ) and end conditions ( $t = t$  and  $q_t = q_t$ ), Equation (21) may be rearranged for linearized data plotting as shown by Equation (22):

$$\log (q_m - q_t) = \log q_m - \frac{k_1}{2.303} t \quad (21)$$



Equation (21) is applied and the parameter  $q_m$  is evaluated, using experimental data. The boundary  $q_m$  does not address the quantity of accessible sites. The boundary  $\log(q_m)$  is a movable boundary, and it's rarely equivalent to the intercept of a plot of  $\log(q_m - q_t)$  against  $t$ , while, in a genuine first-order system,  $\log(q_m)$  ought to be equivalent to the intercept of a plot of  $\log(q_m - q_t)$  against  $t$ . Equation (22) is only an approximate solution to the first-order rate mechanism (10).

2.8.3. Pseudo-first-order model (PFO)

A pseudo-first-order kinetic model equation is given as Equation 22 (15):

$$\ln(q_e - q_t) = \ln q_e - k_1 t \tag{22}$$

Where  $q_e$  is the adsorption capacity at equilibrium (mg/g),  $q_t$  is the amount of pollutant removed at time  $t$  (mg/g),  $k_1$  is the pseudo-first-order rate constant (1/min), and  $t$  is the contact time (min) (10).

2.8.4. Second-order model

A second-order kinetic model is given as Equation 23;

$$\frac{1}{q_t} = \frac{1}{q_0} + K_2 t \tag{23}$$

Where  $q_t$  is the amount of pollutant removed at time  $t$  (mg/g),  $q_0$  is the amount of solute sorbed at time  $t = 0$  (mg/g), and  $K_2$  second-order rate constant (g/mg min). The plot of  $1 / q_t$  against  $t$  gives a straight line and the values for  $K_2$  and  $q_0$  can be calculated from the slope and intercept, respectively (10).

2.8.5. Pseudo-second-order model (PSO)

The pseudo-second-order model is expressed in Equation 24 and its linear form is given in Equation 25.

$$\frac{d q}{d t} = k_2 \tag{24}$$

$$\frac{t}{q_t} = \frac{1}{k_2 q_e^2} + \frac{t}{q_e} \tag{25}$$

Where,  $k_2$  (mg/g/min),  $t$  and  $q_e$  are the pseudo-second-order rate constant, time, and adsorption capacity at equilibrium, respectively. They were determined from the plot of  $t / q_t$  versus  $t$  (10).

2.8.6. Third-order model

The third-order kinetic equation is given as:

$$\frac{1}{q_t^2} = \frac{1}{q_0^2} + K_3 t \tag{26}$$

Where  $q_t^2$  is the amount of pollutant removed at

time  $t$  (mg/g),  $q_0$  is the amount of solute sorbed at time  $t = 0$  (mg/g), and  $K_3$  second-order rate constant (g/mg min). The plot of  $1 / q_t^2$  against  $t$  gives a straight line, and the values for  $K_3$  and  $q_0$  can be calculated from the slope and intercept, respectively (10).

2.8.7. Fractional power model

The nonlinear and linear forms of the fractional power kinetic model equation are depicted in equations 27-28;

$$q_t = K t^v \tag{27}$$

$$\log q_t = \log K + v \log t \tag{28}$$

Where  $\log K$  and  $v$  are the intercept and slope of the plot of  $\log q_t$  against  $\log t$  respectively. Thus, the antilog of intercept gives the value of constant  $K$ .  $v$  is also a constant that is usually less than unity if the adsorption kinetic data fits well into the power function model.  $q_t$  is the quantity of adsorbate adsorbed at time  $t$  (10).

2.9. Mass Transfer Diffusion

2.9.1. Weber-Morris' transfer diffusion

To predict the rate of determining steps in the adsorption process of the pollutants,

$$q_t = K_{wm} t^{0.5} + C \tag{29}$$

A graph of  $q_t$  against  $t^{0.5}$  is plotted. Where  $K_{wm}$  (mg/gmin<sup>0.5</sup>) is the intra-particle diffusion rate constant and  $C$  (mg/g) is proportional to the boundary layer thickness (10).

2.9.2. Dumwald-Wagner transfer diffusion

This is another form of the intra-particle model developed by Dumwald-Wagner. The Equation is given as:

$$\log(1 - F^2) = \frac{-K}{2.303} t \tag{30}$$

$K$  is the diffusion rate constant,  $F$  is the adsorption capacity, and it is gotten as  $F = q_t/q_e$ ,  $q_t$  is the adsorption capacity at each time and  $q_e$  is the adsorption capacity at equilibrium (10).

2.9.3. Matthew-Weber transfer diffusion

The model is used to examine the external mass transfer in the boundary phase around the solid particle. The equation is given as:

$$\log \frac{C_t}{C_e} = \frac{-K_m \cdot A}{2.303} \cdot t \tag{31}$$

Indicating a plot of  $\log C_t/C_0$  against  $t$ , where  $C_t$  and  $C_0$  are the adsorbate concentration at time  $t$  and the initial solute concentration, mg/g,  $K_m$  is the external mass transfer coefficient m/h and  $A$  is the external surface per unit mass, m<sup>2</sup>/g (10).

2.9.4. Banghams transfer diffusion

This model is employed to determine if the rate-limiting step is controlled by pore diffusion alone or not.

$$\log\left(\log\frac{C_o}{C_o - q_t \cdot m}\right) = \log\left(\frac{K_b \cdot m}{2.303 \cdot V}\right) + \theta \log t \quad (32)$$

A graph of  $\log\left(\log\frac{C_o}{C_o - q_t \cdot m}\right)$  against  $\log t$ , where  $V$  is the volume of the liquid phase, mL, is the weight of adsorbent per liter of solution g/L, and  $K_b$  and  $\theta < 1$  are constants (10).

2.9.5. McKay Film transfer diffusion

This involves mass transfer, which is based on film diffusion. It is represented as

$$\ln(1 - F) = -K_m t \quad (33)$$

Where a graph of  $\ln(1-F)$  is plotted against time to obtain  $K_m$  as the slope (16).

2.9.6. Vermeulin transfer diffusion

If the adsorbate diffusion through the adsorbent beads is the slowest step, the particle diffusion will be the rate-determining step. The expression of the model is as follows:

$$-\ln\left(1 - \left(\frac{q_t}{q_e}\right)^2\right) = \left(\frac{2 \pi^2 Dv}{r_0^2}\right) - Kv \cdot t \quad (34)$$

A plot of  $-\ln\left(1 - \left(\frac{q_t}{q_e}\right)^2\right)$  against time is made, where  $Dv$  is the effective diffusion coefficient,  $r_0^2$  is the radius of the adsorbent particles supposed to be spherical particles,  $q_t / q_e$  is the fraction realization

of equilibrium at a time,  $t$  (16).

2.9.7. Film transfer diffusion

The film diffusion model is represented as follows:

$$\log(q_m - q_t) = \log(q_m) - \frac{R}{2.303} t \quad (35)$$

Equation (35) has a similar structure to condition (20), showing that separating between film dissemination control and pseudo-first-order response control will be troublesome. Notwithstanding, doing a progression of sorption at various agitation speeds, as a rule, shows that film dissemination has a lot more grounded reliance on unsettling. In agitated sorption studies, film dispersion is generally just rate-controlling for an initial couple of moments (16).

3. RESULTS AND DISCUSSION

3.1. Characterization of Adsorbents

3.1.1. Morphological Characteristics of the adsorbent Using Scanning Electron Microscopy (SEM)

The scanning electron micrographs of the adsorbent were done before and after adsorption and are presented in Figures 1a-c and 2a-c, respectively. The SEM images indicate the surface area and pore spaces on the adsorbent, as shown in Figure 1a-c. TDX has more surface area and larger pore sizes. This showed that the TDX was viable in making well-developed pores on the outer layer of the antecedent for maximum adsorption, prompting TDX to have a huge surface region and permeable structure. The surface morphology of all the sorbents changed significantly by disturbing the pore spaces. It was identified that MB had been adsorbed onto the pores of the adsorbents, as shown in Figure 2a-c.

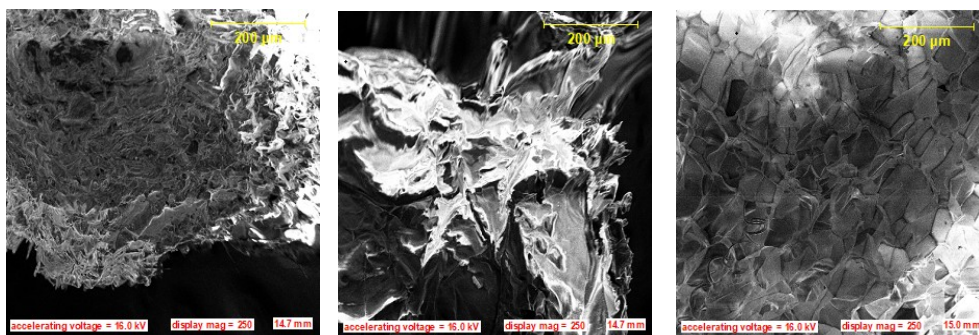
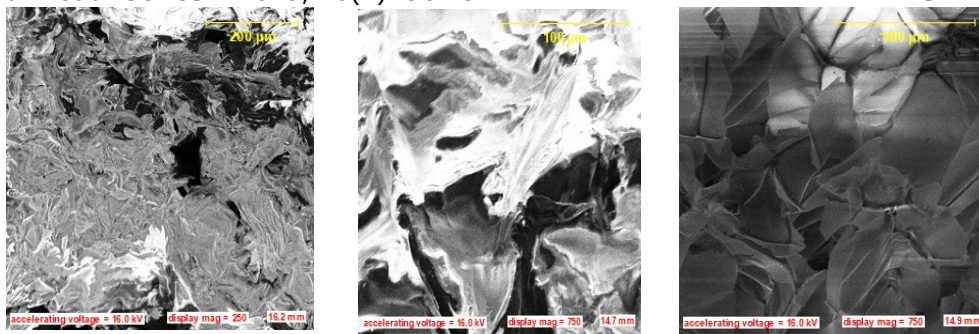


Figure 1: The morphology characteristics of adsorbent before adsorption (a) SEM Image of EPS(b) SEM Image of styrofoam (c) SEM Image of TDX.



**Figure 2:** The morphology characteristics of adsorbent after adsorption (a) SEM Image of EPS(b) SEM Image of styrofoam (c) SEM Image of TDX.

**3.2. Optimization of Concentration and Contact Time**

The impact of concentration and contact time significantly affects the adsorption cycle, as displayed in Figures 3a-b. The impact of initial MB concentration in the range of 40 and 100 mg/L on adsorption was examined and is displayed in Figure 3a. It is clear from the figure that the level of MB removal diminished with the increase in the initial concentration of MB. The initial MB concentration gives the vital impetus to defeat the resistance to the mass transfer of MB between the fluid stage and the solid stage. The increase in initial MB concentration additionally improves the interaction between the material and MB. Hence, an increase in the initial MB concentration improves the adsorption take-up of MB. This is because of an increase in the driving force of the concentration gradient and an increase in the initial MB concentration. While the percentage of MB removal was found as 96.39% for 40 mg/L and 92.70% for 100 mg/L at 100 minutes. In addition, it was likewise seen that the pace of MB

take-up increased rapidly in the initial 10 minutes of contact time. After around 10 minutes, the rate diminished for an additional 10 minutes until a steady MB focus was reached, this happened after around 80 minutes (Figure 3b). It was assumed that this time addressed the equilibrium time at which equilibrium MMB concentration occurred. This agrees with the result obtained by (5-7, 17).

The outcome can additionally be explained as follows, at first, the adsorption sites on the adsorbent were open, and MB cooperated effectively with the site. The concentration difference between the bulk solution and the solid-liquid interface was at first higher, which prompted the higher pace of adsorption after 10 minutes. A while later, MB was accumulated on the enormously accessible surface of adsorption sites on the adsorbent, which prompted the control of surface binding sites, dialing back adsorption. The graph affirmed the possibility of stopping the batch adsorption study at 80 min to optimize time for further study.

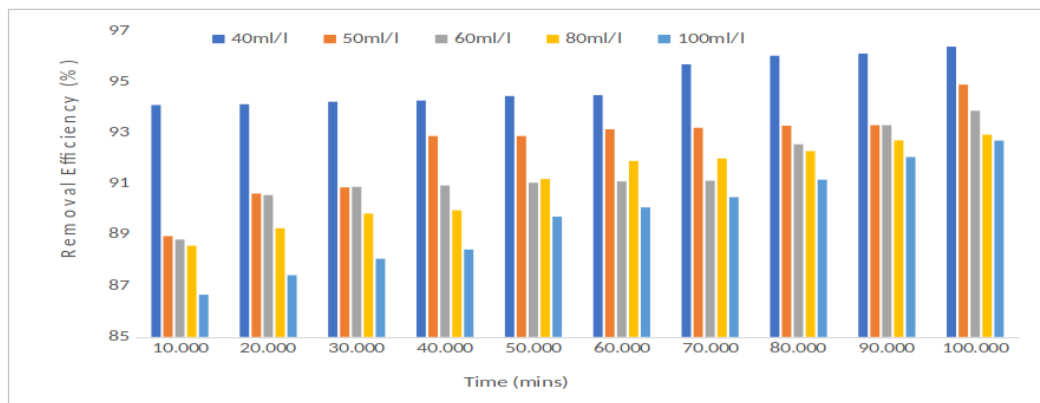


**Figure 3a:** Effect of contact time and concentration on removal efficiency.

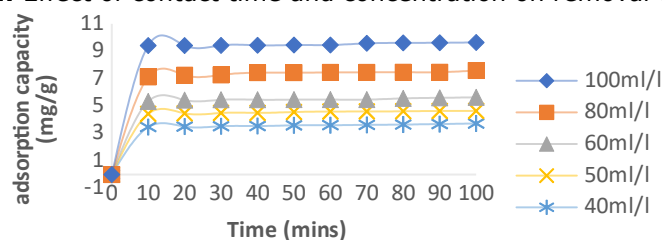


**Figure 3b:** Effect of contact time and concentration on adsorption capacity.

### 3.3. Adsorption Isotherm

Adsorption isotherm models can portray the cooperation between the adsorbate and adsorbent. This is an important criterion for optimizing the use of adsorbents. Eleven adsorption isotherms were studied in the investigation of the adsorption experiments. Langmuir 1-4, Freundlich, Temkin, Harkin-Jura, Hill-DeBoer, Dubinin-Radushkevich, Halsey, and Jovanovich were the isotherms selected because the values of their  $R^2$  are greater than 0.9.

#### 3.3.1. Langmuir model

The plots of Langmuir-1, Langmuir-2, Langmuir-3, and Langmuir-4 models were shown in Figure 4 which provided a linear relationship from which are  $q_m \wedge K_a$  determined from the slope and intercept of the plot. The  $q_m$  values for the contact time of Langmuir-1, Langmuir-2, Langmuir-3, and Langmuir-4 models were -17.0358, 13.4953, 7.9025, and -15.2446 respectively. The  $K_a$  parameters estimated are -0.0341, 0.0407, 0.0582, and -0.0372 for Langmuir-1, Langmuir-2, Langmuir-3, and Langmuir-4 Models, respectively. The correcting coefficient ( $R^2$ ) for the Langmuir-1, Langmuir-2, Langmuir-3, and Langmuir-4 models

was found to be 0.4344, 0.9155, 0.6385, and 0.6385, respectively. The  $R^2$  value of Langmuir-2, which is highly significant than Langmuir-1, Langmuir-3, and Langmuir-4.

The negative values of some of the parameters show that the Langmuir model cannot be fitted, as the adsorption behavior does not follow the assumption on which the model is based (18), which shows that Langmuir isotherms 2 and 3 are more favorable for the treatment of MB in aqueous solution using polymeric adsorbent. The separation factor  $R$  can also be used to describe the essential characteristics of Langmuir. The value of  $R$  indicates the nature of the absorption process and the shape of the isotherm is irreversible ( $R = 0$ ), favorable ( $0 < R < 1$ ), linear ( $R = 1$ ), or unfavorable ( $R > 1$ ) (12). The overall trend obtained for the  $R$  was all below one for all the concentration ranges studied, representing favorable adsorption processes. This showed good linearity for the Langmuir isotherm, which makes the isotherm valid and supports its applicability. The findings of the current study compare well with others reported in the literature (17, 19, 20).

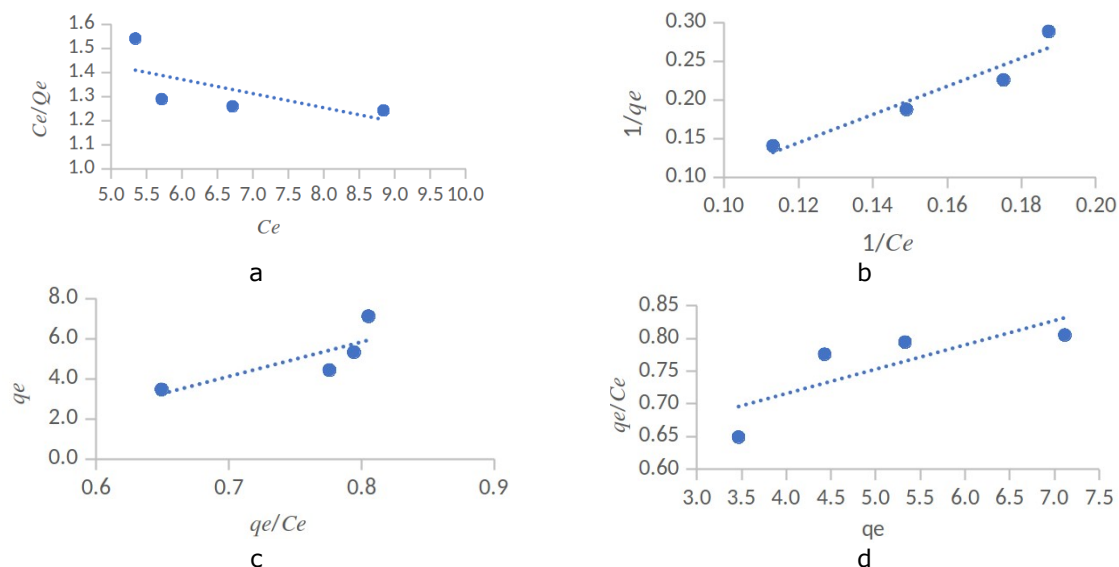


**Figure 4:** (a) Langmuir 1, (b) Langmuir 2, (c) Langmuir 3 and (d) Langmuir 4 Isotherms.

#### 3.3.2. Freundlich model

The plot of  $\ln q_e$  against  $\ln C_e$  (Figure 5a provides a linear relationship from which  $1/n$  and  $\log K_f$  is gotten from the slope and intercept of the plot. The  $K_f$  value for the contact time of the Freundlich model was found to be 0.4172. The  $n$  parameter was also found to be 0.7603 and  $1/n$  was estimated to be 1.3152. The  $R^2$  for Freundlich's model is found to be 0.945. The  $R^2$  value of the Freundlich model is highly significant. The absence of negative values indicates that the Freundlich isotherm can be used. Based on the correlation coefficients, the applicability of the isotherms was compared, and it showed that the Freundlich isotherm was a better fit for the adsorption data than the Langmuir isotherm. The surface heterogeneity of an adsorbent is addressed by utilizing the  $1/n$  value, in which the

adsorption is viewed as great and heterogeneous when the value of  $1/n$  lies somewhere in the range of 0 and 1, the adsorption is homogenous in which there is no cooperation among the adsorbed species when  $1/n = 1$  and the adsorption is unfavorable when  $1/n > 1.46$ . In this situation, the value of  $1/n$  is under 1.46, and the adsorption is good for the Freundlich isotherm. The findings of the current study compare well with others reported in the literature (21).

#### 3.3.3. Temkin model

The plot of  $1-(C_e/C_0)$  against  $\ln C_e$  (Figure 5b provides a linear relationship from which  $RT/\Delta Q$  and  $RT/\Delta Q \ln K_0 C_e$  are determined from the slope and

intercept of the plot. The  $\Delta Q$  value for a contact time was 0.0028. The estimated K parameter is 953.37. The Temkin Model  $R^2$  is estimated as 0.9818. The  $R^2$  value of the Temkin model is highly significant. While comparing the results with Langmuir and Freundlich, the Temkin isotherm model also shown that the  $R^2$  values are close to unity. The findings of the current study compare well with others reported in the literature (22, 23).

3.3.4. Harkin-Jura model

The plot of  $1 / q_e^b$  against  $\log C_e$ , (Figure, 5c) provides a linear relationship from which A and B are determined from the slope and intercept of the plot. The A value for a contact time is 3.9968. The  $q_0$  parameter is estimated as 1.0032. The  $R^2$  of the Harkin-Jura model is 0.8062. The  $R^2$  value is highly significant. Based on  $R^2$  values of these isotherm models, it was concluded that the Freundlich, Jovanovich, Dubinin-Radushkevich, Temkin isotherms, and Langmuir 1,2 were better models than the Harkin-Jura model, however, Harkin-Jura constant, A values greater than 1, suggest better curve fitting, and the adsorption is favorable for Harkin-Jura isotherm (12, 21).

3.3.5. Hill-De Boer model

The plot of  $\ln\left(\frac{C_e^2}{C_0 - C_e}\right) - \frac{C_0 - C_e}{C_e}$  against  $\frac{C_0 - C_e}{C_0}$  (Figure 5d) provides a linear relationship from which  $-K_2 / RT$  and  $-\ln K_1$  is determined from the slope and intercept of the plot. The  $K_2$  value for a contact time is 1553374.67. The  $K_1$  parameter estimated is 4.18E-23. The  $R^2$  for Hill-De Boer model is 0.9566, which is highly significant. The  $R^2$  value of the Hill-De Boer Model is highly significant. While comparing the results with Langmuir, Freundlich, Jovanovich, Dubinin-Radushkevich, and Hill-De Boer isotherm models, it was seen that the  $R^2$  values are closer to unity.

3.3.6. Halsey model

The plot of  $\ln q_e$  against  $\ln C_e$  (Figure 5e) provides a linear relationship from which  $-1 / n_H$  and  $\ln K_H$  are determined from the slope and intercept of the plot. The  $n_H$  value for a contact time is -0.7603. The  $K_H$  parameter was estimated as 1.9439. The Halsey Model  $R^2$  was found to be 0.945. The  $R^2$  value is highly significant. The findings of the current study compare well with others reported in the literature (21).

3.3.7. Dubinin Radushkevich model

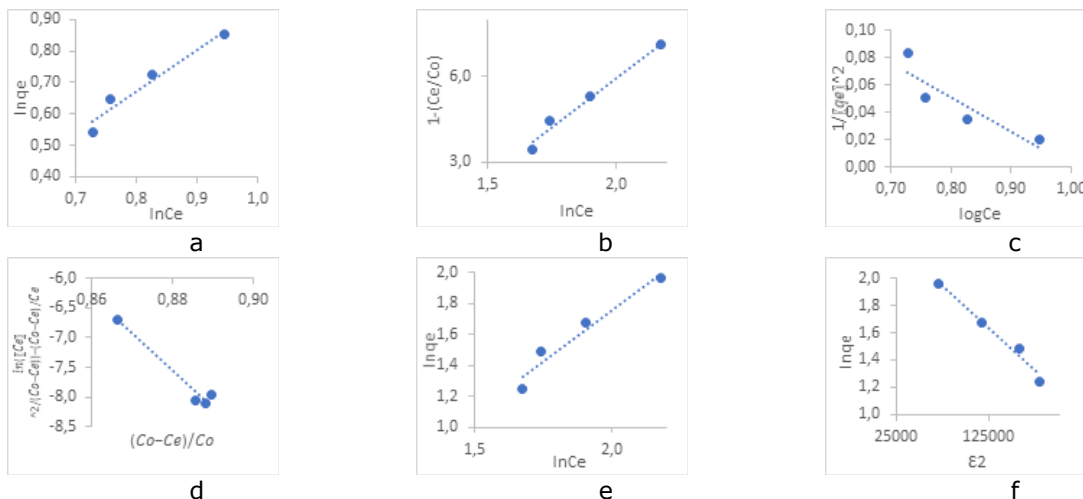
The plot of  $\ln q_e$  against  $\epsilon^2$  (Figure 5f) provides a linear relationship from which  $\beta$  and  $\ln q_m$  are determined from the slope and intercept of the plot. The  $\beta$  value for contact time is -6E-06. The  $q_m$  parameter was estimated as 11.0851. The  $R^2$  for Dubinin Radushkevich model is estimated as 0.975. The  $R^2$  value is highly significant. The findings of the current study compare well with others reported in the literature (24).

3.3.8. Jovanovich model

The plot of  $\ln q_e$  against  $C_e$  (Figure 5g) provides a linear relationship from which  $K_f$  and  $q_{max}$  are determined from the slope and intercept of the plot. The  $K_f$  value for contact time is 0.1853. The  $q_{max}$  parameter is estimated as 1.4329. The  $R^2$  for Jovanovich model is 0.9191. The  $R^2$  value is highly significant. The Jovanovich equilibrium constant  $K_j$  was almost the same as the values reported by (7).

3.3.9. Selection of suitable isotherm

The fitness of the isotherms to the data obtained from the study was analyzed based on the  $R^2$ , and the Temkin isotherm model has the highest value (0.9818) while Langmuir 3 has the least (0.6385). The sequence of the suitability of the isotherms based on average is Temkin > Dubinin > Hill-De > Halsey > Freundlich > Jovanovich > Langmuir -2 > Harkin-J > Langmuir -3, as shown in Table 1. Langmuir 1 and 4 were exempted because some of their isotherm parameters were negative and could not be used to describe the adsorption process.



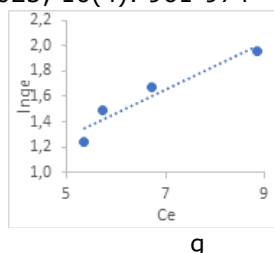


**Figure 5:** Model isotherms. (a) Freundlich, (b) Temkin, (c) Harkin-Jura, (d) Hill-De Boer, (e) Halsey, (f) Dubinin Radushkevich, and (g) Jovanovich.

**Table 1:** Suitable isotherm models.

Model	(R <sup>2</sup> )	Model	(R <sup>2</sup> )
Langmuir-1	0.4344	Temkin	0.9818
Langmuir-2	0.9155	Harkin- Jura	0.8062
Langmuir-3	0.6385	Hill-De Boer	0.9566
Langmuir-4	0.6385	Halsey	0.945
Freundlich	0.945	D-R	0.975

### 3.4. Kinetic Studies for Different Concentrations

#### 3.4.1. Zero Order

The plot of  $q_t^*$  against  $t$  (Figure 6a) provides a linear relationship from which  $K_0$  and  $q_0^*$  are determined from the slope and intercept of the plot, as seen in Table 2. The  $K_0$  values for the contact time of MB at different concentration ranges of 100, 80, 60, 50, and 40 mg/L were 0.0029, 0.0042, 0.0027, 0.0025, and 0.0027, respectively. The  $q_0^*$  parameters estimated at 100, 80, 60, 50 and 40 mg/L are 9.3395, 7.1641, 5.3381, 4.416, and 3.4386 mg/g, respectively. These values were lower compared to their corresponding  $q_e$  experimental values (9.6390, 7.5919, 5.6323, 4.6467, and 3.7241 mg/g respectively). The  $R^2$  values are 0.8689, 0.8254, 0.8558, 0.9600, and 0.9889, respectively. The highest value of  $R^2$  is 0.9889 at 40 mg/L. In addition, it was observed that only  $R^2$  at 40 mg/L is not far from unity, and this implies that a Zeroth order kinetic model can be used to fit the adsorption of MB only for 40 mg/L and is not suitable for higher concentrations.

#### 3.4.2. First Order

The plot of  $\log(q_m - q_t)$  against  $t$  (Figure 6b) provides a linear relationship from which  $K_1$  and  $q_m$  are determined from the slope and intercept of the plot. The  $K_1$  values for a contact time of MB at different concentration ranges of 100, 80, 60, 50, and 40 mg/L were 0.0003, 0.0006, 0.0005, 0.0005, and 0.0008, respectively. The  $q_0^*$  parameters estimated at 100, 80, 60, 50 and 40 mg/L are 9.3409, 7.1657, 5.3393, 4.4172, and 3.4408 mg/g, respectively. These values, just like zeroth order, were also lower compared to their corresponding  $q_e$  experimental values, which were 9.6390, 7.5919, 5.6323, 4.6467, and 3.7241 mg/g, respectively, for 100, 80, 60, 50, and 40 mg/L concentration. The  $R^2$  for 100, 80, 60, 50 and 40 mg/L are 0.8689, 0.8253, 0.8556, 0.9585, and 0.9896, respectively. The highest value of  $R^2$  is 0.9896 at 40 mg/L. In addition, it was observed that only  $R^2$  at 40 mg/L is

not far from unity, and this implies that the first-order kinetic model can also be used to fit the adsorption of MB only at 40 mg/L and is not suitable for higher concentrations.

#### 3.4.3. Pseudo-first Order

The plot of  $\ln(q_e - q_t)$  against  $t$  (Figure 6c) provides a linear relationship from which  $K_1$  and  $\ln q_{e(cal.)}$  are determined from the slope and intercept of the plot. The  $K_1$  values for a contact time of MB at different concentration ranges of 100, 80, 60, 50, and 40 mg/L were -0.0029, -0.0042, -0.0027, -0.0025, and -0.0027, respectively. The  $q_e$  parameters estimated at 100, 80, 60, 50, and 40 mg/L are 1.3487, 1.5338, 1.3421, 1.2596, and 1.3306, respectively. These values were lower compared to Zero and first order and also to their corresponding  $q_e$  experimental values, which were 9.6390, 7.5919, 5.6323, 4.6467, and 3.7241 mg/g, respectively, for 100, 80, 60, 50, and 40 mg/L concentrations. The  $R^2$  for 100, 80, 60, 50 and 40 mg/L are 0.8689, 0.8254, 0.8558, 0.96, and 0.9889, respectively. The highest value of  $R^2$  is 0.9889 at 40 mg/L. In addition, it was observed that only  $R^2$  at 40 mg/L is not far from unity, and this implies that a Zeroth order kinetic model can be used to fit the adsorption of MB only for 40 mg/L and is not suitable for higher concentrations.

#### 3.4.4. Second Order

The plot of  $1/q_t$  against  $t$  (Figure 6d) provides a linear relationship from which  $K_2$  and  $q_0$  are determined from the slope and intercept of the plot. The  $K_1$  values for a contact time of MB at different concentration ranges of 100, 80, 60, 50, and 40 mg/L were -0.0003, -0.0008, -0.0009, -0.0001, and -0.0002, respectively. The  $q_e$  parameters estimated at (100, 80, 60, 50 and 40 mg/L are 9.3457, 7.1684, 5.3418, 4.4189, and 3.4435, respectively. These values just like other kinetic models were also lower compared to their corresponding  $q_e$  experimental which were 9.6390, 7.5919, 5.6323, 4.6467, and 3.7241 mg/g, respectively, for 100, 80, 60, 50, and 40 mg/L concentrations. The  $R^2$  for 100,

80, 60, 50, and 40 mg/L concentrations are 0.9999, 0.9998, 0.9996, 0.9999, and 0.9995, respectively, which were very close to unity and further made the model a better fit than the zeroth, first-order, and pseudo-first-order kinetics models. Thus, it was presumed that the second-order model provides a better correlation of adsorption fit than the zeroth, first-order, and pseudo-first-order models.

3.4.5. Pseudo-second Order

The plot of  $1 / q_t$  against  $t$  (Figure 6e) provides a linear relationship from which  $K_2$  and  $q_o$  are determined from the slope and intercept of the plot. The  $K_1$  values for a contact time of MB at different concentration ranges of 100, 80, 60, 50, and 40 mg/L were -0.0003, -0.0008, -0.0009, -0.0001, and -0.0002, respectively. The  $q_e$  parameters estimated at 100, 80, 60, 50, and 40 mg/L are 9.3457, 7.1685, 5.3418, 4.4189, and 3.4435 mg/g, respectively. These values just like other kinetic models were also lower compared to their corresponding  $q_e$  experimental values, which were 9.6390, 7.5919, 5.6323, 4.6467, and 3.7241 mg/g, respectively, for 100, 80, 60, 50, and 40 mg/L concentrations. The  $R^2$  for 100, 80, 60, 50, and 40 mg/L concentrations are 0.9999, 0.9998, 0.9996, 0.9999, and 0.9995, respectively, which were very close to unity and further made the model a better fit than the zeroth, first-order, pseudo-first-order, and second-order kinetics model. Thus, it was presumed that the pseudo-second-order provides a better correlation of adsorption fit than the zeroth, first-order, pseudo-first-order, and second-order. The results also indicate that the adsorption of MB was consistent with a pseudo-second-order kinetic equation and that its adsorption was mainly via chemisorption.

3.4.6. Third Order

The plot of  $1 / q_t^2$  against  $t$  (Figure 6f) provides a linear relationship from which  $K_3$  and  $q_o$  are determined from the slope and intercept of the plot.

The  $K_1$  values for a contact time of MB at different concentration ranges of 100, 80, 60, 50, and 40 mg/L were -7E-06, -0.00002, -0.00003, -0.00005, and -0.00001, respectively. The  $q_e$  parameters estimated at 100, 80, 60, 50, and 40 mg/L are 9.3250, 7.1611, 5.3452, 4.4194, and 3.4442, respectively. These values just like other kinetic models were also lower compared to their corresponding  $q_e$  experimental values, which were 9.6390, 7.5919, 5.6323, 4.6467, and 3.7241 mg/g respectively for 100, 80, 60, 50, and 40 mg/L concentration. The  $R^2$  for 100, 80, 60, 50, and 40 mg/L are 0.8705, 0.8157, 0.8545, 0.9555, and 0.9902, respectively. The highest value of  $R^2$  is 0.9902 at 40 mg/L. In addition, it was observed that only  $R^2$  at 40 mg/L is not far from unity, and this implies that the third-order kinetic model can also be used to fit the adsorption of MB only at 40 mg/L and is not suitable for higher concentrations.

3.4.7. Selection of suitable isotherm

The suitability of the kinetic model to the data obtained from the study was analyzed based on the  $R^2$ , and it was observed that only  $R^2$  at 40 mg/L is not far from unity zeroth, first-order, pseudo-first-order, third-order, and this implies that these kinetic models can also be used to fit the adsorption of MB only at 40 mg/L and are not suitable for higher concentration. The  $R^2$  for the second-order and pseudo-second-order Kinetic models were very close to unity at all concentrations, which further made the model a better fit than the zeroth, first-order, and pseudo-first-order kinetic models. Thus, it was presumed that the second-order and pseudo-second-order Kinetic models provide a better correlation of adsorption fit than the zeroth, first-order, and pseudo-first-order models. The results also indicate that the adsorption of MB was consistent with a pseudo-second-order kinetic equation, and that its adsorption was mainly via chemisorption.

Table 2: Kinetic Models for Effect of Concentration.

Concentration		100 ml/L	80 ml/L	60 ml/L	50 ml/L	40 ml/L
Zeroth Order	$q_{e(exp)}$	9.639	7.5919	5.6322	4.6467	3.7242
	$q_o$	9.339	7.1641	5.3381	4.4160	3.4386
	$K_o$	0.0029	0.0042	0.0027	0.0025	0.0027
	$R^2$	0.8689	0.8254	0.8558	0.9600	0.9889
First Order	$q_o$	9.3408	7.1656	5.3393	4.4172	3.4408
	$K_1$	0.0003	0.0006	0.0005	0.0005	0.0008
	$R^2$	0.8694	0.8223	0.8556	0.9585	0.9896
Pseudo-First Order	$q_o$	1.3487	1.5338	1.3420	1.2596	1.3306
	$K_1$	-0.0029	-0.0042	-0.0027	-0.0025	-0.0027
	$R^2$	0.8689	0.8254	0.8558	0.9600	0.9889
Second Order	$q_o$	9.3457	7.1685	5.3418	4.4189	3.4435
	$K_2$	-0.00003	-0.00008	-0.00009	-0.0001	-0.0002
	$R^2$	0.87	0.8191	0.8552	0.9571	0.9900
Pseudo-Second Order	$q_o$	9.6805	7.5930	5.6433	4.6838	3.7439
	$K_2$	0.1312	0.1274	0.1510	0.1897	0.1519
	$R^2$	0.9999	0.9998	0.9996	0.9999	0.9995
Third Order	$q_o$	9.3251	7.1611	5.3452	4.4194	3.4442
	$K_3$	-7E-06	-0.00002	-0.00003	-0.00005	-0.0001
	$R^2$	0.8705	0.8157	0.8545	0.9555	0.9902

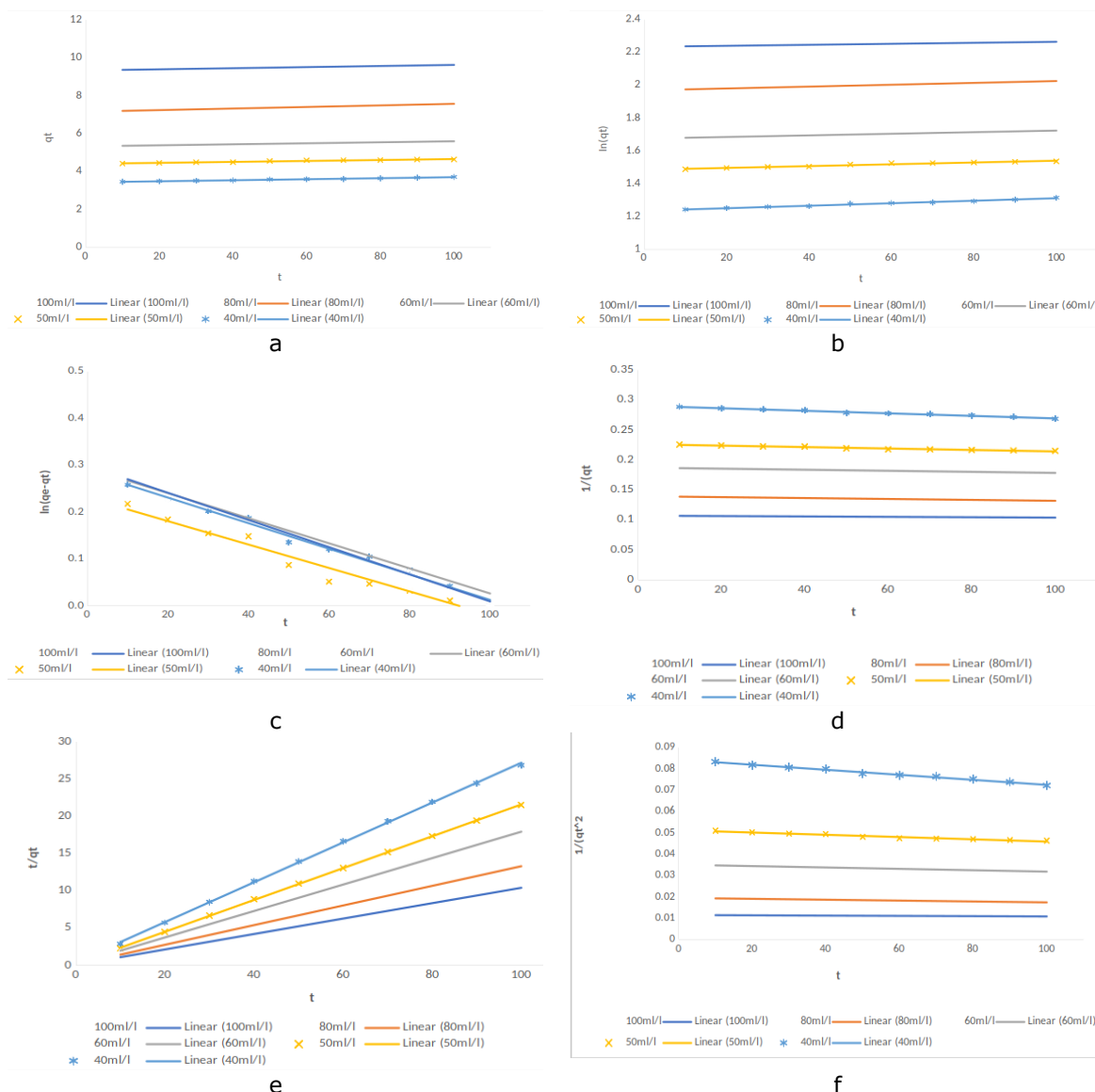


**Figure 6:** (a) Zeroth Order Kinetic Model, (b) First Order Kinetic Model (c): Pseudo-First Order Kinetic Model (d) Second-Order Kinetic Model (e) Pseudo-Second Order Kinetic Model, and (f) Third Order Kinetic Model.

### 3.5. Mass Transfer for Diffusion for Effect of Concentration Model

#### 3.5.1. Webber-Morris Mass Transfer

The plot  $q_e$  against  $t^{1/2}$  (Figure 7a) describes the relationship between the Weber Morris constant as obtained from the slope and intercept of the plot. The intraparticle diffusion parameters obtained from the plot are  $C_{wm}$  and  $R^2$ . Where  $k_{ami}$  is the slope and  $C$  is the intercept. The  $k_{wm}$  values for a contact time of MB at different concentration ranges of 100, 80, 60, 50, and 40 mg/L were 0.0372, 0.0582, 0.037, 0.034, and 0.0364 mg/g/min<sup>0.5</sup>, respectively, which is less than 0.1 mg/g/min<sup>0.5</sup>, which clearly show that adsorption stages did not occur in multiples (16). The  $R^2$  for 100, 80, 60, 50, and 40 mg/L are 0.7841, 0.8896, 0.8327, 0.9731, and 0.9616, respectively. The highest value of  $R^2$  is 0.9731, which is close to unity, suggesting that the adsorption process was surface diffusion dominant

and showed a good fit to the experimental data.

#### 3.5.2. McKay

The plot  $\ln(1-F)$  against  $t$  (Figure 7b) describes the relationship between the McKay constant as obtained from the slope of the plot. The  $k$  values for a contact time of MB at different concentration ranges of 100, 80, 60, 50, and 40 mg/L were -0.0119, -0.0073, -0.0085, -0.0148, and -0.0089, respectively. The  $R^2$  for 100, 80, 60, 50, and 40 mg/L are 0.7632, 0.8327, 0.706, 0.9208 and 0.923, respectively. The highest value of  $R^2$  is 0.923 at 40 mg/L. The negative value of  $km$  and fluctuation of values of  $R^2$  as concentration increased showed a trend that could be derived as not being a good function of concentrations.

#### 3.5.3. Dumwald Wagner

The plot  $\log(1-F^2)$  against  $t$  (Figure 7c), describes the relationship between the Dumwald Wagner



constants. The intraparticle diffusion parameters  $K$  and  $R^2$  are evaluated from the plot. The  $k$  values for a contact time of MB at different concentration ranges of 100, 80, 60, 50, and 40 mg/L were 0.02718, 0.01658, 0.01935, 0.03385, and 0.02004, respectively. The  $R^2$  for 100, 80, 60, 50, and 40 mg/L are 0.7628, 0.8336, 0.7041, 0.9194, and 0.9208, respectively. The highest value of  $R^2$  is 0.9208 at 40 mg/L.

3.5.4. Vermeulin

The plot  $-\ln(q_i/q_e)^2$  against  $t$  (Figure 7d) describes the relationship between the Verneulin constants. The diffusion parameters  $K_v, D_v$ , and  $R^2$  are evaluated from the plot. The  $K_v$  values for a contact time of MB at different concentration ranges of 100, 80, 60, 50 and 40 mg/L were  $-2.72E-02$ ,  $-1.65E-02$ ,  $-1.94E-02$ ,  $-3.39E-02$ , and  $-2.00E-02$ , respectively, and the estimated  $D_v$  values for contact time of MB at different concentrations ranges of 100, 80, 60, 50, and 40 mg/L were 1.4813, 1.3712, 1.2952, 1.1191, and 1.0592, respectively. The  $R^2$  for 100,

80, 60, 50, and 40 mg/L are 0.7628, 0.8336, 0.7041, 0.9194, and 0.9208, respectively. The highest value of  $R^2$  is 0.9208 at 40 mg/L.

3.5.5. Film Transfer

The plot  $\log(q_m - q_t)$  against  $t$  (Figure 7e) describes the relationship between the film transfer constants  $R^*$  and  $q_m$  as obtained from the slope and intercept of the plot. The diffusion parameters  $R^*, q_m$ , and  $R^2$  are derived from the plot. The  $R^*$  values for a contact time of MB at different concentration ranges of 100, 80, 60, 50, and 40 mg/L were 0.027406,  $-0.0073$ ,  $-0.0085$ ,  $-0.0148$ , and  $-0.0089$ , respectively, and the estimated  $q_m$  values for a contact time of MB at the different concentration range of 100, 80, 60, 50, and 40 mg/L were 0.4783, 0.453524, 0.378181, 0.411339, and 0.36686, respectively. The  $R^2$  for 100, 80, 60, 50, and 40 mg/L are 0.7632, 0.8327, 0.706, 0.9208, and 0.923, respectively. The highest value of  $R^2$  is 0.923 at 40 mg/L.

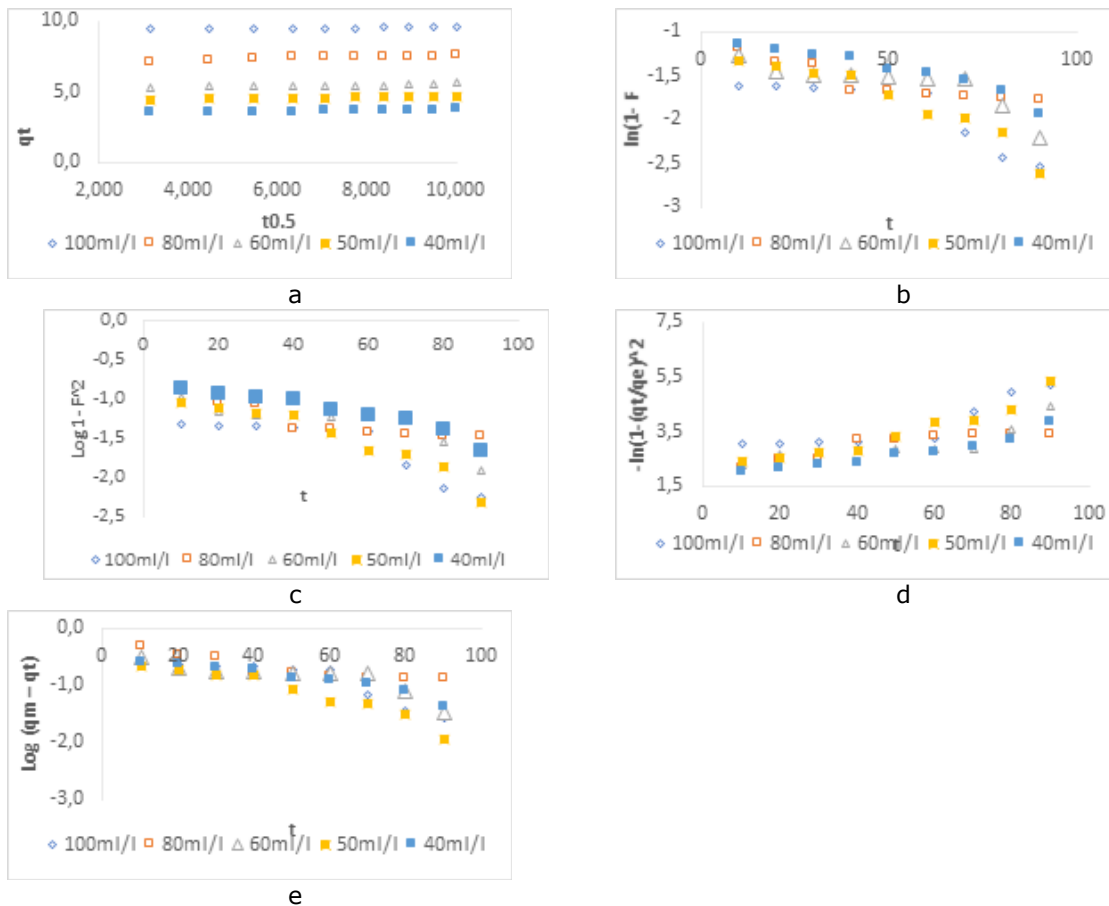


Figure 7: (a) Webber- Morris Mass Transfer, (b) McKay Mass Transfer (c) Dumwald-Wagner Mass Transfer (d) Vermeulin, and (e) Film Mass Transfer.

4. CONCLUSION

The polymeric waste was successfully chemically recycled into the novel functional adsorbent composite. The synthesized adsorbent composite was applied for the treatment of MB wastewater. The adsorption capacity and removal efficiency

showed a linear relationship between the investigated entities, concentration, and contact time. The result also showed that adsorption capacity and removal efficiency increase as concentration and contact time increase. The equilibrium data shows that Langmuir, Freundlich, Temkin, Harkin-J, Hill-De, Dubinin, Halsey, and

Jovanovich isotherms are more suitable for MB removal because the values of their  $R^2$  are greater than 0.9. It can be deduced that the order of isotherms fit for MB is as follows; Temkin > Dubinin > Hill-De > Halsey > Freundlich > Jovanovich > Langmuir -2 > Harkin-J > Langmuir -4 > Langmuir -3 > Langmuir -1. The kinetic model that best describes the adsorption of MB onto the polymeric composite produced is the pseudo-second-order model. The Weber- Morris Mass Transfer has the highest value of  $R^2$  and is the most suitable model for the adsorption of MB onto the polymeric composite.

## 5. REFERENCES

1. Bekri-Abbes I, Bayouh S, Baklouti M. Converting Waste Polystyrene into Adsorbent: Potential Use in the Removal of Lead and Cadmium Ions from Aqueous Solution. *J Polym Environ* [Internet]. 2006 Nov 21;14(3):249–56. Available from: [<URL>](#).
2. Pan B, Pan B, Zhang W, Lv L, Zhang Q, Zheng S. Development of polymeric and polymer-based hybrid adsorbents for pollutants removal from waters. *Chem Eng J* [Internet]. 2009 Aug 15;151(1–3):19–29. Available from: [<URL>](#).
3. Parashar N, Hait S. Plastics in the time of COVID-19 pandemic: Protector or polluter? *Sci Total Environ* [Internet]. 2021 Mar 10;759:144274. Available from: [<URL>](#).
4. Santoso E, Ediati R, Kusumawati Y, Bahruji H, Sulistiono DO, Prasetyoko D. Review on recent advances of carbon based adsorbent for methylene blue removal from waste water. *Mater Today Chem* [Internet]. 2020 Jun 1;16:100233. Available from: [<URL>](#).
5. N'diaye AD, Aoulad El Hadj Ali Y, Bollahi MA, Stitou M, Kankou M, Fahmi D. Adsorption of Methylene Blue from aqueous solution using Senegal River *Typha australis*. *Mediterr J Chem* [Internet]. 2020 Jan 22;10(1):22–32. Available from: [<URL>](#).
6. Song J, Zou W, Bian Y, Su F, Han R. Adsorption characteristics of methylene blue by peanut husk in batch and column modes. *Desalination* [Internet]. 2011 Jan 15;265(1–3):119–25. Available from: [<URL>](#).
7. Alade AO, Amuda OS, Afolabi TJ, Okoya AA. Adsorption of naphthalene onto activated carbons derived from milk bush kernel shell and flamboyant pod. *J Environ Chem Ecotoxicol* [Internet]. 2012 Apr 2;4(7):124–32. Available from: [<URL>](#).
8. Ge M, Wang X, Du M, Liang G, Hu G, S.M. JA. Adsorption Analyses of Phenol from Aqueous Solutions Using Magadiite Modified with Organo-Functional Groups: Kinetic and Equilibrium Studies. *Materials* (Basel) [Internet]. 2018 Dec 28;12(1):96. Available from: [<URL>](#).
9. Langmuir I. The Constitution and Fundamental Properties of Solids and Liquids. Part I. Solids. *J Am Chem Soc* [Internet]. 1916 Nov 1;38(11):2221–95. Available from: [<URL>](#).
10. Unuabonah EI, Omorogie MO, Oladoja NA. Modeling in Adsorption: Fundamentals and Applications. In: *Composite Nanoadsorbents* [Internet]. Elsevier; 2019. p. 85–118. Available from: [<URL>](#).
11. Hall KR, Eagleton LC, Acrivos A, Vermeulen T. Pore- and Solid-Diffusion Kinetics in Fixed-Bed Adsorption under Constant-Pattern Conditions. *Ind Eng Chem Fundam* [Internet]. 1966 May 1;5(2):212–23. Available from: [<URL>](#).
12. Alam MS, Khanom R, Rahman MA. Removal of Congo Red Dye from Industrial Wastewater by Untreated Sawdust. *Am J Environ Prot* [Internet]. 2015 [cited 2023 Aug 29];4(5):207–13. Available from: [<URL>](#).
13. Freundlich H. Über die Adsorption in Lösungen. *Zeitschrift für Phys Chemie* [Internet]. 1907 Oct 1;57U(1):385–470. Available from: [<URL>](#).
14. Hutson ND, Yang RT. Theoretical basis for the Dubinin-Radushkevitch (D-R) adsorption isotherm equation. *Adsorption* [Internet]. 1997 Sep;3(3):189–95. Available from: [<URL>](#).
15. Li Y-H, Wang S, Luan Z, Ding J, Xu C, Wu D. Adsorption of cadmium(II) from aqueous solution by surface oxidized carbon nanotubes. *Carbon N Y* [Internet]. 2003 Jan 1;41(5):1057–62. Available from: [<URL>](#).
16. Dada AO, Latona DF, Ojediran OJ, Nath OO. Adsorption of Cu (II) onto bamboo supported manganese (BS-Mn) nanocomposite: effect of operational parameters, kinetic, isotherms, and thermodynamic studies. *J Appl Sci Environ Manag* [Internet]. 2016 Jul 25;20(2):409–22. Available from: [<URL>](#).
17. Kadhom M, Albayati N, Alalwan H, Al-Furaiji M. Removal of dyes by agricultural waste. *Sustain Chem Pharm* [Internet]. 2020 Jun 1;16:100259. Available from: [<URL>](#).
18. Priyadarshini B, Rath PP, Behera SS, Panda SR, Sahoo TR, Parhi PK. Kinetics, Thermodynamics and Isotherm studies on Adsorption of Eriochrome Black-T from aqueous solution using Rutile TiO<sub>2</sub>. *IOP Conf Ser Mater Sci Eng* [Internet]. 2018 Feb 1;310(1):012051. Available from: [<URL>](#).
19. Boukhemkhem A, Rida K. Improvement adsorption capacity of methylene blue onto modified Tamazert kaolin. *Adsorpt Sci Technol* [Internet]. 2017 Dec 25;35(9–10):753–73. Available from: [<URL>](#).
20. Ozudogru Y, Merdivan M, Gökşan T. Biosorption of Methylene Blue from Aqueous Solutions by Iron Oxide-Coated *Cystoseira barbata*. *J Turkish Chem Soc Sect A Chem* [Internet]. 2016 Oct 5;3(3):551–64. Available from: [<URL>](#).
21. Babalola BM, Babalola AO, Akintayo CO, Lawal OS, Abimbade SF, Oseghe EO, et al. Adsorption and desorption studies of Delonix regia pods and leaves: removal and recovery of Ni(II) and Cu(II) ions from aqueous solution. *Drink Water Eng Sci* [Internet]. 2020 Jul 17;13(2):15–27. Available from: [<URL>](#).
22. Chandran V, Muthuraman P, Rajalekshmi G, Amritha TS, Viji Chandran S, Pandimadevi M. Preparation and characterisation of activated carbon from Delonix regia seeds for the removal of methylene blue dye. *J Ind Pollut Control* [Internet]. 2016;32(2):572–9. Available from: [<URL>](#).
23. Dehghani MH, Tajik S, Panahi A, Khezri M, Zarei A, Heidarinejad Z, et al. Adsorptive removal of noxious cadmium from aqueous solutions using poly urea-formaldehyde: A novel polymer adsorbent. *MethodsX* [Internet]. 2018 Jan 1;5:1148–55. Available from: [<URL>](#).
24. Amole AR, Araromi DO, Alade AO, Afolabi TJ, Adeyi VA. Biosorptive removal of nitrophenol from aqueous solution using ZnCl<sub>2</sub>-modified groundnut shell: optimization, equilibrium, kinetic, and thermodynamic studies. *Int J Environ Sci Technol* [Internet]. 2021 Jul 30;18(7):1859–76. Available from: [<URL>](#).



## Preparation and Characterization of Some Complexes of Nickel(II), Copper (II), and Zinc (II) With Decylxanthate and their Adducts with Nitrogen Base Ligands, and their Biological Activity

Mohammad A. Ali , Fadia J. Ahmad 

University of Mosul, College of Education for Pure Science, Department of Chemistry, Mosul, Iraq

**Abstract:** This research includes the synthesis and characterization of twelve new complexes of mono nuclear xanthate for a number of transition metal ions Ni(II), Cu(II), and Zn(II) and through the interaction with ligand (potassium decyl xanthate) and complexes of formula  $[M(\text{DEXANT})_2]$  were prepared: M= Ni(II), Cu(II), and Zn(II), and then the interaction of these complexes with Lewis bidentate bases, to give complexes with the formula  $[M(\text{DEXANT})_2.L]$ , where L= 1,10-phenanthroline, 8-hydroxyquinoline, and 2,2-bipyridine. The prepared complexes were characterized by melting point, atomic absorption spectrometry, micro elemental analysis, infrared spectroscopy, proton nuclear magnetic resonance spectroscopy, molar electrical conductivity, electronic absorption spectra, and magnetic susceptibility measurements. Magnetic moment and electronic spectra indicated that the complexes of type  $[M(\text{DEXANT})_2]$  had a tetrahedral geometry, while complexes of type  $[M(\text{DEXANT})_2.L]$  had an octahedral geometry. The conductivity measurements proved the non-electrolytic behavior of all compounds. The biological evaluation against bacterial species indicated that the xanthate complexes were effective against all bacterial types.

**Keywords:** Xanthate, Complexes, Nickel(II), Copper(II), Zinc(II), Biological Activity.

**Submitted:** June 08, 2023. **Accepted:** August 14, 2023.

**Cite this:** Ali MA, Ahmad FJ. Preparation and Characterization of Some Complexes of Nickel(II), Copper (II), and Zinc (II) With Decylxanthate and their Adducts with Nitrogen Base Ligands, and their Biological Activity. JOTCSA. 2023;10(4):975-84.

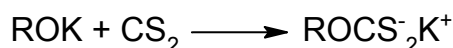
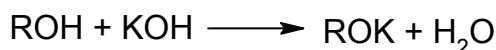
**DOI:** <https://doi.org/10.18596/jotcsa.1311891>.

**\*Corresponding author. E-mail:** [mahameedameen.21esp22@student.uomosul.edu.iq](mailto:mahameedameen.21esp22@student.uomosul.edu.iq).

### 1. INTRODUCTION

Xanthates are sulfur- and oxygen-containing ligands that form a wide variety of coordination complexes with transition and main group metals (1). Xanthates are derived from xanthic acid, and organic molecules with a  $-\text{OCS}_2$  functional group (2). Due to the important roles that several xanthate reactions play, the chemistry of xanthates holds a unique place among sulfur-containing reagents (3). Chemistry professionals have been drawn to the significant class of organic compounds known as xanthates because of their wide range of potential uses (4). Xanthates are

much efficient for removing heavy metals from wastewater due to their low solubility products and high stability constants (5). Xanthates inhibit the replication of both DNA and RNA viruses in vitro and therefore, possess enhanced antiviral and antitumoral activity (6). Metal xanthates are extensively used as fungicides, pesticides, rubber accelerators, corrosion inhibitors, reagents in agriculture, and for treating HIV infections (7). The synthesis of xanthates may involve different processes and substances through a sequence of alkylation and xanthation reactions. However, they are mainly obtained by reacting an alkaline hydroxide with carbon disulfide and alcohol (8).



**Scheme 1:** Preparation of xanthates.

## 2. EXPERIMENTAL PART

### 2.1 Materials and Instrumentation

The primary chemicals and solvents used were all processed by Aldrich Sigma and BDH: 1,10-phenanthroline monohydrate, 8-hydroxyquinoline, 2,2'-bipyridine, ethanol, decanal, diethyl ether, carbon disulfide, dimethylformamide (DMF), potassium hydroxide, NiCl<sub>2</sub>, CuCl<sub>2</sub>, and ZnCl<sub>2</sub>.

The percentage of nickel, copper, and zinc in the complexes was determined by atomic absorption spectrometry (Analytik Jena NovA A350) in Mosul. NMR Ultrashield was used for analyzing <sup>1</sup>H-NMR spectra of synthesized ligand in Turkey, the sample was dissolved in deuterated (DMSO) at room temperature (298 K). FT-IR spectra of ligands and complexes were recorded on a spectrometer (Shimadzu) in the range (400 - 4000 cm<sup>-1</sup>) using a KBr pellet, that was conducted at the University of Tikrit at 25 °C. The electrical conductivity was measured on the conductivity Meter-Model (Eutech pc700) of the complexes, and the samples were dissolved in DMF at a concentration of 10<sup>-3</sup> M and a temperature of 25 °C. A UV spectrophotometer (PG Instruments) was used for recording electronic spectra in dimethylformamide solvent with 10<sup>-3</sup> M at 25 °C using 1 cm quartz cells. The melting point or decomposition temperature for the compounds was measured using (Aparatus-Stuart-SMP Melting point). magnetic measurements were made. using the Gouy method in the solid-state using (Magnetic Susceptibility Balance) at the University of Tikrit. The elements of carbon, hydrogen, nitrogen, and sulfur in the ligand and prepared complexes were estimated using an Elementer Germany-type device at Tehran University/Iran.

### 2.2. Synthesis of Potassium DecylXanthate Ligand

Decanol (38.11 mL, 0.199 mol) was added to potassium hydroxide (11.20 g, 0.199 mol) with stirring. The mixture was cooled in an ice bath, and carbon disulfide was added drop wise to the mixture (12.06 mL, 0.199 mol) while stirring was continued for 30 minutes. The yellow precipitate formed was filtered off in an ice bath, washed with diethyl ether, and dried in vacuum (9).

### 2.3 Synthesis of Complexes [M (DEXANT)<sub>2</sub>] (1:2)

M = Ni(II), Cu(II), and Zn(II) in which NiCl<sub>2</sub> (0.237 g, 0.0018 mol) or CuCl<sub>2</sub> (0.246 g, 0.0018 mol) or ZnCl<sub>2</sub> (0.250 g, 0.0018 mol) potassium hydroxide in ethanol, and decyl xanthate (**1**, 0.0036 mol) was added drop wise to the ethanolic solution while

stirring 30 min to achieve complete precipitation. The precipitate was filtered off, rinsed with ethanol, dried in vacuum, and washed again with diethyl ether.

### 2.4 Synthesis of Complexes [M(DEXANT)<sub>2</sub>.L] (1:2:1)

L = 1,10-phenanthroline, 8-hydroxyquinoline, or 2,2'-bipyridine were prepared similarly to section 2.3. The resulting precipitate was treated with (0.0018 mol) (1,10-phenanthroline, 8-hydroxyquinoline and 2,2'-bipyridine), which were added drop wise for 30 minutes while stirring constantly. The resulting precipitate was filtered off, washed with ethanol and dried.

## 3. RESULT AND DISCUSSION

### 3.1. Molar Conductivity

Molar conductance values of the millimolar solutions of adducts in DMF were found in the range of (2.5-21.5) ohm<sup>-1</sup>mol<sup>-1</sup>cm<sup>2</sup> (Table 1). The values were much smaller than that expected for any univalent electrolyte suggesting that these complexes were neutral and non-ionic in nature (10).

### 3.2. Magnetic Susceptibility Measurements

The effective magnetic moment (*eff*) of Complexes was calculated at 25 °C as shown in Table 2. The magnetic moments for Ni(II) and Cu(II) complexes from **1**, **2** and **3** are in the range in (1.65 - 2.12 B.M) suggesting a tetrahedral geometry (11). The low values of the effective magnetic moments compared to the spin-only magnetic moment for complexes **4** and **5** are due to antiferromagnetic interaction. The magnetic moment values of the other complexes **7-12** were in the range (1.83 - 2.75 B.M) suggesting an octahedral geometry (12). All Zn(II) complexes are diamagnetic.

### 3.3. Atomic Absorption

The proportions of Ni, Cu, and Zn in the resulting complexes were estimated from the results obtained in Table 1 and compared with theoretically calculated values, it was shown that the resulting complexes were consistent with the proposed formula (10).

### 3.4. Elemental Analysis (CHN)

Elemental analysis was carried out on the isolated complexes in order to prove their formation. The results obtained from this analysis are given in Table 1. Looking at the results in Table 1, it can be seen that there is a good consistency between the calculated and experimental ratio of the elements C,H,N and S of the proposed structure. This

agreement supported the formation of synthesized complex (10).

### 3.5. Electronic Spectral Studies

The UV-Vis spectra of the  $10^{-3}$  M (DMF) solution of the ligand and its complex were recorded; the results are shown in (Table 2). For ligands, the high-intensity absorption peaks appearing in the 37037, 49504  $\text{cm}^{-1}$  region are related to  $\pi \rightarrow \pi^*$ ,  $n \rightarrow \pi^*$  intraligand transitions (13).

The UV-Visible spectrum of Ni(II) complex (**1**) shows two absorption bands at 11235  $\text{cm}^{-1}$  and 17793  $\text{cm}^{-1}$  which were assigned to  ${}^3T_1(F) \rightarrow {}^3A_2(F)$  and  ${}^3T_1(F) \rightarrow {}^3T_1(P)$  transitions respectively in a tetrahedral geometry, at the same time, the complexes **4**, **7** and **10** exhibit three absorption bands in the range 11185-11363  $\text{cm}^{-1}$ , 14577-15337  $\text{cm}^{-1}$  and 24154-21789  $\text{cm}^{-1}$  which corresponded to  ${}^3A_{2g}(F) \rightarrow {}^3T_{2g}(F)$ ,  ${}^3A_{2g}(F) \rightarrow {}^3T_{1g}(F)$ , and  ${}^3A_{2g}(F) \rightarrow {}^3T_{1g}(P)$  octahedral transitions respectively (14).

The Cu(II) complex (**2**) shows absorption band at 11235  $\text{cm}^{-1}$  which correlates to  ${}^2T_2 \rightarrow {}^2E$  transition in the tetrahedral geometry, whereas octahedral

complexes (**5**, **8**, and **11**) exhibited broadband in the region 12886-13227  $\text{cm}^{-1}$ , which was assigned to  ${}^2E_g \rightarrow {}^2T_{2g}$  in an octahedral geometry (13). The Zn(II) complexes have no peaks in the visible range ( $d^{10}$  system). This means that no d-d electronic transitions occurred. These metal complexes do not show d-d transitions (14).

### 3.6 IR Spectra

The critical IR bands of the ligand (decylxanthate)K and its complexes are listed in Table 3. The band of FT-IR spectrum at 1128  $\text{cm}^{-1}$  was assigned to  $\nu(\text{C-O})$  in ligand spectra, this band was shifted to a higher frequency and observed in the range 1143-1200  $\text{cm}^{-1}$ . The band at 1075  $\text{cm}^{-1}$  due to  $\nu(\text{C-S})$  of the ligand which shifted to a lower frequency 995-1052  $\text{cm}^{-1}$  (15).

The range (418-470  $\text{cm}^{-1}$ ) of the IR spectra revealed a new band of moderate to strong intensity that provides support for the coordination of metal to sulfur  $\nu(\text{M-S})$ . This phenomenon could be explained by alcohol's release of electrons, which pushes a high electron density toward the sulfur atoms, where the  $\nu(\text{M-N})$  was seen in the 483 - 555  $\text{cm}^{-1}$  region (13).

**Table 2:** Data on the electronic spectra and effective magnetic moment of the ligand and produced compounds ( $\text{cm}^{-1}$ ).

No	Formula of complexes	$\mu_{\text{eff}}$ B.M	U-Vis. Bands ( $\text{cm}^{-1}$ )	Charge transfer	Proposed Structure
L	K-DEXANT	----	----	37037, 49504	----
1	[Ni(DEXANT) <sub>2</sub> ]	2.12	11235, 17793	37037	Tetrahedral
2	[Cu(DEXANT) <sub>2</sub> ]	1.65	11235	35460	Tetrahedral
3	[Zn(DEXANT) <sub>2</sub> ]	Dia	----	33211	Tetrahedral
4	[Ni(DEXANT) <sub>2</sub> (phen)]	2.75	11173, 15337, 21786	34722	Octahedral
5	[Cu(DEXANT) <sub>2</sub> (phen)]	1.83	13227	35971	Octahedral
6	[Zn(DEXANT) <sub>2</sub> (phen)]	Dia	----	35211	Octahedral
7	[Ni(DEXANT) <sub>2</sub> (Bipy)]	2.65	11363, 14577, 24154	37878	Octahedral
8	[Cu(DEXANT) <sub>2</sub> (Bipy)]	1.94	12886	37878	Octahedral
9	[Zn(DEXANT) <sub>2</sub> (Bipy)]	Dia	----	37971	Octahedral
10	[Ni(DEXANT) <sub>2</sub> (8-Qui)]	2.70	11185, 14925, 23923	35211	Octahedral
11	[Cu(DEXANT) <sub>2</sub> (8-Qui)]	2.03	13989	37593	Octahedral
12	[Zn(DEXANT) <sub>2</sub> (8-Qui)]	Dia	----	35791	Octahedral

Dia: Diamagnetic.

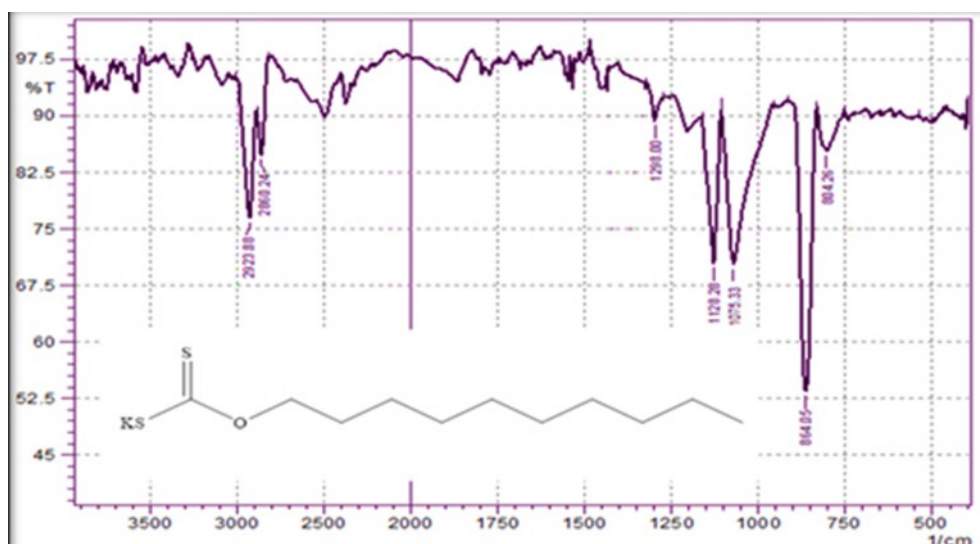
**Table 1:** The closed formulas, the compounds' physical characteristics, molar conductivity, and elemental analysis of the compounds prepared in this study.

NO	Formula of complexes	Color	M.P °C	Molar conductivity $\Omega^{-1} \cdot \text{cm}^2 \cdot \text{mol}^{-2}$	Yield	Elemental analysis theoretical (Practical)				
						C%	H%	N%	S%	M%
L	K-DEXANT	Pale yellow	*260	---	87%	---	23.53 (22.77)	---	7.77 7.13	48.48 (47.83)
1	[Ni(DEXANT) <sub>2</sub> ]	Dark yellow	185	21.5	85%	11.17 (10.67)	24.40 (24.27)	---	8.06 (8.10)	50.28 (49.97)
2	[Cu(DEXANT) <sub>2</sub> ]	Blue	172	16.0	91%	11.98 (11.2)	24.18 (23.77)	---	7.98 (7.91)	49.82 (48.63)
3	[Zn(DEXANT) <sub>2</sub> ]	off White	220	19.3	72%	12.28 (11.65)	24.10 (23.69)	---	7.95 (7.87)	49.65 (49.73)
4	[Ni(DEXANT) <sub>2</sub> (phen)]	Pink	*300	18.0	77%	8.32 (7.55)	18.17 (17.59)	3.97 (3.32)	7.14 (7.09)	57.87 (56.93)
5	[Cu(DEXANT) <sub>2</sub> (phen)]	Deep Blue	120	6.9	85%	8.94 (8.47)	18.05 (18.23)	3.94 (3.69)	7.59 (7.47)	57.47 (57.09)
6	[Zn(DEXANT) <sub>2</sub> (phen)]	Elegant White	*290	10.0	78%	9.18 (8.66)	18.00 (17.79)	3.93 (3.82)	7.57 (7.61)	57.32 (58.02)
7	[Ni(DEXANT) <sub>2</sub> (Bipy)]	Light green	*320	7.0	92%	8.61 (7.81)	18.81 (18.44)	4.11 (3.56)	7.39 (7.23)	56.38 (55.59)
8	[Cu(DEXANT) <sub>2</sub> (Bipy)]	Green	*295	18.0	89%	9.26 (8.55)	18.68 (18.17)	4.08 (3.47)	7.34 (7.39)	55.98 (54.88)
9	[Zn(DEXANT) <sub>2</sub> (Bipy)]	off White	180	6.0	82%	9.50 (8.76)	18.63 (17.87)	4.07 (3.83)	7.32 (7.37)	55.83 (54.67)
10	[Ni(DEXANT) <sub>2</sub> (8-Qui)]	Light brown	200	4.7	87%	8.75 (7.45)	19.12 (19.56)	2.09 (1.87)	7.36 (7.41)	55.52 (54.77)
11	[Cu(DEXANT) <sub>2</sub> (8-Qui)]	Dark green	230	2.5	73%	9.41 (8.23)	18.98 (19.12)	2.07 (2.27)	7.31 (7.25)	55.12 (55.67)
12	[Zn(DEXANT) <sub>2</sub> (8-Qui)]	Yellow	*315	15.0	79%	9.65 (8.27)	18.93 (18.13)	2.07 (2.36)	7.29 (7.22)	54.97 (55.13)

\* = decomposition

**Table 3:** IR bands ( $\text{cm}^{-1}$ ) data of ligand and prepared complexes.

N0	Formula of complexes	$\nu(\text{C-O})$	$\nu(\text{C-S})$	$\nu(\text{M-S})$	$\nu(\text{M-N})$
L	K-DEXANT	---	1075	1128	---
1	$[\text{Ni}(\text{DEXANT})_2]$	448	995	1200	---
2	$[\text{Cu}(\text{DEXANT})_2]$	465	1005	1190	---
3	$[\text{Zn}(\text{DEXANT})_2]$	425	1008	1195	---
4	$[\text{Ni}(\text{DEXANT})_2(\text{phen})]$	465	1035	1175	511
5	$[\text{Cu}(\text{DEXANT})_2(\text{phen})]$	458	1015	1182	483
6	$[\text{Zn}(\text{DEXANT})_2(\text{phen})]$	420	1047	1178	525
7	$[\text{Ni}(\text{DEXANT})_2(\text{Bipy})]$	470	1028	1162	510
8	$[\text{Cu}(\text{DEXANT})_2(\text{Bipy})]$	455	1048	1167	484
9	$[\text{Zn}(\text{DEXANT})_2(\text{Bipy})]$	438	1018	1148	493
10	$[\text{Ni}(\text{DEXANT})_2(8\text{-Qui})]$	462	1043	1151	512
11	$[\text{Cu}(\text{DEXANT})_2(8\text{-Qui})]$	423	1052	1143	487
12	$[\text{Zn}(\text{DEXANT})_2(8\text{-Qui})]$	418	1037	1180	555

**Figure 1:** FTIR Spectrum of Ligand (K-DEXANT).

### 3.7 $^1\text{H-NMR}$

The prepared ligand was studied by  $^1\text{H-NMR}$  spectrometry, and the measurement reference is in this technique is tetramethylsilane ( $\text{SiMe}_4$ ) and using ( $\text{DMSO-d}_6$ ) solvent, or the results were

interpreted depending on the values of the chemical signals, where the ligand spectrum was shown (16).  $^1\text{H-NMR}$  ( $\text{DMSO-d}_6$ ; 400 MHz)  $\delta\text{H}$  (ppm): 0.85- 0.88 (3H, m,  $\text{CH}_3$ ), 1.25-1.30 (12H, m,  $\text{CH}_2$ ), 1.39- 1.42 (4H, m,  $\text{CH}_2$ ), 4.39-4.40 (2H, t,  $\text{CH}_2$ ).

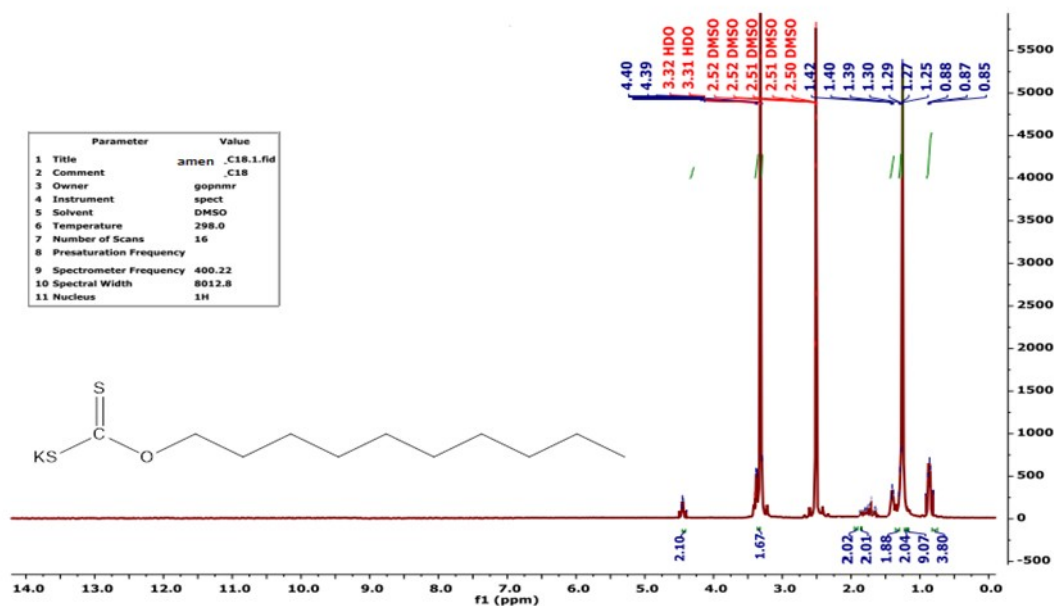


Figure 2:  $^1\text{H}$ -NMR Spectrum of Ligand (K-DEXANT) in  $\text{DMSO-d}_6$ .

### 3.8 Thermogravimetric Analysis

The thermal behavior of the as-prepared complexes was studied at a heating rate of  $25\text{ }^\circ\text{C}$  per minute in a temperature range of  $30\text{--}400\text{ }^\circ\text{C}$ . The results showed the thermogravimetric analysis of the complexes of the type  $[\text{M}(\text{DEXANT})_2\text{L}]$ , there is no loss in the molecule above ( $120\text{ }^\circ\text{C}$ ) and this

indicates the absence of a consistent water molecule within the crystalline network of the complexes as in (Figure 3) and the thermal dissociation of the complex ended with the transformation of the complex completely to a metal oxide at a temperature higher than  $400\text{ }^\circ\text{C}$  (17).

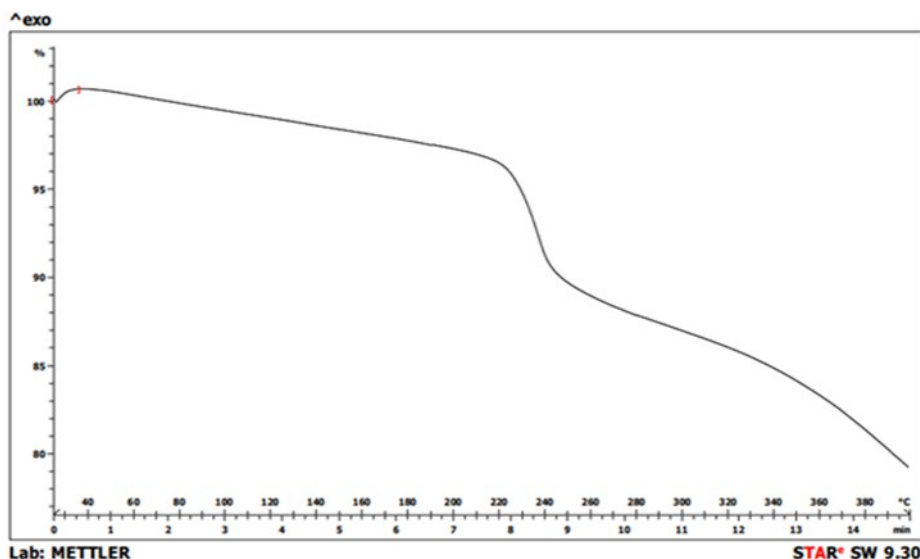


Figure 3: TGA For complexes  $[\text{M}(\text{DEXANT})_2(\text{Bipy})]$ .

### 3.9 Gas chromatography- Mass spectrometry

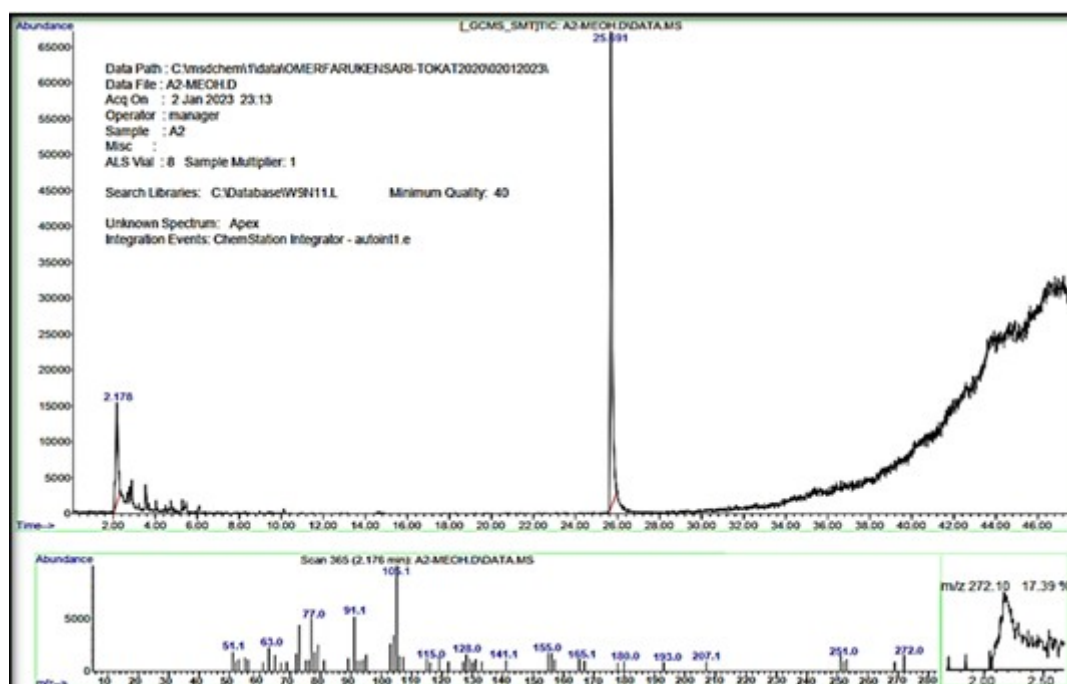
The Gas Chromatography-Mass Spectrometry for K-DEXANT showed multiple peaks with relative abundance of Table 4. This shows where a peak appeared at  $272\text{ m/z}$  at an abundance of  $17.39\%$  that thickened the partial weight of ligand itself, while the mass spectrum of the complex

$[\text{Zn}(\text{DEXANT})_2]$  Peak at  $532\text{ m/z}$  approved for theoretically calculated complex mass, while the mass spectrum of the complex  $[\text{Ni}(\text{DEXANT})_2(\text{Bipy})]$  Peak  $681\text{ m/z}$  approved the theoretically-calculated complex mass, the mass spectrum for complex  $[\text{Cu}(\text{DEXANT})_2(8\text{-Qui})]$  peak at  $675.12\text{ m/z}$  approved the calculated complex mass (10,18).



**Table 4:** Mass spectral data of ligand and the metal(II) complexes.

NO	Compound	Peak m/z	Relative % Abundance
L	K-DEXANT	272.1	17.39
1	[Ni(DEXANT) <sub>2</sub> ]	525.21	32.55
2	[Cu(DEXANT) <sub>2</sub> ]	530.16	49.23
3	[Zn(DEXANT) <sub>2</sub> ]	532.10	17.10
4	[Ni(DEXANT) <sub>2</sub> (phen)]	705.12	28.32
5	[Cu(DEXANT) <sub>2</sub> (phen)]	710.17	52.12
6	[Zn(DEXANT) <sub>2</sub> (phen)]	712.21	21.44
7	[Ni(DEXANT) <sub>2</sub> (Bipy)]	681.10	18.10
8	[Cu(DEXANT) <sub>2</sub> (Bipy)]	686.15	45.12
9	[Zn(DEXANT) <sub>2</sub> (Bipy)]	688.28	12.29
10	[Ni(DEXANT) <sub>2</sub> (8-Qui)]	670.17	62.22
11	[Cu(DEXANT) <sub>2</sub> (8-Qui)]	675.12	38.76
12	[Zn(DEXANT) <sub>2</sub> (8-Qui)]	677.16	53.36

**Figure 4:** Mass Spectrum of ligand.

### 3.10 Biological Activity

The results of evaluating the biological activity of the ligand and the complexes under study on pathogenic bacteria (*Staphylococcus aureus*, *Escherichia coli*, *Pseudomonas aeruginosa* and *Proteus mirabilis* (*Klebsiella* spp)) showed that the ligand and the complexes under study have an

inhibitory ability towards these bacteria. These complexes bind with SH groups of enzyme cells, so they act more strongly than donor atoms in ligands, which should have the lowest (MIC) inhibitory concentration and came in agreement with what was published by many researchers (17,18) (see Table 5).

**Table 5:** Antibacterial activity (inhibition zone) of different concentrations of the ligand and complexes ( $\mu\text{g/mL}$ ).

Compd	<i>Staphylococcus aureus</i>			<i>Escherichia coli</i>			<i>Pseudomonas auruginosa</i>			<i>Klebsiella spp</i>		
	125	250	500	125	250	500	125	250	500	125	250	500
L	-	-	6	-	-	7	-	6	7	-	8	6
1	-	-	8	-	-	9	-	7	7	7	9	8
2	-	-	7	-	-	7	-	9	6	-	8	7
3	-	-	8	-	-	8	-	8	9	-	9	6
4	-	-	11	-	-	7	-	7	8	8	7	8
5	-	6	7	-	-	6	-	6	8	-	9	7
6	-	-	6	-	-	7	-	7	7	-	8	6
7	-	7	7	-	-	9	-	6	6	-	7	8
8	-	8	9	6	7	8	-	9	9	7	8	7
9	-	-	10	-	-	6	-	7	7	-	9	10
10	-	-	7	-	-	8	9	9	7	-	6	7
11	-	7	7	-	-	8	-	8	11	-	10	8
12	-	-	11	-	-	7	-	10	8	-	7	11
CIPS		10			10			10			10	
TMP		12			4			10			0	

#### 4. CONCLUSION

According to the analytical, physical, and spectral results the data observed have brought about the following points:

A- Complexes having a molar ratio of (2:1) are unsymmetrically tetrahedral and they have the formula  $[\text{M}(\text{DEXANT})_2]$  :

B-complexes with a molar ratio of (1:2:1) hexagonal symmetry octahedral and having the formula  $[\text{M}(\text{DEXANT})_2\text{L}]$

C-The ligand and metal complexes showed very good antimicrobial Properties.

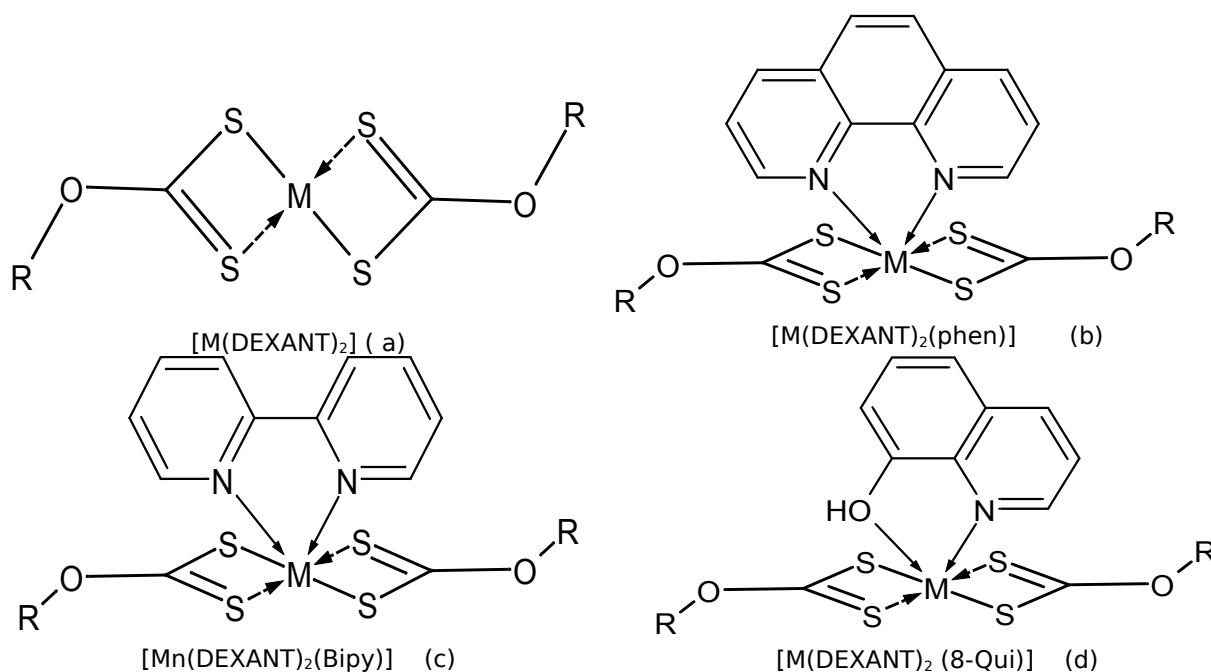


**Figure 3:** Suggested structures (a) complexes (1,2,3), (b) complexes (4,5,6), (c) complexes (7,8,9), (d) complexes (10,11,12), M = Mn(II), Fe(II), Co(II) R =  $(\text{CH}_2)_9\text{CH}_3$

## 5. ACKNOWLEDGMENTS

All the researchers thank the Deanship of the College of Education for Pure Sciences, Department of Chemistry, University of Mosul, Iraq, for completing the research requirements.

## 6. REFERENCES

- Ghoshal S, Jain VK. Gallium(III) and indium(III) dithiolate complexes: versatile precursors for metal sulfides. *Journal of Chemical Sciences*. 2007;119:583-91. Available from: [<URL>](#).
- Chand VT. Synthesis of metal xanthates and their application as latent catalysts for curing of epoxy resin. PhD Thesis, 2015. Kyushu University, Japan. Available from: [<URL>](#).
- Rumyantsev M, Korablev IA, Rumyantsev S. The reaction of potassium xanthates with five-membered cyclic carbonates: Selectivity of the underlying cascade reactions and mechanistic insights. *RSC advances*. 2020;10(60):36303-16. Available from: [<URL>](#).
- Vakalopoulou E, Buchmaier C, Pein A, Saf R, Fischer RC, Torvisco A, et al. Synthesis and characterization of zinc di (O-2, 2-dimethylpentan-3-yl dithiocarbonates) bearing pyridine or tetramethylethylenediamine coligands and investigation of their thermal conversion mechanisms towards nanocrystalline zinc sulfide. *Dalton Transactions*. 2020;49(41):14564-75. Available from: [<URL>](#).
- Görgülü AO, Arslan M, Çil E. Synthesis and characterization of a new pyrrolidine containing sulfur ligand and the transition metal complexes of Co (II), Ni (II) and Cu (I). *Journal of Coordination Chemistry*. 2006;59(17):1913-9. Available from: [<URL>](#).
- Perluigi M, Joshi G, Sultana R, Calabrese V, De Marco C, Coccia R, et al. In vivo protection by the xanthate tricyclodecan-9-yl-xanthogenate against amyloid  $\beta$ -peptide (1-42)-induced oxidative stress. *Neuroscience*. 2006;138(4):1161-70. Available from: [<URL>](#).
- Larsson A-C, Öberg S. Study on potassium isopropylxanthate and its decomposition products: experimental  $^{13}\text{C}$  CP/MAS NMR combined with DFT calculations. *The Journal of Physical Chemistry A*. 2011;115(8):1396-407. Available from: [<URL>](#).
- Ma X, Wang S, Zhong H. Effective production of sodium isobutyl xanthate using carbon disulfide as a solvent: Reaction kinetics, calorimetry and scale-up. *Journal of Cleaner Production*. 2018;200:444-53. Available from: [<URL>](#).
- A Al-Qasser I, E Al-Mukhtar S, F Hana N. Synthesis and Characterization of 2-butoxyethylxanthate complexes with iron(II), cobalt(II), nickel(II), copper(II) and zinc(II) and their adducts with nitrogen base ligands. *Rafidain Journal of Science*. 2014;25(3):57-64. Available from: [<URL>](#).
- Sharma S, Sachar R, Bajju G, Sharma V. Nickel (II) complexes of m-ethylphenylxanthate with nitrogen donors and their biological screening. *Indian Journal of Chemistry-Section A (IJCA)*. 2020;59(11):1618-26. Available from: [<URL>](#).
- Al-Mukhtar SE, Al-Katib HF, Al-Nuaimy LA. Preparation and characterization of some transition metal complexes with crotyl xanthate ligand and their adducts with nitrogen bases. *Rafidain Journal of Science*. 2017;26(1):49-55. Available from: [<URL>](#).
- Al-Jarah FK, Al-Mukhtar SE. Preparation and characterization of some transition metal complexes with oleyl xanthate and 1, 10-phenanthroline. *Rafidain Journal of Science*. 2019;28(2):228-34. Available from: [<URL>](#).
- Al-Fahdawi A, Alsalihi E. Synthesis and characterization of iron(II), cobalt(II), nickel(II), copper(II), and zinc(II) complexes using diphenylmethyl xanthate ligand. *ARO-The Scientific Journal of Koya University*. 2018;6(1):33-7. Available from: [<URL>](#).
- Adel HI, Al-Mukhtar SE. Synthesis and characterization of sulfur donor ligand (Xanthate) Complexes With manganese(II), iron(II), cobalt(II), nickel(II), copper(II), and zinc(II) and their adduct with nitrogen base ligand. *Journal of Duhok University*. 2022;25(2):244-60. Available from: [<URL>](#).
- Al-Mukhtar S. Synthesis and characterization of 3-Methoxypropyldithiocarbamate complexes with iron(II), cobalt(II), nickel(II), copper(II) and zinc(II) and their adducts with nitrogen base ligands. *Rafidain journal of science*. 2013;24(7):50-9. Available from: [<URL>](#).
- Nakamoto K. *Infrared and Raman Spectra of Inorganic and Coordination Compounds, Part A: Theory and Applications in Inorganic Chemistry*, 6th Edition. New York. 2009; 165-322. ISBN: 978-0-471-74339-2
- Abed RR, Mohammed AS, Ahmed FJ. Synthesis and diagnoses of new metal ions complexes derived from trimethoprim schiff bases. *Research Journal of Pharmacy and Technology*, 2021; 14(9), 4963-4968. Available from: [<URL>](#).
- Numan AT, Ibraheem KR, Ibrahim MK. Synthesis, characterization and bacterial evaluation of new mixed-ligand complexes containing dithiocarbamate and 1, 10-phenanthroline with some metal ions. *Journal of Education and Scientific Studies*. 2018;3(12). Available from: [<URL>](#).





## Synthesis and Photodegradation of Bi<sub>2</sub>O<sub>3</sub> and Pb-Bi<sub>2</sub>O<sub>3</sub> Nanoparticles and Their Kinetic Study

Farzana HAIDER\* , Zakia GUL , Kafeel AHMAD KHAN 

Department of Chemistry, Bacha Khan University, Charsadda, Pakistan

**Abstract:** The green synthesis method synthesized the bismuth oxide and lead-doped bismuth oxide nanoparticles using *Ferula Asafoetida* leaves extract. The lead-doped bismuth oxide showed greater degradation efficiency than undoped bismuth oxide. This greater efficiency was due to decreases in the band gap energy between the valence band and the conduction band of the metal oxide and reduced the chances of electron-hole pair recombination with the metal oxide catalyst. The synthesized nanoparticles were characterized by TGA, SEM, FT-IR, EDX, XRD, and UV- visible Spectrometer. XRD diffraction of Bi<sub>2</sub>O<sub>3</sub> nanoparticles reflected a strong and sharp peak at 32.8° shows that Bi<sub>2</sub>O<sub>3</sub> nanoparticles are in crystalline phase. The crystallite size of Bi<sub>2</sub>O<sub>3</sub> nanoparticles is 13.433 nm, and Pb-doped Bi<sub>2</sub>O<sub>3</sub> is 9.6 nm, calculated from the Debye-Scherrer equation. The synthesized Bi<sub>2</sub>O<sub>3</sub> nanoparticles are round in shape with average size of ~ 90-100 nm While Pb doped Bi<sub>2</sub>O<sub>3</sub> is ~ 75 f- 100 nm. The EDX spectra showed no additional peak for any impurities. The degradation rate of Malachite Green dye (MG) increased with the increase in contact time and temperature, while it decreased with increasing dye initial concentration and pH. Initially, the degradation efficiency of the bismuth oxide catalyst is increased with increasing catalyst amount, but after a certain amount of catalyst, it started decreasing as the catalyst amount was further increased. The irradiation time on photodegradation is deliberate, keeping other parameters steady at catalyst quantity 0.01 g at specific reaction conditions. Moreover, the dye showed an increase in degradation at 50 °C. The utmost degradation of 92% was observed for lead-doped bismuth oxide (Bi<sub>2</sub>O<sub>3</sub>) and 76% for undoped bismuth oxide (Bi<sub>2</sub>O<sub>3</sub>).

**Keywords:** Bi<sub>2</sub>O<sub>3</sub> nanoparticles, Debye-Scherrer equation, dye degradation.

**Submitted:** August 18, 2022. **Accepted:** July 25, 2023.

**Cite this:** Haider F, Gul Z, Ahmad Khan K. JOTCSA. Synthesis and Photodegradation of Bi<sub>2</sub>O<sub>3</sub> and Pb-Bi<sub>2</sub>O<sub>3</sub> Nanoparticles and Their Kinetic Study. 2023; 10(4): 985-1000.

**DOI:** <https://doi.org/10.18596/jotcsa.1164065>.

**Corresponding author. E-mail:** [unsty36@gmail.com](mailto:unsty36@gmail.com).

### 1. INTRODUCTION

Nanotechnology has grown to be the most dynamic area of research in various fields of science, having an objective to determine the recompenses of the nano world for the betterment of society (1). Scientists use fine powders for various purposes, such as manufacturing, calculating, and characterization. Practical applications of nanotechnology are increasing with increasing demand for people. Scientists may also use nanotechnology in cosmetics (2), catalysis (3), medicines (4), and biosensing (5). Nanotechnology has a vital role in

chemistry, fabric science, engineering, and physics (6).

Metallic nanoparticles are more significant than metal factors in the bulk state (7). Many nanoparticles have been manufactured from time to time. These fine powders were used in various applications such as terminals of batteries, catalyzers, and components of diesel (8). Bismuth oxide nanoparticles can be used in antibiotic-resistant pathogens on the atomic, thermal, and land physical properties. Bismuth oxide is used in numerous industries, such as optical electronics (9),

solid oxide fuels (10), and cell optical coating (11). It is widely used in applications such as gas sensors (12), optical technology (13), and microelectronics (14).

The plastic, textile, and pharmaceutical industries mainly add pollutants to the environment. These pollutants destroy or reduce the growth and production of local flora and fauna (15). Dyes released by these industries mainly cause water pollution, which reduces the penetration of sun light to water as sunlight is essential for both aquatic and land, so due to the unavailability of light, the plants are unable to synthesize their food. Dyes have diverse distinctiveness and affinities; for example, methylene blue (MB), congo red dye (CR), methyl orange (MO) dye, malachite green dye (MG), and 4-nitrophenol (4-NP) are natural dyes and pollutants. These dyes have complicated molecular structures and are non-biodegradable (16). The elimination of this pollutant from surroundings is of primary importance. Mostly NPs can be unique and best for removing such harmful substances (17).

The malachite green dye is water soluble cationic dye, green in color and crystalline powder in texture. To reduce water pollution, converting these dyes into non-hazardous forms is essential before they are released into water (18). Textile, pharmaceuticals, and leather industries use Nitro phenol (pollutant) for coloring and chemical synthesis, which pollutes the ecosystem. Nitro phenol and other chemicals move down the soil and contaminate the water. This contaminated water may cause mutation and cancer in living organisms. These cancer-causing pollutants are non-biodegradable by routine methods (19, 20).

Nanoparticles produced from plants are safe because toxic chemicals are not used compared to chemicals and physical procedures used for NPS extraction. Plants offer herbal capping marketers for NPs synthesis (21). Silver nanoparticles use diminishes after the surfacing and common use of antibiotics like insecticides and pesticides, but silver nanoparticles in combination with antibiotics are more efficacious (22). Synthesis of silver nanoparticles is low cost in terms of temperature and pressure. It is also non-toxic owing to its industry utilization plant-based AgNPs have been given unique locations in all fields of technological know-how, mainly in medical drugs inclusive for the remedy of wounds, cuts, scratches, burn up, fungal illnesses and different pores skin associated illness (23) From plant *Trianthema decandra*, gold NPs had been prepared which help in coating objects. The scientist takes more interest in manufacturing Gold Nps because gold can bind with organic molecules easily but have a high-cost value (24). M. Mohammadlou et al. synthesized magnetic iron oxide (FeO<sub>2</sub>) NPs from leaves of *Glycosmis Mauritania*. Magnetic iron oxide (FeO<sub>2</sub>) NPs are used for various purposes. Synthesis from the plant is non-toxic than physical procedure and chemicals used for its synthesis (3). The research interest of our group is to synthesize nanoparticles using plants

which is easily approachable, non-toxic, cheap, and safe. Scientists have used different plants, but *Ferula asafoetida* is not used until now, so the plant we are interested in is *Ferula asafoetida*.

## 2. EXPERIMENTAL SECTION

### 2.1. Collection of Sample

*Ferula asafoetida* is widely grown naturally in Abbot Abad (Pakistan). The plants were uprooted and Collected at their Mature Stage during March.

### 2.2. Reagents

The chemicals used for the synthesis of nanoparticles were Bi(NO<sub>3</sub>)<sub>2</sub> and Pb(NO<sub>3</sub>)<sub>3</sub>. The synthesized nanoparticles degraded the organic dye Malachite green with the chemical formula (C<sub>23</sub>H<sub>25</sub>N<sub>2</sub>Cl). All the chemicals used were of analytical Grade.

### 2.3. Instrumentation

The prepared solutions were thoroughly mixed using a magnetic stirrer (Misong Scientific c., Ito Korea). The obtained precipitates were filtered with the help of Whatman filter paper No. 1 (Millipore Corp., Bedford, Mass). The precipitate was dried in an oven (precision, ±1°C, 0.6 kW). The fully dried precipitates were placed in a muffle furnace at 200 ± 5°C (Neycraft™ JFF 2000 Furnace) for a few minutes. The samples were placed in UV light box for photocatalytic reactions using an ultra-violet light source. In order to disperse the particles the sample was centrifuged using an ultracentrifugation machine (Daihan Labtech Co. Ltd., Korea). A double beam UV-visible spectrophotometer (UV-1800 240v, Shimadzu Corporation) was used for determination of concentration and wavelength of maximum absorption. For functional group analysis IR spectra were recorded using a spectrophotometer (Perkin Elmer FT-IR spectrometer model 95120) rotary flash evaporator. The surface morphology and elemental composition were confirmed by using FE-SEM (QUANTA FEG 450) and EDX, respectively. The XRD (Bruker-D8 Advanced X-ray diffraction) was used to find out the crystallinity of the synthesized powder.

### 2.4. Preparation of Leaves Extract

Fresh leaves of *Ferula Asafoetida* were washed with doubly distilled water and dried in the shade at room temperature (22-25 °C). The dried leaves were then crushed using a commercial blender (TSK-949, west point Furnace). The aqueous solution of powder leaves (1 g/100 mL) was placed in the soxhlet apparatus for 3 hours in solvent for continuous solvent extraction. After that, the extract was filtered, and then the sample was concentrated under a vacuum in a rotary flash evaporator. The concentrated extract was air-dried, taken in an air-tight bottle, and stored for further use.

### 2.5. Synthesis of Bismuth Oxide Nanoparticles

#### 2.5.1. Bismuth oxide Nanoparticles

Bismuth oxide nanoparticles were synthesized by using the green synthesis method. A solution of 0.5 M Bi(NO<sub>3</sub>)<sub>2</sub> was prepared in 100 mL double distilled water, and then 5 mL *Ferula Asafoetida* extract was

added dropwise to the prepared solution. The solution was placed on a magnetic stirrer at a constant stirring of 1200 rpm for 10-15 minutes to homogenize. The particles were placed for 2-3 min in the preheated muffle furnace ( $200 \pm 5^\circ\text{C}$ ) for combustion, producing bismuth oxide ( $\text{Bi}_2\text{O}_3$ ) nanoparticles. In order to remove impurities, the sample was washed several times with double distilled water. Furthermore, the synthesized nanoparticles were calcinated for 2 hours to attain purity. Finally, the dried bismuth oxide nanoparticles were stored in an air-tight container for further use.

### 2.5.2. Pb-Doped bismuth Oxide Nanoparticles

To synthesize lead-doped bismuth oxide nanoparticles, 0.05M  $\text{Pb}(\text{NO}_3)_2$  was added to 0.5M  $\text{Bi}(\text{NO}_3)_3$  solution and 5 mL *Ferula asafoetida* extract. The solutions were placed on a magnetic stirrer at a constant stirring of 1200 rpm for 10-15 minutes to homogenize. The obtained particles were placed for 2-3 min in the preheated muffle furnace ( $200 \pm 5^\circ\text{C}$ ) for combustion, resulting in lead-doped bismuth oxide nanoparticles. In order to remove impurities, the sample was washed several times with double distilled water. Furthermore, the synthesized nanoparticles were calcinated for 2 hours to attain purity. Finally, lead-doped bismuth oxide nanoparticles were obtained; the particles were stored in an air-tight container for further use.

## 3. RESULTS AND DISCUSSION

### 3.1. SEM of $\text{Bi}_2\text{O}_3$ and Pb- $\text{Bi}_2\text{O}_3$ Nanoparticles

The SEM analysis of  $\text{Bi}_2\text{O}_3$  is shown in Fig. 1 (a). It is clear from the micrographs that synthesized  $\text{Bi}_2\text{O}_3$  nanoparticles are in round aggregation form. The average size of the nanoparticles calculated from the AGI method of  $\text{Bi}_2\text{O}_3$  is ~ 90-100 nm, while Pb-doped  $\text{Bi}_2\text{O}_3$  is ~ 75- 100 nm. The surface morphology is clear in the micrograph, and the aggregate of nanoparticles is uniformly distributed. While from

the surface morphology of Pb doped  $\text{Bi}_2\text{O}_3$  Fig 1 (b) the lead is small, agglomerating on  $\text{Bi}_2\text{O}_3$ .

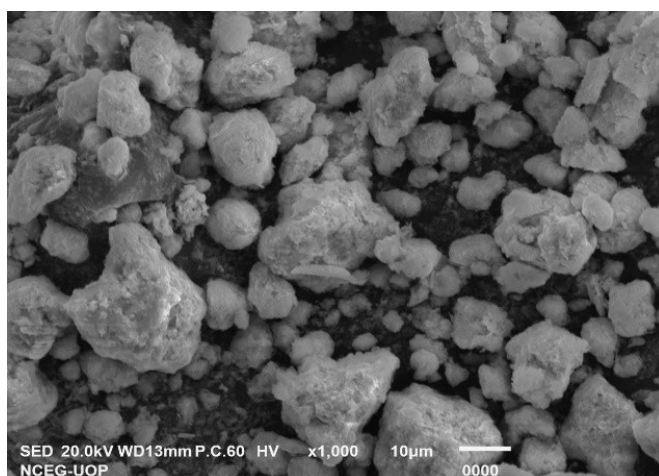
### 3.2. EDX analysis of $\text{Bi}_2\text{O}_3$ and Pb- $\text{Bi}_2\text{O}_3$

Figure 3.2 (a) and (b) display the elemental composition analysis of lead-doped  $\text{Bi}_2\text{O}_3$ , with both elements in oxide form. The mass ratios for Pb, Bi, and O were 23.55, 31.51, and 44.95, respectively, as shown in Figure 4.2(b). Meanwhile, the atomic ratios were 39.84 for Pb, 57.07 for Bi, and 3.09 for oxygen. The EDX spectra did not reveal any additional peaks, indicating the absence of impurities. In contrast, the undoped  $\text{Bi}_2\text{O}_3$ , illustrated in Figure 2 (a), had mass ratios of 13.55 for C, 16.55 for O, and 69.90 for Bi. Correspondingly, the atomic ratios were 45.19 for C, 41.42 for O, and 13.39 for Bi.

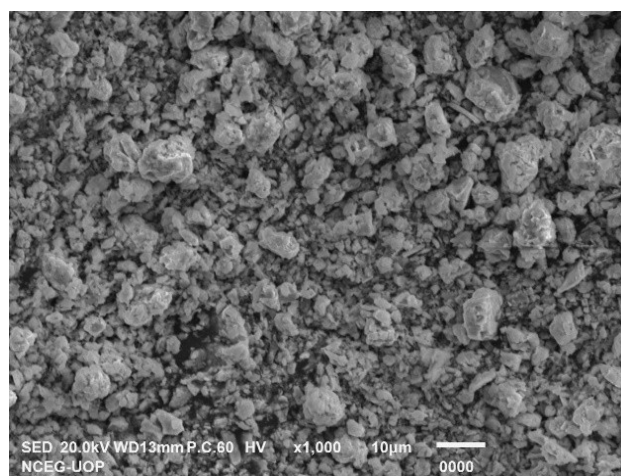
### 3.3. TGA of $\text{Bi}_2\text{O}_3$ and Pb- $\text{Bi}_2\text{O}_3$ Nanoparticles

The thermal stability of pure  $\text{Bi}_2\text{O}_3$  nanoparticles and  $\text{Bi}_2\text{O}_3$  nanoparticles doped by Pb were investigated by thermal gravimetric analysis in Figure 3. The thermograms were recorded in the nitrogen atmosphere by heating the samples from 25 to 600  $^\circ\text{C}$ . The TGA of  $\text{Bi}_2\text{O}_3$  nanoparticles was almost stable with a little weight loss over the given temperature range due to the moisture absorption and combined water. Overall weight loss of 2% is due to moisture in a temperature range of 300 to 400  $^\circ\text{C}$ .

The TGA of doped  $\text{Bi}_2\text{O}_3$  nanoparticles shows weight loss at three stages. The first stage of weight loss from 100 to 200  $^\circ\text{C}$  is attributed to the volatilization of water molecules from the nanoparticles. The second stage of weight loss from 300 to 400  $^\circ\text{C}$  is attributed to the inorganic compound Pb contains a small amount of  $\text{PbO}_2$ , which is thermally decomposed from  $\text{PbO}_2$  to  $\text{PbO}$ . The third stage of weight loss from 500 to 600  $^\circ\text{C}$  shows excellent thermal stability of Pb nanoparticles (25). This shows the high thermal stability of doped  $\text{Bi}_2\text{O}_3$  nanoparticles. The overall stability of  $\text{Bi}_2\text{O}_3$  is higher than the doped  $\text{Bi}_2\text{O}_3$  at 600  $^\circ\text{C}$ . The total weight loss in pure  $\text{Bi}_2\text{O}_3$  is less than that of doped  $\text{Bi}_2\text{O}_3$  (26).



(a)



(b)

**Figure 1:** SEM image for (a)  $\text{Bi}_2\text{O}_3$  Nanoparticles (b) Pb- $\text{Bi}_2\text{O}_3$  nanoparticles.

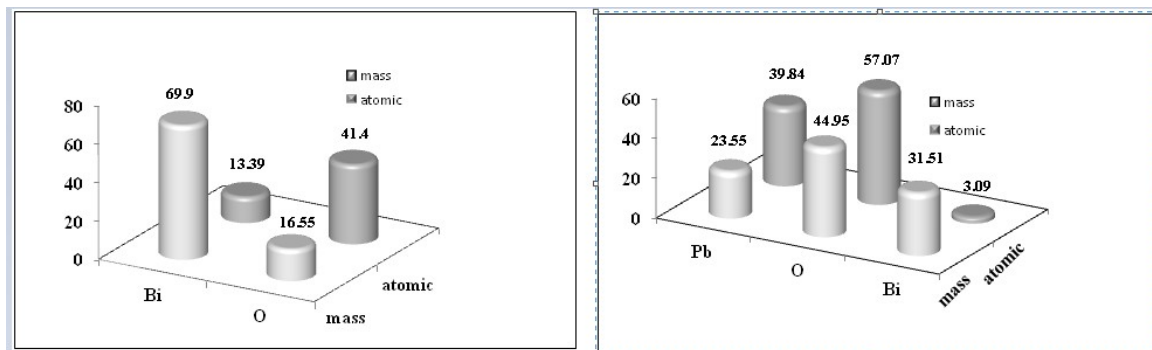


**Figure 2:** EDX analysis of (a) Bi<sub>2</sub>O<sub>3</sub> (b) Pb-Bi<sub>2</sub>O<sub>3</sub> Nanoparticles.

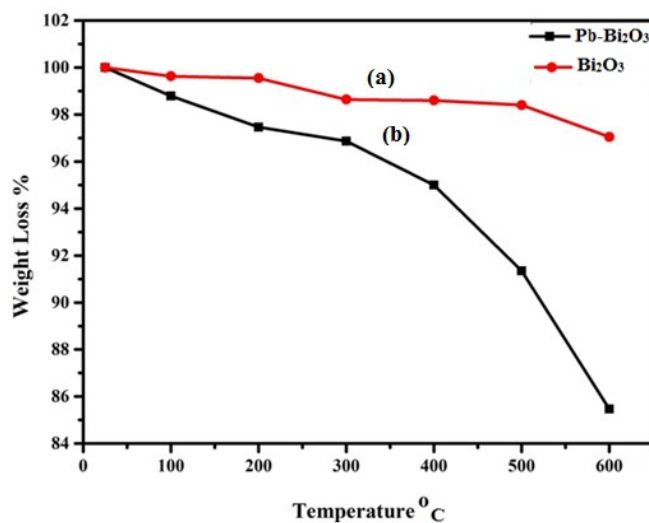


**Figure 3:** TGA of (a) Bi<sub>2</sub>O<sub>3</sub> and (b) Pb-Bi<sub>2</sub>O<sub>3</sub> nanoparticles.

### 3.4. FT-IR of Bi<sub>2</sub>O<sub>3</sub> and Pb-Bi<sub>2</sub>O<sub>3</sub>

FT-IR spectra help study functional groups in a compound, their molecular interaction, and their molecular geometry. Figure 4 (a) shows the FTIR spectra of the calcined Bi<sub>2</sub>O<sub>3</sub> and Pb-Bi<sub>2</sub>O<sub>3</sub> nanoparticles. Generally, the band frequencies within 1000 cm<sup>-1</sup> must be accredited to the bond stretching of metal oxides (27). The spectrum in Figure 4(a) at 3351.07 cm<sup>-1</sup> is because of hydroxyl bond attraction in the water. The absorption

spectrum obtained 1600- 1000 cm<sup>-1</sup> is due to the occurrence of organic residue from the plant leaf extract. The peaks lower than 1000 cm<sup>-1</sup> showed the presence of nanoparticles (28). Figure 4 (b) shows the absorption spectrum 675.49 cm<sup>-1</sup> due to the stretching frequency of the Bi-O bond, and for Pb-Bi<sub>2</sub>O<sub>3</sub> is 465.33 cm<sup>-1</sup> because of Pb-O stretching (29). The result shows that Pb successfully merged in Bi<sub>2</sub>O<sub>3</sub> crystal.



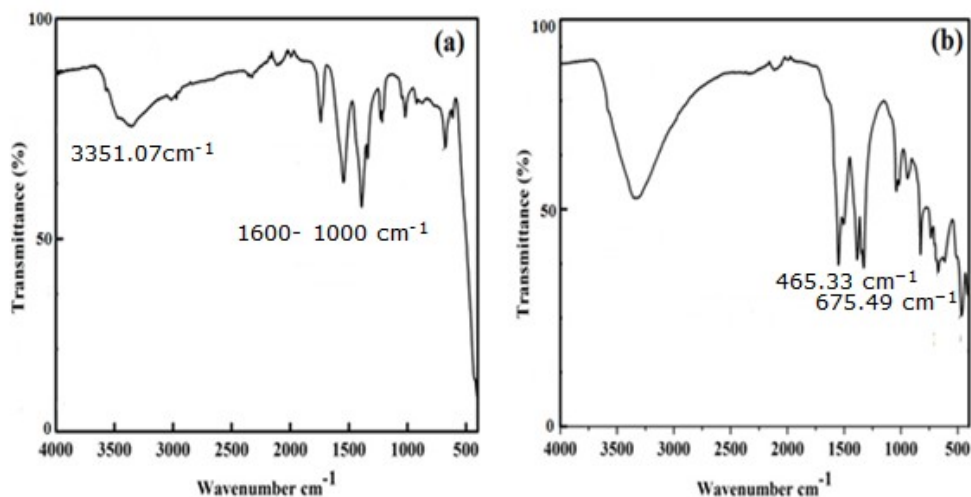


Figure 4: FTIR spectrum of (a)  $\text{Bi}_2\text{O}_3$  and (b)  $\text{Pb-Bi}_2\text{O}_3$  Nanoparticles.

### 3.5. XRD of $\text{Bi}_2\text{O}_3$ and $\text{Pb-Bi}_2\text{O}_3$ Nanoparticles

XRD is the most effective tool for describing the structure and nature of a material. An analytical technique mainly used to identify the crystalline nature of the material. In this technique, an X-ray is bombarded on the crystal. The crystalline properties and purity of the green synthesized  $\text{Bi}_2\text{O}_3$  NPs were analyzed by X-ray diffraction data collected in the  $2\theta$  range. Fig. 5 (a) shows the XRD spectrum of  $\text{Bi}_2\text{O}_3$ . XRD diffraction of  $\text{Bi}_2\text{O}_3$  nanoparticles gives a strong and sharp peak at  $32.8^\circ$ , which confirms the crystalline nature of  $\text{Bi}_2\text{O}_3$ . The  $\text{Bi}_2\text{O}_3$  nanoparticles exhibited peaks at  $23.9^\circ$ ,  $29.2^\circ$ ,  $30.3^\circ$ ,  $32.0^\circ$ ,  $47.09^\circ$ ,  $56.8^\circ$ ,  $42.3^\circ$ . Figure 5 (b) sharp peak at  $2\theta = 28.8^\circ$  and  $32.7^\circ$  was observed for  $\text{Pb-Bi}_2\text{O}_3$ . JCPDS-card no -36-034 for  $\text{Bi}_2\text{O}_3$  and  $\text{pb-Bi}_2\text{O}_3$  JCPDS card no 3-0591. The Debye-Scherrer (Equation 1) was used

to calculate the average crystallite size of  $\text{Bi}_2\text{O}_3$  nanoparticles.

$$D = \frac{k\lambda}{\beta \cos \theta} \quad (\text{Eq. 1})$$

The average crystallite size is denoted by  $D$ , where  $k$  is the dimensionless shape factor with a value of 0.9 close to unity; it varies depending upon the crystallite's shape  $\lambda$  is the wavelength of the X-ray used, and  $\beta$  is the angle of diffraction at full width at half maximum. The crystallite size of  $\text{Bi}_2\text{O}_3$  nanoparticles is 13.433 nm. The crystallite size of  $\text{Pb-Bi}_2\text{O}_3$  nanoparticles is 9.6 nm Figure 5 (a) shows that X-ray diffraction peaks of  $\text{Bi}_2\text{O}_3$  nanoparticles exhibited reflection peaks at  $32.8^\circ$  of glancing angle. The sharp crystalline peak shows that the nanoparticles are crystalline in structure (30).

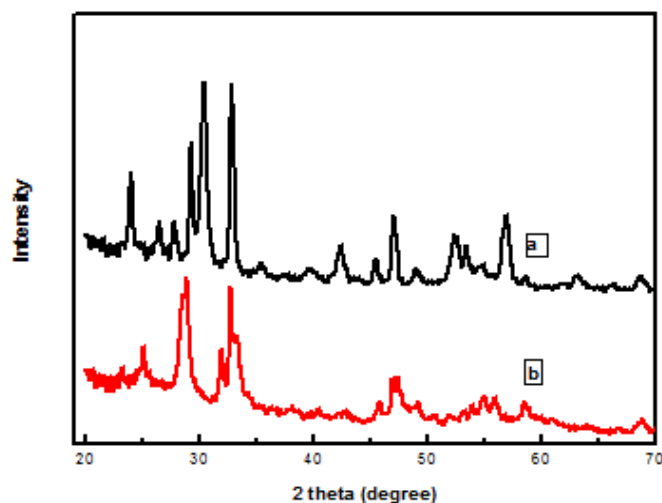


Figure 5: XRD patterns of (a)  $\text{Bi}_2\text{O}_3$  (b)  $\text{Pb-Bi}_2\text{O}_3$  Nanoparticles.

### 3.6. Photocatalytic Activity of Bismuth Oxide Nanoparticles

The photocatalytic activity of bismuth oxide and lead-doped bismuth oxide was studied under UV light to degrade malachite green dye. The effect of various parameters such as catalyst dose, irradiation time, initial dye concentration, pH, and temperature was observed.

### 3.7. Effect of Irradiation Time

UV light plays a primary role in the photodegradation of malachite green dye. The result showing irradiation time on photodegradation is deliberate, keeping other parameters steady at catalyst

quantity 0.01 g, pH 4, time interval 120 minutes, and dye initial concentration 50 ppm, as shown in Figure 6(a). Irradiation time increases by increasing the degradation activity of bismuth oxide nanoparticles. This may be related to the amount of photo-generated electron-hole pair produced due to the sensitization of photocatalyst nanoparticles (31). Under UV light, dye degradation at different time phases is studied. Figure 6(a) depicts a lead-doped bismuth oxide that shows maximum degradation of 98%. The undoped bismuth oxide showed 91% degradation efficiency under a similar experimental condition, as shown in Figure 6(b).

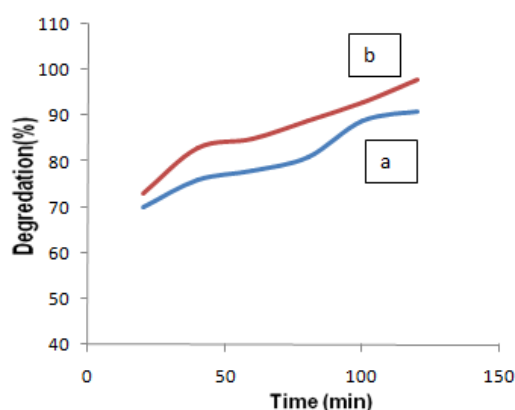


**Figure 6a:** Effect of irradiation time on photocatalytic degradation of MG dye by (a) lead-doped bismuth oxide ( $\text{Bi}_2\text{O}_3$ ), (b) undoped bismuth oxide at catalyst amount of 0.01 g, pH 4, dye initial concentration of 50 ppm, irradiation time 120 minutes.

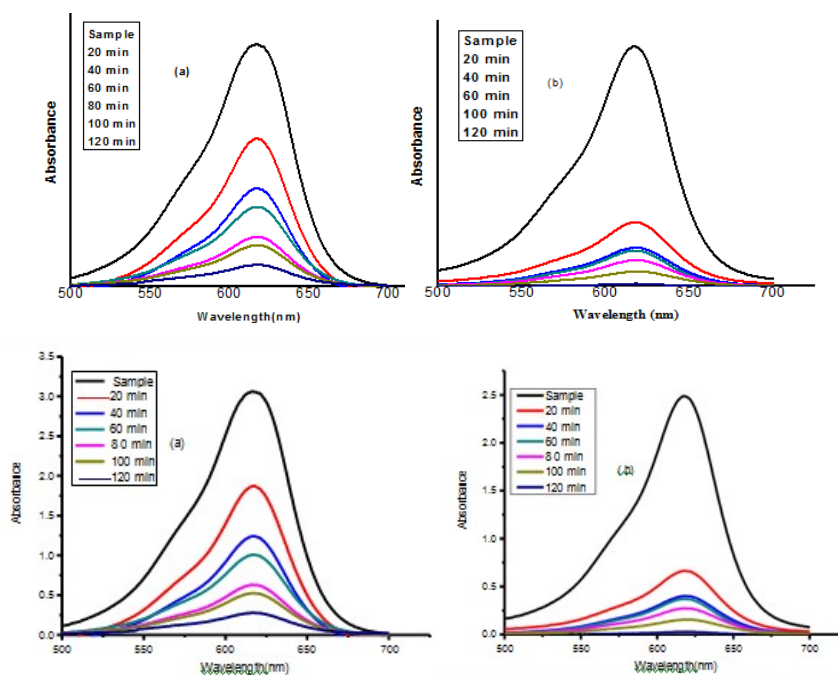


**Figure 6b:** Absorption spectra showing the effect of irradiation time on photocatalytic degradation of Malachite green dye (a) doped and (b) undoped bismuth oxide.

### 3.8. Effect of Dye Concentration

The effect of dye initial concentration on the photodegradation of dye is studied while keeping constant other parameters such as catalyst amount (0.01 g), pH (4), and time interval (120 minutes). It was studied that when the dye's initial concentration increases, then photodegradation decreases; it may be outstanding to the fact that light penetration to nanoparticles surface decreases when dye

concentration is increased (9). More dye molecules will attach in active sites, extensively changing the photodegradation process. It was studied that at little concentration of 50 ppm maximum degradation of 98% for lead-doped bismuth oxide ( $\text{Bi}_2\text{O}_3$ ), as shown in Figure 7(a), and 91% for undoped bismuth oxide ( $\text{Bi}_2\text{O}_3$ ) was observed as depicted in Figure 7(b).

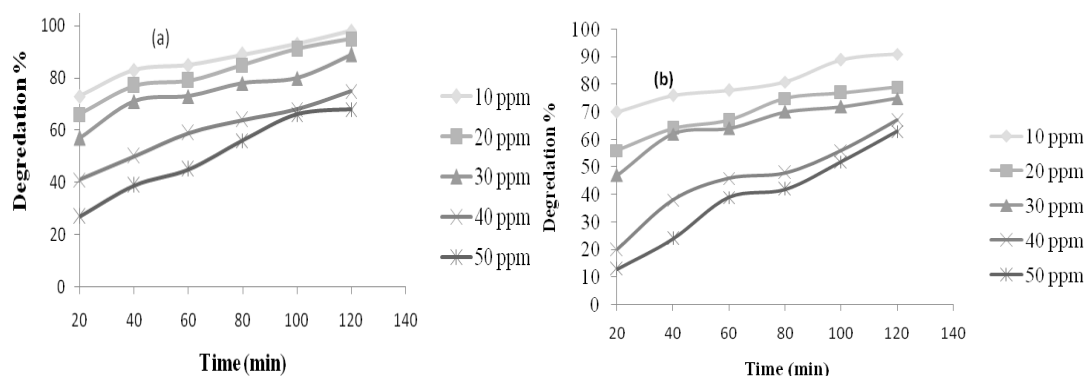


**Figure 7:** Effect of dye initial concentration on photocatalytic degradation of Malachite green dye by (a) lead-doped bismuth oxide (b) undoped bismuth oxide, at catalyst amount 0.01 g, initial dye pH 4.

### 3.9. Effect of Catalyst

The influence of varying catalyst amounts on the photodegradation of the dye was examined using different quantities of catalyst (10 mg, 15 mg, 20 mg, 25 mg, and 30 mg), with a constant radiation time of 120 minutes, an initial dye concentration of 50 ppm, and a pH level of 4. It was observed that the initial degradation rate increased with the addition of more catalysts but subsequently decreased. The reaction rate initially grew with the

addition of more catalysts, reaching an optimal level, after which the nanoparticles began to act as a filter for the incident light, limiting the light intensity from reaching the semiconductor surface (10). The maximum degradation achieved was 82% for lead-doped catalyst, as shown in Figure 8(a), and 79% for undoped bismuth oxide nanoparticles, at an optimal catalyst amount of 20 mg, as illustrated in Figure 8(b).

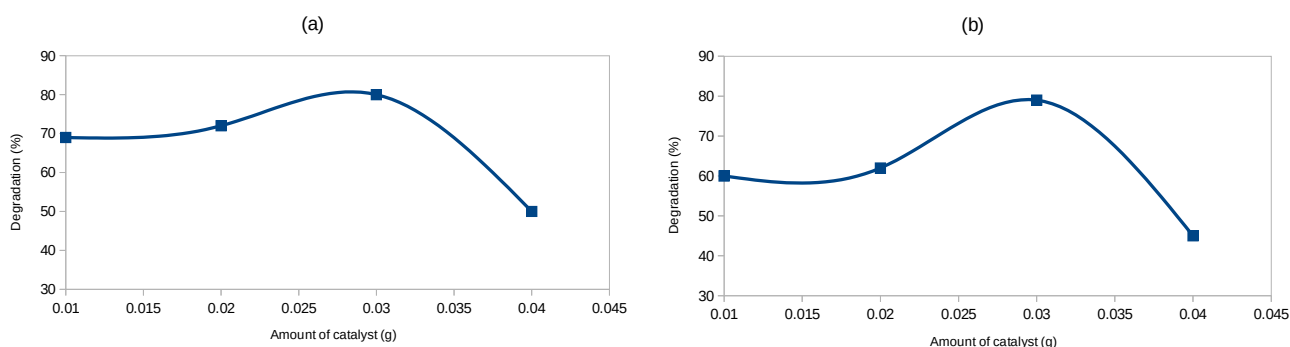


**Figure 8:** Effect of catalyst dose on photocatalytic degradation of MG dye by (a) lead-doped bismuth oxide, (b) undoped bismuth oxide, at catalyst amount 0.01 g, pH 4, and dye initial concentration 50 ppm and time interval 120 minutes.

### 3.10. Effect of pH

The effect of pH on the photodegradation of dye was studied at various pH (4, 5, 10, and 11) at a constant radiation time of 120 minutes with a dye concentration of 50 ppm initial and a catalyst quantity of 10 mg. It was observed that the rate of

degradation increases as pH increases (32). The maximum degradation efficiencies of 79% for lead-doped bismuth oxide in Figure 9(a), while 75% for undoped bismuth oxide was obtained as shown in Figure 9(b).

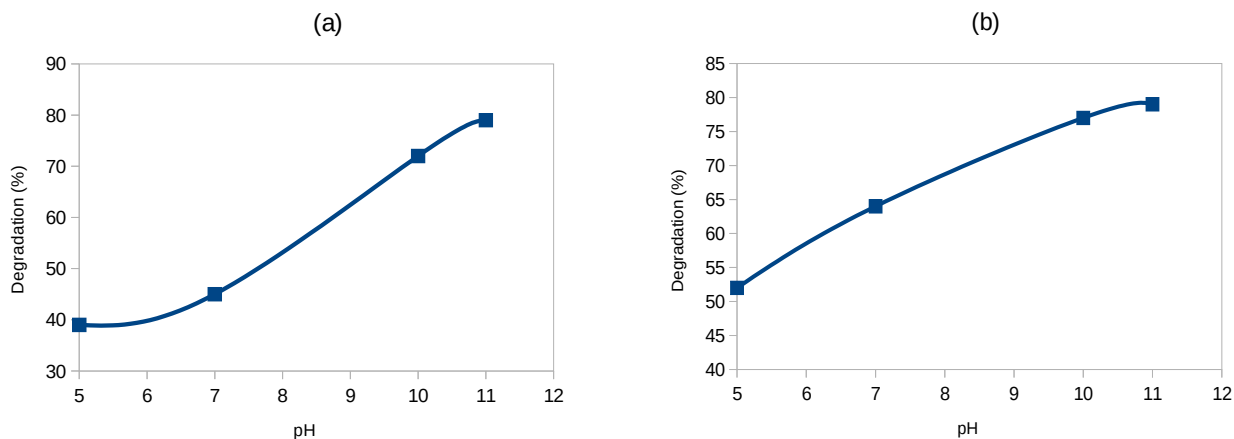


**Figure 9(a, b):** Effect of pH on the photocatalytic degradation of MG dye by (a) lead-doped bismuth oxide (Bi<sub>2</sub>O<sub>3</sub>) (b) undoped bismuth oxide, at Catalyst amount 0.01 g, dye initial concentration 50 ppm, and irradiation time 120 minutes.

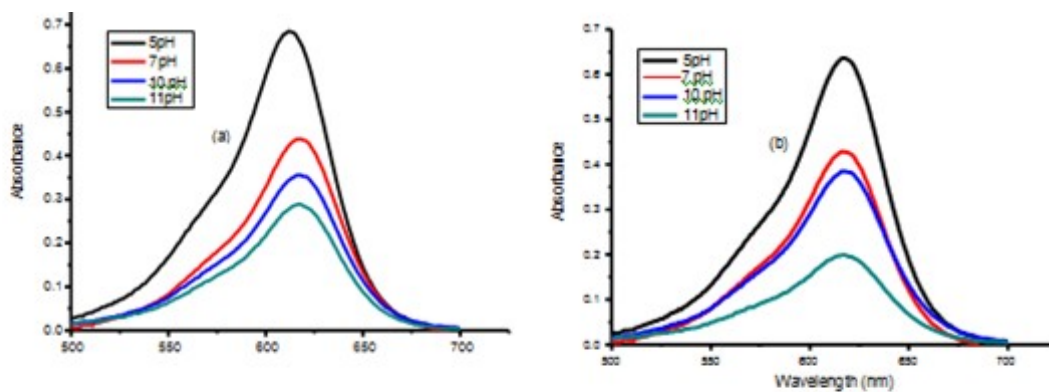


**Figure 9c:** Absorption spectra effect of pH on the photocatalytic degradation of malachite green dye (a) doped (b) undoped bismuth oxide (Bi<sub>2</sub>O<sub>3</sub>).

### 3.11. Effect of Temperature

In the photodegradation of dye, temperature plays a significant role. At different temperatures (30, 40, and 50 °C), the dye degradation was studied, keeping the other parameters steady, i.e., irradiation time 120 minutes, 50 ppm initial dye concen-

tration, and catalyst amount of 10 mg. It was experimentally observed that with the temperature increase, dye degradation increased, and the utmost degradation of 92% for lead-doped bismuth oxide in Figure 10(a) and 76% for undoped bismuth oxide was achieved in Figure 10(b).

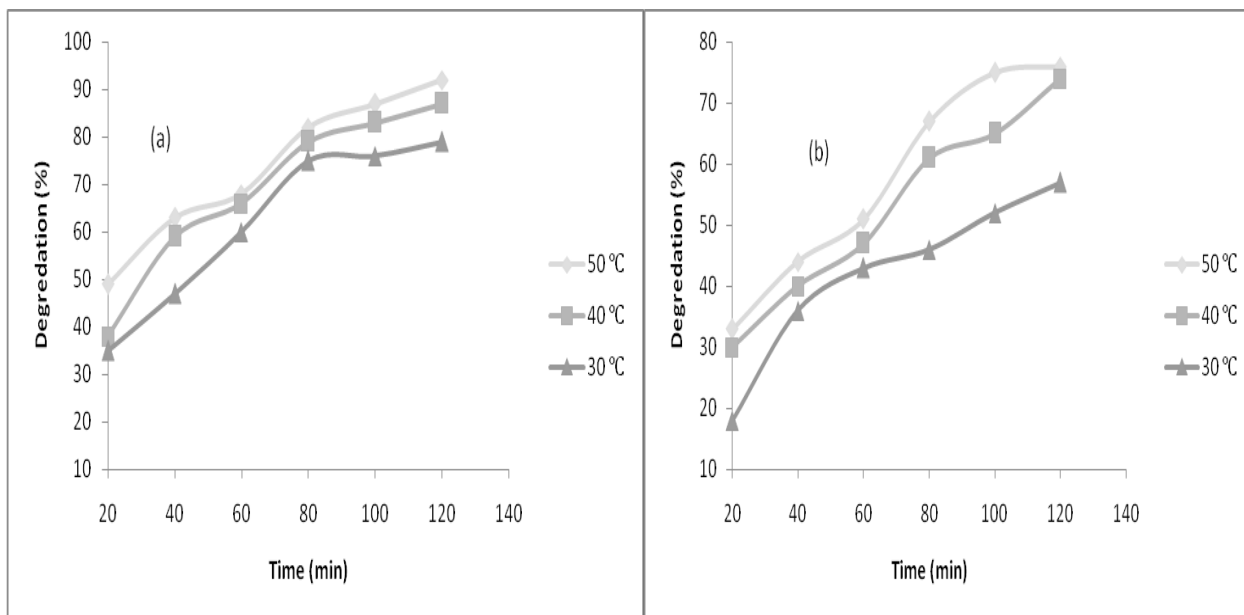


**Figure 10(a, b):** Effect of temperature on photocatalytic degradation of Malachite green dye by (a) lead-doped bismuth oxide (b) undoped bismuth oxide, catalyst amount 0.01 g, pH 4, time initial concentration 50 ppm and time interval 120 minutes.

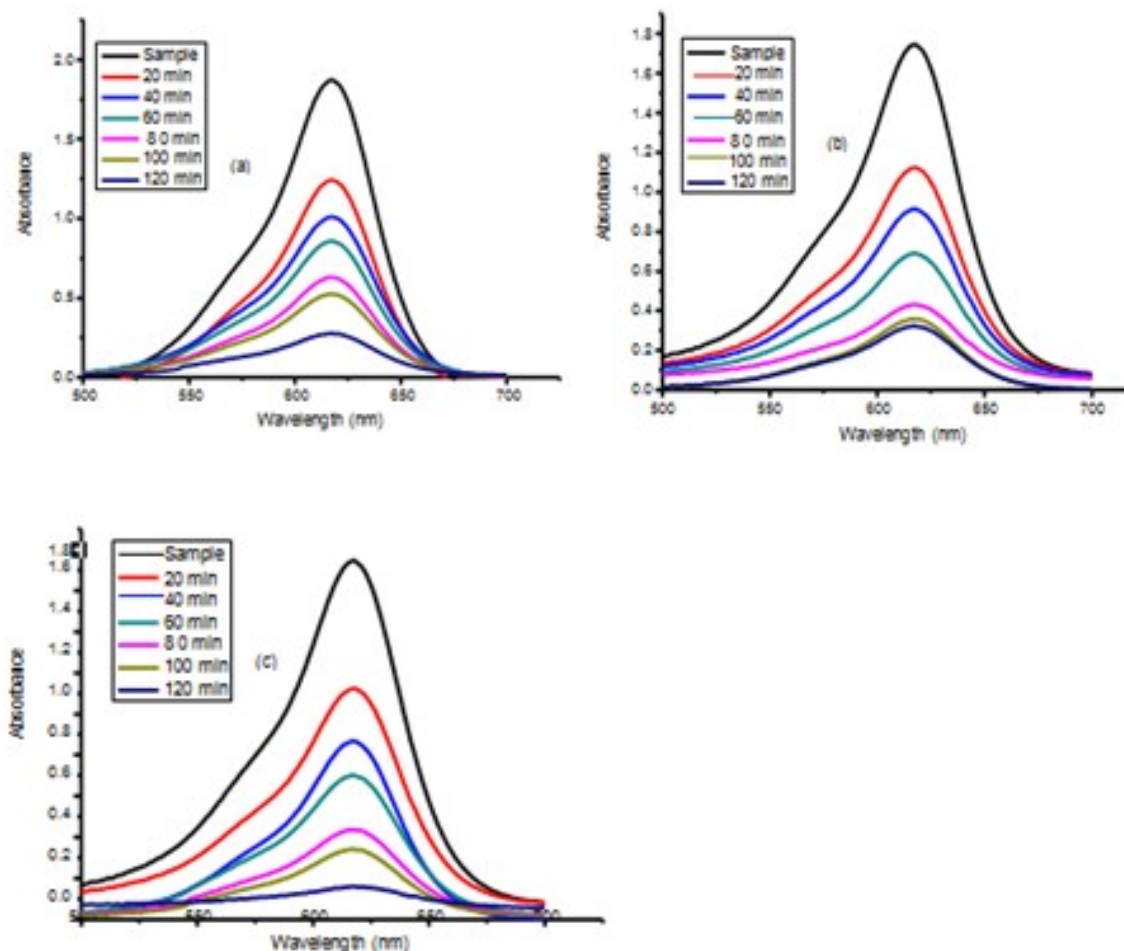


**Figure 10c:** Absorption spectra showing effect of irradiation time at constant (60 °C) on the photocatalytic degradation of MG dye (a) (b) (c) for lead-doped bismuth oxide.

### 3.12. Kinetic Study of Nanoparticles

The Kinetic study of degradation of MG at different temperatures (30 °C, 40°C, 50 °C) by using different concentrations (10 ppm, 20 ppm, 30 ppm, 40 ppm, 50 ppm) of doped  $\text{Bi}_2\text{O}_3$  and undoped  $\text{Bi}_2\text{O}_3$  as a catalyst. The  $k$  values linearization was used to calculate the temperature parameters of doped  $\text{Bi}_2\text{O}_3$  and undoped  $\text{Bi}_2\text{O}_3$ . Table 1 presents the values of  $R^2$ , extracted from the linearization of the rate constants ( $k$ ) by  $\text{Bi}_2\text{O}_3$ . With increasing the concentration of catalyst, the rate of degradation decreases. However, the same trend was observed for temperature parameters. The photodegradation of the samples was evaluated at a different temperature by applying the following equations (Eq. 2 and 3).

$$\frac{dc}{dt} = k_{App} \times C \quad (\text{Eq. 2})$$

where  $k_{App}$  is called the pseudo-first-order rate constant.

The integrated form of the above equation is

$$\ln\left(\frac{C_0}{C}\right) = k_{App} \times t \quad (\text{Eq. 3})$$

$C_0$  and  $C$  represent the initial and final concentration of MG dye, respectively.

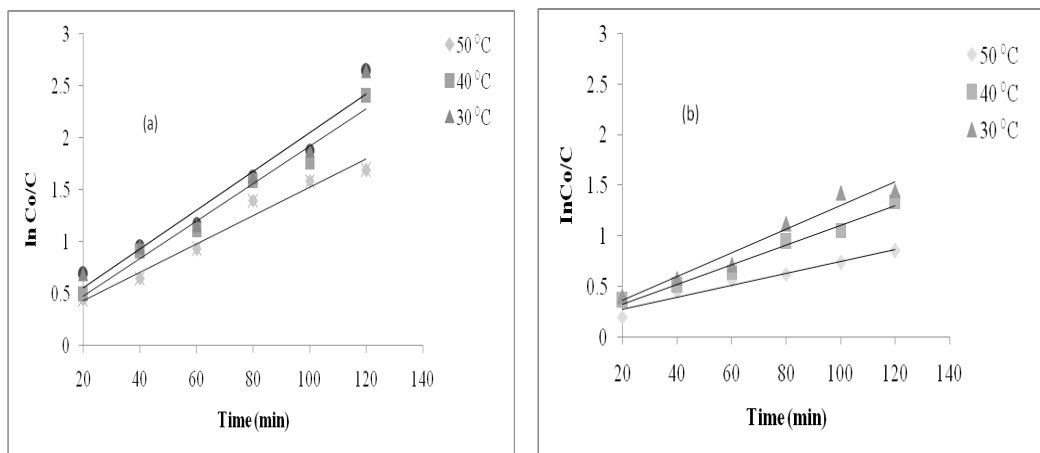
Figure 11(a) and 11(b) show the kinetic study of MG dye. It can be observed that the rate of photocatalytic reaction is significantly affected by the catalyst dose. The  $k_{App}$  and their correlation coefficient values for undoped and Pb-doped  $\text{Bi}_2\text{O}_3$  are given in Tables 1 and 2.

**Table 1:** Parameter of pseudo-first-order kinetics equation of different temperatures using Pb - $\text{Bi}_2\text{O}_3$ .

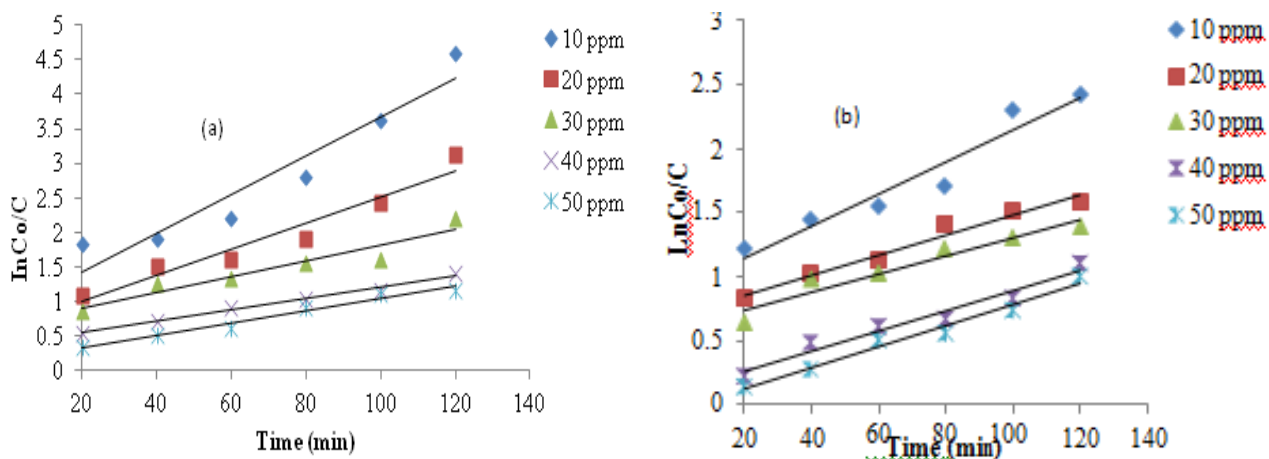
Temp (°C)	Equation	R <sup>2</sup>	kA <sub>pp</sub>
30	y = 0.0136x + 0.1619	R <sup>2</sup> = 0.9679	0.0136
40	y = 0.0186x + 0.186	R <sup>2</sup> = 0.954	0.0186
50	y = 0.018x + 0.1134	R <sup>2</sup> = 0.9778	0.018

**Table 2:** Parameter of pseudo first order kinetics equation of different temperatures using undoped Bi<sub>2</sub>O<sub>3</sub>.

Temp (°C)	Equation	R <sup>2</sup>	kA <sub>pp</sub>
30	y = 0.0117x + 0.1335	R <sup>2</sup> = 0.9586	0.0117
40	y = 0.0098x + 0.1276	R <sup>2</sup> = 0.9824	0.0098
50	y = 0.006x + 0.1531	R <sup>2</sup> = 0.9558	0.006



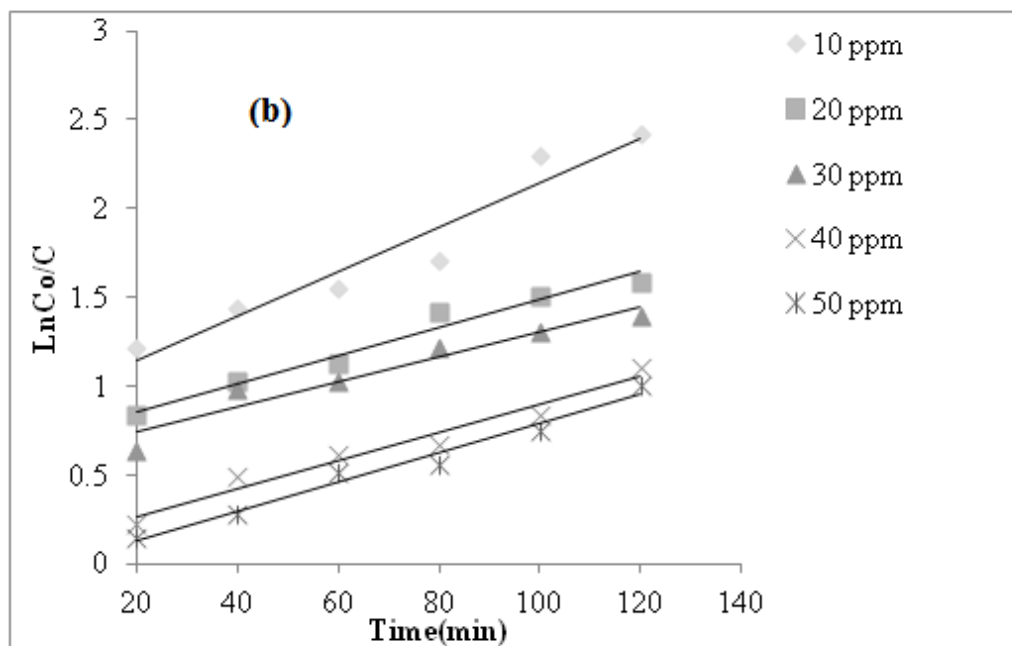
**Figure 11:** Showing the application of pseudo 1<sup>st</sup> orders kinetic to photodegradation of dye on (a) Pb -Bi<sub>2</sub>O<sub>3</sub> (b) undoped Bi<sub>2</sub>O<sub>3</sub> at different temperatures.



**Figure 11c:** Application of pseudo first order kinetic to photodegradation of dye on (a) Pb -Bi<sub>2</sub>O<sub>3</sub> (b) undoped Bi<sub>2</sub>O<sub>3</sub> at different concentrations.

**Table 3:** Parameter of first-order kinetics equation of different concentrations using undoped  $\text{Bi}_2\text{O}_3$ .

Conc. (mg/L)	Equation	$R^2$	$kA_{pp}$
10	$y = 0.0125x + 0.897$	$R^2 = 0.9348$	0.0125
20	$y = 0.0078x + 0.6997$	$R^2 = 0.9656$	0.0078
30	$y = 0.007x + 0.6016$	$R^2 = 0.927$	0.007
40	$y = 0.0079x + 0.1069$	$R^2 = 0.9604$	0.0079
50	$y = 0.0082x - 0.0359$	$R^2 = 0.9753$	0.0082

**Figure 11(d):** Application of pseudo first order kinetic to photodegradation of dye on  $\text{Pb-Bi}_2\text{O}_3$  at different concentrations.**Table 4:** Parameter of first-order kinetics equation of different concentrations using  $\text{Pb-Bi}_2\text{O}_3$ .

Conc.(mg/L)	Equation	$R^2$	$kA_{pp}$
10	$y = 0.0279x + 0.8719$	$R^2 = 0.9141$	0.0279
20	$y = 0.019x + 0.6111$	$R^2 = 0.9405$	0.019
30	$y = 0.0115x + 0.6653$	$R^2 = 0.9027$	0.0115
40	$y = 0.0084x + 0.3716$	$R^2 = 0.9873$	0.0084
50	$y = 0.0089x + 0.1458$	$R^2 = 0.9723$	0.0089

### 3.13. Arrhenius Equation

The effect of temperature was studied at 50 ppm dye concentration, irradiation time 120 min with catalyst amount 10 mg. A linear relation was found

between  $\ln k$  and  $1/T$  with a negative slope for doped  $\text{Bi}_2\text{O}_3$  and undoped  $\text{Bi}_2\text{O}_3$  nanoparticles, as shown in Figure 12(a, b).



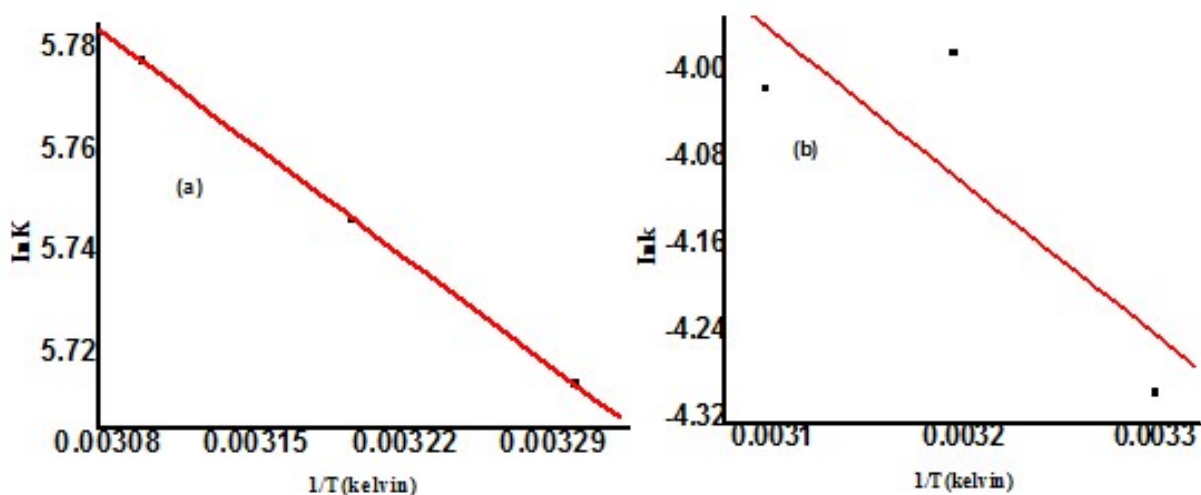


**Figure 12:** Arrhenius plot  $\ln k$  vs.  $1/T$  (a) doped (b) undoped  $\text{Bi}_2\text{O}_3$ .

#### 4. CONCLUSION

Many processes have been used for water purification, but out of all these various processes employed, a major improvement of the photocatalytic activity was observed in the system using a combination of oxidant and photocatalyst irradiation under ultraviolet light. The concentration of both the oxidant and the photocatalyst greatly influenced the degradation rate. Also, the process was observed to be strongly pH dependent. Photodegradation could be an advocate approach for managing wastewater containing MG dye as a pollutant. The study found that the degradation process depends on various parameters like temperature, pH, dye concentration, amount of catalyst, and contact time; by changing any of the above parameters, the extent of degradation changed. The optimum conditions for degradation of Malachite Green dye by bismuth oxide catalyst were pH 4, catalyst amount 0.03 g dye initial concentration 50 ppm, contact time 120 minutes, and temperature 30 °C. The techniques such as SEM, FTIR, XRD, and TGA analysis indicated satisfactory formation of NPs. The bismuth oxide nanoparticles have an average size of 90 nm, and lead-doped bismuth oxide is 75 nm, showed by SEM analysis. The FTIR spectrum shows the occurrence of alcoholic compounds and metal oxide in the *Ferula Asafoetida* leaves extract. However, the TGA of undoped  $\text{Bi}_2\text{O}_3$  nanoparticles was almost stable with a little weight loss (2%). The total weight loss in pure  $\text{Bi}_2\text{O}_3$  was less than the doped  $\text{Bi}_2\text{O}_3$ . XRD diffraction of  $\text{Bi}_2\text{O}_3$  nanoparticles reflected a strong and sharp peak at 32.8°, showing that  $\text{Bi}_2\text{O}_3$  nanoparticles are in the crystalline phase. The crystallite size of  $\text{Bi}_2\text{O}_3$  nanoparticles is 13.433 nm, and Pb-doped  $\text{Bi}_2\text{O}_3$  is 9.6 nm, calculated from the Debye-Scherrer equation.

#### 5. REFERENCES

1. Heera P, Shanmugam S. Nanoparticle characterization and application: an overview. *Int J Curr Microbiol App Sci*. 2015;4(8):379-86.
2. Hani Ramli R, Soon CF, Mohd Rus AZ. Characterisation of silver nanoparticles produced by three different methods based on Borohydride reducing agent. Sharif S, Abdullah MMAB, Abd Rahim SZ, Ghazali MF, Mat Saad N, Ramli MM, et al., editors. *MATEC Web Conf*. 2016;78:01032. Available from: [<URL>](#).
3. Mohammadlou M, Maghsoudi H, Jafarizadeh-Malmiri H. A review on green silver nanoparticles based on plants: Synthesis, potential applications and eco-friendly approach. *International Food Research Journal*. 2016;23(2):446.
4. Miri A, Sadat Shakib E, Ebrahimi O, Sharifi-Rad J. Impacts of Nickel Nanoparticles on Growth Characteristics, Photosynthetic Pigment Content and Antioxidant Activity of *Coriander sativum* L. *Orient J Chem*. 2017 Jun 28;33(3):1297-303. Available from: [<URL>](#).
5. Duman F, Ocsoy I, Kup FO. Chamomile flower extract-directed CuO nanoparticle formation for its antioxidant and DNA cleavage properties. *Materials Science and Engineering: C*. 2016 Mar;60:333-8. Available from: [<URL>](#).

6. Geethalakshmi R, Sarada DVL. Characterization and antimicrobial activity of gold and silver nanoparticles synthesized using saponin isolated from *Trianthema decandra* L. *Industrial Crops and Products*. 2013 Nov;51:107-15. Available from: [<URL>](#).
7. Firdhouse MJ, Lalitha P, Sripathi SK, others. Novel synthesis of silver nanoparticles using leaf ethanol extract of *Pisonia grandis* (R. Br). *Der Pharma Chemica*. 2012;4(6):2320-6.
8. Gangula A, Podila R, M R, Karanam L, Janardhana C, Rao AM. Catalytic Reduction of 4-Nitrophenol using Biogenic Gold and Silver Nanoparticles Derived from *Breynia rhamnoides*. *Langmuir*. 2011 Dec 20;27(24):15268-74. Available from: [<URL>](#).
9. Raza W, Haque MM, Muneer M, Harada T, Matsumura M. Synthesis, characterization and photocatalytic performance of visible light induced bismuth oxide nanoparticle. *Journal of Alloys and Compounds*. 2015 Nov;648:641-50. Available from: [<URL>](#).
10. Falagas ME, Fragoulis KN, Karydis I. A Comparative Study on the Cost of New Antibiotics and Drugs of Other Therapeutic Categories. Baune B, editor. *PLoS ONE*. 2006 Dec 20;1(1):e11. Available from: [<URL>](#).
11. Camilleri J. Color Stability of White Mineral Trioxide Aggregate in Contact with Hypochlorite Solution. *Journal of Endodontics*. 2014 Mar;40(3):436-40. Available from: [<URL>](#).
12. Marchaim D, Lemanek L, Bheemreddy S, Kaye KS, Sobel JD. Fluconazole-Resistant *Candida albicans* Vulvovaginitis: *Obstetrics & Gynecology*. 2012 Dec;120(6):1407-14. Available from: [<URL>](#).
13. Figueroa-Quintanilla D, Salazar-Lindo E, Sack RB, Leon-Barua R, Sarabia-Arce S, Campos-Sanchez M, et al. A Controlled Trial of Bismuth Subsalicylate in Infants with Acute Watery Diarrheal Disease. *N Engl J Med*. 1993 Jun 10;328(23):1653-8. Available from: [<URL>](#).
14. Khodashenas B, Ghorbani HR. Synthesis of silver nanoparticles with different shapes. *Arabian Journal of Chemistry*. 2019 Dec;12(8):1823-38. Available from: [<URL>](#).
15. Yasin S, Liu L, Yao J. Biosynthesis of silver nanoparticles by bamboo leaves extract and their antimicrobial activity. *J Fiber Bioeng Inform*. 2013;6(6):77-84.
16. Princy KF, Gopinath A. Spectroscopic Investigation on the Catalytic Efficacy of Biofabricated Gold Nanoparticles using Marine Macroalgae. *Materials Today: Proceedings*. 2019;9:38-45. Available from: [<URL>](#).
17. Lee HJ, Kim JH, Park SS, Hong SS, Lee GD. Degradation kinetics for photocatalytic reaction of methyl orange over Al-doped ZnO nanoparticles. *Journal of Industrial and Engineering Chemistry*. 2015 May;25:199-206. Available from: [<URL>](#).
18. Goel M, Das A, Ravikumar K, Asthana A. A study on the enhancement of sonochemical degradation of eosin B using other advanced oxidation processes. *Desalination and Water Treatment*. 2014;52(34-36):6770-6. Available from: [<URL>](#).
19. Peng F, Cai L, Yu H, Wang H, Yang J. Synthesis and characterization of substitutional and interstitial nitrogen-doped titanium dioxides with visible light photocatalytic activity. *Journal of Solid State Chemistry*. 2008 Jan;181(1):130-6. Available from: [<URL>](#).
20. Tetenbaum M, Hash M, Tani BS, Luo JS, Maroni VA. Oxygen stoichiometry, phase stability, and thermodynamic behavior of the lead-doped Bi-2223 and Ag/Bi-2223 systems. *Physica C: Superconductivity*. 1995 Jul;249(3-4):396-402. Available from: [<URL>](#).
21. Al-Shamali SS. Photocatalytic degradation of methylene blue in the presence of TiO<sub>2</sub> catalyst assisted solar radiation. *Australian Journal of Basic and Applied Sciences*. 2013;7(4):172-6.
22. Omrani AA, Taghavinia N. Photo-induced growth of silver nanoparticles using UV sensitivity of

- cellulose fibers. *Applied Surface Science*. 2012 Jan;258(7):2373-7. Available from: [<URL>](#).
23. Patil CD, Borase HP, Patil SV, Salunkhe RB, Salunke BK. Larvicidal activity of silver nanoparticles synthesized using *Pergularia daemia* plant latex against *Aedes aegypti* and *Anopheles stephensi* and nontarget fish *Poecillia reticulata*. *Parasitol Res*. 2012 Aug;111(2):555-62. Available from: [<URL>](#).
24. Sylvestre JP, Kabashin AV, Sacher E, Meunier M, Luong JHT. Stabilization and Size Control of Gold Nanoparticles during Laser Ablation in Aqueous Cyclodextrins. *J Am Chem Soc*. 2004 Jun 1;126(23):7176-7. Available from: [<URL>](#).
25. Al-Shamali SS. Photocatalytic degradation of methylene blue in the presence of TiO<sub>2</sub> catalyst assisted solar radiation. *Australian Journal of Basic and Applied Sciences*. 2013;7(4):172-6.
26. Bhuiyan MSH, Miah MY, Paul SC, Aka TD, Saha O, Rahaman MM, et al. Green synthesis of iron oxide nanoparticle using *Carica papaya* leaf extract: application for photocatalytic degradation of remazol yellow RR dye and antibacterial activity. *Heliyon*. 2020;6(8). Available from: [<URL>](#).
27. Alem AF, Worku AK, Ayele DW, Wubieneh TA, Teshager AA, Tadele Mihret Kndie, et al. Ag doped Co<sub>3</sub>O<sub>4</sub> nanoparticles for high-performance supercapacitor application. *Heliyon*. 2023 Feb;9(2):e13286. Available from: [<URL>](#).
28. ElBatal FH, Marzouk MA, ElBatal HA, EzzElDin FM. Impact effect of gamma irradiation on the optical, FTIR, ESR spectral properties and thermal behavior of some mixed (PbO + Bi<sub>2</sub>O<sub>3</sub>) borate glasses searching for shielding effects. *Journal of Molecular Structure*. 2022 Nov;1267:133602. Available from: [<URL>](#).
29. Wahlbeck PG, Myers DL, Salazar KV. Bismuth activities in a lead-doped bismut-2223 superconductor. *Physica C: Superconductivity*. 1995 Oct;252(1-2):147-54. Available from: [<URL>](#).
30. Lu CH, Chen YC. Characterization of lead cation-incorporated strontium bismuth tantalate ferroelectrics. *Integrated Ferroelectrics*. 2000;31(1-4):129-38.
31. Koli Prashant B, Kapadnis Kailas H. Green synthesis and characterization of SnO<sub>2</sub> and ZnO nanoparticles: Study their electrical conductivity and gas sensing properties. *Der ChemicaSinica*. 2016;7(2):29-35.
32. Li R, Chen W, Kobayashi H, Ma C. Platinum-nanoparticle-loaded bismuth oxide: an efficient plasmonic photocatalyst active under visible light. *Green Chem*. 2010;12(2):212. Available from: [<URL>](#).
33. Mohammed-Brahim B, Buchet JP, Lauwerys R. Erythrocyte pyrimidine 5'-nucleotidase activity in workers exposed to lead, mercury or cadmium. *International archives of occupational and environmental health*. 1985;55:247-52.





## Influence of Peptide Bioregulators on Indicators of Hemostasis in Blood of Irradiated Experimental Animals at Low Altitude Conditions

Gulbubu Kurmanbekova<sup>1</sup>, Salkyn Beyshenalieva<sup>2</sup>, Nurzhamal Omurzakova<sup>1</sup>,  
Bermet Kydyralieva<sup>1\*</sup>

<sup>1</sup> Kyrgyz-Turkish Manas University, Biology Department, Bishkek, 720005, Kyrgyzstan.

<sup>2</sup> Kyrgyz State University named after I. Arabaeva, Department of General Biology and Learning Technologies, Bishkek, 720005, Kyrgyzstan.

**Abstract:** In modern biology and medicine, much attention is paid to the study of the hemostasis regulation of some cell populations by substances of a peptide nature. They have the ability to regulate the functional and proliferative activity of cells and ensure communication in normal and pathological conditions. Research data showed that significant violations of the hemostatic system also occur with radiation damage to the body. One of the first radiation responses involves the coagulation cascade's activation, which leads to the breakdown of fibrinogen and the formation of fibrin clots. The potential threat of this is quite evident due to the existence of uranium mining tailings in several regions of the Kyrgyz Republic. Considering that significant disturbances of the hemostatic system occur during radiation damage to the body, and effective means are clearly not enough, the study of the effect of bioregulatory peptides in these conditions is of great importance. In the study, we carried out the total X-ray irradiation of laboratory animals on the X-ray therapeutic apparatus RUM-17. Peptide bioregulators peptide-1 and peptide-2 were administered intramuscularly to irradiated animals. Throughout the research, we used methods characterizing all links of hemostasis: vascular-platelet hemostasis, coagulation hemostasis, and fibrinolysis. The study has shown that the use of the peptide bioregulators in the background of acute radiation pathology leads to a decrease in the intensity of the chronic course of post-radiation thrombo hemorrhagic syndrome, contributing to an increase in the content of antithrombin III in the blood and modulating the versatile effects of endogenous heparin, which undoubtedly have a beneficial effect on the pathogenesis of radiation sickness.

**Keywords:** Experimental animals, Irradiation, Hemostasis, Low altitude, Peptide bioregulators.

**Submitted:** July 6, 2022. **Accepted:** August 10, 2023.

**Cite this:** Kurmanbekova G, Beyshenalieva S, Omurzakova N, Kydyralieva B. Influence of Peptide Bioregulators on Indicators of Hemostasis in Blood of Irradiated Experimental Animals at Low Altitude Conditions. JOTCSA. 2023;10(4):1001-8.

**DOI:** <https://doi.org/10.18596/jotcsa.1141531>

**\*Corresponding author's E-mail:** [bermet.kidiraliyeva@manas.edu.kg](mailto:bermet.kidiraliyeva@manas.edu.kg)

### 1. INTRODUCTION

Much attention in modern biology and medicine is paid to studying the involvement of peptidic nature's substances in regulating the hemostasis of some cell populations and their role as signaling molecules providing communicative links in normal and pathological conditions (1, 2). Such studies include various works on the primary participants in the blood coagulation system and their functioning (3), mechanisms of platelet activation (4), as well as the interaction between them (5) and active agents during thrombosis and thrombo-inflammation (6).

In addition to the main participants of the process of hemostasis regulation, such as blood cells and blood clotting factors, the most interesting are physiologically active peptides, which have been isolated from almost all internal organs. They have the ability to regulate the functional and proliferative activity of tissue cells, which are the starting material for their production (7,8). Our work focuses on the study of the functioning of polypeptides isolated from the spleen (conventionally designated as peptide-1) and erythrocytes (respectively peptide-2) in radiation damage of the organism. The potential threat of radiation exposure is exceptionally relevant to the study due to the presence of uranium mine

tailings in the regions of the Kyrgyz Republic. In addition, the wide use of radioactive sources in production, medicine, and other spheres of life of modern man increases the reality of his contact with radionuclides in various conditions of life and damage to various systems of the organism. Data from several studies (9–11) showed that the many identified violations and stepwise changes occur in the hemostasis system in radiation damage to the body. One of the first reactions to radiation involves the activation of the blood coagulation cascade, which leads to fibrinogen cleavage and the formation of fibrin clots. Effective means of therapy are clearly insufficient, and the study of the state of bioregulatory peptides that eliminate multidirectional changes in plasma hemostasis after irradiation is of great importance, which was the basis for this experiment.

## 2. MATERIALS AND METHODS

The experiments were carried out in the spring-summer and autumn periods of the year on 80 outbred rabbits of both sexes, weighing 2-3 kg, and 350 white outbred laboratory rats of both sexes, weighing 120-180 g, in low-mountain conditions (Bishkek, Kyrgyzstan, 760 above sea level). All animals were kept in the vivarium for at least two weeks on a regular diet before the start of the experiments. Due to the fact that the quality of nutrition and the content of microelements in food have a pronounced effect on hemostasis, the diet and quality of nutrition were the same for both intact and irradiated rabbits and rats in Bishkek. Hemostasis in experimental animals was studied in low altitude conditions on the 8th and 14th days of the experiment (that is, on the 3rd and 9th days after the end of the bioregulator administration).

In low-mountain conditions, total X-ray irradiation of animals was carried out on an X-ray therapeutic apparatus, RUM-17. Animals were placed in special cages during irradiation. Two rats were exposed simultaneously at a dose of 3–5 Gy (dose rate 26.1 Gy/min, tube voltage 200 kV, current strength 15 mA, filter 0.5 ml, focal length 92 cm). The dose of irradiation of animals (radiation sickness of moderate severity) was chosen to consider the fact that, on the one hand, the maximum radiation effects in irradiated animals could be detected according to the studied parameters, and on the other hand, the maximum radiation effect was estimated during long periods of observation.

Obtaining blood and plasma. Blood was taken through a fluoroplastic cannula in a fluoroplastic dish with sodium citrate (3.8%) in a ratio of 9:1 and immediately centrifuged for 10 minutes at 1500 rpm. The resulting plasma was pipetted into a siliconized test tube and used in the experiment.

Bioregulatory peptides were obtained by acetic acid extraction according to the Khavinson method. Peptide bioregulators peptide-1 and peptide-2 in our experiments were administered to irradiated animals intramuscularly at a dose of 1 mg/kg of bodily weight. Before administration, peptide bioregulators

were diluted in sterile saline. The solutions were administered once a day for 5 days. As a control, the animals were simultaneously injected with a sterile 0.9% sodium chloride solution in the same volume.

Throughout the research, we used methods characterizing all links of hemostasis: vascular-platelet hemostasis, coagulation hemostasis, and fibrinolysis (12).

The resulting material was processed by methods of variation statistics for Student's related and unrelated observations, and the confidence score differences (P) were calculated (13).

## 3. RESULTS AND DISCUSSION

### 3.1. Results

In the available literature, we did not find any studies on the effect of peptide-1 on the hemostasis of irradiated animals in low-mountain conditions. We studied the effects of peptide-1 on the hemostasis of animals compared to the effect of physiological saline. So, if the number of platelets in irradiated animals (compared to healthy animals) fell and amounted to  $282.7 \pm 12.6 \times 10^9/L$  (Table 1), then after a five-day injection of saline, an even more significant decrease in their number was noted ( $262.6 \pm 8.9 \times 10^9/L - 210.6 \pm 1.3 \times 10^9/L$ ) (Figure 1).

In the control group of animals, fluctuations in the adhesive function of blood platelets were statistically insignificant; however, the platelet aggregation time was extended both on the 8th day of the experiment (from  $18.6 \pm 2.2$  to  $35.5 \pm 6.0$  s) (Table 1) and on the 14th day (Table 2) of the examination (from  $18.6 \pm 2.2$  to  $24.7 \pm 1.3$  s).

So, in animals irradiated in the conditions in low mountains, which were injected with physiological saline, pronounced thrombocytopenia, inhibition of the aggregation function of platelets, and an increase in the time of plasma recalcification were determined.

In addition, the kaolin clotting time of plasma in this group of animals changed in different directions - on the 8th day of the examination, it was shortened from  $67.2 \pm 1.0$  to  $59.3 \pm 1.0$  s, and on the 14th day, it was lengthened from  $67.2 \pm 1.0$  to  $90.1 \pm 4.7$  s. According to the autoagglutination test, pronounced hypocoagulation was detected at the specified time. Also, on the 8th day of development of acute radiation sickness, plasma tolerance to heparin decreased (from  $23.1 \pm 1.3$  to  $29.3 \pm 0.9$ ), while on the 14th day, it increased from  $23.1 \pm 1.3$  up to  $16.3 \pm 2.0$  min. This indicates that thrombin that binds to heparin is apparently formed in the bloodstream of irradiated rabbits. Along with this, on the 8th day of the examination, the prothrombin time was shortened from  $22.4 \pm 0.7$  to  $20.0 \pm 0.2$  s, and the thrombin time remained practically unchanged, the concentration of fibrinogen in the blood plasma decreased from  $4.2 \pm 0.28$  to  $3.4 \pm 0.06$  g/l (Table 1-2).

On the 8th and 14th days of the experiment in the control group of animals, the plasma recalcification time was extended (respectively from  $78.5 \pm 1.2$  to  $93.8 \pm 1.3$  s and from  $78.5 \pm 1.2$  to  $86.0 \pm 0.2$  s).

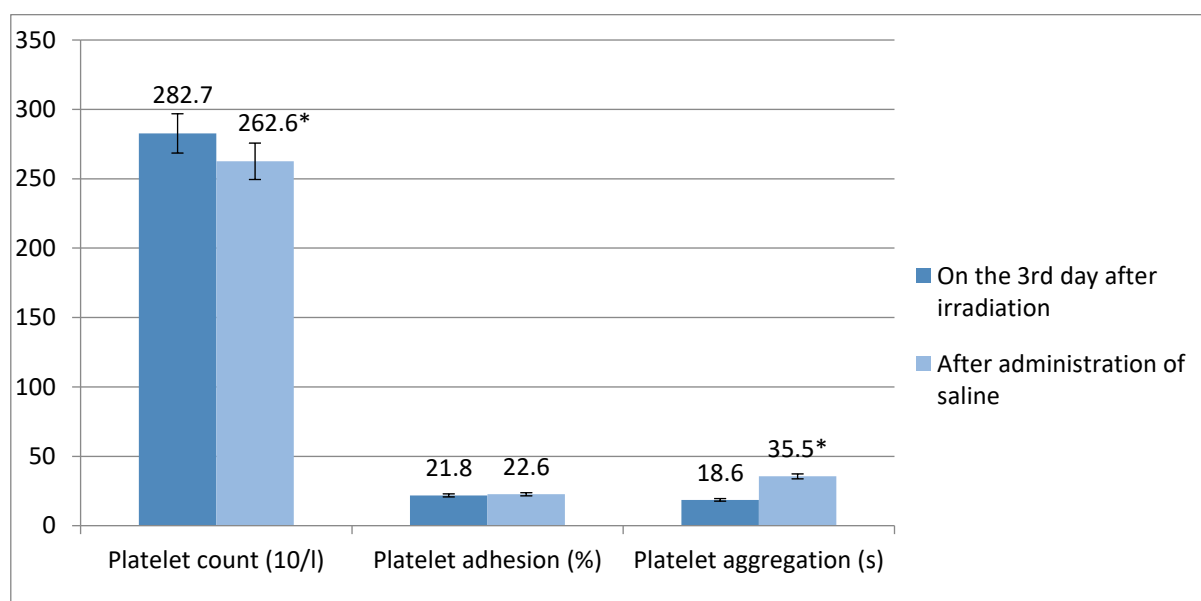


**Figure 1:** Influence of saline solution on hemostasis of irradiated animals in low mountains (on the 8th day of examination)

**Table 1:** Influence of saline solution on hemostasis of irradiated animals in low mountains (on the 8th day of examination)

Indicators	On the 3rd day after irradiation	After administration of saline
Plasma recalcification time (s)	$78.5 \pm 1.2$	$93.8 \pm 1.3$
Kaolin clotting time (s)	$67.2 \pm 1.0$	$59.3 \pm 1.0^*$
Autocoagulation test (c)		
at 6 <sup>th</sup> minute	$12.5 \pm 0.4$	$14.8 \pm 0.2^*$
at 8 <sup>th</sup> minute	$11.3 \pm 0.3$	$12.6 \pm 0.2^*$
at 10 <sup>th</sup> minute	$9.1 \pm 0.6$	$11.5 \pm 0.1^*$
Prothrombin time (s)	$22.4 \pm 0.7$	$20.0 \pm 0.2$
Thrombin time (s)	$25.7 \pm 0.3$	$26.2 \pm 1.2$
Kaolin-cephalin clotting time (s)	$33.7 \pm 0.8$	$108.7 \pm 5.4^*$
Plasma tolerance to heparin (min)	$23.1 \pm 1.3$	$29.3 \pm 0.9^*$
Antithrombin III (c)	$47.1 \pm 0.6$	$88.6 \pm 15.3^*$
Fibrinogen (g/l)	$4.2 \pm 0.2$	$3.4 \pm 0.06^*$
Euglobulin fibrinolysis (min)	$141.1 \pm 7.2$	$150.0 \pm 10.8$
Ethanol test (%)	55.0	62.5
Protamine sulfate test (%)	44.0	50.0

NOTE: \*  $P < 0.05$  when compared with control (3rd day after irradiation)

Based on the fact that in irradiated animals (who received and did not receive saline), in addition to the above changes, positive ethanol, and protamine sulfate tests were also noted in 55% and 44% of cases, respectively, we can talk about the formation of post-radiation thrombohemorrhagic syndrome on

the indicated days of observation. At the same time, total fibrinolysis was sharply activated in these animals, which indicated that the plasminogen activator entered the bloodstream from the vascular wall and tissues.

**Table 2:** Influence of saline solution on hemostasis of irradiated animals at low mountain conditions (on the 14<sup>th</sup> day of examination)

Indicators	On the 3rd day after irradiation	After administration of saline
Platelet count (10/l)	282.7±12.6	210.6±1.3*
Platelet adhesion (%)	21.8±0.6	22.5±0.9
Platelet aggregation (s)	18.6±2.2	24.7±1.3*
Plasma recalcification time (s)	78.5±1.2	86.0±0.2*
Kaolin clotting time (s)	67.2±1.0	90.1±4.7*
Autocoagulation test (c)		
at 6 <sup>th</sup> minute	12.5±0.4	13.2±0.5
at 8 <sup>th</sup> minute	11.3±0.3	11.8±0.5
at 10 <sup>th</sup> minute	9.1±0.6	11.7±0.4*
Prothrombin time (s)	22.4±0.7	19.8±0.5*
Thrombin time (s)	25.7±0.3	23.1±1.2
Kaolin-cephalin clotting time (s)	33.7±0.8	78.7±2.1*
Plasma tolerance to heparin (min)	23.1±1.3	16.3±2.0*
Antithrombin III (c)	47.1±0.6	118.8±4.7*
Fibrinogen (g/l)	4.2±0.2	3.2±0.3
Euglobulin fibrinolysis (min)	141.1±7.2	113.2±8.7*
Ethanol test	55.0	62.5
Protamine sulfate test	44.0	50.0

NOTE:\* P<0.05 when compared with control (3rd day after irradiation)

Thus, the administration of physiological saline to irradiated animals in the conditions of Bishkek does not significantly affect the state of multidirectional changes in hemostasis parameters, indicating the development of post-radiation thrombohemorrhagic syndrome.

In experiments to study the effect of a 5-day administration of peptide-1, it was shown that on the 8th day of the examination, the number of platelets in the blood of irradiated animals increased (from 262.6±8.9 to 286.0±9.6×10<sup>9</sup> g/l) (Figure 2) and their adhesion increased against the background of unchanged platelet aggregation.

From the data in Table 3, it can be seen that against the background of the use of peptide-1 in irradiated animals, the time of plasma recalcification was

prolonged (from 93.8±1.3 to 128.3±2.0 s), as well as the kaolin time of plasma (from 59.3±1.0 to 107.6±3.3 s). However, according to the autocoagulation test, at the 6th minute, an acceleration of the fibrin clot formation time was detected.

Shortening (from 20.0±0.2 to 17.5±0.1 s) of prothrombin and thrombin (from 26.2±2.2 to 24.0±0.4 s) plasma time also testified about hypercoagulation shifts in hemostasis after the administration of peptide-1. The addition of cephalin significantly shortened (from 108.7±5.4 to 73.3±0.8 s) the kaolin-cephalin clotting time. At the same time, plasma tolerance to heparin increased (from 20.3±0.9 to 24.2±0.6 min), and the content of antithrombin III, fibrinogen in the blood, and the time of euglobulin clot lysis did not change.

**Table 3:** Effect of bioregulatory peptide-1 on hemostasis of irradiated animals in low mountains (on the 8th day of examination)

Indicators	After administration of saline	After administration of peptide 1
Plasma recalcification time (s)	93.8 ±1.3	128.3±2.0*
Kaolin clotting time (s)	59.3±1.0	107.6±3.3*
Autocoagulation test (c)		
at 6 <sup>th</sup> minute	14.8±0.2	13.1±0.8*
at 8 <sup>th</sup> minute	12.6±0.2	12.2±0.6
at 10 <sup>th</sup> minute	11.5±0.1	11.5±0.4
Prothrombin time (s)	20.0±0.2	17.5±0.1*
Thrombin time (s)	26.2±1.2	24.0±0.4
Kaolin-cephalin clotting time (s)	108.7±5.4	73.3±0.8*
Plasma tolerance to heparin (min)	20.3±0.9	24.2±0.6*
Antithrombin III (c)	68.6±15.3	39.2±0.9*
Fibrinogen (g/l)	3.4±0.06	3.5±0.2
Euglobulin fibrinolysis (min)	150.0±10.8	141.8±13.5
Ethanol test	62.5	25.0
Protamine sulfate test	50.0	25.0

NOTE:\* P<0.05 when compared with control (after administration of saline)



On the 14th day of the examination of irradiated rabbits, after a 5-day administration of peptide-1, an increase in the number of platelets (from  $210.6 \pm 1.3$  to  $252.1 \pm 4.3$ ) in platelet blood plasma was noted (Figure 2). At the same time, adhesion increased (from  $22.5 \pm 0.9$  to  $25.2 \pm 0.6\%$ ), and the time of ADP aggregation of platelets shortened (from  $24.7 \pm 1.3$  to  $19.8 \pm 0.6$  s), recalcification time lengthened (from  $86.0 \pm 0.2$  to  $109.2 \pm 1.8$  s) and plasma kaolin time shortened (from  $90.1 \pm 4.7$  to  $74.1 \pm 1.3$  s). According

to the ACT indicators, a pronounced hypercoagulation was revealed at the analysis's 6th, 8th, and 10th minutes. It should also be noted that in irradiated animals, the administration of peptide-1 led to prolongation of prothrombin (from  $19.8 \pm 0.5$  to  $21.7 \pm 0.5$  s) and thrombin time. The addition of phospholipids to plasma against the background of activation of the Hageman factor by kaolin caused a sharp shortening (from  $78.3 \pm 2.7$  to  $55.3 \pm 2.7$  s) of the time of formation of a fibrin plasma clot.

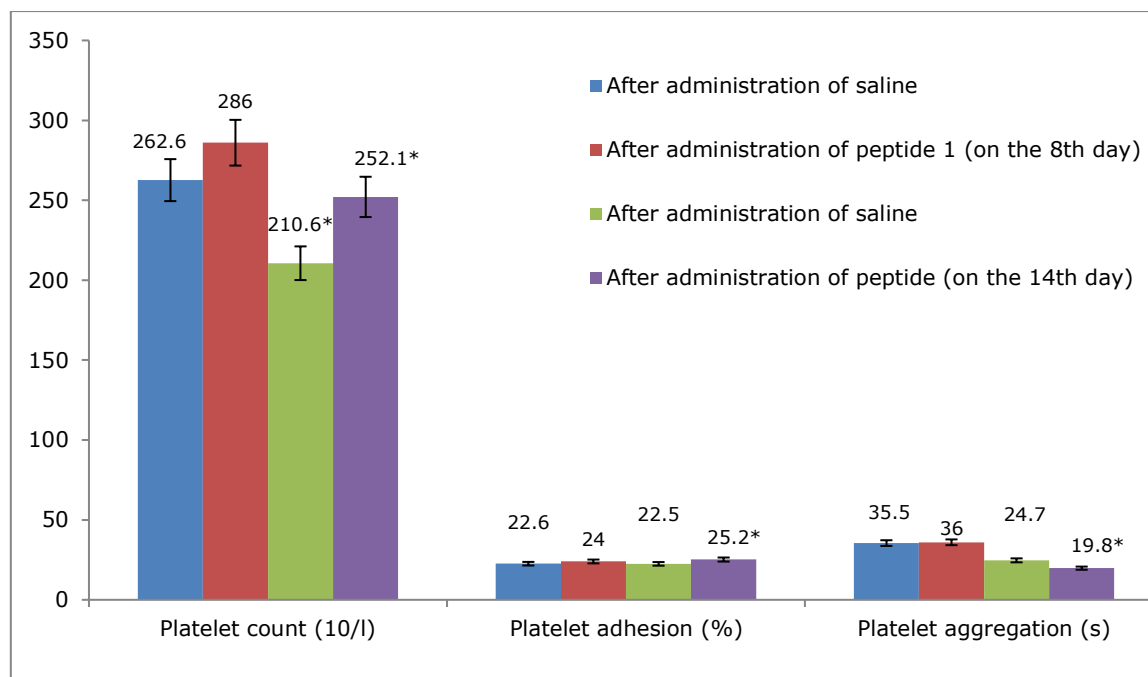


**Figure 2:** Influence of bioregulatory peptide-1 on hemostasis of irradiation of animals in low mountains (on the 8th and 14th day of the examination)

However, the degree of plasma tolerance to heparin in control and experimental animals did not differ much from each other. At the same time, on the 14th day of the examination (the 9th day after the end of the administration of peptide-1), in irradiated

animals after the administration of the drug, a decrease (from  $118.4 \pm 4.7$  to  $104.5 \pm 1.3$  s) was noted in the content of antithrombin III, the concentration of fibrinogen in the blood plasma did not actually change (Table 4).

**Table 4:** Influence of bioregulatory peptide-1 on hemostasis of irradiated animals in low mountains (on the 14th day of examination)

Indicators	After administration of saline	After administration of peptide 1
Plasma recalcification time (s)	86	109.2
Kaolin clotting time (s)	90.1	74.1
Autocoagulation test (c)		
at 6 <sup>th</sup> minute	13.2	10.6
at 8 <sup>th</sup> minute	11.8	8.3
at 10 <sup>th</sup> minute	11.7	6.8
Prothrombin time (s)	19.8	21.7
Thrombin time (s)	23.1	30.1
Kaolin-cephalin clotting time (s)	78.7	55.3
Plasma tolerance to heparin (min)	16.3	16
Antithrombin III (c)	118.8	104.5
Fibrinogen (g/l)	3.2	3.4
Euglobulin fibrinolysis (min)	113.2	76.2

Particular attention should be paid to the fact that on the 14th day of the examination, the irradiated animals showed a rather sharp activation of total fibrinolysis, as well as a decrease in the number of

positive ethanol and protamine sulfate tests, against the background of the use of peptide-1.

Thus, in conditions of low mountains, 5-day intramuscular administration of peptide-1 at a dose

of 1 mg/kg of body weight to irradiated animals, against the background of the existing pronounced post-radiation thrombohemorrhagic syndrome, led to a significant decrease in the intensity of its course. The favorable effect of peptide-1 on the state of the hemostasis and erythropoiesis system was more pronounced on the 14th day of the examination by the preservation of platelets and their dynamic function in the vascular bed, a decrease in the multidirectional hypo- and hypercoagulation shifts in hemostasis, activation of the fibrinolytic activity of the blood, and a decrease in the number of positive ethanol and protamine sulfate tests for paracoagulation products of fibrin and fibrinogen.

The next series of experiments showed that (Table 4) in irradiated animals after a 5-day administration of the peptide-2 polypeptide, the platelet content did not change significantly on the 8th and 14th days of observation.

Although the Lee-White clotting time for this period of examination in animals after the administration of

peptide-2 indicated hypercoagulation, the plasma recalcification time and kaolin clotting time remained practically unchanged, and the plasma kaolin-cephalin time shortened (from  $108.7 \pm 5.4$  to  $91.2 \pm 2.8$  s). Shortening on the 8th ( $12.6 \pm 0.2$  to  $9.0 \pm 1.1$  s) and 10th minutes (from  $11.5 \pm 0.1$  to  $7.5 \pm 1.1$  c) of fibrin clot formation evidenced the hypercoagulation orientation of hemostasis. At the same time, prothrombin (from  $20.02$  to  $25.0 \pm 1.1$  s) and thrombin (from  $26.0 \pm 1.2$  to  $50.1 \pm 4.2$  s) plasma time was lengthened. However, the plasma tolerance to heparin in irradiated animals after the administration of peptide-2 (on the 8th day of observation) increased (from  $29.3 \pm 0.9$  to  $16.0 \pm 1.4$  s) and the content of antithrombin III sharply decreased. Hypofibrinogenemia was also detected, and euglobulin fibrinolysis was inhibited (from  $150.0 \pm 13.5$  to  $245.0 \pm 45.7$  min.,  $P < 0.05$ ). Evidence of the positive effect of peptide-2 on the hemostasis of irradiated animals in Bishkek is the decrease in positive ethanol tests (from 62.5% to 25%).

**Table 5:** Effect of bioregulatory peptide-2 on hemostasis of irradiated animals in low mountains (on the 8th day of examination)

Indicators	After administration of saline	After administration of peptide 2
Platelet count (10/l)	$262.6 \pm 8.9$	$280.0 \pm 10.0$
Platelet adhesion (%)	$22.6 \pm 0.6$	$23.2 \pm 1.1$
Platelet aggregation (s)	$35.5 \pm 6.0$	$25.0 \pm 2.7$
Plasma recalcification time (s)	$93.8 \pm 1.3$	$90.0 \pm 1.8$
Kaolin clotting time (s)	$59.3 \pm 1.0$	$35.0 \pm 8.5^*$
Autocoagulation test (c)		
at 6 <sup>th</sup> minute	$14.8 \pm 0.2$	$14.0 \pm 1.4$
at 8 <sup>th</sup> minute	$12.6 \pm 0.2$	$9.2 \pm 1.1$
at 10 <sup>th</sup> minute	$11.5 \pm 0.1$	$7.5 \pm 1.1^*$
Prothrombin time (s)	$20.0 \pm 0.2$	$25.0 \pm 1.1^*$
Thrombin time (s)	$26.2 \pm 1.2$	$50.0 \pm 4.2^*$
Kaolin-cephalin clotting time (s)	$108.7 \pm 5.4$	$91.2 \pm 2.8^*$
Plasma tolerance to heparin (min)	$20.3 \pm 0.9$	$16.0 \pm 1.4^*$
Antithrombin III (c)	$68.6 \pm 15.3$	$34.0 \pm 8.0^*$
Fibrinogen (g/l)	$3.4 \pm 0.06$	$2.3 \pm 0.2^*$
Euglobulin fibrinolysis (min)	$150.0 \pm 10.8$	$245.0 \pm 45.7^*$
Ethanol test (%)	62.5	25.0
Protamine sulfate test (%)	50.0	50.0

NOTE: \*  $P < 0.05$  when compared with control (after administration of saline)

On the 14th day after the administration of peptide-2 to irradiated animals, according to the hemostasiogram parameters, an elongation ( $86.0 \pm 0.2$  to  $102.2 \pm 2.8$  s) of the plasma recalcification time was detected along with a simultaneous shortening (from  $80.0 \pm 2.8$  s) of kaolin and kaolin-cephalin (from  $78.7 \pm 2.7$  to  $53.0 \pm 1.4$  s) plasma time. According to the autocoagulation test, hypercoagulation was detected at the 6th, 8th, and 14th minutes. However, on the 14th day after the administration of peptide-2 in irradiated animals, the prothrombin and thrombin (from  $23.1 \pm 1.2$  to  $27, 0 \pm 1.4$  s  $P > 0.05$ ) plasma time lengthened. The content of the natural anticoagulant antithrombin III in the blood decreased (from  $118.8 \pm 4.3$  to  $108.0 \pm 4.2$  s at  $P < 0.05$ ). The fact of an increase (from

$2.3 \pm 0.2$  to  $3.4 \pm 0.6$  g/l, at  $P < 0.05$ ) of fibrinogen in the blood on the 8th day of examination attracts attention on the 14th day of observation after the administration of peptide-2 concentration did not change. There was a significant decrease (from 62% to 25%) in positive ethanol and protamine sulfate tests (from 50% to 25%) for fibrin and fibrinogen paracoagulation products (Table 5).

Thus, intramuscular 5-day administration of peptide-2 at a dose of 1 mg/kg of body weight to irradiated animals in low-mountain conditions against the background of post-radiation thrombohemorrhagic syndrome expressed in them led to a significant decrease in the intensity of this syndrome.

**Table 6:** Effect of bioregulatory peptide-2 on hemostasis of irradiated animals in low mountains (on the 14th day of examination)

Indicators	After administration of saline	After administration of peptide 2
Platelet count (10/l)	210.6±1.3	270.0±4.2*
Platelet adhesion (%)	22.5±0.9	25.0±0.5*
Platelet aggregation (s)	24.7±1.3	25.7±2.8
Plasma recalcification time (s)	86.0±0.2	102.2±2.8*
Kaolin clotting time (s)	90.1±4.7	80.0±2.8*
Autocoagulation test (c)		
at 6 <sup>th</sup> minute	13.2±0.5	10.2±0.8*
at 8 <sup>th</sup> minute	11.8±0.5	8.0±0.5*
at 10 <sup>th</sup> minute	11.7±0.4	5.7±0.2*
Prothrombin time (s)	19.8±0.5	21.2±0.5
Thrombin time (s)	23.1±1.2	27.0±1.4*
Kaolin-cephalin clotting time (s)	78.7±2.1	53.0±1.4*
Plasma tolerance to heparin (min)	16.3±2.0	15.7±0.5*
Antithrombin III (c)	118.8±4.7	108.0±4.2*
Fibrinogen (g/l)	3.2±0.3	3.3±0.3
Euglobulin fibrinolysis (min)	113.2±8.7	125.0±10.0*
Ethanol test (%)	62.5	25.0
Protamine sulfate test (%)	50.0	25.0

NOTE:\* P<0.05 when compared with control (after administration of saline)

This favorable pharmacological effect of peptide-2 in terms of hemostasiogram is manifested by hypercoagulation shifts in the clotting time of whole blood appears in siliconized and non-siliconized tubes and as well as a shortening of the fibrin clot formation time according to the kaolin-cephalin time and autocoagulation test. It is also important to note that this effect in irradiated animals under conditions of low mountains after the administration of peptide-2 persisted on the 14th day of examination of these animals.

### 3.2. Discussion

Bioregulatory peptide-1 increases the content of antithrombin III in the blood, apparently modulating the pharmacological and pharmacokinetic parameters of heparin. Also, peptide-1 in all our studies in the low mountains caused the activation of fibrinolysis. Stimulation by peptide-1 of blood fibrinolytic activity in healthy and irradiated animals in low altitude conditions can be carried out with the development of erythrocytosis. Strengthening fibrinolysis leads to the dissolution of fibrinogen and the appearance in the vascular bed of fibrin-monomers with anticoagulant properties. These so-called secondary anticoagulants can prevent the development of thrombohemorrhagic syndrome.

According to our data, after a 5-day administration of peptide-2 in the conditions of the city of Bishkek, pronounced hypocoagulation was noted in the hemostasis of healthy animals. How can one explain the nature of this, at first glance, the paradoxical reaction of animals in low-mountain conditions to introducing the polypeptide used? As we know, the hemostasis system generally reacts very sensitively and subtly to the slightest changes in the strength and nature of disturbing factors, both endogenous and exogenous. In addition, the response of this system and its stability have biorhythmological and specific features of the organism. Therefore, peptide-2, administered parenterally, acts against the

background of a pronounced stress state, which necessarily creates the preconditions for increased thrombus formation in the body. It is precisely by acting as a regulator of reciprocal relations in the hemostasis system that, in this case, erythrolin exhibits a hypocoagulant effect in healthy animals in low altitude conditions. The formation of a hypocoagulable state in the hemostasis system is assessed by us as a positive effect of peptide-2 since it prevents stress thrombus formation in low-altitude conditions. This is confirmed by the fact that in this group of animals, there was an increase in the number of platelets in the blood and, most importantly, the content of the natural anticoagulant antithrombin III in the blood increased (on the 14th day of the experiment), and the concentration of fibrinogen increased (from 3.0 ± 0.3 up to 4.1±0.2%). The effect of peptide-2 on hemostasis is associated with the fundamental processes of multilevel regulation of vital functions, including hemostasis of the hemocoagulation system. Based on this, it seems that peptide-2 can block primary and secondary platelet receptors and thereby reduce the "release reaction" of platelets, i.e., keep their number. In addition, depending on the initial physiological state of the hemostasis system, it can either compensate the lack of erythrocyte coagulation factors or reduce their excess activity. As a result, its regulatory function is manifested against the background of the hypercoagulation orientation of hemostasis, peptide-2 forms hypocoagulation, and conversely, against the background of hypocoagulation leads to hypercoagulable shifts.

It is known that profound disorders in the blood coagulation system develop with radiation damage to the body, which usually have a hypocoagulant orientation. In conditions of low mountains after total X-ray irradiation on the 8th and 14th days in rabbits, we revealed pronounced hypocoagulation, a decrease in the content of antithrombin III and activation of fibrinolysis. The presence of

thrombohemorrhagic syndrome explains, in part, a drop in the number of platelets, a decrease in the prothrombin index, an increase in fibrinogen levels, and the appearance of paracoagulation products. Yet, we consider the development of thrombohemorrhagic syndrome to be the main one in the genesis of acute radiation injury, which causes hemorrhagic symptoms in acute radiation sickness.

#### 4. CONCLUSION

The introduction of peptide bioregulators in low altitude conditions in healthy animals leads to the development of hypocoagulation, which is expressed in an increase in the number of platelets, the content of fibrinogen and antithrombin III in the blood, an increase in the time of formation of a fibrin clot, kaolin, kaolin-cephalin plasma time. Under conditions of low mountains, bioregulatory peptides peptide-1 and peptide-2 significantly reduce the intensity of secondary post-radiation hypocoagulation, which is manifested by a shortening of the whole blood clotting time in siliconized and non-siliconized tubes, kaolin, kaolin-cephalin time and plasma recalcification time. This effect of bioregulatory peptides is more pronounced on the 14th day of the examination and is manifested by an increase in the number of platelets in the blood with their full function and activation of fibrinolysis. Functional inferiority of hemostasis subsystems can be effectively corrected by peptide bioregulators peptide-1 and peptide-2 in low-mountain conditions.

Thus, the use of peptide bioregulators against the background of acute radiation pathology in low altitude conditions leads to a decrease in the intensity of the chronic course of post-radiation thrombohemorrhagic syndrome, contributing to an increase in the content of antithrombin III in the blood and modulating the versatile effects of endogenous heparin, which undoubtedly have a beneficial effect on the pathogenesis of radiation sickness.

#### 5. REFERENCES

1. Toktosunovna Kurmanbekova G, Tursunaliyeva Beishenalieva S, Ananievich Rachkov I, Beckbalaevich Chekirov K, Taichiyeva Omurzakova N. Advances in Environmental Biology Bioregulatory Basic Peptides Liberated from Gall-Bladder Inflammatory Wall of People Who are Sick with Acute Cholecystitis after Laparotomy Cholecystectomy. *Adv Environ Biol* [Internet]. 2014;8(10):303–8. Available from: [<URL>](#).
2. Rehfeld JF, Bundgaard JR. Cellular Peptide Hormone Synthesis and Secretory Pathways

[Internet]. Rehfeld JF, Bundgaard JR, editors. Berlin, Heidelberg: Springer Berlin Heidelberg; 2010. (Results and Problems in Cell Differentiation; vol. 50). Available from: [<URL>](#).

3. Versteeg HH, Heemskerk JWM, Levi M, Reitsma PH. New Fundamentals in Hemostasis. *Physiol Rev* [Internet]. 2013 Jan 1;93(1):327–58. Available from: [<URL>](#).

4. Holinstat M. Normal platelet function. *Cancer Metastasis Rev* [Internet]. 2017 Jun 30;36(2):195–8. Available from: [<URL>](#).

5. Sang Y, Roest M, de Laat B, de Groot PG, Huskens D. Interplay between platelets and coagulation. *Blood Rev* [Internet]. 2021 Mar 1;46:100733. Available from: [<URL>](#).

6. Kuijpers MJE, Heemskerk JWM, Jurk K. Molecular Mechanisms of Hemostasis, Thrombosis and Thrombo-Inflammation. *Int J Mol Sci* [Internet]. 2022 May 23;23(10):5825. Available from: [<URL>](#).

7. Ivanov VT. Peptides as universal biological regulators. *Her Russ Acad Sci* [Internet]. 2010 Oct 14;80(5):419–29. Available from: [<URL>](#).

8. Shpakov AO. Peptides derived from the extracellular loop of receptors: structure, mechanisms of action and application in physiology and medicine. *Russ Fiziol Zhurnal Im IM Sechenova* [Internet]. 2011 May 1;97(5):441–58. Available from: [<URL>](#).

9. Rachkov AG. Trombogemorragicheskiy sindrom pri ostroi krovopotere i luchevoi bolezni v usloviyakh vysokogor'ya. 1989;

10. Kennedy AR, Maity A, Sanzari JK. A Review of Radiation-Induced Coagulopathy and New Findings to Support Potential Prevention Strategies and Treatments. *Radiat Res* [Internet]. 2016 Aug 1;186(2):121–40. Available from: [<URL>](#).

11. Treml B, Wallner B, Blank C, Fries D, Schobersberger W. The Influence of Environmental Hypoxia on Hemostasis—A Systematic Review. *Front Cardiovasc Med* [Internet]. 2022 Feb 18;9:813550. Available from: [<URL>](#).

12. Favaloro EJ, Lippi G. Hemostasis and Thrombosis Methods and Protocols [Internet]. Favaloro EJ, Lippi G, editors. New York, NY: Springer New York; 2017. (Methods in Molecular Biology; vol. 1646). Available from: [<URL>](#).

13. Glantz SA. Primer of Biostatistics [Internet]. McGraw-Hill; 2012. 327 p. Available from: [<URL>](#).



## Removal of Methylene Blue Dye from Aqueous Solution Using Trichlorovinylsilane Chitosan-g-polyacrylamide Hydrogel

Anthony U. Awode<sup>1,2\*</sup>, Sunday E. Elaigwu<sup>3\*</sup> , Akeem A. Oladipo<sup>1</sup>, Osman Yilmaz<sup>1</sup>, Mustafa Gazi<sup>1\*</sup>

<sup>1</sup> Polymeric Materials Research Laboratory, Chemistry Department, Faculty of Arts and Science, Eastern Mediterranean University, TR North Cyprus, Famagusta via Mersin 10, Turkey

<sup>2</sup> Department of Chemistry, Faculty of Natural Sciences, University of Jos, Plateau State, Nigeria

<sup>3</sup> Department of Chemistry, Faculty of Physical Sciences, University of Ilorin, Kwara State, Nigeria.

**Abstract:** A new hydrogel based on vinylsilane-chitosan and acrylamide was synthesized as VSi-CTS-g-PAAM and was used to remove methylene blue (MB) from aqueous solution using batch adsorption technique. The VSi-CTS-g-PAAM hydrogel interacted with methylene blue (MB) dye solution at different mass-liquid ratios, pH, and temperature. The amount of MB dye removal was estimated using a UV-Vis spectrophotometer at an optical density of  $\lambda_{\max} = 665$  nm. The MB dye removal was most effective at pH 12, with about 98 % removal at 50 °C. The study's findings also indicated that the equilibrium data exhibited the highest degree of conformity with the Langmuir isotherm model. Additionally, the adsorption process adhered to the pseudo-second-order kinetics and was characterized as endothermic. Therefore, our study suggests that the utilization of prepared materials may have potential advantages in treating wastewater containing dyes.

**Keywords:** Acrylamide, Adsorption, Chitosan, Hydrogel, Vinylsilane.

**Submitted:** May 4, 2023. **Accepted:** August 21, 2023.

**Cite this:** Awode AU, Elaigwu SE, Oladipo AA, Yilmaz O, Gazi M. Removal of Methylene Blue Dye from Aqueous Solution Using Trichlorovinylsilane Chitosan-g-polyacrylamide Hydrogel. JOTCSA. 2023;10(4):1009-18.

**DOI:** <https://doi.org/10.18596/jotcsa.1292604>

**\*Corresponding author's E-mail:** [awodea@unijos.edu.ng](mailto:awodea@unijos.edu.ng); [elaigwu.se@unilorin.edu.ng](mailto:elaigwu.se@unilorin.edu.ng)

### 1. INTRODUCTION

Over 280,000 tonnes per year of various dyes are estimated to be discharged into water bodies globally (1). A good percentage of these dyes are not effectively treated before their release into water bodies and thus pose a substantial environmental challenge to the biodiversity and usability of these water bodies (2). The need to rid water bodies of these dyes from textile effluent is of utmost necessity, as water is becoming a scarce commodity.

Various methods have been developed to treat wastewater; these include adsorption, photocatalytic degradation, biological treatment, chemical oxidation, and precipitation (3). These methods are effective but time-consuming and usually involve high-energy demand, leading to higher costs. An extensive review of the advantages and disad-

vantages of these methods has been published (4,5). Adsorption technology, a hybrid of physical and chemical treatment methods, has gained prominence due to its low operation cost and effectiveness (6-8).

Diverse techniques utilizing low-cost adsorbents have been successfully advanced for dye removal (9,10). In recent years, hydrogel-based materials, which are polymeric materials with three-dimensional networks retaining a large quantity of water within their structures, have been widely studied because of their beneficial properties and have been used in wastewater treatment and other applications such as bio-sensing, biomedical engineering, agriculture and horticulture, drug delivery, and sanitary products (11-14).

However, hydrogel made purely from synthetic materials and metal ions have their drawbacks due

to their environmental impact and toxicity to living cells when used as an antibacterial agent (15). Moreover, nanoparticle-based hydrogel development has been restricted due to their physical and chemical instability (16). To address these drawbacks, researchers have focused on synthesizing polysaccharide-based hydrogel, which can be prepared by polymer grafting and cross-linking reactions, making them more beneficial as adsorbents than conventional hydrogels. This is not only because of the hydrophilic groups, such as  $-\text{OH}$ ,  $-\text{NH}_2$ ,  $-\text{COOH}$ , and  $-\text{CONH}_2$  on their surface that help in the adsorption of the pollutants via electrostatic interaction and hydrogen bonding, but due to their low-cost, non-toxic, environmentally friendly, and highly biodegradable and biocompatible nature (17-19, 3).

Chitosan is a deacetylated version of chitin (the second most abundant natural polysaccharide biopolymer after cellulose). It is made up of 2-acetamido-2-deoxy- $\beta$ -D-glucopyranose and 2-amino-2-deoxy- $\beta$ -D-glucopyranose linked by  $\beta(1,4)$ -linkage and possesses important properties of biopolymers such as non-toxicity, biocompatibility, and biodegradability than chitin (20,21). In addition, chitosan has positive charges on its surface, which helps when bonding with negatively charged groups, thus making it a compelling candidate in wastewater remediation. Despite the advantages of using chitosan, there are disadvantages associated with its use, namely low porosity, low thermal resistance, high solubility, and low stability in acidic medium (20,21). These disadvantages limit its use, especially in the adsorption of acidic pollutants such as dyes from their aqueous solutions. Modifying the chitosan chains is crucial to avert these challenges and improve performance. Hence, techniques such as crosslinking, blending with other polymers, and grafting copolymerization have been used to achieve it (22-25).

Therefore, to prevent the aforementioned limitations of chitosan and to improve its ability to remove dyes from aqueous solutions, we synthesized a new adsorbent material (hydrogel) in this study by blending chitosan with trichlorovinylsilane and subsequent cross-linking with polyacrylamide. To the best of our knowledge, no previous work has reported using this material to remove dye (methylene blue) from an aqueous solution. The effect of different parameters such as adsorbent dosage, temperature, initial concentration of dye, contact time, and pH on the adsorption process was investigated to understand the adsorption process's kinetics and equilibrium adsorption isotherms.

## 2. MATERIALS AND METHODS

### 2.1. Materials

Low molecular weight (LMW) chitosan (75-85 % DDA) was purchased from Sigma-Aldrich Co. (St. Louis, USA) and used as supplied. Acetone and acetic acid were purchased from Merck, Germany. Trichlorovinylsilane, acrylamide, N,N'-Methylenebisacrylamide, Methylene blue (MB) and ammonium

persulfate were obtained from Sigma-Aldrich, Germany.

### 2.2. Synthesis of Trichlorovinylsilane Chitosan-g-acrylamide Hydrogel (VSi-CTS-g-PAAm)

4 g of low molecular weight chitosan (CTS) was weighed into a bottle; 10 mL of trichlorovinylsilane (VSi) was added and allowed to soak the chitosan for 3 days. After complete soaking and interaction with chitosan, the bottle was opened and excess fumes of trichlorovinylsilane allowed to escape. The product (VSi-CTS) produced was properly stored in a corked container.

50 mL of 2.5 % acetic acid was added into a conical flask containing 0.5 g of VSi-CTS, and it was allowed to stir overnight until complete dissolution. 10 mL of the VSi-CTS acetic acid solution was used in the preparation of the hydrogel by adding varying amount of acrylamide (0.9 g, 0.7 g, 0.5 g, 0.3 g), 0.05 g N,N'-methylenebisacrylamide (crosslinker) and 0.05 g ammonium persulfate (initiator). The reaction was carried out at 75 °C until gel was formed.

Finally, the synthesized hydrogel was washed several times with distilled water and acetone, and then dried at room temperature until a constant weight was obtained.

### 2.3. Adsorption Experiments

Batch adsorption experiments were performed at 25 – 50 °C temperature range using a set of 250 mL Erlenmeyer flask containing 0.025 g of adsorbent and 25 mL of MB solution of different initial concentrations (10 – 100 mg/L). The MB solution was adjusted to varying pH range (2 – 12) using 0.1 M HCl and 0.1 M NaOH solutions. It was then shaken at an agitation speed of 205 rpm for 24 h (1440 min). After equilibrium is achieved, decantation and filtration were carried out and the equilibrium concentration of the dye was determined using a UV-visible spectrophotometer (2377 double beam) at maximum wavelength of 665 nm. The percentage removal of MB dye and amount of dye adsorbed were calculated using the following equations.

$$\% \text{ Removal} = \frac{(C_0 - C_e)}{C_0} \times 100 \quad (1)$$

$$q_e = \frac{(C_0 - C_e)}{M} V \quad (2)$$

where  $C_0$  and  $C_e$  (mg/L) are the initial dye concentration and equilibrium dye concentration at a given time,  $q_e$  (mg/g) amount of MB dye in mg per gram of adsorbent,  $V$  ( $\text{dm}^3$ ) volume of solution,  $M$  (g) mass of hydrogel used.

## 3. RESULTS AND DISCUSSION

### 3.1. Effect of Adsorbent Dosage on the Adsorption Process

The effect of adsorbent dosage was studied using 0.025 – 0.075 g, 25 mL of 10 mg/L adsorbate at 25 °C, pH 12 for 24 h. As can be seen in Figure 1, the adsorption efficiency of the adsorbent was very high at low adsorbent dosage and remained almost stable

with increase the adsorbent dosage. The observed trend under the studied conditions could be attributed to the presence of large numbers of active adsorption sites on the adsorbent, which made it possible for the high adsorption efficiency to be

recorded at low adsorbent dosage. This study result is consistent with previous studies, which reported adsorption sites to be responsible for high adsorption efficiency of adsorbents (26,27).

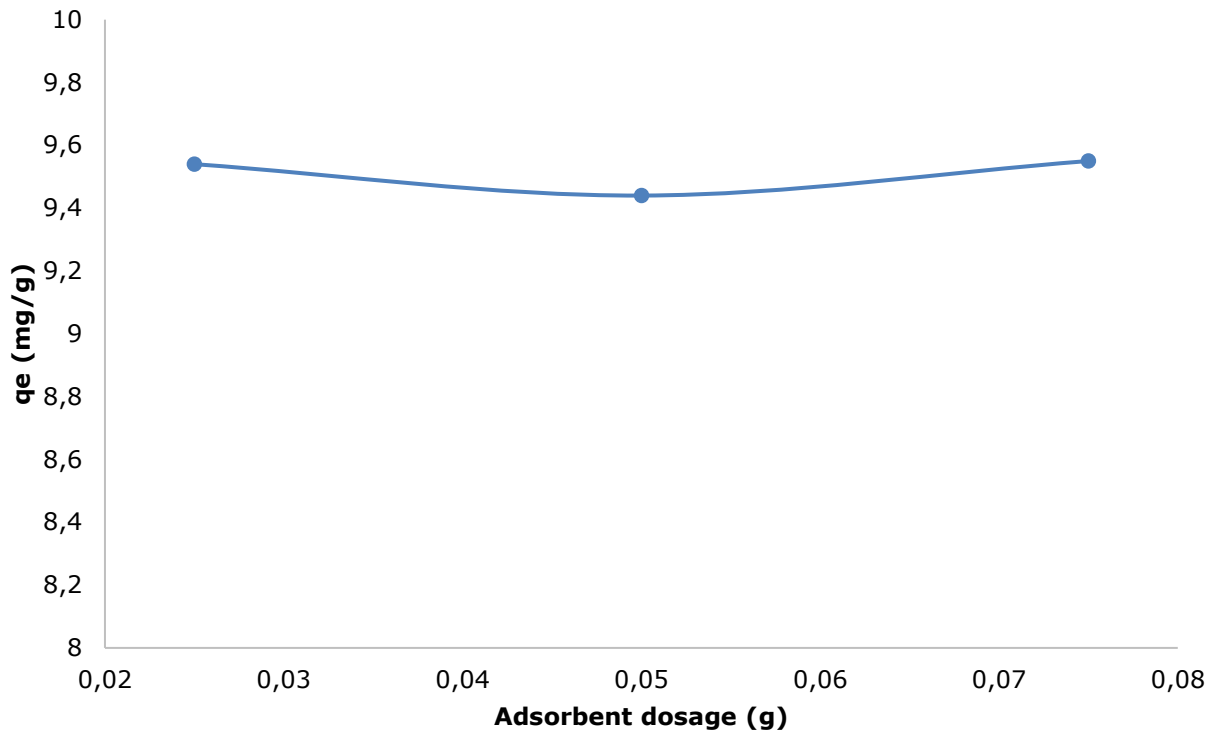


**Figure 1:** Effect of adsorbent dosage on the adsorption of MB onto VSi-CTS-g-PAAm hydrogel.

### 3.2. Effect of Initial Dye Concentration and Adsorption Isotherm

The effect of initial concentration on the amount of MB adsorbed is shown in Figure 2. Different concentrations of MB were prepared ranging from 10 – 120 mg/L and the experiment was carried out at 25 °C, pH 12, with 0.025 g of the adsorbent for 24 h. As the concentration of MB increases there was an increase in the uptake of MB dye onto VSi-CTS-g-PAAm hydrogel. This could be attributed to increased collisions between the dye molecules as a result of bulk density of the dye molecules thereby prevailing over any liquid to solid phase barrier (28,29). Nevertheless, as the adsorbent active sites continued to bind to the dye molecules, it got to a point of saturation (100 mg/L), and further increase in MB concentration led to decrease in the amount of dye molecules adsorbed.

To fully understand the adsorption behavior of the prepared VSi-CTS-g-PAAm hydrogel, the Langmuir and Freundlich adsorption isotherm models were used. The linearized forms of their equations are given in equations 3 and 4 respectively.

$$\frac{1}{q_e} = \frac{1}{q_m} + \frac{1}{K_L q_m C_e} \quad (3) \text{ Langmuir model}$$

$$\ln q_e = \ln K_F + \frac{1}{n} \ln C_e \quad (4) \text{ Freundlich model}$$

Where  $C_e$  is the (mg/dm<sup>3</sup>) is the equilibrium dye concentration in solution,  $q_e$  (mg/g) is the equi-

librium dye concentration on the adsorbent,  $q_m$  (mg/g) is the MB concentration onto the adsorbent when monolayer forms,  $C_0$  (mg/dm<sup>3</sup>) is the initial dye concentration, and  $K_L$  is the Langmuir constant (dm<sup>3</sup>/mg).

Figures 3 and 4 illustrate the different isotherms of Langmuir and Freundlich respectively. The obtained experimental data fitted well into the two models. However, the correlation coefficient for Langmuir ( $R^2 = 0.986$ ) was observed to be a better fit with a maximum adsorption capacity of 68.02 mg/g. The values for the parameters in the Langmuir and Freundlich are summarized in Table 1. The most important feature of the Langmuir isotherm is the  $R_L$ , which is known as the dimensionless constant separation factor that helps to foretell if an adsorption system is favorable or unfavorable and is given by equation (5). Adsorption system is favorable when ( $0 < R_L < 1$ ), unfavorable ( $R_L > 1$ ), linear ( $R_L = 1$ ), irreversible ( $R_L = 0$ ) (30,31).

$$R_L = \frac{1}{1 + K_L C_0} \quad (5) \text{ Separation factor}$$

The plot of the Separation Factor is shown in Figure 5. The  $R_L$  values obtained ranged from 0.283–0.703, indicating that the monolayer adsorption of MB onto VSi-CTS-g-PAAm hydrogel was favorable. It also established that the adsorption data fitted into the Langmuir isotherm at the optimal conditions in this study (30,31).

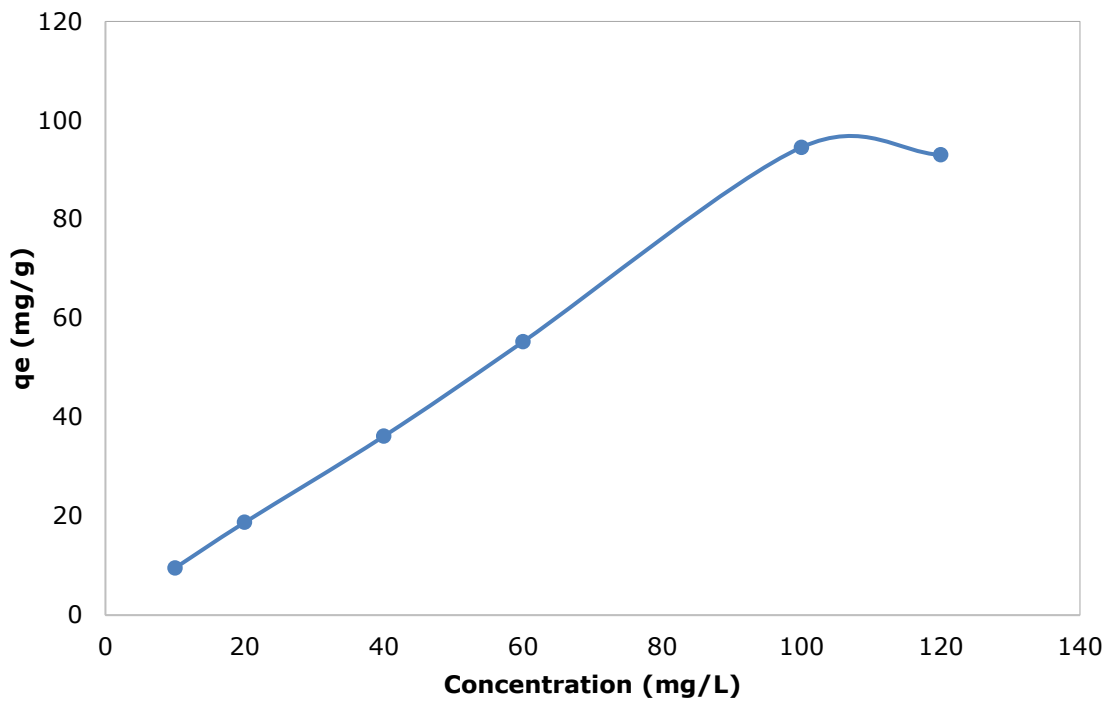


Figure 2: Effect of initial dye concentration on the adsorption of MB onto VSi-CTS-g-PAAm hydrogel.

Table 1: Summary of adsorption isotherm parameters.

Langmuir model				Freundlich model		
qm (mg/g)	KL	RL	R <sup>2</sup>	n	K <sub>F</sub>	R <sup>2</sup>
68.02	0.042	0.283-0.703	0.986	1.42	1.21	0.978

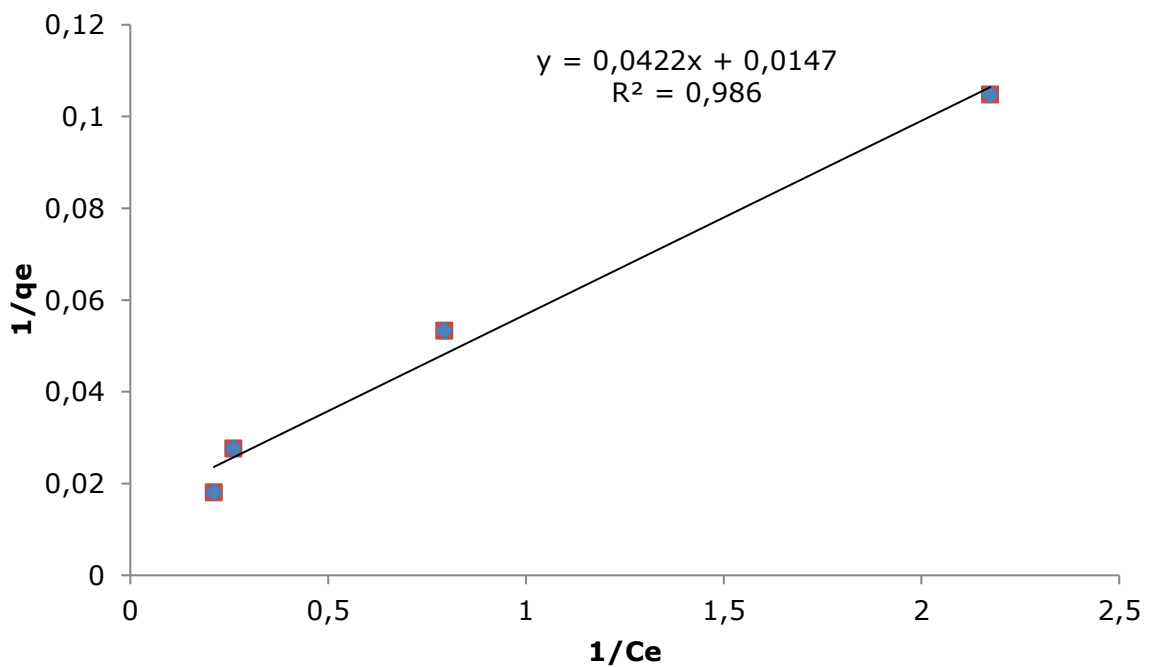
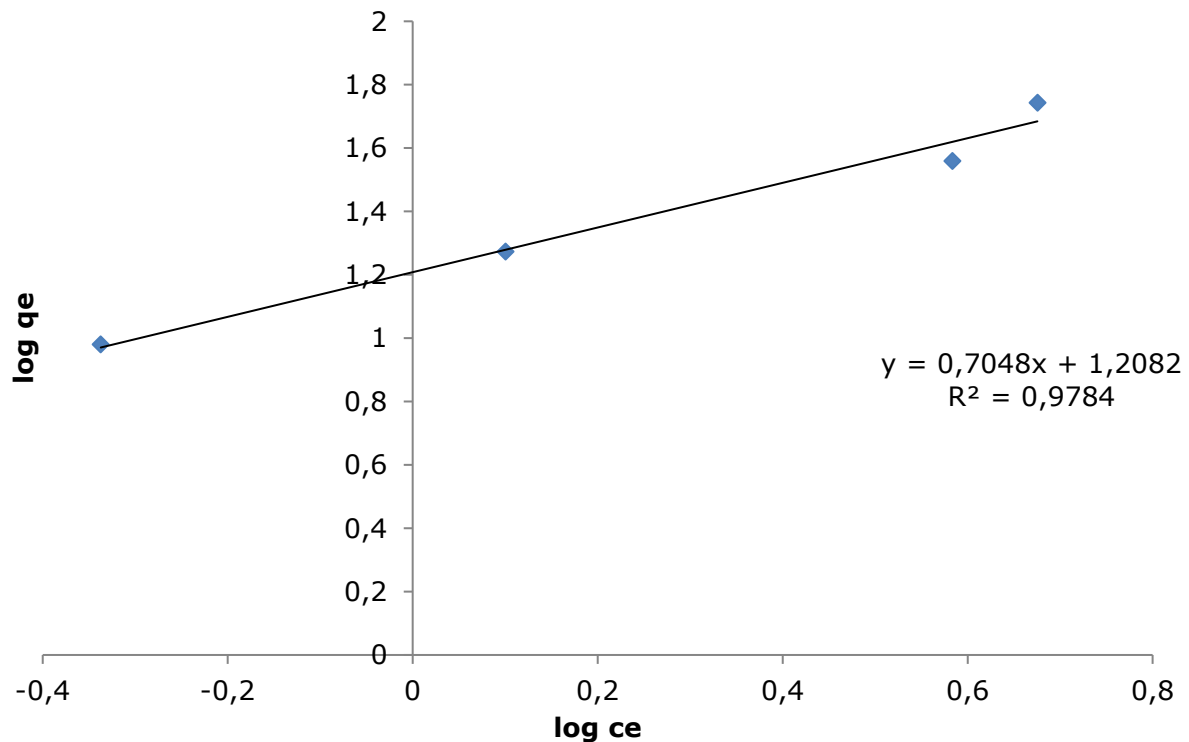
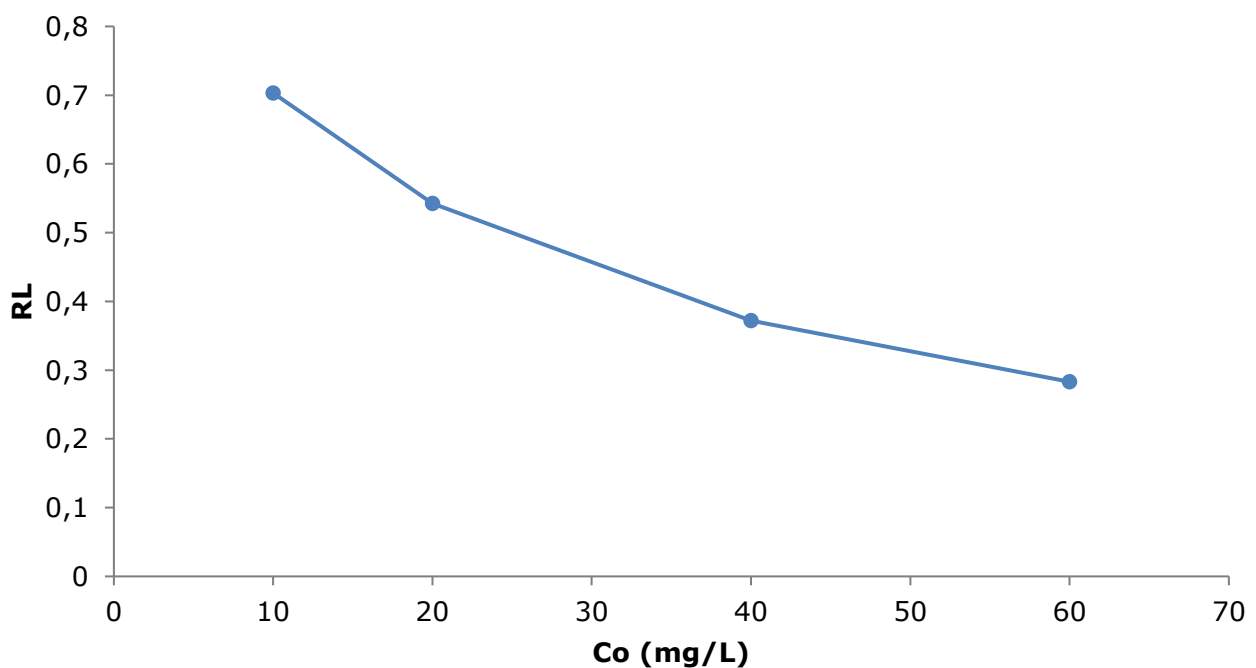


Figure 3: Langmuir adsorption Isotherm for the adsorption of MB onto VSi-CTS-g-PAAm hydrogel.





**Figure 4:** Freundlich adsorption isotherm for the adsorption of MB onto VSi-CTS-g-PAAm hydrogel.



**Figure 5:** Separation factor  $R_L$  versus the initial MB dye concentration at 25 °C.

### 3.3. Effect of pH on The Adsorption Process

The effect of pH of the dye solution was studied using 0.025 g of the adsorbent, 25 mL of 10 mg/L adsorbate at 25 °C for 24 h, while the pH was varied between 2-12. From the results obtained the adsorption of MB increased with increase in the pH as can be seen from Fig. 6 with the maximum

adsorption occurring at pH 12. The observed trend is as a result of protonation of functional groups such as carboxyl and alcoholic groups at pH < 3 that decreased the adsorption efficiency, while deprotonation of these functional groups occurs at pH > 8 and increases the adsorption efficiency (32).

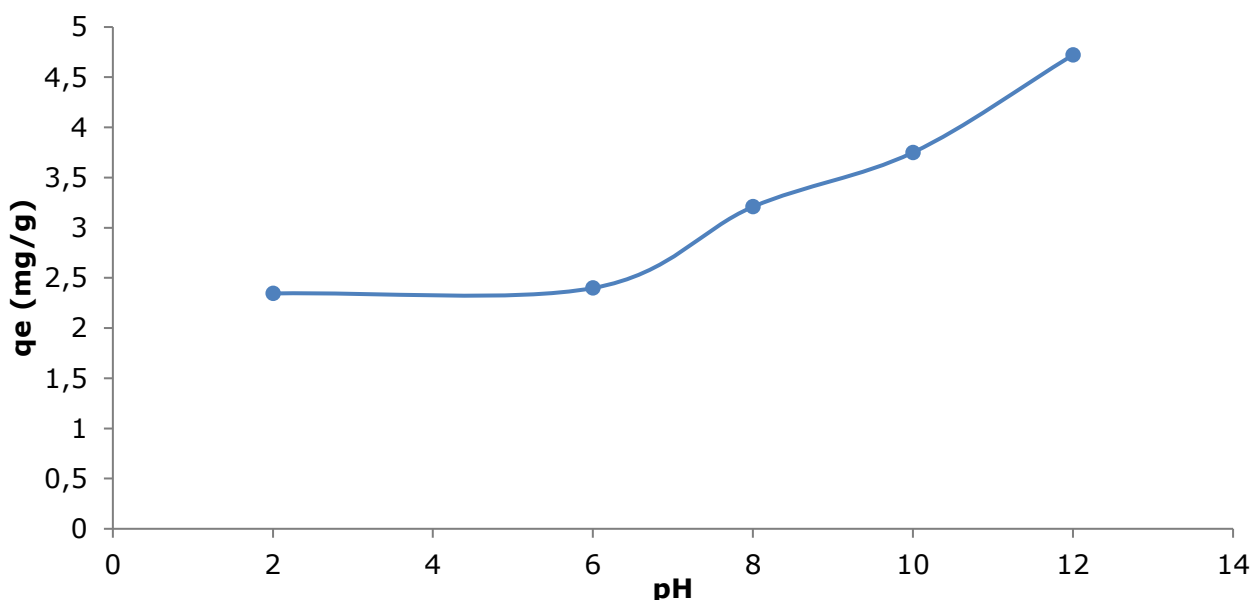


**Figure 6:** Effect of pH on the adsorption of MB onto VSi-CTS-g-PAAm hydrogel.

### 3.4. Effect of Temperature on the Adsorption Process

The effect of temperature on the adsorption of MB onto VSi-CTS-g-PAAm was performed at 25, 35 and 50 °C for 24 h using 25 mL of 10 mg/L adsorbate solution and 0.025 g of adsorbate at pH 12. There was an increase in the adsorption of MB as the temperature was increased signifying an endother-

mic process (27). The adsorption capacity of MB increased from 4.722 – 9.777 mg/g onto the VSi-CTS-g-PAAm hydrogel at 25 – 50 °C as seen from Fig. 7. This can be ascribed to the increase in the kinetic energy of the MB molecules giving them adequate energy to prevail over the bulk layer and be adsorbed onto the crevice of the hydrogel network (33).

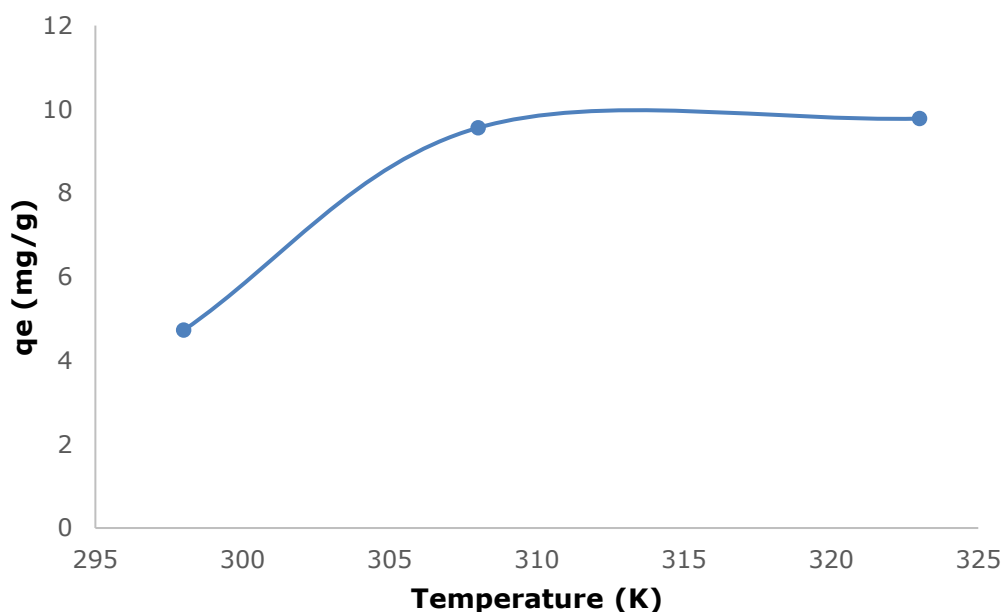


**Figure 7:** Effect of temperature on the adsorption of MB onto VSi-CTS-g-PAAm hydrogel.

### 3.5. Effect of Time and Adsorption Kinetics

The effect of contact time of the adsorbent with MB was studied from 30 – 1440 min (0.5 – 24 h) using an adsorbent dosage of 0.025 g, 25 mL of 10 mg/L adsorbate at pH 12. The result obtained is as presented in Fig. 8. It can be seen that the quantity of MB adsorbed increased rapidly at the beginning and became gradual afterward until equilibrium was

achieved. The optimum time was attained at 1440 min; thereafter, the percentage of dye adsorption remained relatively constant. The increase in adsorption ab initio could be attributed to many vacant adsorption sites; these sites became occupied over time, resulting in reduced adsorption of MB (28). A similar trend in adsorption has been previously reported (27).

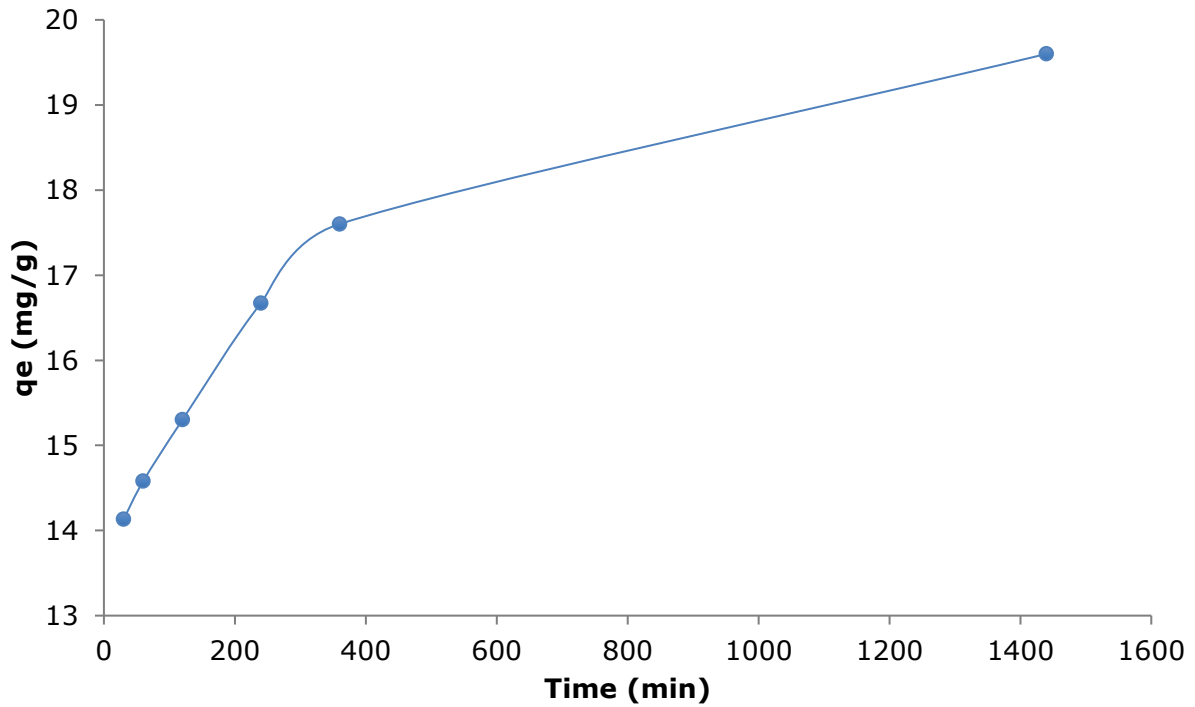


Figure 8: Effect of time on the adsorption of MB onto VSi-CTS-g-PAAm hydrogel.

Two kinetic models, namely the pseudo-first order and pseudo-second orders (Equations 6 and 7, respectively), were used to fit the experimental data and propose a mechanism for the adsorption process. The results are presented in Fig. 9 and 10, respectively. The correlation coefficient ( $R^2$ ) values obtained show that the experimental data better fits into the pseudo-second-order kinetic model. This suggests that a pseudo-second-order kinetic model could be applied in describing the entire adsorption

process, with chemisorption as the rate-determining step (27). The kinetics parameters for the adsorption of MB onto VSi-CTS-g-PAAm hydrogel are presented in Table 2.

$$\ln(q_e - q_t) = \ln(q_e) - (K_1)t \quad (6) \text{ Pseudo first order}$$

$$\frac{t}{q_t} = \frac{1}{k_2 q_e^2} + \frac{t}{q_e} \quad (7) \text{ Pseudo second order}$$

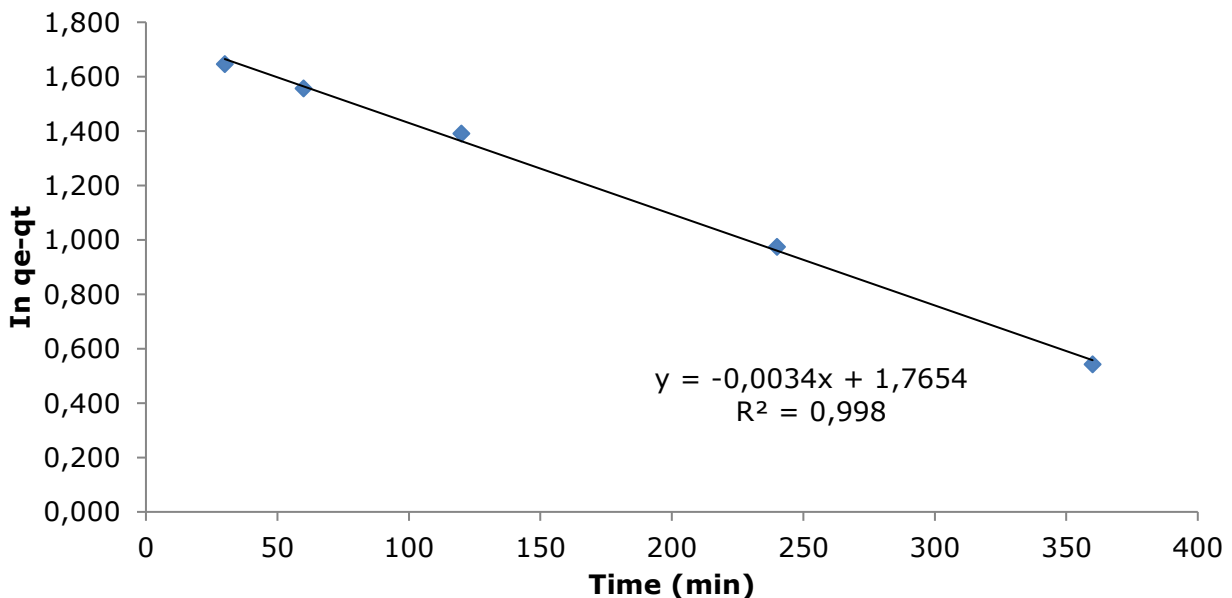


Figure 9: Pseudo-first-order kinetics for the adsorption of MB onto VSi-CTS-g-PAAm hydrogel.

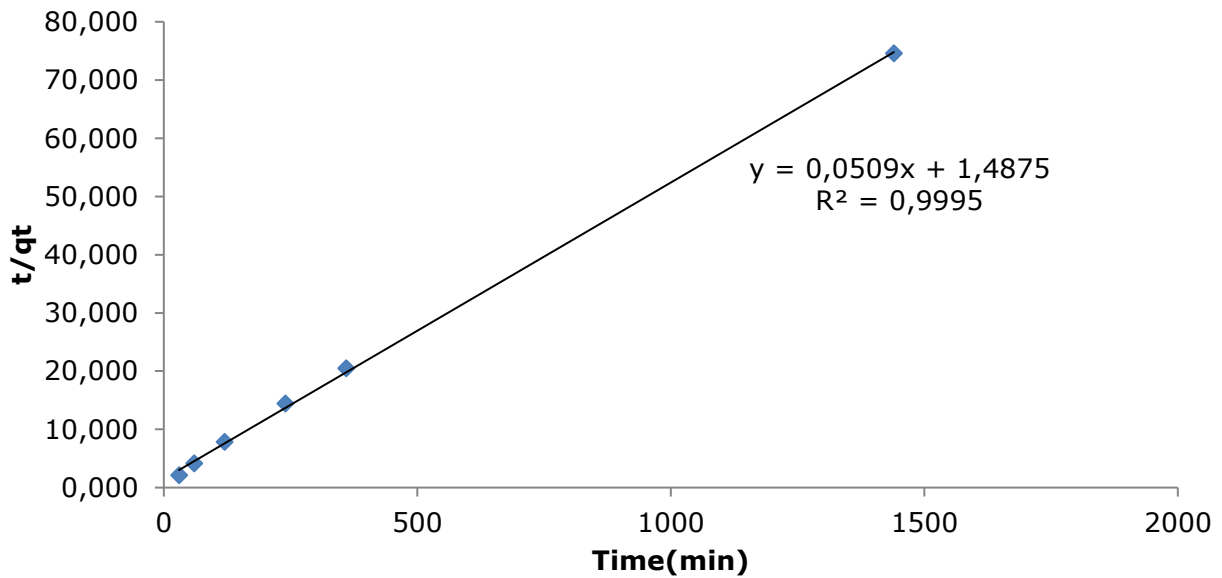


Figure 10: Pseudo-second-order kinetics for the adsorption of MB onto VSi-CTS-g-PAAm hydrogel.

Table 2: Kinetic parameters for the adsorption of MB onto VSi-CTS-g-PAAm hydrogel

Kinetic Model	Parameter	Value
Pseudo first order model	$K_1$ ( $\text{min}^{-1}$ )	0.0034
	$R^2$	0.998
Pseudo second order model	$K_2$ ( $\text{gmg}^{-1}\text{min}^{-1}$ )	1.4875
	$R^2$	0.999
Boyd model	$R^2$	0.998

To get further information regarding the mechanism of the adsorption process, the experimental data was fitted into the Boyd kinetic model using equation 8, and the result is shown in Figure 11. It can be seen that the straight does not pass through the origin; therefore, film diffusion or bulk mass transport mechanism could be suggested for the sorption

process, which may be attributed to electrostatic interaction between the VSi-CTS-g-PAAm hydrogel surface and the cationic MB dye molecules (34).

$$B_t = -0.4978 - \ln\left(1 - \frac{qt}{q\alpha}\right) \quad (8) \text{ Boyd kinetic model}$$

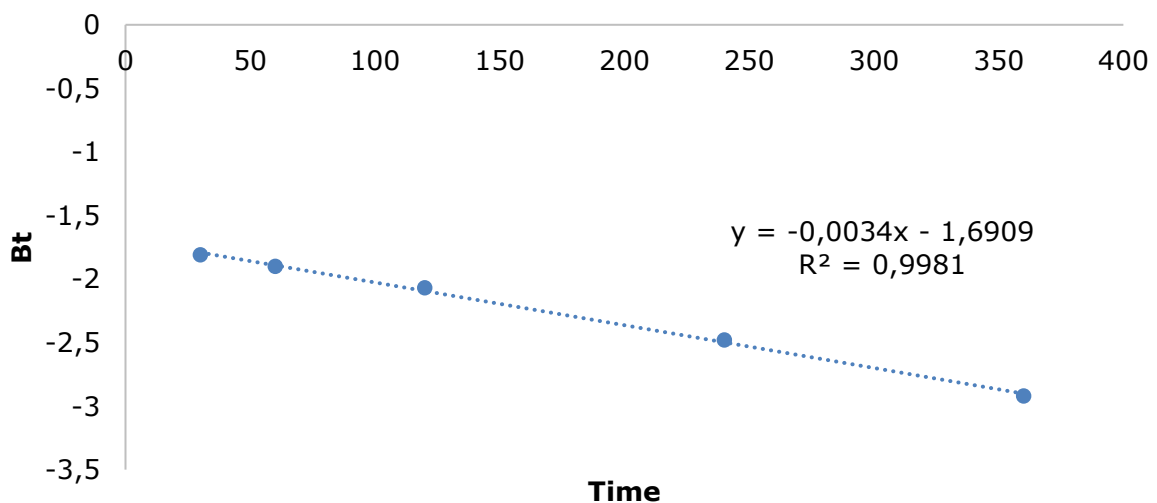


Figure 11: Boyd kinetic model for MB adsorption onto VSi-CTS-PAAm.

#### 4. CONCLUSION

Hydrogels prepared as VSi-CTS-g-PAAm were tested for the adsorption of MB dye from an aqueous solution. The study's findings indicate that several

elements, including the adsorbent dosage, the adsorbate concentration, the duration of contact, the pH level, and the temperature, influence the adsorption process. The obtained experimental data exhibited a favorable agreement with the Langmuir

isotherm model, indicating that the adsorption process adhered to a chemisorption mechanism, as evidenced by the pseudo-second-order kinetic behavior. The adsorption process was hypothesized to occur by either film diffusion or bulk mass transfer mechanisms, as indicated by the plot of the Boyd kinetic model. The hydrogel, known as VSi-CTS-g-PAAm, has been successfully synthesized and demonstrates the ability to adsorb methylene blue (MB) from aqueous solutions. This characteristic makes it a promising candidate for potential utilization in the remediation of wastewater contaminated with dyes.

## 5. CONFLICT OF INTEREST

There is no conflict of interest to declare.

## 6. REFERENCES

- Ogugbue CJ, Sawidis T. Bioremediation and detoxification of synthetic wastewater containing triarylmethane dyes by *Aeromonas hydrophila* Isolated from Industrial Effluent. *Biotechnol Res Int* [Internet]. 2011 Jul 25;2011:967925. Available from: [<URL>](#).
- Samchetshabam G, Hussan A, Choudhury TG. Impact of textile dyes waste on aquatic environments and its treatment revival of fisheries cooperatives and fisheries federation of Assam View project Hilsa Project View project. *Environ Ecol* [Internet]. 2017;35(3C):2349–53. Available from: [<URL>](#).
- Cai J, Zhang D, Xu W, Ding W-P, Zhu Z-Z, He J-R, et al. Polysaccharide-based hydrogels derived from cellulose: the architecture change from nanofibers to hydrogels for a putative dual function in dye wastewater treatment. *J Agric Food Chem* [Internet]. 2020 Sep 9;68(36):9725–32. Available from: [<URL>](#).
- Hameed BH. Spent tea leaves: A new non-conventional and low-cost adsorbent for removal of basic dye from aqueous solutions. *J Hazard Mater* [Internet]. 2009 Jan 30;161(2–3):753–9. Available from: [<URL>](#).
- Salleh MAM, Mahmoud DK, Karim WAWA, Idris A. Cationic and anionic dye adsorption by agricultural solid wastes: A comprehensive review. *Desalination* [Internet]. 2011 Oct 3;280(1–3):1–13. Available from: [<URL>](#).
- Bhatti HN, Akhtar N, Saleem N. Adsorptive Removal of Methylene Blue by Low-Cost Citrus sinensis Bagasse: Equilibrium, Kinetic and Thermodynamic Characterization. *Arab J Sci Eng* [Internet]. 2012 Jan 13;37(1):9–18. Available from: [<URL>](#).
- Bhatti HN, Safa Y. Removal of anionic dyes by rice milling waste from synthetic effluents: equilibrium and thermodynamic studies. *Desalin Water Treat* [Internet]. 2012 Oct;48(1–3):267–77. Available from: [<URL>](#).
- Mittal A, Jain R, Mittal J, Varshney S, Sikarwar S. Removal of Yellow ME 7 GL from industrial effluent using electrochemical and adsorption techniques. *Int J Environ Pollut* [Internet]. 2010;43(4):308–23. Available from: [<URL>](#).
- Daraei H, Mittal A, Noorisepehr M, Mittal J. Separation of chromium from water samples using eggshell powder as a low-cost sorbent: kinetic and thermodynamic studies. *Desalin Water Treat* [Internet]. 2015 Jan 2;53(1):214–20. Available from: [<URL>](#).
- Noreen S, Bhatti HN, Nausheen S, Sadaf S, Ashfaq M. Batch and fixed bed adsorption study for the removal of Drimarine Black CL-B dye from aqueous solution using a lignocellulosic waste: A cost affective adsorbent. *Ind Crops Prod* [Internet]. 2013 Oct 1;50:568–79. Available from: [<URL>](#).
- Puoci F, Iemma F, Spizzirri UG, Cirillo G, Curcio M, Picci N. Polymer in Agriculture: a Review. *Am J Agric Biol Sci* [Internet]. 2008 Jan 1;3(1):299–314. Available from: [<URL>](#).
- Kosemund K, Schlatter H, Ochsenhirt JL, Krause EL, Marsman DS, Erasala GN. Safety evaluation of superabsorbent baby diapers. *Regul Toxicol Pharmacol* [Internet]. 2009 Mar 1;53(2):81–9. Available from: [<URL>](#).
- Buenger D, Topuz F, Groll J. Hydrogels in sensing applications. *Prog Polym Sci* [Internet]. 2012 Dec 1;37(12):1678–719. Available from: [<URL>](#).
- Holback H, Yeo Y, Park K. Hydrogel swelling behavior and its biomedical applications. In: *Biomedical Hydrogels* [Internet]. Elsevier; 2011. p. 3–24. Available from: [<URL>](#).
- Grade S, Eberhard J, Neumeister A, Wagener P, Winkel A, Stiesch M, et al. Serum albumin reduces the antibacterial and cytotoxic effects of hydrogel-embedded colloidal silver nanoparticles. *RSC Adv* [Internet]. 2012 Jul 30;2(18):7190. Available from: [<URL>](#).
- Li S, Dong S, Xu W, Tu S, Yan L, Zhao C, et al. Antibacterial Hydrogels. *Adv Sci* [Internet]. 2018 May 1;5(5):1700527. Available from: [<URL>](#).
- Yang J, Chen Y, Zhao L, Feng Z, Peng K, Wei A, et al. Preparation of a chitosan/carboxymethyl chitosan/AgNPs polyelectrolyte composite physical hydrogel with self-healing ability, antibacterial properties, and good biosafety simultaneously, and its application as a wound dressing. *Compos Part B Eng* [Internet]. 2020 Sep 15;197:108139. Available from: [<URL>](#).
- Lu H, Wang X, Shi X, Yu K, Fu YQ. A phenomenological model for dynamic response of double-network hydrogel composite undergoing transient transition. *Compos Part B Eng* [Internet]. 2018 Oct 15;151:148–53. Available from: [<URL>](#).
- Jana S, Pradhan SS, Tripathy T. Poly(N,N-dimethylacrylamide-co-acrylamide) Grafted hydroxyethyl cellulose hydrogel: a useful congo red dye remover. *J Polym Environ* [Internet]. 2018 Jul

13;26(7):2730–47. Available from: [<URL>](#).

20. Ravi Kumar MN. A review of chitin and chitosan applications. *React Funct Polym* [Internet]. 2000 Nov 1;46(1):1–27. Available from: [<URL>](#).

21. Al-Harby NF, Albahly EF, Mohamed NA. Synthesis and characterization of novel uracil-modified chitosan as a promising adsorbent for efficient removal of congo red dye. *Polymers (Basel)* [Internet]. 2022 Jan 10;14(2):271. Available from: [<URL>](#).

22. Mohamed NA, Abd El-Ghany NA. Synthesis, characterization, and antimicrobial activity of carboxymethyl chitosan-graft-poly(n-acryloyl,n'-cyanoacetohydrazide) copolymers. *J Carbohydr Chem* [Internet]. 2012 Mar 1;31(3):220–40. Available from: [<URL>](#).

23. Abraham A, Solomon PA, Rejini VO. Preparation of chitosan-polyvinyl alcohol blends and studies on thermal and mechanical properties. *Procedia Technol* [Internet]. 2016 Jan 1;24:741–8. Available from: [<URL>](#).

24. Elmehbad NY, Mohamed NA. Terephthalohydrazido cross-linked chitosan hydrogels: synthesis, characterization and applications. *Int J Polym Mater Polym Biomater* [Internet]. 2022 Sep 2;71(13):969–82. Available from: [<URL>](#).

25. Elsayed NH, Monier M, Youssef I. Fabrication of photo-active trans -3-(4-pyridyl)acrylic acid modified chitosan. *Carbohydr Polym* [Internet]. 2017 Sep 15;172:1–10. Available from: [<URL>](#).

26. Anwar J, Shafique U, Waheed-uz-Zaman, Salman M, Dar A, Anwar S. Removal of Pb(II) and Cd(II) from water by adsorption on peels of banana. *Bioresour Technol* [Internet]. 2010 Mar 1;101(6):1752–5. Available from: [<URL>](#).

27. Elaigwu SE, Rocher V, Kyriakou G, Greenway GM. Removal of Pb<sup>2+</sup> and Cd<sup>2+</sup> from aqueous solution using chars from pyrolysis and microwave-assisted hydrothermal carbonization of *Prosopis africana* shell. *J Ind Eng Chem* [Internet]. 2014 Sep

25;20(5):3467–73. Available from: [<URL>](#).

28. Olgun A, Atar N. Equilibrium, thermodynamic and kinetic studies for the adsorption of lead (II) and nickel (II) onto clay mixture containing boron impurity. *J Ind Eng Chem* [Internet]. 2012 Sep 25;18(5):1751–7. Available from: [<URL>](#).

29. Shokry A, El Tahan A, Ibrahim H, Soliman M, Ebrahim S. Polyaniline/akaganeite superparamagnetic nanocomposite for cadmium uptake from polluted water. *Desalin Water Treat* [Internet]. 2019;171:205–15. Available from: [<URL>](#).

30. Bamgbose JT, Elaigwu SE, Adimula VO, Okeowo HO, Olayemi VT, Ameen OA, et al. Green route synthesis and adsorption studies of copper-benzimidazole coordination polymer for removal of methyl orange from water. *Chem Africa* [Internet]. 2023 Apr 14;Article in Press:1–12. Available from: [<URL>](#).

31. Tella AC, Bamgbose JT, Adimula VO, Omotoso M, Elaigwu SE, Olayemi VT, et al. Synthesis of metal-organic frameworks (MOFs) MIL-100(Fe) functionalized with thioglycolic acid and ethylenediamine for removal of eosin B dye from aqueous solution. *SN Appl Sci* [Internet]. 2021 Jan 13;3(1):136. Available from: [<URL>](#).

32. Al-qudah YHF, Mahmoud GA, Abdel Khalek MA. Radiation crosslinked poly (vinyl alcohol)/acrylic acid copolymer for removal of heavy metal ions from aqueous solutions. *J Radiat Res Appl Sci* [Internet]. 2014 Apr 1;7(2):135–45. Available from: [<URL>](#).

33. Chen X, Chen G, Chen L, Chen Y, Lehmann J, McBride MB, et al. Adsorption of copper and zinc by biochars produced from pyrolysis of hardwood and corn straw in aqueous solution. *Bioresour Technol* [Internet]. 2011 Oct 1;102(19):8877–84. Available from: [<URL>](#).

34. Elkady MF, El-Aassar MR, Hassan HS. Adsorption profile of basic dye onto novel fabricated carboxylated functionalized co-polymer nanofibers. *Polymers (Basel)* [Internet]. 2016 Apr 29 [cited 2023 Sep 5];8(5):177. Available from: [<URL>](#).



## Fabrication of Carbonaceous-Modified Halloysite Nanotubes for the Removal of Metal Ions from Aqueous Solution

Bahar Meryemoglu<sup>1\*</sup>, Burcak Kaya Ozsel<sup>2</sup>, Berna Nis<sup>2</sup>

<sup>1</sup> Cukurova University, Central Research Laboratory, Adana, 01330, Turkey.

<sup>2</sup> Bursa Technical University, Department of Chemistry, Bursa, 16310, Turkey.

**Abstract:** Halloysite nanotube-carbonaceous (HNT-C) composites were fabricated through one-pot hydrothermal carbonization of fructose and sodium carboxymethyl cellulose for use as an adsorbent for the removal of Pb(II), Zn(II), and Cu(II) from wastewater. The composites were chemically treated with sulfuric acid after carbonization. The acidic treatment of HNT-C structures contributed to a larger specific surface area and surface functionality, which was favorable for adsorbing more metal ions. Carbonaceous-modified HNTs were characterized by elemental analysis, FT IR, XRD, and BET analysis. Metal ion adsorption experiments were conducted with solutions containing low and high total metal ion concentrations (Cu, Zn, Pb) by mixing with HNT-C composites at a solid/liquid ratio of 1.0 and 10.0 g/L. The results indicated that the HNT C composites exhibited promising Zn(II) adsorption up to 94%, while no Zn(II) adsorbed onto unmodified HNTs. The amount of Pb(II), Zn(II), and Cu(II) ions that were taken up increased as the amount of adsorbent was increased up to 10 g/L in an aqueous solution. The HNT-C composites exhibited the highest adsorption efficiency for Pb(II) ions.

**Keywords:** Adsorbent, adsorption, halloysite nanotube, heavy metal, wastewater.

**Submitted:** February 8, 2023. **Accepted:** August 15, 2023.

**Cite this:** Meryemoglu M, Kaya Ozsel B, Nis B. Fabrication of Carbonaceous-Modified Halloysite Nanotubes for the Removal of Metal Ions from Aqueous Solution. JOTCSA. 2023;10(4):1019-24.

**DOI:** <https://doi.org/10.18596/jotcsa.1248970>

**\*Corresponding author's E-mail:** [meryemoglubahar@gmail.com](mailto:meryemoglubahar@gmail.com)

### 1. INTRODUCTION

Water pollution, which increases due to different factors day by day, is very dangerous not only for living things in the water but also for humans and plants in nature. Therefore, it is important to provide preventive measurements against water pollution and to create a culture in this regard. The main reason for the pollution of water is the different pollutants that are drained into nature without any treatment. These pollutants mix with the surface and groundwater and both disrupt their chemical formula and affect it physically (1). Water may become contaminated by the accumulation of heavy metals such as lead, copper, zinc, cadmium, and mercury through emissions from rapidly expanding industrial areas, mine tailings, disposal of high metal wastes, leaded gasoline and paints, pesticides, wastewater irrigation, and electronic waste (2). Heavy metal accumulation is the most dangerous dimension of chemical water pollution. Heavy metals have toxic effects when they exceed their concentration limits in both water and living organisms. They can cause health problems by affecting the psychological structure, even at very

low concentrations. The negative effects of polluted water on people are investigated by many disciplines, and the importance of measures to prevent pollution is emphasized. The World Health Organization (WHO) recommends 1.5, 0.015, and 5.0 mg/L as the maximum tolerable levels of copper (Cu (II)), lead (Pb (II)), and zinc (Zn (II)) ions in drinking water, respectively (3).

Halloysite nanotube (HNT) is a nanoclay with a tube-like morphology, and is composed of a bilayer aluminosilicate structure with a 1:1 Al:Si ratio (4). It has been shown that HNTs are good adsorbents used to remove metal ions from wastewater (5) due to the specific crystal formations, and the electrical and chemical characteristics of the external and internal surfaces of HNT. The applications of HNT structures are developing, particularly because HNTs are environmentally friendly, inexpensive, and have compatible behavior in preparing composites (6-10). Modified HNTs usually exhibit increased stability, due to reduced agglomeration and increased zeta potential values (11). HNTs can be used to adsorb various compounds and contaminated substances (12, 13). Kiani et al.

utilized the Taguchi technique to identify the optimal conditions for HNTs to remove Zn (II) from aqueous solutions (14).

In this study, HNT-carbonaceous composite adsorbents have been successfully synthesized through hydrothermal carbonization using two different carbon precursors and used to remove metal ions from wastewater. Functionalization of HNTs by incorporation of carbonaceous structure followed by acid treatment enhances the adsorption ability of the clay mineral, thus making the nanoclay a good candidate for metals' removal from aqueous solutions.

## 2. MATERIALS AND METHODS

### 2.1. Materials

Halloysite nanotube (HNT) (nanopowder, 1.26-1.34 mL/g pore volume) and sodium carboxymethyl cellulose (average mw ~90000) were supplied from Aldrich Chemistry. Sulfuric acid (98.0%) was purchased from Merck, d-fructose was purchased from VWR Chemicals, and ethanol (>99.9%) was supplied from ISOLAB.

### 2.2. Preparation and Characterization of HNT-C Composites

0.40 g of carbon precursor (fructose, sodium carboxymethyl cellulose) was dissolved in 40 mL DI water, and 0.50 g of HNT was added to the solution and stirred at a speed of 200 rpm at 25 °C for 12 h. The prepared mixture was heated in a 100 mL Teflon-lined stainless steel reactor at 160 °C for 48 h. The cooled sample was filtered through a 0.45 µm Teflon filter, washed sequentially with water and ethanol, and dried in a vacuum oven at 60°C (15). For acid treatment; 0.50 g of HNT-C composite was dispersed in 12.5 mL of a 4.0 M H<sub>2</sub>SO<sub>4</sub> solution. The dispersion was heated at 85 °C under stirring for 8 h, then allowed to cool to 25 °C and again stirred for 16 h at room temperature. The obtained powder was filtered, washed with ethanol, and dried in a vacuum oven at 60 °C (16). The fructose and sodium carboxymethyl cellulose-modified HNTs were abbreviated to HNT-FC and HNT-CC, respectively. For comparison, unmodified-HNTs were also used in adsorption experiments.

The carbon contents of composites were determined using a Thermo Scientific FlashSmart Elemental Analyzer. The total surface area and pore size of the composites were obtained from N<sub>2</sub> adsorption-desorption analysis using a Micromeritics Gemini VII instrument, and prior to the analysis, the samples were outgassed for 10 h at 473 K. The pore volume data were obtained using the Barrett-Joyner-

Halenda (BJH) method, and the surface areas were obtained using the Brunauer, Emmet, and Teller (BET) method. The X-ray diffraction patterns were obtained using a PANalytical Empyrean XRD diffractometer with Cu K $\alpha$  radiation (0.1540 nm) at 45KV. Scanned data was detected in the 2 $\theta$ =7° to 60° range. The FT-IR spectra of composites were collected using a JASCO FT-IR spectrophotometer using ATR from 4000 to 400 cm<sup>-1</sup>.

### 2.3. Adsorption Experiments

Metal ion adsorption experiments were conducted with a solution containing 1.0 (low) and 10.0 (high) ppm total metal ions' concentration (Cu, Zn, Pb) mixed with HNT-C composites at a solid/liquid ratio of low and high amounts of adsorbents (1.0 and 10.0 g/L). The mixture was stirred continuously for 24 h at 21 °C to determine the adsorption capacity. The amounts of ions adsorbed on HNT-C composites were calculated from the concentrations in the solution before and after adsorption. An inductively coupled plasma atomic emission spectroscopy (ICP-OES, Perkin Elmer Optima 7000) method was used to determine the content of the following elements in the solution: zinc (Zn), copper (Cu), and lead (Pb).

## 3. RESULTS AND DISCUSSION

### 3.1. Characterization of HNT-Carbonaceous Composites

It can be observed from the result of the elemental analysis that carbonaceous structure was successfully incorporated into the HNTs after the carbonization process (Table 1). The specific surface area and pore structure are both crucial factors affecting adsorption performance. The specific surface area and pore volume values of raw HNTs decreased after the carbonization process (HNT-FC\*). After the acid treatment, the specific surface areas and the pore volumes of the HNT-C composites increased (HNT-FC and HNT-CC) suggesting that the acid treatment significantly contributed to the specific surface area and pore volume increment without affecting the carbon ratio on the HNT structure. It was notable that the C loading ratio was higher for the composite prepared with fructose (HNT-FC) than for the one prepared with sodium carboxymethyl cellulose (HNT-CC). The use of fructose as a carbon precursor was more effective than the use of carboxymethyl cellulose as a hydrothermal carbonization precursor probably due to its simple structure, which makes it easier to incorporate and disperse into the HNT structure. The lowest C loading detected for HNT-CC can be attributed to the polymeric structure of the precursor.

**Table 1:** Specific surface areas, pore characteristics, and carbon contents of HNT and HNT-C composites.

Samples	BET Surface Area (m <sup>2</sup> /g)	Pore Volume (cm <sup>3</sup> /g)	Pore width (nm)	Carbon (%)
HNT	64.0	1.26-1.34	-	-
HNT-FC*	40.7	0.34	30.2	8.5
HNT-FC	117.9	0.44	16.2	9.9
HNT-CC	126.6	0.60	20.3	7.5

\* HNT-C composite sample prepared without sulfuric acid treatment.

Figure 1 exhibits the FT-IR spectra of unmodified-HNTs and HNT-C composites. The double absorption peaks at 3695.2 and 3622.5 cm<sup>-1</sup> were attributed to

the stretching vibration of the inner-surface hydroxyl group of HNTs (17-19). The small peak in unmodified-HNTs spectra occurred at 3543 cm<sup>-1</sup> for



O-H with an intermolecular hydrogen group, but it disappeared in HNT-C composite spectra. One possible reason for the disappearance of this peak is the breakage of bonds due to the acid treatment (19). The in-plane stretching vibration of the Si-O bonds as indicated by peaks in the HNTs spectra in the fingerprint region between 2000 and 500  $\text{cm}^{-1}$ ,

at 1027 and 911  $\text{cm}^{-1}$ , respectively, while symmetric stretching of Si-O-Si was seen at 794  $\text{cm}^{-1}$ . The band at 1116  $\text{cm}^{-1}$ , which is indicative of Si-O stretching vibrations of  $\text{SiO}_2$ , was still observed in the spectra of HNT-composites despite the modification (Figure 1) (20).

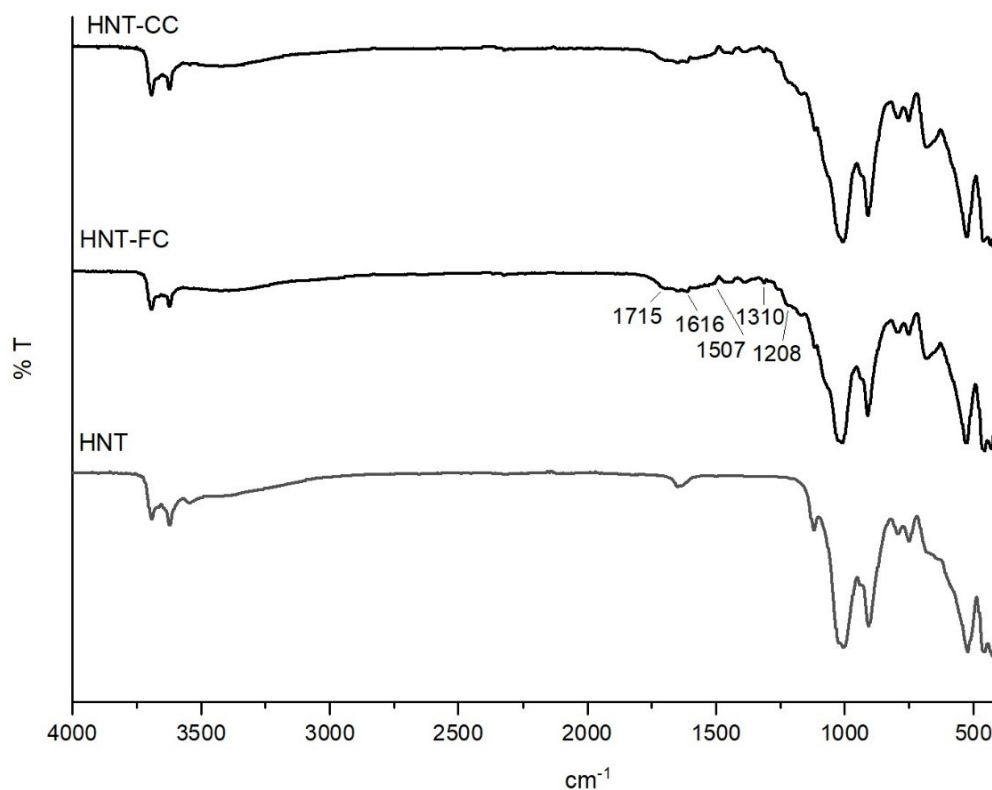


**Figure 1:** The FT-IR spectra of unmodified HNT and HNT-C composites.

Compared to the unmodified-HNTs some new peaks appeared around 1700  $\text{cm}^{-1}$ , 1300  $\text{cm}^{-1}$ , 1600  $\text{cm}^{-1}$ , and 1200  $\text{cm}^{-1}$  on the spectra of HNT-C structures. The peak at 1715  $\text{cm}^{-1}$  is assigned to C=O stretching vibrations, while the peaks at 1310  $\text{cm}^{-1}$  and 1208  $\text{cm}^{-1}$  are attributed to C-O stretching vibrations. The peaks at 1616  $\text{cm}^{-1}$  and 1507  $\text{cm}^{-1}$  are ascribed to C=C stretching vibrations (21). These results indicated that carbonaceous materials were successfully introduced into the HNT structure.

The XRD patterns of the HNT-C composites and unmodified- HNTs are shown in Figure 2. All samples showed the typical characteristic diffraction angles of HNTs at  $2\theta=12.2^\circ$ ,  $20^\circ$ ,  $24.8^\circ$ ,  $26.6^\circ$ ,  $30^\circ$ ,  $35^\circ$ , and  $55.4^\circ$  as marked in Figure 2 (22, 23). The main diffraction at  $2\theta$ , which is associated with the planes at  $12^\circ(001)$ , is visible in the XRD pattern of HNTs. But similar peaks were visible at a slightly shifted angle ( $2\theta=9^\circ$ ) in unmodified HNT. It has been proven that HNT can continue to be structurally stable even after chemical changes (24). After the modification and following acid treatment, there was no significant change in the XRD peaks, implying that the crystal structure of HNTs was not damaged. The diffraction spectrum of the produced HNT-C composites has a broad peak at  $2\theta=24.8^\circ$

which is the typical peak of the 002 crystal plane of carbon (25).

### 3.2. Adsorption Performance of HNT-Carbonaceous Composites

Adsorption experiments were carried out to compare the adsorption capacities of HNT-C composites and unmodified-HNTs on the removal of heavy metals from water. To determine the effect of total ion concentration on the adsorption behavior of HNT-C composites, adsorption experiments were first achieved with a constant low dosage of adsorbent (1.0 g/L) at total ion concentration ranges of 1.0 and 10.0 ppm. As can be seen from Figure 3.a., HNT-FC and HNT-CC have a higher adsorption capacity than unmodified-HNTs at 1.0 ppm total ion concentration. It was interesting that there was a significant difference in the adsorption of  $\text{Zn}^{2+}$ . While unmodified-HNTs have no capability to adsorb  $\text{Zn}^{2+}$ , the adsorption of  $\text{Zn}^{2+}$  was significantly increased up to 19.0% by using the HNT-FC composite. After modifying the HNT structure by hydrothermal carbonization of fructose or carboxymethyl cellulose, a carbonaceous layer was introduced on the HNTs with organic functional groups (-OH and -COOH) that play an important role in the adsorption of ions. On the other hand, before

the acid treatment, the specific surface area of HNT-FC was only 40.7 m<sup>2</sup>/g, a small specific surface area for adsorption, and this value reached 117.9 m<sup>2</sup>/g (or more) by the acid treatment. The results showed that acid treatment is an effective method of

improving the adsorption properties by increasing the surface area of the structures.

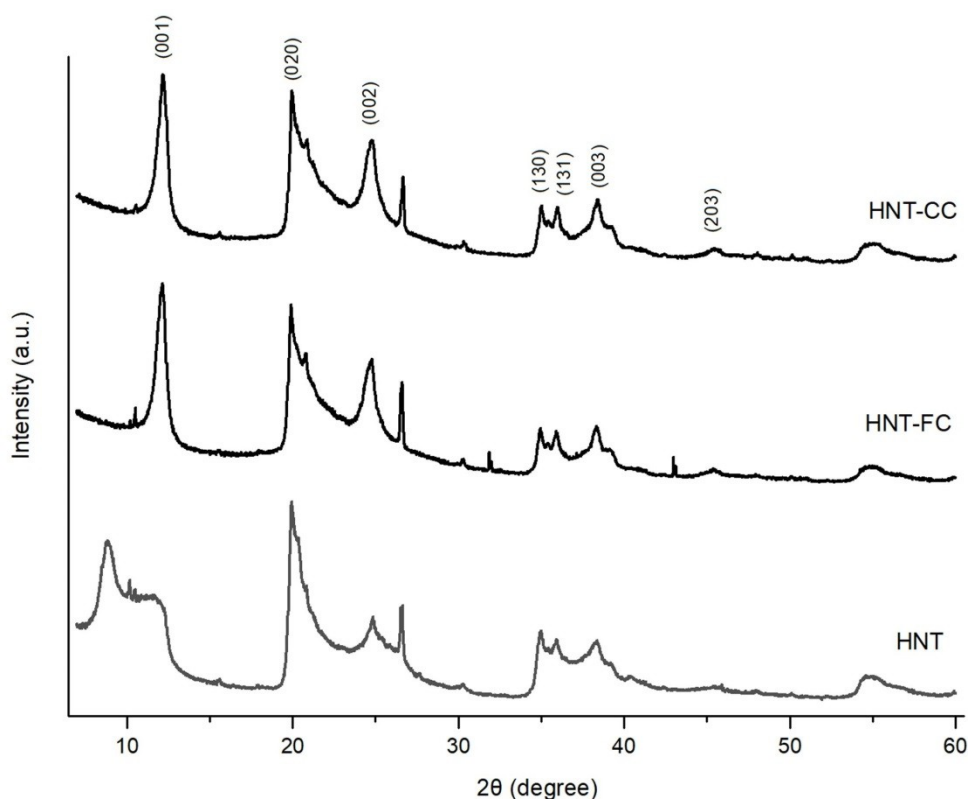


**Figure 2:** The XRD patterns of unmodified-HNT and HNT-C composites.

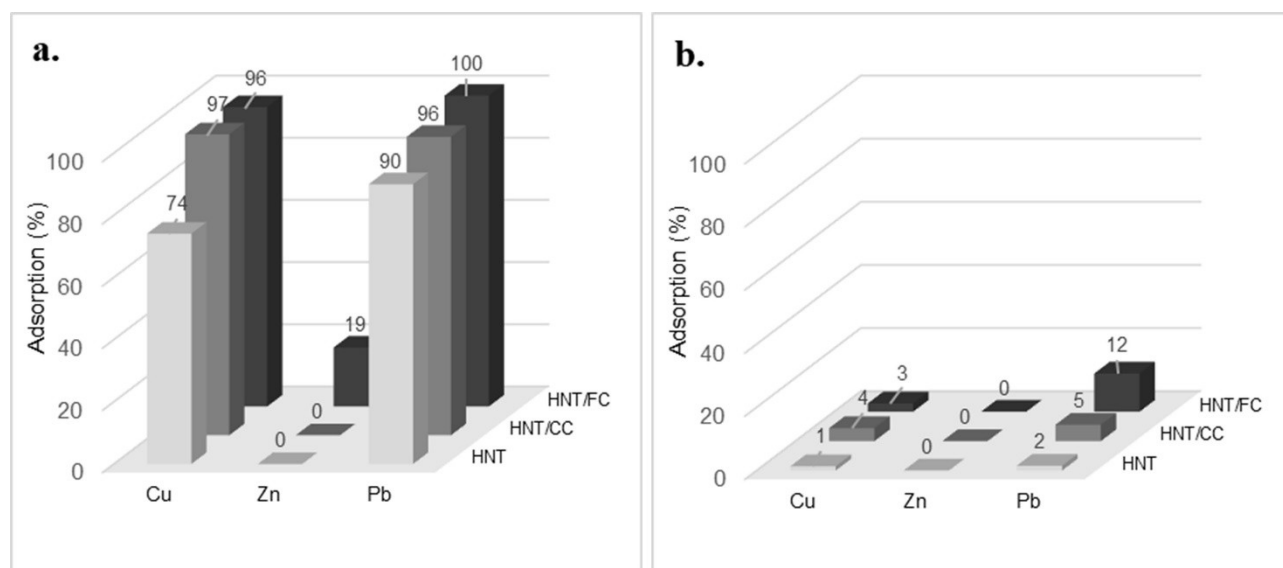


**Figure 3:** Effect of metal concentration a. 1.0 ppm, b. 10.0 ppm at a 1.0 g/L adsorbent dosage.

As can be seen in Figure 3. b., the removal efficiency of adsorbents decreased with the increase in total ion concentration. For instance, the removal ratio of Pb(II) with HNT-FC from the solution decreased from 100% to 12% when the total ion concentration increases from 1.0 to 10.0 ppm. The overall reduction in the removal efficiency of ions was probably due to the saturation of adsorption

sites with the increase in the quantity of ions in the solution. Zn(II) absorption was not observed on unmodified-HNTs and HNT-CC structures, regardless of initial total ion concentration. The sorption capacity of HNT-FC for Zn(II) was higher than that of HNT-CC probably due to the higher carbon content that provides more active acidic sites for metal adsorption.

As a continuation of the study, HNT-C composites' adsorption experiments were also achieved with a constant high dosage of adsorbent (10.0 g/L) at a total ion concentration range of 1.0 and 10.0 ppm. As can be seen in Figure 4.a., Cu and Pb removal efficiency was nearly 100% at low initial metal concentrations for all adsorbents. The removal efficiency of Zn(II) ions increased sharply with increasing the adsorbent concentrations from 1 to 10 g/L for HNT-C composites, while no Zn(II) adsorbed onto unmodified HNT. The HNT-CC and HNT-FC composites exhibited a promising performance in the removal of Zn (II) ions. The percentage adsorption increased from 0% to 84.0% and from 19.0% to 94.0% for Zn(II) with HNT-CC and HNT-FC, respectively, over the same total ion concentration (Figure 3.a. and Figure 4.a.) It might

have been attributed to the fact that increasing the adsorbent dosage provided a larger surface area and more binding sites for the metal ions. On the other hand, according to Fig. 4.b., the percentage adsorption efficiency sharply decreased with increasing the total ion concentration to 10.0 ppm at 10.0 g/L adsorbent dosage, probably due to the adsorbent saturation. These three metal cations also have different sorption capacities for the adsorbents. The obtained HNT-C composites show good adsorption capacity, especially for Pb(II), a higher adsorption efficiency was obtained for Pb(II) compared to Cu(II) and Zn(II). This may be explained by the low hydration enthalpy of Pb(II) that permits the detachment of water molecules from cations and then lets the ion interact with the functional groups on adsorbents (26, 27).

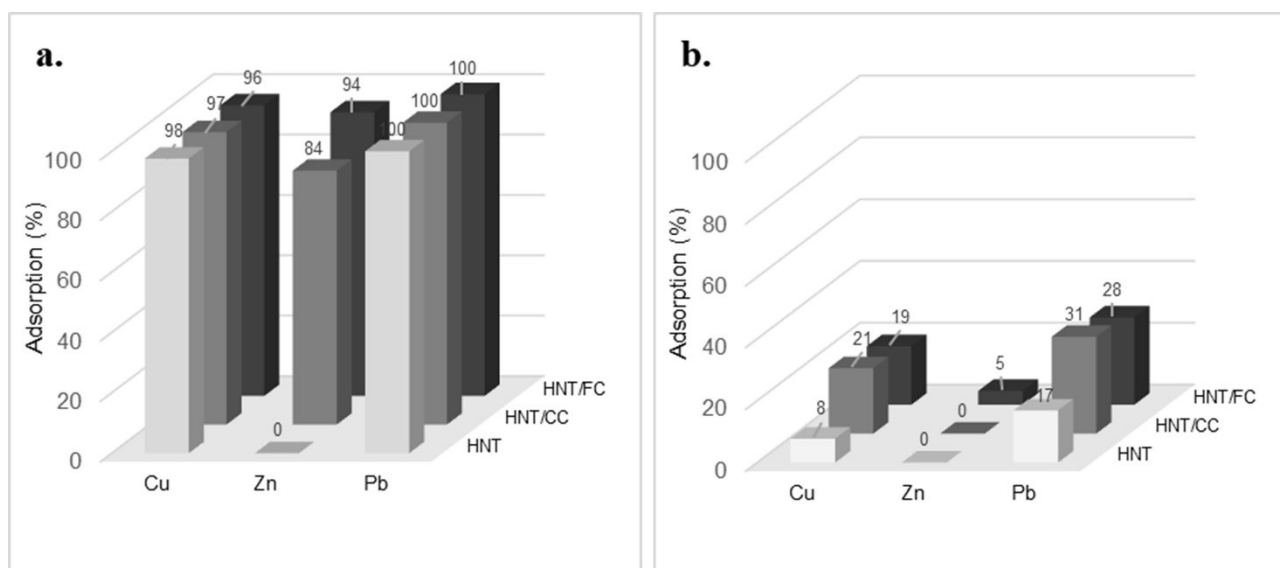


**Figure 4:** Effect of metal concentration a. 1.0 ppm, b. 10.0 ppm at a 10.0 g/L adsorbent dosage.

#### 4. CONCLUSION

In the study, halloysite nanotubes, a naturally occurring clay mineral, were used as raw materials to produce functional HNT-C adsorbents for the removal of heavy metals, including Cu(II), Pb(II), and Zn(II), from wastewater. The experimental results demonstrate that the adsorption capacity of the HNTs increases significantly with the incorporation of carbonaceous layers into the structure. The acid treatment after the hydrothermal carbonization process provided significant enhancement of specific surface area and pore characteristics of HNT-C composites. HNT-C composites can be evaluated as a potential low-cost and eco-friendly adsorbent material.

#### 5. CONFLICT OF INTEREST

No potential conflict of interest was reported by the authors.

#### 6. ACKNOWLEDGMENTS

The authors gratefully acknowledge Cukurova University and Bursa Technical University for providing research infrastructure support.

#### 7. REFERENCES

1. Sönmez AY, Hisar O, Karataş M, Arslan G, Aras MS. Sular Bilgisi. 2nd edition. Ankara: Nobel Yayın Dağıtım A.Ş.; 2008.
2. Sankhla MS, Kumari M, Nandan M, Kumar R, Agrawal P. Heavy Metals Contamination in Water and their Hazardous Effect on Human Health-A Review. *Int J Curr Microbiol Appl Sci* [Internet]. 2016 Oct 15;5(10):759–66. Available from: [<URL>](#).
3. World Healthy Organization (WHO). Guidelines for drinking-water quality: recommendations. World Healthy Organization; 2004.
4. Allalou S, Kheribet R, Benmounah A. Effects of calcined halloysite nano-clay on the mechanical properties and microstructure of low-clinker cement mortar. *Case Stud Constr Mater* [Internet]. 2019 Jun 1;10:e00213. Available from: [<URL>](#).
5. Kiani G. High removal capacity of silver ions from aqueous solution onto Halloysite nanotubes. *Appl Clay Sci* [Internet]. 2014 Mar 1;90:159–64. Available from: [<URL>](#).
6. Cataldo S, Lazzara G, Massaro M, Muratore N, Pettignano A, Riela S. Functionalized halloysite

- nanotubes for enhanced removal of lead(II) ions from aqueous solutions. *Appl Clay Sci* [Internet]. 2018 May 1;156:87–95. Available from: [<URL>](#).
7. Hermawan AA, Chang JW, Pasbakhsh P, Hart F, Talei A. Halloysite nanotubes as a fine grained material for heavy metal ions removal in tropical biofiltration systems. *Appl Clay Sci* [Internet]. 2018 Aug 1;160:106–15. Available from: [<URL>](#).
8. Luo P, Zhang J, Zhang B, Wang J, Zhao Y, Liu J. Preparation and Characterization of Silane Coupling Agent Modified Halloysite for Cr(VI) Removal. *Ind Eng Chem Res* [Internet]. 2011 Sep 7;50(17):10246–52. Available from: [<URL>](#).
9. Yu L, Wang H, Zhang Y, Zhang B, Liu J. Recent advances in halloysite nanotube derived composites for water treatment. *Environ Sci Nano* [Internet]. 2016 Feb 11;3(1):28–44. Available from: [<URL>](#).
10. Jiang L, Zhang C, Wei J, Tjiu W, Pan J, Chen Y, et al. Surface modifications of halloysite nanotubes with superparamagnetic Fe<sub>3</sub>O<sub>4</sub> nanoparticles and carbonaceous layers for efficient adsorption of dyes in water treatment. *Chem Res Chinese Univ* [Internet]. 2014 Dec 18;30(6):971–7. Available from: [<URL>](#).
11. Tharmavaram M, Pandey G, Rawtani D. Surface modified halloysite nanotubes: A flexible interface for biological, environmental and catalytic applications. *Adv Colloid Interface Sci* [Internet]. 2018 Nov 1;261:82–101. Available from: [<URL>](#).
12. Maziarz P, Prokop A, Matusik J. A comparative study on the removal of Pb(II), Zn(II), Cd(II) and As(V) by natural, acid activated and calcinated halloysite. *Geol Geophys Environ* [Internet]. 2015 Aug 5;41(1):108–9. Available from: [<URL>](#).
13. Deng L, Yuan P, Liu D, Annabi-Bergaya F, Zhou J, Chen F, et al. Effects of microstructure of clay minerals, montmorillonite, kaolinite and halloysite, on their benzene adsorption behaviors. *Appl Clay Sci* [Internet]. 2017 Jul 1;143:184–91. Available from: [<URL>](#).
14. Kiani G, Soltanzadeh M, Ahadzadeh I. Adsorption study of Zinc ion onto halloysite nanotubes using taguchi's design of experimental methodology. *Int J Nano Dimens* [Internet]. 2018 Aug 1;9(3):246–59. Available from: [<URL>](#).
15. Tian X, Wang W, Tian N, Zhou C, Yang C, Komarneni S. Cr(VI) reduction and immobilization by novel carbonaceous modified magnetic Fe<sub>3</sub>O<sub>4</sub>/halloysite nanohybrid. *J Hazard Mater* [Internet]. 2016 May 15;309:151–6. Available from: [<URL>](#).
16. Silva SM, Peixoto AF, Freire C. HSO<sub>3</sub>-functionalized halloysite nanotubes: New acid catalysts for esterification of free fatty acid mixture as hybrid feedstock model for biodiesel production. *Appl Catal A Gen* [Internet]. 2018 Nov 25;568:221–
30. Available from: [<URL>](#).
17. Leng Y. *Materials Characterization: Introduction to Microscopic and Spectroscopic Methods*. Singapore: John Wiley & Sons (Asia) Pte Ltd; 2008.
18. Peixoto AF, Fernandes AC, Pereira C, Pires J, Freire C. Physicochemical characterization of organosilylated halloysite clay nanotubes. *Microporous Mesoporous Mater* [Internet]. 2016 Jan 1;219:145–54. Available from: [<URL>](#).
19. Gaaz T, Sulong A, Kadhum A, Nassir M, Al-Amiery A. Impact of Sulfuric Acid Treatment of Halloysite on Physico-Chemic Property Modification. *Materials (Basel)* [Internet]. 2016 Jul 26;9(8):620. Available from: [<URL>](#).
20. Peña L, Hohn KL, Li J, Sun XS, Wang D. Synthesis of Propyl-Sulfonic Acid-Functionalized Nanoparticles as Catalysts for Cellobiose Hydrolysis. *J Biomater Nanobiotechnol* [Internet]. 2014 Sep 30;5(4):241–53. Available from: [<URL>](#).
21. Wang P, Tang Y, Liu Y, Wang T, Wu P, Lu X-Y. Halloysite nanotube@carbon with rich carboxyl groups as a multifunctional adsorbent for the efficient removal of cationic Pb(II), anionic Cr(VI) and methylene blue (MB). *Environ Sci Nano* [Internet]. 2018 Oct 11;5(10):2257–68. Available from: [<URL>](#).
22. Gaaz T, Sulong A, Kadhum A, Nassir M, Al-Amiery A. Surface Improvement of Halloysite Nanotubes. *Appl Sci* [Internet]. 2017 Mar 16;7(3):291. Available from: [<URL>](#).
23. Feng J, Fan H, Zha D, Wang L, Jin Z. Characterizations of the Formation of Polydopamine-Coated Halloysite Nanotubes in Various pH Environments. *Langmuir* [Internet]. 2016 Oct 11;32(40):10377–86. Available from: [<URL>](#).
24. Liu J, Wang C, Cui J, Li J, Li Q, Liu M, et al. Mesoporous carbon prepared by etching halloysite nanotubes (HNTs) with pyrrole as a precursor for a sulfur carrier of superior lithium–sulfur batteries. *RSC Adv* [Internet]. 2019 Apr 23;9(22):12331–8. Available from: [<URL>](#).
25. Wang A, Kang F, Huang Z, Guo Z, Chuan X. Synthesis of mesoporous carbon nanosheets using tubular halloysite and furfuryl alcohol by a template-like method. *Microporous Mesoporous Mater* [Internet]. 2008 Feb 1;108(1–3):318–24. Available from: [<URL>](#).
26. Amarasinghe BMWPK, Williams RA. Tea waste as a low cost adsorbent for the removal of Cu and Pb from wastewater. *Chem Eng J* [Internet]. 2007 Aug 1;132(1–3):299–309. Available from: [<URL>](#).
27. Zendelska A, Golomeova M. Effect of competing cations (Cu, Zn, Mn, Pb) adsorbed by natural zeolite. *Int J Sci Eng Technol* [Internet]. 2014;2(5):483–92. Available from: [<URL>](#).



## Stability Indicating RP-HPLC Method Development and Validation for Simultaneous Estimation of Dapagliflozin Propanediol Monohydrate and Teneligliptin Hydrobromide Hydrate in Synthetic Mixture

Hiteksha Dobariya<sup>1\*</sup> , Urvi Chotaliya<sup>1</sup>

<sup>1</sup> B. K. Mody Government Pharmacy College, Rajkot, Gujarat, India, Postal code: 360003

**Abstract:** For the quantitative measurement of Dapagliflozin propanediol monohydrate and Teneligliptin hydrobromide hydrate in synthetic mixture form in the presence of its degradants, precise, accurate, robust, cost-effective, and isocratic stability indicating RP-HPLC method was developed and validated. The mobile phase comprises [Methanol: 20 mM Ammonium formate (70:30 v/v)] at a flow rate of 1.0 ml/min, injection volume of 20  $\mu$ l, and UV detection at 225 nm. Separation was accomplished using Gemini, C18 column. Teneligliptin hydrobromide hydrate and Dapagliflozin propanediol monohydrate were eluted with retention times of 6.65 minutes and 4.20 minutes, respectively. This procedure was approved following ICH guideline Q2 (R1). The calibration plots for Dapagliflozin propanediol monohydrate and Teneligliptin hydrobromide hydrate have correlation coefficients of 0.9995 and 0.9996 over the concentration ranges of 5-100  $\mu$ g/ml and 10-200  $\mu$ g/ml respectively. For Dapagliflozin propanediol monohydrate and Teneligliptin hydrobromide hydrate, accuracy ranged from 99.81-100.78% and 99.13-100.69%, respectively. For Dapagliflozin propanediol monohydrate and Teneligliptin hydrobromide hydrate, the LOD was found to be 0.947  $\mu$ g/ml and 1.355  $\mu$ g/ml. In contrast, the LOQ was 2.869  $\mu$ g/ml and 4.107  $\mu$ g/ml, respectively. The findings demonstrated the applicability of the devised approach for routine analysis of Teneligliptin hydrobromide hydrate and Dapagliflozin propanediol monohydrate in a synthetic mixture form with its degradants.

**Keywords:** Dapagliflozin propanediol monohydrate, Teneligliptin hydrobromide hydrate, RP- HPLC, Stability indicating method, Validation

**Submitted:** April 26, 2023. **Accepted:** August 17, 2023.

**Cite this:** Dobariya H, Chotaliya U. Stability Indicating RP-HPLC Method Development and Validation for Simultaneous Estimation of Dapagliflozin Propanediol Monohydrate and Teneligliptin Hydrobromide Hydrate in Synthetic Mixture. JOTCSA. 2023;10(4):1025-1034.

**DOI:** <https://doi.org/10.18596/jotcsa.1288000>.

**\*Corresponding author.** E-mail: [hiteksha134@gmail.com](mailto:hiteksha134@gmail.com)

### 1. INTRODUCTION

The chemical name of Dapagliflozin propanediol monohydrate (DAPA) is (2S)-propane-1,2-diol (2S,3R,4R,5S,6R)-2-[(4-chloro-3-[(4-ethoxyphenyl)methyl]phenyl)-6-

(hydroxymethyl)oxane-3,4,5-triol hydrate, Structure shown in Figure 1. Dapagliflozin propanediol monohydrate is an SGLT-2 inhibitor and treats type-2 diabetes mellitus (1).

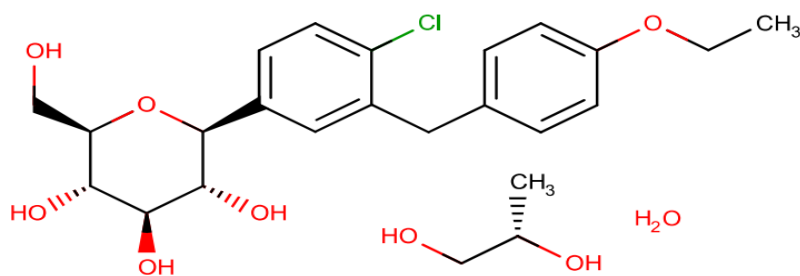


**Figure 1:** Structure of Dapagliflozin propanediol monohydrate

Teneligliptin hydrobromide hydrate (TENE) is {(2*S*,4*S*)-4-[4-(5-Methyl-2-phenylpyrazol-3-yl) piperazin-1-yl] pyrrolidin-2-yl} (1,3 thiazolidin-3-

yl) methanone; hydrate; pentahydrobromide, Structure shown in Figure 2. It is indicated for treating type 2 diabetes mellitus (2).

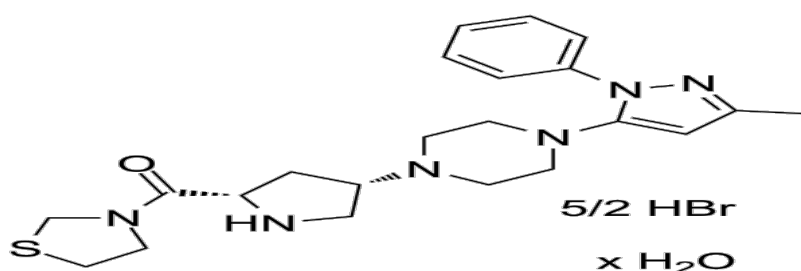


**Figure 2:** Structure of Teneligliptin hydrobromide hydrate

Analytical quality by design (AQbD) and CCD help in regulatory compliance for RP-HPLC method development, stress testing, or stability-indicating methods (3-6). UV spectrophotometric methods (simultaneous equation method/ Vierodt') and LC-MS are widely acceptable for the simultaneous estimation of pharmaceutical combinations (7-9). The presence of impurities or degradants critically affects the stability and pharmacological action of pharmaceutical API and drug products (10-14). The purpose of stability and related substance study is to provide evidence on how the quality of a drug substance or product varies with time under the influence of various environmental factors (15-16).

Developing this approach has been clearly mandated since the International Council for Harmonization of Technical Requirements for Pharmaceuticals for Human Use (ICH) was created. The information on how the quality of the drug changes with changes in environmental elements, such as pH, humidity, temperature, light, etc., can be provided by stability-indicating methods. Moreover, SIM aids a formulator in selecting appropriate vehicles when creating novel formulations (17-18).

A literature review showed a UV (19) method for combining Dapagliflozin propanediol monohydrate and Teneligliptin hydrobromide hydrate. Still, no

single approach is available for stability, indicating simultaneous estimation of Dapagliflozin propanediol monohydrate and Teneligliptin hydrobromide hydrate (20-33). There were many analytical methods reported for Dapagliflozin propanediol monohydrates, such as RP-HPLC (34-36), RP-HPLC (stability indicating method) (37), and UV spectroscopy (38-39) in combination with saxagliptin, metformin, and sitagliptin. There were few analytical methods reported for Teneligliptin hydrobromide hydrates, such as RP-HPLC (40-43), RP-HPLC (stability indicating method) (44-45), and UV spectroscopy (46-47) reported in combination with metformin, rosuvastatin, remogliflozin, and pioglitazone.

## 2. MATERIALS AND METHODS

### 2.1. Materials and Chemicals

Dapagliflozin propanediol monohydrate and Teneligliptin hydrobromide hydrate were supplied by Merrill Pharma Pvt. Ltd. as gift samples and manufactured by Morphan Laboratories and Aalidhra Pharma Chem. respectively. This fixed dose combination is under clinical trial phase 3. So, the synthetic mixture was used for the estimation. Dapagliflozin propanediol monohydrate is White to off-white powder, and Teneligliptin hydrobromide hydrate is White/off-white crystalline powder.

## 2.2. HPLC Instrumentation and Chromatographic Conditions

The method was developed using a Shimadzu HPLC instrument with a Photodiode Array Detector. At 40°C, [MeOH:20mM Ammonium formate (70:30 v/v)] was used as mobile phase, which was pumped at a flow rate of 1 ml per minute, and Gemini, C18, (250×4.6 mm, 5µm) column as a stationary phase. The successful detection had a wavelength of 225 nm.

## 2.3. Preparation of Solutions

### 2.3.1. Preparation of standard stock solution of 400 µg/ml of Dapagliflozin propanediol monohydrate

A 100 ml volumetric flask combined 40 mg of Dapagliflozin propanediol monohydrate with 70% of the diluent. The resulting mixture was subjected to sonication to facilitate dissolution. Subsequently, the remaining diluent was added to reach the desired volume mark on the flask, followed by additional sonication to ensure complete dissolution. The concentration of Dapagliflozin propanediol monohydrate in the resulting solution will be 400 µg/ml.

### 2.3.2. Preparation of Standard stock solution of 800 µg/ml of Teneligliptin hydrobromide hydrate

An 80 mg of atorvastatin calcium was introduced into a volumetric flask with a capacity of 100 ml. Subsequently, 70% of the diluent was added, followed by sonication to facilitate dissolution. The remaining diluent was added, and the resulting mixture was stirred well. The resulting solution will contain a Teneligliptin hydrobromide hydrate concentration at 800 µg/ml.

## 3. FORCED DEGRADATION STUDIES

Acid hydrolysis was carried out by using 1 N HCl for 48 hours, and base hydrolysis was carried out by using 1 N NaOH for 6 hours and then neutralized the mixture solution and made up to the final volume. Oxidative hydrolysis was carried out using 3% H<sub>2</sub>O<sub>2</sub> for 30 minutes in a thermal degradation sample placed in a hot air oven at 70°C for 60 hours. The photodegradation sample was carried out using a UV chamber for 60 hours.

## 4. METHOD VALIDATION

Analytical validation parameters for this proposed method were determined according to the ICH Q2(R1) guideline (48).

### 4.1. Linearity

Linearity has been established over six different concentrations by plotting the calibration curve of peak area v/s concentration.

### 4.2. Accuracy

Drug to drug spiking accuracy was done at three levels: 80%, 100%, and 120%. Three sets were prepared for each level, and the percentage recovery was calculated.

### 4.3. Precision

Interday and intraday precision were performed by taking 80, 100, and 120 percent of the target concentration. Repeatability was achieved by taking six replicate injections of the standard preparation. The outcome was noted as Relative Standard Deviation (RSD).

### 4.4. Limit of detection (LOD) and limit of quantitation (LOQ)

LOD and LOQ were found by the equation as per ICH guidelines.

$$LOD = 3.3 \times \sigma / S \text{ and } LOQ = 10 \times \sigma / S$$

Where,  $\sigma$  was the SD of the response, and S was the mean slope of the calibration curves.

### 4.5. Specificity

In specificity, % interference was measured after injecting a blank (mobile phase), placebo; standard DAPA and TENE solution spiked with excipients, and a test solution.

### 4.6. Robustness

Robustness was performed by deliberate change in flow rate ( $\pm 0.1$  ml/min), column oven temperature ( $40 \pm 1^\circ\text{C}$ ), and mobile phase composition. Robustness was calculated in terms of RSD.

### 4.7. Assay of synthetic mixture

10 mg of dapagliflozin propanediol monohydrate and 20 mg of teneligliptin hydrobromide hydrate were added into a 100 ml volumetric flask, followed by excipients used in single oral unit dosage form, to determine the concentration of dapagliflozin propanediol monohydrate and teneligliptin hydrobromide hydrate in a synthetic mixture. Both substances were evaluated for assay at 40 µg/ml final concentrations for dapagliflozin propanediol monohydrate and 80 µg/ml for teneligliptin hydrobromide hydrate.

## 5. RESULTS AND DISCUSSION

### 5.1. Optimized chromatographic conditions

In Figure 3, Dapagliflozin propanediol monohydrate had a retention time of 6.65 min, while Teneligliptin hydrobromide hydrate had a retention time of 4.20 min under optimized chromatographic conditions.

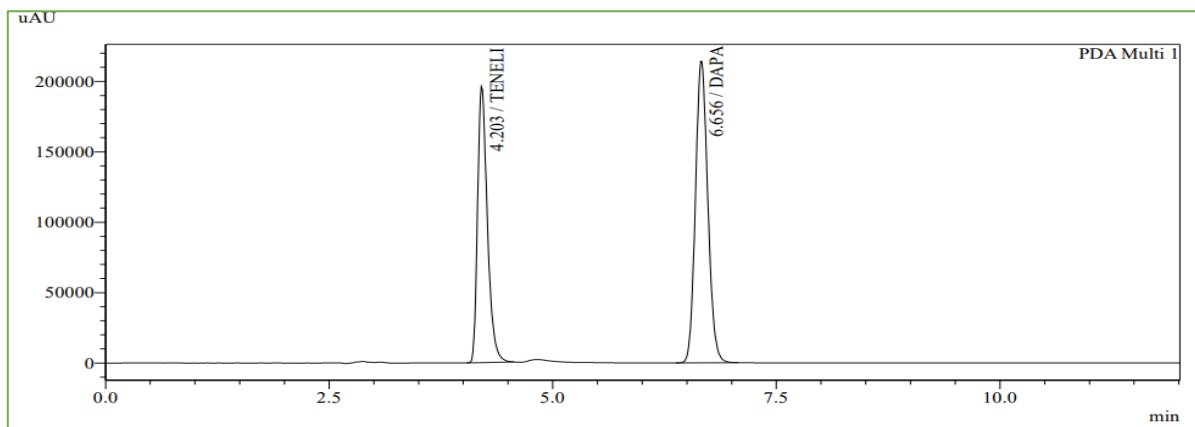


Figure 3: Optimized Chromatogram of Standard DAPA TENE

**5.2. System suitability parameter**

The system suitability parameters were calculated, and it was found that every

parameter was within the acceptable range. It is mentioned in Table 1.

Table 1: System suitability parameter of optimized condition

Peak	Ret. Time	Area	Theoretical Plate	Resolution	Tailing Factor
DAPA	6.65 ± 0.1	2063684	10017 ± 100	10.211	1.14 ± 0.1
TENE	4.20 ± 0.1	1498051	6141 ± 100	0.00	1.36 ± 0.1

**5.3. Forced degradation study**

Acid hydrolysis was carried out as specified, and as shown in Figure 4, the percent degradation for DAPA and TENE was 4.84 and 5.77, respectively. According to Figure 5, the degradation amount was 5.30 for DAPA and 24.13 for TENE during base hydrolysis. In oxidative hydrolysis, the percent degradation for the DAPA and TENE shown in

Figure 6 was 5.81 for DAPA and 23.93 for TENE. Thermal degradation was carried out as instructed, and as shown in Figure 7, the percent degradation was 0.29 for DAPA and 0.57 for TENE. According to Figure 8 and Table 2, the results for photo deterioration were 0.24 for DAPA and 0.35 for TENE in terms of percent degradation.

Table 2: Forced degradation summary

Degradation Condition Name	R.T.		%Degradation		Peak purity index	
	DAPA	TENE	DAPA	TENE	DAPA	TENE
Acid hydrolysis	6.67	4.27	4.84	5.77	1	1
Base hydrolysis	6.66	4.19	5.30	24.13	1	1
Oxidative hydrolysis	6.65	4.13	5.81	23.93	1	1
Thermal degradation	6.66	4.14	0.29	0.57	1	1
Photolytic degradation	6.67	4.13	0.24	0.35	1	1

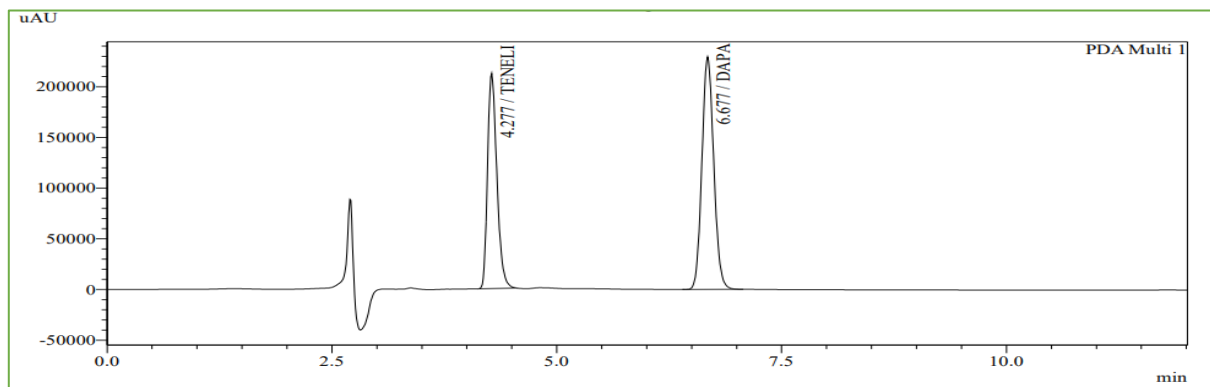


Figure 4: Forced degradation chromatogram of acid degradation



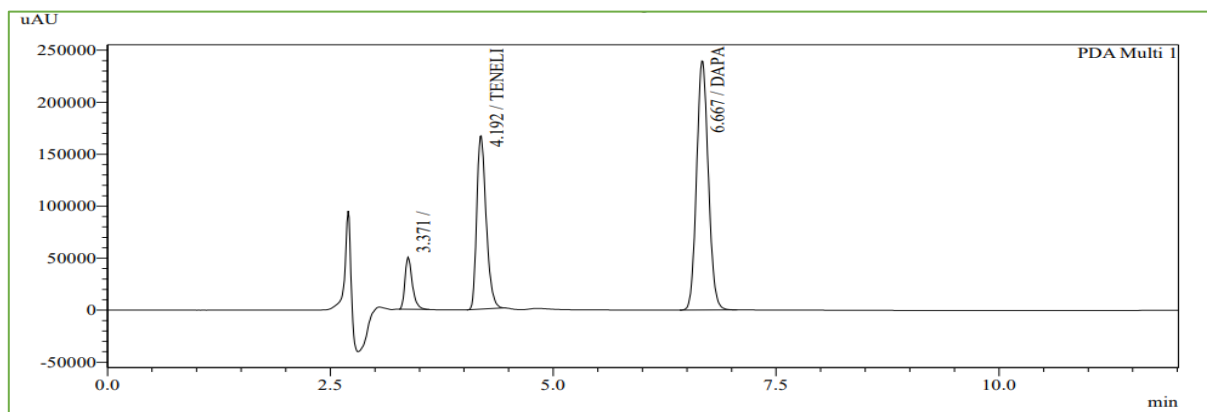


Figure 5: Forced degradation chromatogram of base degradation

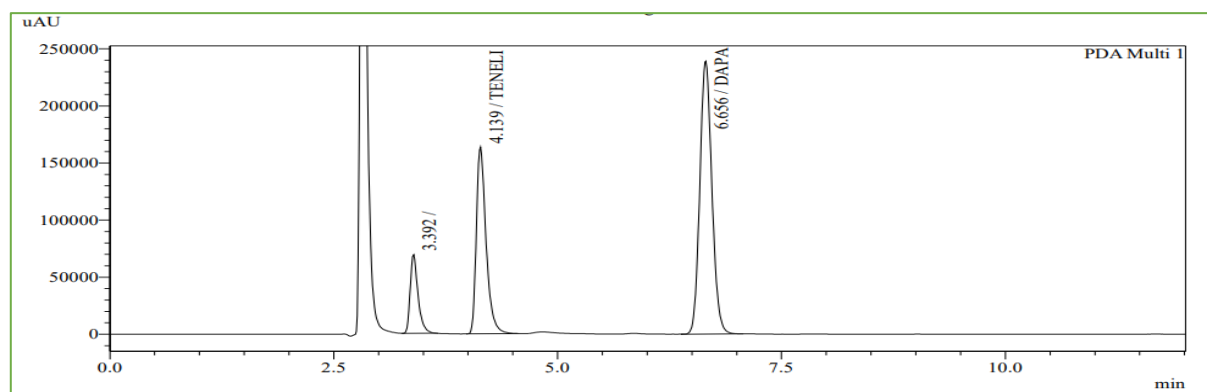


Figure 6: Forced degradation chromatogram of oxidative degradation

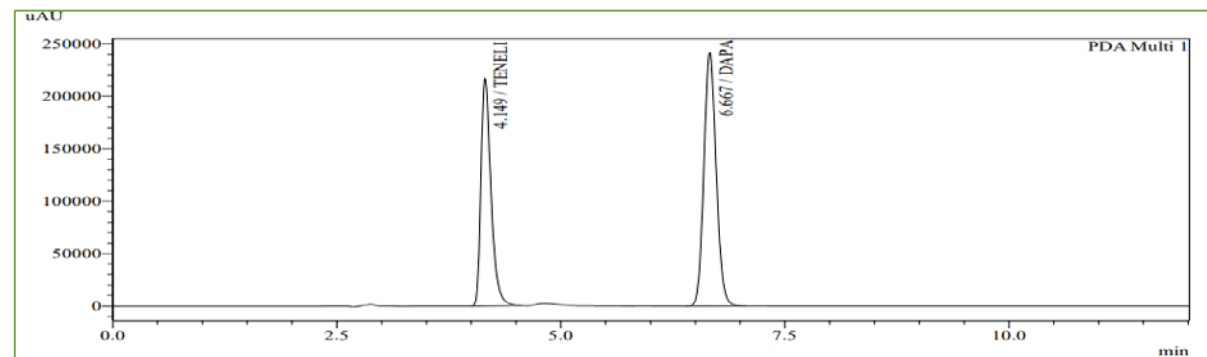


Figure 7: Forced degradation chromatogram of thermal degradation

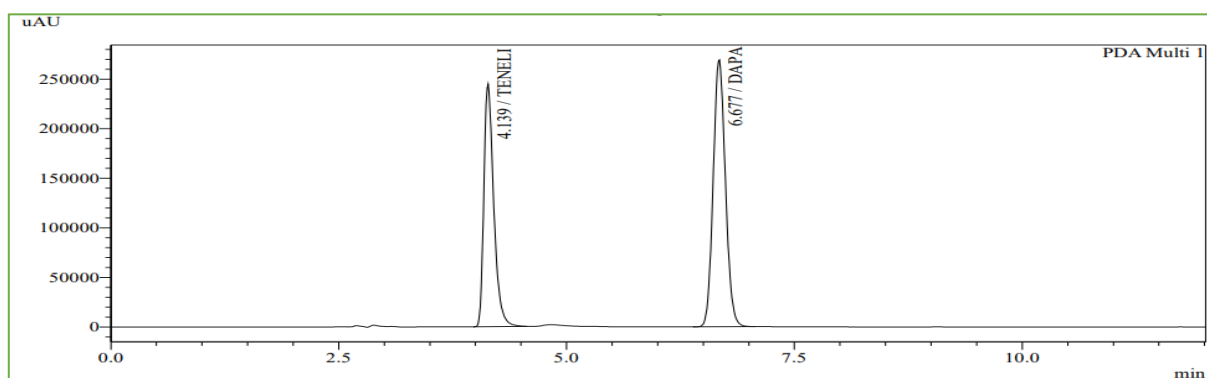


Figure 8: Forced degradation chromatogram of photodegradation

5.4. METHOD VALIDATION

5.4.1. Linearity

DAPA was found to have linear responses in the concentration range of 5-100 µg/ml, and TENE was

found to have linear responses in the concentration range of 10-200 µg/ml. The calibration curves for Dapagliflozin propanediol monohydrate and Teneligliptin hydrobromide hydrate, respectively, are shown in Figures 9 and 10.

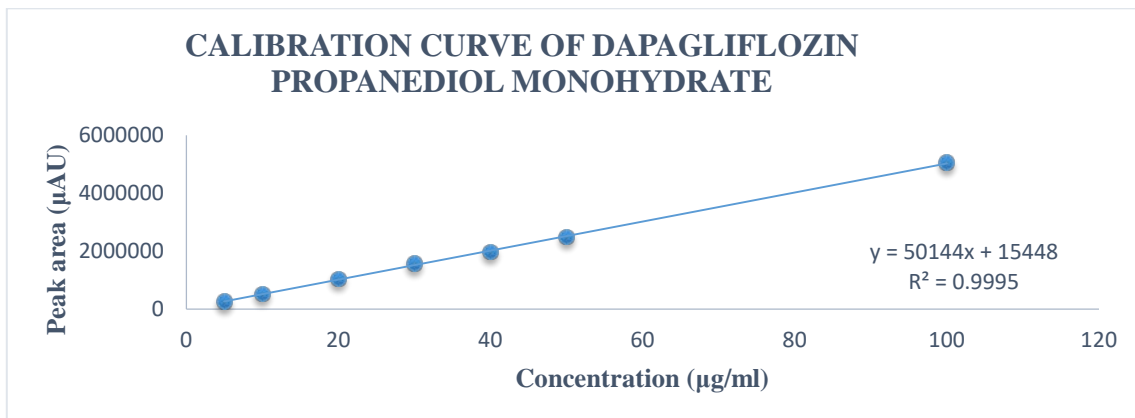


Figure 9: Calibration curve of Dapagliflozin propanediol monohydrate

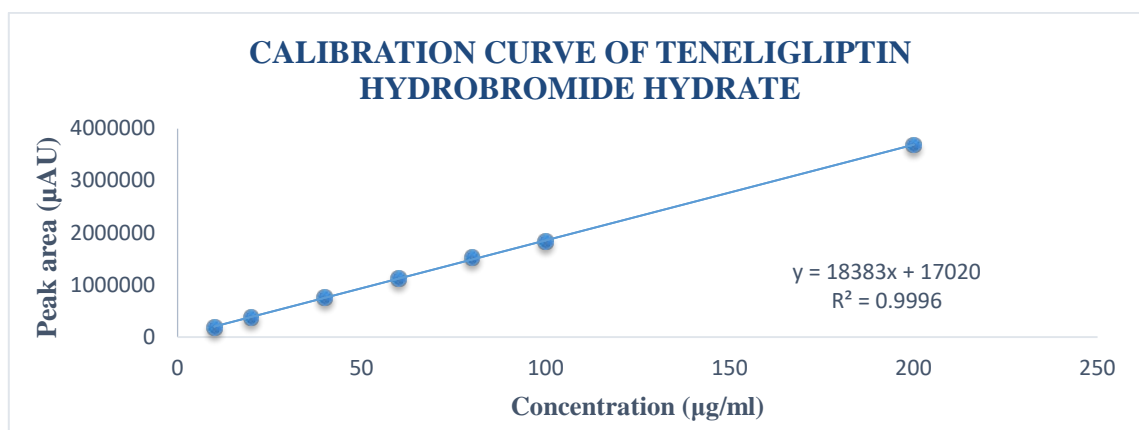


Figure 10: Calibration curve of Teneligliptin hydrobromide hydrate

5.4.2. Accuracy

As indicated in Table 3, the percentage recovery for Dapagliflozin propanediol monohydrate ranged from 99.81-100.78%, whereas the percentage recovery for Teneligliptin hydrobromide hydrate ranged from 99.13-100.69%.

5.4.3. Precision

The repeatability, intraday, and interday precision of the RP-HPLC method were tested using RSD, which was found to be greater than 2. Results are shown in Table 3, demonstrating the precision of the analyzed method.

Table 3: Accuracy and Precision data of DAPA & TENE

LEVEL	ACCURACY		PRECISION					
	%Drug recovery		%RSD					
	DAPA	TENE	Repeatability		Intra-day		Inter-day	
	DAPA	TENE	DAPA	TENE	DAPA	TENE	DAPA	TENE
80	100.66	100.67			0.014	0.011	0.017	0.009
100	99.90	99.31	0.0018	0.014	0.032	0.023	0.004	0.003
120	100.77	99.12			0.025	0.029	0.009	0.010

5.4.4. LOD and LOQ

Using the average slope and standard deviation of intercepts, the LOD and LOQ were calculated. For DAPA and TENE, the LOD was discovered to be 0.94 g/ml and 1.35 µg/ml, respectively. For DAPA and TENE, the LOQ was found to be 2.86 µg/ml and 4.10 µg/ml, respectively.

5.4.5. Specificity

By comparing the chromatograms of the blank, mobile phase, and standard solution, it is demonstrated that no excipient interference with the peak of dapagliflozin propanediol monohydrate

and teneligliptin hydrobromide hydrate has ever been seen.

#### 5.4.6. Robustness

When various parameters, including flow rate, wavelength, and mobile phase ratio, were purposefully altered, it was discovered that the method was reliable and robust. When the parameters were intentionally altered, the relative standard deviation of the peak area was less than 2%.

#### 5.4.7. Assay of synthetic mixture

The concentrations of Dapagliflozin propanediol monohydrate and Teneligliptin hydrobromide hydrate in a synthetic mixture containing 10 mg of Dapagliflozin propanediol monohydrate and 20 mg of Teneligliptin hydrobromide hydrate were calculated using the developed method, and the results showed that they were 100.3% and 101.7%, respectively.

## 6. CONCLUSION

This study presents the development and validation of a stability-indicating reversed-phase high-performance liquid chromatography (RP-HPLC) method for the identification of Dapagliflozin propanediol monohydrate and Teneligliptin hydrobromide hydrate in a synthetic combination. Validation was conducted for Dapagliflozin propanediol monohydrate and Teneligliptin hydrobromide hydrate in accordance with the ICH Q2(R1) requirements. Through the utilization of RP-HPLC, the obtained results indicate that the accuracy falls within the range of 99.81-100.78 percent for DAPA and 99.13-100.69 percent for TENE. The precision of Dapagliflozin propanediol monohydrate and Teneligliptin hydrobromide hydrate was found to be less than 2% in terms of relative standard deviation (RSD). Additionally, all other parameters met the guidelines set by the International Council for Harmonization of Technical Requirements for Pharmaceuticals for Human Use (ICH). These results indicate that the method employed in this study was effective and suitable for accurately quantifying Dapagliflozin propanediol monohydrate and Teneligliptin hydrobromide hydrate in a synthetic mixture. The approach that has been devised effectively achieves the total separation of alkali and oxidative degradants from the primary peak. The pharmacological combination under investigation is currently in phase 3 of clinical trials, indicating that there are currently no commercially available formulations. Consequently, a synthetic combination is employed for the purpose of technique development.

## 7. CONFLICT OF INTEREST

The authors report no conflicts of interest.

## 8. ACKNOWLEDGMENTS

The authors are grateful to MERRIL PHARMA PVT. LTD. for providing standard samples of Dapagliflozin propanediol monohydrate and teneligliptin hydrobromide hydrate and B.K. MODY GOVERNMENT PHARMACY COLLEGE, RAJKOT, and SAURASHTRA UNIVERSITY to offer facilities to work.

## 9. REFERENCES

1. "Drug Profile and Information of Dapagliflozin Propanediol Monohydrate", October 2023, Available from: [<URL>](#)
2. "Drug Profile and Information of Dapagliflozin Propanediol Monohydrate", October 2023, Available from: [<URL>](#)
3. Vyas AJ, Gol DA, Patel AI, Patel AB, Patel NK, Chavda JR, Lumbhani A, Chudasama A. Implementing Analytical Quality by Design (AQbD) Approach for Simultaneous Estimation of Tadalafil and Macitentan by RP-HPLC Method. *Analytical Chemistry Letters*. 2021;11(4):539-552. Available from: [<URL>](#)
4. Vyas AJ, Patel SM, Patel AB, Patel AI, Patel NK. Stability testing: An Essential study for Vaccine Formulation Development. *Asian Journal of Pharmaceutical Analysis*. 2022;12(1):29-6. Available from: [<URL>](#)
5. Vyas AJ, Visana NM, Patel AI, Patel AB, Patel NK. Analytical Quality by Design in Stress Testing or Stability-Indicating Method. *Asian Journal of Pharmaceutical Analysis*. 2021;11(2):170-178. Available from: [<URL>](#)
6. Patel AI, Prajapati KB, Jolapara SH, Vyas AJ, Patel AB, Patel NK, Pandey MN. RP-HPLC method for determination of gemfibrozil using central composite design (CCD). *Research Journal of Pharmacy and Technology*. 2021;14(6):3009-3014. Available from: [<URL>](#)
7. Vyas AJ, Jha SA, Patel AB, Patel AI, Shah SR. Review on simultaneous equation method (Vierodt's method). *Asian Journal of Pharmaceutical Analysis*. 2022;12(2):149-156. Available from: [<URL>](#)
8. Patel AI, Ram K, Guttikar S, Vyas AJ, Patel AB, Patel NK, Trivedi V. Rapid, sensitive and simple LC-MS/MS method development and validation for estimation of phenytoin in human plasma by using deuterated internal standard. *Research Journal of Pharmacy and Technology*. 2021;14(6):2937-2944. Available from: [<URL>](#)
9. Vaghela A, Patel AB, Patel AI, Vyas AJ, Patel NK. Sample Preparation in Bioanalysis: A Review. *International Journal of Scientific & Technology Research*. 2016;5(5):6-10. Available from: [<URL>](#)
10. Patel AB, Asnani AH, Vyas AJ, Patel NK, Patel AI. A brief review on genotoxic impurities in pharmaceuticals. *Asian Journal of Pharmaceutical Research*. 2021;11(3):187-193. Available from: [<URL>](#)
11. Patel AB, Bundheliya AR, Vyas AJ, Patel NK, Patel AI. A Review on Metal Impurities in Pharmaceutical. *Asian Journal of Pharmaceutical Analysis*. 2021;11(3):212-222. Available from: [<URL>](#)

12. Vyas AJ, Godhaniya JP, Patel AI, Patel AB, Patel NK, Chudasama A, Shah SR. A review on carcinogenic impurities found in marketed drugs and strategies for its determination by analytical methods. *Asian Journal of Pharmaceutical Analysis*. 2021;11(2):159-169. Available from: [<URL>](#)
13. Patel AI, Prajapati KB, Vyas AJ, Patel AB, Patel NK. Determination and validation of phthalate impurities in milk by UV-spectrophotometry method. *Pharma Science Monitor*. 2021;10(4):49-58.
14. Vyas AJ, Rajput M, Patel NK, Chotaliya U, Patel AB, Patel AI. Determination of genotoxic Impurity by Chromatographic Method. *An International Journal of Pharmaceutical Sciences*. 2017;8(2):24-31. Available from: [<URL>](#)
15. Vyas AJ, Taviyad M, Patel NK, Chotaliya U, Singh S, Patel AB, Patel AI. Chromatographic Method Development and Validation for Related Substance. *Pharma Science Monitor*. 2017;8(2):32-39.
16. Vyas AJ, Rathod N, Patel AI, Prajapati R, Patel NK, Patel AB. Analytical Method Development and Validation of Stability Indicating Method and Related Substance by Using RP-HPLC of Drug Substance. *Pharma Science Monitor*. 2017;8(2):409-419.
17. Bakshi M, Singh S. Development of validated stability-indicating assay methods-critical review. *Journal of Pharm. and Bio. Ana*. 2002;28:1011-40. Available from: [<URL>](#)
18. Vyas AJ, Gol DA, Patel AI, Patel AB, Patel NK, Chudasama A. A stress degradation kinetic study of Tadalafil bulk and tablet dosage form by UV Spectrophotometry. *Asian Journal of Pharmaceutical Analysis*. 2020;10(4):177-181. Available from: [<URL>](#)
19. Patel A, Jadeja P, Mashru R. Analytical Method Development and Validation for Simultaneous Estimation of Dapagliflozin and Teneligliptin Hydrobromide Hydrate from Synthetic Mixture by Three Different UV Spectrophotometric Methods. *World Journal of Pharmaceutical Research*. 2022;11(7):770-783. Available from: [<URL>](#)
20. Debata J, Kumar S, Jha SK, Khan A. A New RP-HPLC Method Development and Validation of Dapagliflozin in Bulk and Tablet Dosage Form. *International Journal of Drug Development and Research*. 2017;9(2):48-51. Available from: [<URL>](#)
21. Sravanthi S, Zarin N, Shruthi B, Ramya KD, Manjeera A. A New Analytical Method Development and Validation for the Estimation of Dapagliflozin by Using Reverse Phase-High Performance Liquid Chromatography. *International Journal of Advanced Research in Medical & Pharmaceutical Sciences*. 2021;6(4):13-20. Available from: [<URL>](#)
22. Manasa S, Dhanalakshmi K, Reddy GN, Sreenivasa S. Method development and validation of dapagliflozin in API by RP-HPLC and UV-spectroscopy. *International Journal of Pharmaceutical Sciences and Drug Research*. 2014;6(3):250-252. Available from: [<URL>](#)
23. Basha SS, Sravanthi P. Development and Validation of Dapagliflozin by Reversed-Phase High-Performance Liquid Chromatography Method and Its Forced Degradation Studies. *Asian Journal of Pharmaceutical Clinical Research*. 2017;10(11):101-105. Available from: [<URL>](#)
24. Vaghela YV, Patani P, Patel D. Development and Validation of Stability Indicating Estimation Method of Dapagliflozin in Its Tablet Dosage Form. *International Journal of Research and Analytical Reviews*. 2019;6(2):206-213.
25. Bodiwala KB, Shah J, Sureja DK, Dhameliya TM. Generation of predictive models for oxidative degradation kinetics of dapagliflozin with the applications of DOE and stability indicating HPLC method, *International Journal of Chemical Kinetics*. 2022;54(12):712-725. Available from: [<URL>](#)
26. Nagwanshi S, Aher S, Bachhav R. Stability Indicating RP-HPLC Method Development and Validation of Dapagliflozin in Bulk and Tablet Dosage Form. *World Journal of Pharmacy and Pharmaceutical Sciences*. 2021;10(9):2251-2262.
27. Sanagapati M, Dhanalakshmi K, Reddy NG, Kavitha B. Method Development and Validation of Dapagliflozin API by UV Spectroscopy. *International Journal of Pharmaceutical Sciences Review and Research*. 2014;27(1):270-272. Available from: [<URL>](#)
28. Biswas B, Kumar M, Sharma JB, Saini V, Bhatt S. Method Development and Validation for Estimation of Teneligliptin in Tablet Dosage Form by RP-HPLC. *Research Journal of Pharmacy and Technology*. 2020;13(4):1774-1778. Available from: [<URL>](#)
29. Reddy GS, Swetha V, Venu G, Pavani J. Analytical Method Development and Validation of Teneligliptin Hydrobromide Hydrate in Active Pharmaceutical Ingredient by using RP-HPLC. *International Journal of Biology, Pharmacy and Allied Sciences*. 2021;10(7):2250-2262. Available from: [<URL>](#)
30. Lokhande P. Analytical Method Development and Validation of Teneligliptin by using RP-HPLC with ICH Guidelines. *International Journal of Trend in Scientific Research and Development*. 2019;3(3):259-263. Available from: [<URL>](#)
31. Luhar SV, Pandya KR, Jani GK, Narkhed SB. Simultaneous Estimation of Teneligliptin Hydrobromide Hydrate and its Degradation Product by RP-HPLC Method. *Journal of Pharmaceutical Science and Bioscientific Research*. 2016;6(3):254-261. Available from: [<URL>](#)
32. Yadav N, Goyal A. Method development and validation of Teneligliptin in pharmaceutical dosage form by UV spectrophotometric methods. *International Journal of Pharmaceutical Chemistry and Analysis*. 2017;4(3):54-58. Available from: [<DOI>](#)
33. Ghuge BS, Pendhari SS, Malode PA, Anantwar SP. Development and Validation of Simple UV Spectrophotometric Method for The Determination of Teneligliptin Hydrobromide Hydrate in API and its Bulk Dosage Form. *International Journal for Pharmaceutical Research Scholars*. 2017;6(2):44-53. Available from: [<URL>](#)
34. Gadi VL, Devanaboyina N. Method Development and Validation for Simultaneous Estimation of Dapagliflozin & Saxagliptin by RP-HPLC Method. *World Journal of Pharmaceutical and Medical Research*. 2020;6(7):243-248.
35. Urooj A, Shyam Sundar P, Vasanthi R, Raja MA, Dutt KR, Rao KNV. Development and Validation of RP-HPLC Method for Simultaneous Estimation of Dapagliflozin and Metformin in Bulk and in Synthetic Mixture. *World Journal*

- of Pharmacy and Pharmaceutical Sciences. 2017; 6(7):2139-2150. Available from: [<URL>](#)
36. Gupta A, Mishra SK. A Novel Analytical Method for Simultaneous Quantification of Dapagliflozin and Sitagliptin by Reverse Phase High Performance Liquid Chromatography. *Journal of Medical Pharmaceutical and Allied Sciences*. 2021;10(3):2861-2865. Available from: [<DOI>](#)
37. Rao SS, Srinivas S, Gupta VR, Babu VJ. Stability Indicating Method Development and Validation of Dapagliflozin and Saxagliptin Drugs by Using RP-HPLC Method. *Journal of Global Trends in Pharmaceutical Sciences*. 2021;12(3):9554-9559.
38. Ahmad S, Usman R, Shaikh T, Imran MD, Akhtar R. Development and Validation of UV Spectrophotometric Method for Estimation of Saxagliptin and Dapagliflozin in Bulk and Dosage Form. *International Journal of Pharmaceutical Sciences and Research*. 2021;12(4):2185-2192. Available from: [<DOI>](#)
39. Janil S, Shukla R, Patel P, Mehta B, Detholia K. Quantitative estimation of sitagliptin and dapagliflozin propanediol monohydrate in synthetic mixture using 1st order derivative spectroscopy simultaneous spectrophotometric analysis. *International Journal of Pharmaceutical Chemistry and Analysis*. 2022;9(1):28-34. Available from: [<URL>](#)
40. Shirisha K, Amina begum K, Sravya K, Swarna K, Neelima K, Rao SS. Analytical Method Development and Validation of Teneigliptin and Metformin HCL by using RP-HPLC Method. *Journal of Global Trends in Pharmaceutical Sciences*. 2020;11(3):8051-8056.
41. Patel F, Dalwadi P, Patel D, Mehta N. Development and Validation of RP-HPLC Method for Simultaneous Estimation of Teneigliptin Hydrobromide Hydrate and Rosuvastatin Calcium in Synthetic Mixture. *International Journal of All Research Education and Scientific Methods*. 2021;9(4), 2712-2719. Available from: [<URL>](#)
42. Vashi D, Gamit D. Development and Validation of RP-HPLC Method for Simultaneous Estimation of Remogliflozin Etabonate and Teneigliptin in Pharmaceutical Dosage Form. *World Journal of Pharmacy and Pharmaceutical Sciences*. 2022;11(8):1504-1516. Available from: [<DOI>](#)
43. Gheewala JA, Maheshwari DG. Development and Validation of UV Spectrophotometric Method and RP-HPLC Method for Simultaneous Estimation of Teneigliptin and Pioglitazone in Synthetic Mixture. *Asian Journal of Pharmaceutical Technology & Innovation*. 2017;23(5):66-78.
44. Chotaliya UJ, Dobariya HJ, Barad DL, Vyas AJ, Gol DA. Stability Indicating RP-HPLC-DAD Method For Simultaneous Estimation of Atorvastatin Calcium and Teneigliptin Hydrobromide Hydrate in Synthetic Mixture. *Analytical Chemistry Letters*. 2022;12(5):629-638. Available from: [<URL>](#)
45. Mane SS, Mhaske MS. Development and Stability Indicating RP-HPLC Method for Simultaneous Estimation of Metformin HCL and Teneigliptin HBR Hydrate in Bulk and Pharmaceutical Dosage Form. *Indo American Journal of Pharmaceutical Science*. 2022;9(6):499-518. Available from: [<URL>](#)
46. Solanki MS, Goyal PK. Simultaneous Estimation of Teneigliptin and Metformin Hydrochloride in Tablet Formulation by UV Spectrophotometric Method. *Chemistry Research Journal*. 2021;6(6):160-165. Available from: [<URL>](#)
47. Vashi D, Gamit D. Development and Validation of UV-Spectroscopic Method for Simultaneous Estimation of Remogliflozin Etabonate and Teneigliptin in Bulk and Pharmaceutical Dosage Form by Simultaneous Equation Method. *World Journal of Pharmaceutical and Life Science*. 2022;8(8):149-153.
48. ICH-Harmonized Tripartite Guideline (2005) Validation of analytical procedures: text and methodology Q2 (R1). In: International conference on harmonization, ICPMA, Geneva, Switzerland.





## Microencapsulation of Hemp Oil in Gelatin and Gum Arabic and Investigation of Cumulative Release Properties in n-Hexane Medium

Okan Bayram<sup>1\*</sup>, Fethiye Göde<sup>2</sup>

<sup>1</sup> Department of Chemistry, Graduate School of Applied and Natural Sciences, Süleyman Demirel University, Isparta, Turkey.

<sup>2</sup> Department of Chemistry, Faculty of Science and Arts, Süleyman Demirel University, Isparta, Turkey.

**Abstract:** In this study, hemp oil was microencapsulated with gelatin (GE) and gum arabic (GA) polymers by complex coacervation method. The effects of three parameters (stirring speed 1000.0–1500.0 rpm, temperature 50–60 °C, surfactant concentration 0.3–0.7 w/v%) selected in the response surface methodology (RSM) on the encapsulation efficiency were investigated. The obtained results were maximized by multiple response prediction, and the release characteristics were investigated in n-hexane at different times (1 min, 3 min, 5 min, 7 min, 10 min, 30 min, 60 min, 120 min, 240 min, 360 min, 720 min, 1440 min, 2160 min, 2880 min). When the release results were examined, it was observed that the microcapsules started with a rapid release, and the release value remained constant as time progressed. Obtained microcapsules were examined under optical microscope and scanning electron microscope (SEM) devices under special conditions. The microcapsules were observed to be smooth and round in shape under the optical microscope.

**Keywords:** Gelatin, gum arabic, hemp oil, microencapsulation, n-hexane.

**Submitted:** May 4, 2023. **Accepted:** September 6, 2023.

**Cite this:** Bayram O, Göde F. Microencapsulation of Hemp Oil in Gelatin and Gum Arabic and Investigation of Cumulative Release Properties in n-Hexane Medium. JOTCSA. 2023;10(4):1035-44.

**DOI:** <https://doi.org/10.18596/jotcsa.1292222>

**\*Corresponding author's E-mail:** [okan.bayram.32@gmail.com](mailto:okan.bayram.32@gmail.com)

### 1. INTRODUCTION

The active component is shielded from the environment using microencapsulation technology, which involves encasing the active ingredient (core material) in a second material or materials. Hence, the core component is the active ingredient, while the surrounding component is the shell (wall). This technique is employed in a wide range of industries, including textiles, cosmetics, and pharmaceuticals (1). Complex coacervation is one of the chemical microencapsulation techniques. Complex coacervation is one of the easiest, least expensive, scalable, repeatable, and most efficient ways to microencapsulate hydrophobic materials (2). This technique provides the core with strong oxidative stability, little surface oil, and good encapsulation efficiency (3,4). Since ancient times, people in Asia and Europe have utilized hemp (*Cannabis sativa L.*), an annual herbaceous plant with several uses, as a source of food, dietary oil, medicine, and fiber. Moreover, notably in North America, the hemp plant is now favored and utilized in significant sectors,

including textiles, animal feed, and fiber manufacturing (5). *Cannabis sativa L.* seeds are used to make hemp seed oil, which is prized for its wholesome properties. High levels of polyunsaturated fatty acids and other bioactive minor components can be found in hemp oil. It is a particularly rich source of linoleic acid and alpha-linolenic acid when compared to other vegetable oils. Furthermore, significant are the moderate to high concentrations of tocopherols and tocotrienols, phytosterols, phospholipids, carotenes, and minerals found in hemp seed oil (6). Hemp seed oil is nutritionally better than similar seed oils since it contains gamma-linolenic acid (GLA) (7). In this study, hemp oil was microencapsulated in gelatin and gum Arabic polymers in an experimental set formed with the help of RSM. The obtained results were optimized, reproduced with optimized values, and characterized in SEM and optic microscope devices. In addition, their cumulative release in n-hexane medium was investigated.

## 2. EXPERIMENTAL SECTION

### 2.1. Response Surface Methodology and Parameters

Three parameters were chosen for the experimental design of the microencapsulation of hemp oil with gelatin and gum arabic polymers. These parameters are; stirring speed (A, 1000.0–1500.0 rpm), temperature (B, 50–60 °C) and surfactant concentration (C, 0.3–0.7 w/v%). Input responses were analyzed according to the percent yield response. The minimum and maximum points of the selected parameters were determined with the help of preliminary experiments and similar studies in the literature.

### 2.2. Microencapsulation of Hemp Oil by Complex Coacervation Method

4.0 g of hemp oil (core material) was used for each experiment. In all experiments, the stirring speed was adjusted between 1000.0–1500.0 rpm in the first stage, 400.0 rpm in the second stage, and the temperature (50–60 °C) was adjusted in the heating magnetic stirrer (Weightlab WNH550). GE/GA (1.25 w/v%) was used at a 1:1 ratio. In the first stage, hemp oil was mixed with the prepared GE solution for 20 minutes in the experimental environment and brought to the desired temperature (50–60 °C) from the experimental set. 0.25 mL of sodium dodecyl sulphate (SDS), determined in the experimental sets, was added to the mixture as a surfactant and mixed for another 20 minutes. GA (1.25 w/v%) was added, and mixing was continued for another 20 minutes. Then the pH value of the mixture was adjusted with acetic acid solution (10 v/v%) and stirred at 400 rpm for a further 90 minutes. At the end of the period, the heater was turned off, and 300 mL of cold deionized water and 2 mL of glutaraldehyde (10 v/v%) were added to the mixture. The temperature drop was checked with a digital thermometer and the probe of the heater. Stirring was continued at 400 rpm at this stage. Total stirring time was 4.5 hours. Afterward, the obtained mixture was kept for one day and washed, filtered, and processed (8–11). The diagram of the experiments is shown in Figure 1.

### 2.3. Microencapsulation Efficiency and Cumulative Release Calculation

While calculating the encapsulation efficiency and cumulative release, Equations 1 and 2, which were created with the help of similar studies in the literature, were used. The encapsulation efficiency was initially calculated with the help of the known amount of cannabis oil and the amount of cannabis oil taken from the surface. For cumulative release, firstly, a calibration set was prepared by mixing hemp oil and n-hexane. 1 mL of sample solutions from the medium at predetermined time intervals (1 min, 3 min, 5 min, 7 min, 10 min, 30 min, 60 min, 120 min, 240 min, 360 min, 720 min, 1440 min, 2160 min, and 2880 min) was withdrawn and replaced with fresh medium to maintain a constant volume and absorbance values were measured (12). UV readings were made at 209 nm.

$$EE\% = \frac{\text{Total Hemp Oil Amount} - \text{Surface Hemp Oil Amount}}{\text{Total Hemp Oil Amount}} \times 100 \quad (1)$$

$$CR\% = \frac{\text{Hemp Oil Released Amount}}{\text{Initial Hemp Oil Amount}} \times 100 \quad (2)$$

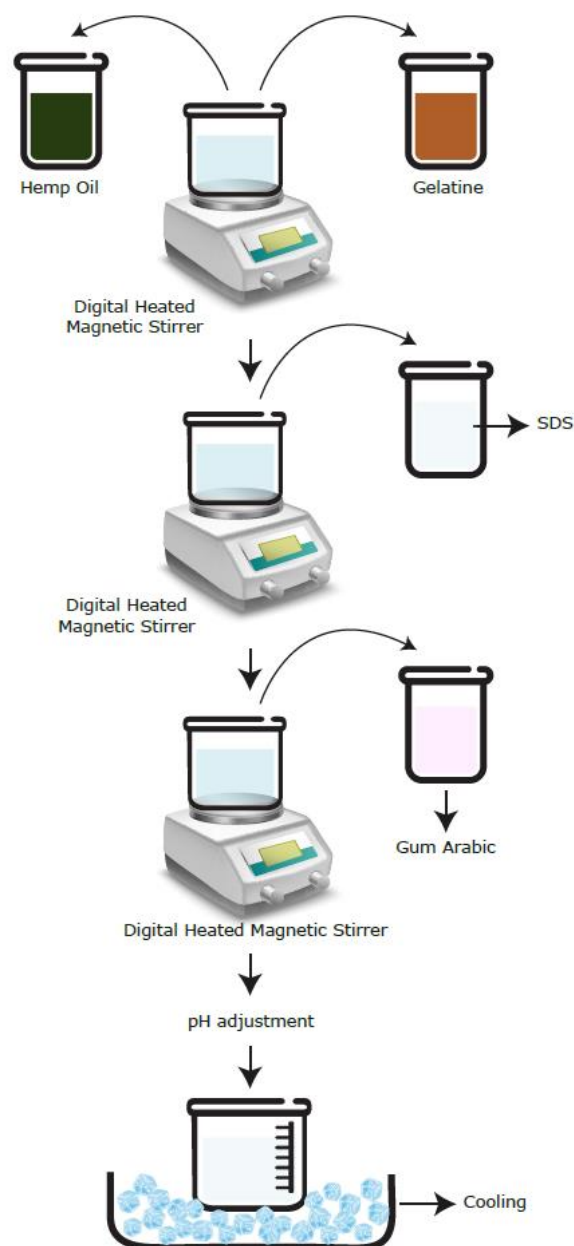


**Figure 1:** Diagram of the experiment with the complex coacervation method.

### 2.4. SEM and Optic Microscope Analysis

The obtained microcapsules were imaged with a Bueco BM-2000 optical microscope and Quanta™ 250 FEG brand SEM device to evaluate their size, shape, and color features.

## 3. RESULTS AND DISCUSSION

The experimental design, experimental yield, and calculated yield values for microcapsules containing hemp oil in gelatin and gum Arabic wall material are shown in Table 1.

ANOVA values calculated over the results obtained are shown in Table 2.



**Table 1:** Hemp oil-GE/GA experimental design results.

A (rpm)	B (°C)	C (%w/v)	Experimental Efficiency	Calculated Efficiency
1000.0	50.0	0.3	50.610	48.029
1250.0	55.0	0.5	59.360	59.857
1250.0	55.0	0.5	59.050	59.857
1500.0	60.0	0.3	62.780	62.779
1500.0	50.0	0.7	63.850	63.284
1000.0	60.0	0.7	51.850	52.944
1250.0	55.0	0.5	58.720	59.857
1250.0	46.8	0.5	52.520	56.687
1250.0	55.0	0.5	59.890	59.857
1250.0	55.0	0.8	66.850	66.481
1658.3	55.0	0.5	58.550	59.797
1250.0	55.0	0.2	58.950	62.557
1250.0	63.2	0.5	61.480	60.533
841.8	55.0	0.5	34.580	36.584
1000.0	60.0	0.3	49.820	49.024
1000.0	50.0	0.7	49.960	48.609
1250.0	55.0	0.5	59.660	59.857
1500.0	60.0	0.7	65.780	66.999
1500.0	50.0	0.3	64.850	62.404
1250.0	55.0	0.5	61.980	59.857
		R-square	96.070%	
		Lack-of-fit ( $p>0.050$ )	0.072	

**Table 2:** ANOVA results for hemp oil-GE/GA

Source	DF	Adj SS	Adj MS	F-Value	P-Value
Model	11	1037.940	94.358	17.800	0.000
Blocks	2	18.210	9.106	1.720	0.240
Linear	3	703.110	234.370	44.210	0.000
A	1	665.000	664.998	125.450	0.000
B	1	18.230	18.232	3.440	0.101
C	1	19.880	19.880	3.750	0.089
Square	3	310.800	103.599	19.540	0.000
A*A	1	253.460	253.456	47.810	0.000
B*B	1	2.890	2.889	0.550	0.481
C*C	1	40.200	40.202	7.580	0.025
2-Way Interaction	3	5.820	1.939	0.370	0.780
A*B	1	0.190	0.192	0.040	0.854
A*C	1	0.050	0.048	0.010	0.926
B*C	1	5.580	5.578	1.050	0.335
Error	8	42.410	5.301		
Lack-of-Fit	5	38.980	7.797	6.830	0.072
Pure Error	3	3.420	1.141		
Total	19	1080.340			

The model reached as a result of the analysis is significant ( $p<0.050$ ). The model ( $p<0.050$ ) shows linearity. A ( $p<0.050$ ) shows linearity. In addition, B and C do not show linearity ( $p>0.050$ ). Square is significant in the model ( $p<0.050$ ). B\*B and C\*C squares are not significant ( $p>0.050$ ). 2-Way Interaction is not significant ( $p>0.050$ ). The p-value

of the lack-of-fit was found to be 0.072 ( $p>0.050$ ). A lack of fit value of  $p>0.050$  indicates that the model fits the data. The  $R^2$  value was found to be 96.070%. The equation showing the calculated encapsulation efficiency obtained as a result of the analysis is given in Equation 3.

$$EE\% = -131.3 + 0.2095 A + 2.03 B - 85.4 C - 0.000070 A^*A - 0.0187 B^*B + 43.6 C^*C - 0.000124 A^*B + 0.0015 A^*C + 0.835 B^*C \tag{3}$$

Three-dimensional surface plots of how the three parameters selected for the encapsulation process with the complex coacervation method (stirring speed, surfactant concentration, and temperature)

relate to the independent variables for hemp oil-GE/GA encapsulation efficiency are shown in Figure 2.

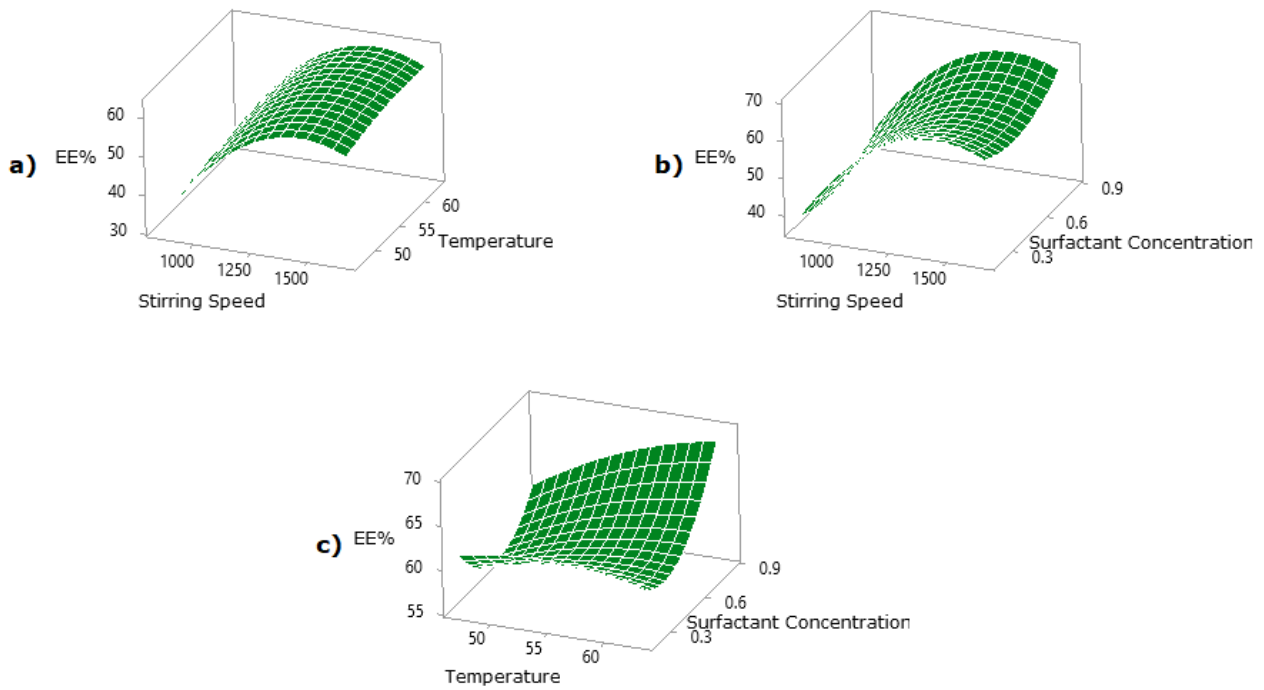


**Figure 2:** Hemp oil-GE/GA 3D surface plot for temperature, surfactant concentration, stirring speed.

When Figure 2a is examined, the EE% reaches its maximum value and then decreases with the increase in stirring speed and temperature together. When Figure 2b is examined, the EE% reaches its maximum value and then decreases with the increase in stirring speed and surfactant concentration. When Figure 2c is examined, the EE% value reaches its maximum, and a concave structure is observed as the temperature and surfactant concentration increase together up to a certain point.

The encapsulation efficiency relationship as a function of the three parameters (stirring speed, temperature, and surfactant concentration) selected for the microencapsulation process is shown in the contour plots in Figure 3.

The distribution of the residuals was examined and the normality test graph performed is shown in Figure 4.

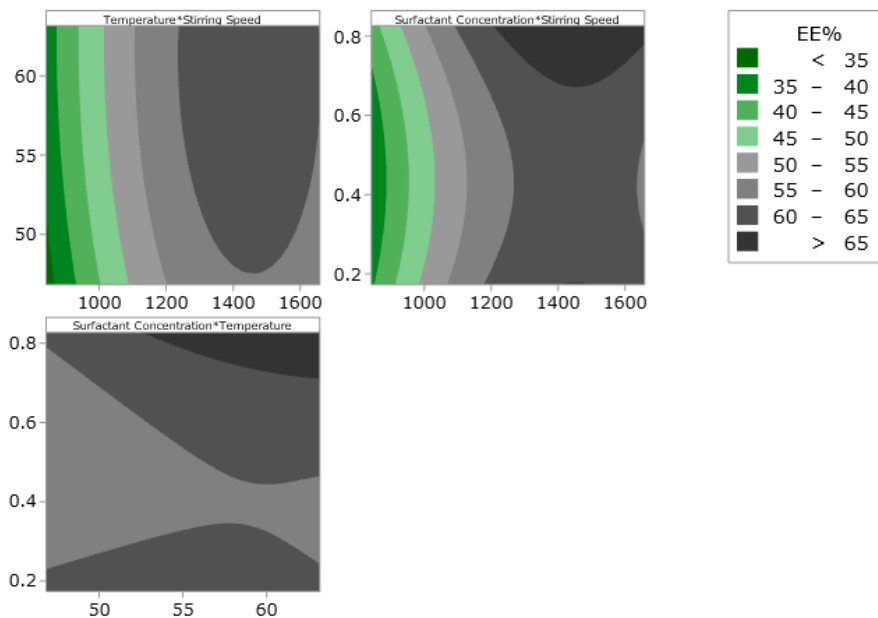


**Figure 3:** Temperature, stirring speed, and surfactant concentration contour plots for hemp oil-GE/GA.

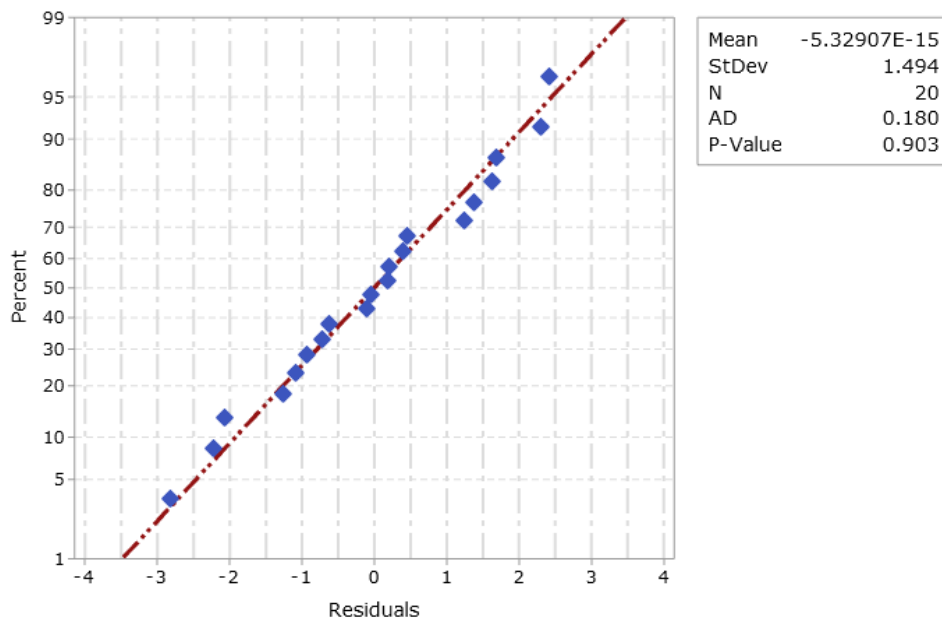


**Figure 4:** Graph of the distribution of residues for hemp oil-GE/GA.

In the analysis of the graph, the mean and standard deviation of the residuals were found to be  $0.000 \pm 1.494$  ( $n=20$ ). According to the AD test, which is one of the normality tests,  $p=0.903$ . The residuals show a normal distribution. Multiple response predictions for hemp oil-GE/GA as a result of the maximization optimization are given in Table 3 (13,14).

The multiple response prediction graph obtained as a result of the optimization is shown in Figure 5.

The theoretical and experimental %EE results of hemp oil-GE/GA microcapsules produced with optimized parameters are given in Table 4.

Images obtained from the hemp oil-GE/GA optical microscope analysis are shown in Figures 6 and 7.

**Table 3:** Multiple response prediction for hemp oil-GE/GA.

Variable				
A (rpm)	B (°C)	C (%w/v)		
1443.820	63.165	0.827		
Response	Fit	SE Fit	95% CI	95% PI
EE%	72.026	3.590	(63.750; 80.310)	(62.190; 81.860)

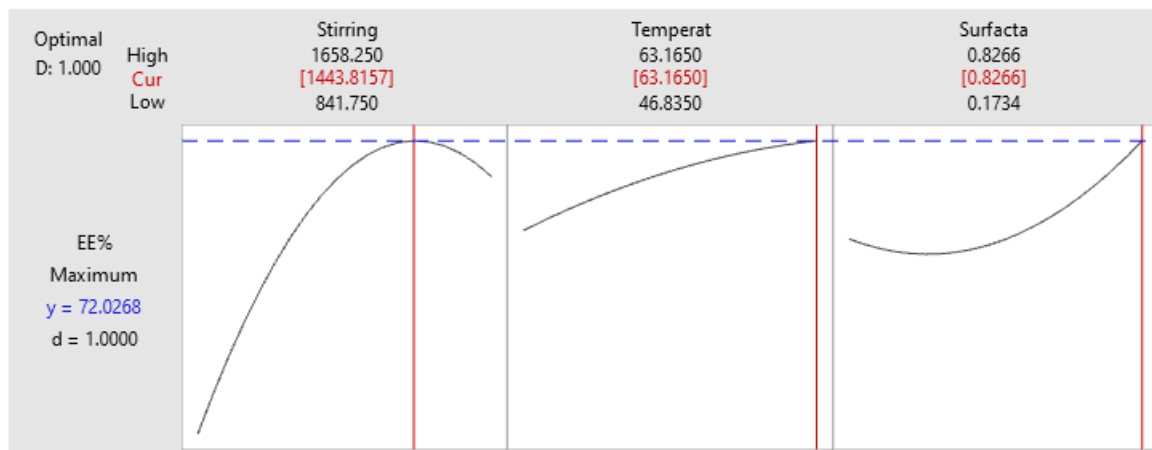


**Figure 5:** Hemp oil-GE/GA optimization graph.

**Table 4:** EE% result of hemp oil-GE/GA optimized parameters.

Core Material-Wall Material:	Hemp Oil-GE/GA
Maximized Theoretical EE%:	72.026%
Experimental EE%:	71.351%

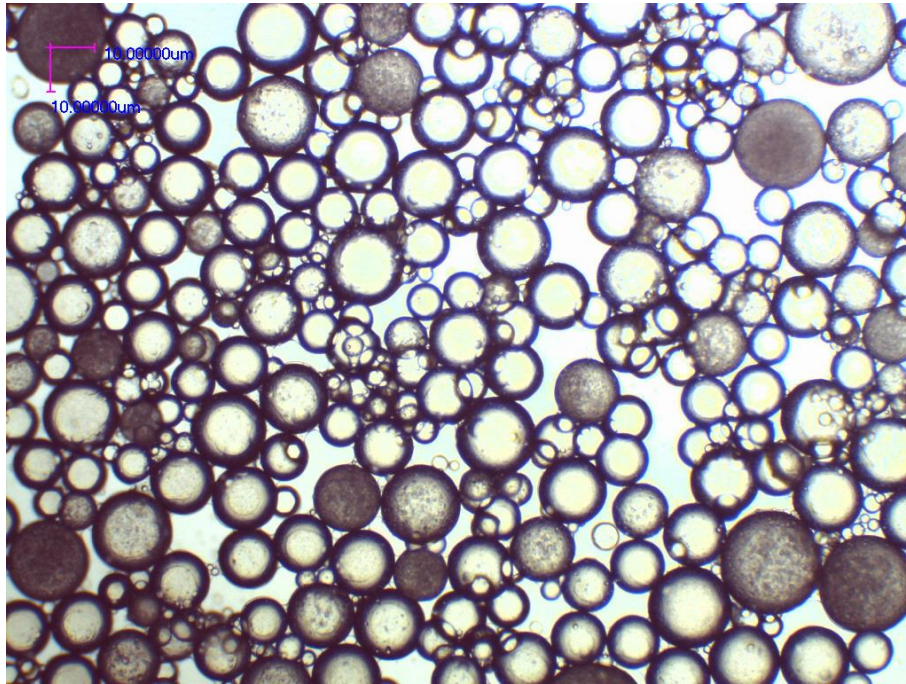


**Figure 6:** Hemp oil-GE/GA optical microscope image.

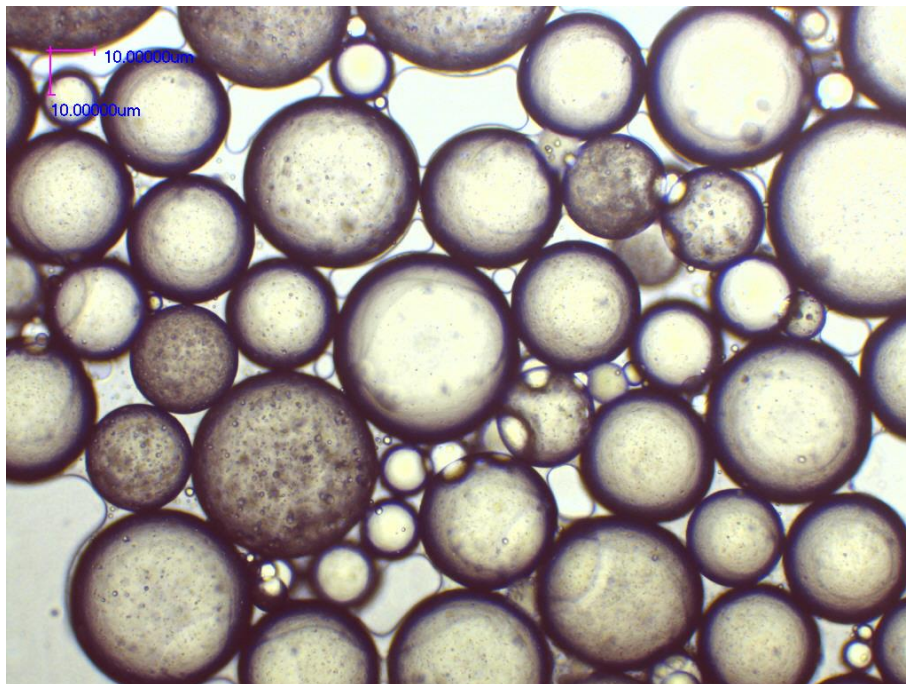


**Figure 7:** Hemp oil-GE/GA optical microscope image.

Images from the hemp oil-GE/GA SEM analysis are shown in Figures 8 and 9.

The investigated cumulative release properties of hemp oil-GE/GA microcapsules in n-hexane medium are shown in Figure 10. The cumulative release

value, which was calculated as 0.289% at the 1st minute, was 20.140% at the 30th minute, 26.128% at the 60th minute, 49.319% at the 360th minute, 58.689% at the 720th minute, and 67.282% at the 2160th minute.

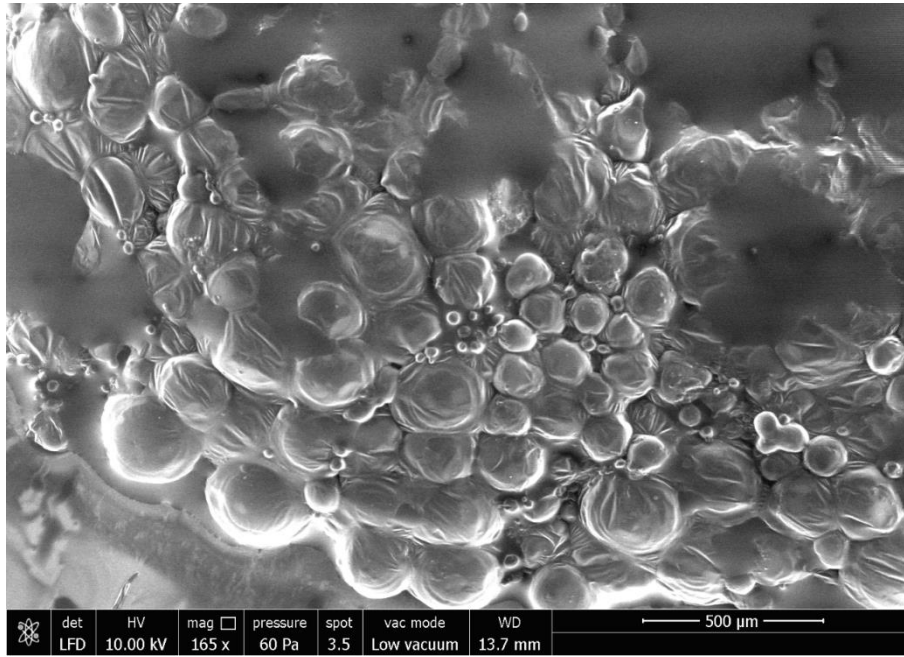


**Figure 8:** Hemp oil-GE/GA SEM image.

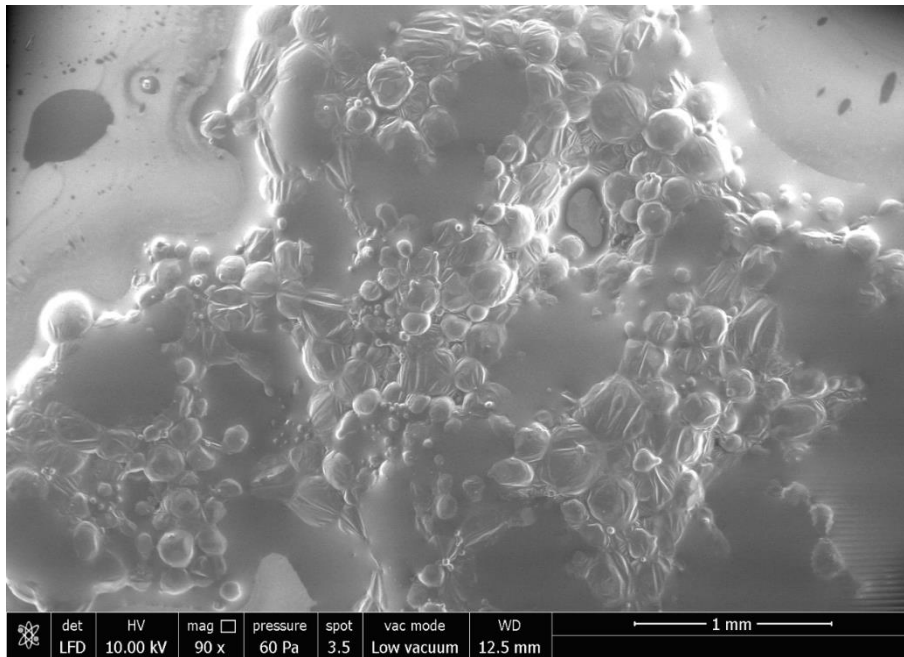


**Figure 9:** Hemp oil-GE/GA SEM microscope image.

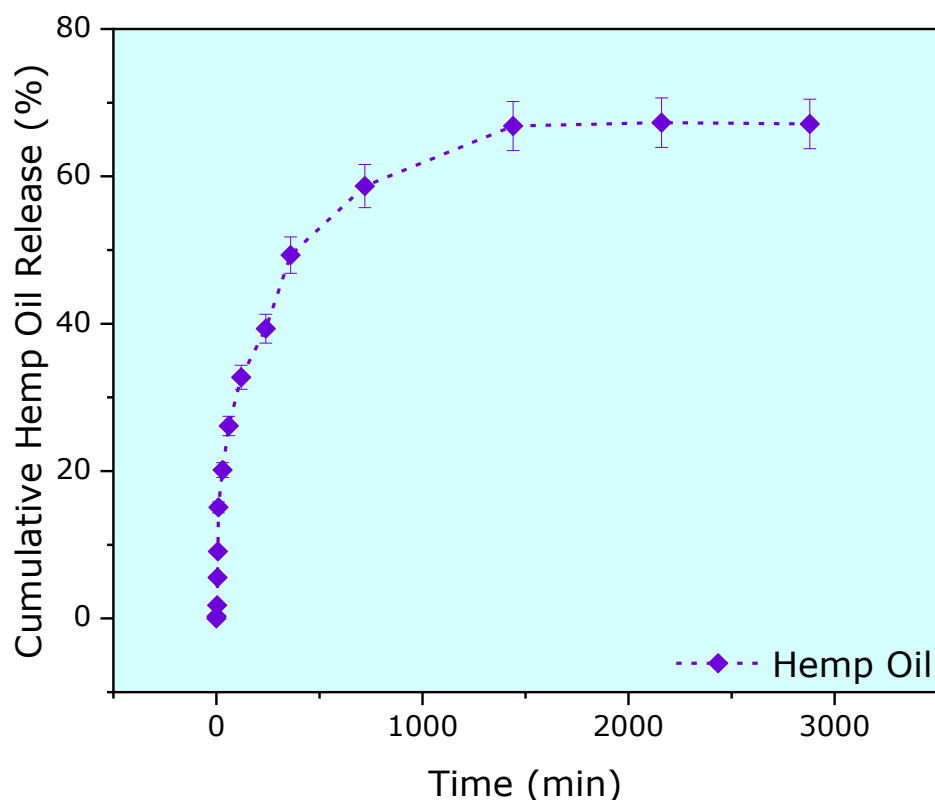


**Figure 10:** Hemp oil-GE/GA cumulative release graph.

#### 4. CONCLUSION

In our study, we aimed to use hemp oil for different purposes by microencapsulating it with gelatin and gum Arabic polymers. In order to bring the process to the most optimal values, an experimental design was first created with RSM. RSM parameters were determined with the help of preliminary experiments and similar studies in the literature (A: 1000.0–1500.0 rpm, B: 50–60 °C, C: 0.3–0.7 w/v%). Microcapsules produced according to efficiency were examined in terms of efficiency and applied to RSM as a response. When the results were optimized to achieve maximum efficiency (EE% = 72.026%), the following conditions were found: stirring speed of 1443.820 rpm, temperature of 63.165 °C, and surfactant concentration of 0.827 w/v%." EE%=71.351% was found in the experiment with the multiple response prediction parameters. Microcapsules produced with maximized values were examined with an optical microscope and SEM devices. Optical microscope images showed that the microcapsules had a smooth round shape. On the other hand, in SEM images, since the device operates in low vacuum mode, some parts of the image are distorted. However, the presence of microcapsules could also be visualized under the SEM device. Obtained microcapsules were evaluated in terms of release in n-hexane medium at 1 min, 3 min, 5 min, 7 min, 10 min, 30 min, 60 min, 120 min, 240 min, 360 min, 720 min, 1440 min, 2160 min, and 2880 min. The microcapsules started with a rapid release, and the release value was found to be constant as time progressed (0.289% at the 1st min, was 20.140% at the 30th min, 26.128% at the 60th min, 49.319% at the 360th min, 58.689% at the 720th min and 67.282% at the 2160th min). In our study,

hemp oil was successfully encapsulated with gelatin and gum Arabic polymers by complex coacervation method, which is a chemical method. It is thought that the findings obtained from our study will contribute to the literature and further studies.

#### 5. CONFLICT OF INTEREST

There is no conflict of interest.

#### 6. ACKNOWLEDGMENTS

This study was supported by Süleyman Demirel University BAP FDK-2019-7334 project number.

#### 7. REFERENCES

1. Dubey R, Shami TC, Bhasker Rao KU. Microencapsulation Technology and Applications. Def Sci J [Internet]. 2009;59(1):82–95. Available from: [<URL>](#).
2. Barrow C, Shahidi F. Marine nutraceuticals and functional foods. CRC press; 2007.
3. Wang B, Adhikari B, Barrow CJ. Optimisation of the microencapsulation of tuna oil in gelatin–sodium hexametaphosphate using complex coacervation. Food Chem [Internet]. 2014 Sep 1;158:358–65. Available from: [<URL>](#).
4. Timilsena YP, Wang B, Adhikari R, Adhikari B. Advances in microencapsulation of polyunsaturated fatty acids (PUFAs)-rich plant oils using complex coacervation: A review. Food Hydrocoll [Internet]. 2017 Aug 1;69:369–81. Available from: [<URL>](#).

5. Blade S. How does hemp measure up? Low-THC Hemp Research Report. Alberta Agric Food, Rural Dev Proj 96CR03, 97NW13. 1997;
6. Mikulcová V, Kašpárková V, Humpolíček P, Buňková L. Formulation, Characterization and Properties of Hemp Seed Oil and Its Emulsions. *Molecules* [Internet]. 2017 Apr 27;22(5):700. Available from: [<URL>](#).
7. Deferne J-L, Pate DW. Hemp seed oil: A source of valuable essential fatty acids. *J Int Hemp Assoc*. 1996;3(1):1-7.
8. de Souza VB, Thomazini M, Echalar Barrientos MA, Nalin CM, Ferro-Furtado R, Genovese MI, et al. Functional properties and encapsulation of a proanthocyanidin-rich cinnamon extract (*Cinnamomum zeylanicum*) by complex coacervation using gelatin and different polysaccharides. *Food Hydrocoll* [Internet]. 2018 Apr 1;77:297-306. Available from: [<URL>](#).
9. Shaddel R, Hesari J, Azadmard-Damirchi S, Hamishehkar H, Fathi-Achachlouei B, Huang Q. Use of gelatin and gum Arabic for encapsulation of black raspberry anthocyanins by complex coacervation. *Int J Biol Macromol* [Internet]. 2018 Feb 1;107:1800-10. Available from: [<URL>](#).
10. Bayram O, Köksal E, Göde F. Yanıt Yüzey Metodolojisi Şartlarında Karabaş Otu Yağının Kompleks Koaservasyon Yöntemi İle Enkapsülasyonu. *Süleyman Demirel Üniversitesi Fen Bilim Enstitüsü Derg* [Internet]. 2020 Aug 26;24(2):508-15. Available from: [<URL>](#).
11. Moral E, Bayram O, Köksal E, Danaş F, Göde F. Kabak Çekirdeği Yağının Kompleks Koaservasyon Yöntemi ile Mikroenkapsülasyonu. *Karaelmas Fen ve Müh Derg* [Internet]. 2021;11(2):91-7. Available from: [<URL>](#).
12. Bulbul YE, Okur M, Demirtas-Korkmaz F, Dilsiz N. Development of PCL/PEO electrospun fibrous membranes blended with silane-modified halloysite nanotube as a curcumin release system. *Appl Clay Sci* [Internet]. 2020 Mar 1;186:105430. Available from: [<URL>](#).
13. Bezerra MA, Santelli RE, Oliveira EP, Villar LS, Escalera LA. Response surface methodology (RSM) as a tool for optimization in analytical chemistry. *Talanta* [Internet]. 2008 Sep 15;76(5):965-77. Available from: [<URL>](#).
14. Ko W-C, Chang C-K, Wang H-J, Wang S-J, Hsieh C-W. Process optimization of microencapsulation of curcumin in  $\gamma$ -polyglutamic acid using response surface methodology. *Food Chem* [Internet]. 2015 Apr 1;172:497-503. Available from: [<URL>](#).







## Radon gas in the indoor air of primary schools of Al-Najaf city, Iraq

Rukia Jabar Dosh<sup>1</sup>, Ali K. Hasan<sup>2</sup>, Ali Abid Abojassim<sup>1\*</sup> 

<sup>1</sup>University of Kufa, Faculty of Science, Department of Physics, Al-Najaf, Iraq

<sup>2</sup>University of Kufa, Faculty of Education for Girls, Department of Physics, Al-Najaf, Iraq

**Abstract:** The indoor radon concentration of 100 primary schools in Al-Najaf province, Iraq, was measured to determine students' and staff's safety in these schools using a CR-39 nuclear track detector based on the sealed can improve technique. The results of indoor radon concentration for all schools vary from (7.47 to 44.84) Bq / m<sup>3</sup> with an arithmetic mean (AM) of 22.26 Bq /, while the geometric mean (GM) was 20.67 Bq / m<sup>3</sup>. The concentration of <sup>222</sup>Rn was lower than the worldwide level. Some radiological parameters like annual effective dose (AED), potential alpha energy (PAEC), exposure to radon progeny (EP), and lung cancer cases per year per million people (CPPP) were also determined. The results of these parameters point toward normal levels in the primary schools, according to ICRP, UNCER, and NCRP data.

**Keywords:** Indoor radon, CR-39 detector, annual effective dose, primary schools, Al-Najaf province.

**Submitted:** October 23, 2022. **Accepted:** August 21, 2023.

**Cite this:** Dosh RJ, Hasan AK, Abojassim AA. Radon gas in the indoor air of primary schools of Al-Najaf city, Iraq. JOTCSA. 2023;10(4):1045-1054.

**DOI:** <https://doi.org/10.18596/jotcsa.1193534>.

\*Corresponding author. E-mail: [ali.alhameedawi@uokufa.edu.iq](mailto:ali.alhameedawi@uokufa.edu.iq)

### 1. INTRODUCTION

Radon is the naturally occurring radioactive gas formed by uranium's radioactive decay. Natural uranium (mainly <sup>238</sup>U) is found among most earthen construction materials and is present in the earth's crust at an average of 33Bq/m<sup>3</sup> (1). There are two primary radioisotopes for radon in nature: - <sup>222</sup>Rn (also known as radon with half-live  $T_{1/2}=3.82$  day) with its short-lived daughters: <sup>218</sup>Po, <sup>214</sup>Pb, <sup>214</sup>Bi, <sup>214</sup>Po, <sup>210</sup>Pb, <sup>210</sup>Bi, <sup>210</sup>Po (uranium sequence). The second isotope is <sup>220</sup>Rn (commonly known as thoron with a half-live  $T_{1/2}=55.6$ s) with its daughters: <sup>216</sup>Po, <sup>212</sup>Pb, <sup>212</sup>Bi, <sup>212</sup>Po, and <sup>208</sup>Tl (thorium sequence) (2). Although radon evaporates quickly if released into the open air, it could concentrate and accumulate to dangerous levels throughout the built environment. Indoor radon can have both external and internal sources. The external source is primarily outdoor air, while internal sources include soil, construction materials, basement air, and water. In most cases, higher indoor radon concentrations result from increased radon formation and mobility in soils, as well as fissures in floor slabs and other pores in

the building's foundation. Typically, the radon concentration in outdoor air at 1 meter above ground is between 4 and 15 Bq/m<sup>3</sup>. Depending on factors like uranium content and the soil's moisture, humidity, winds, and building materials, the radon concentration in indoor air might change from region to region. Because of the elevated radon concentrations in indoor areas of closed buildings, inhalation of air is one of the main causes of radiation exposure for humans. Radon and its daughters are in secular equilibrium in a closed system. However, this equilibrium cannot be conserved in a residential environment because daughters are constantly eliminated from the interior air through radioactive disintegration, surface deposition, and ventilation. The main causes of variation in indoor radon concentrations are often variations in ventilation rate, pressure, and temperature. The rate of air exchange between indoor and outdoor settings is affected by the ventilation rate. When radon becomes trapped indoors, particularly during temperature inversions or when homes are not vented (naturally or artificially), it will accumulate to unsafe levels. The radon concentration in the environment varies with time, meteorological circumstances, and the air

mass source at a sample site (2, 3). Long-term radon exposure may irradiate lung tissue, raising the risk of developing cancer. Inhalation of the short-lived radon daughters is predicted to produce roughly half the effective dosage of natural sources. As a result, radon is currently the most "popular" issue in environmental radioactivity research (4). When radon and its daughters were breathed, the  $\alpha$ -particles released by the depositing radon progeny predominated the radiation dosage for lung tissue. These progenies, particularly those adhering to tiny aerosols or those that stay unattached, cause harm to sensitive lung cells, raising the developing cancer risk. As a result, radon primarily serves as the origin of its daughters, which provide the lung dose (5). Lung cancer risk is elevated by 8.4% for every 100 Bq/m<sup>3</sup> (2.7 pCi/L) elevation in detected radon. Domestic studies show a link between radon exposure at home and an increased risk of lung cancer. WHO (the World Health Organization) and USEPA (the United States Environmental Protection Agency) list radon as one of the primary causes of lung cancer, next to smoking. According to studies on radon's behavior in the geological environment, there is a clear relationship between indoor radon levels and soil gas concentrations. As a result, conducting radon concentration studies at as many home and school locations as feasible would be one of the more efficient and expedient methods of lowering potential threats for children in schools and other facilities. Radon exposure in schools could have significant public health effects. The risk of lung cancer from radon exposure in children

may be up to three times higher than that of adults exposed to the same amount of radon due to morphologic distinctions between children's and adults' lungs and faster respiration rates in children. Children are more susceptible to environmental risks as well as spending extra time inside. (6, 7). For these reasons, there has been a rise in interest in indoor radon assessments in primary schools. As a result, assessing indoor radon levels in these facilities is important. Radon studies have been done widely in several countries (8–11). This study aimed to determine radon concentration and its risks to human health in one hundred primary schools in Al-Najaf province and to calculate the annual effective dose of radon for students and teachers in primary schools. Potential alpha energy concentration, exposure to radon progeny, and lung cancer cases per year per million people (CPPP) were calculated using CR-39 nuclear track detector (NTDs).

### 1.1. Sampling Sites

The studied area of Najaf (Figure 1) is located in southwestern Iraq, about 160 km southwest of Baghdad. It is situated at the intersection of line length 44.019E and latitude 31.059N. It is rising 70 meters above sea level (12). One hundred primary public schools were chosen to study the indoor radon concentration in these schools in Najaf city. The location of schools in the current research was identified using a GPS and plotted using a GIS approach (ArcGIS 10.7.1.) as depicted in Figure 1.

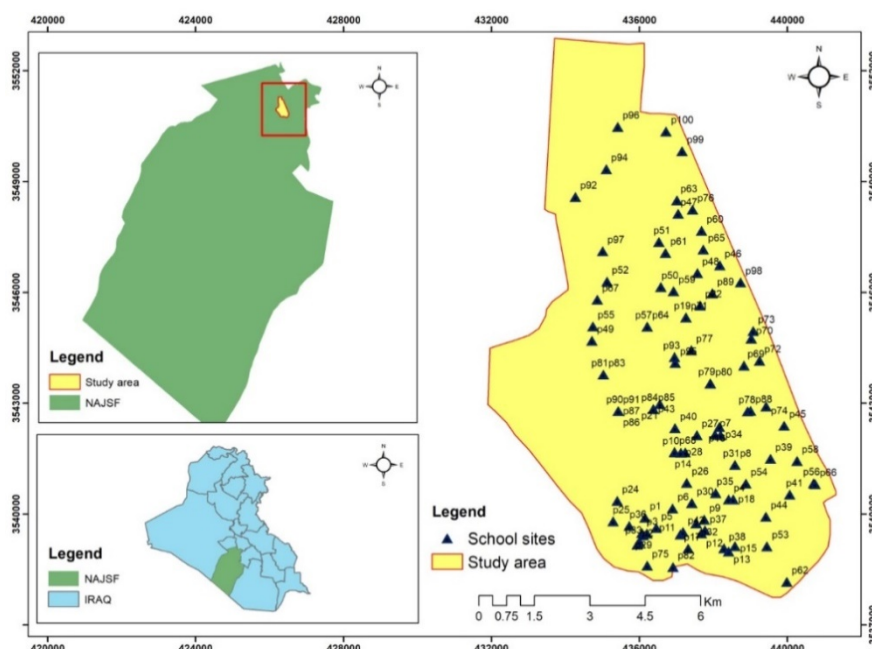


Figure 1: A map of the field of study.

## 2. MATERIAL AND METHOD

Radon concentration levels were assessed in 100 schools throughout the AL- Najaf city area using the solid state nuclear track detectors (SSNTDs) technique with a CR-39 detector. The dosimeter

measures <sup>222</sup>Rn in a very reproducible and unambiguous manner. One detector was exposed in each school's classroom, away from the doors and windows, and located in an inaccessible area to reduce loss throughout measurement time. In each of the 100 schools, around one hundred

detectors were distributed. Age, size, and construction materials vary among the school buildings. Natural ventilation is provided by windows as well as fans. A passive track detector inside a sealed hollow holder, which allows  $^{222}\text{Rn}$  to penetrate it, is used to investigate radon concentration and the annual effective dose within elementary schools.

The hollow holder has a diameter of 5.2 cm and a height of 9 cm. A circular aperture with a radius of 0.75 cm is drilled in the middle of the lid. A 3 cm × 3 cm sponge piece with a thickness of 0.3 cm is glued onto the internal surface of the lid to enclose the aperture. A bit of CR-39 with an area of around 2.5 cm × 2.5 cm and a thickness of 1 mm, density 0.32 gm/m<sup>3</sup>, is placed inside the holder and settled to its bottom with double-sided adhesive tape. The holder is placed around 1.5 m above the floor to represent the exhalation height inside the classrooms. The can's design guarantees that all aerosols and radon daughters are deposited from outside on the soft sponge while radon, along with other components, passes across it to the can's sensitive region. This type of detector generates data that correlate to the accurate mean radon concentration during the period of exposure, which extends from March to July 2022. The number of tracks left by alpha particles on the detector was proportional to the average radon concentration. After the end of the exposure time, the detectors were removed from the containers and placed in a solution of NaOH of about 6.25 N in a water bath at 98 C for one hour (13). The detectors were eliminated from the bath and adequately rinsed and cleaned using distilled water to eliminate surface digging leftovers. Following the chemical process, these detectors were dry. They scanned with an optical microscope at a magnification of about (400X) connected to a micro camera connected to a personal computer to count the number of tracks per cm<sup>2</sup> in each detector according to the following equation (14).

$$\text{The density of tracks } (\rho) = \frac{\text{number of tracks in sample}}{\text{Area of field view}} \quad (1)$$

## 2.1. Theoretical Considerations

### 2.1.1. Radon Concentrations

Radon concentration levels in the air of specific schools in Al-Najaf city are evaluated in the unit (Bq / m<sup>3</sup>), in which the highest degree reference levels are calculated. The following equations are employed to calculate radon concentration (15, 16).

$$C = \frac{\rho}{k t} \quad (2)$$

$\rho$  is the evaluated number of tracks for every cm<sup>2</sup> on the CR-39 detectors within the spread dosimeters utilized in the research,  $t$  would be the exposure time of the CR-39 detector (90 days), and  $k$  is a calibration factor equal to 0.28 Track.cm<sup>-2</sup> / Bq.m<sup>-3</sup>.day.

### 2.2.2. Annual Effective Dose (AED)

The annual effective dose (AED) in (mSv/y) units is directly affected by the occupancy factor (H), which can be calculated for students and teachers in schools by the following equation:

$$30 \text{ h/wk} \times 37 \text{ d /y} = 1110 \text{ hours per year}$$

$$H = 1110 / 8760 = 13\%$$

The annual effective dose can be calculated as (17, 18):

$$\text{AED (m Sv/y)} = C \times F \times H \times T \times D \quad (3)$$

Where;  $F$  indicates the worldwide average of the equilibrium factor of radon and its daughters equal to (0.4).

$T=8760$  h/y, which represents the time in hours per year

$D$ : represents the dose conversion factor and equal  $(9 \times 10^{-6} \text{ (m Sv) / (Bq.h.m}^{-3}\text{)})$

### 2.2.3. PAEC, EP, CPPP

Potential Alpha Energy Concentration (PAEC) can be calculated using the following equation (19-21):

$$\text{PAEC (WL)} = F \times C / 3700 \quad (4)$$

The following equation can be used to evaluate Exposure to radon progeny (EP) (22):

$$\text{EP (WLM Y}^{-1}\text{)} = T \times H \times F \times C / 170 \times 3700 \quad (5)$$

170 : is the number of hours spent per month.

WL represents the working level, in which (1WL = 3.7 Bq / L= 3.7 × 10<sup>3</sup>PP Bq / m<sup>3</sup>) .

Where 1 L=1000 m<sup>3</sup>

The lung cancer cases per year per million person (CPPP) were found by using the equation (19, 23, 24):

$$\text{CPPP} = \text{AED} \times (18 \times 10^{-6} \text{ mSv}^{-1} \cdot \text{y}) \quad (6)$$

## 3. RESULTS AND DISCUSSION

This study covered the public primary schools in Najaf, Iraq, in which 100 classrooms on the ground floor from 100 schools were chosen to measure indoor radon using the passive technique with a CR39 detector. The study area is divided into 22 districts. The descriptive statistics of the results for indoor radon concentration are summarized in Table 1. The results of indoor radon concentrations for all schools vary from (7.47 to 44.84) Bq / m<sup>3</sup> with an arithmetic mean (AM) 22.26 Bq / m<sup>3</sup> and standard deviation (SD) 8.43. The geometric mean (GM) was 20.67 Bq / m<sup>3</sup> with a geometric standard deviation (GSD) of 1.48. The Abotalib district has the maximum indoor radon concentration with an arithmetic mean (32.14) Bq / m<sup>3</sup> and a standard deviation of 2.25, whereas the geometric mean was 32.06 Bq / m<sup>3</sup> with a geometric standard deviation of 1.1. The minimum indoor radon concentration was in the AL Gari district, with AM equal to 12.74 Bq / m<sup>3</sup> and SD equal to 3.30, while GM was 12.24 Bq / m<sup>3</sup> with a GSD of 1.41. The maximum radon concentrations seemed to be below the worldwide average of radon gas in air (100) Bq/m<sup>3</sup> according to WHO (25), as shown in Figure (2). The variation in indoor radon results between different schools is

due to geological considerations, ventilation, and the type of soil in the schools.

**Table 1:** Descriptive statistics of indoor radon concentrations for studied schools.

District	N°. Of Schools	AM (Bq/m <sup>3</sup> )	SD (Bq/m <sup>3</sup> )	Min (Bq/m <sup>3</sup> )	Max (Bq/m <sup>3</sup> )	GM (Bq/m <sup>3</sup> )	GSD
old city	15	21.03	9.46	8.97	40.36	18.87	1.64
Al.Karama	4	20.55	3.72	14.95	25.41	20.19	1.25
Al.Moalmen	5	21.67	4.38	16.44	26.9	21.23	1.25
Alhussein	4	19.80	5.83	10.46	25.41	18.75	1.49
Al.Ameer	4	31.82	7.95	24.14	44.84	30.92	1.31
Al.Ansar	6	23.42	9.52	13.45	40.36	21.67	1.53
Al.Zahraa	6	20.99	4.18	13.45	25.41	20.53	1.27
AL gari	4	12.74	3.30	7.47	16.59	12.24	1.41
Aloroba	4	17.19	6.02	10.46	26.9	16.22	1.48
Al.Mothana	4	25.78	4.65	17.94	29.89	25.30	1.26
Aladala	3	27.77	3.06	23.91	31.39	27.60	1.15
Alwafaa	5	28.92	9.004	17.56	41.1	27.49	1.43
Al.Askary	6	26.90	6.85	14.95	34.38	25.88	1.38
Alnasor	2	19.24	2.81	16.44	22.05	19.04	1.23
Alresalah	3	19.06	2.42	16.81	22.42	18.91	1.16
Alnidaa	5	19.13	3.19	14.95	23.91	18.86	1.21
Aljamea	4	25.04	10.27	14.95	40.36	23.04	1.59
Alsalam	5	19.13	6.08	11.96	28.4	18.20	1.423
Alforat	3	27.77	10.263	13.45	36.98	25.38	1.74
Abotalib	2	32.14	2.25	29.89	34.38	32.06	1.10
Alrahma	4	14.95	5.69	7.47	22.42	13.77	1.62
Algahdeer village	2	16.45	1.49	14.95	17.94	16.38	1.14
All	100	22.26	8.43	7.47	44.84	20.68	1.48

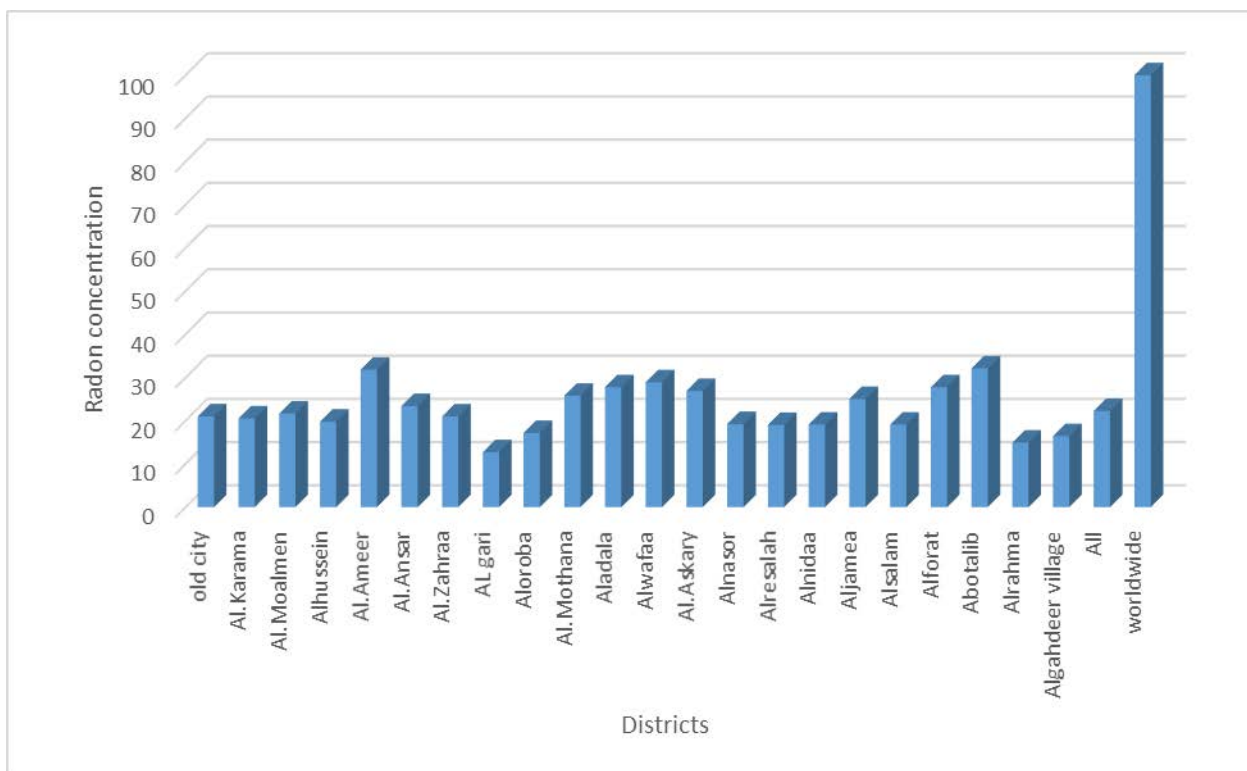


**Figure 2:** Indoor radon concentrations at the primary schools in the districts of AL- Najaf city.

The frequency distribution of indoor radon levels in investigated schools is illustrated in Figure (3), which explains the normal distribution of indoor radon for all schools under study. The skewness of this distribution, indicating its deviation from a symmetrical normal distribution, is 0.608,

suggesting a positive skew in indoor radon levels. This skewness implies that many indoor radon test results have lower values, with means exceeding the medians. The central tendency of the positively skewed data is also illustrated in figure (4), which represents the box plot of the indoor radon concentration for the primary schools. It is clear that quartile Q2 exists nearer to quartile Q1, and the mean value is larger than the median. Also, the length of the upper whisker is greater than that of the bottom. All this refers to a positively skewed distribution. The kurtosis of this distribution, which tested whether the results were heavy-tailed or light-tailed compared to the normal

distribution, is (-0.029), indicating that the distribution is a platykurtic distribution. This means that the majority of the indoor radon results are very close to the mean value. Figure (5) represents the normal quantile-quantile plot (Q-Q plot) for radon concentration for all schools under study, assessing indoor radon results relative to the normal distribution. We can see from this plot that our results are normally distributed. Also, the ends of the Q-Q plot deviated with a slight deviation from the normal distribution reference line, indicating there is a thin-tailed distribution (platykurtic distribution).

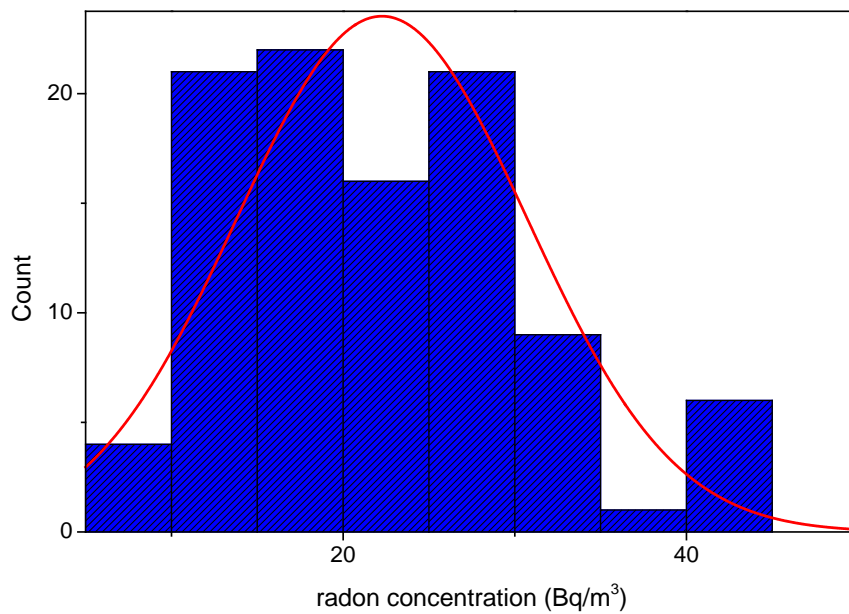


Figure 3: Histogram of indoor radon concentrations at the primary schools in the AL- Najaf city.

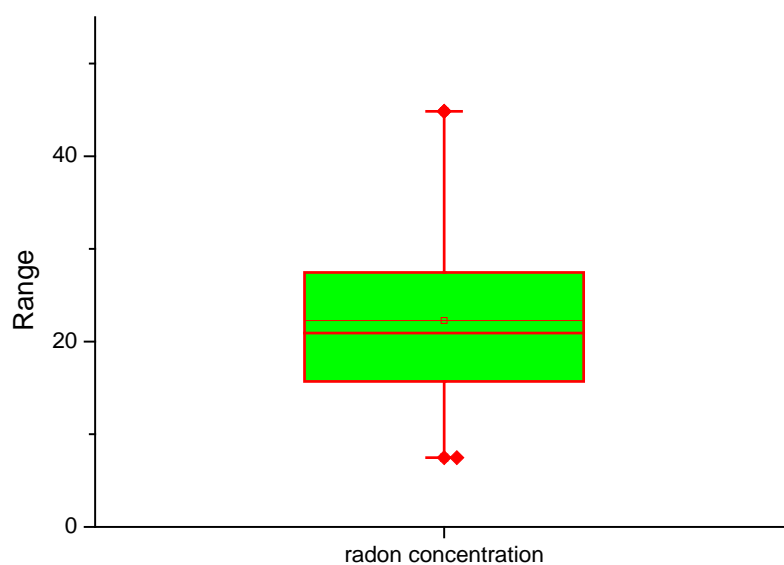
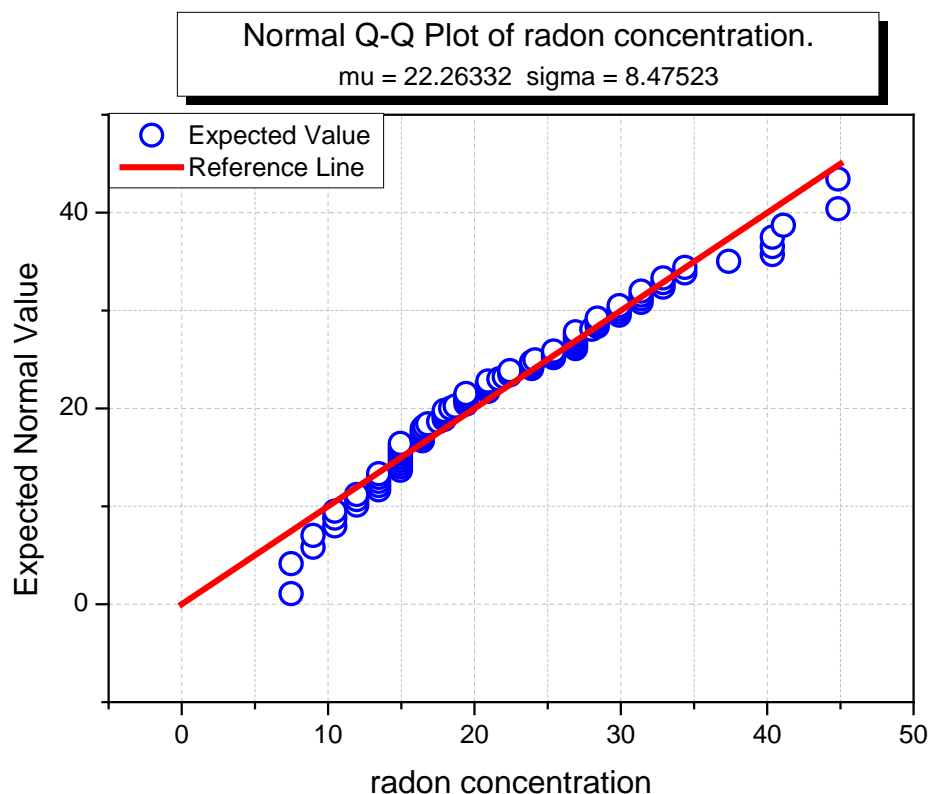


Figure 4: Box plot of indoor radon concentrations at the AL- Najaf city primary schools.



**Figure 5:** Normal quantile plot of indoor radon concentrations at the investigated primary schools.

Figure 6 displays the relationship between the indoor radon levels and the school buildings' age. The higher level of indoor radon was in buildings

with ages between 1979 and 1999 (consisting of 36 schools), while the lower level was in schools between 1919-1939 (consisting of 3 schools).

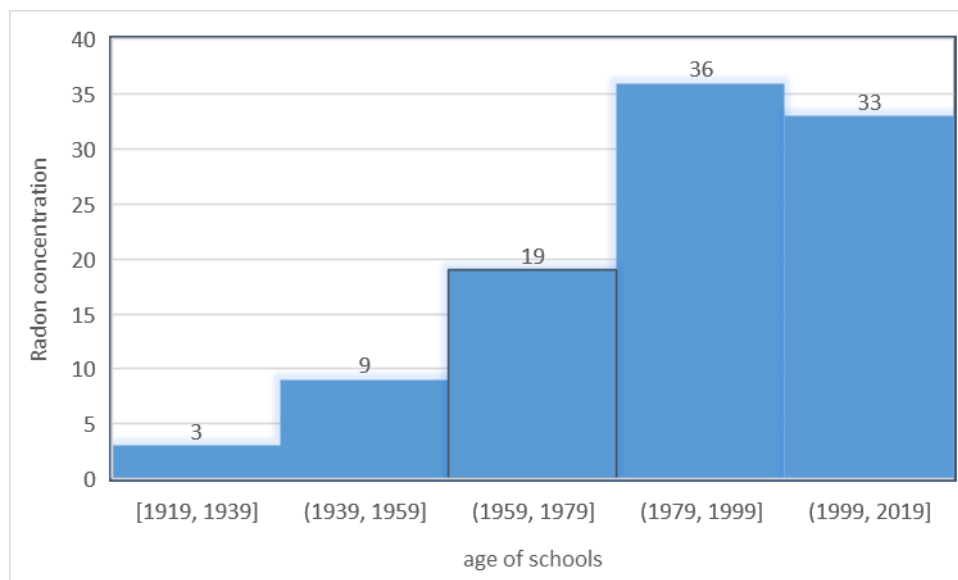


**Figure 6:** The relation between radon concentration in studied schools and the age of schools.

Table 2 displays the results of the annual effective dose (AED), potential alpha energy concentration (PAEC), exposure to radon progeny (EP), and lung cancer cases per year per million people (CPPP) for the primary schools in the districts of AL- Najaf city. The maximum values of AED, PAEC, EP, and CPPP were 0.132 mSv/y, 3.474 mWL, 23.272 mWLM Y<sup>-1</sup>, and 2.371, respectively, found in Abotalib district. The minimum values of AED,

PAEC, EP, and CPPP were 0.052 mSv/y, 1.377mWLM, 9.228 mWLM Y<sup>-1</sup>, and 0.940, respectively, and found in the AL gari district. The maximum values of AED are much lower than the (ICRP,1993) limit that lies between 3 and 10 mSv/y (26). PAEC results were significantly lower than (UNCER,1993) (27) level that equals 53.33 mWL, and the measurements of EP lowered the recommended values of (NCRP,1989) (28) that

range between (1-2) mWLM Y<sup>-1</sup>. The results of CPPP were below the values of (ICRP ,1993) (26) limit that lies between 170 and 230 per year per million people. Figure 7 illustrates the annual

effective dose and lung cancer cases per year per million people for the primary schools in the districts of AL-Najaf city.

**Table 2:** The annual effective dose (AED), potential alpha energy concentration (PAEC), exposure to radon progeny (EP), and lung cancer cases per year per million people (CPPP) for the primary schools in the districts of AL-Najaf city.

District	N°. Of Schools	AED (mSv/y)	PAEC (mWL)	EP (mWLM Y <sup>-1</sup> )	CPPP (×10 <sup>-6</sup> )
Old city	15	0.086	2.273	15.226	1.551
Al.Karama	4	0.084	2.222	14.883	1.517
Al.Moalmen	5	0.089	2.343	15.695	1.599
Alhussein	4	0.081	2.141	14.342	1.461
Al.Ameer	4	0.130	3.440	23.042	2.348
Al.Ansar	6	0.096	2.531	16.958	1.728
Al.Zahraa	6	0.086	2.270	15.208	1.550
AL gari	4	0.052	1.377	9.228	0.940
Aloroba	4	0.070	1.858	12.448	1.268
Al.Mothana	4	0.106	2.787	18.672	1.903
Aladala	3	0.114	3.003	20.115	2.050
Alwafaa	5	0.119	3.127	20.945	2.134
Al.Askary	6	0.110	2.908	19.483	1.985
Alnasor	2	0.079	2.080	13.936	1.420
Alresalah	3	0.078	2.060	13.801	1.406
Alnidaa	5	0.078	2.068	13.855	1.412
Aljamea	4	0.103	2.706	18.130	1.847
Alsalam	5	0.078	2.068	13.855	1.412
Alforat	3	0.125	3.286	22.009	2.243
Abotalib	2	0.132	3.474	23.272	2.371
Alrahma	4	0.061	1.616	10.824	1.103
Algahdeer village	2	0.067	1.777	11.907	1.213
All	100	0.091	2.407	16.123	1.643

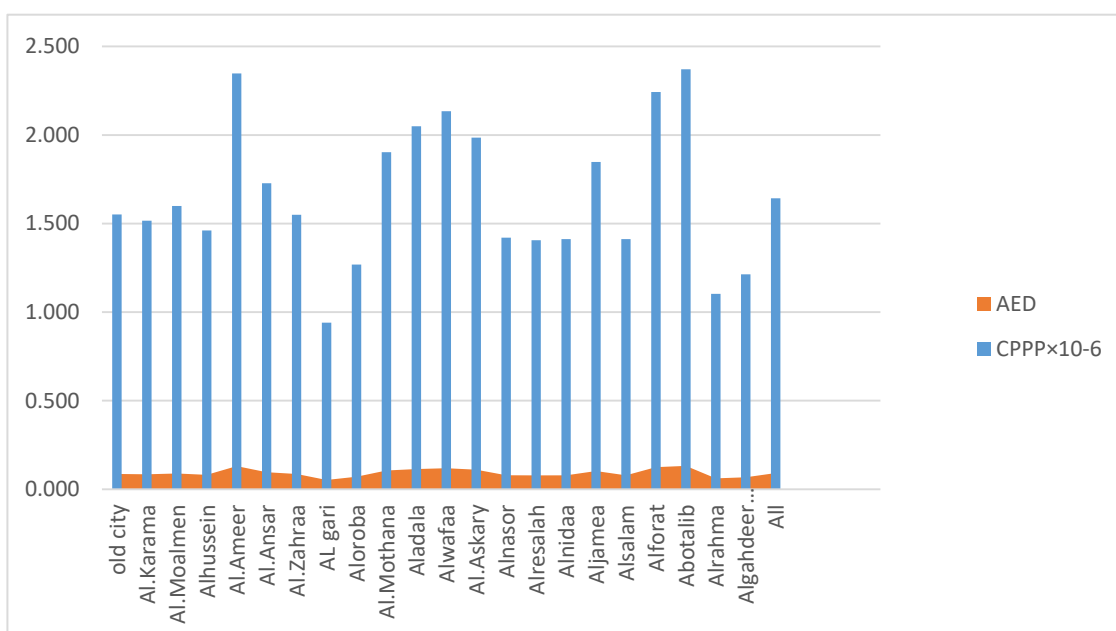


**Figure 7:** The annual effective dose (AED) and lung cancer cases per year per million people (CPPP) at the primary schools in the districts of AL-Najaf city.

**Table 3:** The average value of the indoor radon concentrations compared to other similar research in primary schools across different countries.

country	Average radon concentration	reference
Bulgaria	339	(29)
Kuwait	18	(1)
Greece.	149	(30)
Macedonia	211	(31)
Poland	49.0	(32)
Sudan	59	(33)
Serbia	119	(34)
Tunisia	26.9	(35)
Palestine	40.42	(36)
Italy	77	(37)
Iraq (Karbala)	25.4	(38)
Turkey	49	(39)
Present Study	22.26	

Table 3 compares the indoor radon measured within schools in several countries. The results vary because numerous factors influence indoor radon concentrations, including geology.

#### 4. CONCLUSION

The study of radon levels in the primary schools in AL-Najaf city indicates a normal level. The average values of  $C_{Rn}$  are substantially below the global limit. The results of AED for the studied schools are lower than those of ICRP and lower than the results of UNSCEAR. The results of potential alpha energy concentration, exposure to radon progeny, and lung cancer cases per year per million people are lower than the global limits. As a result, the occupants of these schools (children and staff) are not at risk of radiological exposure from their immediate surroundings.

#### 5. REFERENCES

- Maged AF. Radon concentrations in elementary schools in Kuwait. *Health physics*. 2006;90(3):258-62. Available from: [<URL>](#)
- Hussein A. Radon in the environment: friend or foe? 2008. Available from: [<URL>](#)
- Khan F, Ali N, Khan EU, Khattak NU, Raja IA, Baloch MA, et al. Study of indoor radon concentrations and associated health risks in the five districts of Hazara division, Pakistan. *Journal of Environmental Monitoring*. 2012;14(11):3015-23. Available from: [<URL>](#)
- Clouvas A, Xanthos S, Takoudis G. Indoor radon levels in Greek schools. *Journal of environmental radioactivity*. 2011;102(9):881-5. Available from: [<URL>](#)
- Ismail AH, Jaafar MS, editors. Indoor radon concentration and its health risks in selected locations in Iraqi Kurdistan using CR-39 NTDs. 2010 4th International Conference on Bioinformatics and Biomedical Engineering; 2010: IEEE. Available from: [<URL>](#)
- Gordon K, Terry PD, Liu X, Harris T, Vowell D, Yard B, et al. Radon in schools: a brief review of state laws and regulations in the United States. *International journal of environmental research and public health*. 2018;15(10):2149. Available from: [<URL>](#)
- Obed R, Ademola A, Vascotto M, Giannini G. Radon measurements by nuclear track detectors in secondary schools in Oke-Ogun region, Nigeria. *Journal of environmental radioactivity*. 2011;102(11):1012-7. Available from: [<URL>](#)
- Al-Awadi L, Khan A. Indoor radon levels in schools and residential dwellings in Kuwait. *International Journal of Environmental Science and Technology*. 2019;16:2627-36. Available from: [<URL>](#)
- Malanca A, Gaidolfi L, Fava R. Natural radioactivity in kindergartens and play schools of Parma, Italy. *Environment international*. 1997;23(4):541-6. Available from: [<URL>](#)
- Kurt A, Yalcin LS, Oktem Y, Akkus B, Bozkurt E, Hafizoglu N, et al., editors. Determination of indoor radon concentrations at the elementary schools of Fatih district in Istanbul. *AIP conference proceedings*; 2016: AIP Publishing.
- Papaefthymiou H, Georgiou C. Indoor radon levels in primary schools of Patras, Greece. *Radiation protection dosimetry*. 2007;124(2):172-6. Available from: [<URL>](#)
- Abojassim AA. Comparative study between active and passive techniques for measuring radon concentrations in groundwater of Al-Najaf city, Iraq. *Groundwater for Sustainable Development*. 2020;11:100476. Available from: [<URL>](#)
- Tate B, Long S. Acceptance testing of the tasl radon dosimetry system. *Technical Report*. 2016:175.
- Al-Gharabi M, Al-Hamzawi A. Measurement of radon concentrations and surface exhalation rates using CR-39 detector in soil samples of Al-Diwaniyah Governorate, Iraq. *Iranian journal of medical physics*. 2020;17(4):220-4. Available from: [<URL>](#)



15. Hashim AK. A study of radon concentration in the soil and air of some villages in Irbid governorate: M. Sc. Thesis, Yarmouk University, Jordan; 2003.
16. Mayya Y, Eappen K, Nambi K. Methodology for mixed field inhalation dosimetry in monazite areas using a twin-cup dosimeter with three track detectors. *Radiation protection dosimetry*. 1998;77(3):177-84. Available from: [<URL>](#)
17. Annex I. Epidemiological evaluation of radiation-induced cancer. Vienna: United Nations. 2000.
18. Mowlavi AA, Fornasier MR, Binesh A, Denaro Md. Indoor radon measurement and effective dose assessment of 150 apartments in Mashhad, Iran. *Environmental monitoring and assessment*. 2012;184:1085-8. Available from: [<URL>](#)
19. Kansal S, Mehra R, Singh N. Life time fatality risk assessment due to variation of indoor radon concentration in dwellings in western Haryana, India. *Applied Radiation and Isotopes*. 2012;70(7):1110-2. Available from: [<URL>](#)
20. Ismail A, Hussyin Z, editors. Study of seasonal variations of radon levels and its risks inside different schools in Iraqi Kurdistan region for the first time. *Proceedings of the 10 th*; 2007.
21. Ismail AH, Jaafar MS, editors. Indoor radon concentration and its health risks in selected locations in Iraqi Kurdistan using CR-39 NTDs. 2010 4th International Conference on Bioinformatics and Biomedical Engineering; 2010: IEEE. Available from: [<URL>](#)
22. Protection ICoR, Clarke RH. Protection against radon-222 at home and at work: Pergamon published for the International Commission on Radiological Protection; 1994. Available from: [<URL>](#)
23. Mansour H, Per Khdar S, Abdulla H, Muhamad N, Othman M, Qader S. Measurement of indoor radon levels in Erbil capital by using solid state nuclear track detectors. *Radiation measurements*. 2005;40(2-6):544-7. Available from: [<URL>](#)
24. Abdullah AA. Internal and external radiation exposure evaluation amongst selected workers and locations in Iraq: Universiti Sains Malaysia; 2013.
25. Organization WH. WHO handbook on indoor radon: a public health perspective: World Health Organization; 2009.
26. Brenner D. Protection against radon-222 at home and at work. ICRP publication 65. Taylor & Francis; 1994.
27. Radiation UNSaEol. Report to the General Assembly, with Scientific Annexes. United Nations sales publication E. 94. IX. 2. United Nations New York; 1993.
28. Wagner LK. Exposure of the US Population from Diagnostic Medical Radiation. JSTOR; 1989.
29. Vuchkov D, Ivanova K, Stojanovska Z, Kunovska B, Badulin V. Radon measurement in schools and kindergartens (Kremikovtsi municipality, Bulgaria). *Romanian Journal of Physics*. 2013;58(S):S328-S35. Available from: [<URL>](#)
30. Clouvas A, Xanthos S, Takoudis G. Indoor radon levels in Greek schools. *Journal of environmental radioactivity*. 2011;102(9):881-5. Available from: [<URL>](#)
31. Stojanovska Z, Boev B, Zunic ZS, Bossew P, Jovevska S. Results of radon CR-39 detectors exposed in schools due two different long-term periods. *Nukleonika*. 2016;61(3):385-9. Available from: [<URL>](#)
32. Bem H, Bem EM, Krawczyk J, Płotek M, Janiak S, Mazurek D. Radon concentrations in kindergartens and schools in two cities: Kalisz and Ostrów Wielkopolski in Poland. *Journal of Radioanalytical and Nuclear Chemistry*. 2013;295(3):2229-32. Available from: [<URL>](#)
33. Elzain, AEA. Assessment of indoor radon doses received by the students and staff in schools in some towns in Sudan. *Rn*. 2015;19(34), 35.
34. Bochicchio F, Žunić ZS, Carpentieri C, Antignani S, Venoso G, Carelli V, et al. Radon in indoor air of primary schools: a systematic survey to evaluate factors affecting radon concentration levels and their variability. *Indoor air*. 2014;24:315-326. Available from: [<URL>](#)
35. Labidi S, Al-Azmi D, Mahjoubi H, Salah RB. Radon in elementary schools in Tunisia. *Radioprotection*. 2010;45(2):209-217. Available from: [<URL>](#)
36. Al Zabadi H, Mallah K, Saffarini G. Indoor exposure assessment of radon in the elementary schools. Palestine. 2015. Available from: [<URL>](#)
37. Loffredo F, Opoku-Ntim I, Meo G, Quarto M. Indoor Radon Monitoring in Kindergarten and Primary Schools in South Italy. *Atmosphere*. 2015;13(3):478. Available from: [<URL>](#)
38. Hashim AK, Nayif SS. Assessment of Internal Exposure to Radon in Schools in Karbala, Iraq. *Journal of Radiation and Nuclear Applications*. 2019;4:25-34. Available from: [<URL>](#)
39. Damla N, Aldemir K. Radon survey and soil gamma doses in primary schools of Batman, Turkey. *Isotopes in environmental and health studies*. 2014;50:226-234. Available from: [<URL>](#)





## Oleic Acid-PVA Based Amphiphilic Polymer Micelles for Vitamin D Encapsulation

Hatice Birtane<sup>1\*</sup> 

<sup>1</sup>Marmara University Faculty of Science, Department of Chemistry, Goztepe 34722 Istanbul, Türkiye

**Abstract:** In this study, oleic acid-PVA based amphiphilic polymer micelles were prepared for vitamin D encapsulation. The amphiphilic polymer encapsulations were characterized using Fourier transformed infrared spectroscopy (FTIR) and nuclear magnetic resonance spectroscopy (<sup>1</sup>H-NMR). The goal of the study was to create micelles by using a lipophilic and biocompatible polymer. An oleic acid-substituted polyvinyl alcohol polymer was created through an acidic esterification reaction. The chemical structure of the polymer was disclosed by FTIR. To calculate the polymer's substitution ratio, <sup>1</sup>H-NMR was used. Micellization was used to encapsulate vitamin D. Scanning electron microscope (SEM) analysis was used to determine the crucial micelle concentration and the size of the oleic acid-modified PVA. Ultraviolet-visible (UV) spectroscopy was used to analyze the release of vitamin D at various pH levels. As a result, vitamin D can be enclosed in PVA polymer that has been substituted with oleic acid.

**Keywords:** Encapsulation, Vitamin D, Oleic Acid, Drug Release, Micelle

**Submitted:** June 20, 2023. **Accepted:** August 21, 2023.

**Cite this:** Birtane H. Oleic Acid-PVA Based Amphiphilic Polymer Micelles for Vitamin D Encapsulation. JOTCSA. 2023;10(4):1055-1062.

**DOI:** <https://doi.org/10.18596/jotcsa.1317320>.

**\*Corresponding author.** E-mail: [hatice.ceylan@marmara.edu.tr](mailto:hatice.ceylan@marmara.edu.tr)

### 1. INTRODUCTION

The process of covering solid, liquid, or gaseous components with a film coating material is referred to as encapsulation (1,2). The outer material is referred to as the shell, the shield, or the wall, and the inside substance is referred to as the core, corona, or active substance. It is frequently employed in a variety of industries, including medicine, nanotechnology, paint, cosmetics, and many more. Typically, one of the generated blocks is found to be hydrophilic, while the other is hydrophobic. Amphiphilic polymers can also be used to encapsulate molecules with a lipophilic structure (3).

Drug delivery systems that facilitate the transport of low-resolution drugs in the body have high interest. Such systems often allow the drug to be transported within the body and released in the targeted area (4,5). Polymeric carriage systems are used due to their easy adaptation in the body, protection of the drug from external factors, formation of phase separation, facilitation of distribution and easy movement within the vessels

(6). In addition, drug transportation systems reduce side effects, inactivate body areas where unnecessary, and increase bioavailability, in addition to their easier production and lower costs (7).

Due to their capacity for absorption by the body, biodegradable polymers have become necessary as medication carriers in controlled-release technologies. Natural or artificial, biodegradable polymers can be broken down in vivo either enzymatically or non-enzymatically. They generate by-products that are biocompatible and toxicologically safe and can be further removed through regular metabolic function (8). Researchers currently have access to a wide variety of degradable polymers with a variety of breakdown rates thanks to the field of biodegradable polymers' rapid development (9). Polyvinyl alcohol (PVA), polylactic acid (PLA), and polylactic-co-glycolic acid (PLGA) are the most commonly utilized and researched biodegradable polymers. These polymers have been used in the formulation of numerous micro- and nanoparticulate systems.

The following benefits (16,17,18) should be provided by the encapsulation technique: the encapsulation should not have any negative consequences on the drug's stability or biological activity, the drug should not be affected during the final phase of the microsphere process, the effectiveness of the drug's encapsulation should not be subpar, and the yield of microspheres should be sufficient (up to 250 nm, ideally 125 nm). Additionally, the medication release profile and microsphere quality should be repeatable within the predetermined ranges. The microspheres must be manufactured in a powder that flows freely and exhibit neither agglomeration nor adhesion.

The coacervation technique (19,20), interfacial polymerization (21,22), and "in situ" polymerization (23,24) are the most frequently used techniques for microencapsulation.

Vitamin D, is a fat-soluble vitamin. Some types of vitamin D, such as ergocalciferol, play an important role in terms of their effects in the in vivo metabolism of calcium and phosphorus. Vitamin D has an important role in human health, from bone fractures to cardiovascular disease, neuromuscular problems, and diabetes. D vitamins could also be preferred as provitamin for the body's needs. Vitamin D precursors turns into Vitamin D by UV rays, which makes calcium binding faster (25).

In this study, PVA is modified with oleic acid, and optimum conditions for the encapsulation of vitamin D have been studied.

## 2. MATERIALS AND METHODS

### 2.1. Material

PVA (Mw ~150,000) (89% Hydrolyzed), oleic acid, sulfuric acid, ethanol, and citric acid were purchased from Sigma Aldrich. Vitamin D (98 %) was obtained from Merck.

### 2.2. Characterization techniques

A Shimadzu UV-Vis spectrophotometer 2450 (Kyoto Japan) was used for the spectrophotometric analysis. Using a Perkin-Elmer Spectrum 100 ATR-FTIR spectrophotometer, synthetic oligomers' chemical structures were determined (WA). A Varian Unity Inova Spectrometer (CAL USA) running at 400 MHz was used to generate <sup>1</sup>H-NMR spectra. SEM images of the resultant composites were captured using a Philips XL30 ESEM-FEG/EDAX. In order to prepare specimens for SEM, liquid nitrogen was used to solidify them, break them, and then cover them in platinum.

### 2.3. Synthesis of oleic acid modified polyvinyl alcohol

The oleic acid modified PVA (OA-PVA) was prepared according to previous studies (3,26). Briefly, PVA (600 g, 4 mmol) dissolved in 200 mL

of distilled water and oleic acid (0.34 g, 1.2 mmol) were put into to a three-necked glass flask equipped with a nitrogen inlet, a magnetic stirrer, a reflux condenser, and a thermometer. 1 mL of H<sub>2</sub>SO<sub>4</sub> was added with 250 rpm stirring at 80 °C in an oil bath through a dropping funnel. The mixture was refluxed at a temperature of 80 °C for 24 hours. The obtained product was precipitated with ethanol. The oleic acid-modified PVA was filtered and dried overnight at room temperature in a vacuum.

<sup>1</sup>H-NMR: δ5.26-5.41(2H, 5.33 (dt, J=11.0, 7.4 Hz), 5.33 (dt, J=11.0, 7.4 Hz), 4.69 (1H, q, J=7.1 Hz), 3.57-3.6 (3H, 3.59 (q, J=7.4 Hz), 3.6 (tt, J=6.2,2.7 Hz), 3.6 (qt, J=6.2,2.6 Hz), 2.19-2.31 (2H, 5.33 (dt, J=11.0, 7.4 Hz), 2.25(t, J=7.4Hz), 1.91-2.03 (4H, 1.97(q, J=7.4 Hz), 1.97 (q, J=7.4 Hz), 1.97(q, J=7.4 Hz), 1.97 (q, J=7.4 Hz)), 1.35-1.84 (14 H, 1.42(tt, J=7.4,7.0 Hz), 1.42 (tt, J=7.4, 7.0 Hz), 1.43 (tt, J=7.4,7.0 Hz), 1.43 (tt, J=7.4, 7.0 Hz), 1.56 (tt, J=7.7,7.4 Hz), 1.56 (tt, J=7.7,7.4 Hz), 1.62 (qd, J=7.5, 6.2 Hz), 1.62 (qd, J=7.5, 6.2 Hz), 1.71 (t, J=2.6 Hz), 1.71 (t, J=2.6 Hz), 1.77 (dd, J=7.1, 2.7 Hz), 1.77 (dd, J=7.1, 2.7 Hz), 1.77 (dd, J=7.1, 2.7 Hz), 1.77 (dd, J=7.1, 2.7 Hz), 1.11-1.34 (21H, 1.17 (d, J=6.2 Hz), 1.23 (tt, J=7.0, 6.9 Hz), 1.23 (tt, J=7.0, 6.9 Hz), 1.23(q, J=7.0 Hz), 1.23 (q, J=7.0 Hz), 1.23 (q, J=7.0 Hz), 1.23 (q, J=7.0 Hz), 1.23 (q, J=7.0 Hz), 1.24 (tt, J=7.0, 6.9 Hz), 1.24 (q, J=7.0 Hz), 1.24 (q, J=7.0 Hz), 1.25 (tt, J=7.7, 6.9Hz), 1.24 (q, J=7.0 Hz), 1.24 (q, J=7.0 Hz), 1.25 (tt, J=7.7,6.9 Hz), 1.25 (tt, J=7.7,6.9 Hz), 1.28 (tt, J=7.0,6.9 Hz), 1.28 (tt, J=7.0,6.9 Hz), 1.28 (h, J=7.0 Hz), 1.28 (h, J=7.0 Hz), 0.81-1.02 (6H, 0.86 (t, J=7.0 Hz), 0.96 (t, J=7.5 Hz).

### 2.4. Vitamin D encapsulation by using OA-PVA and determination of optimum capsulation parameters

Vitamin D encapsulation was performed by the direct dissolution method at optimum critical micelle concentration (CMC), resulting in the self-assembling of the drug and polymer to form polymeric micelles. In the encapsulation study, 0.6 g oleic acid-modified PVA was dissolved in 50 mL distilled water, stirred for 2 h, and 1 mL of vitamin D was added to the solution. After 1 h, 4 mL of 1M citric acid were added. The resulting mixture was stirred for 2 h at 500 rpm (27). The obtained capsules were filtered and dried.

The CMC is the minimum quantity of wall material necessary for micelle formation during the manufacturing of a capsule. Both SEM analysis and visual inspection revealed that different amounts of OA-PVA (0.2, 0.4, 0.6, 0.8, and 1 g) were used to make capsule walls, and varying amounts of vitamin D (0.5, 1 and 1.5 mL) were placed into the micelle that served as the cores of the capsules to determine the optimal encapsulation parameters.

## 2.5. Decomposition of nanocapsules at various pH values

The release studies were carried out at different pHs to monitor the pH dependence of vitamin D encapsulated wall material for the critical micelle concentration and the optimum vitamin D amount. The solutions were stirred for 20 minutes, followed by changing pH values. Capsule deterioration has been revealed by means of changes in its color

with a UV-Vis spectrophotometer in addition to visual inspection.

## 3. RESULTS

### 3.1. Synthesis and characterization

Oleic Acid Substituted Polyvinyl Alcohol was prepared via Fisher esterification according to Figure 1.

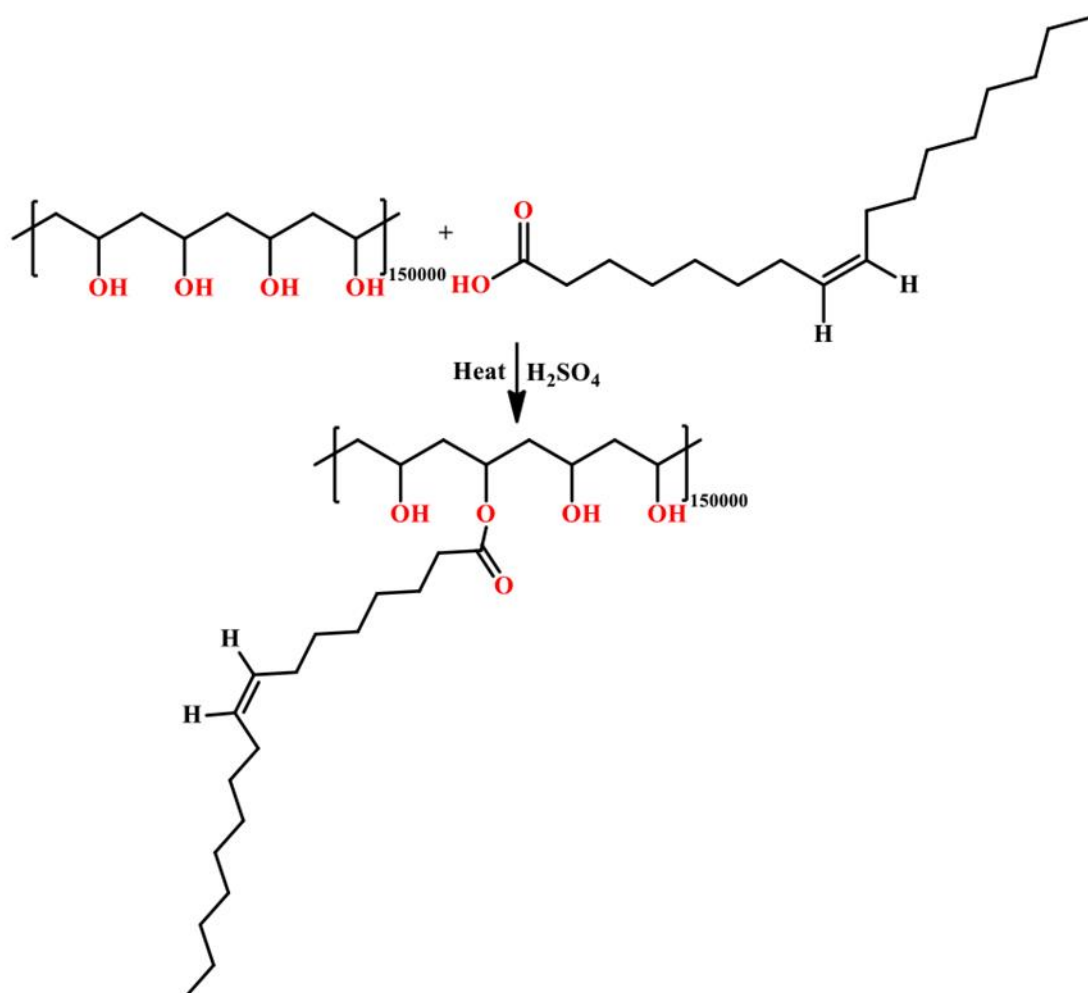


**Figure 1:** Synthesis of oleic acid substituted polyvinyl alcohol

In Section 2.3, the <sup>1</sup>H-NMR spectrum of oleic acid modified polyvinyl alcohol can be seen. The double bond proton signals for the oleic acid substituted polyvinyl alcohol appeared at 5.33 ppm and at 4.69-4.75 ppm for oleic acid bonded C-H. Additionally, the spectrum exhibits OH protons signals of PVA at 3.60 and 3.57 ppm. At 2.25 ppm, the first protons of oleic acid and, at 1.96 and 1.25 ppm, methyl protons (-CH<sub>2</sub>-) of oleic acid can be seen. In addition, the methyl protons of PVA appear at 1.72, 1.76, and 1.50 ppm. Moreover, the terminal methyl protons of the oleic acid are seen at 0.86 ppm. The obtained results were in accordance with the literature (28). The substitution was calculated by comparing the areas of the peaks at 4.69-4.75 ppm oleic acid bonded C-H and OH protons signals of PVA at 3.60 and

3.57 ppm. The ratio is calculated as 1: 4. The substitution range is close to the calculated value and matches the literature (29). The results of <sup>1</sup>H-NMR analysis demonstrated that the expected structure was synthesized successfully.

Additionally, the FTIR analysis supports the <sup>1</sup>H-NMR results. Figure 2a demonstrated that the carbonyl stretching of PVA's acetate groups emerged at 1693 cm<sup>-1</sup> and that the typical CH<sub>2</sub> stretching band for PVA appeared at 2915 cm<sup>-1</sup>. Moreover, at 3307 cm<sup>-1</sup> typical strong hydroxyl bands for PVA can be seen. Crystallization-sensitive band of PVA at 1090 cm<sup>-1</sup> Similar results could also be found in the literature for the PVA (30). Figure 2b showed that the characteristic carbonyl strength band of oleic acid at 1711 cm<sup>-1</sup>

and the peaks at 2900 and 2850  $\text{cm}^{-1}$  were attributed to the asymmetric  $\text{CH}_2$  stretch and the symmetric  $\text{CH}_2$  stretch, respectively, in-plane and out-of-plane. The peak at 3005  $\text{cm}^{-1}$  belongs to  $\text{CH}=\text{CH}$  strength of oleic acid. The results are consistent with the literature (31). Figure 2c showed that oleic acid modified polyvinyl alcohol

FTIR. The key parameter of the stretching vibration of carbonyl groups in esters ( $\text{C}-\text{O}-\text{C}=\text{O}$ ) was observed at 1644  $\text{cm}^{-1}$  (figure 2c). The results are consistent with the data of Zagonel et al. (32). The emergence of the ester peak 1644  $\text{cm}^{-1}$ , and the double bond peak at 3005  $\text{cm}^{-1}$  demonstrates successful binding.

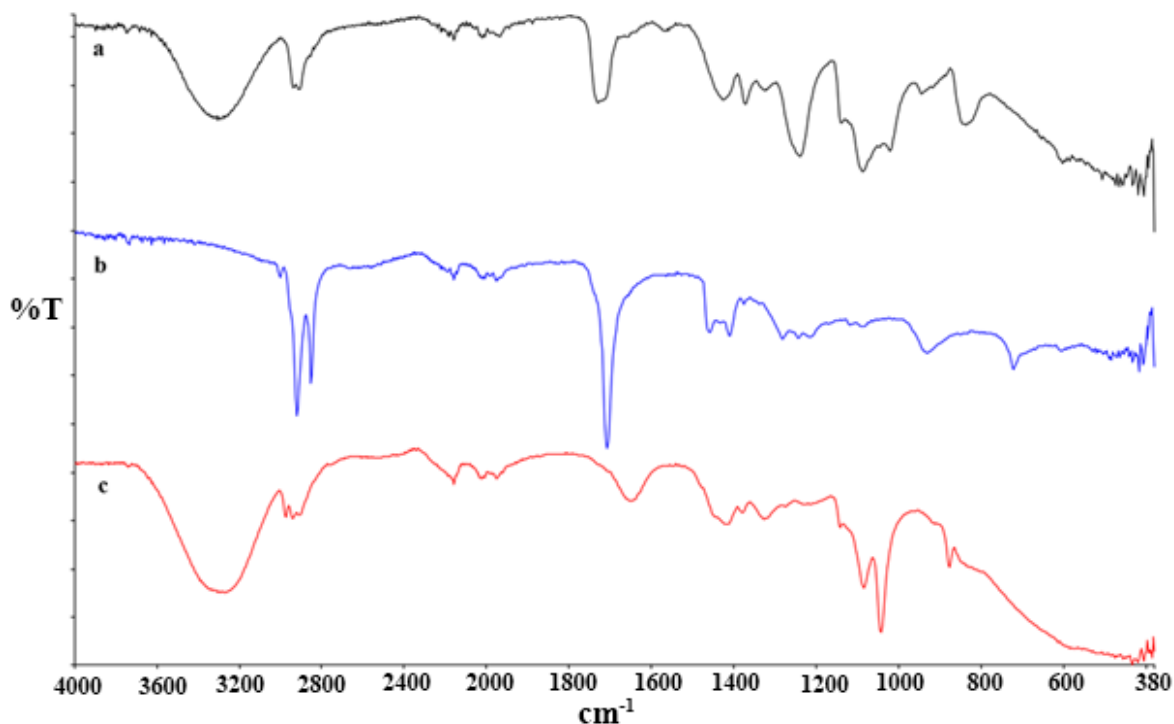


**Figure 2:** FTIR spectra a. PVA b. oleic acid c. oleic acid substituted polyvinyl alcohol

The FTIR spectrum of the encapsulated vitamin D at the optimum amount of vitamin D and polymer content, which are determined with critic micelle concentration and oil amount study (Figure 3). Figure 3 shows the FTIR spectrum of vitamin D with bands of 2915-2917  $\text{cm}^{-1}$  free  $\text{CH}_3$  stretching, 1730  $\text{cm}^{-1}$  ester stretching, and 1088  $\text{cm}^{-1}$  carbonyl stretching (33). Comparing the FTIR spectra of vitamin D and the capsule according to

Figure 3, the vibration band at 965  $\text{cm}^{-1}$  due to sulfoxide ( $\text{S}=\text{O}$ ) and sulfhydryl groups for vitamin D disappeared in the FTIR spectrum of the capsule. It is seen that all the vitamin D was encapsulated in the core and only the polymeric peaks at the wall appeared in the spectrum (34). The absence of a vitamin D band indicates that capsulation has been achieved successfully.

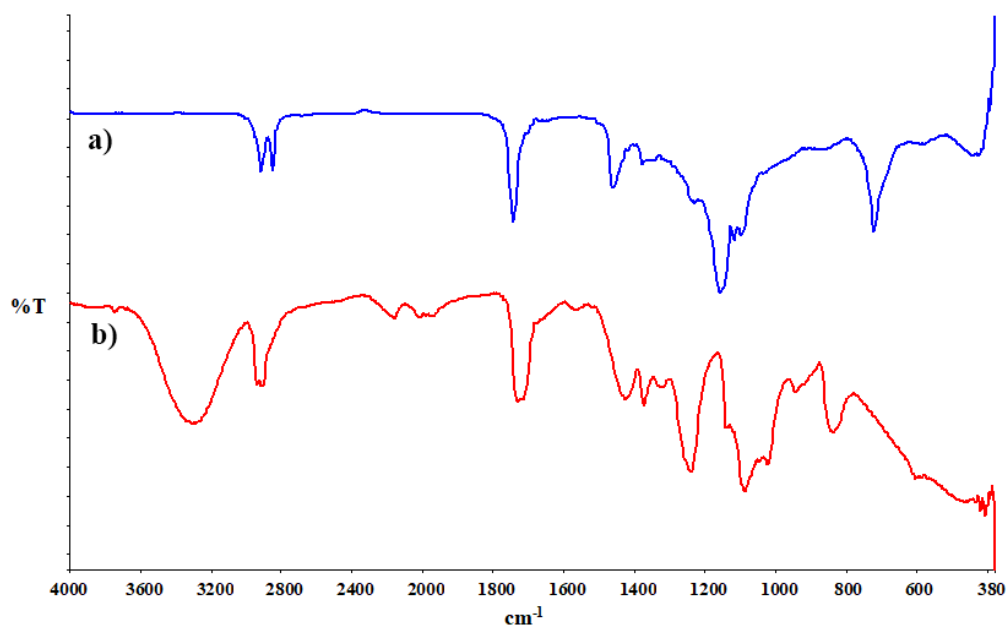


**Figure 3:** FTIR spectra of a) vitamin D and b) vitamin D-oleic acid modified polyvinyl alcohol capsule

The encapsulation of vitamin D was prepared under acidic conditions. When the pH dependence of encapsulation was examined (Figure 4a), it was concluded that encapsulation does not occur at a basic pH and only occurs at an extreme acidic pH (35). In addition, when the SEM images were

examined, it was determined that the capsule size was homogeneous and about 6.5 nm (Figure 4b). When the size of the obtained capsules was compared with the literature, it was determined that 10 times smaller capsules were synthesized (36).

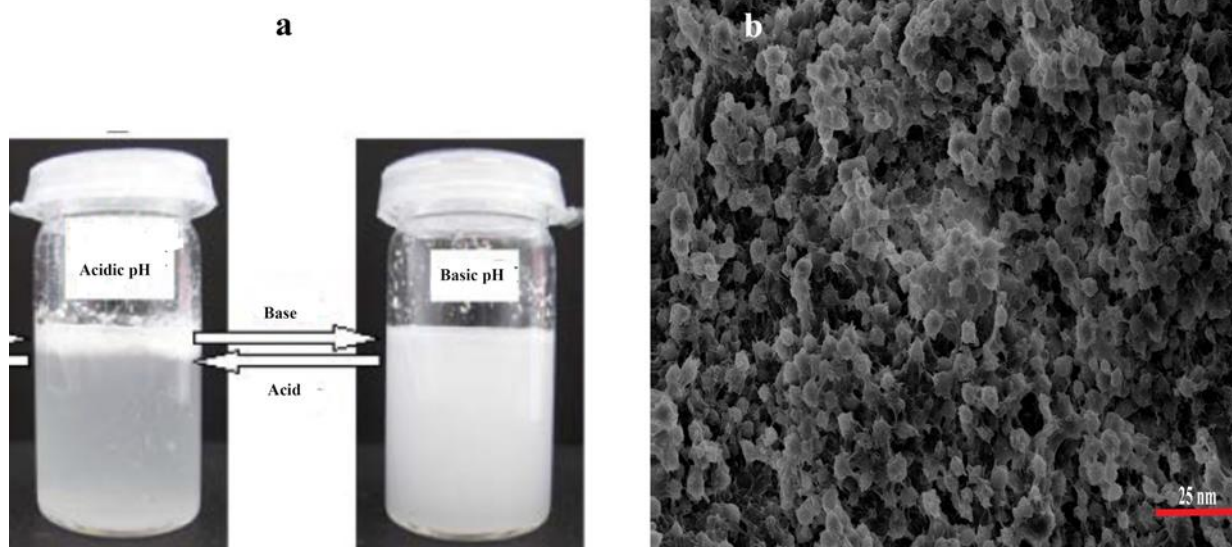


**Figure 4:** a. Encapsulation condition image b. SEM images of vitamin D-oleic acid modified polyvinyl alcohol capsules

The minimum oleic acid modified polyvinyl alcohol polymer that is needed to achieve critical micelle concentration for the encapsulation of vitamin D was determined. It was visually found that the encapsulation did not occur at the concentration of OA-PVA under 0.6 g/50 mL water. This result is

also supported by the literature (37). In addition, when the SEM images were examined, it was seen that the capsules were agglomerated at a concentration of 1 g/50 mL, whereas the capsules were not formed at a concentration of 0.4 g/50 mL at 50.000x magnification.

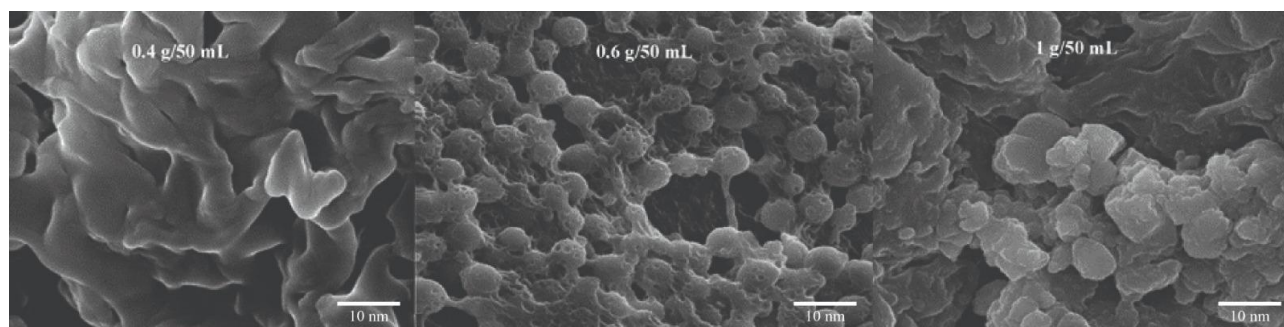


**Figure 5:** SEM images of capsules obtained with various amount of OA-PVA

To investigate the effect of vitamin D concentration on encapsulation, different concentrations were added to of 0.6 g of OA-PVA, and the encapsulation was visually inspected. The encapsulations of 0.5 mL and 1 mL of vitamin D were performed without issues, but when the vitamin D was further increased, the emulsion could not be formed completely with the OA-PVA. The untreated vitamin D remained on the surface. As a result, the upper limit for micellization of vitamin D was determined to be 1 mL.

### 3.2. Decomposition of nanocapsules at various pH values

The decomposition of capsules due to the pH changes was investigated by UV spectroscopy. The decomposition of capsules release profiles of vitamin D (Figure 6) from micelles prepared with OA-PVA polymer showed significant differences with pH. It was observed that OA- PVA polymer stabilized the vitamin D at acidic pH, but the capsules were deteriorated at pH 6 and above. The oil phase containing vitamin D was separated above pH 6. This observation was also compatible with the literature (38).

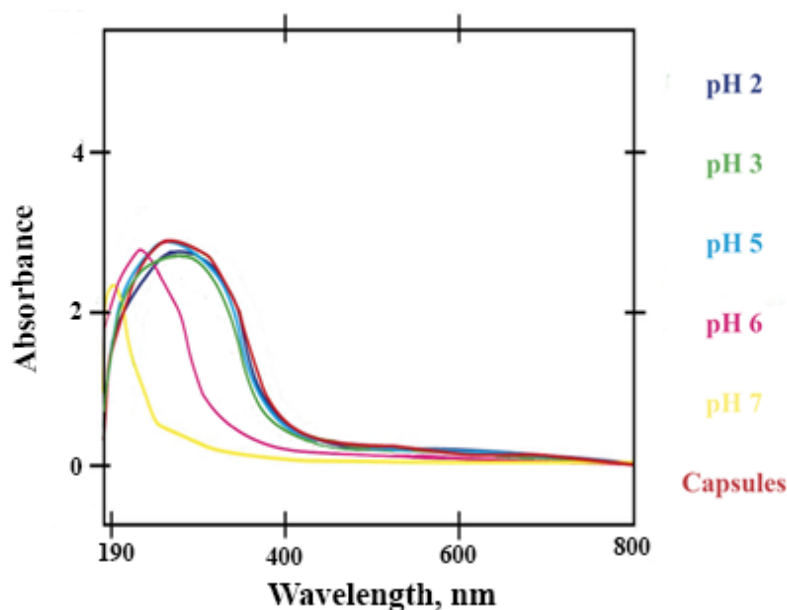


**Figure 6:** UV spectrum of capsules at different pH

## 4. CONCLUSION

OA-PVA amphiphilic polymer was prepared with Fisher acidic esterification.  $^1\text{H-NMR}$  and ATR-FTIR confirmed the expected structures. The vibration band belonging to sulfoxide ( $\text{S=O}$ ) and sulfhydryl groups of vitamin D at  $965\text{ cm}^{-1}$  disappeared in the FTIR spectrum of the capsule. The absence of vitamin D bands indicates that capsulation has been achieved successfully. Herein, vitamin D encapsulation with the obtained polymer is reported for the first time. The optimum conditions

for encapsulation were determined visually and by SEM. In light of the results obtained, it was concluded that the optimum capsulation conditions were 0.6 g / 50 mL polymer solution, 1 mL vitamin D, and an extremely acidic environment. The decomposition of vitamin D capsules at various pH values was investigated. It was observed that oleic acid-substituted PVA polymer stabilized the capsule at acidic pH. Considering all of the results, it could be stated that oleic acid substituted polyvinyl alcohol polymer can be used for encapsulation applications of vitamin D.



## 5. CONFLICT OF INTEREST

There is no conflict of interest.

## 6. REFERENCES

- Dubey R. Microencapsulation technology and applications. Defence Science Journal. 2009; 59(1): 82-95. Available from: [<URL>](#)
- Mars G, Scher H. Controlled delivery of crop protecting agents. Taylor and Francis, London. 1990:65-90.
- Ozcan A, Kandirmaz EA, editors. Poly [(vinyl alcohol)-(stearic acid)] synthesis and use in lavender oil capsulation. 9th International symposium on graphic engineering and design, <https://doi.org/10.24867/GRID-2018-p23> (2018, accessed 29 December 2020); 2018.
- Yang L, Alexandridis P. Physicochemical aspects of drug delivery and release from polymer-based colloids. Current opinion in colloid & interface science. 2000;5(1-2):132-43. Available from: [<URL>](#)
- Allen, C., Eisenberg, A., Maysinger, D. Copolymer drug carriers: conjugates, micelles and microspheres. STP. Pharma Sciences. 1999;9(1):139-151.
- Luppi B, Orienti I, Bigucci F, Cerchiara T, Zuccari G, Fazzi S, Zecchi, V. Poly (vinylalcohol-co-vinyloleate) for the preparation of micelles enhancing retinyl palmitate transcutaneous permeation. Drug Delivery. 2002;9(3):147-152. Available from: [<URL>](#)
- Kataoka K, Harada A, Nagasaki Y. Block copolymer micelles for drug delivery: design, characterization and biological significance. Advanced Drug Delivery Reviews. 2012;64:37-48. Available from: [<URL>](#)
- Wise DL. Encyclopedic handbook of biomaterials and bioengineering: v. 1-2. Applications: CRC Press; 1995.
- Vert M, Li SM, Spenlehauer G, Guérin P. Bioresorbability and biocompatibility of aliphatic polyesters. Journal of Materials Science: Materials in Medicine. 1992;3(6):432-446. Available from: [<URL>](#)
- Chacon M, Berges L, Molpeceres J, Aberturas MR, Guzman M. Optimized preparation of poly D, L (lactic-glycolic) microspheres and nanoparticles for oral administration. International Journal of Pharmaceutics. 1996;141(1-2):81-91. Available from: [<URL>](#)
- Ammoury N, Dubrasquet M, Fessi H, Devissaguet JP, Puisieux F, Benita S. Indomethacin-loaded poly (D,L-lactide) nanocapsules, protection from gastrointestinal ulcerations and antiinflammatory-activity, evaluation in rats. Clinical Materials. 1993;13(1-4):121-130. Available from: [<URL>](#)
- Uchida T, Yoshida K, Nakada Y, Nagareya N, Konishi Y, Nakai A, Matsuyama K. Preparation and characterization of polylactic acid microspheres containing water-soluble anesthetics with small molecular weight. Chemical and Pharmaceutical Bulletin. 1997;45(3):513-517. Available from: [<URL>](#)
- Soriano I, Evora C, Llabrés M. Preparation and evaluation of insulin-loaded poly (DL-lactide) microspheres using an experimental design. International Journal of Pharmaceutics. 1996;142(2):135-142. Available from: [<URL>](#)
- Yamakawa I, Tsushima Y, Machida R, Watanabe S. *In vitro* and *in vivo* release of poly (DL-lactic acid) microspheres containing neurotensin analogue prepared by novel oil-in-water solvent evaporation method. Journal of Pharmaceutical Sciences. 1992;81(8):808-811. Available from: [<URL>](#)
- Niwa T, Takeuchi H, Hino T, Kunou N, Kawashima Y. Preparations of biodegradable nanospheres of water-soluble and insoluble drugs with D,L-lactide/glycolide copolymer by a novel spontaneous emulsification solvent diffusion method, and the drug release behavior. Journal of Controlled Release. 1993;25(1-2):89-98. Available from: [<URL>](#)
- Jalil R, Nixon JR. Biodegradable poly(lactic acid) and poly(lactide-co-glycolide) microcapsules: problems associated with preparative techniques and release properties. Journal of Microencapsulation. 1990;7(3):297-325. Available from: [<URL>](#)
- Southern TRT, Tabibi SE. Parenteral Drug Delivery: Injectables. Treatise on Controlled Drug Delivery: Fundamentals-optimization-applications. 2017:315.
- Fong J. Microencapsulation by solvent evaporation and organic phase separation processes. Controlled release systems: fabrication technology. 1988;1:81-108.
- Moutinho IMT, Kleen AM, Figueiredo MML, Ferreira PJT. Effect of surface sizing on the surface chemistry of paper containing eucalyptus pulp. Holzforschung. 2009;63(3):282-289. Available from: [<URL>](#)
- Pruszyński P, editor Recent developments in papermaking chemicals. Chemical Technology of Wood, Pulp and Paper, Proceedings of the International Conference" Chemical Technology of Wood, Pulp and Paper; 2003;82-90.
- Zhu GY, Xiao ZB, Zhou RJ, Yi FP. Fragrance and flavor microencapsulation technology. Advanced Materials Research. 2012;535:440-445. Available from: [<URL>](#)
- Moutinho IM, Ferreira PJ, Figueiredo ML. Paper surface chemistry as a tool to improve inkjet printing quality. BioResources. 2011;6(4):4259-4270. Available from: [<URL>](#)
- Singh MN, Hemant KSY, Ram M, Shivakumar HG. Microencapsulation: A promising technique for controlled drug delivery. Research in Pharmaceutical Sciences. 2010;5(2):65-77.
- Mervosh TL, Stoller EW, Simmons FW, Ellsworth TR, Sims GK. Effects of starch encapsulation on clomazone and atrazine movement in soil and clomazone volatilization. Weed Science. 1995;43(3):445-453. Available from: [<URL>](#)
- Nieves JW. Skeletal effects of nutrients and nutraceuticals, beyond calcium and vitamin D. Osteoporosis International. 2013; 24(3): 771-786. Available from: [<URL>](#)

26. Özgülsün A, Karaosmanoglu F, Tüter M. Esterification reaction of oleic acid with a fusel oil fraction for production of lubricating oil. *Journal of the American Oil Chemists' Society*. 2000;77(1):105-109. Available from: [<URL>](#)
27. Kikuchi A, Okano T. Pulsatile drug release control using hydrogels. *Advanced Drug Delivery Reviews*. 2002;54(1):53-77. Available from: [<URL>](#)
28. Chetri P, Dass NN. Development of a new method for synthesis of poly (vinyl oleate) from poly (vinyl alcohol). *Polymer*. 1996;37(23):5289-5293. Available from: [<URL>](#)
29. Crini G, Torri G, Guerrini M, Martel B, Lekchiri Y, Morcellet M. Linear cyclodextrin-poly (vinylamine): Synthesis and NMR characterization. *European Polymer Journal*. 1997;33(7):1143-1151. Available from: [<URL>](#)
30. Mansur HS, Sadahira CM, Souza AN, Mansur AA. FTIR spectroscopy characterization of poly (vinyl alcohol) hydrogel with different hydrolysis degree and chemically crosslinked with glutaraldehyde. *Materials Science and Engineering: C*. 2008;28(4):539-548. Available from: [<URL>](#)
31. Zhang L, He R, Gu HC. Oleic acid coating on the monodisperse magnetite nanoparticles. *Applied Surface Science*. 2006;253(5):2611-2617. Available from: [<URL>](#)
32. Zagonel GF, Peralta-Zamora P, Ramos LP. Multivariate monitoring of soybean oil ethanolysis by FTIR. *Talanta*. 2004;63(4):1021-1025. Available from: [<URL>](#)
33. Molavesi M, Shahidi-Noghabi M, Naji-Tabasi S. Vitamin D3-loaded nanophytosomes for enrichment purposes: Formulation, structure optimization, and controlled release. *Journal of Food Process Engineering*. 2020;43:13560-13572. Available from: [<URL>](#)
34. Miyamoto K, Murayama E, Ochi K, Watanabe H, Kubodera N. Synthetic studies of vitamin D analogues. XIV. Synthesis and calcium regulating activity of vitamin D3 analogues bearing a hydroxyalkoxy group at the 2 $\beta$ -position. *Chemical and Pharmaceutical Bulletin*. 1993;41(6):1111-1113. Available from: [<URL>](#)
35. Ziani K, Fang Y, McClements DJ. Encapsulation of functional lipophilic components in surfactant-based colloidal delivery systems: vitamin E, vitamin D, and lemon oil. *Food Chemistry*. 2012;134(2):1106-1112. Available from: [<URL>](#)
36. Mu L, Feng SS. Vitamin E TPGS used as emulsifier in the solvent evaporation/extraction technique for fabrication of polymeric nanospheres for controlled release of paclitaxel (Taxol). *Journal of Controlled Release*. 2002;80(1-3):129-144. Available from: [<URL>](#)
37. Domínguez A, Fernandez A, Gonzalez N, Iglesias E, Montenegro L. Determination of critical micelle concentration of some surfactants by three techniques. *Journal of Chemical Education*. 1997;74(10):1227. Available from: [<URL>](#)
38. Luppi B, Bigucci F, Cerchiara T, Andrisano V, Pucci V, Mandrioli R, Zecchi V. Micelles based on polyvinyl alcohol substituted with oleic acid for targeting of lipophilic drugs. *Drug Delivery*. 2004;12(1):21-26. Available from: [<URL>](#)



## Aqueous Extract of Onion Peels as A Biowaste-Based Sensitizer for Photovoltaic Cells

Risna Erni Yati Adu<sup>1\*</sup> , Gebhardus Gelyaman<sup>1</sup> 

<sup>1</sup> Universitas Timor, Department of Chemistry, Faculty of Agriculture, Science and Health, Kefamenanu 85613, Indonesia.

**Abstract:** In the present paper, two natural photosensitizers extracted from red onion peels have been experimentally studied to sensitize the photovoltaic cells. The two natural dyes were prepared overnight, soaking the red onion peel powder in distilled water without acidification (UW) and acidified water (AW). Dye characteristics were identified by UV-vis Spectrophotometer and FT-IR Spectrophotometer. The cell performance was assessed by calculating the produced voltage and current by multi-meter. Red onion peel dyes absorb visible light at a wavelength of 507 nm and promote electron transfer into the porous semiconductor surface. A higher power conversion efficiency ( $\eta=0.0535\%$ ) was featured by an unacidified solvent with a short circuit current density ( $J_{sc}$ ) of  $0.96\text{ mA}\cdot\text{cm}^{-2}$ , an open circuit voltage ( $V_{oc}$ ) of 338 mV and a fill factor of 0.2576. This paper presents a fascinating preliminary study to develop renewable and sustainable energy sources using bulky biowaste.

**Keywords:** Aqueous extracts, biowaste-based sensitizer, onion dyes, photovoltaic cells.

**Submitted:** March 6, 2023. **Accepted:** September 15, 2023.

**Cite this:** Adu REY, Gelmayan G. Aqueous Extract of Onion Peels as A Biowaste-Based Sensitizer for Photovoltaic Cells. JOTCSA. 2023;10(4):1063-70.

**DOI:** <https://doi.org/10.18596/jotcsa.1260709>

\*Corresponding author's E-mail: [adoe.risna@yahoo.com](mailto:adoe.risna@yahoo.com), [risnaadu12@unimor.ac.id](mailto:risnaadu12@unimor.ac.id)

### 1. INTRODUCTION

Energy crises, fossil fuel depletion, and environmental issues encourage researchers to strive for sustainable and renewable energy sources. One of the efforts is to utilize solar radiation, which is abundant, accessible, and eco-friendly. Solar radiation provides energy of  $3 \times 10^{24}$  J per year to the Earth or about ten thousand times more than the world population demands (1). Solar cells, also called photovoltaic cells, can be used to utilize this freely available energy. The key parameter in harvesting solar energy is the capability of the cells to transform solar radiation into electrical power.

Dye-sensitized solar cells (DSCs) represent a promising device for directly converting solar radiation. It can be fabricated cheaply and produces high power conversion efficiency. This device involves a photoelectrochemical process to convert solar radiation into electrical power based on the sensitization of wide-band gap semiconductors. Generally, the DSSCs structure comprises a

photoanode, dye molecules or sensitizer, a redox electrolyte, and a counter electrode as cathode (2–4). The dye sensitizer is the main component in capturing solar radiation and transforming it into electrical power (5). To enhance the DSSC performance, a dye sensitizer should have absorption from UV-visible to near-infrared spectrum and contain carboxyl and hydroxyl groups required for proper binding to the semiconductor (6,7). The functional groups promote negative charge transfer into the  $\text{TiO}_2$  conduction band; thus, the power conversion capability of DSSC can be improved.

Ruthenium complexed with carboxylated polypyridyl ligands is a synthetic inorganic sensitizer with the highest power conversion efficiency of 11%-12% (8,9). However, due to the high cost and tedious manufacturing method, sensitizer-based natural dyes are considered a favorable option for DSSC devices. Sensitizer-based natural dyes can be safely prepared at a low cost from flowers, fruits, and plants (3). Using biowaste-based materials as natural dye sources is important due to their

seasonal independence, uncompetitive-to-food products, and eco-friendly properties. Biowaste-based materials have shown significant advantages in utilization as natural sensitizers (1,10,11). Red onion peel, an abundant biowaste from agroindustry, has drawn significant attention as a novel raw material for photosensitizer purposes. This waste occurs in huge quantities because onion is a daily-consumed staple from the household to the restaurant. Anthocyanin is one of the natural pigments easily found in onion biowaste. It is a watery soluble compound and contains carbonyl (C=O) and hydroxyl group (OH) that can be absorbed to the TiO<sub>2</sub> surface and stabilize the excited states (12–14). Anthocyanin shows a wide absorption band in the visible light spectrum and accelerates the electronic transitions of the dye molecules. Onion peel analysis exhibits a high anthocyanin content (15,16), making it possible to apply as a natural, affordable, and sustainable sensitizer.

An important parameter to prepare the pigment is the choice of extracting solvent. Various extracting solvents can affect the absorption spectrum of natural pigments as well as the bonding between the pigments and the TiO<sub>2</sub> surface (17). Acidified ethanol: water mixture (1) as extracting solvent of red onion peel dyes gives a higher efficiency than ethanol and acidified ethanol (18) as much as 0.29%, 0.049%, and 0.0034%. Additionally, previous studies have found that combinations of ethanol and water encourage widespread visible spectrum absorption between 490 and 532 nm. The current study evaluated the effectiveness of acidified and non-acidified water as extracting solvents. Two different types of red onion peel extracts were used as photosensitizers to create dye-sensitized solar cells. The power conversion efficiencies were calculated using a UV-vis and FT-IR spectrometer to examine the extracted dyes' absorption properties.

## 2. EXPERIMENTAL SECTION

### 2.1. Material

The types of equipment used for the research are FT-IR Spectrometer Bruker Alpha, UV-vis Spectrophotometer (Genesys 10S Thermo Scientific), blender, water bath, solar simulator (ORIEL S013A), and I-V meter (Keithley 2400). The materials are acetonitrile (99.8%, Merck), distilled water, HCl 37%, TiO<sub>2</sub> (99.5%, Merck), KI (99.7%, Merck), I<sub>2</sub> (99.8%, Merck) and 4-pyridinecarboxylic acid hydra-zide (97%, Merck).

### 2.2. Dye Extraction and Characterization

Onion peels were randomly taken from local food stalls. Onion peel dyes were prepared by grinding the sample in a mixer and sieving with a size of 200 mesh. The peel powder (100 g) was mixed with unacidified water (250 mL) and macerated for 24 hours in the chamber that was stored away from direct sun rays. The macerated solution was separated from the solids by using Whatman Filter

paper, concentrated at 40 °C on a hot plate, and used to fabricate solar cells. The same procedure was carried out against the acidified distilled water. Both extracts were labeled as AW (acidified water) and UW (unacidified water). The dye absorption band against UV and visible light was characterized by UV-vis spectrophotometer; meanwhile, the functional groups were analyzed by FT-IR spectrometer.

### 2.3. DSSC Fabrication and Performance

The present DSSC was prepared according to our earlier study (19). DSSC device was assembled from four main components (photoanode, nature-based sensitizer, electrolyte solution, and auxiliary electrode). TiO<sub>2</sub> paste was printed to the conductive side of Indium Tin Oxide/ITO glass to prepare the working electrode. TiO<sub>2</sub>-coated glass was dehydrated for 15 minutes at 120 °C in a bath. TiO<sub>2</sub>-coated glass was annealed at a temperature of 500 °C for 1 hour. This working electrode was subsequently immersed for 20 hours in aqueous extracts of red onion dyes and then washed with C<sub>3</sub>H<sub>7</sub>OH. The stained electrode was gently dried at 80 °C on a water bath for further use in dye sensitization. To prepare a redox electrolyte solution containing iodine and potassium iodide, KI, I<sub>2</sub>, and 4-pyridinecarboxylic acid hydrazide were dissolved in acetonitrile; meanwhile, the cathode was fabricated by painting the glass slide with synthetic graphite. The graphite-painted slide was covered through screen printing with Graphite: PANI (3:1) paste. It was heated at 120 °C for 15 minutes before being allowed to cool at room temperature. Before examining the DSSC performance, electrolyte solution was injected into the working electrode, and two binder clips were used to clamp the photoanode and counter electrode. These DSSCs were set under irradiation of light (100 mW) using a solar simulator (ORIEL S013A), whereas the current and voltage were measured by a Keithley 2400 I-V meter. Photovoltaic cell performance in terms of energy-transforming efficiency was determined using the equation according to Richhariya et al. (2) as follows:

$$\eta (\%) = \frac{J_{sc} \times V_{oc} \times FF}{P_{in}} \times 100 (\%) \quad (1)$$

where J<sub>sc</sub> is the short-circuit photocurrent (mAcm<sup>-2</sup>), η is the cell efficiency (%), V<sub>oc</sub> is open-circuit voltage (V), FF is the fill factor, and P<sub>in</sub> is the power of the solar simulator lamp (100 mW).

## 3. RESULTS AND DISCUSSION

### 3.1. Dye Extraction

Red onion (*Allium cepa* L.) has a red color peel and dry peel characteristics. Red onion contains anthocyanins and phenolics in the dry outer skin and epidermis layer (20,21). Anthocyanin can be extracted from onion peel through several extracting methods, i.e., maceration, reflux, percolation, and soxhletation (22,23). Maceration

was considered a suitable extracting method in this work because of its effectiveness in cell lysis, less solvent consumption, longer solvent-solute interaction, and lower temperature demand. Saptarini and Herawati (24) achieved a higher total anthocyanin content through the immersion method (maceration and reflux extraction) compared to the flowing solvent method (percolation and soxhlet methods). The choice of anthocyanins extracting solvent predominantly affects the total anthocyanin level. Anthocyanins are a group of water-soluble flavonoid compounds; therefore, distilled water was chosen as the proper solvent. Ali et al. (25) stated that onion peel extraction using acidified ethanol (0.01% HCl) gave a higher efficiency than acidified methanol (0.01% HCl). pH solution was reported elsewhere as another important factor that can affect the color stability of anthocyanin. Natural anthocyanin extracts showed the greatest stability at lower pH (2.0 and 3.0) (26,27). Therefore, an acid solution (0.01% HCl) was added to the distilled water in the current work (Figure 1) to stabilize the flavylium cation, which is stable in highly acidic conditions.

### 3.2. Dye Absorption

UV-visible light absorption capacity of the natural sensitizer and the transport of expelled electrons through the porous TiO<sub>2</sub> film determine the overall performance of DSSC. The absorption capability of the extracted onion peel dyes was measured using a UV-vis spectrophotometer between the wavelength of 400 to 780 nm and illustrated in Figure 2. There are two identical absorption peaks in the visible spectrum with a maximum absorption of 507 nm featured by extracted onion peel dyes, both unacidified and acidified water. These intense wide-band absorptions in the visible spectrum approximately meet the value noted by Hosseinnzhad et al. (28) for extracted anthocyanin from onion peel using ethanol (508 nm). However,

they are slightly different from the maximum absorption reported by Ammar et al. (10) and Adolaju (1) using water (486 nm) and the mixture of ethanol-water (532 nm) as extracting solvent, respectively. Absorption peak difference is attributed to the different quantities of functional groups and the color of extracted anthocyanins. Moreover, the presence of unnecessary particles potentially resulted in different absorption.

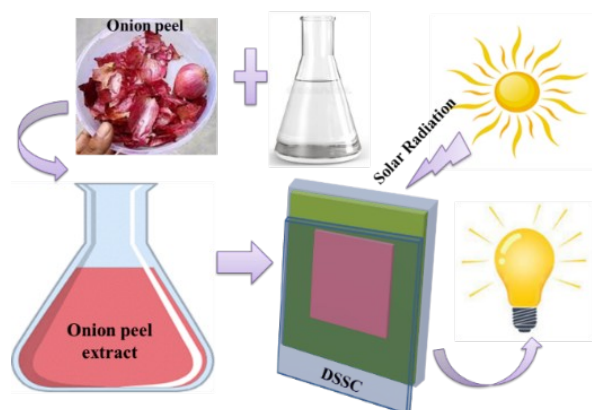


**Figure 1:** Workflow of The Current Work.

In the present work, the two extracted dyes (AW and UW) absorb visible light photons, resulting in  $n \rightarrow \pi^*$  and  $\pi \rightarrow \pi^*$  transition. The absorption capability of these extracts is responsible for the efficient conversion of photons into electrical power in DSSC. Photon absorption leads to the generating of excited electrons from HOMO to LUMO (29,30). The presence of anthocyanins functional groups in the extracts allows their adsorption into the TiO<sub>2</sub> surface (Figure 4). This adsorption promotes the electron transfer from the dye to the TiO<sub>2</sub> conduction band, ultimately improving the DSSC power conversion efficiency.

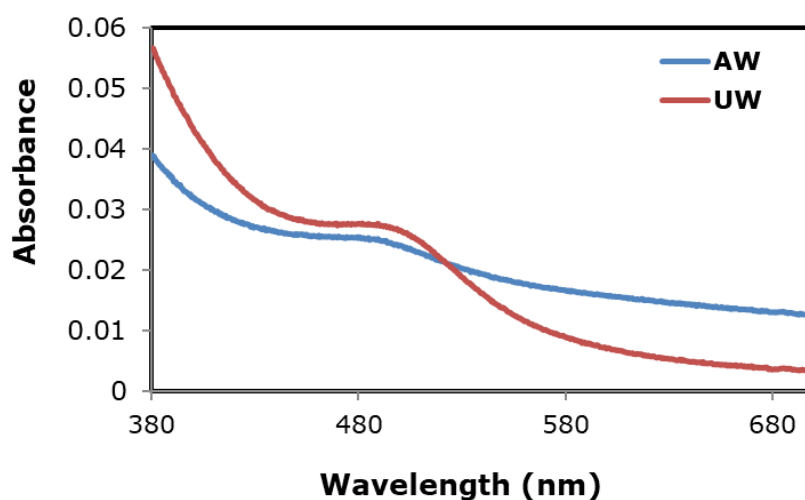


**Figure 2:** UV-vis Absorption of Extracted Red Onion Peel Dyes.

In order to effectively adsorb in  $\text{TiO}_2$  surface, the dye sensitizer needs to have specific functional groups. Functional groups contained in onion peel

extracts were identified by FT-IR Spectrometer at a wavenumber of  $4000\text{-}500\text{ cm}^{-1}$ . Figure 3 reveals identical absorption of the two extracts.

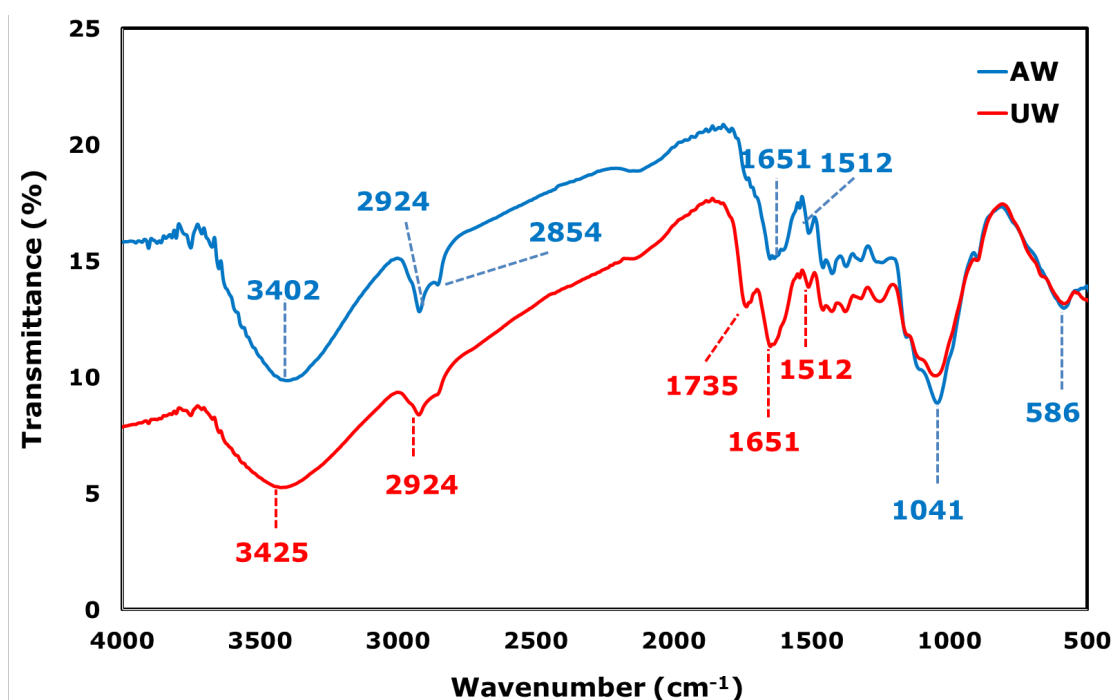


**Figure 3:** FT-IR Spectra of Extracted Dyes.

The absorption band in the  $3402$  and  $3425\text{ cm}^{-1}$  wavenumber is attributed to the  $\text{-OH}$  strain vibration. The absorption band of  $\text{C=C}$  strain vibration aromatic and  $\text{C-H}$  aromatics is observed in the wavenumber of  $1651$  and  $655\text{ cm}^{-1}$ . The  $\text{C-O}$  group is detected at  $1041\text{ cm}^{-1}$ ; meanwhile, the  $\text{C-H}$  strain appears at wavenumber  $2854$  and  $2924\text{ cm}^{-1}$  for  $\text{C-H}_3$  and  $\text{C-H}_2$ . Absorption peak showing  $\text{C=O}$  vibration that is characteristic of anthocyanin is detected in UW extract ( $1735\text{ cm}^{-1}$ ) but totally disappears in the AW spectra, presumably due to the rapid transformation of  $\text{C=O}$  groups into  $\text{-O-}$  groups under acidic conditions. The presence of these groups is similar to the previous report (10,27,28). According to Swer et al. (31) the presence of  $\text{O-H}$ ,  $\text{C=O}$ ,  $\text{C=C}$ , and  $\text{C-O-C}$  functional groups in the FT-IR spectra is the absorption characteristic of anthocyanin compounds; therefore, onion peel extracts in this study have characteristics as an anthocyanin. These specific functional groups possess anchoring capability on the  $\text{TiO}_2$  layer, promoting a high electron transfer rate. The different absorption intensity of the two extracts is also confirmed by FT-IR Spectra. Under acidic conditions, functional groups absorb less

intensely than in nonacidic conditions because of pigment degradation during extraction. As previously reported, pigment degradation can occur in unstable residues of acyl groups and sugars because of acid hydrolysis (32).

### 3.3. DSSC Performance

As revealed in Figure 4, the present photoelectrochemical solar cell was arranged by an opposite electrode (conductive glass covered with platinum), photoanode (conductive glass coated with  $\text{TiO}_2$  film), dye and electrolyte solution (redox pairs  $\text{I}^-/\text{I}_3^-$ ) (14). In order to examine the prepared onion peel dyes as a natural photosensitizer, the DSSC device was fabricated by varying the extracts (acidified water extract and unacidified water extract). The addition of a low content of hydrochloric acid (0.01%) in the present work may improve the stability of the produced flavylum ion in an aqueous solution. Generally, the effective light exposure domain of the DSSC was retained at  $1\text{ cm}^2$ ; meanwhile, the  $\text{I}^-/\text{I}_3^-$  solution and Pt thin film were used as the redox mediator and the counter electrode, respectively.

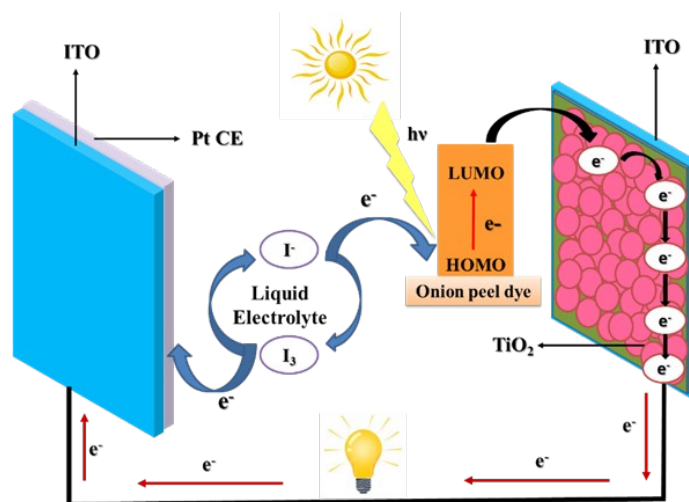


**Figure 4:** Schematic Diagram of The Fabricated Cell.

The photovoltaic variables such as short-circuit photocurrent density ( $J_{sc}$ ), open-circuit voltage ( $V_{oc}$ ), fill factor (FF), and total power conversion efficiencies (%) for the aqueous extract of onion peels are summarized in Table 1. These parameters are determined by measuring the photocurrent-voltage (J-V) curves which are displayed in Figure 5. The power conversion efficiency of the fabricated cell mainly depends on two key variables: open circuit voltage and short circuit current. Short circuit current production primarily relies on the quantity of adsorbed dyes on the porous  $TiO_2$ , device framework, sunlight converting efficiency, and capability of the prepared dye to accelerate electron injection (3). The more adsorbed dye molecules on the surface site of  $TiO_2$ , the more the generated photons that are heading to the rapid electron flow (33,34).

On the other hand, the open circuit voltage or output voltage was defined as the difference

between the quasi-Fermi level of free electron of the  $TiO_2$  electrode and the redox couple potential of mediator, which mostly counts on the recombination rate of electron and adsorption mode of the prepared sensitizer (29,35). In this work, photovoltaic cells based on the unacidified extract of onion peels performed the better power conversion efficiency of 0.0535%, whereas the other exhibited efficiency of 0.0021%. The cell's efficiency is still low because of a lower fill factor than normal values. The fill factor value in this study is only influenced by the  $J_{sc}$ , and the  $V_{oc}$  value does not affect the FF because of the use of the same redox pair and semiconductor. To achieve the proper  $V_{oc}$  value, active layer which is dye with high band gap is needed. Generally, natural pigments which act as DSSC photosensitizers exhibited lower power conversion efficiencies than that of synthetically prepared dyes owing to the less presence of particular functional groups (36).

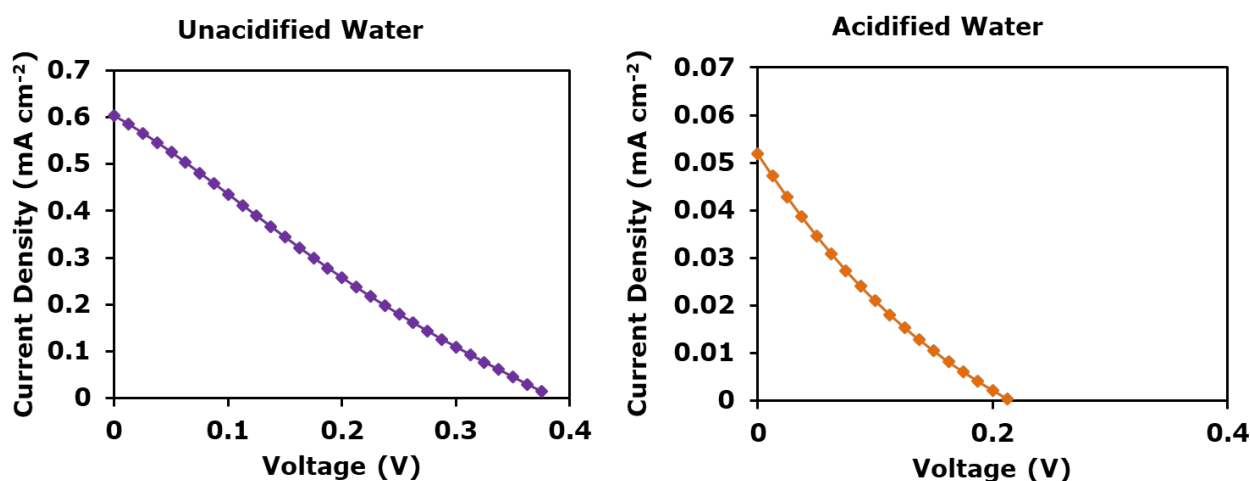


**Figure 5:** Current-voltage density (J-V) curve of DSSC sensitized by aqueous extracts of onion peel dyes.

A higher power conversion of the photovoltaic device based on unacidified water extract is attributed to the high presence of extracted anthocyanin containing hydroxyl and carbonyl groups. The more content of functional groups may

amend the maximum electron injection into the  $TiO_2$  surface by the chemical adsorption process. In contrast, the acidified aqueous extract of onion peels has less quantity of adsorbing functional groups, as featured in Figure 3, due to the

destruction of anthocyanin molecules by hydrochloric acid during the dye storage. Anthocyanin extraction using solvents that are acidified with strong acids like hydrochloric acid can contribute to pigment destruction during the preconcentration stage, especially at dryness. Concentrated acid could hydrolyze important compounds that are responsible for their stability, such as unstable groups of acyl, pale substances, or metal complexes contained in the essential form of anthocyanin (37). To establish this, using weak acids (i.e., formic acid, citric acid, or acetic acid) is

highly recommended since using strong concentrated acids may destroy anthocyanin molecules. Anthocyanin instability during the study decreases its binding capability to the TiO<sub>2</sub> surface. Moreover, fewer electron donating and withdrawing groups are most important for the electron injection rate from the dye compounds to porous semiconductors under light illumination. Therefore, the relatively higher J<sub>sc</sub> generated by sensitized cells with unacidified extract of onion peels might be ascribed to its good performance in harvesting solar radiation.

**Table 1:** The Photovoltaic Parameters of Fabricated DSSC.

Onion Peel Dyes	J <sub>sc</sub> (mAcm <sup>-2</sup> )	V <sub>oc</sub> (mV)	FF	Efficiency (%)
Unacidified water	0.6031	338	0.2576	0.0535
Acidified water	0.0518	338	0.1204	0.0021

The measured power conversion efficiency of unacidified water in our present device is higher than that of our previous photovoltaic cells when unacidified methanol and ethanol were used as extracting solvent (0.0413 and 0.0491 %) (18,19). It was reported elsewhere that anthocyanins are highly soluble in water. Their polyphenolic compounds increase the hydrophobic characteristic, which makes them soluble in organic solvents (38). Furthermore, compared to recently reported natural sensitizers using similar samples and solvents, our power conversion efficiencies of the produced devices are slightly inferior (1,28). Its different efficiency could be due to the different treatments applied to the crude extract. It appears that adding the purification stage using hexane and adjusting the temperature to 90 °C, as performed by previous workers, is highly needed to improve the efficiencies. Therefore, it is suggested to optimize the other analytical parameters in the future, such as extraction pH and time, powder size of the solid, and solvent-to-solid ratio, in addition to the purification and temperature to ensure the maximum yields of anthocyanins.

#### 4. CONCLUSION

Two extracted dyes from onion peels were examined as natural photosensitizers in DSSC. The aqueous extracts of onion peel dyes can transform solar radiation into electrical power through a photoelectrochemical solar cell. The acidified and unacidified extracts have anchoring groups and strongly absorb the visible spectrum at 507 nm. The DSSC device assembled from the unacidified red onion peel dye extract demonstrated a higher power conversion efficiency of 0.0535% than the acidified extract.

#### 5. CONFLICT OF INTEREST

The authors declare that there is no conflict of interest.

#### 6. ACKNOWLEDGMENTS

The Institute for Research and Community Service (LPPM) of Timor University is acknowledged for financial support to this work according to the Novice Lecturer Research Program with grant number 45/UN60/LPPM/PP/2021.

#### 7. REFERENCES

- Aduloju KA, Shitta MB. Dye sensitized solar cell using natural dyes extracted from red leave onion. *Int J Phys Sci* [Internet]. 2012 Jan 30;7(5):709–12. Available from: [<URL>](#).
- Richhariya G, Kumar A, Tekasakul P, Gupta B. Natural dyes for dye sensitized solar cell: A review. *Renew Sustain Energy Rev* [Internet]. 2017 Mar 1;69:705–18. Available from: [<URL>](#).
- Calogero G, Bartolotta A, Di Marco G, Di Carlo A, Bonaccorso F. Vegetable-based dye-sensitized solar cells. *Chem Soc Rev* [Internet]. 2015;44(10):3244–94. Available from: [<URL>](#).
- Marques A dos S, da Silva VAS, Ribeiro ES, Malta LFB. Dye-sensitized solar cells: Components screening for glass substrate, counter-electrode, photoanode and electrolyte. *Mater Res* [Internet]. 2020;23(5):e20200168. Available from: [<URL>](#).
- Rahman S, Haleem A, Siddiq M, Hussain MK, Qamar S, Hameed S, et al. Research on dye sensitized solar cells: recent advancement toward the various constituents of dye sensitized solar cells for efficiency enhancement and future prospects. *RSC Adv* [Internet]. 2023;13(28):19508–29. Available from: [<URL>](#).
- Sharma K, Sharma V, Sharma SS. Dye-sensitized solar cells: Fundamentals and current status. *Nanoscale Res Lett* [Internet]. 2018 Dec 28;13(1):381. Available from: [<URL>](#).
- Pandey AK, Ahmad MS, Rahim NA, Tyagi V V., Saidur R. Natural sensitizers and their applications in dye-sensitized solar cell. In: environmental



- biotechnology: For sustainable future [Internet]. Singapore: Springer Singapore; 2019. p. 375–401. Available from: [<URL>](#).
8. Adedokun O, Titilope K, Awodugba AO. Review on Natural Dye-Sensitized Solar Cells (DSSCs). *Int J Eng Technol IJET* [Internet]. 2016 Jun 22;2(2):34. Available from: [<URL>](#).
9. Ye M, Wen X, Wang M, Iocozzia J, Zhang N, Lin C, et al. Recent advances in dye-sensitized solar cells: from photoanodes, sensitizers and electrolytes to counter electrodes. *Mater Today* [Internet]. 2015 Apr 1;18(3):155–62. Available from: [<URL>](#).
10. Ammar AM, Mohamed HSH, Yousef MMK, Abdel-Hafez GM, Hassanien AS, Khalil ASG. Dye-Sensitized Solar Cells (DSSCs) Based on Extracted Natural Dyes. *J Nanomater* [Internet]. 2019 Apr 18;2019:1867271. Available from: [<URL>](#).
11. Hardeli, Zainul R, Isara LP. Preparation of Dye Sensitized Solar Cell (DSSC) using anthocyanin color dyes from jengkol shell (*Pithecellobium lobatum* Benth.) by the gallate acid copigmentation. *J Phys Conf Ser* [Internet]. 2019 Apr 1;1185(1):012021. Available from: [<URL>](#).
12. Syafinar R, Gomesh N, Irwanto M, Fareq M, Irwan YM. Potential of purple cabbage, coffee, blueberry and turmeric as nature based dyes for dye sensitized solar cell (dssc). *Energy Procedia* [Internet]. 2015 Nov 1;79:799–807. Available from: [<URL>](#).
13. Al Batty S, Al-Jubouri SM, Wali Hakami M, Sarief A, Haque SM. Innovative economic anthocyanin dye source for enhancing the performance of dye-sensitized solar cell. *J Taibah Univ Sci* [Internet]. 2022 Dec 31;16(1):415–22. Available from: [<URL>](#).
14. Kim J-H, Kim D-H, So J-H, Koo H-J. Toward eco-friendly dye-sensitized solar cells (DSSCs): Natural Dyes and Aqueous Electrolytes. *Energies* [Internet]. 2021 Dec 29;15(1):219. Available from: [<URL>](#).
15. Collings DA. Anthocyanin in the vacuole of red onion epidermal cells quenches other fluorescent molecules. *Plants* [Internet]. 2019 Dec 12;8(12):596. Available from: [<URL>](#).
16. Celano R, Docimo T, Piccinelli AL, Gazzero P, Tucci M, Di Sanzo R, et al. Onion peel: Turning a food waste into a resource. *Antioxidants*. 2021 Feb 16;10(2):304. Available from: [<URL>](#).
17. Prabavathy N, Shalini S, Balasundaraprabhu R, Velauthapillai D, Prasanna S, Walke P, et al. Effect of solvents in the extraction and stability of anthocyanin from the petals of *Caesalpinia pulcherrima* for natural dye sensitized solar cell applications. *J Mater Sci Mater Electron*. 2017 Jul 23;28(13):9882–92. Available from: [<URL>](#).
18. Adu REY, Gelyaman G, Kabosu M. Pemanfaatan ekstrak antosianin dari limbah kulit bawang merah (*Allium cepa*) sebagai zat pemeka (sensitizer) pada dye sensitized solar cell (DSSC). *ALCHEMY J Penelit Kim* [Internet]. 2022 Feb 9;18(1):103–11. Available from: [<URL>](#).
19. Adu REY. Dye sensitized solar cell (DSSC) fabrication using methanol extract of onion peel as a natural sensitizer. *J Turkish Chem Soc Sect A Chem* [Internet]. 2022 Nov 30;9(4):1285–94. Available from: [<URL>](#).
20. Zhang S, Deng P, Xu Y, Lü S, Wang J. Quantification and analysis of anthocyanin and flavonoids compositions, and antioxidant activities in onions with three different colors. *J Integr Agric* [Internet]. 2016 Sep;15(9):2175–81. Available from: [<URL>](#).
21. Samota MK, Sharma M, Kaur K, Sarita, Yadav DK, Pandey AK, et al. Onion anthocyanins: Extraction, stability, bioavailability, dietary effect, and health implications. *Front Nutr* [Internet]. 2022 Jul 27;9:917617. Available from: [<URL>](#).
22. Constantin OE, Istrati DI. Extraction, quantification and characterization techniques for anthocyanin compounds in various food matrices—a review. *Horticulturae* [Internet]. 2022 Nov 16;8(11):1084. Available from: [<URL>](#).
23. Tena N, Asuero AG. Up-to-date analysis of the extraction methods for anthocyanins: principles of the techniques, optimization, technical progress, and industrial application. *Antioxidants* [Internet]. 2022 Jan 30;11(2):286. Available from: [<URL>](#).
24. Saptarini NM, Herawati IE. Extraction methods and varieties affect total anthocyanins content in acidified extract of papery skin of onion (*Allium cepa* L.). *Drug Invent Today* [Internet]. 2018;10(4):471–4. Available from: [<URL>](#).
25. Ali O-H, Al-sayed H, Yasin N, Afifi E. Effect of different extraction methods on stability of anthocyanins extracted from red onion peels (*Allium cepa*) and Its Uses as Food Colorants. *Bull Natl Nutr Inst* [Internet]. 2016 Nov 1;47(2):1–24. Available from: [<URL>](#).
26. Giusti MM, Polit MF, Ayvaz H, Tay D, Manrique I. Characterization and Quantitation of Anthocyanins and other phenolics in native andean potatoes. *J Agric Food Chem* [Internet]. 2014 May 14;62(19):4408–16. Available from: [<URL>](#).
27. Oancea S, Draghici O. pH and thermal stability of anthocyanin-based optimised extracts of Romanian red onion cultivars. *Czech J Food Sci* [Internet]. 2013 Jun 30;31(3):283–91. Available from: [<URL>](#).
28. Hosseinnezhad M, Gharanjig K, Moradian S, Saeb MR. In quest of power conversion efficiency in nature-inspired dye-sensitized solar cells: Individual, co-sensitized or tandem configuration? *Energy* [Internet]. 2017 Sep 1;134:864–70. Available from: [<URL>](#).

29. Ghann W, Kang H, Sheikh T, Yadav S, Chavez-Gil T, Nesbitt F, et al. Fabrication, optimization and characterization of natural dye sensitized solar cell. *Sci Rep* [Internet]. 2017 Jan 27;7(1):41470. Available from: [<URL>](#).
30. Lee C-P, Lin RY-Y, Lin L-Y, Li C-T, Chu T-C, Sun S-S, et al. Recent progress in organic sensitizers for dye-sensitized solar cells. *RSC Adv* [Internet]. 2015 Mar 4;5(30):23810–25. Available from: [<URL>](#).
31. Swer TL, Mukhim C, Bashir K, Chauhan K. Optimization of enzyme aided extraction of anthocyanins from *Prunus nepalensis* L. *LWT* [Internet]. 2018 May 1;91:382–90. Available from: [<URL>](#).
32. Amelia F, Afnani GN, Musfiroh A, Fikriyani AN, Ucche S, Murrukmihadi M. Extraction and stability test of anthocyanin from buni fruits (*Antidesma bunius* L) as an alternative natural and safe food colorants. *J Food Pharm Sci* [Internet]. 2013 May 8;1(2):49–53. Available from: [<URL>](#).
33. Ramanarayanan R, P. N, C.V. N, S. S. Natural dyes from red amaranth leaves as light-harvesting pigments for dye-sensitized solar cells. *Mater Res Bull* [Internet]. 2017 Jun 1;90:156–61. Available from: [<URL>](#).
34. Castillo-Robles JA, Rocha-Rangel E, Ramírez-de-León JA, Caballero-Rico FC, Armendáriz-Mireles EN. Advances on dye-sensitized solar cells (DSSCs) nanostructures and natural colorants: A review. *J Compos Sci* [Internet]. 2021 Oct 29;5(11):288. Available from: [<URL>](#).
35. Almalki ASA, Shoair AGF, Badawi A, Al-Baradi AM, Atta AA, Algarni SA, et al. Enhancement of the open-circuit voltage of the dye-sensitized solar cells using a modified ruthenium dye. *Appl Phys A* [Internet]. 2021 Mar 6;127(3):171. Available from: [<URL>](#).
36. Shanmugam V, Manoharan S, Anandan S, Murugan R. Performance of dye-sensitized solar cells fabricated with extracts from fruits of ivy gourd and flowers of red frangipani as sensitizers. *Spectrochim Acta Part A Mol Biomol Spectrosc* [Internet]. 2013 Mar 1;104:35–40. Available from: [<URL>](#).
37. Rodriguez-Saona LE, Wrolstad RE. Extraction, isolation, and purification of anthocyanins. *Curr Protoc Food Anal Chem* [Internet]. 2001 Apr 1;00(1):F1.1.1-F1.1.11. Available from: [<URL>](#).
38. Taghavi T, Patel H, Rafie R. Anthocyanin extraction method and sample preparation affect anthocyanin yield of strawberries. *Nat Prod Commun* [Internet]. 2022 May 13;17(5):1–7. Available from: [<URL>](#).



## Surface Physicochemical Characterization of Shepherd's Purse (*Capsella bursa-pastoris*) by Inverse Gas Chromatography

Biol Isik<sup>1\*</sup> 

<sup>1</sup> Yildiz Technical University, Faculty of Arts & Sciences, Department of Chemistry, Esenler, Istanbul, 34220, Turkey.

**Abstract:** Shepherd's purse (*Capsella bursa-pastoris*) is one of the plants widely utilized in conventional medicine and can grow in different parts of the world. The determination of the surface properties of a solid material is extremely important for the industrial use of the material and the improvement of material properties. Therefore, in this study, this plant was used as a stationary phase, and its surface characterization was performed by inverse gas chromatography technique. In this context, firstly, the plant was prepared with several pretreatments to be used in the experimental tests. The  $V_N$  values were found from the retention data obtained by passing organic solvents over the plant filled into the chromatographic column in the temperature range of 303.2–328.2 K and linear retention diagrams were drawn. The  $\gamma_s^D$  of the plant was calculated according to Schultz, Dorris-Gray, and Donnet-Park methods, and the suitability of the methods was compared. The  $\Delta G_A^S$  values were calculated with the data obtained from the Schultz method, and the  $\Delta H_A^S$  values were calculated using these data. The acidity and basicity of the plant surface were examined. According to the  $K_D/K_A$  value (0.93), it was determined that the surface of the plant was acidic.

**Keywords:** Adsorption, surface properties, inverse gas chromatography, shepherd's purse.

**Submitted:** April 6, 2023. **Accepted:** September 10, 2023.

**Cite this:** Isik B. Surface Physicochemical Characterization of Shepherd's Purse (*Capsella bursa-pastoris*) by Inverse Gas Chromatography. JOTCSA. 2023;10(4):1071-80.

**DOI:** <https://doi.org/10.18596/jotcsa.1278025>

**\*Corresponding author's E-mail:** [19birol91@gmail.com](mailto:19birol91@gmail.com), [isikb@yildiz.edu.tr](mailto:isikb@yildiz.edu.tr)

### 1. INTRODUCTION

A popular technique for analyzing volatiles is gas chromatography, which combines a stationary phase with known properties and an inert mobile phase. Several different types of volatile chemicals can be examined using gas chromatography (1–3). Nevertheless, this technique cannot be used to analyze large molecular weights and non-volatile components such as lignocellulosic materials (4), clays (5), liquid crystals (6), polymers (7), and composites (8). To examine such compounds, inverse gas chromatography (IGC) was improved for the task (9–11).

Unlike traditional gas chromatography, the IGC method analyzes solid materials by passing them through a chromatographic column loaded with known-property volatile solvents. The IGC approach uses retention data from experimental research to characterize the physicochemical properties of solid materials in a simple, rapid, reliable, and generally low-cost manner (12–14). The IGC approach allows

for the study of both infinite dilution and restricted concentration. The parameters surface energy, acidity-basicity constants, adsorption enthalpy, entropy, and Gibbs free energy can all be obtained by doing experimental tests at infinite dilution (15,16).

The development of a solid material's qualities and optimum efficiency all depend heavily on the surface properties of the material that will be used in various industrial applications. Surface-free energy in particular is crucial for the processing and use of materials. This energy plays a crucial role in the identification, assessment, and development of material surface characteristics such as ornamentation, wetting capacity, adhesion, and coating (17,18). Measurements of liquid adsorption, flow micro-calorimetry, and contact angle can all be used to calculate the surface energy of solid materials (19,20). Researchers have recently favored the IGC methodology over these methods, however, because it is simpler to use, has higher efficiency, and produces data with higher accuracy.

This is because determining surface energy using these methods is rather limited and complex. The IGC method also determines whether the material's surface is acidic or alkaline. The material surface's acidity or basicity offers crucial preliminary data for assessing the adsorption behavior of the materials and choosing the right pollutant to maximize the efficiency of the adsorption process. Several techniques, including  $pH_{pzc}$  determination, zeta potential tests, and the Boehm titration method, can be used to determine the acidity or alkalinity of the material surface. The IGC approach, however, offers straightforward and quick findings and enables the evaluation of several surface properties in addition to acidity and alkalinity parameters (21–23).

One plant that is commonly used in conventional medicine is the shepherd's purse (*Capsella bursa-pastoris*), which is a global plant that may grow anywhere. Shepherd's purse contains a wide variety of chemicals, including flavonoids, fatty acids, organic acids, amino acids, many trace elements, vitamins, and many other compounds. This plant can be widely used for antimicrobial, anti-inflammatory, antioxidant, cardiovascular, reproductive, anticancer, sedative, and other pharmacological fields and purposes (24–27). Shepherd's purse can be utilized in many areas. Besides, as a lignocellulosic material, it has the potential to be used as an efficient sorbent for the removal of various organic contaminants and

heavy metals from aqueous environments. For this purpose, it is extremely significant to investigate the surface properties of the shepherd's purse plant.

In this work, the IGC method was used to determine the surface characteristics of the shepherd's purse at infinite dilution. In this case, a chromatographic column was loaded with the powdered shepherd's purse following specific pretreatments. The plant's retention behavior was then evaluated by running various organic solvents through the column. Net retention volumes and linear retention diagrams were calculated using the retention information gleaned from the experimental research. The information obtained from these linear diagrams was used to determine the surface characteristics of the shepherd's purse.

## 2. EXPERIMENTAL SECTION

### 2.1. Materials and methods

All chemicals were illustrated in Table 1. All chemicals were acquired from Sigma Aldrich and Merck, Inc. For the chromatographic investigations, a 0.5 m stainless steel column from Alltech Associates Inc. was employed. Furthermore, from Alltech Associates Inc., silanized glass wool was utilized to fill the column tips. As the mobile phase in the IGC investigations, high-purity inert helium (He) gas was used.

**Table 1.** The chemicals used in this work.

Chemicals	Abbreviation	Source	CAS Registry Number	Assay
n-Hexane	Hx	Sigma Aldrich	110-54-3	≥99.7%
n-Heptane	Hp	Sigma Aldrich	142-82-5	≥99.0%
n-Octane	O	Sigma Aldrich	111-65-9	≥99.0%
n-Nonane	N	Sigma Aldrich	111-84-2	≥99.0%
n-Decane	D	Sigma Aldrich	124-18-5	≥94.0%
Tetrahydrofuran	THF	Sigma Aldrich	109-99-9	≥99.8%
Acetone	Ace	Sigma Aldrich	67-64-1	≥99.8%
Ethyl acetate	EA	Sigma Aldrich	141-78-6	≥99.8%
Chloroform	TCM	Sigma Aldrich	67-66-3	≥99.8%
Dichloromethane	DCM	Sigma Aldrich	75-09-2	≥99.8%
Diethyl ether	DEE	Sigma Aldrich	60-29-7	≥97.5%

A thermal conductivity detector-equipped Agilent Technologies 6890N gas chromatograph was used to carry out the IGC studies. The temperature of the sample injection unit and detector of the gas chromatography device used throughout the studies is 523.2 K. Several organic solvents were applied to the prepared adsorbent using a 1 mL Hamilton syringe, and their retention behavior was examined. The air peak was also obtained using a Hamilton syringe of 10 mL. Each solvent and air injection received at least four successive injections for each set of measurements to ensure the correctness of the experimental data. Retention times were calculated based on the solvents' behavior during retention on the stationary phase, and retention diagrams were drawn. The surface characteristics of the materials in the temperature range of 303.2–328.2 K were determined using these retention diagrams, and the results were evaluated. For infinite dilution, the probe (0.1  $\mu$ L) was taken into the syringe and flushed

into the air. Then, the air and probe retention times were calculated. For every set of measurements, each probe and air injection were received at least four consecutive times.

### 2.2. Preparation of the Adsorbent and Chromatographic Column

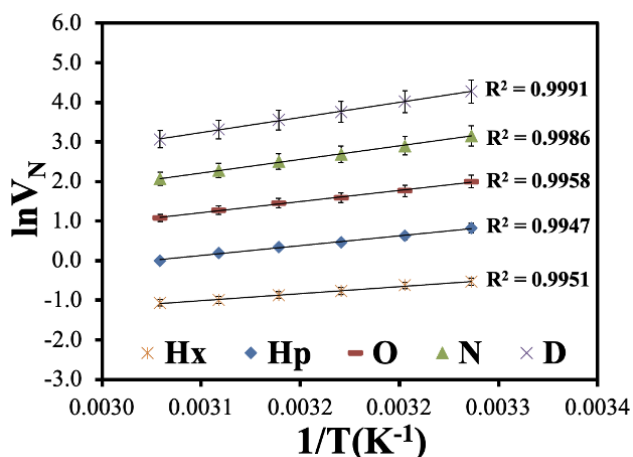
Shepherd's purse plants were bought from herbalists in Istanbul, Turkey, and then they were scrubbed clean of any dirt and dust. Then, to get rid of different pollutants and impurities, they were extensively cleaned with distilled water. At 383.2 K for 24 h, an oven was used to dry the completely washed plants (23,28). With a grinder, they were further ground to 80–100 mesh. For further research, the ground plants were dried again in an oven at 383.2 K for 48 h after being cleaned many times with distilled water.

A stainless-steel chromatographic column was cut into 0.5 m in length. It was first washed with distilled

water and then with chromic acid to remove organic and inorganic contaminants. It was then cleaned again with distilled water and passed through acetone. After this process, it was dried in an oven at 383.2 K for 24 hours. Then, sorbent was filled into the column at approximately 0.6 g. After this process, the column ends were completely plugged with silanized glass wool.

### 3. RESULTS AND DISCUSSION

The interaction between the shepherd's purse and organic solvents is determined by the retention time of the selected solvent. A net retention volume ( $V_N$ ) is calculated by the following equation (29,30):



$$V_N = Q \times J \times (t_R - t_A) \times T/T_f \quad (1)$$

Here,  $t_R$  and  $t_A$  are the retention times of solvents and air, respectively.  $Q$  is the volumetric flow rate,  $J$  is the James-Martin constant,  $T$  is the column temperature (K), and  $T_f$  is the ambient temperature (K).

Using the retention data of the solvents on the stationary phase (shepherd's purse) in the column,  $V_N$  values were determined by equation (1) utilizing the data. Figure 1 illustrates linear retention diagrams.

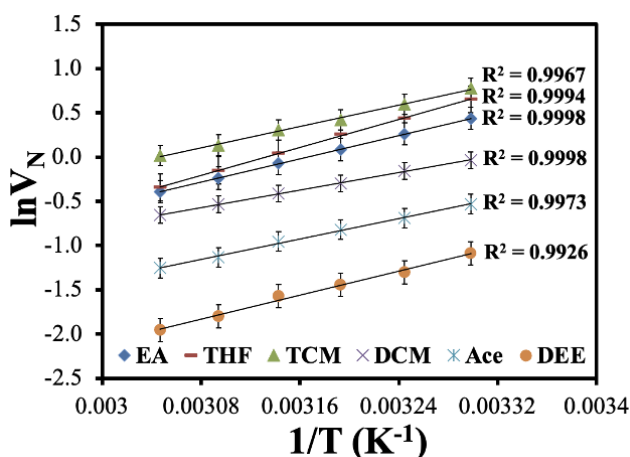


**Figure 1.** The linear retention diagrams of organic solvents onto shepherd's purse.

By employing the  $V_N$  values derived by equation (1) with the aid of the raw data collected from the IGC tests, it is possible to determine the Gibbs free energy of adsorption ( $\Delta G_A^o$ ), which is a crucial parameter for the sorption process. The  $\Delta G_A^o$  values were calculated from the following equation (31–33):

$$\Delta G_A = -R \times T \times \ln(V_N) + K \quad (2)$$

The chemical composition, physical characteristics, and composition of solid materials can all affect how energetically active they are on the surface. Van der Waals interactions, which are weak, London forces, and strong interactions like acid-base and polar interactions are what cause the interactions between the solid material and organic solvent to occur (34). The dispersive surface energy ( $\gamma_S^D$ ) is a result of the weak interaction between the solid material and solvent molecules. There are several ways to compute the  $\gamma_S^D$  values, including the Dorris-Gray (equation (3)) (35), Donnet-Park (36–38), and Schultz (equation (4)) (39) approaches.

$$-\Delta G_{[CH_2]} = 2 \times N_A \times a_{[CH_2]} \times (\gamma_S^D \times \gamma_{[CH_2]}^D)^{0.5} \quad (3)$$

$$-\Delta G_A = R \times T \times \ln(V_N) = 2 \times N_A \times a \times (\gamma_S^D \times \gamma_L^D)^{0.5} + K \quad (4)$$

Here,  $\Delta G_{[CH_2]}$  is the Gibbs free energy of a surface including only the  $-CH_2$  group, calculated according

to equation (5).  $a_{[CH_2]}$  refers to the surface area of the  $-CH_2$  group ( $0.06 \text{ nm}^2$ ). " $a$ " refers to the cross-sectional area of solvents, and  $\gamma_L^D$  refers to the dispersive energy of solvents. These values were taken from the literature and are presented in Table 2.

$\gamma_{[CH_2]}^D$  refers to the dispersive energy of the  $-CH_2$  group, calculated according to the Dorris-Gray (Equation (5)) (35) and Donnet-Park (Equation (6)) (36–38) approaches.

$$\Delta G_{[CH_2]} = -R \times T \times \ln\left(\frac{V_{N,n}}{V_{N,n+1}}\right) \quad (5)$$

$$\gamma_{[CH_2]}^D = 35.6 - 0.058 \times t \quad (6)$$

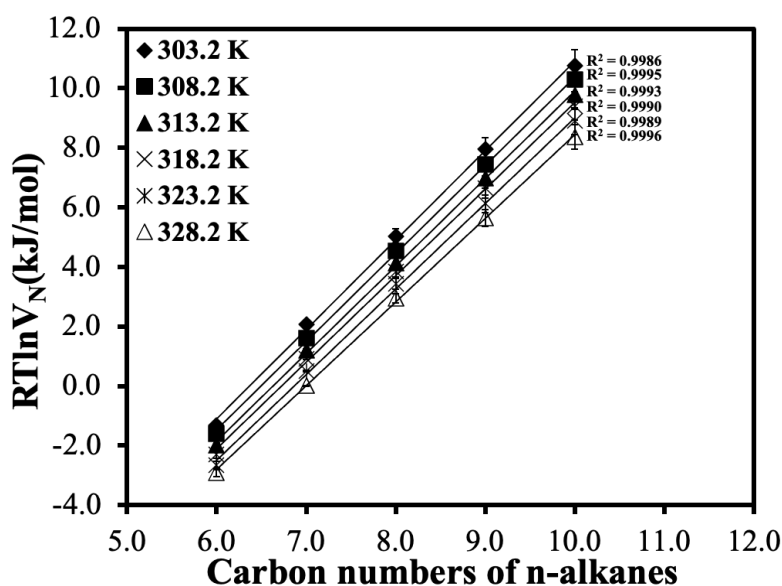
$$\gamma_{[CH_2]}^D = 35.6 - 0.058 \times (t - 20) \quad (7)$$

Here,  $t$  refers to the column temperature.  $V_{N,n}$  and  $V_{N,n+1}$  refer to the net retention volumes of  $n$ -alkanes consisting of a  $n$  and  $n+1$  carbon atoms, respectively.

Figure 2 displays  $RT \ln V_N$  linear graphs versus the carbon number of  $n$ -alkanes according to equation (7), used to calculate the  $\gamma_S^D$  values using the Dorris-Gray equation in equation (3).

**Table 2.** The values of  $a$  and  $\gamma_L^D$  for organic solvents (29).

Probes	$a$ ( $\times 10^{-10}$ m <sup>2</sup> )	$\gamma_L^D$ (mJ/m <sup>2</sup> )
n-Hexane (Hx)	51.5	18.4
n-Heptane (Hp)	57.0	20.3
n-Octane (O)	62.8	21.3
n-Nonane (N)	69.0	22.7
n-Decane (D)	75.0	23.4
Dichloromethane (DCM)	31.5	27.6
Chloroform (TCM)	44.0	25.9
Tetrahydrofuran (THF)	45.0	22.5
Ethyl acetate (EA)	48.0	19.6
Acetone (Ace)	42.5	16.5
Diethyl ether (DEE)	47.0	15.0

**Figure 2.** The linear plot of  $RT \ln V_N$  versus carbon numbers of n-alkanes.

According to the Dorris-Gray and Donnet-Park methods,  $\gamma_{[CH_2]}^D$  values were calculated according to equations (6) and (7), respectively, and illustrated in Table 3. By substituting the  $\Delta G_{[CH_2]}$  values found from

Figure 2 and the  $\gamma_{[CH_2]}^D$  values calculated from equations (6) and (7) into equation (3), the  $\gamma_S^D$  values were found from the Dorris-Gray and Donnet-Park methods, and the results are given in Table 3.

**Table 3.** Dispersive surface energy ( $\gamma_S^D$ , mJ/m<sup>2</sup>) values determined using the Dorris-Gray and Donnet-Park method of shepherd's purse.

T (K)	Dorris-Gray method			Donnet-Park method	
	$\gamma_{CH_2}$ (mJ/m <sup>2</sup> )	$-\Delta G_{ads}(CH_2)$ (kJ/mol)	$\gamma_S^D$ (mJ/m <sup>2</sup> )	$\gamma_{CH_2}$ (mJ/m <sup>2</sup> )	$\gamma_S^D$ (mJ/m <sup>2</sup> )
<b>303.2</b>	33.86	3.01	51.13	35.02	49.44
<b>308.2</b>	33.57	2.96	50.05	34.73	48.38
<b>313.2</b>	33.28	2.93	49.61	34.44	47.94
<b>318.2</b>	32.99	2.91	49.21	34.15	47.54
<b>323.2</b>	32.70	2.87	48.36	33.86	46.71
<b>328.2</b>	32.41	2.82	46.89	33.57	45.27

From Table 3, the  $\gamma_S^D$  values of the shepherd's purse were found in the range of 51.13–46.89 mJ/m<sup>2</sup> by the Dorris-Gray method and in the range of 49.44–46.89 mJ/m<sup>2</sup> by the Donnet-Park method. It was observed that the  $\gamma_S^D$  values gradually decreased with increasing temperature. In this case, it can be concluded that the decrease in surface energy with

increasing temperature may facilitate coating, wetting, and bonding to different surfaces at higher temperatures. Similar results were also found in the literature. Perez-Mendoza et al. calculated the surface energies of activated carbons and found that the surface energy decreased with increasing temperature (40). Ocak et al. reported that the

surface energy of 5-((S)-3,7-dimethyloctyloxy)-2-[[[4-(dodecyloxy)phenyl]imino]-methyl]phenol liquid crystal decreases with increasing temperature (15). Erol et al. reported that the dispersive surface energy of 4-[4-((S)-citronellyloxy) benzoyloxy] benzoic acid thermotropic liquid crystal decreases with increasing temperature (30). Sreekanth et al. reported that the dispersive surface energy of thiourea and melamine polymerized graphitic carbon nitride sheets decreases with increasing temperature (41). Similarly, Papadopoulou et al. reported that the dispersive surface energy of 1-butyl-1-ethylpiperidinium bromide decreases with increasing temperature (42).

The  $\gamma_S^D$  values were also calculated from the linear plots (Figure 3) from the Schultz method (Equation (4)). The results were listed in Table 4. As can be seen from Table 4, the  $\gamma_S^D$  values were found to decrease with increasing temperature in the Schultz method. The methods used for the calculation of the  $\gamma_S^D$  values were found to be compatible with each other. There is a difference between the three methods because the Schultz approach determines the surface area of hydrocarbon solvent molecules based on the assumption that they are spherical, which is usually stated as a constant (43).

**Table 4.** Dispersive surface energy ( $\gamma_S^D$ , mJ/m<sup>2</sup>) values obtained using the Schultz method of shepherd's purse.

Temperature (K)	303.2	308.2	313.2	318.2	323.2	328.2
Schultz method	49.21	47.75	46.92	46.13	44.93	43.18

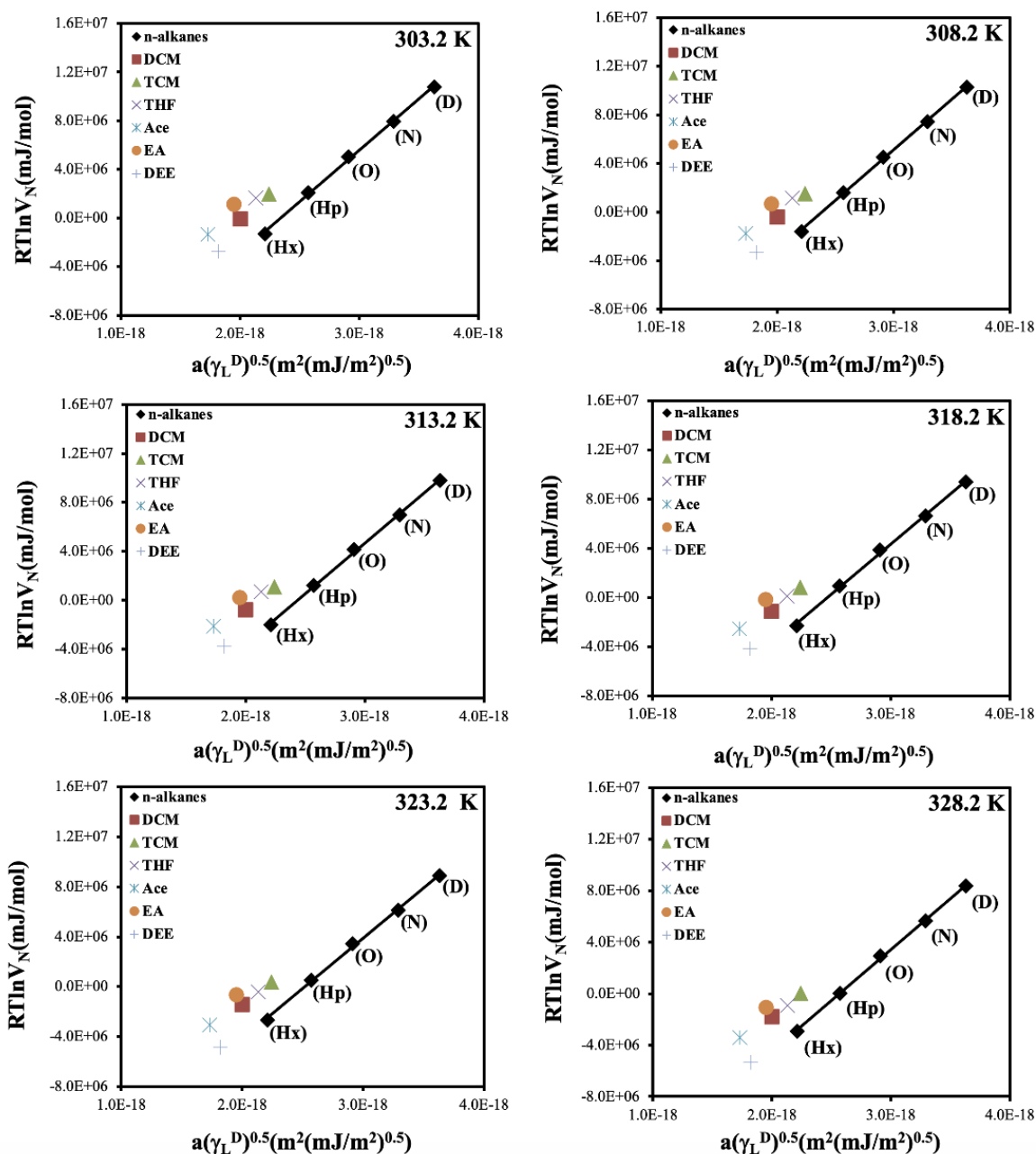


**Figure 3.** The linear plots drawn between  $a(\gamma_L^D)^{0.5}$  and  $RT \ln V_N$  values according to the Schultz method.

Figure 4 shows the comparison and temperature dependence of the three different methods applied in this study to calculate the  $\gamma_s^D$  values. As can be seen in Figure 4, the  $\gamma_s^D$  values decreased with temperature in all three approaches. From all the

results, the best correlation coefficient ( $R^2 = 0.9822$ ) was found in the Schultz method. The correlation coefficients of the Dorris-Gray and Donnet-Park methods are also very close to each other.

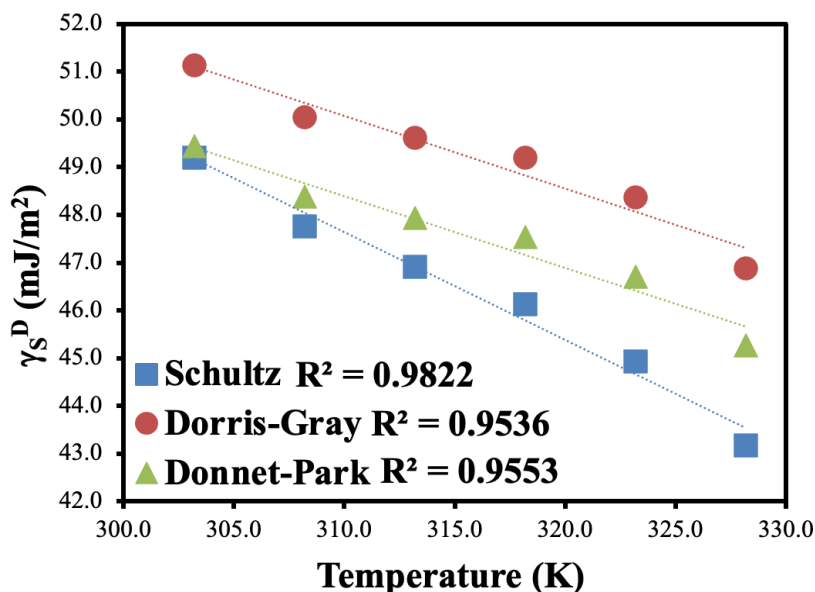


**Figure 4.** Variation of the  $\gamma_s^D$  values of shepherd's purse with temperature, as obtained by the Schultz, Dorris-Gray, and Donnet-Park approaches.

In the Schultz plots given in Figure 3, the specific Gibbs free energies ( $\Delta G_A^S$ ) of polar solvents were found from the distances of polar solvents to the linear line of n-alkanes and given in Table 5. From

Table 5, the sorption process appears to be spontaneous. It was also found that  $-\Delta G_A^S$  values decreased gradually with rising temperature.

**Table 5.** The  $-\Delta G_A^S$  (kJ/mol) values of polar solvents onto shepherd's purse.

T (K)	EA	Ace	DCM	TCM	THF	DEE
303.2	4.41	3.83	2.80	2.82	3.44	1.66
308.2	4.31	3.70	2.81	2.75	3.27	1.37
313.2	4.22	3.67	2.81	2.69	3.19	1.30
318.2	4.06	3.52	2.74	2.69	2.88	1.15
323.2	3.95	3.31	2.74	2.61	2.73	0.80
328.2	3.52	2.94	2.40	2.29	2.21	0.30

Based on the  $-\Delta G_A^S$  values presented in Table 5, the sorption enthalpy ( $\Delta H_A^S$ ) values were calculated using equation (8), which are then provided in Table 6 (14, 44).

$$-\frac{\Delta G_A^S}{T} = -\frac{\Delta H_A^S}{T} + \Delta S_A^S \quad (8)$$

As seen in Table 6, the sorption process was found to be exothermic. The  $\Delta H_A^S$  values for polar solvents follow the order of magnitude THF > DEE > EA > Ace > TCM > DCM. Here, THF ( $DN = 84.4, AN = 2.1$ ) interacts better with acidic surfaces since it is a relatively basic solvent. On the contrary, since DCM ( $DN = 0.0, AN = 16.4$ ) is a relatively acidic solvent, it interacts more with basic surfaces (45–47).

**Table 6.**  $-\Delta H_A^S$  (kJ/mol) values of shepherd's purse for the polar solvents.

Polar Solvents	Ace	EA	THF	DCM	TCM	DEE
$-\Delta H_A^S$ (kJ/mol)	13.72	14.17	17.36	6.64	8.05	16.63



Polar solvents were used to determine details regarding the surface acidity or basicity of the shepherd's purse. According to the method suggested by Gutmann, the behavior of acidity or basicity can be analyzed using the following equation (48,49). The  $-\Delta H_A^S$  values given in Table 6 were used to calculate the acidity or basicity character.

$$-\Delta H_A^S = K_A \times (DN) + K_D \times (AN^*) \quad (9)$$

Here,  $DN$  and  $AN^*$  refer to the donor and acceptor numbers, respectively.  $K_A$  and  $K_D$  refer to the acidity and basicity constants, respectively. If the  $K_D/K_A > 1$ ,

the sorbent surface is basic. If the  $K_D/K_A < 1$ , the sorbent surface is acidic.

Figure 5 shows the linear plot to calculate the acidity-basicity constants. From the slope and intercept of this linear plot,  $K_A$  and  $K_D$  values were calculated, respectively. Accordingly, the  $K_A$  value was found to be 0.1989 and the  $K_D$  value was found to be 0.1847. The  $K_D/K_A$  value calculated by using these values was found to be 0.93. According to this value, it can be said that the surface of the shepherd's purse has an acidic character. This study provides preliminary information about which type of pollutant to choose for sorption studies.

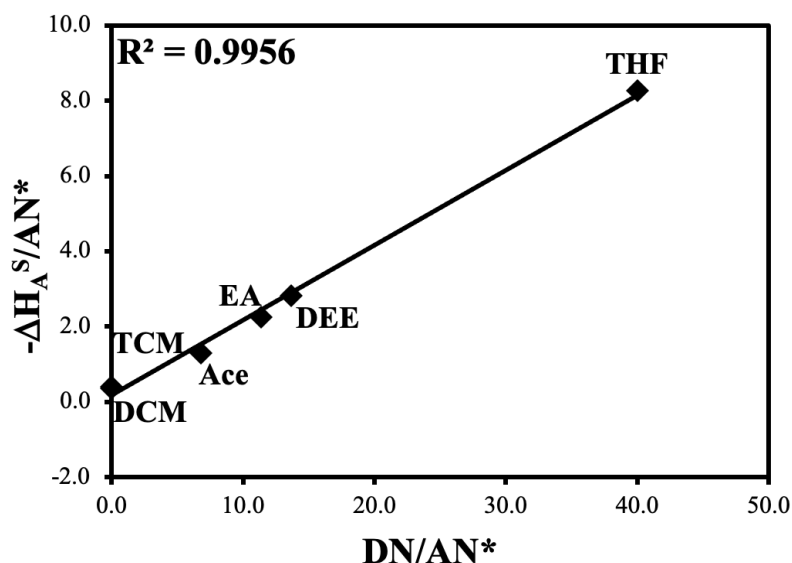


**Figure 5.** The plot of  $-\Delta H_A^S/AN^*$  vs  $DN/AN^*$  of shepherd's purse.

#### 4. CONCLUSION

In the current work, the stationary phase of the shepherd's purse was generated, and its surface properties were assessed using the IGC approach at infinite dilution. The retention diagrams were obtained between 303.2 and 328.2 K, and then calculations were made based on these diagrams to determine the  $\gamma_S^D$ ,  $\Delta H_A^S$ ,  $\Delta G_A^S$ , and  $K_A$  and  $K_D$  constants. The  $\gamma_S^D$  values of shepherd's purse were ranging from 51.13 to 46.89 mJ/m<sup>2</sup> (Dorris-Gray), 49.44 to 45.47 mJ/m<sup>2</sup> (Donnet-Park), and 49.21 to 43.18 mJ/m<sup>2</sup> (Schultz). These values were shown to be high and to decrease linearly with the increasing temperature.  $K_D/K_A = 0.93$  indicate that the surface of the shepherd's purse has an acidic behavior. The process of solvents adsorbing on the shepherd's purse was found to be exothermic based on the results of enthalpy measurements. According to these results, preliminary information can be obtained about which type of pollutant should be removed from aqueous solutions when shepherd's purse is used as an adsorbent. Since the shepherd's purse surface is acidic, it can be concluded that functional groups that may show acidic properties may be present on the surface, and cationic pollutants can be removed from wastewater.

#### 5. CONFLICT OF INTEREST

The authors declare that they have no known competing financial interests or personal relationships that could have appeared to influence the work reported in this paper.

#### 6. REFERENCES

1. Dettmer-Wilde K, Engewald W. Practical gas chromatography [Internet]. Berlin, Heidelberg: Springer; 2014. 904 p. Available from: [<URL>](#).
2. Smidsrød O, Guillet JE. Study of polymer-solute interactions by gas chromatography. *Macromolecules* [Internet]. 1969 May 1;2(3):272-7. Available from: [<URL>](#).
3. Aresta AM, De Vietro N, Picciariello A, Rotelli MT, Altomare DF, Dezi A, et al. Volatile organic compounds determination from intestinal polyps and in exhaled breath by gas chromatography-mass spectrometry. *Appl Sci* [Internet]. 2023 May 15;13(10):6083. Available from: [<URL>](#).
4. Bai W, Pakdel E, Li Q, Wang J, Tang W, Tang B, et al. Inverse gas chromatography (IGC) for studying the cellulosic materials surface characteristics: a mini review. *Cellulose* [Internet]. 2023 Apr 6;30(6):3379-96. Available from: [<URL>](#).

5. Boudriche L, Calvet R, Chamayou A, Hamdi B. Influence of different wet milling on the properties of an attapulgite clay, contribution of inverse gas chromatography. Powder Technol [Internet]. 2021 Jan 22;378:29–39. Available from: [<URL>](#).
6. Cakar F, Ocak H, Ozturk E, Mutlu-Yanic S, Kaya D, San N, et al. Investigation of thermodynamic and surface characterisation of 4-[4-(2-ethylhexyloxy)benzoyloxy]benzoic acid thermotropic liquid crystal by inverse gas chromatography. Liq Cryst [Internet]. 2014 Sep 2;41(9):1323–31. Available from: [<URL>](#).
7. Yampolskii Y, Belov N. Investigation of polymers by inverse gas chromatography. Macromolecules [Internet]. 2015 Oct 13;48(19):6751–67. Available from: [<URL>](#).
8. Cakar F. Synthesis and thermodynamic characterization of poly(methyl methacrylate)/multiwall carbon nanotube nanocomposite. Surf Interface Anal [Internet]. 2021 Feb 4;53(2):258–67. Available from: [<URL>](#).
9. Adıgüzel A, Korkmaz B, Çakar F, Cankurtaran, Şenkal BF. Investigation of the surface properties of dibutyl amine modified poly(styrene) based polymer by inverse gas chromatography method. J Polym Res [Internet]. 2021 Mar 1;28(3):83. Available from: [<URL>](#).
10. Nawawi WMFW, Lee K-Y, Kontturi E, Bismarck A, Mautner A. Surface properties of chitin-glucan nanopapers from Agaricus bisporus. Int J Biol Macromol [Internet]. 2020 Apr 1;148:677–87. Available from: [<URL>](#).
11. Zhu Q-N, Wang Q, Hu Y-B, Abliz X. Practical Determination of the Solubility Parameters of 1-alkyl-3-methylimidazolium bromide ([C<sub>n</sub>C<sub>1</sub>im]Br, n = 5, 6, 7, 8) ionic liquids by inverse gas chromatography and the hansen solubility parameter. Molecules [Internet]. 2019 Apr 5;24(7):1346. Available from: [<URL>](#).
12. Saada A, Papirer E, Balard H, Siffert B. Determination of the surface properties of illites and kaolinites by inverse gas chromatography. J Colloid Interface Sci [Internet]. 1995 Oct 1;175(1):212–8. Available from: [<URL>](#).
13. Cordeiro N, Gouveia C, John MJ. Investigation of surface properties of physico-chemically modified natural fibres using inverse gas chromatography. Ind Crops Prod [Internet]. 2011 Jan 1;33(1):108–15. Available from: [<URL>](#).
14. van Asten A, van Veenendaal N, Koster S. Surface characterization of industrial fibers with inverse gas chromatography. J Chromatogr A [Internet]. 2000 Aug 4;888(1–2):175–96. Available from: [<URL>](#).
15. Ocak H, Mutlu-Yanic S, Cakar F, Bilgin-Eran B, Guzeller D, Karaman F, et al. A study of the thermodynamical interactions with solvents and surface characterisation of liquid crystalline 5-((S)-3,7-dimethyloctyloxy)-2-[[[4-(dodecyloxy)phenyl]imino]-methyl]phenol by inverse gas chromatography. J Mol Liq [Internet]. 2016 Nov 1;223:861–7. Available from: [<URL>](#).
16. Uhlmann P, Schneider S. Acid–base and surface energy characterization of grafted polyethylene using inverse gas chromatography. J Chromatogr A [Internet]. 2002 Sep 6;969(1–2):73–80. Available from: [<URL>](#).
17. Król P, Król B. Determination of free surface energy values for ceramic materials and polyurethane surface-modifying aqueous emulsions. J Eur Ceram Soc [Internet]. 2006 Jan 1;26(12):2241–8. Available from: [<URL>](#).
18. Ugraskan V, Isik B, Yazici O, Cakar F. Surface characterization and synthesis of boron carbide and silicon carbide. Solid State Sci [Internet]. 2021 Aug 1;118:106636. Available from: [<URL>](#).
19. Faria PC., Órfão JJ., Pereira MF. Adsorption of anionic and cationic dyes on activated carbons with different surface chemistries. Water Res [Internet]. 2004 Apr 1;38(8):2043–52. Available from: [<URL>](#).
20. Nassar NN, Hassan A, Pereira-Almao P. Effect of surface acidity and basicity of aluminas on asphaltene adsorption and oxidation. J Colloid Interface Sci [Internet]. 2011 Aug 1;360(1):233–8. Available from: [<URL>](#).
21. Isik B, Cakar F, Cankurtaran O. A comparative study of surface properties of *Urtica dioica* (nettle) leaves, roots, and seeds and examination of their ability to separate xylene isomers. Phytochem Anal [Internet]. 2022 Aug 29;33(6):886–94. Available from: [<URL>](#).
22. Gamelas JAF. The surface properties of cellulose and lignocellulosic materials assessed by inverse gas chromatography: a review. Cellulose [Internet]. 2013 Dec 1;20(6):2675–93. Available from: [<URL>](#).
23. Isik B, Avci S, Cakar F, Cankurtaran O. Adsorptive removal of hazardous dye (crystal violet) using bay leaves (*Laurus nobilis* L.): surface characterization, batch adsorption studies, and statistical analysis. Environ Sci Pollut Res [Internet]. 2023 Jan 2;30(1):1333–56. Available from: [<URL>](#).
24. Grosso C, Vinholes J, Silva LR, Pinho PG de, Gonçalves RF, Valentão P, et al. Chemical composition and biological screening of *Capsella bursa-pastoris*. Rev Bras Farmacogn [Internet]. 2011 Aug;21(4):635–43. Available from: [<URL>](#).
25. Al-Snafi AE. The chemical constituents and pharmacological effects of *capsella bursa-pastoris*-a review. Int J Pharmacol Toxicol [Internet]. 2015;5(2):76–81. Available from: [<URL>](#).
26. Al-Douri NA, Al-Essa LY. A survey of plants used in Iraqi traditional medicine. Jordan J Pharm Sci [Internet]. 2010 Jul 12;3(2):100–18. Available from: [<URL>](#).
27. Alizadeh H, Club YR, Branch A, Jafari B, Babae T. The Study of Antibacterial Effect of *Capsella Bursa-*

- Pastoris on Some of Gram Positive and Gram Negative Bacteria. *J Basic Appl Sci Res* [Internet]. 2012;2(7):6940–5. Available from: [<URL>](#).
28. Ali NS, Jabbar NM, Alardhi SM, Majdi HS, Albayati TM. Adsorption of methyl violet dye onto a prepared bio-adsorbent from date seeds: isotherm, kinetics, and thermodynamic studies. *Heliyon* [Internet]. 2022 Aug 1;8(8):e10276. Available from: [<URL>](#).
29. Işık B, Çakar F, Cankurtaran H, Cankurtaran Ö. Evaluation of the surface properties of 4-(Decyloxy) benzoic acid liquid crystal and its use in structural isomer separation. *Turkish J Chem* [Internet]. 2021 Jun 30;45(3):845–57. Available from: [<URL>](#).
30. Erol I, Cakar F, Ocak H, Cankurtaran H, Cankurtaran Ö, Bilgin-Eran B, et al. Thermodynamic and surface characterisation of 4-[4-((S)-citronellyloxy)benzyloxy]benzoic acid thermotropic liquid crystal. *Liq Cryst* [Internet]. 2016 Jan 2;43(1):142–51. Available from: [<URL>](#).
31. Mukhopadhyay P, Schreiber HP. Aspects of acid-base interactions and use of inverse gas chromatography. *Colloids Surfaces A Physicochem Eng Asp* [Internet]. 1995 Jul 25;100:47–71. Available from: [<URL>](#).
32. Isik B, Cakar F, Cankurtaran O, Cankurtaran H. Liquid crystal entrapped porous films for ammonia sensing and determination of surface properties of liquid crystal molecule. *ChemistrySelect* [Internet]. 2021 Jul 13;6(26):6740–7. Available from: [<URL>](#).
33. Ugraskan V, Isik B, Yazici O, Cakar F. Comparative physicochemical characterization of ULTEM/SWCNT nanocomposites: Surface, thermal and electrical conductivity analyses. *J Polym Res* [Internet]. 2022 Jul 2;29(7):254. Available from: [<URL>](#).
34. Ugraskan V, Isik B, Yazici O, Cakar F. Removal of Safranin T by a highly efficient adsorbent (*Cotinus Coggyria* leaves): Isotherms, kinetics, thermodynamics, and surface properties. *Surfaces and Interfaces* [Internet]. 2022 Feb 1;28:101615. Available from: [<URL>](#).
35. Dorris GM, Gray DG. Adsorption of n-alkanes at zero surface coverage on cellulose paper and wood fibers. *J Colloid Interface Sci* [Internet]. 1980 Oct 1;77(2):353–62. Available from: [<URL>](#).
36. Donnet J-B, Park S-J. Surface characteristics of pitch-based carbon fibers by inverse gas chromatography method. *Carbon N Y* [Internet]. 1991 Jan 1;29(7):955–61. Available from: [<URL>](#).
37. Donnet JB, Park SJ, Balard H. Evaluation of specific interactions of solid surfaces by inverse gas chromatography. *Chromatographia* [Internet]. 1991 May;31(9–10):434–40. Available from: [<URL>](#).
38. Donnet JB, Park SJ, Brendle M. The effect of microwave plasma treatment on the surface energy of graphite as measured by inverse gas chromatography. *Carbon N Y* [Internet]. 1992 Jan 1;30(2):263–8. Available from: [<URL>](#).
39. Schultz J, Lavielle L, Martin C. The Role of the interface in carbon fibre-epoxy composites. *J Adhes* [Internet]. 1987 Sep 3;23(1):45–60. Available from: [<URL>](#).
40. Pérez-Mendoza M, Almazán-Almazán MC, Méndez-Liñán L, Domingo-García M, López-Garzón FJ. Evaluation of the dispersive component of the surface energy of active carbons as determined by inverse gas chromatography at zero surface coverage. *J Chromatogr A* [Internet]. 2008 Dec 19;1214(1–2):121–7. Available from: [<URL>](#).
41. Sreekanth TVM, Basivi PK, Nagajyothi PC, Dillip GR, Shim J, Ko TJ, et al. Determination of surface properties and Gutmann's Lewis acidity–basicity parameters of thiourea and melamine polymerized graphitic carbon nitride sheets by inverse gas chromatography. *J Chromatogr A* [Internet]. 2018 Dec 14;1580:134–41. Available from: [<URL>](#).
42. Papadopoulou SK, Papaiconomou N, Baup S, Iojoiu C, Svecova L, Thivel P-X. Surface characterization of 1-butyl-1-ethylpiperidinium bromide by inverse gas chromatography. *J Mol Liq* [Internet]. 2019 Aug 1;287:110945. Available from: [<URL>](#).
43. Wang Q, Wang Q. Evaluation of the surface properties of poly(ionic liquid) materials by inverse gas chromatography. *Eur Polym J* [Internet]. 2020 Jan 15;123:109451. Available from: [<URL>](#).
44. Isik B, Cakar F, Cankurtaran O. The study on cholesteryl chloroformate liquid crystal for separation of isomers and determination of its surface properties. *Sep Sci Technol* [Internet]. 2022 Nov 22;57(17):2843–51. Available from: [<URL>](#).
45. Santos JMRCA, Guthrie JT. Study of a core-shell type impact modifier by inverse gas chromatography. *J Chromatogr A* [Internet]. 2005 Apr 8;1070(1–2):147–54. Available from: [<URL>](#).
46. Santos JMRCA, Guthrie JT. Analysis of interactions in multicomponent polymeric systems: The key-role of inverse gas chromatography. *Mater Sci Eng R Reports* [Internet]. 2005 Oct 31;50(3):79–107. Available from: [<URL>](#).
47. Santos JMRCA, Fagelman K, Guthrie J. Characterisation of the surface Lewis acid–base properties of poly(butylene terephthalate) by inverse gas chromatography. *J Chromatogr A* [Internet]. 2002 Sep 6;969(1–2):111–8. Available from: [<URL>](#).
48. Gutmann V. The donor-acceptor approach to molecular interactions [Internet]. Springer New York, NY; 1978. 279 p. Available from: [<URL>](#).
49. Bauer F, Meyer R, Czihal S, Bertmer M, Decker U, Naumov S, et al. Functionalization of porous siliceous materials, Part 2: Surface characterization by inverse gas chromatography. *J Chromatogr A* [Internet]. 2019 Oct 11;1603:297–310. Available from: [<URL>](#).





## The Role of Molecularly Imprinted Polymers in Sensor Technology: Electrochemical, Optical and Piezoelectric Sensor Applications

Hilmiye Deniz Ertuğrul Uygun<sup>1\*</sup> , M. Nalan Demir<sup>2</sup> 

<sup>1</sup> Center for Fabrication and Application of Electronic Materials, Dokuz Eylül University, Buca İzmir, Turkey.

<sup>2</sup> Department of Chemistry, Faculty of Science, Dokuz Eylül University, Buca İzmir, Turkey.

**Abstract:** With the help of molecular imprinting technology, artificial receptors can be made and used for identification. This technique's limitless application increases polymer technology and makes it adaptable to other technologies. In this study, examples of sensor applications are used to explain molecular imprinting technology (MIT) and its brief history. MIT can be used to create polymer-based artificial receptors with remarkable selectivity and affinity to detect any target molecules that can be imprinted on a polymer. A monomer is synthesized around a template molecule to create a selective cavity that serves as an artificial receptor. Molecularly imprinted polymers (MIP) offer a wide range of uses and have recently garnered much attention. These polymers' production methods, production kinds, and molecular imprinting techniques are all thoroughly detailed. The outstanding properties of MIPs make a crucial contribution to sensor applications offering selective, fast, easy, and cost-effective analysis, which became very popular after Clark published his first biosensor study. Apart from the biological recognition receptors, MIPs have the advantage that they are not affected by physical conditions of the environment, such as temperature, pH, and ion strength. To overcome the biological recognition receptors' disadvantages, molecularly imprinted polymers can be used for sensor development. From the point of view of the review, the combination of MIPs and sensors was explained and proposed as an informative paper.

**Keywords:** Sensor, molecular imprinting, molecularly imprinted sensors, polymerization, electropolymerization.

**Submitted:** April 19, 2023. **Accepted:** August 30, 2023.

**Cite this:** Ertuğrul Uygun HD, Demir MN. The Role of Molecularly Imprinted Polymers in Sensor Technology: Electrochemical, Optical and Piezoelectric Sensor Applications. JOTCSA. 2023;10(4):1081-98.

**DOI:** <https://doi.org/10.18596/jotcsa.1285655>

**\*Corresponding author's E-mail:** [deniz.uygun@deu.edu.tr](mailto:deniz.uygun@deu.edu.tr)

### 1. INTRODUCTION

Recently, it has been exciting to follow the development of biosensor technology, especially with its applications in the health field, which has high miniaturization and almost unlimited application potential. The growth rate of these small systems, which are formed by combining a biological molecule with a non-biological element, increases almost exponentially. They are interesting because they can develop quickly, their research and development costs are low, and the innovative aspects of the developed technologies are high. On the other hand, one of the most significant advantages of biosensor technology is that it includes interdisciplinary fields.

It can consist of organic chemistry, biochemistry, electrochemistry, nanotechnology, electronics, material chemistry, and many other areas. Like

every field, biosensor technology's advantages and disadvantages cause new developments, especially in this field.

The biosensor concept first met the literature with the system used by Clark to measure the amount of oxygen in the blood (1). That design turned into a product and has recently been used as a commercial glucose monitoring device known in the scientific community as glucose biosensors (2–5). From the oxygen-measuring biosensor technology, miniaturized analyzer systems have been produced and developed in different fields with each developed biorecognition agent. Although it is not a specific area, there have been developments in many areas, from health to food, from environmental factors to hazardous chemicals (6). The most critical point in the biosensor system is that it can analyze the target analyte in a specific, selective, and sensitive manner,

as in every analyzer. The biorecognition receptor element in the biosensor technology, which contains these most important features, provides specificity, sensitivity, and selectivity for target molecule detection. Since it is known that biosensors consist of a transmitter and a biorecognition receptor, they are systems that generally work by monitoring the signal created by the interaction of the analyte molecule with the biorecognition receptor immobilized on the transducer. This interaction can be monitored by electrochemical, optical, or mass transfer (piezoelectric) based transducers with different interactions (7). All these methods divide into subgroups and transducers used by the biochemical reaction, targeting the interaction of the target molecule and the biorecognition receptor. The most used electrochemical sensors can be subdivided into different classes as amperometric (current-based), potentiometric (voltage-based), impedimetric (resistance-based), and capacitance (double layer charges based) measurement due to the interactions between the selective layer and the target molecule on the transducer (electrode) surface (8).

On the other hand, optical sensors are based on the measurement of absorbance, fluorescence, chemiluminescence, or surface plasmon resonance. In optical systems, measurement is carried out with an optical transducer; on the contrary, the detection is different in surface plasmon resonance (SPR) systems. Here, the reflection of a laser transmitted on a chip is changed over time by the biorecognition receptor and analyte interacting on the other side of that chip. SPR systems are based on the fact that the interaction of the receptor with the analyte changes the dielectric constant of the chip. Piezoelectric systems, which are mass-based measurement systems, are based on the principle of changing the resonance in piezoelectric crystals with the interaction of the receptor and the analyte. Based on all systems, the analog signal is released by the reaction of the biorecognition receptor with the analyte detection by the transducer and converted into a digital signal (9). The combustion agent that creates the analog signal can be different biomolecules. As described in the previous sections, these biomolecules can interact with the catalytic or affinity-based analyte molecule. Catalytic biomolecules can be enzymes, whereas affinity-based ones can be molecules that do not react with the analyte, such as antibodies, DNA, and cell surface receptors that can interact with each other in a specific way (10).

Although biological receptors (enzyme, DNA, antibody) used in biosensor systems offer high sensitivity measurement due to their high cost, special storage conditions, and optimum operating conditions (such as pH and temperature), their use is limited (11). Due to this restriction, new physical-based recognition receptors are being developed. This technology, which is seen as a technology to create similar biorecognition receptors, is called molecular imprinting technology (MIT). Simply called, it is the name given to the polymerization of a monomer in a certain way. Molecularly imprinted

polymers (MIPs) have been seen as a solution to the usage limitations of biorecognition systems since they do not require special physical conditions such as temperature, pH, or ionic strength optimization required by the receptors used in biosensors. A broad spectrum of solutions is offered in this technology, which has not only sensor technology but also different application areas. Molecularly imprinted polymers have applications in different areas, such as solid phase extraction (11), affinity chromatography (12), controlled drug release (13), catalysis (14), and chemical/biochemical sensors (15). Although they are primarily used in affinity-based separation applications, their use in sensor systems has increased recently (16).

## 2. MOLECULAR IMPRINTING TECHNOLOGY

Molecular imprinting technology (MIT) can be explained in the most general sensor technology as the technique of creating artificial receptors containing specific cavities around the target molecule to be analyzed, and polymeric structures created with this technology can find applications in a wide range of industries, from food to health (17). In other words, when these polymers, developed as synthetic, smart receptor technology, are used in biosensors, they are called sensors because synthetic receptors are used instead of biorecognition receptors. Because the recognition receptor of biological origin leaves the system. In this way, a more resistive element of the system makes it extremely easy to use, although it has disadvantages in some usages. Molecular imprinting technology allows the production of synthetic polymers that mimic the antigen-antibody relationship in nature. These polymers enable new measurement systems with the sensitivity and selectivity of biological sensors but are unaffected by the harsh conditions in which they are affected (18). Molecularly imprinted polymers have been prepared by the copolymerization of the desired molecule (target), one or more monomers containing appropriate functional groups, and crosslinking chemicals in a suitable solvent environment (Figure 1). After removing the target molecule from the synthesized polymer, gaps are formed similar to the target molecule in shape, size, and chemical composition. By reattaching the target molecule to these gaps, systems allowing selective, sensitive, and rapid determination of the target molecule can be prepared (19). M. V. Polyakov is credited with creating the first instance of the idea of molecular imprinting in 1931 for his work on polymerization with sodium silicate and ammonium carbonate utilizing a novel synthesis method (20). However, the concept of the imprinted polymer was first used by K. Mosbach and B. Sellergren (21) in a study published in 1984 - the first study using the imprinted polymer definition, written by G. Wulff (22), was published in 1985, although Wulff had been publishing a series of articles since 1973, entitled "Polymers of Enzyme-Analog Structure" (16). Both of these researchers are working on molecular imprinting technology, but they have focused on different methods in polymer synthesis: Wulf has used covalent bond-based synthesis methods, while Mosbach has prepared polymers with

non-covalent interactions-based methods. The significant difference between the two methods is the desorption process, defined as releasing the analyte from the polymer. Although covalent imprinting offers a very stable and homogeneous binding environment, the non-covalent method is considered more valuable because of the difficulties in the desorption process of covalent imprinting (23).

Non-covalent procedures are considered to be more technically convenient when compared to covalent ones. In this context, separating the imprinted molecule is comparatively more straightforward compared to the covalent bond. A notable benefit of the proposed methodology is the substantially reduced detrimental impact on the polymer during the non-covalent separation process. Consequently, this contributes to an extended lifespan of the molecularly imprinted polymer (MIP). Furthermore, the enhancement of repeatability is a highly desirable characteristic often sought in sensor technology. The interaction between the analyte and polymer is contingent upon the characteristics of the cavity. However, it is also desirable for the overall structure of the polymer to remain unchanged. The ability to customize the design of this cavity further enhances its selectivity. Although a cavity in the form of a target molecule is produced, the properties of the chemical parts in this cavity are also found in the non-imprinted parts of the polymer. This usually causes non-specific binding. This is a handicap in large molecules. This handicap causes a false-positive signal, especially in susceptible systems such as EIS, SPR, or QCM. Different imprinting techniques have been used to overcome this situation. The most popular type of molecular imprinting, epitope imprinting, improves selectivity in molecularly imprinted polymers. Therefore, MIPs offer a wide area of use, especially in sensor

technology, with features like high selectivity, durability, long-term stability, and easy preparation. Epitope imprinting provides the opportunity to replace the antibodies used in biosensors and is called artificial biomimetic antibodies (7).

Molecular recognition reactions are one of the most essential elements of biological mechanisms. Molecularly imprinted polymers are designed to mimic molecular recognition elements in nature. Molecular recognition often includes non-covalent interactions such as van der Waals forces, ionic interactions, dipole-dipole interactions, pi bonds, and hydrogen bonds. Molecular recognition is based on the key-lock relationship between the enzyme and substrate. Molecularly imprinted polymers are also specific to the template molecule on which they are based, just as a key is specific to a lock. The molecular imprinting technique is used to produce polymer materials that mimic the structure and properties of a particular target molecule. This target molecule is used as a template during the imprinting process. Just as a key fits into a particular lock, molecularly imprinted polymers are designed to have the ability to recognize a particular target molecule. The template molecule forms the basis of this recognition feature and creates a specific shape and structure within the polymer material. This shape and structure provide similarity between the template molecule and the target molecule so that the polymer material can selectively capture the target molecule. A different template molecule must be designed for each target molecule because each has its unique structure and properties. Thanks to this design, the polymer material can recognize and select the target molecule; similarly, a key fits only in a suitable lock (24). Figure 1 shows a schematic summary of recognition by molecularly imprinted polymers.

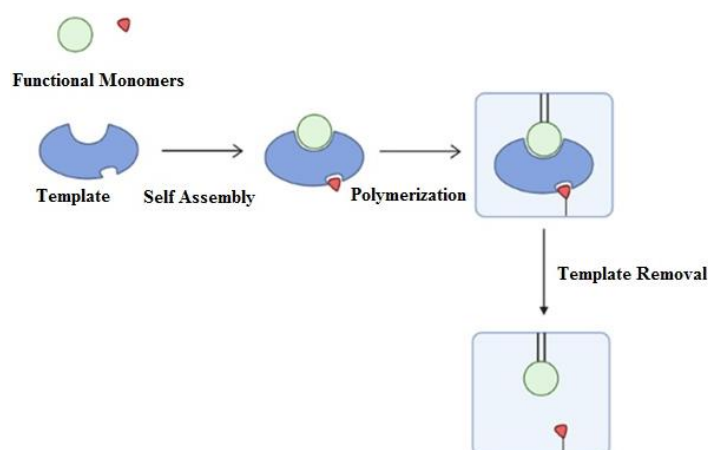


**Figure 1:** The principle of molecular imprinting recognition.

### 2.1. MIP Synthesizing Methods

In polymers produced with molecular imprinting technology, the first thing to consider is the physical structure of the target molecule. Since this structure will be directly related to the functional groups on the monomer, the biggest handicap lies here. When an analyte-containing multi-functional group, e.g., protein, is selected, one monomer may not be sufficient. The presence of a homopolymer can

reduce selectivity. Therefore, it is crucial to turn to copolymers. Problems with the polymer synthesis process arise as the amount of monomers rises. For this reason, when we look at the sensors developed with molecular printing technology, it can be seen that sensor systems targeting simple molecules have been produced in general.

Universal polymer production reactions are used in the production technique, which is generally a

biomimetic technique. In these systems, if the target is a molecule that can be denatured, some polymerization techniques may experience problems. Because if the polymerization liquid is organic, a biological molecule will be denatured, and the resulting cavity will be shaped to recognize the denatured structure. Considering these, the target analyte should be measured before denaturation.

As we mentioned before, a wide variety of production methods are available for MIP synthesis. The only difference is that the imprinted molecule is added to the mixture. The polymer composition ratio is another critical point except for the target molecule structure (25). After selecting the target to be imprinted, the next step is to select the monomer. This is crucial for the sensor system's functionality since the monomer will grow together with the target molecule's binding. It should also avoid binding unspecific targets.

The target molecule's physical size and the presence of different reactive side groups suggest that selectivity will be a significant challenge. The cross-reactivity in question here may occur with molecules with similar properties. One of the ways to overcome this is to produce multiple but weak interactions. Another critical point is the concentration of the cross-linker. In this case, it is necessary to decrease the concentration of the cross-linker with the increase in the size of the molecule, that is, the target molecule. As a result, the properties of the template molecule and the required monomer have an important place in determining the composition of the polymer.

In MIP synthesis, more than one monomer can be used to increase the selectivity for the target molecule. The monomer-target ratio, on the other hand, is based on preparing a functional monomer group for each chemical bond due to the nature of the polymerization. Experimental conditions optimize this ratio, and it is imperative to prevent non-specific binding. The effect on the monomer/target ratio can also be in the form of copolymerization. The creation of steric effects has an essential place in molecular imprinting technology.

By copolymerizing functional monomers and the required target molecule with cross-linker molecules present, MIPs can be created. The bonding herein may be by covalent or non-covalent interactions, depending on the method chosen (26). The functional monomers selected for polymer synthesis are responsible for providing the functional groups required for non-covalent bonding or the reactive substituents required for covalent bonding. Examples of highly preferred monomers are acrylamide, methacrylic acid, pyrrole, and aniline. In addition, conductive functional monomers such as pyrrole, o-phenylenediamine, thiophene, aniline, dopamine, o-aminophenol, and p-amino thiophenol are preferred for the polymerization process by electropolymerization. Acidic and basic monomers with the capacity to make covalent bonds, hydrogen bonds, and other interactions can be used. Polymerization is carried out by adding functional monomer and

template molecule to the polymerization medium, as well as cross-linkers such as ethylene glycol dimethacrylate (EGDMA) and tetraethyl orthosilicate (TEOS) (18,27). Most often employed techniques include precipitation polymerization, electropolymerization, and photopolymerization. In some polymerization methods, a chemical may be required to initiate the reaction; hence, Azobisisobutyronitrile (AIBN) and N,N,N',N'-tetramethylethane-1,2-diamine (TEMED) are the most commonly used initiators.

The new technology MIP's is not just a mixture of polymer and template. The use of nanomaterials as polymer composites in sensor technology has increased in recent years due to their properties, such as increasing the surface area and having high conductivity (28). With these advantages that nanomaterials add to sensor technology, sensor technology has advanced. They are very useful in reducing the potential required for electropolymerization, especially in studies where electrical conductivity is effective on polymerization. High surface area increases the quality of the polymer formed. Nanomaterial-modified polymers, which are generally very useful in terms of forming a thin layer to reduce limitations, also eliminate many disadvantages in sensor technology.

MIPs have several disadvantages, such as containing target molecule residues, limited selectivity, and limited mass-carrying ability. Various methods have been used to overcome these disadvantages: the thin film polymerization method has been used on the electrode surface to increase mass transport, and nanomaterials have been used to increase the surface stabilization and sensitivity of the method by increasing the surface area. In addition, nanomaterials such as carbon nanotubes, graphene, and fullerene help to increase reusability and surface conductivity (29). Additionally, through the reaction between both the polymer and the template molecule, imprinting, polymerization, and manufacturing can all be accomplished using imprinting procedures. This interaction can be covalent, non-covalent or semi-covalent (30). A covalent link is created between the functional monomer and the template in the covalent imprinting technique. With this bond, the template molecule is chemically modified to form this bond before monomer-pattern formation. The covalent bond on the polymer produced as a result of this modification is broken, and the template is eliminated. This removal causes covalent bonds to rebuild, contributing to backlinking's selectivity. This method is called the pre-organized approach.

The non-covalent method is based on the self-assembly principle. There will be non-covalent interactions active here. These are hydrogen bonds between donor and acceptor, electrostatic/hydrophobic interactions, and Van der Waals forces. Imprinting is performed with these interactions. An important point in this technique is that the interaction between the functional monomer and the template that will interact should be strong. Another method is the semi-covalent interaction. In this



instance, the functional monomer is covalently linked to the target, the template. After polymerization, the covalent bond does not re-form, unlike the covalent approach, but the interaction occurs with non-covalent bonds.

Among these imprinting methods, the covalent method is believed to be more effective and provides more homogeneous imprinting. Its stability is also higher than non-covalent methods. The most significant handicap is the step of designing the binding sites of the covalently imprinted molecule. In addition, extreme care must be taken to avoid breaking the covalent bond and damaging the polymer. In contrast, non-covalent imprinting is simpler than covalent imprinting. It is one step because there is a direct polymerization between the template and the monomer molecule. Heterogeneity is higher in contrast to covalent modification.

MIP-based sensor systems must have an appropriate interaction between the recognition element and the transducing surface. The process considered while producing the polymer is how the template molecule to be measured is desired to be stamped. If polymerization on the transducer surface is not suitable, external polymerization is more suitable if electrical polymerization is possible on the electrode surface. In this case, it should be taken into account that the template molecule is imprinted on the transducer surface without losing its solubility and natural structure. The success of the polymerization must be determined by proving that there is no loss of activity with a validated method.

There are two approaches to the preparation of these systems. First, in situ polymerization prepares the recognition element on the conductive surface. Conversely, the prepared MIP is coated on the conductive surface (ex-situ) with a suitable method.

#### 2.1.1. Ex-Situ Polymerization

Ex-situ synthesis methods for MIPs refer to methods in which the polymer material is produced ex-situ under laboratory conditions to develop proper recognition properties on the target molecule. Ex-situ polymerization means polymer synthesized externally, in other words, not on the transducer surface. The polymerization reaction requires a monomer and a chemical initiator that can be a chemical substance. In this way, it can be synthesized in large quantities, stored, and used consistently. It is not necessary to produce in every usage. In this type of polymerization, the polymers to be synthesized are prepared directly in a container without being treated with the support material. They are advantageous because they can be prepared at high temperatures as desired. High temperatures are not feasible for protein or biological element imprinting because denaturation can be problematic.

Additionally, from the perspective of sensor technology, polymer sizes and shapes can be changed in a controlled manner. The most significant handicap here is placing these polymers on the transducer surface, which is the support material. While it is easy to place on large surfaces such as

SPR chips, on the other hand, it is quite challenging to fix polymers on the surfaces of microelectrodes. Even if successful, the homogeneous distribution of polymers may affect sensor applications, but when it is achieved, extremely durable and reproducible signals can be obtained. The most significant advantage of polymerization is that the monomer and initiator molecules can be prepared in high volume, and the template molecule can show good distribution. The polymerization components that are well dispersed in the solution successfully produce a homogeneous polymer (31).

Bulk polymerization (32), suspension polymerization (33), emulsion polymerization (34), and surface imprinted molecular imprinting (35) can be given as an example of ex-situ polymerization types. In bulk polymerization, monomers and basic template molecules are combined in a solution or mixture. Then, polymerization is carried out using polymerization initiators. As a result of this process, polymer material is obtained. The polymer material contains cavities with recognition properties around the target molecule in this method. Suspension polymerization is a polymer production method in which insoluble monomers are dispersed in solid particles, and polymer particles are obtained as a result of polymerization of these monomers. In this method, since the solubility of the monomers is low, the monomers are dispersed in suspension in the solid carrier. Emulsion polymerization is frequently used to produce latex paint and latex rubber products. Since the polymer particles produced by this method are dispersed in the liquid in the form of small droplets, the properties and usage areas of the final product can be controlled to a great extent. However, the complexity of the method and the need for careful control of the process parameters can present some challenges that need to be optimized. The surface-printed molecular imprinting method uses a substrate with the target molecule on the surface. Polymerization is carried out around the target molecules on the surface. This method develops specific recognition properties for target molecules on the surface.

Examples of free radical initiators used in polymerization are peroxides, azo compounds (Azobisisobutyronitrile (AIBN)), and persulfates (Sodium, ammonium, or potassium persulfate) (36).

#### 2.1.2. In-situ Polymerization

Another molecularly imprinted polymer preparation process is in-situ polymerization. In this approach, the transducer serves as the surface on which the polymer imprinting process is conducted (37). Same as in ex-situ polymerization, a monomer, template molecule, and an initiator are needed on this support material. The initiator can also be a chemical component or a direct electric current. Because functional semiconductors that can be polymerized electrically can be used today. With these methods, polymerization, that imprinting, can be facilitated. The handicap of the method is that it has to be regenerated each time. This reduces repeatability. However, the consumption of the substance reduces the suppression of the proteins obtained in small

amounts. Another advantage is that if the amount of target molecule is low, the polymer can be produced on this structure by covalent or non-covalent immobilization of the molecule directly onto the transducer surface. This facilitates the imprinting of particularly large proteins or cells. In this way, a large amount of material can be imprinted with a small amount of monomer.

Moreover, *in situ* polymerization is synthesized on the support material by direct polymerization on the transducer. In this way, sensor production can be carried out directly. The most commonly used technique in polymerization is electropolymerization. Here, the electric current, the electron, is used as an initiator. In this way, rapid polymerization can be achieved.

In addition to electrochemical polymerization, it is crucial to exercise caution when conducting polymerization on undesired regions, particularly the transducer. Failure to do so may result in the generation of false positive signals due to polymerization occurring outside the working electrode. The sensor is ready for usage after direct polymerization on the transducer. There is no retention problem of polymers produced on the transducer. Reproducible production and measurements are therefore possible. *In situ* polymerization is more effective, especially when the template molecule needs to be imprinted at a low concentration (biomolecule). Although there is no loss of template molecules, high-efficiency suppression is achieved. Efficiency increases with a low amount of monomers and templates (38). In both methods, the imprinting method and the transducer are selected based on the properties of the template molecule.

Each of the molecularly imprinted polymer synthesis methods has several advantages and disadvantages. Their superiority depends entirely on where and for what purpose this polymer will be used. The researcher needs to consider the needs and priorities of the use area when choosing between these methods. When deciding which method is most suitable, factors such as the properties of the target molecule, the properties of the polymer material to be used, the complexity of the manufacturing process, and cost should be considered.

### 3. MIP SENSORS AND APPLICATIONS

Surface characterization is important after the production of molecularly imprinted polymers. This

characterization is carried out primarily with sensor technology, a measurement technique. Secondly, the bonds and interactions between the target analyte and the polymer should be determined by different methods and the adhesion of the polymer to the transducer surface. Bond structures are usually determined by Fourier Transform Infrared Spectroscopy (FTIR). The polymer's bonds with the target molecule should be shown here. The target polymer can then be imaged on the transducer surface after that. The morphological structure can be visualized by examining the transducer surface with an electron or atomic force microscope.

By determining this, optimization processes can be started. In the sensor optimization processes, the polymer binding capacity is determined first. This process is considered by calculating the polymer surface and the concentration of the target molecule. Sensitivity, selectivity, and storage stability tests can be performed, and sensor applications can be started.

Various physicochemical techniques can be applied according to the transducer type to analyze molecules in sensor systems using MIP instead of biological molecules as biorecognition receptors. Optimization of physicochemical techniques is crucial to preserve the durability of polymers. For example, when electropolymerization is performed, applying excessive current may cause excessive polymer oxidation, creating undesirable structures and rendering the imprinting process useless.

The stability of the imprinted polymers with the sensitivity of the sensors and their usability under all conditions increase the commercialization potential of these systems. Therefore, the interest in these systems is increasing day by day. In Figure 2, the Scopus data obtained by scanning "molecular imprinting" and sensor illustrate this increasing interest. MIP-based sensors can be used in many areas, such as the environment, food, and biomedicine, by differentiating the targeted analyte (39). The template molecule can be a small ion-molecule or a macromolecule, such as enzymes and proteins (40). In Figure 3, the working principle of a MIP-based sensor is schematized. With the change of the analyte, the analytical signal and, therefore, the measurement method can also vary widely. These methods can be examined under 3 headings: electrochemical, optical, and piezoelectric methods (41).

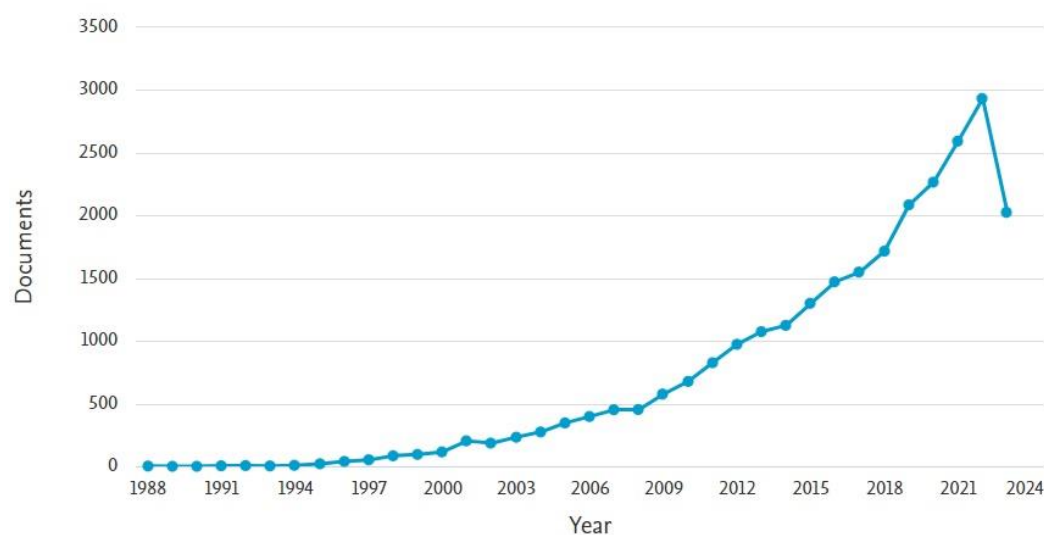


**Figure 2:** The Scopus data showing articles published from 1988-2023 on MIP-based sensors.

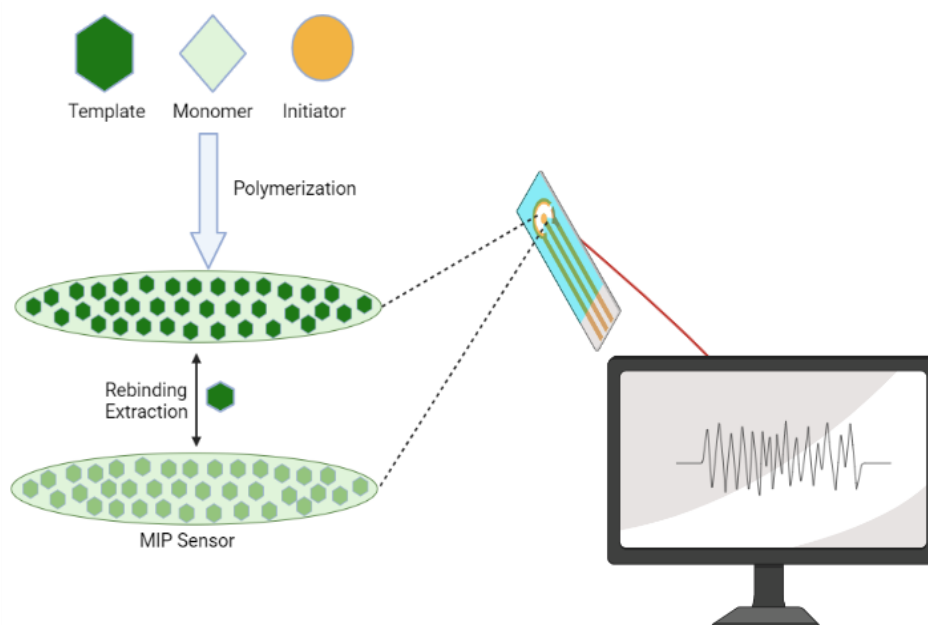


**Figure 3:** The modification principle of a MIP based sensor.

As we have mentioned before, molecular imprinting technology is carried out using existing polymerization techniques. The most well-known of these techniques is the Bulk imprinting method. Here, the target molecule is directly imprinted into the entire polymer matrix without needing a specific region. The polymer is then mechanically broken down, removing the mold (42). It is preferred for small molecules that are small and will not degrade from mechanical degradation. Apart from imprinting on the entire polymer, only surface imprinting can be performed. Here, the target creates high affinity. Target molecule-polymer interaction is easier because the cavities are not embedded (43). Therefore, it is the ideal method for imprinting large molecules such as proteins. Although this method has the disadvantage of sensitivity to bulk polymerization in itself, it is widely used with different method designs. Among the surface imprinting methods, the soft lithography method, in

other words, stamping, can be used on sensor surfaces (44,45). The polymer can be produced by forming a mold with UV curing. Assistance is provided with support solver support. Performing two-dimensional imprinting instead of 3D imprinting allows the development of micro or nano-size polymers (46). Another surface imprinting method is the template immobilization method (47). Here, self-assembling polymerization is performed on the target molecule.

In this way, immobilization of large biomolecules over multiple groups is possible. Another method is emulsion polymerization.

Covalent bonds are used in this instance to imprint the surface. Selective microspheres with a large surface area can be created during the manufacture of spherical polymers by polymerization on a substance in the center (48). Instead of imprinting

the entire molecule in polymerization techniques, the epitope imprinting method is carried out over a portion from which a domain is specifically selected (49). The epitope imprinting method allows for using a tiny fragment or portion of a macromolecule to produce stronger and more precise connections. As a result, affinity can be raised while non-specific binding is reduced. When the sequence is revealed, the imprinted polymer can recognize both the template and the protein. In this way, imprinting can be done with different methods, especially considering the target molecule. It can form a film of the desired thickness in a simple, fast, and low-cost way to prepare MIP by electropolymerization (50).

### 3.1. Electrochemical MIP Sensors

The engagement of analytes with receptors on an electrode surface can be converted into an analytical signal by electrochemical sensors, detectors with electrochemical transducers. The working electrode, the reference electrode, and the counter electrode are all present in these systems. Gold electrodes and glassy carbon electrodes are preferred as working electrodes. In addition, disposable screen-printed electrodes are also widely used in MIP sensors. Differential pulse voltammetry (DPV), Cyclic voltammetry (CV), amperometry, and electrochemical impedance spectroscopy (EIS) are the most widely used electrochemical measurement methods. These methods are preferred because of their low cost and easy preparation (51). Electrochemical-based MIP sensors are used in areas such as environmental analysis and food and medical applications. The most important point of the electrochemical-based sensor technology is that it can detect molecules in any kind of sample structure. Table 1 provides examples of several MIP-based electrochemical sensors.

In their study, Sundhoro et al. devised a sensor to facilitate the monitoring of allergens present in soy-based food products. The MIP-modified sensor has the capability to detect food allergens at a concentration of 100 parts per billion (ppb). The

basis of the method is electrochemical surface investigation techniques such as CV and EIS. The method was also compared with food allergen lateral flow tests. In this study, genistein-specific cavities were formed by electropolymerization of *o*-phenylenediamine dihydrochloride at 1.2 V in one minute. Imprinted occurred via N-H bonds. However, this study is an analyte-centered redox method, therefore, quercetin and 7-hydroxy flavone redox potentials were used to detect food allergens on the screen-printed electrode in the presence of the genistein. The method was based on the non-covalent technique and performed successfully (52). Aghoutane et al. prepared a sensor based on electrochemical impedance spectroscopy for the determination of malathion (MAL), an organophosphate pesticide in olive oil and olives. The imprinting was carried out via the N group of the MAL, and the MIP formation was carried out by using TEMED, acrylamide, and ammonium persulfate as initiators including MAL detection was carried out electrochemically by CV, EIS, and DPV methods were also used for the electrochemical characterization of the surface. The detection limit was calculated as 0.06 pg/mL, and the calibration curve was between 0.1 to 1000 pg/mL (53). Ayankojo et al. prepared a MIP-based sensor for monitoring the antibiotic erythromycin in water. The erythromycin selective MIP surface was prepared by polymerizing *m*-phenylenediamine (mPD) on the electrode surface and analyzed by cyclic voltammetry. The limit of detection (LOD) was calculated as 0.1 M (54). Mazouz et al. developed a sensor for prostate-specific antigen (PSA) detection by electropolymerization of pyrrole. The basis of the imprinting is NH groups hydrogen bond formation to LOD protein amino acid residues. The MIP formation was observed by chronoamperometric technique and square wave voltammetry for PSA analysis in the study. It is calculated by Hill equation  $K_d = (1.02 \pm 0.54) \times 10^{-14}$  M. The method's applicability was examined by contrasting it with ELISA utilizing actual serum samples (55).

**Table 1:** Electrochemical sensors with performance parameters.

Method	Monomer	Target Molecule	L.O.D.	Ref.
DPV	mPD	ncovNP	27 fM	(56)
SWV	Acrylic acid	Tetracycline	$1.5 \times 10^{-7}$ mol/L	(57)
DPV	Pyrrole	5-HIAA	$15 \times 10^{-12}$ M	(58)
EIS	APBA-Pyrrole	Glucose	6.064 mg/dL	(59)
CV, EIS	<i>o</i> -PD	Trypsin	70.9-ng/mL	(60)
Amperometry	MAA	Tetracycline	0.026 mg/L	(61)
SWV	MAA-DVB	2-furaldehyde	$4.67 \times 10^{-5}$ M	(62)
EIS	Acrylamide	Cortisol	0.14 nM	(38)
EIS	<i>o</i> PD	SARS-CoV-2-RBD	0.7 pg mL	(63)
SWV	Pyrrole	PSA	n.d	(55)
SWV	MAA	Melamine	$1.75 \times 10^{12}$ mol/L	(64)
DPV	MAA	Milk amyloid A	5 pg/mL	(65)
DPV	Pyrrole	Troponin T	0.006 ng/mL	(66)
EIS	PVC COOH	Myoglobin	2.25 µg/mL	(67)
DPV	<i>o</i> PD	TGF-β1	0.09 ng/mL	(68)
DPV and EIS	Acrylamide	Tofacitinib citrate	$3.48 \times 10^{-13}$ M	(69)
DPV	<i>o</i> -PD	Amyloid-β(1-42)	0.018 ng/mL	(70)
DPV	Itaconic acid	Metribuzin	0.1 pg/mL	(71)
Potentiometric	Polyaniline	Ketamine	$1.0 \times 10^{-6}$ M	(72)

### 3.2. Optical MIP Sensors

From the perspective of matter-light interactions, optically active molecularly imprinted polymers are used to develop optical sensor technologies. Surface plasmon resonance is the most widely used technique among optical systems (73). This technique works by changing the laser's reflection angle projected onto a gold chip. This reflection angle is realized by the modifications made on the gold chip. In addition, MIPs interferometry used in optical sensor technology can be used with Reflectometric Interference Spectroscopy (RIfS) (74) and Surface-enhanced Raman spectroscopy (SERS) (75) techniques. Most MIP-based sensors in the literature are optical methods such as surface plasmon resonance based on refractive index change (23). These sensors convert optical property changes on the electrode surface into readable signals. Optical sensor systems can be examined in two classes (76).

Affinity-based optical systems, which assess changes in optical properties like fluorescence, absorbance, and refractive index, are the first class. Surface plasmon resonance (SPR), which is dependent on the measurement of refraction of light, is the method that falls into this class and is frequently used in the literature (77,78). Second-class optical sensors are called optoelectronic sensors. The usage of monomers that can change the optical property on the surface forms the basis of these systems. These monomers are expected to have high quantum yields and molar absorption coefficients (76).

Application areas of MIP-based optical sensors can be listed as disease diagnosis, food analysis, and environmental pollution monitoring (See Table 2) (50).

A nanoparticle-based optical sensor for pharmaceutical monitoring was created by Altıntaş et al. The synthesized MIP nanoparticles, whose dimensions were determined as  $\sim 132.3 \text{ nm} \pm 3.2$ , were immobilized on the SPR gold sensor with EDC/NHS. The prepared sensor was used to monitor diclofenac in water and was verified by the LC-MS method. A study of the kinetic data revealed that a dissociation constant of  $1.48 \times 10^{-9} \text{ M}$  was attained. (79). Motaharian et al. created an optical sensor for detecting the antibiotic sulfasalazine (SSZ) (MIP-SG) by combining molecular imprinting with sol-gel methods. The UV-Vis spectroscopy technique was used to determine the binding characteristics of the sulfasalazine sensor. The 0.26 g/mL detection limit was chosen because of its high reproducibility (RSD = 4.1%) (80). An optical sensor device based on fluorescence was created by Chen et al. to measure anthracene. Bisphenol A and *p,p'*-diisocyanatodiphenylmethane were chosen as monomers, and trihydroxybenzene, *p,o,p'*-trisisocyanatodiphenylmethane as cross-linkers for MIP synthesis (81). Sanguanprang et al. prepared an Opto sensor to determine thiamphenicol using a mesoporous and quantum dot hybrid fluorescence sensing probe with molecularly imprinted polymer technology. Meso-

porous carbon and CdTe\*CdS\*ZnS quantum dots were trapped inside the molecularly imprinted polymer to create the hybrid probe. The prepared probe was characterized by SEM, TEM, and particle size analyses, and all the conditions for determining thiamphenicol were optimized. The thiamphenicol analysis is determined based on the fluorescence quenching of the hybrid nanostructure by thiamphenicol. The linear detection range of the system is between 0.10 and 100  $\mu\text{g/L}$  with a coefficient of determination ( $R^2$ ) of 0.9979, and the detection limit is 0.04  $\mu\text{g/L}$ . The developed optosensor's accuracy was assessed by assessing the spiked milk samples, and the results were compared to those obtained using high-performance liquid chromatography (HPLC) analysis. The recoveries were determined in the range of 93.5% to 100.1% with high sensitivity (R.S.D. < 5%) (82). Chullasat and colleagues created a sensor system for the selective and sensitive monitoring of amoxicillin using molecularly imprinted polymers (MIP-QDs) coated on CdTe quantum dots as photoluminescence probes. MIP-QDs were prepared by the sol-gel method using 3-aminopropylethoxysilane as the functional monomer, tetraethoxysilane as the cross-linker, and amoxicillin as a template molecule. Following the desorption of the target chemical from the polymer using ethanol as the desorption agent, amoxicillin-specific cavities in MIP-QDs were produced. The functional groups of amoxicillin and the amino group of the 3-aminopropylethoxysilane chosen as a functional monomer formed a hydrogen bond, and the cavity's size and shape helped to give good selectivity. Amoxicillin more effectively quenched the photoluminescence of MIP-QDs than NIP-QDs, the unimprinted polymer made without the template molecule. Under ideal circumstances, it was discovered that the system's linear detection range and detection limit were 0.20-50.0 g/L and 0.14 g/L, respectively. With a relative standard deviation of less than 6%, it can be said that the system has strong repeatability and reproducibility. The developed method determined amoxicillin in egg, milk, and honey samples, and a recovery of 85-102% was obtained (83). Yu et al. prepared molecularly imprinted phase change microcapsules embedded in carbon quantum dots (CQDs) and developed an innovative fluorescence detection system (MIP@CQDPCM) to determine tetracycline under high-temperature conditions. The system was made ready by microencapsulation of n-eicosan as a phase change material in a SiO shell embedded in CQDs. A molecularly imprinted polymer with cavities specific to this molecule was obtained by removing tetracycline from this polymeric structure. This prepared structure was characterized by SEM, TEM, and fluorescence microscope imaging analysis. Observing fluorescence quenching by binding the tetracycline molecule to the MIP structure, it was seen that the system worked successfully. A sample application of the MIP@CQD-PCM structure was done with local water samples, and the results showed high selectivity and good reusability (84).

**Table 2:** Optical sensors with performance parameters.

Method	Monomer	Target Molecule	L.O.D.	Ref.
SPR	Methacrylic acid	Ciprofloxacin	9.71 nM	(85)
SPR	Multi monomer	Secreted bacterial factor	0.23 nM	(86)
SPR	2-methacryloyloxy ethyl phosphorylcholine	Cortisol	4.8 pM	(87)
SPR	Graphene-Dopamine	L-Tryptophan	0.105 mM	(88)
SPR	PGA	Kanamycin	12 nM	(89)
SPR	NanoMIP	Casein	127 ng/mL	(90)
RIFS	Methacrylamide	PenG	4.32 mM	(91)
Reflectance spectra	IIP-AMPSA	Pb(II)	85 ng/L	(92)
Fluorescence	a-CQDs	Tannic acid	0.6 nmol/L	(93)
Fluorescence	PANV-GMA	Paracetamol	$1.00 \times 10^{-6}$ M	(94)
Fluorescence	AA, MBAA, AMPSA, DEAEM, and allylamine	Aflatoxin B1	20 ng/mL	(95)
SERS	4-MBA and 4-VP	Patulin	$5.37 \times 10^{-12}$ M	(96)
SPR	Methacrylic acid	Adenosine	0.018 M	(97)
SPR-LMR	NanoMIP	Transferrin (HTR)	13.6 fM	(98)
SPR	Methacryloylamidoglutamic acid (MAGA)	Zearalenone	0.33 ng/L	(99)
SPR	N-methacryloyl-L-phenylalanine	Benzo[a]Pyrene	14.97 ng/L	(100)
SPR-POF	Acrylamide	Glyphosate	0.04 $\mu$ g/L	(101)

### 3.3. Piezoelectric MIP Sensors

The piezoelectric effect can be described in its simplest form by the voltage applied to a material, creating a wave in the crystal. The potential applied to the piezoelectric material's surface creates vibrations in the substance. Crystals without a center of symmetry are piezoelectric materials, such as quartz (SiO<sub>2</sub>), aluminum phosphate (berlinite), potassium sodium tartrate tetrahydrate (Rochelle salt), and polyvinylidene fluoride (102). Piezoelectric measurements are preferred methods, especially in affinity-based biosensor applications, because they can be analyzed without any label application (such as fluorescence or chemiluminescence).

This approach is based on detecting the oscillation with the mass attached to the surface of the electrodes on the piezoelectric crystal, which is a part

of the sensor system, and the measurement of this change (78). Piezoelectric sensors have become popular in recent years with their simplicity, ease of use, low cost, and measurement speed, among other methods that do not require labels. Quartz crystal microbalance (QCM) is one of the most commonly used piezoelectric measurement methods (Table 3). Quartz microbalance is preferred for mass-sensitive measurements and chemical analysis (103). Another type of piezoelectric sensor system is the surface acoustic wave method. Acoustic wave sensors can vary in their use of different vibration levels and wave modes. In sensors of all classes, physical changes in the material in contact with the wave propagation level can be monitored in real-time. Current research using these sensors focuses on measuring samples and their molecular types and concentrations.

**Table 3:** QCM-based sensors with performance parameters.

Method	Monomer	Target Molecule	L.O.D.	Ref.
QCM	Pyrrrole	Trichloroacetic acid	1.0 $\mu$ g/L	(104)
QCM	MAA	Methimazole	0.109 mg/L	(105)
QCM	Methacryloylamido tryptophan	Bilirubin	0.45 $\mu$ g/mL	(106)
QCM	MAA	Methomyl	n.d.	(107)
QCM	MIP Monolayer	Thiacloprid	10 $\mu$ M	(108)
QCM	Methacrylic acid	Formaldehyde	500 ppb	(109)
QCM	mPD	Amoxicillin	0.2 nM	(110)
QCM	3-TAA	Melphalan	5.40 ng/mL	(111)
QCM	Methacrylic acid	L-tryptophan	0.73 ng/mL	(112)
E.QCM	<i>p</i> -Phenylene diamine	S-cathinone	0.12 ng/mL	(113)
QCM	MAGA	Chlorpyrifos	$3.0 \times 10^{-13}$ M	(114)
QCM	MAGA	Zearalenone	0.30 ng/L	(115)
QCM	Methacrylic acid	Diethylstilbestrol	2.63 ng/mL	(116)
QCM	Acrylamide	AHL	0.055 ng/mL	(117)
QCM	MAA	<i>Bactrocera dorsalis</i>	24.68 mg/m <sup>3</sup>	(118)
QCM	PVAc/BA	NH <sub>3</sub>	22.9 ppm	(119)

By monitoring physical and chemical changes, these sensors can be used in fields such as medicine, food, and environmental sciences. Two sensing principles exist in such systems: the first is when the voltage field is affected, and the other is when the piezoelectric field (potential) is affected (120). In the study of Ermolaeva et al., molecularly imprinted polymers synthesized by the precipitation method were used to prepare sensors for Ractopamine determination. Methacrylic acid was chosen as the monomer for MIP synthesis. Cyanoacrylate was used to immobilize the produced nanoparticles on the electrode surface. MIP and cyanoacrylate solution were dropped on the piezoelectric crystal, and the spin coating method was used. The study's detection limit was discovered to be 12 g/mL (121). To detect terpinyl acetate in small doses, Debabhuti et al. created a QCM gas sensor (aTA-MIP-QCM) by covering the quartz crystal with a polymer containing polymethacrylic acid (PMAA). The limit of detection was calculated as 4.46 ppm (122).

#### 4. CONCLUSION AND FUTURE REMARKS

Molecular imprinting, which is less or almost unaffected by physical conditions, creates the sensors of the future, where artificial receptors can be created. Molecular imprinting technology has been developed with artificial receptor logic in determining different analytes, and sensor applications are also pervasive. Among its advantages, reducing measurement costs is the most significant factor. While providing this, time-saving in the production phase, easy reproduction, and low cost of consumables used to play a crucial role. Thanks to the advantage of overcoming the problem of denaturation, which is the most significant handicap of biosensor technology, it can be easily predicted that sensor technologies that can increase shelf life will be available soon. The fact that the optimum working conditions, essential for biological receptors, are not sought for performance shows the system's usefulness. Although the selectivity as the selectivity of a biological molecule has not been achieved, the sensor as a promising technology attracts the attention of scientists.

Another advantage is the regeneration potential of molecularly imprinted polymers unaffected by physical conditions. This stage reduces the measurement costs.

For example, biomolecules such as cell surface receptors are extremely sensitive to external factors used in biosensor systems and have a low regeneration potential. The reason for this is the tendency of the method applied for regeneration to disrupt the structure of this biomolecule due to its high affinity for the target molecule. At this stage, MIPs stand out, especially with their regeneration potential. The inability to regenerate some biorecognition receptors also makes using MIPs interesting. In addition, it can be said as another advantage that optimum conditions are required for the biorecognition receptor to act, but these are eliminated in the use of MIP. Developments in this technology will

enable the development of technologies such as enzymes that can dynamically change according to the target molecule or technologies where more than one monomer can be produced in a controlled manner. The engineering of more than one monomer remains the biggest challenge. This is an obstacle to overcome in imprinting high-structure target molecules. When this obstacle is removed, it is inevitable to develop more futuristic technologies.

The introduction of monomers, copolymers, and additional monomers leads to the formation of cavities, subsequently enhancing the structure's selectivity. This augmentation will be feasible through the utilization of cross-linkers or materials that possess the capability to generate diverse composites. The utilization of nanoparticles in polymer technology has the potential to enhance sensitivity and selectivity due to their increased surface area. This phenomenon expands the boundaries of its programmable capacity, enhancing molecular imprinting technology's utility. The fast evolution observed in the characteristics of molecularly imprinted sensors holds great potential. Given the tremendous pace of advancement in this field, one may hypothesize that integrating artificial enzymes onto the surface of sensors may be within close reach.

#### 5. CONFLICT OF INTEREST

Authors declare that they have no conflict of interest in The Role of Molecularly Imprinted Polymers In Sensor Technology: Electrochemical, Optical and Piezoelectric Sensor Applications.

#### 6. REFERENCES

1. Clark LC, Kaplan S, Matthews EC, Edwards PK, Helmsworth JA. Monitor and control of blood oxygen tension and pH during total body perfusion. *J Thorac Surg* [Internet]. 1958 Oct;36(4):488–96. Available from: [<URL>](#).
2. Clark LC, Lyons C. Electrode systems for continuous monitoring in cardiovascular surgery. *Ann N Y Acad Sci* [Internet]. 1962 Oct 15;102(1):29–45. Available from: [<URL>](#).
3. Turner A, Swain A. Commercial perspectives for diagnostics using biosensor technologies. *Am Biotechnol Lab* [Internet]. 1988;6(8):10. Available from: [<URL>](#).
4. Wang J. Glucose Biosensors: 40 Years of Advances and Challenges. *Electroanalysis* [Internet]. 2001;13(12):983–8. Available from: [<URL>](#).
5. Newman JD, Turner APF. Home blood glucose biosensors: a commercial perspective. *Biosens Bioelectron* [Internet]. 2005 Jun 15;20(12):2435–53. Available from: [<URL>](#).
6. Marli C, Gouvea CP. Biosensors for health applications. In: Serra PA, editor. *Biosensors for Health, Environment and Biosecurity* [Internet]. InTech; 2011. Available from: [<URL>](#).

7. Cieplak M, Kutner W. Artificial Biosensors: How Can Molecular Imprinting Mimic Biorecognition? *Trends Biotechnol* [Internet]. 2016 Nov 1;34(11):922–41. Available from: [<URL>](#).
8. Hasan MR, Ahommed MS, Daizy M, Bacchu MS, Ali MR, Al-Mamun MR, et al. Recent development in electrochemical biosensors for cancer biomarkers detection. *Biosens Bioelectron X* [Internet]. 2021 Sep 1;8:100075. Available from: [<URL>](#).
9. Mehrotra P. Biosensors and their applications – A review. *J Oral Biol Craniofacial Res* [Internet]. 2016 May 1;6(2):153–9. Available from: [<URL>](#).
10. Yano K, Karube I. Molecularly imprinted polymers for biosensor applications. *TrAC Trends Anal Chem* [Internet]. 1999 Mar 1;18(3):199–204. Available from: [<URL>](#).
11. Jia S, Zhou Y, Li J, Gong B, Ma S, Ou J. Highly selective enrichment and direct determination of imazethapyr residues from milk using magnetic solid-phase extraction based on restricted-access molecularly imprinted polymers. *Anal Methods* [Internet]. 2021 Jan 28;13(3):426–35. Available from: [<URL>](#).
12. Fang X, Wang Z, Sun N, Deng C. Magnetic metal oxide affinity chromatography-based molecularly imprinted approach for effective separation of serous and urinary phosphoprotein biomarker. *Talanta* [Internet]. 2021 May 1;226:122143. Available from: [<URL>](#).
13. Mohebbi A, Abdouss M, Kazemi Y, Daneshnia S. Fabrication and characterization of pH-responsive poly (methacrylic acid)-based molecularly imprinted polymers nanosphere for controlled release of amitriptyline hydrochloride. *Polym Adv Technol* [Internet]. 2021 Nov 6;32(11):4386–96. Available from: [<URL>](#).
14. Kirsch N, Hedin-Dahlström J, Henschel H, Whitcombe MJ, Wikman S, Nicholls IA. Molecularly imprinted polymer catalysis of a Diels-Alder reaction. *J Mol Catal B Enzym* [Internet]. 2009 Jun 1;58(1–4):110–7. Available from: [<URL>](#).
15. Ertuğrul Uygun HD, Demir MN. A Novel Fullerene- Pyrrole- Pyrrole- 3- Carboxylic Acid Nanocomposite Modified Molecularly Imprinted Impedimetric Sensor for Dopamine Determination in Urine. *Electroanalysis* [Internet]. 2020 Sep 27;32(9):1971–6. Available from: [<URL>](#).
16. BelBruno JJ. Molecularly Imprinted Polymers. *Chem Rev* [Internet]. 2019 Jan 9;119(1):94–119. Available from: [<URL>](#).
17. Ramström O, Ansell RJ. Molecular Imprinting Technology: Challenges and Prospects for the Future. *Chirality* [Internet]. 1998;10(3):195–209. Available from: [<URL>](#).
18. Turiel E, Martín-Esteban A. Molecularly imprinted polymers for sample preparation: A review. *Anal Chim Acta* [Internet]. 2010 Jun 4;668(2):87–99. Available from: [<URL>](#).
19. Gui R, Jin H, Guo H, Wang Z. Recent advances and future prospects in molecularly imprinted polymers-based electrochemical biosensors. *Biosens Bioelectron* [Internet]. 2018 Feb 15;100:56–70. Available from: [<URL>](#).
20. Ali HR. New Trends for Removal of Water Pollutants. In: Heimann RB, editor. *Prime Archives in Material Science* [Internet]. India: Vide Leaf; 2020. p. 1–57. Available from: [<URL>](#).
21. Andersson L, Sellergren B, Mosbach K. Imprinting of amino acid derivatives in macroporous polymers. *Tetrahedron Lett* [Internet]. 1984 Jan 1;25(45):5211–4. Available from: [<URL>](#).
22. Wulff G, Oberkobusch D, Minárik M. Enzyme-analogue built polymers, 18 chiral cavities in polymer layers coated on wide-pore silica. *React Polym Ion Exch Sorbents* [Internet]. 1985 Oct 1;3(4):261–75. Available from: [<URL>](#).
23. Cao Y, Feng T, Xu J, Xue C. Recent advances of molecularly imprinted polymer-based sensors in the detection of food safety hazard factors. *Biosens Bioelectron* [Internet]. 2019 Sep 15;141:111447. Available from: [<URL>](#).
24. Cormack PA., Elorza AZ. Molecularly imprinted polymers: synthesis and characterisation. *J Chromatogr B* [Internet]. 2004 May 5;804(1):173–82. Available from: [<URL>](#).
25. Hasanah AN, Safitri N, Zulfa A, Neli N, Rahayu D. Factors Affecting Preparation of Molecularly Imprinted Polymer and Methods on Finding Template-Monomer Interaction as the Key of Selective Properties of the Materials. *Molecules* [Internet]. 2021 Sep 16;26(18):5612. Available from: [<URL>](#).
26. Kryscio DR, Peppas NA. Critical review and perspective of macromolecularly imprinted polymers. *Acta Biomater* [Internet]. 2012 Feb 1;8(2):461–73. Available from: [<URL>](#).
27. Iskierko Z, Sharma PS, Bartold K, Pietrzyk-Le A, Noworyta K, Kutner W. Molecularly imprinted polymers for separating and sensing of macromolecular compounds and microorganisms. *Biotechnol Adv* [Internet]. 2016 Jan 1;34(1):30–46. Available from: [<URL>](#).
28. Ouyang Y, Bai L, Tian H, Li X, Yuan F. Recent progress of thermal conductive polymer composites: Al<sub>2</sub>O<sub>3</sub> fillers, properties and applications. *Compos Part A Appl Sci Manuf* [Internet]. 2022 Jan 1;152:106685. Available from: [<URL>](#).
29. Wackerlig J, Schirhagl R. Applications of Molecularly Imprinted Polymer Nanoparticles and Their Advances toward Industrial Use: A Review. *Anal Chem* [Internet]. 2016 Jan 5;88(1):250–61. Available from: [<URL>](#).
30. Caro E, Masqué N, Marcé RM, Borrull F, Cormack PA., Sherrington DC. Non-covalent and semi-covalent molecularly imprinted polymers for selective on-line solid-phase extraction of 4-nitrophenol from



- water samples. *J Chromatogr A* [Internet]. 2002 Jul;963(1-2):169-78. Available from: [<URL>](#).
31. Uygun ZO, Ertugrul Uygun HD, Ermis N, Canbay E. Molecularly Imprinted Sensors — New Sensing Technologies. In: Rincken T, editor. *Biosensors - Micro and Nanoscale Applications* [Internet]. InTech; 2015. p. 85-108. Available from: [<URL>](#).
32. Włoch M, Datta J. Synthesis and polymerisation techniques of molecularly imprinted polymers. In: *Comprehensive Analytical Chemistry* [Internet]. Elsevier; 2019. p. 17-40. Available from: [<URL>](#).
33. Brooks B. Suspension Polymerization Processes. *Chem Eng Technol* [Internet]. 2010 Nov 25;33(11):1737-44. Available from: [<URL>](#).
34. Lovell PA, Schork FJ. Fundamentals of Emulsion Polymerization. *Biomacromolecules* [Internet]. 2020 Nov 9;21(11):4396-441. Available from: [<URL>](#).
35. Dong C, Shi H, Han Y, Yang Y, Wang R, Men J. Molecularly imprinted polymers by the surface imprinting technique. *Eur Polym J* [Internet]. 2021 Feb 15;145:110231. Available from: [<URL>](#).
36. Bisht HS, Chatterjee AK. Living free-radical polymerization-A review. *J Macromol Sci Part C Polym Rev* [Internet]. 2001 Jul 31;41(3):139-73. Available from: [<URL>](#).
37. Renkecz T, László K, Horváth V. In situ synthesis of molecularly imprinted nanoparticles in porous support membranes using high- viscosity polymerization solvents. *J Mol Recognit* [Internet]. 2012 Jun 25;25(6):320-9. Available from: [<URL>](#).
38. Ertuğrul Uygun HD, Uygun ZO, Canbay E, Girgin Sağın F, Sezer E. Non-invasive cortisol detection in saliva by using molecularly cortisol imprinted fullerene-acrylamide modified screen printed electrodes. *Talanta* [Internet]. 2020 Jan 1;206:120225. Available from: [<URL>](#).
39. Uzun L, Turner APF. Molecularly-imprinted polymer sensors: realising their potential. *Biosens Bioelectron* [Internet]. 2016 Feb 15;76:131-44. Available from: [<URL>](#).
40. Pohanka M. Sensors Based on Molecularly Imprinted Polymers. *Int J Electrochem Sci* [Internet]. 2017 Sep 1;12(9):8082-94. Available from: [<URL>](#).
41. Ramanavicius S, Jagminas A, Ramanavicius A. Advances in Molecularly Imprinted Polymers Based Affinity Sensors (Review). *Polymers (Basel)* [Internet]. 2021 Mar 22 [cited 2023 Sep 28];13(6):974. Available from: [<URL>](#).
42. Brüggemann O, Haupt K, Ye L, Yilmaz E, Mosbach K. New configurations and applications of molecularly imprinted polymers. *J Chromatogr A* [Internet]. 2000 Aug 11;889(1-2):15-24. Available from: [<URL>](#).
43. Zahedi P, Ziaee M, Abdouss M, Farazin A, Mizaikoff B. Biomacromolecule template-based molecularly imprinted polymers with an emphasis on their synthesis strategies: a review. *Polym Adv Technol* [Internet]. 2016 Sep 1;27(9):1124-42. Available from: [<URL>](#).
44. Whitesides GM, Ostuni E, Takayama S, Jiang X, Ingber DE. Soft Lithography in Biology and Biochemistry. *Annu Rev Biomed Eng* [Internet]. 2001 Aug 28;3(1):335-73. Available from: [<URL>](#).
45. Mujahid A, Iqbal N, Afzal A. Bioimprinting strategies: From soft lithography to biomimetic sensors and beyond. *Biotechnol Adv* [Internet]. 2013 Dec;31(8):1435-47. Available from: [<URL>](#).
46. Voicu R, Faid K, Farah AA, Bensebaa F, Barjovanu R, Py C, et al. Nanotemplating for Two-Dimensional Molecular Imprinting. *Langmuir* [Internet]. 2007 May 1;23(10):5452-8. Available from: [<URL>](#).
47. Bonatti AF, De Maria C, Vozzi G. Molecular Imprinting Strategies for Tissue Engineering Applications: A Review. *Polymers (Basel)* [Internet]. 2021 Feb 12;13(4):548. Available from: [<URL>](#).
48. Tan CJ, Chua HG, Ker KH, Tong YW. Preparation of Bovine Serum Albumin Surface-Imprinted Submicrometer Particles with Magnetic Susceptibility through Core-Shell Miniemulsion Polymerization. *Anal Chem* [Internet]. 2008 Feb 1;80(3):683-92. Available from: [<URL>](#).
49. Rachkov A, Minoura N. Towards molecularly imprinted polymers selective to peptides and proteins. The epitope approach. *Biochim Biophys Acta - Protein Struct Mol Enzymol* [Internet]. 2001 Jan 12;1544(1-2):255-66. Available from: [<URL>](#).
50. Fang L, Jia M, Zhao H, Kang L, Shi L, Zhou L, et al. Molecularly imprinted polymer-based optical sensors for pesticides in foods: Recent advances and future trends. *Trends Food Sci Technol* [Internet]. 2021 Oct 1;116:387-404. Available from: [<URL>](#).
51. Cui F, Zhou Z, Zhou HS. Molecularly Imprinted Polymers and Surface Imprinted Polymers Based Electrochemical Biosensor for Infectious Diseases. *Sensors* [Internet]. 2020 Feb 13;20(4):996. Available from: [<URL>](#).
52. Sundhoro M, Agnihotra SR, Amberger B, Augustus K, Khan ND, Barnes A, et al. An electrochemical molecularly imprinted polymer sensor for rapid and selective food allergen detection. *Food Chem* [Internet]. 2021 May 15;344:128648. Available from: [<URL>](#).
53. Aghoutane Y, Diouf A, Österlund L, Bouchikhi B, El Bari N. Development of a molecularly imprinted polymer electrochemical sensor and its application for sensitive detection and determination of malathion in olive fruits and oils. *Bioelectrochemistry* [Internet]. 2020 Apr 1;132:107404. Available from: [<URL>](#).
54. Ayankojo AG, Reut J, Ciocan V, Öpik A, Syritski V. Molecularly imprinted polymer-based sensor for electrochemical detection of erythromycin. *Talanta* [Internet]. 2020 Mar 1;209:120502. Available from: [<URL>](#).

55. Mazouz Z, Mokni M, Fourati N, Zerrouki C, Barbault F, Seydou M, et al. Computational approach and electrochemical measurements for protein detection with MIP-based sensor. *Biosens Bioelectron* [Internet]. 2020 Mar 1;151:111978. Available from: [<URL>](#).
56. Raziq A, Kidakova A, Boroznjak R, Reut J, Öpik A, Syritski V. Development of a portable MIP-based electrochemical sensor for detection of SARS-CoV-2 antigen. *Biosens Bioelectron* [Internet]. 2021 Apr 15;178:113029. Available from: [<URL>](#).
57. Zeb S, Wong A, Khan S, Hussain S, Sotomayor MDPT. Using magnetic nanoparticles/MIP-based electrochemical sensor for quantification of tetracycline in milk samples. *J Electroanal Chem* [Internet]. 2021 Nov 1;900:115713. Available from: [<URL>](#).
58. Moncer F, Adhoum N, Catak D, Monser L. Electrochemical sensor based on MIP for highly sensitive detection of 5-hydroxyindole-3-acetic acid carcinoid cancer biomarker in human biological fluids. *Anal Chim Acta* [Internet]. 2021 Oct 9;1181:338925. Available from: [<URL>](#).
59. Onur Uygun Z, Ertuğrul Uygun HD. A Novel Chronoimpedimetric Glucose Sensor in Real Blood Samples Modified by Glucose- imprinted Pyrrole- Aminophenylboronic Acid Modified Screen Printed Electrode. *Electroanalysis* [Internet]. 2020 Feb 24;32(2):226–9. Available from: [<URL>](#).
60. Choi DY, Yang JC, Park J. Optimization and characterization of electrochemical protein Imprinting on hemispherical porous gold patterns for the detection of trypsin. *Sensors Actuators B Chem* [Internet]. 2022 Jan 1;350:130855. Available from: [<URL>](#).
61. Zhao H, Wang H, Quan X, Tan F. Amperometric Sensor for Tetracycline Determination Based on Molecularly Imprinted Technique. *Procedia Environ Sci* [Internet]. 2013 Jan 1;18:249–57. Available from: [<URL>](#).
62. Pesavento M, Merli D, Biesuz R, Alberti G, Marchetti S, Milanese C. A MIP-based low-cost electrochemical sensor for 2-furaldehyde detection in beverages. *Anal Chim Acta* [Internet]. 2021 Jan 15;1142:201–10. Available from: [<URL>](#).
63. Amouzadeh Tabrizi M, Fernández-Blázquez JP, Medina DM, Acedo P. An ultrasensitive molecularly imprinted polymer-based electrochemical sensor for the determination of SARS-CoV-2-RBD by using macroporous gold screen-printed electrode. *Biosens Bioelectron* [Internet]. 2022 Jan 15;196:113729. Available from: [<URL>](#).
64. Bakas I, Salmi Z, Jouini M, Geneste F, Mazerie I, Floner D, et al. Picomolar Detection of Melamine Using Molecularly Imprinted Polymer- Based Electrochemical Sensors Prepared by UV- Graft Photopolymerization. *Electroanalysis* [Internet]. 2015 Feb 15;27(2):429–39. Available from: [<URL>](#).
65. Zhang Z, Chen S, Ren J, Han F, Yu X, Tang F, et al. Facile construction of a molecularly imprinted polymer-based electrochemical sensor for the detection of milk amyloid A. *Microchim Acta* [Internet]. 2020 Dec 1;187(12):1–10. Available from: [<URL>](#).
66. Silva BVM, Rodríguez BAG, Sales GF, Sotomayor MDPT, Dutra RF. An ultrasensitive human cardiac troponin T graphene screen-printed electrode based on electropolymerized-molecularly imprinted conducting polymer. *Biosens Bioelectron* [Internet]. 2016 Mar 15;77:978–85. Available from: [<URL>](#).
67. Moreira FTC, Dutra RAF, Noronha JPC, Sales MGF. Electrochemical biosensor based on biomimetic material for myoglobin detection. *Electrochim Acta* [Internet]. 2013 Sep 30;107:481–7. Available from: [<URL>](#).
68. Siciliano G, Chiriaco MS, Ferrara F, Turco A, Velardi L, Signore MA, et al. Development of an MIP based electrochemical sensor for TGF-β1 detection and its application in liquid biopsy. *Analyst* [Internet]. 2023 Sep 11;148(18):4447–55. Available from: [<URL>](#).
69. Budak F, Cetinkaya A, Kaya SI, Atici EB, Ozkan SA. A molecularly imprinted polymer-based electrochemical sensor for the determination of tofacitinib. *Microchim Acta* [Internet]. 2023 Jun 10;190(6):205. Available from: [<URL>](#).
70. Ding M, Niu H, Guan P, Hu X. Molecularly imprinted sensor based on poly-o-phenylenediamine-hydroquinone polymer for β-amyloid-42 detection. *Anal Bioanal Chem* [Internet]. 2023 Mar 18;415(8):1545–57. Available from: [<URL>](#).
71. Atef Abdel Fatah M, Abd El-Moghny MG, El-Deab MS, Mohamed El Nashar R. Application of molecularly imprinted electrochemical sensor for trace analysis of Metribuzin herbicide in food samples. *Food Chem* [Internet]. 2023 Mar 15;404:134708. Available from: [<URL>](#).
72. Soliman SS, Mahmoud AM, Elghobashy MR, Zaazaa HE, Sedik GA. Point-of-care electrochemical sensor for selective determination of date rape drug “ketamine” based on core-shell molecularly imprinted polymer. *Talanta* [Internet]. 2023 Mar 1;254:124151. Available from: [<URL>](#).
73. Ma J, Yan M, Feng G, Ying Y, Chen G, Shao Y, et al. An overview on molecular imprinted polymers combined with surface-enhanced Raman spectroscopy chemical sensors toward analytical applications. *Talanta* [Internet]. 2021 Apr 1;225:122031. Available from: [<URL>](#).
74. Ahmad OS, Bedwell TS, Esen C, Garcia-Cruz A, Piletsky SA. Molecularly Imprinted Polymers in Electrochemical and Optical Sensors. *Trends Biotechnol* [Internet]. 2019 Mar 1;37(3):294–309. Available from: [<URL>](#).
75. Matsui J, Akamatsu K, Hara N, Miyoshi D, Nawafune H, Tamaki K, et al. SPR Sensor Chip for Detection of Small Molecules Using Molecularly

- Imprinted Polymer with Embedded Gold Nanoparticles. *Anal Chem* [Internet]. 2005 Jul 1;77(13):4282–5. Available from: [<URL>](#).
76. Singh P. SPR Biosensors: Historical Perspectives and Current Challenges. *Sensors Actuators B Chem* [Internet]. 2016 Jun 28;229:110–30. Available from: [<URL>](#).
77. Luo Q, Yu N, Shi C, Wang X, Wu J. Surface plasmon resonance sensor for antibiotics detection based on photo-initiated polymerization molecularly imprinted array. *Talanta* [Internet]. 2016 Dec 1;161:797–803. Available from: [<URL>](#).
78. Naresh V, Lee N. A Review on Biosensors and Recent Development of Nanostructured Materials-Enabled Biosensors. *Sensors* [Internet]. 2021 Feb 5;21(4):1109. Available from: [<URL>](#).
79. Altintas Z, Guerreiro A, Piletsky SA, Tothill IE. NanoMIP based optical sensor for pharmaceuticals monitoring. *Sensors Actuators B Chem* [Internet]. 2015 Jul 5;213:305–13. Available from: [<URL>](#).
80. Motaharian A, Hajebrahimi M, Hosseini MRM, Khosrokhavar R. Molecularly Imprinted Sol-Gel Sensing Film-Based Optical Sensor for Determination of Sulfasalazine Antibiotic. *ChemistrySelect* [Internet]. 2020 Nov 13;5(42):13191–7. Available from: [<URL>](#).
81. Chen Y-C, Brazier JJ, Yan M, Bargo PR, Prael SA. Fluorescence-based optical sensor design for molecularly imprinted polymers. *Sensors Actuators B Chem* [Internet]. 2004 Sep 1;102(1):107–16. Available from: [<URL>](#).
82. Sa-nguanprang S, Phuruangrat A, Bunkoed O. An optosensor based on a hybrid sensing probe of mesoporous carbon and quantum dots embedded in imprinted polymer for ultrasensitive detection of thiamphenicol in milk. *Spectrochim Acta Part A Mol Biomol Spectrosc* [Internet]. 2022 Jan 5;264:120324. Available from: [<URL>](#).
83. Chullasat K, Nurerk P, Kanatharana P, Davis F, Bunkoed O. A facile optosensing protocol based on molecularly imprinted polymer coated on CdTe quantum dots for highly sensitive and selective amoxicillin detection. *Sensors Actuators B Chem* [Internet]. 2018 Jan 1;254:255–63. Available from: [<URL>](#).
84. Yu J, Liu H, Wang Y, Li J, Wu D, Wang X. Fluorescent sensing system based on molecularly imprinted phase-change microcapsules and carbon quantum dots for high-efficient detection of tetracycline. *J Colloid Interface Sci* [Internet]. 2021 Oct 1;599:332–50. Available from: [<URL>](#).
85. Sari E, Üzek R, Duman M, Denizli A. Detection of ciprofloxacin through surface plasmon resonance nanosensor with specific recognition sites. *J Biomater Sci Polym Ed* [Internet]. 2018 Jul 24;29(11):1302–18. Available from: [<URL>](#).
86. Ertürk Bergdahl G, Andersson T, Allhorn M, Yngman S, Timm R, Lood R. *In Vivo* Detection and Absolute Quantification of a Secreted Bacterial Factor from Skin Using Molecularly Imprinted Polymers in a Surface Plasmon Resonance Biosensor for Improved Diagnostic Abilities. *ACS Sensors* [Internet]. 2019 Mar 22;4(3):717–25. Available from: [<URL>](#).
87. Suda N, Sunayama H, Kitayama Y, Kamon Y, Takeuchi T. Oriented, molecularly imprinted cavities with dual binding sites for highly sensitive and selective recognition of cortisol. *R Soc Open Sci* [Internet]. 2017 Aug 16;4(8):170300. Available from: [<URL>](#).
88. Xu X, Zhang Y, Wang B, Luo L, Xu Z, Tian X. A novel surface plasmon resonance sensor based on a functionalized graphene oxide/molecular-imprinted polymer composite for chiral recognition of L-tryptophan. *RSC Adv* [Internet]. 2018 Sep 19;8(57):32538–44. Available from: [<URL>](#).
89. Zhang L, Zhu C, Chen C, Zhu S, Zhou J, Wang M, et al. Determination of kanamycin using a molecularly imprinted SPR sensor. *Food Chem* [Internet]. 2018 Nov 15;266:170–4. Available from: [<URL>](#).
90. Ashley J, Shukor Y, D’Aurelio R, Trinh L, Rodgers TL, Temblay J, et al. Synthesis of Molecularly Imprinted Polymer Nanoparticles for  $\alpha$ -Casein Detection Using Surface Plasmon Resonance as a Milk Allergen Sensor. *ACS Sensors* [Internet]. 2018 Feb 23;3(2):418–24. Available from: [<URL>](#).
91. Weber P, Riegger BR, Niedergall K, Tovar GEM, Bach M, Gauglitz G. Nano-MIP based sensor for penicillin G: Sensitive layer and analytical validation. *Sensors Actuators B Chem* [Internet]. 2018 Aug 15;267:26–33. Available from: [<URL>](#).
92. Meza López F de L, Khan S, Picasso G, Sotomayor MDPT. A novel highly sensitive imprinted polymer-based optical sensor for the detection of Pb(II) in water samples. *Environ Nanotechnology, Monit Manag* [Internet]. 2021 Dec 1;16:100497. Available from: [<URL>](#).
93. Sistani S, Shekarchizadeh H. Fabrication of fluorescence sensor based on molecularly imprinted polymer on amine-modified carbon quantum dots for fast and highly sensitive and selective detection of tannic acid in food samples. *Anal Chim Acta* [Internet]. 2021 Nov 22;1186:339122. Available from: [<URL>](#).
94. Huang J, Tong J, Luo J, Zhu Y, Gu Y, Liu X. Green Synthesis of Water-Compatible Fluorescent Molecularly Imprinted Polymeric Nanoparticles for Efficient Detection of Paracetamol. *ACS Sustain Chem Eng* [Internet]. 2018 Aug 6;6(8):9760–70. Available from: [<URL>](#).
95. Sergeeva T, Yarynka D, Piletska E, Linnik R, Zaporozhets O, Brovko O, et al. Development of a smartphone-based biomimetic sensor for aflatoxin B1 detection using molecularly imprinted polymer membranes. *Talanta* [Internet]. 2019 Aug 15;201:204–10. Available from: [<URL>](#).
96. Wu L, Yan H, Li G, Xu X, Zhu L, Chen X, et al.

- Surface-Imprinted Gold Nanoparticle-Based Surface-Enhanced Raman Scattering for Sensitive and Specific Detection of Patulin in Food Samples. *Food Anal Methods* [Internet]. 2019 Jul 25;12(7):1648–57. Available from: [<URL>](#).
97. Kurt ZT, Çimen D, Denizli A, Bereli N. Development of Optical-Based Molecularly Imprinted Nanosensors for Adenosine Detection. *ACS Omega* [Internet]. 2023 May 30;8(21):18839–50. Available from: [<URL>](#).
98. Arcadio F, Noël L, Del Prete D, Maniglio D, Seggio M, Soppera O, et al. Soft molecularly imprinted nanoparticles with simultaneous lossy mode and surface plasmon multi-resonances for femtomolar sensing of serum transferrin protein. *Sci Rep* [Internet]. 2023 Jul 11;13(1):11210. Available from: [<URL>](#).
99. Çapar N, Yola BB, Polat İ, Bekerecioğlu S, Atar N, Yola ML. A zearalenone detection based on molecularly imprinted surface plasmon resonance sensor including sulfur-doped g-C<sub>3</sub>N<sub>4</sub>/Bi<sub>2</sub>S<sub>3</sub> nanocomposite. *Microchem J* [Internet]. 2023 Oct 1;193:109141. Available from: [<URL>](#).
100. Çorman ME, Armutcu C, Karasu T, Özgür E, Uzun L. Highly Selective Benzo[a]Pyrene Detection Even under Competitive Conditions with Molecularly Imprinted Surface Plasmon Resonance Sensor. *Polycycl Aromat Compd* [Internet]. 2023 May 28;43(5):3896–909. Available from: [<URL>](#).
101. Alberti G, Spina S, Arcadio F, Pesavento M, De Maria L, Cennamo N, et al. MIP-Assisted 3-Hole POF Chip Faced with SPR-POF Sensor for Glyphosate Detection. *Chemosensors* [Internet]. 2023 Jul 22;11(7):414. Available from: [<URL>](#).
102. Pohanka M. Overview of Piezoelectric Biosensors, Immunosensors and DNA Sensors and Their Applications. *Materials (Basel)* [Internet]. 2018 Mar 19;11(3):448. Available from: [<URL>](#).
103. Spieker E, Lieberzeit PA. Molecular Imprinting Studies for Developing QCM-sensors for *Bacillus Cereus*. *Procedia Eng* [Internet]. 2016 Jan 1;168:561–4. Available from: [<URL>](#).
104. Suedee R, Intakong W, Lieberzeit PA, Wanichapichart P, Chooto P, Dickert FL. Trichloroacetic acid-imprinted polypyrrole film and its property in piezoelectric quartz crystal microbalance and electrochemical sensors to application for determination of haloacetic acids disinfection by-product in drinking water. *J Appl Polym Sci* [Internet]. 2007 Dec 15;106(6):3861–71. Available from: [<URL>](#).
105. Pan M, Fang G, Lu Y, Kong L, Yang Y, Wang S. Molecularly imprinted biomimetic QCM sensor involving a poly(amidoamine) dendrimer as a functional monomer for the highly selective and sensitive determination of methimazole. *Sensors Actuators B Chem* [Internet]. 2015 Feb 1;207(PartA):588–95. Available from: [<URL>](#).
106. Çiçek Ç, Yılmaz F, Özgür E, Yavuz H, Denizli A. Molecularly Imprinted Quartz Crystal Microbalance Sensor (QCM) for Bilirubin Detection. *Chemosensors* [Internet]. 2016 Nov 18;4(4):21. Available from: [<URL>](#).
107. Mirmohseni A, Houjaghan MR. Measurement of the pesticide methomyl by modified quartz crystal nanobalance with molecularly imprinted polymer. *J Environ Sci Heal Part B* [Internet]. 2013 Mar;48(4):278–84. Available from: [<URL>](#).
108. Bi X, Yang K-L. On-Line Monitoring Imidacloprid and Thiocloprid in Celery Juice Using Quartz Crystal Microbalance. *Anal Chem* [Internet]. 2009 Jan 15;81(2):527–32. Available from: [<URL>](#).
109. Hussain M, Kotova K, Lieberzeit P. Molecularly Imprinted Polymer Nanoparticles for Formaldehyde Sensing with QCM. *Sensors* [Internet]. 2016 Jun 30;16(7):1011. Available from: [<URL>](#).
110. Ayankojo AG, Reut J, Boroznjak R, Öpik A, Syritski V. Molecularly imprinted poly(meta-phenylenediamine) based QCM sensor for detecting Amoxicillin. *Sensors Actuators B Chem* [Internet]. 2018 Apr 1;258:766–74. Available from: [<URL>](#).
111. Kumar Singh A, Singh M. QCM sensing of melphalan via electropolymerized molecularly imprinted polythiophene films. *Biosens Bioelectron* [Internet]. 2015 Dec 15;74:711–7. Available from: [<URL>](#).
112. Prabakaran K, Jandas PJ, Luo J, Fu C, Wei Q. Molecularly imprinted poly(methacrylic acid) based QCM biosensor for selective determination of L-tryptophan. *Colloids Surfaces A Physicochem Eng Asp* [Internet]. 2021 Feb 20;611:125859. Available from: [<URL>](#).
113. Kushwaha A, Srivastava J, Singh M. EQCM sensor for targeting psychoactive drug via rationally designed molecularly imprinted polymeric nanoparticles (nanoMIPs). *Mater Today Proc* [Internet]. 2022 Jan 1;49:3345–56. Available from: [<URL>](#).
114. Kadirsoy S, Atar N, Yola ML. Molecularly imprinted QCM sensor based on delaminated MXene for chlorpyrifos detection and QCM sensor validation. *New J Chem* [Internet]. 2020 Apr 27;44(16):6524–32. Available from: [<URL>](#).
115. Çapar N, Polat İ, Yola BB, Atar N, Yola ML. A novel molecular imprinted QCM sensor based on MoS<sub>2</sub>NPs-MWCNT nanocomposite for zearalenone determination. *Microchim Acta* [Internet]. 2023 Jul 17;190(7):262. Available from: [<URL>](#).
116. Cai X, Liu J, Liang D, Tang S, Xu B. Construction of a QCM sensor for detecting diethylstilbestrol in water based on the computational design of molecularly imprinted polymers. *Arab J Chem* [Internet]. 2023 Apr 1;16(4):104601. Available from: [<URL>](#).
117. Acet Ö, Odabaşı M. Detection of N-hexanoyl-L-homoserine lactone via MIP-based QCM sensor: preparation and characterization. *Polym Bull*

- [Internet]. 2023 Jun 22;80(6):6657–74. Available from: [<URL>](#).
118. Wen T, He W, Nie Q, Gong Z, Li D, Wen L, et al. Discrimination of citrus infested with *Bactrocera dorsalis* (Hendel) using an olfactory detection system based on MIPs-QCM sensor array and Bayesian optimized classification algorithms. *Sensors Actuators B Chem* [Internet]. 2023 Jun 15;385:133687. Available from: [<URL>](#).
119. Humairah NA, Nurijal I, Ainus Sofa S, Chaerunnisa A, Roto R, Kusumaatmaja A, et al. Molecularly imprinted polyvinyl acetate doped with boric acid for sensitivity and selectivity of ammonia sensing by QCM. *Biosens Bioelectron X* [Internet]. 2023 May 1;13:100320. Available from: [<URL>](#).
120. Shiokawa S, Kondoh J. Surface Acoustic Wave Sensors. *Jpn J Appl Phys* [Internet]. 2004 May 1;43(5S):2799. Available from: [<URL>](#).
121. Ermolaeva TN, Farafonova O V., Chernyshova VN, Zyablov AN, Tarasova N V. A Piezoelectric Sensor Based on Nanoparticles of Ractopamine Molecularly Imprinted Polymers. *J Anal Chem* [Internet]. 2020 Oct 2;75(10):1270–7. Available from: [<URL>](#).
122. Debabhuti N, Neogi S, Mukherjee S, Dhar A, Sharma P, Vekariya RL, et al. Development of QCM sensor to detect  $\alpha$ -terpinyl acetate in cardamom. *Sensors Actuators A Phys* [Internet]. 2021 Mar 1;319:112521. Available from: [<URL>](#).





## Effect of AOT/Heptane Reverse Micelles on Oxidation of Ferriin by Metaperiodate: Kinetic and Mechanistic Aspects

Bodasingi Leela Kumari<sup>1</sup> , Pulipaka Shyamala<sup>2\*</sup> , Venkata Nagalakshmi Kilana<sup>3</sup> 

<sup>1</sup>Chaitanya Women's Degree & P.G College, Visakhapatnam-530026, Andhra Pradesh, India.

<sup>2</sup>Andhra University, Department of Chemistry, Visakhapatnam-530017, Andhra Pradesh, India.

<sup>3</sup>Gayatri Vidya Parishad College of Engineering (Autonomous), Department of Chemistry, Madhurawada, Visakhapatnam-530048, Andhra Pradesh, India.

**Abstract:** A kinetic study of the oxidation of Ferriin,  $[\text{Fe}(\text{phen})_3]^{2+}$  by metaperiodate ( $\text{IO}_4^-$ ) has been carried out in AOT/heptane reverse micelles by changing  $W = ([\text{H}_2\text{O}]/[\text{AOT}])$  and AOT concentration. The reaction order is first order with respect to Ferriin, while zero order with respect to  $\text{IO}_4^-$ . The reaction rate is faster in aqueous medium compared to AOT reverse micelles by eight times. The oxidation rate increases with an increase in the value of  $W$  (at fixed surfactant concentration,  $[\text{AOT}]$ ) and decreases with AOT concentration. The effect of  $W$  on rate is elucidated based on the low dielectric constant of the water pool. Berezin's pseudo-phase model has been applied to explain the effect of AOT on rate.

**Keywords:** Ferriin, periodate, AOT, Reverse micelles, and water pool.

**Submitted:** December 31, 2022. **Accepted:** September 19, 2023.

**Cite this:** Leela Kumari B, Shyamala P, Klina VN. Effect of AOT/Heptane Reverse Micelles on Oxidation of Ferriin by Metaperiodate: Kinetic and Mechanistic Aspects. JOTCSA. 2023;10(4):1099-106.

**DOI:** <https://doi.org/10.18596/jotcsa.1226805>

**\*Corresponding author's E-mail:** [shyamalapulipaka06@gmail.com](mailto:shyamalapulipaka06@gmail.com)

### 1. INTRODUCTION

Reverse micelles are stable surfactant aggregates formed spontaneously in organic solvents. Their hydrophilic head groups combine to create structures with polar cores, while their hydrophobic tails extend outward into the surrounding organic solvent, unlike normal micelles. One important feature of reverse micelles is their ability to solubilize water within them, resulting in optically transparent and thermodynamically stable structures. This water-containing region within the reverse micelle is referred to as the "water pool" and is characterized by its radius ( $r$ , in nanometers), which is linearly related to an externally controlled parameter known as  $W$  ( $W = [\text{H}_2\text{O}]/[\text{Surfactant}]$ ) (1-4).

The water solubilized within reverse micelles hydrates the hydrophilic head groups of the surfactants. This water is tightly bound and exhibits lower mobility compared to bulk water. It is important to note that only the initial portions of water added to the reverse micelle are tightly bound, and as solvation progresses, free water becomes available. The behavior exhibited by these initial

water portions is characterized by certain anomalies, including a diminished dielectric constant, decreased activity, limited mobility, modified pH, and heightened nucleophilicity compared to conventional aqueous solutions. As the water content within the reverse micelle increases, the physical properties of the water pool gradually approach those of ordinary aqueous solutions (5-9). Three structural changes occur within reverse micelles when varying the water and surfactant concentrations can be categorized (10). They are:

1. When water and surfactant concentrations are adjusted simultaneously while keeping  $W$  constant, the reverse micelle concentration changes, but its size remains unchanged.
2. An increase in the amount of water results in an enlargement of the micelle size.
3. Increasing water and surfactant concentrations simultaneously increases micelle concentration while maintaining a fixed micelle size. Conversely, an increase in surfactant concentration causes a reduction in micelle size.

Reverse micelles have many advantages compared to aqueous media. For example, they offer a unique capacity to accommodate a wide range of substrate molecules, regardless of their hydrophilic, hydrophobic, or amphiphilic nature. The compartmentalization of reactants in reverse micelles is a key aspect of their utility in various chemical and biochemical applications. The localization of reactants gives rise to catalytic effects on the rates of the reactions, thereby controlling the kinetics and mechanism of reactions (11-14).

We have reported a few reactions taking place in the presence of CTAB/CHCl<sub>3</sub>/Hexane reverse micelles, explored the unique properties of CTAB reverse micelles, and applied Berezin's pseudo-phase model to explain the results (15-19). To explore the unique properties of AOT/Heptane reverse micelles, oxidation of ferrioxalate by metaperiodate has been chosen.

## 2. EXPERIMENTAL SECTION

### 2.1. Materials

Double distilled water was used for the preparation of solutions. All the chemicals used were of Analytical grade. Sodium bis(2-ethylhexyl)sulfosuccinate (AOT) (Fluka) was used without further purification. Heptane was distilled before use. A solution of AOT with a concentration of 0.3 mol/dm<sup>3</sup> was prepared by dissolving 66.68 g of AOT in heptane. Additionally, solutions with concentrations of 0.2 mol/dm<sup>3</sup> and 0.1 mol/dm<sup>3</sup> were prepared similarly by dissolving the appropriate amount of AOT in heptane. The stock solutions of ferrioxalate (0.02 mol/dm<sup>3</sup>) were produced by dissolving the necessary amount of FeSO<sub>4</sub>·7H<sub>2</sub>O and 1,10-phenanthroline in water. Sodium metaperiodate (Merck, India) solution was prepared by dissolving the necessary quantities in water.

### 2.2. Determination of binding constants of [Fe(phen)<sub>3</sub>]<sup>2+</sup>

The binding constants of [Fe(phen)<sub>3</sub>]<sup>2+</sup> in AOT reverse micelles have been determined at different concentrations of AOT. For each concentration, the absorbance of [Fe(phen)<sub>3</sub>]<sup>2+</sup> has been noted at λ=510 nm (Fig. 1). The absorbances recorded are

A<sub>M</sub>, the absorbance of the complex in the presence of reverse micellar medium; A<sub>W</sub><sup>0</sup>, is the absorbance of the complex in the presence of water and C, the concentration of surfactant (20). The binding constant has been determined by following Benesi-Hildebrand equation,

$$\frac{1}{(A_M - A_W^0)} = \frac{1}{(A_M^0 - A_W^0)} + \frac{1}{(A_M^0 - A_W^0)K_S C}$$

A graph between 1 / (A<sub>M</sub> - A<sub>W</sub><sup>0</sup>) vs 1/C gives straight line, binding constant values determined from slope and intercept given in Table 1.

### 2.3. Experimental method:

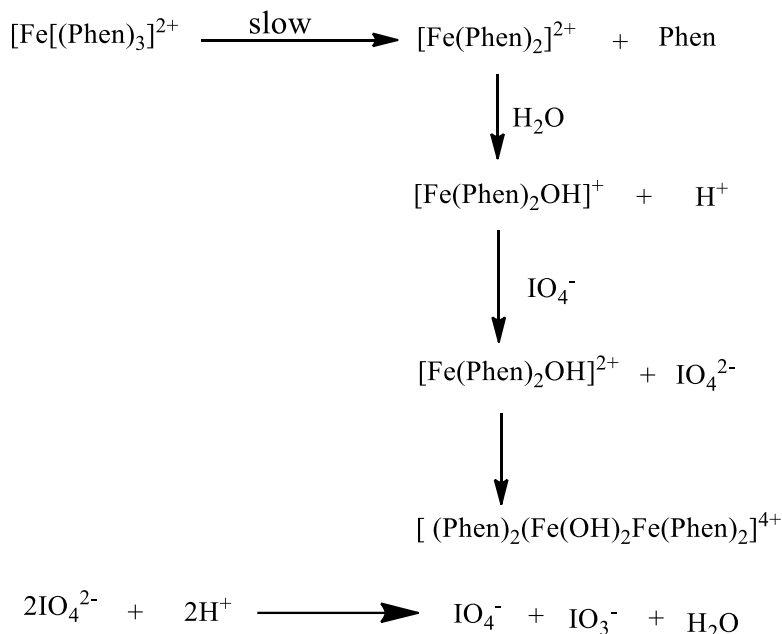
[Fe(phen)<sub>3</sub>]<sup>2+</sup> (0.02 mol/dm<sup>3</sup>, 0.02 mL) was taken into 0.1 mol/dm<sup>3</sup>, 10 mL of AOT solution using a micropipette followed by IO<sub>4</sub><sup>-</sup> solution (0.2 mol/dm<sup>3</sup>, 0.04 mL/dm<sup>3</sup>) the reaction mixtures were thoroughly shaken to obtain a clear solution. W was varied in the range of 3.33 to 12.2 in the subsequent experiments, and the concentration of IO<sub>4</sub><sup>-</sup> was varied from (4-40) × 10<sup>-4</sup> mol/dm<sup>3</sup>.

The decrease in absorbance of [Fe(phen)<sub>3</sub>]<sup>2+</sup> at a wavelength of 510 nm was measured as a function of time. [IO<sub>4</sub><sup>-</sup>] >> [[Fe(phen)<sub>3</sub>]<sup>2+</sup>]. Good linear plots were obtained for log(absorbance) vs. time, showing first-order kinetics with respect to [Fe(phen)<sub>3</sub>]<sup>2+</sup>. Triplicate runs were performed, and averages were taken. A UV-Vis double-beam spectrophotometer was used.

## 3. RESULTS AND DISCUSSION

The kinetics of the reaction have been carried out in the presence of AOT reverse micelles under pseudo-first-order conditions, taking [IO<sub>4</sub><sup>-</sup>] >> [Fe(phen)<sub>3</sub>]<sup>2+</sup>. [Fe(phen)<sub>3</sub>]<sup>2+</sup> is therefore isolated. Good linear plots between log (A<sub>t</sub>) versus time (Figure 2) were obtained, indicating first-order kinetics with respect to [Fe(phen)<sub>3</sub>]<sup>2+</sup>. The pseudo-first-order rate constant, k<sub>1</sub>, has no dependence on [IO<sub>4</sub><sup>-</sup>], confirming zero-order kinetics with respect to IO<sub>4</sub><sup>-</sup> (Table 2). Based on these results, the mechanism has been given in Scheme 1.





**Scheme 1:** The reaction between metaperiodate and ferroin.

The reaction is around eight times slower in AOT reverse micellar medium compared to aqueous medium under the same conditions. The present reaction is a cation-anion reaction. Since the reverse micelles have a low dielectric constant, which does not favor a cation-anion reaction, the reaction is slower in the AOT reverse micellar medium. Similar results based on the dielectric constant effect on reaction rates have been reported by Ayoko G et al. (12).

#### Effect of molar ratio (*W*) on rate

The pseudo-first-rate constant,  $k_1$ , increases slightly with an increase in molar ratio ( $W = [\text{H}_2\text{O}]/[\text{AOT}]$ ) (Table 3). The slight rate increase is because of two factors.

1. The first is the dielectric constant of the medium: It is well known that the rate of the reaction is dependent on the dielectric constant of the medium (21)

$$\ln k = \ln k_0 - \frac{Z_A Z_B e^2}{(4\pi\epsilon_0 \epsilon d_{AB} kT)}$$

Since the present reaction is an anion-cation reaction, according to the above equation, as *W* increases, the dielectric constant increases, and therefore the reaction rate increases with *W*.

2.  $\text{IO}_4^-$  is a hydrophilic species, and because of the lack of electrostatic attraction with AOT, it exists totally in the water pool.  $[\text{Fe}(\text{phen})_3]^{2+}$  is partitioned between the water pool and AOT surface (Figure 3). As *W* increases  $[\text{Fe}(\text{phen})_3]^{2+}$  goes more into the water pool while  $\text{IO}_4^-$  is already available in the water pool, so there is an increase in rate with change in *W*.

#### Effect of concentration of AOT

At constant *W*, with an increase in AOT concentration,  $k_1$  decreases. This is because the positively charged  $[\text{Fe}(\text{phen})_3]^{2+}$  is increasingly

bound by the negatively charged micellar surface, whereas  $\text{IO}_4^-$  is left behind only at the core of the water pool. This results in a decrease in rate with an increase in concentration of AOT. Berezin's pseudo-phase model has been applied to explain this behavior, and accordingly, the expression related to a reaction involving one strongly bound reactant and another strongly repelled reactant has been applied (22). The observed rate constant  $k_1$  is thus given by:

$$k_1 = \frac{k_m P_{\text{IO}_4^-} K_{[\text{Fe}(\text{Phen})_3]^{2+}} C + k_w (1 - CV)}{(1 + K_{\text{IO}_4^-} C)(1 + K_{[\text{Fe}(\text{Phen})_3]^{2+}} C)}$$

Where,  $k_m$  is the rate constant at the micellar phase,  $k_w$  is the rate constant of reaction in the water pool, *C* is  $[\text{AOT}]$ , and *V* is the molar volume of AOT ( $P_{\text{IO}_4^-}$ ) is the partition coefficient of the periodate.  $K_{[\text{Fe}(\text{phen})_3]^{2+}}$  and  $K_{\text{IO}_4^-}$  are the binding constants of  $[\text{Fe}(\text{phen})_3]^{2+}$  and  $\text{IO}_4^-$  and  $K_{[\text{Fe}(\text{phen})_3]^{2+}} = P_{[\text{Fe}(\text{phen})_3]^{2+}} V$  and  $K_{\text{IO}_4^-} = P_{\text{IO}_4^-} V$ .  $\text{IO}_4^-$  is repelled by the micellar surface and is water-soluble, and therefore  $K_{\text{IO}_4^-}$  can be neglected in the above equation. Since  $k_w > k_m$ , the above equation changes to

$$\begin{aligned}
 & k_1 = \frac{k_w}{(1 + K_{[\text{Fe}(\text{Phen})_3]^{2+}} C)} \\
 + & \frac{1}{k_1} = \frac{1}{k_w} + \frac{K_{[\text{Fe}(\text{Phen})_3]^{2+}} C}{k_w}
 \end{aligned}$$

According to the above equation,  $1/k_1$  versus *C* was found to be linear, showing the applicability of Berezin's pseudo-phase model to reverse micelles (Fig. 4). The binding constant of  $[\text{Fe}(\text{phen})_3]^{2+}$  was calculated from slope and intercept of the above plot (Table 1). It was found that the binding constants thus obtained agree with the binding constant obtained from spectral data (experimental section). This shows the validity of Berezin's model to the present reaction.

**Table 1:** Binding constants of  $[\text{Fe}(\text{phen})_3]^{2+}$ 

W	Spectral data	Kinetic data
4.44	17.80	18.81
6.66	16.60	10.46
12.2	10.02	8.65

**Table 2.** Influence of periodate on reaction rate  
 $[\text{Fe}(\text{phen})_3]^{2+} = 4.0 \times 10^{-5} \text{ mol/dm}^3$ ;  $T = 304 \text{ K}$ 

		W = 5.55		W = 12.2	
$[\text{IO}_4^-]_0 \times 10^4$ (mol/dm <sup>3</sup> )	$[\text{IO}_4^-]_e$ (mol/dm <sup>3</sup> )	$k_1 \times 10^4$ (sec <sup>-1</sup> )	$[\text{IO}_4^-]_e$ (mol/dm <sup>3</sup> )	$k_1 \times 10^4$ (sec <sup>-1</sup> )	
4.0	0.04	1.30	0.018	1.90	
12.0	0.12	1.30	0.054	2.00	
16.0	0.16	1.60	0.072	1.79	
20.0	0.20	1.64	0.090	1.81	

**Table 3:** Influence of W and [AOT] on observed first-order rate constant ( $k_1$ )  
 $[\text{Fe}(\text{phen})_3]^{2+} = 4.0 \times 10^{-5} \text{ mol/dm}^3$ ;  $[\text{IO}_4^-] = 8.0 \times 10^{-4} \text{ mol/dm}^3$ ;  $T = 304 \text{ K}$ 

[AOT] (mol/dm <sup>3</sup> )	W	$k_1 \times 10^4$ (sec <sup>-1</sup> )
0.1	3.33	1.1
	4.44	1.50
	5.55	1.53
	6.66	1.70
	7.77	1.80
	8.88	1.97
	12.2	1.99
0.2	3.33	0.94
	4.44	1.35
	5.55	1.53
	6.66	1.54
	7.77	1.60
	8.88	1.61
	12.2	1.72
0.3	3.33	0.75
	4.44	0.78
	5.55	0.90
	6.66	1.00
	7.77	1.27
	8.88	1.35
	12.2	1.47

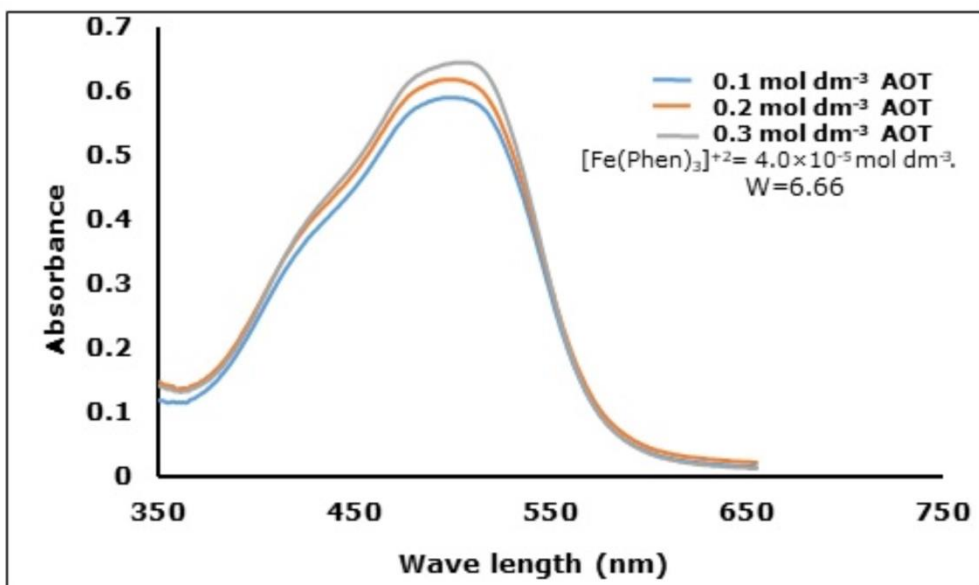


Figure 1: Spectra of Absorbance of  $[\text{Fe}(\text{phen})_3]^{2+}$  versus wavelength (nm) at different [AOT].

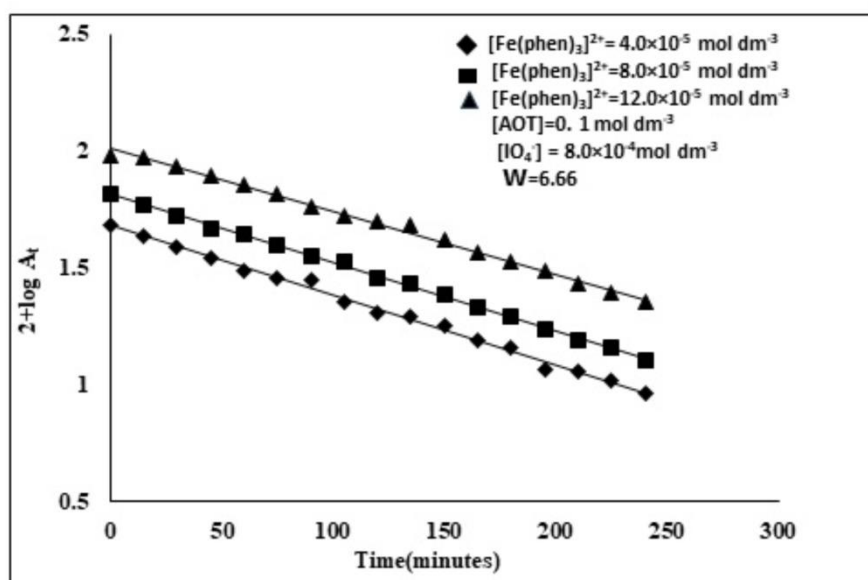


Figure 2: A Plot of  $2 + \log (\text{Absorbance})$  versus Time (min) at different concentrations of  $[\text{Fe}(\text{phen})_3]^{2+}$

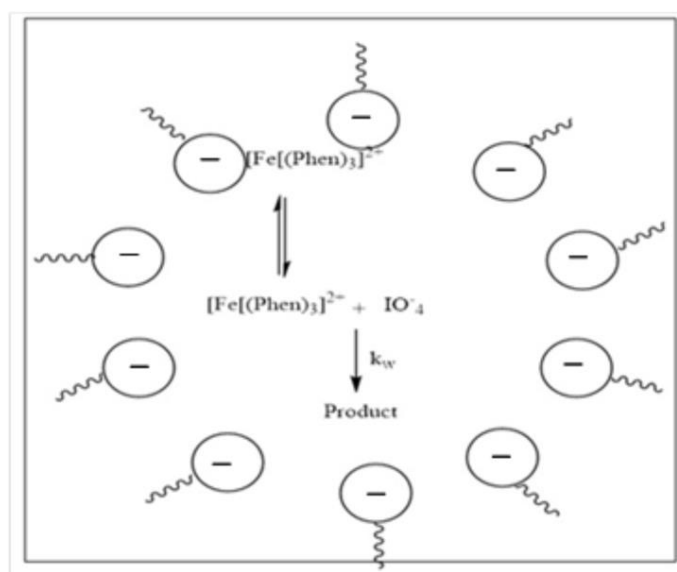


Figure 3: Graphical representation of the distribution of reactants in AOT/Heptane reverse micelles.

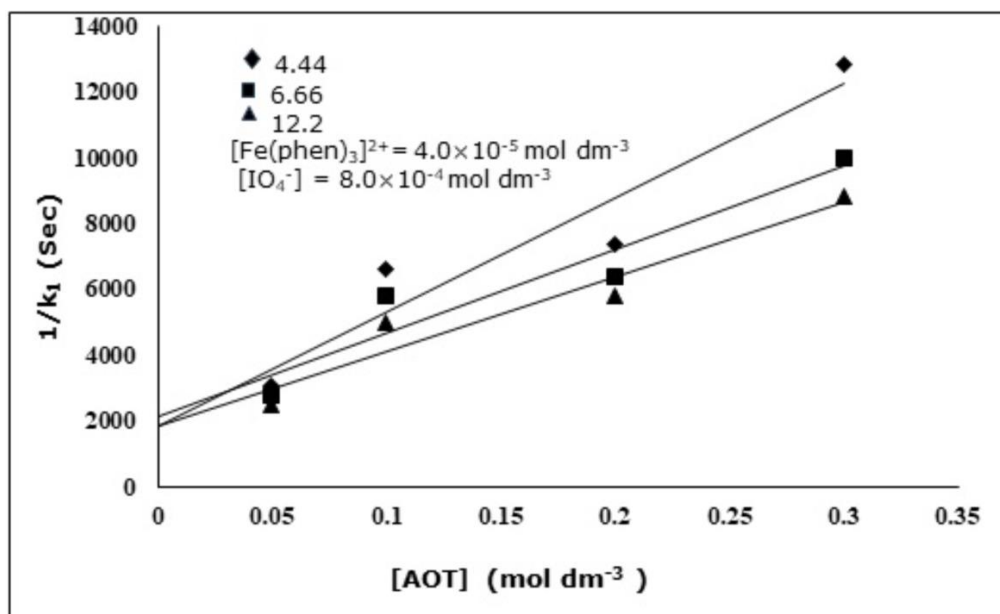


Figure 4: A Plot of  $1/k_1$  versus [AOT].

#### 4. CONCLUSION

- The reaction's order is zero concerning  $\text{IO}_4^-$  while the first is concerning  $[\text{Fe}(\text{phen})_3]^{2+}$ .
- The reaction is inhibited eight times in the presence of AOT reverse micelles.
- As  $W$  increases, the rate of the reaction increases slightly due to an increase in the availability of  $[\text{Fe}(\text{phen})_3]^{2+}$  in the water pool, and also, with an increase of  $W$ , the dielectric constant increases, which favors the reaction between two oppositely charged reactants.
- The rate constant,  $k_1$ , decreases with an increase in AOT concentration. This is because the positively charged  $[\text{Fe}(\text{phen})_3]^{2+}$  is increasingly bound by the negatively charged micellar surface and less available for reaction.

#### 5. CONFLICT OF INTEREST

We have no conflicts of interest to disclose.

#### 6. ACKNOWLEDGMENTS

P. Shyamala thanks the Ministry of Earth Sciences (MOES), National Centre for Coastal Research (NCCR), and the Government of India for financial support under major project No MOES/ICMAM - PD/Supply. Order/81/2017.

B. Leela Kumari is thankful to the Management of Chaitanya Women's Degree & P.G College of Gajuwaka, Visakhapatnam, for their encouragement.

#### 7. REFERENCES

1. Muñoz E, Gómez-Herrera C, Graciani M del M, Moyá ML, Sánchez F. Kinetics of the oxidation of iodide by persulphate in AOT-oil-water microemulsions. *J Chem Soc, Faraday Trans* [Internet]. 1991 Jan 1;87(1):129-32. Available from: [<URL>](#).
2. Sunamoto J, Hamada T. Solvchromism and Thermochromism of Cobalt(II) Complexes Solubilized in

Reversed Micelles. *Bull Chem Soc Jpn* [Internet]. 1978 Nov 19;51(11):3130-5. Available from: [<URL>](#).

3. Bridge NJ, Fletcher PDI. Time-resolved studies of fluorescence quenching in a water-in-oil microemulsion. *J Chem Soc Faraday Trans 1 Phys Chem Condens Phases* [Internet]. 1983 Jan 1;79(9):2161-9. Available from: [<URL>](#).

4. Nicholson J, Clark J. Surfactants in solution. Mittal K, editor. Vol. 3, Ed. KL Mittal, Plenum Press, New York—London. New York: Plenum Press; 1984. 1663-1674 p.

5. Mandal HK, Majumdar T, Mahapatra A. Kinetics of basic hydrolysis of tris(1,10-phenanthroline)iron(II) in macromolecular assemblies of CTAB. *Int J Chem Kinet* [Internet]. 2011 Oct 1;43(10):579-89. Available from: [<URL>](#).

6. Johnson MD, Lorenz BB, Wilkins PC, Lemons BG, Baruah B, Lamborn N, et al. Switching off electron transfer reactions in confined media: Reduction of  $[\text{Co}(\text{dipic})_2]$  - and  $[\text{Co}(\text{edta})]$  - by hexacyanoferrate(II). *Inorg Chem* [Internet]. 2012 Mar 5;51(5):2757-65. Available from: [<URL>](#).

7. García-Río L, Mejuto JC, Pérez-Lorenzo M. Microheterogeneous Solvation for Aminolysis Reactions in AOT-Based Water-in-Oil Microemulsions. *Chem - A Eur J* [Internet]. 2005 Jul 18;11(15):4361-73. Available from: [<URL>](#).

8. Yao C, Tang S, He Z, Deng X. Kinetics of lipase-catalyzed hydrolysis of olive oil in AOT/isooctane reversed micelles. *J Mol Catal B Enzym* [Internet]. 2005 Sep 1;35(4-6):108-12. Available from: [<URL>](#).

9. Eskici G, Axelsen PH. The size of AOT reverse micelles. *J Phys Chem B* [Internet]. 2016 Nov 10;120(44):11337-47. Available from: [<URL>](#).

10. Bru R, Sánchez-Ferrer A, García-Carmona F. Kinetic models in reverse micelles. *Biochem J* [Internet]. 1995 Sep 15;310(3):721-39. Available from: [<URL>](#).

11. Cid A, Acuña A, Alonso-Ferrer M, Astray G, García-Río L, Simal-Gándara J, et al. Pseudophase Model in Microemulsions. In: Mejuto JC, editor. *Microemulsion - A Chemical Nanoreactor* [Internet]. IntechOpen; 2019. Available from: [<URL>](#).

12. Goto A, Kishimoto H. The Addition of the Cyanide Ion to the *N*-Methyl-3-carbamoylpyridinium Ion in Reversed Micelles. Bull Chem Soc Jpn [Internet]. 1989 Sep 27;62(9):2854–61. Available from: [<URL>](#).
13. Rathman JF. Micellar catalysis. Curr Opin Colloid Interface Sci [Internet]. 1996 Aug 1;1(4):514–8. Available from: [<URL>](#).
14. Venkateswarlu G, Rao GSRK. Kinetics of the dissociation of tris (2, 2'-bipyridyl) iron (II) and tris (1, 10-phenanthroline) iron (II) in the reverse micelles of Tween-85 in cyclohexane. J Indian Chem Soc. 2009;86(8):822–5.
15. Nagalakshmi K V, Shyamala P, Rao S. Notes Catalytic effect of CTAB reverse micelles on the oxidation of indigo carmine by periodate. Indian J Chem [Internet]. 2015;54:351–5. Available from: [<URL>](#).
16. Nagalakshmi K V., Padma M, Shyamala P, Srikanth V, Satyanarayana A, SubbaRao P V. Catalytic effect of CTAB reverse micelles on the kinetics of dissociation of bis(2,4,6-tripyridyl-s-triazine) iron(II). Transit Met Chem [Internet]. 2013 Aug 3;38(5):523–7. Available from: [<URL>](#).
17. Nagalakshmi K V., Shyamala P. Acid Hydrolysis of Bis(2,2'; 6',2''-Terpyridyl) Iron(II) Complex in the Water Pools of CTAB/Hexane/Chloroform Reverse Micelles-A Kinetic Study in Confined Medium. Bull Chem React Eng Catal [Internet]. 2020 Dec 28;15(3):853–60. Available from: [<URL>](#).
18. Nagalakshmi K V, Shyamala P. Effect of CTAB reverse micelles on the kinetics of aminolysis of p-nitrophenyl acetate by hydrazine. J Indian Chem Soc [Internet]. 2020;97:737–41. Available from: [<URL>](#).
19. Nagalakshmi KV, Shyamala P, Subba Rao PV. Kinetics of oxidation of toluidine blue by periodate: Catalysis by water pools of CTAB. Curr Chem Lett [Internet]. 2018;7(3):93–100. Available from: [<URL>](#).
20. Azum N, Rub MA, Alfaiifi SY, Asiri AM. Interaction of Diphenhydramine Hydrochloride with Cationic and Anionic Surfactants: Mixed Micellization and Binding Studies. Polymers (Basel) [Internet]. 2021 Apr 9;13(8):1214. Available from: [<URL>](#).
21. Laidler KJ. Chemical kinetics. 3rd edition. 1987. 197 p.





## Recent Developments in Nanostructured Materials for Supercapacitor Electrodes

Emre Yilmazoğlu<sup>1\*</sup> , Selcan Karakuş<sup>2</sup> 

<sup>1</sup>Department of Chemical Engineering, Faculty of Engineering, Istanbul University-Cerrahpasa, Istanbul, 34320, Turkey.

<sup>2</sup>Department of Chemistry, Faculty of Engineering, Istanbul University-Cerrahpasa, Istanbul, 34320, Turkey.

**Abstract:** This review focuses on nanostructures-based systems and aims to provide a comprehensive overview of recent advancements in energy storage technologies and modified energy storage materials. The transition towards a sustainable and carbon-free energy system hinges on the progress of efficient and safe energy storage technologies. Supercapacitors have garnered significant interest in diverse energy storage applications due to their rapid charge/discharge rates, high power density, and extended cycle life. Nanostructures have conclusively demonstrated their capability to significantly enhance supercapacitor electrodes' performance. MXene, an innovative category of 2D materials, has emerged as a promising candidate for energy storage applications due to its substantial surface area, exceptional electrical conductivity, and versatile characteristics. Supercapacitors, nanostructures, and MXene are the main topics of the research articles and reviews in this special issue, highlighting recent developments in the design, synthesis, and characterization of advanced energy storage materials and devices. Additionally, this study presents an in-depth investigation of various carbon-based nanomaterials, their synthesis techniques, and their performance in supercapacitors. It also emphasizes the potential of recycling waste materials for developing high-performance nanomaterials for energy storage applications. Finally, this review encourages further research and development of advanced energy storage technologies by giving readers a thorough overview of the current state-of-the-art and future directions in this rapidly expanding sector.

**Keywords:** Supercapacitor, MXene, nanostructures, energy storage systems.

**Submitted:** June 27, 2023. **Accepted:** September 6, 2023.

**Cite this:** Yilmazoğlu E, Karakuş S. Recent Developments in Nanostructured Materials for Supercapacitor Electrodes. JOTCSA. 2023;10(4):1107-22.

**DOI:** <https://doi.org/10.18596/jotcsa.1320655>

**\*Corresponding author's E-mail:** [emre.yilmazoglu@iuc.edu.tr](mailto:emre.yilmazoglu@iuc.edu.tr)

### 1. INTRODUCTION

In recent years, the global population growth rate has surged, paralleled by a corresponding expansion in the size of industries. As these industries proliferate and extend their reach across broader geographical regions, the demand for energy experiences a steep and substantial rise. Due to reasons such as global warming and the limited availability of fossil fuels, the significance of equipment necessary for efficient energy storage, transmission, and alternative fuels becomes increasingly prominent. The storage of energy derived from renewable resources and its efficient conversion into power necessitate a more sophisticated infrastructure. This requirement fosters equipment production, such as new battery types and supercapacitors, driven by advancements in

materials science (1–3).

Enhancing energy efficiency through the development of capacitors and batteries is a focal point of research driven by the need to address various drawbacks. These drawbacks include limited energy storage capacity, a short operational lifespan characterized by a small number of cycles, as well as restricted charge and discharge rates. While certain studies focus on refining existing devices, a significant portion of research strives to create energy storage and transmission devices using innovative techniques and novel materials. Consequently, the goal is to fabricate equipment characterized by remarkable attributes such as high energy storage capacity, rapid charging/discharging capabilities, lightweight design, resistance to corrosion and external influences, cost-effectiveness,

and ease of production. One of the foremost concerns is the realization of equipment boasting elevated charge/discharge speeds, commonly referred to as high energy density, while preserving their initial stability over numerous charging/discharging cycles. In the contemporary landscape, there is a prevalent shift towards adopting wireless, portable, and compact devices that demand substantial energy due to their technological functionalities. This contrasts with the traditional use of stationary devices tethered to networks via cables. Consequently, the imperative to harness novel materials and technologies to advance sophisticated batteries and capacitors becomes exceedingly significant. These developments cater to devices designed for everyday and specialized applications, including biomedical devices (4–6).

In this context, a multitude of novel products have emerged as a direct outcome of conscientious research endeavors focused on ecologically friendly and sustainable advancements in capacitors and batteries. Among this array of products, several stand out prominently owing to their diverse advantages.

**Solid-state battery:** Solid-state battery manufacturing is an intriguing study area for enhanced energy storage materials (7). Due to the solid electrolytes used instead of liquid ones, these batteries' cycle life, safety, and energy density can all be improved. Solid-state batteries. They are a desirable alternative for electric car applications because they can produce better energy densities than lithium-ion batteries. These battery systems replace conventional liquid electrolytes, enhancing security, power density, and cycle stability.

**Redox flow battery:** Redox flow batteries are another cutting-edge energy storage method that is gaining popularity since they are simple to scale up and down (8). The energy reservoir in these batteries is derived from the liquid electrolyte, which can be physically isolated from the electrodes. With enhanced adaptability and customization, energy storage technologies are more suitable for large-scale energy applications. As a result, storage technology options are becoming increasingly scalable and flexible.

**Lithium-ion battery:** One of the most widely acclaimed intricate energy storage devices is the lithium-ion battery. Lithium batteries have emerged as the best choice for many applications, including stationary energy storage, portable devices, and electric vehicles. Lithium-ion batteries are an excellent solution for several applications due to their high energy capacity and prolonged cycle stability. They rely on the electrochemical properties of electrolytes to produce and store electricity. Furthermore, due to their size, weight, and suboptimal performance, conventional lithium-ion batteries (LiB), characterized by an energy density of less than 500 watt-hours per kilogram, are not advisable for application in portable or wearable electronic devices (9–11).

**Supercapacitors:** A supercapacitor, also known as

an energy storage device or an electrochemical capacitor, is a high-tech energy storage device that generates electricity by separating negative and positive charges on opposite sides of a membrane. Unlike batteries, which store energy through chemical reactions, supercapacitors do so through electrostatic interactions. They are perfect for applications demanding a high power density because of their quick charging and discharging characteristics. Due to their ability to quickly charge (i.e., short discharge times of 1–10 seconds compared to 10–60 minutes for Li-ion batteries) and maintain performance over an extended period (over 30,000 hours compared to 500 hours for batteries), supercapacitors have grown in popularity (12).

Compared to traditional batteries, supercapacitors have several benefits. Because they have a higher power density, they can deliver more power in less time. They may also be charged and discharged more often than batteries before their performance starts to decline. Supercapacitors can be more dependable in challenging circumstances since they are more resistant to temperature changes than batteries. Advanced energy storage materials play a crucial role in facilitating the transition to a future dominated by renewable and sustainable energy sources, as they have the capability to enhance the efficiency, dependability, and availability of energy storage systems.

Supercapacitors can be categorized into several types based on how they store their charge. These types include pseudocapacitors, hybrid supercapacitors, and electric double-layer capacitors (EDLCs). Among these, pseudocapacitors utilize redox reactions occurring at the electrode surface to store energy. At the same time, EDLCs achieve energy storage by forming an electric double layer at the interface between the electrolyte and electrode surface. Combining the EDLC and pseudocapacitive mechanisms to enhance charge storage, hybrid supercapacitors demonstrate significantly higher energy and power densities than EDLCs or pseudocapacitive mechanisms used separately. EDLCs are a specific type of supercapacitor that stores electrical charge by creating an electric double layer at the interface between the electrode and the electrolyte. This double layer enables EDLCs to have high capacitance, allowing for storing large amounts of energy through electrostatic means. Carbon-based materials such as carbon nanowires, carbon nanotubes, activated carbon, graphene, and graphene oxide are commonly used as electrodes in EDLCs due to their extensive surface area, facilitating efficient charge storage.

On the other hand, pseudocapacitors store charge by utilizing electrochemical Faradaic redox reactions that take place at the electrode surface. This mechanism allows pseudocapacitors to store more energy than EDLCs, giving them a higher power density. Pseudocapacitive materials, including metal oxides like ruthenium oxide and manganese oxide, as well as conducting polymers like polyaniline (PANI) and polypyrrole (PPy), are commonly employed as electrodes in pseudocapacitors. It is worth noting



that while pseudocapacitors offer higher energy storage capabilities, the long-term stability of these devices can be limited by changes in the electrolyte and modifications to the electrode surface over time. These factors can lead to performance degradation in pseudocapacitors, highlighting the need to consider the materials and design used in their construction carefully.

## 2. CLASSIFICATIONS OF SUPERCAPACITORS

Supercapacitors can be divided into three categories: thin film, flexible, and planar. Thin film supercapacitors, frequently used in small electronic devices, comprise thin layers of materials like metal oxides and carbon. Flexible supercapacitors, on the other hand, are more common and can continue to perform even when bent, twisted, or stretched. Because of their great power density, planar supercapacitors, which have a rectangular, level architecture, are frequently utilized in bigger electronic equipment. Depending on the special needs of the device, each of these three types of supercapacitors offers a different set of advantages and can be applied to various applications. Supercapacitors can be categorized based on their construction, which includes electrochemical capacitors, pseudocapacitors, and hybrid capacitors. Electrochemical capacitors are composed of two conductive plates separated by an electrolyte, having a high capacitance but lower energy density compared to other supercapacitor types. On the other hand, pseudocapacitors employ electrode materials such as metal oxides or conducting polymers, leading to higher energy density but lower capacitance.

By striking a balance between high energy density and high capacitance, hybrid capacitors amalgamate the benefits of electrochemical and pseudocapacitors. High power density, energy density, low internal resistance, and quick charge-discharge periods are just a few of the characteristics of supercapacitors. High energy density refers to storing a significant quantity of energy in a compact device, whereas high power density allows for great power delivery in a short time. Effective energy transfer between the powered device and the supercapacitor is facilitated by low internal resistance, thus enhancing overall performance. Quick charge-discharge times are essential for applications requiring an immediate power boost, like electric automobiles or regenerative braking systems. Due to their categorization and physical characteristics, supercapacitors present an intriguing solution for a wide range of applications requiring high power and rapid energy transfer.

The materials utilized for the electrodes in supercapacitors are classified due to their charge storage mechanism. Additionally, electric double-layer capacitors (EDLCs), pseudocapacitors, and hybrid capacitors are the three main varieties (13,14). Activated carbon serves as the electrode material in EDLCs, also known as electrostatic capacitors, which exploit the electric double layer they produce at the electrode-electrolyte interface to

store energy. In a non-Faradaic process, where the concentration of electrons at the electrode is electrostatic, EDLCs use the electrical double-layer between the electrode and electrolyte to store energy. This procedure has no chemical mechanism or charge transfer between the electrode and electrolyte. Because no chemical connections are formed or broken, charges are therefore dispersed evenly across surfaces by physical processes, leading to great reversibility and cycle stability. Moreover, electrode polarization can distort the solvation shell around ions, potentially leading to partial desolvation. EDLCs feature a rapid energy storage system that enables swift charging, discharging, and high-power output.

## 3. SUPERCAPACITORS: HIGH-POWER ENERGY STORAGE DEVICES

Supercapacitors are divided into three according to the material class they are made from, apart from these classifications. All of them are nano-sized, but chemically and morphologically, they can be formed from classical nanomaterials, structures occurring with innovative MXenes, and various carbon-based structures. Material-based classification of supercapacitors is given in Figure 1.

### 3.1. Nanostructure-Enhanced Supercapacitor Electrodes

The electrodes of supercapacitors can benefit specifically from nanostructures. Nanostructures have significantly improved the functionality of supercapacitor electrodes thanks to their enormous surface area, better electrical conductivity, and adjustable properties. Nanostructured materials have improved charge transfer kinetics, better electrochemical stability, and energy storage capabilities. This section thoroughly analyzes several nanostructures used in supercapacitor electrode design, emphasizing the synthesis methods used and the resulting performance gains.

Metal oxide-based nanostructures have gained significant popularity in various energy applications due to their exceptional characteristics, such as a high surface area-to-volume ratio and small particle sizes. These qualities make them highly desirable for energy-related applications, including energy storage, catalysis, and sensors. The large surface area facilitates enhanced interactions with reactants and electrolytes, promoting efficient charge transfer and overall performance improvement. Furthermore, the smaller particle sizes allow for greater accessibility to active sites, improving functionality and responsiveness. Utilizing metal oxide-based nanostructures holds great promise in advancing energy technologies by enhancing their effectiveness and performance. In line with this approach, Haldorai et al. conducted a study focused on synthesizing a novel composite material (15). The study involved decorating reduced graphene oxide (rGO) with zinc oxide nanoparticles (ZnO NPs) using a one-pot method in a supercritical carbon dioxide medium. The primary objective of this study was to enhance the performance of supercapacitors by leveraging ZnO NPs as nanostructures, thereby achieving improved

energy storage capabilities. In another study, Sivakumar et al. presented a study on the synthesis of novel copper-doped zinc oxide nanoparticles (Cu-doped ZnO NPs) with an average crystallite size ranging from 25 to 22 nm (16). These nanoparticles demonstrated remarkable electrochemical performance, exhibiting an outstanding specific capacitance of 539.87 F/g at a scan rate of 10 mV/s. The primary objective of this research was to enhance both the photocatalytic activities and electrochemical performance of the Cu-doped ZnO NPs, with potential applications in wastewater treatment and supercapacitors. Integrating nanostructures, particularly metal oxide-based nanomaterials, holds immense potential for advancing energy storage technologies. Research findings suggest that thorough exploration and optimization of ZnO nanostructured materials can significantly enhance the efficiency and performance of supercapacitors. This progress contributes to developing more efficient and sustainable energy storage techniques. To further improve energy storage technologies, it is crucial to fully unlock the potential of nanostructures and continuously

evaluate the benefits derived from their utilization. By doing so, we can drive innovation, foster continuous improvement, and achieve remarkable advancements in the field of energy storage. In 2023, Kambale et al. used spray pyrolysis to produce copper oxide (CuO) nanorods (17). The obtained CuO electrode was extremely appropriate for supercapacitor applications since it had a maximum specific energy of 108.18 Wh/kg and had outstanding cycling stability by maintaining 87.78% of its capacitance after 5000 cycles. For the advancement of energy storage systems, the incorporation of nanostructures, in particular metal oxide-based nanomaterials, offers great promise. Exploring and utilizing the potential of metal oxide nanostructured materials has improved supercapacitor performance and efficiency, opening the door for more efficient and long-lasting energy storage options. Enhancing energy storage systems requires employing nanostructures to their maximum capacity and continually assessing the benefits received from doing so. These continual research and development efforts are crucial for stimulating innovation and attaining more improvements in the sector.

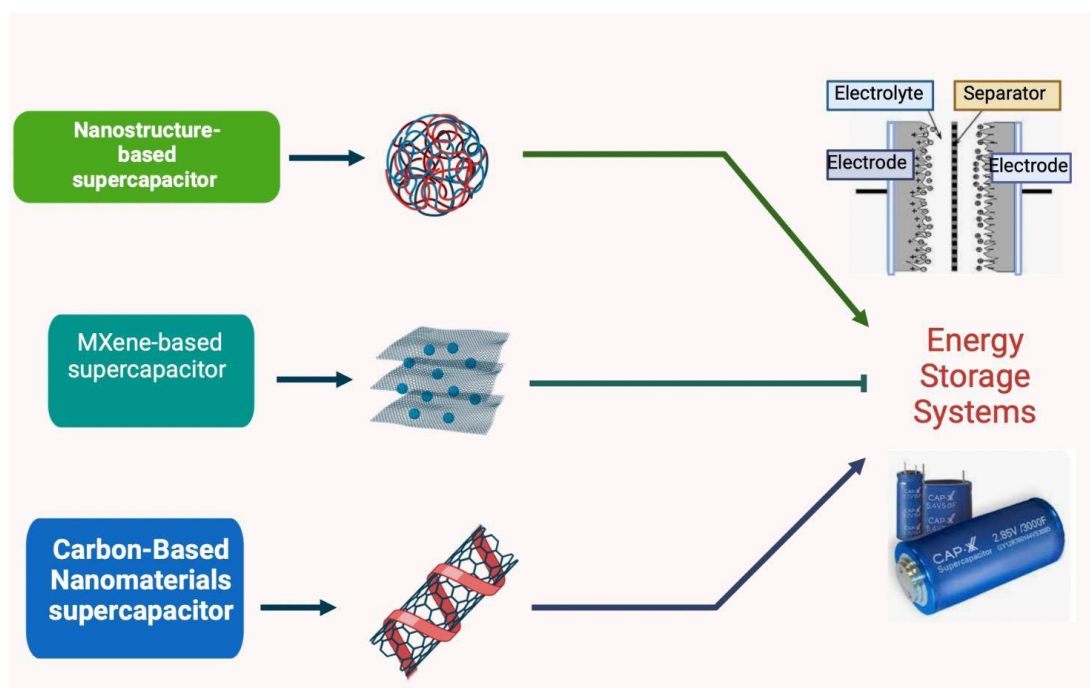


**Figure 1:** Material-based classification of supercapacitors.

Metal-organic frameworks (MOFs) consist of porous, crystalline compounds formed by metal ions or clusters bonded to organic ligands. Their properties can be highlighted for various purposes based on the utilized metal, the valency of metal ions in the structure, and the type of organic molecule. Concerning supercapacitors, MOFs with a smooth crystal structure, substantial surface area, and easy adjustability are preferred for producing high-capacity electrodes. One significant drawback of these materials lies in their inherent low electrical conductivity and weak stability in their pristine state, especially when compared to their diverse composite structures. Nevertheless, MOFs remain extensively employed in this field due to their adaptability to alternative structures and compatibility with

additives. Discovered by Yaghi et al. in 1995, MOFs have continued to undergo development and customization since then (18). In the realm of energy, MOFs and their derivatives find application in various areas, including hydrogen production and storage, fuel cells, lithium-ion batteries, superconductors, and solar cells. Three alternatives exist for employing MOFs in superconductor fabrication: a) Pristine MOFs can be utilized due to electrolyte ions adsorbed on their inner surfaces or due to reversible redox reactions occurring at their metallic centers. b) Metal oxides obtained by the transformation of MOFs are employed, with charge transfer between the electrolyte and the electrode safeguarding electrons. c) The MOFs are subjected to pyrolysis, resulting in a porous carbonaceous structure that enhances

conductivity and capacitance (19).

The notable advantages of MOFs over traditional supercapacitors include their expansive design possibilities and the capability to fine-tune composition, adjust porosity, and control surface area width. Furthermore, their distinctive structures enable a harmonious fusion of organic molecule flexibility with the inherent rigidity of inorganic molecules. Nonetheless, challenges such as low conductivity, potential particle aggregation, and structural degradation during cycling must be addressed. Consequently, research on MOFs has reached advanced stages, with the integration of newly discovered materials into these frameworks being actively explored. MOF-derived composites harness the favorable attributes of MOFs and other materials. The metallic content within MOFs furnishes redox sites that exhibit Faraday pseudocapacitive behavior, while the organic components contribute a conjugated  $\pi$  electron cloud and a porous structure that elicits EDLC behavior. The resultant structure can exhibit hybrid capacitive behavior when both behaviors are sufficiently developed. The high stability of the structures can reach extraordinary degrees when compared to batteries. Ni-MOF sample structures produced by electrophoretic deposition,  $\text{Ni}_3(\text{HAB})_2$  showed 81% stability after 50,000 cycles (20),  $\text{Ni}_3(\text{HITP})_2$  showed 84% capacitance stability after 100,000 cycles (21). It has been shown that crystallization in the desired direction can be achieved by adjusting the concentrations of organic ligands in Ni(Tdc)(Bpy) based 3D MOF nanocrystals (22). Considering this, it has been asserted that a diverse range of shapes can be synthesized, including nanorods, nanosheets, and 3D structures.

Using Co as the metal is a common practice. The widespread utilization of Co-MOFs can be attributed to factors such as low cost, straightforward synthesis, excellent structural stability, and environmentally friendly attributes. An exemplary illustration is the Co(II)-TMU-63 MOF structure, wherein both  $\mu_4\text{-tpa}_2$  and  $\mu\text{-dapz}$  ligands are simultaneously employed. This structure showcases the incorporation of multiple organic compounds and has demonstrated remarkable performance concerning capacitance, energy density, and cyclic life (23). The investigation of polymetallic MOFs featuring multiple metallic constituents has also garnered attention. Comparative to structures comprising solely Ni or Co, Ni/Co-MOF nanoflakes exhibited heightened efficiency (24). While the solvothermal method was employed in this study for material fabrication, an alternative investigation utilizing ultrasound treatment yielded greater capacitance due to the creation of more electroactive sites (25). Furthermore, the advancement of solvothermal synthesis, achieved via metal ion exchange, has increased capacitance. This is attributed to the facilitated diffusion of the electrolyte, achieved by augmenting the gap between layers within the multilayer structure alongside the augmentation of the count of electroactive sites (26). In conjunction with Ni and Co, the incorporation of Mn into the MOF structure has also demonstrated an elevation in capacitance

(27). Mn-based MOFs offer electrochemical advantages such as a hierarchical configuration and shortened ion diffusion pathways (28). The profound impact of morphologies on capacitive behavior has been explored from various vantage points. For instance, the amorphous form of UiO-66 MOF outperformed its crystalline counterpart (29). Ni-MOF and Cu-MOF stand as instances where different MOFs have been combined to augment dimensions (30).

Additionally, introducing diverse compounds into the structure is recommended to bolster capacity (31). Employing MOFs as composite constituents represents a strategy for enhancing their electrochemical or physical attributes. For instance, incorporating Cu-MOF onto  $\delta\text{-MnO}_2$  resulted in nanosheets that amplified the original structure's capacitance and extended its cyclic lifespan (32). While integrating metal oxides into the materials leads to composite formation, an additional boost in capacitance can be achieved by grafting them with metallic compounds (33).

Certain polymers, recognized for their remarkable electrical conductivity, are often favored in supercapacitor fabrication. Due to their adaptable attributes, diverse functional groups, isomeric variety, flexibility, ease of production, and cost-effectiveness, polymers emerge as preferred choices in this field and various other domains. The presence of conjugated bonds between monomers imparts these exceptional characteristics to conducting polymers. Moreover, non-inherently conductive polymers can acquire conductive attributes by incorporating dopants during monomer bonding. These dopants may also confer additional functional properties. Neutral ( $\text{Br}_2$ ,  $\text{I}_2$ ), ionic ( $\text{FeClO}_4$ ,  $\text{LiClO}_4$ ), organic ( $\text{CH}_3\text{COOH}$ ,  $\text{CF}_3\text{SO}_3\text{Na}$ ), polymeric (PVA, PVS), metal oxide ( $\text{SnO}_2$ ,  $\text{TiO}_2$ ) dopants can be selected based on the material and the desired trait (34). Polyaniline (PANI), polypyrrole (PPy), polythiophene (PTh), and their derivatives rank among the most frequently utilized conductive polymers. The rate of dopant incorporation hinges on the proximity of positive charges along the polymeric chain. For instance, while this ratio stands at 0.5 for polyaniline, it is 0.33 for the polymers listed above (35).

The initial high capacitance observed in stand-alone conductive polymers typically experiences a significant reduction after a short cyclic life (36). Naturally, exceptional cases exist, and performance varies based on factors such as synthesis method, dopant, nanostructure morphology, and more. For instance, the practical performance of PANI was found to lag its theoretical potential (37,38). In investigations where PPy and PTh were utilized in their pure forms, incorporating a surfactant (39) or dopant (40,41) substantially elevated capacitance and cyclic stability. However, the advantageous attributes of polymeric materials, even if not exhibiting exceedingly high performance on their own, find utility when integrated into composite structures within supercapacitors. For instance, carbon materials exhibit relatively low capacitance despite their notable electrical conductivity, physical

resilience, and adaptable surface properties. Numerous studies have been undertaken to surmount this limitation by employing polymers. Graphite (42), graphene (43), graphene oxide (44), and carbon nanoparticles of diverse configurations (45–49) have been combined with conductive polymers, yielding performance surpassing that of pure constituents. Moreover, the range of synthesis methods employed is considerably extensive (50–54). A recent study presents specific capacitance values for various polymers and polymeric composites alongside their respective synthesis methods (55). For example, producing a PPy/graphene composite featuring a uniform nanosheet morphology, in contrast to a cauliflower-like structure, bolstered electrochemical properties by creating ion diffusion pathways (56). In examining a PANI/graphene composite, an increase in the graphene ratio led to a more orderly placement of PANI monomers and heightened conductivity due to robust structural bonding (57). Alongside the research conducted by scholars who established a similar correlation within the PPy/MWCNT blend (54), another study revealed that the performance of the composite material exhibited enhancement up to a 15% MWCNT ratio, after which it declined at higher proportions (58). The utilization of PANI with graphene oxide yielded a more than twofold increase in capacitance, accompanied by elevated material conductivity (59). When subjected to a current density of 0.3 A/g, among PANI, PEDOT, and PPy combined with reduced graphene oxide, PEDOT displayed the highest stability (88%) after 1000 cycles despite possessing the lowest specific capacitance (108 F/g). PANI, boasting a higher specific capacitance (361 F/g) compared to PPy (248 F/g), also exhibited superior stability (82% vs. 81%) (60). Furthermore, when coated onto a pencil graphite electrode, PTh exhibited the lowest specific capacitance but demonstrated the greatest stability when compared to poly(3-methylthiophene) and PEDOT (61).

As elucidated in the preceding section, metal oxides are frequently employed in conjunction with polymers due to their inherent low conductivity and susceptibility to instability in acidic environments, notwithstanding their notable high capacity (62). Especially the wide band gaps of the oxides of the transition metals are the main reason for their low conductivity. However, for example, n-octadecyl-trimethyl-ammonium-intercalated  $\text{MnO}_2$  used with PANI both maintained its high conductivity and increased the specific capacity of PANI from 187 F/g to 220 F/g at a current density of 1 A/g (63). There are many other studies in which the same binary mixture is used in different morphologies (27,64,65). The PANI/CuO composite performed better than PEDOT/CuO and PPy/CuO (51). On the other hand, PPy has still been evaluated in producing supercapacitors by using it with many metal oxides. CoO (66),  $\text{WO}_3$  (67),  $\text{MnO}_2$  (68), and  $\text{V}_2\text{O}_5$  (69) are some metal oxides whose electrochemical properties are strengthened thanks to their synergistic effects with PPy. In addition to carbonaceous materials and metal oxides, compounds can also be incorporated to create composites with polymers for application in

supercapacitors. PANI, for instance, facilitates the crystal growth of  $\text{Ni}(\text{OH})_2$ , resulting in enhanced electrochemical performance (52). It also bolsters the conductivity of hydroquinone, rendering it suitable for utilization in supercapacitors (70). Moreover, PANI contributes to the capacitance and stability of  $\text{MoS}_2$  (71).

Table 1 comprehensively compares recent breakthroughs in nanomaterials tailored for supercapacitor applications. The table outlines specific capacitance, energy, power densities, cycling stability, and rate capability, highlighting the significant impact of nano-based materials on elevating supercapacitor electrodes' design and operational prowess, ultimately leading to enhanced efficiency and effectiveness.

### 3.2. An Innovative Class of 2D Materials for Energy Storage: MXene

MXene has emerged as a promising contender among the most recent developments in energy storage materials. MXene is a name for a class of two-dimensional materials made of carbides, nitrides, or carbonitrides of transition metals. These substances have outstanding qualities such a high conductivity, a sizable surface area, and customizable surface chemistry. MXene is an appealing option for energy storage applications, such as supercapacitors, due to its distinctive qualities. The synthesis, characterization, and performance of MXene-based energy storage materials are covered in detail in this section, along with information on their potential to play a significant role in developing new energy storage technologies. The improved MXene-based composites outperform traditional materials regarding cycle lifetime and energy density while dramatically lowering the MXene stacking phenomenon and enhancing oxidation resistance. They work well with a variety of materials, including small molecules, polymers, and oxides. The complex relationship between their structural properties and electrochemical performance has been revealed through extensive investigation. This includes the way in which the characteristics are organized, the microstructure, the steric arrangement, and the makeup of the material, all of which influence the charge storage processes, ion transport, conductivity, and stability. Thanks to their systematic analysis of these interactions, researchers have made it possible to construct MXene-based electrodes with knowledge, resulting in more effective and efficient energy storage systems. These composite materials predominantly comprise conductive polymers, metal oxides, and carbon nanostructures. Approximately 40% of MXene-based composite publications focus on metal oxides, conducting polymers, and carbon nanomaterials. In the literature, Vigneshwaran made a significant contribution by successfully developing a novel three-dimensional (3D) nickel cobalt tungstate-MXene nanocomposite specifically designed for coin cell supercapacitors (83). The nanocomposite demonstrated remarkable capacitance, achieving an impressive value of 587 F/g at a current density of 1 A/g in a three-electrode cell configuration. These

outstanding results highlight the exceptional performance of this nanocomposite and its tremendous potential for high-performance supercapacitor applications. In 2023, MXene-bacterial cellulose (MXene-BC) composite sheets, a novel substance that Weng et al. reported, have enormous potential for the creation of self-charging supercapacitors. These composite films have exceptional qualities that allow it possible to store and discharge electrical energy effectively. This research's ability to achieve a charging voltage of 0.6 V for the self-chargeable supercapacitor is one of its notable accomplishments. This substantial voltage milestone was reached using synthetic sweat as the electrolyte, further boosting the supercapacitor's efficiency and usefulness. The MXene-BC composite films are formed by combining MXene, a two-dimensional nanomaterial with high surface area and outstanding electrical conductivity, with bacterial cellulose, a biocompatible and durable material. This

effective combination creates a material with effective charge storage and great mechanical characteristics (84). Tin-cobalt-sulfide (Sn-Co-S) coated on 2D MXene sheets was the ground-breaking cathode material for high-performance asymmetric supercapacitors developed by Kim et al. in a recent work (85). A high specific capacity value of 305.71 mAh/gm at 1 A/g is one of the innovative 0D/2D Sn-Co-S/MXene hybrid material's impressive features. The Sn-Co-S/MXene hybrid material's remarkable electrochemical performance is due to its highly electroactive and conductive design. This study produces outstanding efficiency qualities by enabling effective charge storage and transfer. Hence, the deliberate integration of precisely engineered binary sulfide nanoparticles in conjunction with 2D scaffold-like MXene sheets presents exciting prospects for developing energy storage systems with outstanding performance and long-term stability.

**Table 1:** Comparative overview of nanomaterials for supercapacitors.

Nanomaterials	Results	Reference
Graphene	The specific capacitance: 523 F/g at 1.0 A/g, good rate capability and cycling stability.	(72)
Silver (Ag)-doped reduced graphene oxide (rGO)/PANI composite	The specific capacitance: 0.5–30 A/g, the highest capacitance value: 379 F/g	(73)
N-doped crumpled carbon nanotubes (CNTs)	The high capacitance: 336 F/g, cycling stability: 96.1% capacitance retention after 10,000 cycles, and good rate capability.	(74)
SmNiO <sub>3</sub> /Multi walled carbon nanotube (SWCNT)//CNT	Capacitance retention: 79.34% and coulombic efficiency: 97.52% (20,000 cycles)	(75)
Multi-walled carbon nanotube (MWCNTs)/MgMn <sub>2</sub> O <sub>4</sub> composite	The specific capacitance: 1208 F/g at 1 A/g, high energy density of 54.39 W h/kg, and power density of 775.46 W/kg at 1 A/g.	(76)
Zn-Co metal-organic frameworks (MOFs) nanospheres/rGO	The specific capacitance: 2925 F/g at 0.5 A/g, and good rate capability of 45.4% capacitance at a high current density of 50 A/g.	(77)
MOF-derived NiS <sub>2</sub> @carbon microspheres wrapped with CNTs	The specific capacitance: 1572 F/g at 0.5 A/g, energy density: 21.6 Wh/kg and 94.8% cycling stability after 10,000 cycles.	(78)
MOF derived NiCo <sub>2</sub> O <sub>4</sub> nanosheets	Energy density: 84.26 Wh/kg, power density: 1185 W/kg with 83.23% capacitance retention after 10,000 cycles.	(79)
3D MXene@graphene hydrogel	The maximum area capacitance: 4.33 F/cm <sup>2</sup> at 10 mA/cm <sup>2</sup> and a high area capacitance: 1.76 F/cm <sup>2</sup> at 1000 mA/cm <sup>2</sup> , the high capacitance retention: 40.6%, a high cyclic stability of 8.37% decrease after 100,000 cycles.	(80)
PANI-MXene composite	The specific capacitance: 222 F/g. The capacitance retention of 98.5% after 10,000 charges.	(81)
CuMn <sub>2</sub> O <sub>4</sub> /Ti <sub>3</sub> C <sub>2</sub> MXene composite	The specific capacitance: 496 mF/cm <sup>2</sup> at 6 mA/cm <sup>2</sup> with cyclic stability of 80% for up to 10,000 cycles, and a power density: 1.5 m/cm <sup>2</sup> at a higher energy density of 0.073 mWh/cm <sup>2</sup>	(82)

### 3.3. Carbon-Based Nanomaterials: Synthesis Techniques and Performance in Supercapacitors

Due to their superior electrochemical qualities, carbon-based nanomaterials have attracted a lot of interest in the field of energy storage. This section examines several carbon-based nanomaterials and their synthesis processes, including carbon nanotubes, graphene, and carbon nanofibers.

Additionally, it looks at how well they work as electrode materials in supercapacitors, concentrating on elements like pore structure, surface chemistry, and morphology that affect how much energy they can store. The promise of these materials for upcoming energy storage applications is also highlighted in this section, along with current developments in modifying carbon-based nanoparticles to enhance their electrochemical

performance. The performance of carbon-based nanomaterials in supercapacitors can vary depending on various factors such as material structure, surface area, pore size, and electrode configuration. The green method for Carbon Dots (CDs), hydrothermal synthesis of Graphene Quantum Dots, Chemical Vapor Deposition (CVD) for Graphene and Reduced Graphene Oxide, electrochemical exfoliation for Reduced Graphene Oxide and Carbon Nanotubes (CNTs), and the template method for Mesoporous Carbon/nanoparticles have all been investigated for carbon-based nanomaterials in supercapacitor applications.

In fabricating electrodes especially designed for supercapacitors, various deposition processes, including physical vapor deposition, chemical vapor deposition, and electrodeposition, are employed (86–88). These techniques offer various ways to create electrode materials with specific characteristics and

enable fine control over the thickness of the deposited films. The electrodes produced because of this customized process are guaranteed to have the best properties, such as increased surface area, electrical conductivity, and charge storage capacity, all of which are essential for the greater performance of supercapacitor devices. Additionally, the ability to precisely control the film thickness helps optimize the supercapacitor's energy and power density, allowing it to transmit and store electrical energy effectively in various applications. These techniques yield materials with a wide range of performance characteristics, including affordability, straightforward growth, high stability, excellent rate capability, high specific capacitance, long cycle life, low resistance, and good electrical conductivity, enabling researchers to choose materials based on specific application requirements. The Table 2 provides a general overview of their performance characteristics.

**Table 2:** A general overview of the performance characteristics of nanomaterial in supercapacitor applications.

Synthesis Method	Nanostructure	Performance	Characterization Results	Reference
Green Method	Carbon Dots (CDs)	Low specific capacitance, cost-effectiveness, simple growth, and high stability	10-20 nm	(89)
Hydrothermal Method	Graphene quantum dots	Low specific capacitance, cost-effectiveness, simple growth, and high stability	Lateral dimensions: 10–20 nm	(90)
Chemical Vapor Deposition (CVD)	Graphene	Excellent rate capability, high specific capacitance, long cycle life, and low resistance	Spherical nanoparticles diameter: 80±8 nm and the lateral size 500 nm (PPY grown on dopamine-coated graphene)	(91)
Chemical Vapor Deposition (CVD)	Reduced graphene oxide	Excellent rate capability, high specific capacitance, long cycle life, and low resistance	the average crystallite size of GO and thermally reduced graphene oxide (TRGO)/Ni-Foam (NF) 35.43 and 1.61 nm	(92)
Electro-chemical Exfoliation	Carbon nanotubes	Excellent electrical conductivity, high specific capacitance, and rapid charge/discharge rates	The high specific surface area: 219 - 210 m <sup>2</sup> /g	(93)
Electro-chemical Exfoliation	Carbon nanofibers	Long cycle life, good electrical conductivity, and moderate specific capacitance	Diameter: 10–40 nm	(94)
One-pot synthesis technique	Mesoporous carbon/nanoparticles	Excellent ion accessibility, high specific capacitance, and good stability	The high specific surface area: 686 m <sup>2</sup> /g	(95)
Solvothermal Method	Heterostructure hollow spheres	Low cost, good stability, moderate specific capacitance, and simple scalability	Size: 1140 and 1520 nm.	(96)
Pyrolysis	Porous carbon	Large surface area, low cost, strong stability, and moderate specific capacitance	Pores with width between 10 nm and 50 nm	(97)
Sonication	Nb <sub>2</sub> C MXenes composites	Good cycling stability, electrical conductivity, and high specific capacitance	100 nm for single layer	(98)
Sonication	MnFe <sub>2</sub> O <sub>4</sub> /MXene/NF nanosized composite	Good cycling stability, electrical conductivity, and high specific capacitance	quasi-2D MXene sheets	(99)

#### 4. CHALLENGES AND FUTURE OPPORTUNITIES

In the realm of energy storage, the pursuit of innovative solutions remains paramount to meet the escalating demand for environmentally sustainable and carbon-neutral power sources. This review, focused on nanostructure-based systems, endeavors to provide a comprehensive panorama of recent advancements in energy storage technologies and refined energy storage materials. Facilitating the transition to a sustainable energy landscape necessitates the development of efficient and secure energy storage techniques. Supercapacitors have emerged as a central focus across a diverse array of

energy storage applications, driven by their swift charge/discharge kinetics, high power density, and extended cycle life. The integration of nanostructures has incontrovertibly demonstrated their potential to significantly amplify supercapacitor electrodes' effectiveness. Running parallel to this, the evolution of MXene, an inventive class of two-dimensional materials, holds great promise as a formidable contender in the energy storage arena. MXene's expansive surface area, remarkable electrical conductivity, and adaptable properties render it an appealing candidate for diverse energy storage applications.

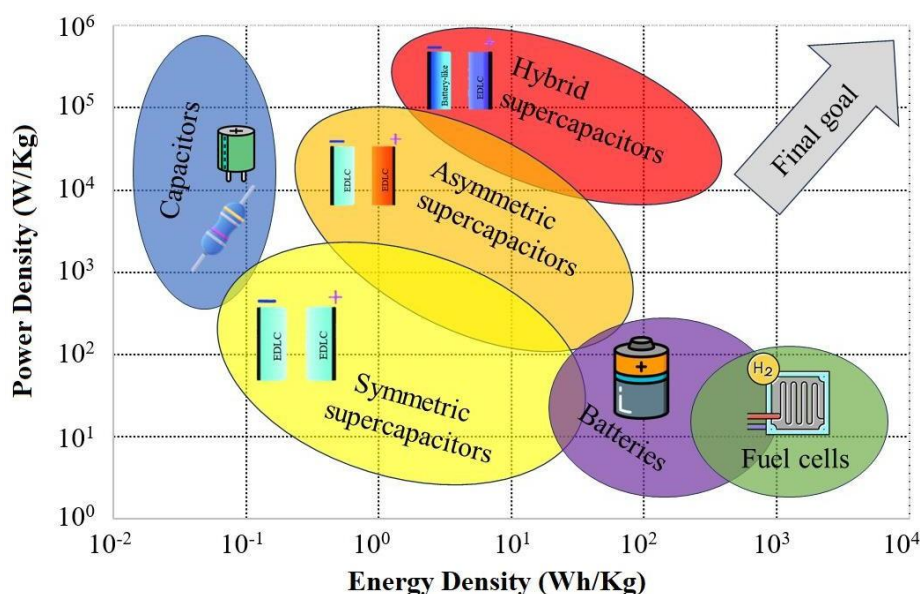


**Figure 2:** Energy density vs power density of capacitors, batteries, fuel cells, and supercapacitors.

The Ragone plot (Fig. 2), a graph that juxtaposes electricity storage and transmission devices along the energy density (Wh/kg) -power density (W/kg) axes, offers valuable insights. As data points populate this graph, batteries, characterized by their high storage capacities and low transmission forces, populate the high energy density-low power density quadrant. In contrast, classical capacitors occupy a different region. Fuel cells notably exhibit higher energy density compared to batteries. Devices closest to the ideal region align with mechanical components like engines and turbines. Supercapacitors, positioned along the graph's axial line, showcase their structure and composition diversity. This expansive variety positions supercapacitors, spanning a wide spectrum, to deliver superior densities. To encapsulate, the journey from EDLC to asymmetric and hybrid structures progressively enhances energy density.

Biological materials are used too, besides polymeric and other chemical materials in the separators that are expected to prevent unwanted ions' transition and be stable throughout the working life. Materials can present negative features along with some superior features. For example, PVA, which is preferred in terms of properties such as permeability, biodegradability, can withstand low voltages (100). In addition to organic structures, it is seen that ceramic-like inorganic structures are also

developed. Eggshell is one of the biologically based separators (101). In general, in addition to the stability of the separators, flexibility is another desired feature. Conductive liquids used as electrolytes can also be supplemented with other solutions that can give ions. For example, adding a solution that will make the pH move away from neutral but will not adversely affect other components will increase the power density (102). Materials such as anodic aluminum oxide, polystyrene colloidal particles, and sugar cubes are some of the auxiliary materials that can be used to increase the surface area of the electrodes. The smaller size of the ions also increases the performance, providing a faster transfer. While carbon itself, as active material, shows a weak capacitance, its derivatives with various morphological properties can improve performance. Although metal oxides, which are frequently used for this purpose, have different energy levels that facilitate charge transfer, they can be disadvantageous regarding environmental pollution, cyclic life, and charging efficiency (103). Conductive polymers, which are environmentally friendly, easily produced, and provide high power density, are another material class used as active material. Polypyrrole, polyaniline, polythiophene, polyphenylenevinylene, and polyacetylene are the most widely used conductive polymers. They can also be easily used in composite production with other materials and increase the

adjustability of properties (104). The diffusion rate of immobilized ions into the electrolyte is a parameter that affects the energy density. Materials with very different contents and structures have been designed to develop this speed in a controlled way. Hierarchical nanoarrays offer an advantageous approach when the one-pot strategy of hierarchical structures is used for dimension increase. Asymmetric fiber structures create folds and twists on the surface, creating a 3D morphology, which increases capacitance and power density. The properties of some supercapacitors, such as transparency, flexibility, lightness, small size, and biodegradability, increase the possibility of using these materials in biomedical engineering. This is a very important development in the field of medical electronics. It is possible to use supercapacitors in wearable electronics, electric vehicles, solar cells, etc (105).

In contrast to lithium-ion batteries, supercapacitors boast safer and more straightforward electrolytes. Moreover, the realm of biodegradable supercapacitors introduces an added advantage in this domain. Their distinctive structural makeup ensures an extended cyclic life and elevated power density. As illustrated in the examples, many of these supercapacitors exhibit substantial performance retention even after enduring thousands or even up to 100 thousand cycles. While their relatively lower energy densities may be perceived as a drawback; this aspect often pales compared to their many advantages. Furthermore, the emergence of novel materials and techniques holds the promise of surmounting this limitation. Various production methods, including lithography, electrospinning, printing, laser scribing, deposition (electrophoretic, electrolytic, physical/chemical vapor), and sputtering, form the backbone of supercapacitor fabrication from diverse materials. Within this comprehensive review, the exploration spans diverse nanomaterials, their synthesis processes, and their functional performance within supercapacitor frameworks. Reported studies also spotlight the untapped potential inherent in waste recycling, underscoring the capacity to craft high-performance nanomaterials tailored exclusively for energy storage applications. Ultimately, the overarching objective is to establish a robust foundation for advancing energy storage technologies, thereby catalyzing a surge of research and development endeavors.

## 5. CONCLUSION

Recent developments in energy storage technology have focused on nanostructures for modifying energy storage materials. Creating effective and secure energy storage systems is necessary to transition to a carbon-free and sustainable energy system. As a result of their high power density, quick charge/discharge rates, and long cycle life, supercapacitors have attracted a lot of attention. Supercapacitor electrode performance has been demonstrated to be improved by the incorporation of nanostructures. MXene, a 2D material renowned for its sizable surface area, superior electrical conductivity, and varied features, is one promising

substance in this domain. With a focus on supercapacitors, nanostructures, and MXene, this special issue includes various research articles and reviews highlighting the most recent advancements in advanced energy storage materials and systems. While highlighting the possibility of recycling waste materials to produce high-performance nanomaterials for energy storage applications, the paper also examines the synthesis methods of carbon-based nanomaterials and their performance in supercapacitors. Overall, regarding the current state-of-the-art and future directions in this quickly developing sector, this study seeks to encourage more research and development in energy storage technologies.

## 6. CONFLICT OF INTEREST

The authors have no conflicts of interest to declare.

## 7. REFERENCES

1. Meenu PC, Roy S, Chakraborty C, Roy S. Electro catalytic oxidation reactions for harvesting alternative energy over non noble metal oxides: Are we a step closer to sustainable energy solution? *Adv Powder Technol* [Internet]. 2021 Aug;32(8):2663–89. Available from: [<URL>](#).
2. Adetokun BB, Oghorada O, Abubakar SJ. Superconducting magnetic energy storage systems: Prospects and challenges for renewable energy applications. *J Energy Storage* [Internet]. 2022 Nov;55(Part C):105663. Available from: [<URL>](#).
3. Niu D, Fang J, Yau W, Goetz SM. Comprehensive evaluation of energy storage systems for inertia emulation and frequency regulation improvement. *Energy Reports* [Internet]. 2023 Dec;9:2566–76. Available from: [<URL>](#).
4. Dascalu A, Sharkh S, Cruden A, Stevenson P. Performance of a hybrid battery energy storage system. *Energy Reports* [Internet]. 2022 Nov;8:1–7. Available from: [<URL>](#).
5. Muzaffar N, Afzal AM, Hegazy HH, Iqbal MW. Recent advances in two-dimensional metal-organic frameworks as an exotic candidate for the evaluation of redox-active sites in energy storage devices. *J Energy Storage* [Internet]. 2023 Aug;64:107142. Available from: [<URL>](#).
6. Ren G, Wang J, Li Y, Zhang G. Power distribution optimization of a fully active hybrid energy storage system configuration for vehicular applications. *J Ind Inf Integr* [Internet]. 2023 Jun;33:100459. Available from: [<URL>](#).
7. Jiang W, Zhu X, Liu Y, Zhao S, Huang R, Ling M, et al. Design of composite cathodes for sulfide-based all-solid-state batteries. *eTransportation* [Internet]. 2023 Jul;17:100246. Available from: [<URL>](#).
8. Hu B, Li H, Fan H, Song J. A long-lifetime aqueous organic redox flow battery utilizing multi-redox anolyte. *Energy Storage Mater* [Internet]. 2023 May;59:102789. Available from: [<URL>](#).



9. Muralee Gopi CVV, Vinodh R, Sambasivam S, Obaidat IM, Kim H-J. Recent progress of advanced energy storage materials for flexible and wearable supercapacitor: From design and development to applications. *J Energy Storage* [Internet]. 2020 Feb;27:101035. Available from: [<URL>](#).
10. Ghadi BM, Hekmatnia B, Fu Q, Ardebili H. Stretchable fabric-based lithium-ion battery. *Extrem Mech Lett* [Internet]. 2023 Jun;61:102026. Available from: [<URL>](#).
11. Abdalla AM, Abdullah MF, Dawood MK, Wei B, Subramanian Y, Azad AT, et al. Innovative lithium-ion battery recycling: Sustainable process for recovery of critical materials from lithium-ion batteries. *J Energy Storage* [Internet]. 2023 Sep;67:107551. Available from: [<URL>](#).
12. Ji C, Cui H, Mi H, Yang S. Applications of 2D MXenes for Electrochemical Energy Conversion and Storage. *Energies* [Internet]. 2021 Dec 6;14(23):8183. Available from: [<URL>](#).
13. Inagaki M, Konno H, Tanaike O. Carbon materials for electrochemical capacitors. *J Power Sources* [Internet]. 2010 Dec 15;195(24):7880–903. Available from: [<URL>](#).
14. Kraiwattanawong K. A review on the development of a porous carbon-based as modeling materials for electric double layer capacitors. *Arab J Chem* [Internet]. 2022 Feb;15(2):103625. Available from: [<URL>](#).
15. Haldorai Y, Voit W, Shim J-J. Nano ZnO@reduced graphene oxide composite for high performance supercapacitor: Green synthesis in supercritical fluid. *Electrochim Acta* [Internet]. 2014 Feb;120:65–72. Available from: [<URL>](#).
16. Sivakumar S, Robinson Y, Mala NA. Studies on photocatalytic performance and supercapacitor applications of undoped and Cu-doped ZnO nanoparticles. *Appl Surf Sci Adv* [Internet]. 2022 Dec;12:100344. Available from: [<URL>](#).
17. Kambale S V., Lokhande BJ. Morphologically modified CuO nanorod structure @ stainless steel as high performing supercapacitor electrode prepared by spray pyrolysis. *Mater Chem Phys* [Internet]. 2023 Feb;295:127166. Available from: [<URL>](#).
18. Yaghi OM, Li H. Hydrothermal Synthesis of a Metal-Organic Framework Containing Large Rectangular Channels. *J Am Chem Soc* [Internet]. 1995 Oct 1;117(41):10401–2. Available from: [<URL>](#).
19. Wang L, Han Y, Feng X, Zhou J, Qi P, Wang B. Metal-organic frameworks for energy storage: Batteries and supercapacitors. *Coord Chem Rev* [Internet]. 2016 Jan;307:361–81. Available from: [<URL>](#).
20. Wechsler SC, Amir FZ. Superior electrochemical performance of pristine nickel hexaaminobenzene mof supercapacitors fabricated by electrophoretic deposition. *ChemSusChem* [Internet]. 2020 Mar 20;13(6):1491–5. Available from: [<URL>](#).
21. Nguyen DK, Schepisi IM, Amir FZ. Extraordinary cycling stability of Ni<sub>3</sub>(HITP)<sub>2</sub> supercapacitors fabricated by electrophoretic deposition: Cycling at 100,000 cycles. *Chem Eng J* [Internet]. 2019 Dec;378:122150. Available from: [<URL>](#).
22. Zheng S, Sun Y, Xue H, Braunstein P, Huang W, Pang H. Dual-ligand and hard-soft-acid-base strategies to optimize metal-organic framework nanocrystals for stable electrochemical cycling performance. *Natl Sci Rev* [Internet]. 2022 Aug 9;9(7):nwab197. Available from: [<URL>](#).
23. Sanati S, Abazari R, Morsali A, Kirillov AM, Junk PC, Wang J. An asymmetric supercapacitor based on a non-calcined 3D pillared cobalt(II) metal-organic framework with long cyclic stability. *Inorg Chem* [Internet]. 2019 Dec 2;58(23):16100–11. Available from: [<URL>](#).
24. Xia H, Zhang J, Yang Z, Guo S, Guo S, Xu Q. 2D MOF Nanoflake-Assembled Spherical Microstructures for Enhanced Supercapacitor and Electrocatalysis Performances. *Nano-Micro Lett* [Internet]. 2017 Oct 28;9(4):43. Available from: [<URL>](#).
25. Wang Y, Liu Y, Wang H, Liu W, Li Y, Zhang J, et al. Ultrathin NiCo-MOF nanosheets for high-performance supercapacitor electrodes. *ACS Appl Energy Mater* [Internet]. 2019 Mar 25;2(3):2063–71. Available from: [<URL>](#).
26. Li H, Wang X, Dai L, Guo F, Mi H, Ji C, et al. Kinetics-favorable ultrathin NiCo-MOF nanosheets with boosted pseudocapacitive charge storage for quasi-solid-state hybrid supercapacitors. *Inorg Chem* [Internet]. 2022 Mar 7;61(9):3866–74. Available from: [<URL>](#).
27. Zhang B, Song S, Li W, Zheng L, Ma X. Asymmetric supercapacitors with high energy density and high specific capacitance based on Ni-Co-Mn multiphase metal structure MOF. *Ionics (Kiel)* [Internet]. 2021 Aug 27;27(8):3553–66. Available from: [<URL>](#).
28. Liu J, Wang Z, Bi R, Mao F, Wang K, Wu H, et al. A polythreaded Mn<sup>II</sup>-MOF and its super-performances for dye adsorption and supercapacitors. *Inorg Chem Front* [Internet]. 2020;7(3):718–30. Available from: [<URL>](#).
29. Yang F, Li W, Tang B. Facile synthesis of amorphous UiO-66 (Zr-MOF) for supercapacitor application. *J Alloys Compd* [Internet]. 2018 Feb;733:8–14. Available from: [<URL>](#).
30. Deng T, Shi X, Zhang W, Wang Z, Zheng W. In-plane Assembly of Distinctive 2D MOFs with Optimum Supercapacitive Performance. *iScience* [Internet]. 2020 Jun;23(6):101220. Available from: [<URL>](#).
31. Cui L, Yu K, Lv J, Guo C, Zhou B. A 3D POMOF based on a {AsW<sub>12</sub>} cluster and a Ag-MOF with interpenetrating channels for large-capacity aqueous asymmetric supercapacitors and highly selective biosensors for the detection of hydrogen peroxide. *J*

- Mater Chem A [Internet]. 2020;8(43):22918–28. Available from: [<URL>](#).
32. Xu J, Wang Y, Cao S, Zhang J, Zhang G, Xue H, et al. Ultrathin Cu-MOF@ $\delta$ -MnO<sub>2</sub> nanosheets for aqueous electrolyte-based high-voltage electrochemical capacitors. J Mater Chem A [Internet]. 2018;6(36):17329–36. Available from: [<URL>](#).
33. Cao X, Cui L, Liu B, Liu Y, Jia D, Yang W, et al. Reverse synthesis of star anise-like cobalt doped Cu-MOF/Cu<sub>2</sub>O hybrid materials based on a Cu(OH)<sub>2</sub> precursor for high performance supercapacitors. J Mater Chem A [Internet]. 2019;7(8):3815–27. Available from: [<URL>](#).
34. Madgula K, Pattathil SD, Puli VS, Venkataraman A. Materials and Chemistry of Conducting Polymers. In: Gupta RK, editor. Conducting Polymers for Advanced Energy Applications [Internet]. 1st ed. Boca Raton: CRC Press; 2021. Available from: [<URL>](#).
35. Snook GA, Kao P, Best AS. Conducting-polymer-based supercapacitor devices and electrodes. J Power Sources [Internet]. 2011 Jan;196(1):1–12. Available from: [<URL>](#).
36. Meng Q, Cai K, Chen Y, Chen L. Research progress on conducting polymer based supercapacitor electrode materials. Nano Energy [Internet]. 2017 Jun;36:268–85. Available from: [<URL>](#).
37. Sivakkumar SR, Kim WJ, Choi J-A, MacFarlane DR, Forsyth M, Kim D-W. Electrochemical performance of polyaniline nanofibres and polyaniline/multi-walled carbon nanotube composite as an electrode material for aqueous redox supercapacitors. J Power Sources [Internet]. 2007 Sep;171(2):1062–8. Available from: [<URL>](#).
38. Li H, Wang J, Chu Q, Wang Z, Zhang F, Wang S. Theoretical and experimental specific capacitance of polyaniline in sulfuric acid. J Power Sources [Internet]. 2009 May;190(2):578–86. Available from: [<URL>](#).
39. Yang Q, Hou Z, Huang T. Self-assembled polypyrrole film by interfacial polymerization for supercapacitor applications. J Appl Polym Sci [Internet]. 2015 Mar 15;132(11):4–8. Available from: [<URL>](#).
40. Rajesh M, Raj CJ, Kim BC, Cho B-B, Ko JM, Yu KH. Supercapacitive studies on electropolymerized natural organic phosphate doped polypyrrole thin films. Electrochim Acta [Internet]. 2016 Dec;220:373–83. Available from: [<URL>](#).
41. Gnanakan SRP, Muruganatham N, Subramania A. Organic acid doped polythiophene nanoparticles as electrode material for redox supercapacitors. Polym Adv Technol [Internet]. 2011 Jun 15;22(6):788–93. Available from: [<URL>](#).
42. Raj CJ, Kim BC, Cho W-J, Lee W, Jung S-D, Kim YH, et al. Highly Flexible and Planar Supercapacitors Using Graphite Flakes/Polypyrrole in Polymer Lapping Film. ACS Appl Mater Interfaces [Internet]. 2015 Jun 24;7(24):13405–14. Available from: [<URL>](#).
43. Gómez H, Ram MK, Alvi F, Villalba P, Stefanakos E (Lee), Kumar A. Graphene-conducting polymer nanocomposite as novel electrode for supercapacitors. J Power Sources [Internet]. 2011 Apr;196(8):4102–8. Available from: [<URL>](#).
44. Sun H, She P, Xu K, Shang Y, Yin S, Liu Z. A self-standing nanocomposite foam of polyaniline@reduced graphene oxide for flexible super-capacitors. Synth Met [Internet]. 2015 Nov;209:68–73. Available from: [<URL>](#).
45. Imani A, Farzi G. Facile route for multi-walled carbon nanotube coating with polyaniline: tubular morphology nanocomposites for supercapacitor applications. J Mater Sci Mater Electron [Internet]. 2015 Oct 9;26(10):7438–44. Available from: [<URL>](#).
46. Tran C, Singhal R, Lawrence D, Kalra V. Polyaniline-coated freestanding porous carbon nanofibers as efficient hybrid electrodes for supercapacitors. J Power Sources [Internet]. 2015 Oct;293:373–9. Available from: [<URL>](#).
47. Shen K, Ran F, Zhang X, Liu C, Wang N, Niu X, et al. Supercapacitor electrodes based on nanopolyaniline deposited on hollow carbon spheres derived from cross-linked co-polymers. Synth Met [Internet]. 2015 Nov;209:369–76. Available from: [<URL>](#).
48. Cai J, Niu H, Li Z, Du Y, Cizek P, Xie Z, et al. High-Performance Supercapacitor Electrode Materials from Cellulose-Derived Carbon Nanofibers. ACS Appl Mater Interfaces [Internet]. 2015 Jul 15;7(27):14946–53. Available from: [<URL>](#).
49. Keskinen J, Tuurala S, Sjödin M, Kiri K, Nyholm L, Flyktman T, et al. Asymmetric and symmetric supercapacitors based on polypyrrole and activated carbon electrodes. Synth Met [Internet]. 2015 May;203:192–9. Available from: [<URL>](#).
50. Niu Z, Luan P, Shao Q, Dong H, Li J, Chen J, et al. A “skeleton/skin” strategy for preparing ultrathin free-standing single-walled carbon nanotube/polyaniline films for high performance supercapacitor electrodes. Energy Environ Sci [Internet]. 2012;5(9):8726–33. Available from: [<URL>](#).
51. Ates M, Serin MA, Ekmen I, Ertas YN. Supercapacitor behaviors of polyaniline/CuO, polypyrrole/CuO and PEDOT/CuO nanocomposites. Polym Bull [Internet]. 2015 Oct 7;72(10):2573–89. Available from: [<URL>](#).
52. Zhang J, Shi L, Liu H, Deng Z, Huang L, Mai W, et al. Utilizing polyaniline to dominate the crystal phase of Ni(OH)<sub>2</sub> and its effect on the electrochemical property of polyaniline/Ni(OH)<sub>2</sub> composite. J Alloys Compd [Internet]. 2015 Dec;651:126–34. Available from: [<URL>](#).

53. Tang Q, Chen M, Yang C, Wang W, Bao H, Wang G. Enhancing the energy density of asymmetric stretchable supercapacitor based on wrinkled CNT@MnO<sub>2</sub> cathode and CNT@polypyrrole anode. ACS Appl Mater Interfaces [Internet]. 2015 Jul 22;7(28):15303–13. Available from: [<URL>](#).
54. Song H, Cai K, Wang J, Shen S. Influence of polymerization method on the thermoelectric properties of multi-walled carbon nanotubes/polypyrrole composites. Synth Met [Internet]. 2016 Jan;211:58–65. Available from: [<URL>](#).
55. Islam MM, Sheikh MSI, Susan MABH, Islam MM. Conjugated Polymers as the Materials for Supercapacitor Electrodes. In: Gupta RK, editor. Organic Electrodes [Internet]. Cham: Springer International Publishing; 2022. p. 265–88. (Engineering Materials). Available from: [<URL>](#).
56. Zhu J, Xu Y, Wang J, Wang J, Bai Y, Du X. Morphology controllable nano-sheet polypyrrole-graphene composites for high-rate supercapacitor. Phys Chem Chem Phys [Internet]. 2015;17(30):19885–94. Available from: [<URL>](#).
57. Du Y, Shen SZ, Yang W, Donelson R, Cai K, Casey PS. Simultaneous increase in conductivity and Seebeck coefficient in a polyaniline/graphene nanosheets thermoelectric nanocomposite. Synth Met [Internet]. 2012 Jan;161(23–24):2688–92. Available from: [<URL>](#).
58. Wang J, Cai K, Shen S, Yin J. Preparation and thermoelectric properties of multi-walled carbon nanotubes/polypyrrole composites. Synth Met [Internet]. 2014 Sep;195:132–6. Available from: [<URL>](#).
59. Wang H, Hao Q, Yang X, Lu L, Wang X. Graphene oxide doped polyaniline for supercapacitors. Electrochem Commun [Internet]. 2009 Jun;11(6):1158–61. Available from: [<URL>](#).
60. Zhang J, Zhao XS. Conducting Polymers Directly Coated on Reduced Graphene Oxide Sheets as High-Performance Supercapacitor Electrodes. J Phys Chem C [Internet]. 2012 Mar 8;116(9):5420–6. Available from: [<URL>](#).
61. Hür E, Varol GA, Arslan A. The study of polythiophene, poly(3-methylthiophene) and poly(3,4-ethylenedioxythiophene) on pencil graphite electrode as an electrode active material for supercapacitor applications. Synth Met [Internet]. 2013 Nov;184:16–22. Available from: [<URL>](#).
62. Wang X, Liu J, Wang Y, Zhao C, Zheng W. Ni(OH)<sub>2</sub> nanoflakes electrodeposited on Ni foam-supported vertically oriented graphene nanosheets for application in asymmetric supercapacitors. Mater Res Bull [Internet]. 2014 Apr;52:89–95. Available from: [<URL>](#).
63. Zhang X, Ji L, Zhang S, Yang W. Synthesis of a novel polyaniline-intercalated layered manganese oxide nanocomposite as electrode material for electrochemical capacitor. J Power Sources [Internet]. 2007 Nov;173(2):1017–23. Available from: [<URL>](#).
64. Chen L, Sun L-J, Luan F, Liang Y, Li Y, Liu X-X. Synthesis and pseudocapacitive studies of composite films of polyaniline and manganese oxide nanoparticles. J Power Sources [Internet]. 2010 Jun 1;195(11):3742–7. Available from: [<URL>](#).
65. Anu Prathap MU, Satpati B, Srivastava R. Facile preparation of polyaniline/MnO<sub>2</sub> nanofibers and its electrochemical application in the simultaneous determination of catechol, hydroquinone, and resorcinol. Sensors Actuators B Chem [Internet]. 2013 Sep;186:67–77. Available from: [<URL>](#).
66. Zhou C, Zhang Y, Li Y, Liu J. Construction of High-Capacitance 3D CoO@Polypyrrole Nanowire Array Electrode for Aqueous Asymmetric Supercapacitor. Nano Lett [Internet]. 2013 May 8;13(5):2078–85. Available from: [<URL>](#).
67. Wang F, Zhan X, Cheng Z, Wang Z, Wang Q, Xu K, et al. Tungsten Oxide@Polypyrrole Core-Shell Nanowire Arrays as Novel Negative Electrodes for Asymmetric Supercapacitors. Small [Internet]. 2015 Feb;11(6):749–55. Available from: [<URL>](#).
68. Ji J, Zhang X, Liu J, Peng L, Chen C, Huang Z, et al. Assembly of polypyrrole nanotube@MnO<sub>2</sub> composites with an improved electrochemical capacitance. Mater Sci Eng B [Internet]. 2015 Aug;198:51–6. Available from: [<URL>](#).
69. Sun X, Li Q, Mao Y. Understanding the influence of polypyrrole coating over V<sub>2</sub>O<sub>5</sub> nanofibers on electrochemical properties. Electrochim Acta [Internet]. 2015 Aug;174:563–73. Available from: [<URL>](#).
70. Chen C, Fan W, Zhang Q, Ma T, Fu X, Wang Z. In situ synthesis of cabbage like polyaniline@hydroquinone nanocomposites and electrochemical capacitance investigations. J Appl Polym Sci [Internet]. 2015 Aug 5;132(29):42290. Available from: [<URL>](#).
71. Zhu J, Sun W, Yang D, Zhang Y, Hoon HH, Zhang H, et al. Multifunctional architectures constructing of PANI nanoneedle arrays on MoS<sub>2</sub> thin nanosheets for high-energy supercapacitors. Small [Internet]. 2015 Sep;11(33):4123–9. Available from: [<URL>](#).
72. Wang J, Wang Z, Li Z, Liu N, Luo Y, Chu Y, et al. High-energy-density flexible graphene-based supercapacitors enabled by atypical hydroquinone dimethyl ether. J Colloid Interface Sci [Internet]. 2023 Oct 15;648:231–41. Available from: [<URL>](#).
73. Kerli S, Bhardwaj S, Lin W, Gupta RK. Silver-doped reduced graphene oxide/Pani composite synthesis and their supercapacitor applications. J Organomet Chem [Internet]. 2023 Aug 15;995:122725. Available from: [<URL>](#).
74. Zong S, Du J, Chen A, Gao X, Otun KO, Liu X, et al. N-doped crumpled carbon nanotubes as advanced electrode material for supercapacitor. J Alloys Compd [Internet]. 2022 Dec 20;928:167222. Available

from: [<URL>](#).

75. Isacfranklin M, Yuvakkumar R, Ravi G, Thambidurai M, Nguyen HD, Velauthapillai D. SmNiO<sub>3</sub>/SWCNT perovskite composite for hybrid supercapacitor. J Energy Storage [Internet]. 2023 Sep 15;68:107786. Available from: [<URL>](#).

76. Bhagwan J, In Han J. Construction of high performance aqueous asymmetric supercapacitor based on multi walled carbon nanotube/MgMn<sub>2</sub>O<sub>4</sub> composite. J Energy Storage [Internet]. 2023 Nov 20;72:108350. Available from: [<URL>](#).

77. Wu H, Li S, Liu Y, Shi Y. Self-assembled Zn-Co MOF nanospheres/rGO as cathode material for an asymmetric supercapacitor with high energy density. Electrochim Acta [Internet]. 2023 Sep 10;462:142740. Available from: [<URL>](#).

78. Zhao J, Wang M, Wang S, Zhang S, Wang J, Qiao X, et al. MOF-derived NiS<sub>2</sub>@carbon microspheres wrapped with carbon nanotubes for high cycle performance supercapacitors. Electrochim Acta [Internet]. 2023 Oct 1;464:142920. Available from: [<URL>](#).

79. Salunkhe AD, Pawar PS, Pagare PK, Kadam AN, Katkar PK, Torane AP. MOF derived NiCo<sub>2</sub>O<sub>4</sub> nanosheets for high performance asymmetric supercapacitor. J Electroanal Chem [Internet]. 2023 Jun 15;939:117475. Available from: [<URL>](#).

80. Shi C, Liu Z, Tian Z, Li D, Chen Y, Guo L, et al. Fabrication of 3D MXene@graphene hydrogel with high ion accessibility via Al-induced self-assembly and reduction for high-performance supercapacitors. Electrochim Acta [Internet]. 2023 Oct 1;464:142892. Available from: [<URL>](#).

81. Bai W, Yong Z, Wang S, Wang X, Li C, Pan F, et al. Polyaniline-MXene composite electrode with excellent electrochemical properties for all-solid flexible supercapacitors. J Energy Storage [Internet]. 2023 Nov 1;71:108053. Available from: [<URL>](#).

82. Beknalkar SA, Teli AM, Khot AC, Mane SM, Shin JC. Preparation of CuMn<sub>2</sub>O<sub>4</sub>/Ti<sub>3</sub>C<sub>2</sub> MXene composite electrodes for supercapacitors with high energy density and study on their charge transfer kinetics. Ceram Int [Internet]. 2023 Oct 1;49(19):31236-47. Available from: [<URL>](#).

83. Vigneshwaran J, Narayan RL, Ghosh D, Chakkravarthy V, Jose SP. Robust hierarchical three dimensional nickel cobalt tungstate-MXene nanocomposite for high performance symmetric coin cell supercapacitors. J Energy Storage [Internet]. 2022 Dec;56(Part C):106102. Available from: [<URL>](#).

84. Weng M, Zhou J, Ye Y, Qiu H, Zhou P, Luo Z, et al. Self-chargeable supercapacitor made with MXene-bacterial cellulose nanofiber composite for wearable devices. J Colloid Interface Sci [Internet]. 2023 Oct;647:277-86. Available from: [<URL>](#).

85. Chang Kim M, Saeed G, Alam A, Choi Y, Zhang L, Lee D, et al. Ultrafine nanoparticles of tin-cobalt-

sulfide decorated over 2D MXene sheets as a cathode material for high-performance asymmetric supercapacitor. J Ind Eng Chem [Internet]. 2023 Aug;124:294-303. Available from: [<URL>](#).

86. Lai W, Wang Y, Wang X, Nairan A, Yang C. Fabrication and engineering of nanostructured supercapacitor electrodes using electromagnetic field-based techniques. Adv Mater Technol [Internet]. 2018 Jan 25;3(1):1700168. Available from: [<URL>](#).

87. Zaccagnini P, Heß LH, Baudino L, Laurenti M, Serrapede M, Lamberti A, et al. From aluminum dissolution in supercapacitors to electroplating: A new way for Al thin film deposition? Adv Mater Interfaces [Internet]. 2023 Jul 4;10(20):2202470. Available from: [<URL>](#).

88. Dianatdar A, Mukherjee A, Bose RK. Oxidative chemical vapor deposition of polypyrrole onto carbon fabric for flexible supercapacitive electrode material. Synth Met [Internet]. 2023 Sep 1;298:117444. Available from: [<URL>](#).

89. Başlak C, Öztürk G, Demirel S, Kocyigit A, Doğu S, Yıldırım M. Green synthesis of carbon quantum dots from *Sideritis vuralii* and its application in supercapacitors. Inorg Chem Commun [Internet]. 2023 Jul;153:110845. Available from: [<URL>](#).

90. Zhu Y, Huang Z, Huang X, Li Y, Li H, Zhou B, et al. One-step hydrothermal synthesis of manganese oxide nanosheets with graphene quantum dots for high-performance supercapacitors. J Energy Storage [Internet]. 2023 Jun;62:106948. Available from: [<URL>](#).

91. Kim YK, Shin K-Y. Dopamine-assisted chemical vapour deposition of polypyrrole on graphene for flexible supercapacitor. Appl Surf Sci [Internet]. 2021 May;547:149141. Available from: [<URL>](#).

92. Maphiri VM, Bakhoun DT, Sarr S, Sylla NF, Rutavi G, Manyala N. Low temperature thermally reduced graphene oxide directly on Ni-Foam using atmospheric pressure-chemical vapour deposition for high performance supercapacitor application. J Energy Storage [Internet]. 2022 Aug;52(Part B):104967. Available from: [<URL>](#).

93. Ghodhbane M, Ashraf JM, Karam Z, Lonkar S, Alshaya A, Busà C. Cellulose nanofibers as a green binder for symmetric carbon nanotubes-based supercapacitors. Electrochim Acta [Internet]. 2023 Sep;461:142584. Available from: [<URL>](#).

94. Costa LH, Vicentini R, Almeida Silva T, Vilela Franco D, Morais Da Silva L, Zanin H. Identification and quantification of the distributed capacitance and ionic resistance in carbon-based supercapacitors using electrochemical techniques and the analysis of the charge-storage dynamics. J Electroanal Chem [Internet]. 2023 Jan;929:117140. Available from: [<URL>](#).

95. Pooladi M, Zerfat MM. Controlled micro/mesoporous carbon aerogel structure as a template for Bi<sub>2</sub>O<sub>3</sub> nano-particles/rods to improve

- the performance of asymmetric supercapacitors. *J Energy Storage* [Internet]. 2021 Oct;42:102994. Available from: [<URL>](#).
96. Cheng Y, Xia K, Li H, Liu P, Zhao Z, Xu G, et al. One-pot synthesis of NiO-MnCo<sub>2</sub>O<sub>4</sub> heterostructure hollow spheres via template-free solvothermal method for high-performance supercapacitors. *Colloids Surfaces A Physicochem Eng Asp* [Internet]. 2023 Jul;669:131544. Available from: [<URL>](#).
97. Wu H, Yuan W, Yuan X, Cheng L. Atmosphere-free pyrolysis of harakeke fiber: A new chamber-induced activation methodology for porous carbon electrodes in supercapacitors. *Energy Storage Mater* [Internet]. 2022 Sep;50:514–24. Available from: [<URL>](#).
98. Yang W, Yang Z, Wang J, Lu W, Wang W. A bean catching double pigeons: Sonication assisted modification of Nb<sub>2</sub>C MXenes composites by O-doping porous biomass-carbons for supercapacitors and zinc-ion batteries. *J Energy Storage* [Internet]. 2023 Aug 15;65:107334. Available from: [<URL>](#).
99. Althubiti NA, Aman S, Taha TAM. Synthesis of MnFe<sub>2</sub>O<sub>4</sub>/MXene/NF nanosized composite for supercapacitor application. *Ceram Int* [Internet]. 2023 Aug 15;49(16):27496–505. Available from: [<URL>](#).
100. Ahankari S, Lasrado D, Subramaniam R. Advances in materials and fabrication of separators in supercapacitors. *Mater Adv* [Internet]. 2022;3(3):1472–96. Available from: [<URL>](#).
101. Yu H, Tang Q, Wu J, Lin Y, Fan L, Huang M, et al. Using eggshell membrane as a separator in supercapacitor. *J Power Sources* [Internet]. 2012 May;206:463–8. Available from: [<URL>](#).
102. Tan R, Wang A, Malpass-Evans R, Williams R, Zhao EW, Liu T, et al. Hydrophilic microporous membranes for selective ion separation and flow-battery energy storage. *Nat Mater* [Internet]. 2020 Feb 2;19(2):195–202. Available from: [<URL>](#).
103. Abdel Maksoud MIA, Fahim RA, Shalan AE, Abd Elkodous M, Olojede SO, Osman AI, et al. Advanced materials and technologies for supercapacitors used in energy conversion and storage: a review. *Environ Chem Lett* [Internet]. 2021 Feb 28;19(1):375–439. Available from: [<URL>](#).
104. Abdelhamid ME, O'Mullane AP, Snook GA. Storing energy in plastics: A review on conducting polymers & their role in electrochemical energy storage. *RSC Adv* [Internet]. 2015;5(15):11611–26. Available from: [<URL>](#).
105. Su Y, Sawan M. Supercapacitors: Fabrication Challenges and Trends. In: Stevic Z, editor. *Updates on Supercapacitors* [Internet]. IntechOpen; 2023. Available from: [<URL>](#).





## Preparation of PLGA-PEG/Hydroxyapatite Composites via Simple Methodology of Film Formation and Assessment of Their Structural, Thermal, and Biological Features

Fatih Ciftci<sup>1\*</sup>, Ali Can Özarlan<sup>2</sup>

<sup>1</sup>Department of Biomedical Engineering, Fatih Sultan Mehmet Vakif University, Istanbul, 34445, Turkey.

<sup>2</sup>Faculty of Chemistry Metallurgy, Department of Bioengineering, Yildiz Technical University, Istanbul, 34220, Turkey.

**Abstract:** This study aimed to develop polymeric composite films suitable for applications in the field of bone tissue engineering. The preparation of PLGA-PEG/HAP composite films was achieved using a simple methodology, including mixing, sonication, and casting-drying stages. Characterization analyses, including FTIR, SEM, TGA-DSC, and XRD, were conducted to assess the properties of the composite films. The results showed that the PEG polymer decreased the glass transition temperature of the composite, while the HAP did not change. Further, weight remaining (%) values of HAP, PLGA-PEG, and PLGA-PEG/HAP were found as 94.04, 88.28, and 90.57, respectively. Thus, it can be concluded that HAP improves the thermal stability of PLGA-PEG. The outcomes of the analysis, encompassing the evaluation of physical, morphological, and thermal properties, demonstrate that the composite structure comprising PLGA and PEG polymers along with HAP ceramic material may attain the intended quality. Moreover, fluorescence microscopy was employed to visualize the interaction between cells and the composite films following DAPI staining to evaluate cell adhesion and proliferation on the PLGA-PEG/HAP composite films. PLGA-PEG/HAP composite films have no adverse effects on cells, such as toxicity, and they have also exhibited a favorable influence on cell proliferation, supporting an augmentation in cellular growth and adhesion. Overall, the results indicate that the synthesized PLGA-PEG/HAP composite films may hold the potential to serve as a promising candidate for applications in the field of bone tissue engineering.

**Keywords:** Bone tissue engineering, PLGA, PEG, Hydroxyapatite, Composite, Film.

**Submitted:** June 12, 2023. **Accepted:** September 30, 2023.

**Cite this:** Ciftci F, Özarlan AC. Preparation of PLGA-PEG/Hydroxyapatite Composites via Simple Methodology of Film Formation and Assessment of Their Structural, Thermal, and Biological Features. JOTCSA. 2023;10(4):1123-32.

**DOI:** <https://doi.org/10.18596/jotcsa.1313562>

**\*Corresponding author's E-mail:** [faciftci@gmail.com](mailto:faciftci@gmail.com)

### 1. INTRODUCTION

Tissue engineering is an emerging field in biomaterial research with great therapeutic potential (1). Recent studies in the treatment of spinal cord injury have utilized tissue engineering technology, particularly for the design of a biological scaffold containing polymers, support cells and growth factors (2). We have investigated a three-dimensional tissue scaffold that can mimic the properties of the spinal cord to enable axonal regeneration in spinal cord injury (3). When placed in the damaged area, this scaffold needs to be orientated along the injured area to regenerate neuronal tissue and provide adequate mechanical support for regenerating nerve fibers (4).

An ideal neural scaffold should be biocompatible, biodegradable to avoid toxicity, permeable for nutrient and gas exchange, and have sufficient mechanical strength (5). The scaffold should gain elasticity to reduce stress at the injured point. The balance between the flexibility and rigidity of the scaffold should also be well balanced. Excessively hard scaffolds may dislodge easily, while overly soft ones may not support axonal regeneration (6).

The use of synthetic polymers instead of natural polymers in scaffolding offers a wider scope for designing and controlling the properties of the material. The most commonly used synthetic polymers in the spinal cord are either polyester-

based biodegradable materials such as PLA and PGA, or biodegradable hydrogels based on PEG. PLGA, a copolymer of PLA and PGA, was preferred as a synthetic polymer (5). This material is biocompatible and biodegradable. The degradation of PLGA produces glycolic and lactic acids that lower the pH and may inhibit the tissue repair process. Studies have shown that PLGA promotes axonal regeneration in nerve canals (5,7).

Poly (lactic-co-glycolic acid) (PLGA), a synthetic blend comprising polylactic acid and polyglycolic acid, is both biocompatible and biodegradable (8). Adjusting the proportion of polylactic acid to polyglycolic acid allows for control over the rate of copolymer degradation (9). PLGA-based neural conduits were inserted into fully severed rat spinal cords, resulting in observed axonal regeneration within these nerve conduits (10). However, it was noted that the degradation of PLGA produces glycolic and lactic acids, subsequently lowering the local pH and potentially hindering the tissue repair process (11).

PEG is a water-soluble compound belonging to the polyether family, known for its non-toxic nature and resistance to protein adsorption and cell adhesion (12). These characteristics make PEG a polymer that remains largely unrecognizable by the immune system upon implantation. Furthermore, PEG assists in sealing cell membranes post-injury. By manipulating the cross-links, PEG hydrogels can be tailored to degrade at various rates and employed as carriers for drug delivery (13). Additionally, they can be modified to promote improved cell adhesion (14). PEG possesses exceptional attributes for spinal cord repair, such as high hydrophilicity, biocompatibility, lack of immunogenicity, and neuroprotective qualities (15). Nevertheless, the degradation of PEG within the body hinges on the specific polyether structure. For instance, Mahoney et al. synthesized hydrolysable PEG hydrogels that were enhanced with poly (lactic acid) (PLA) and poly (glycolic acid) (PGA) (16). These PEG hydrogels exhibited remarkable resistance to protein adsorption, which can be attributed to properties like neutrality and enhanced mobility.

Hydroxyapatite (HAP) is the main inorganic component of natural bone. HAP has properties such as being biocompatible, bioactive (the ability to form direct chemical bonds with surrounding tissues), osteoconductive, non-toxic, non-inflammatory, and non-immunogenic (17). HAP is one of the ideal materials widely used in bone tissue engineering due to its biocompatibility and mechanical strength (18,19). The degradation rate of HAP implants must match the regeneration rate of native tissue and this is currently one of the biggest challenges in this field. Another purpose of using HAP is its excellent biocompatibility in soft tissue regeneration (17). Studies have shown that HAP forms a scaffold that supports the growth of fibroblasts. This in turn produces and deposits new collagen, a natural volumizing substance. Hydroxyapatite degradation is synchronized with neo-collagen deposition at the injection site, providing a lasting, natural, complete

and new appearance. The use of HAP in the scaffold promotes the growth of fibroblast cells, allowing the injured area to heal and gain a new appearance (20).

Both polymers and ceramics hold individual merit as viable biomaterials, while concurrently, researchers are exploring the potential of composite materials, including polymer-polymer and polymer-ceramic blends, as promising candidates within the biomaterial domain. The composite biomaterials paradigm exhibits versatility by encompassing different production methodologies to fabricate the constituent polymers and/or ceramics. The resultant diversity in fabrication techniques may enable various forms of these materials and, moreover, can help create new materials that exhibit different properties (21). Scaffaro et al. (22) undertook the fabrication of biocomposite nanofiber scaffolds employing a combination of polycaprolactone (PCL) and graphene oxide (GO) via the electrospinning methodology. Their investigation encompassed an exhaustive evaluation, encompassing morphological and mechanical analyses, aimed at providing an in-depth understanding of the structural influence and reinforcing efficacy introduced by GO within these scaffolds. The study revealed that the diameter of PLA/GO electrospun nanofibers decreased with increased filler content, while GO-g-PEG increased the diameter. Both nanofillers enhanced PCL hydrophilicity, with PCL/GO-g-PEG showing better wettability. The addition of GO improved Young's modulus, especially when GO was surface grafted with PEG at lower concentrations. This indicates improved dispersion due to PEG grafting. Additionally, MC3T3-E1 cell culture on PCL and PCL/GO-g-PEG scaffolds provided preliminary insights into their potential for tissue engineering. In a previous study conducted by Yavuz et.al. (23), HAP was synthesized using the sol-gel method, followed by surface modification with PEG-400Si. Subsequently, nanofibrous biomembranes containing unmodified (PCL/PEG-HAp) and modified HAp (PCL/PEG-400Si-HAp) were produced via electrospinning. In vitro assessments demonstrated biocompatibility for all biomembranes, with the PCL/PEG-400Si-HAp biomembrane exhibiting notably higher cellular protein expression, approximately 1.5 times more than the PCL biomembrane, over 24 h, 48 h, and 72 h. They concluded that the electrospun biomembrane composed of PCL/PEG-400Si-HAp holds promise as a prospective candidate for applications in bone tissue engineering scaffolds. In a different study performed by Santos et. al. (24), PLGA/hydroxyapatite/ $\beta$ -tricalcium phosphate membranes were fabricated with two different methods (dry phase inversion and electrospinning). This investigation demonstrated the feasibility of fabricating bilayer membranes comprising PLGA, HAp, and  $\beta$ -TCP, which exhibited suitable in vitro degradation, a mechanical profile striking a balance between rigidity and flexibility, well-defined pore architecture and dimensions, robust interlayer bonding, and enhanced potential for bone regeneration.

The principal objective of this inquiry is to ascertain and discuss the attributes of a tissue scaffold with the potential to facilitate the restoration of functional



connections in cases of spinal cord injury. This objective involves the straightforward methodological preparation of a composite film, serving as a promising scaffold that prominently combines synthetic polymers (PLGA and PEG) with ceramic material (HAP).

## 2. EXPERIMENTAL

### 2.1. Synthesis of Hydroxyapatite

A procedure called wet precipitation was used for HAP synthesis. This method was chosen because it offers high yield, simplicity, and low cost in contrast to other methods of obtaining HAP. For HAP synthesis, a reaction of 250 mL of 0.6 M  $\text{H}_3\text{PO}_4$  (purchased from Merck/Sigma-Aldrich, 80%) and 18.56 g  $\text{Ca}(\text{OH})_2$  (purchased from Merck/Sigma-Aldrich, 99%) was prepared, and then NaOH (purchased from Merck | Sigma-Aldrich, 99%) was added and stirred at room temperature for 7 days, keeping the pH above 11. After 7 days, the mixture was centrifuged three times for 5 min at 3000 rpm. Then, a filtration system was set up, and the mixture was poured into a Buchner funnel for separation. Finally, the obtained wet product was incubated in a dry oven at a temperature of 80 °C for 5 days. A portion of the HAP obtained during the synthesis process was sintered at 1050 °C for two hours to evaluate the effect of sintering.

### 2.2. Preparation of PLGA-PEG/HAP Composite Film

In this study, a PLGA-PEG/HAP composite film was prepared, wherein the central objective revolved around the attainment of a uniform dispersion of the constituent elements through a methodical process involving uncomplicated mixing and meticulous sonication. Firstly, the PLGA (purchased from Sigma Aldrich, 50:50, CAS Number: 26780-50-7,  $m_w$  30000-60000 g/mol) and PEG (purchased from Sigma Aldrich, CAS Number: 25322-68-3,  $m_w$  ~1500) polymer solutions were prepared, incorporating a 5% polymer content by weight, while maintaining a volumetric ratio of 95% chloroform. Subsequently, equal amounts of PLGA and PEG solutions were blended until achieving a homogeneous solution at ambient temperature. In addition, a chloroform-based solution of HAP was prepared, subsequently followed by the meticulous blending of PLGA-PEG/HAP solutions at a specific proportion of 65% PLGA-PEG to 35% HAP. The mixture was left to agitate at 40 °C for 24 h and sonicated as stated in a previous report (25) where the sonication time was divided into 10 s intervals with an amplitude of 100 using a Qsonica Q700 sonicator model CL-334. The Petri dishes were enveloped within a hermetically sealed container exhibiting a substantial headspace and maintained in an immobile state until solvent evaporation ensued. Following the completion of film formation, the resulting constructs were retrieved for subsequent characterization endeavors.

### 2.3. Characterizations

#### 2.3.1. Fourier-Transform Infrared Spectroscopy Analysis (FTIR)

FTIR spectra were collected for the composite films between 4000 - 650  $\text{cm}^{-1}$  at 20 °C. The spectra were recorded and stored on an ATR (Attenuated Total Reflectance) Perkin Elmer spectrometer. Four scans were performed at 4  $\text{cm}^{-1}$  resolution.

#### 2.3.2. X-ray Diffraction Analyses (XRD)

The equipment used in this analysis was a Bruker 8 with a powder method. A metal sample holder was used and a small amount of sample was placed so that it covered an area 1 cm long and 3 mm wide. The sample holder was then placed inside the equipment and secured inside the equipment. The analysis conditions were then programmed in the equipment, a speed between 15 and 30 rpm was programmed. The lamp used was a copper (Cu) lamp at 30 kV. Tests were performed in the  $2\theta = 20\text{-}80^\circ$  range and  $0.02^\circ$  step size.

#### 2.3.3. Scanning electron microscopy (SEM)

Morphological examination of all prepared composite films was conducted using scanning electron microscopy (SEM; EVO LS 10, ZEISS). A metal sample holder was prepared with graphite adhesive tape, onto which a small section of the specimen was positioned. Subsequently, a fine layer of gold was deposited onto the samples via assisted deposition at approximately 1 kV for a duration of 8 minutes. The prepared samples were placed onto an electron microscope tray, and images were captured across various magnifications and distinct regions.

#### 2.3.4. Thermogravimetric Analysis (TGA) and Differential Scanning Calorimetry (DSC) Analysis

Thermogravimetric analysis was carried out by measuring the mass change, thermal stability, and maximum decomposition temperature of all samples with increasing temperature. The test was carried out in an unsealed platinum flask using a nitrogen atmosphere at a flow rate of 20 mL/min, using a heating period of 10 °C/min from room temperature ( $\pm 20$  °C) to 700 °C at a flow rate of 20 mL/min. The equipment used was a Shimadzu TGA-50 model. Composite films were characterized using Shimadzu DSC model DSC-50 DSC equipment and programmed for room temperature heating ( $\pm 20$  °C) up to 120 °C for a period of 10 °C/min (initial run). The mass of the samples analyzed ranged from 5 to 10 mg. At the end of the run, the furnace was cooled with liquid nitrogen to a temperature of -20 °C or -30 °C.

#### 2.3.5. In vitro cell studies

Prior to culturing, the composite films underwent a sterilization procedure. Subsequently, they were cultured in Dulbecco's Modified Eagle Medium (DMEM), which served as a nutritive medium akin to the extracellular matrix (ECM). The experimental approach employed NIH 3T3 mouse embryonic fibroblast cells, obtained subsequent to their isolation from a designated cell line. Each composite film sample was meticulously seeded with an approximate population of  $7 \times 10^4$  NIH-3T3 cell lines. At intervals of the 1<sup>st</sup>, 3<sup>rd</sup>, 5<sup>th</sup>, and 7<sup>th</sup> days within the course of cell culture, the cells were subjected to staining with Dio6 and DAPI (5 mM) dyes. Subsequent to staining, an in-depth examination of

the cellular attributes and behaviors was undertaken utilizing fluorescence microscopy.

### 3. RESULT AND DISCUSSION

#### 3.1. FTIR Analysis

The purpose of this analysis is to determine the presence of both reagents in the sample. For the spectrum in Figure 1.A, the characteristic 5 signal of the PLGA structure was observed. The peak around 1765 - 1740  $\text{cm}^{-1}$  was assigned to C=O bonds, while the signal for -C-C-O bonds was assigned between 1300 - 1080  $\text{cm}^{-1}$ . The ether type appeared between 1085 and 1190  $\text{cm}^{-1}$  for -C-O-C- bonds. The -CH, -CH<sub>2</sub> and -CH<sub>3</sub> stretching group of the polymer was observed around 3000 - 2900  $\text{cm}^{-1}$ . It was assigned to methyl (-CH<sub>3</sub>) at 1383  $\text{cm}^{-1}$  and methylene (-CH<sub>2</sub>) at 1423  $\text{cm}^{-1}$ . Finally, the peaks observed around 869  $\text{cm}^{-1}$  correspond to the C-C bond. Between 1500 and 1250  $\text{cm}^{-1}$ , deformation of the -CH<sub>2</sub> and -CH<sub>3</sub> bond may be observed; CH and CH<sub>2</sub> vibrations between 1350 and 1150  $\text{cm}^{-1}$  and stretching of the -C-O ester bonds between 1300 and 1150  $\text{cm}^{-1}$  (26–29).

#### 3.2. XRD Analysis

The purity and crystallinity of the synthesized HAP were evaluated by XRD. Thanks to the interaction of X-rays with HAP powders, a diffraction diagram was

obtained. Since the diffraction diagram produced was considered as the fingerprint of the crystalline phase that produced it, it was possible to identify and determine whether the product obtained was really what we expected. The diffraction diagram obtained was plotted as a function of density versus angle  $2\theta$ . Figure 1.B shows the X-ray spectrum of the HAP powder. The first four peaks with the highest intensity located between the angular region  $20 < 2\theta < 60$  were assigned indices attributed to hydroxyapatite with Miller indices 002, 211, 112, and 300, respectively. These spectra were calculated with the structural parameters as in the previous study (30), in which a very similar behavior was observed, although the pattern presents narrower and more intense peaks. The spectra obtained were compared with JCPDS 09-432 (catalogue number) and it was proved that the sample obtained from HAP by wet precipitation method represents the typical pattern of this type of bioceramics (31–33). PLGA-PEG patterns were observed approximately at 211 and 300. PEG was observed at 211 and 202, while PLGA was observed in 211, 300, and 202 bands. When HAP bioceramic material was added to PLGA-PEG composite structures, the presence of HAP crystal structure continued to be observed at miller indices of 310, 222, 213 and, 411.

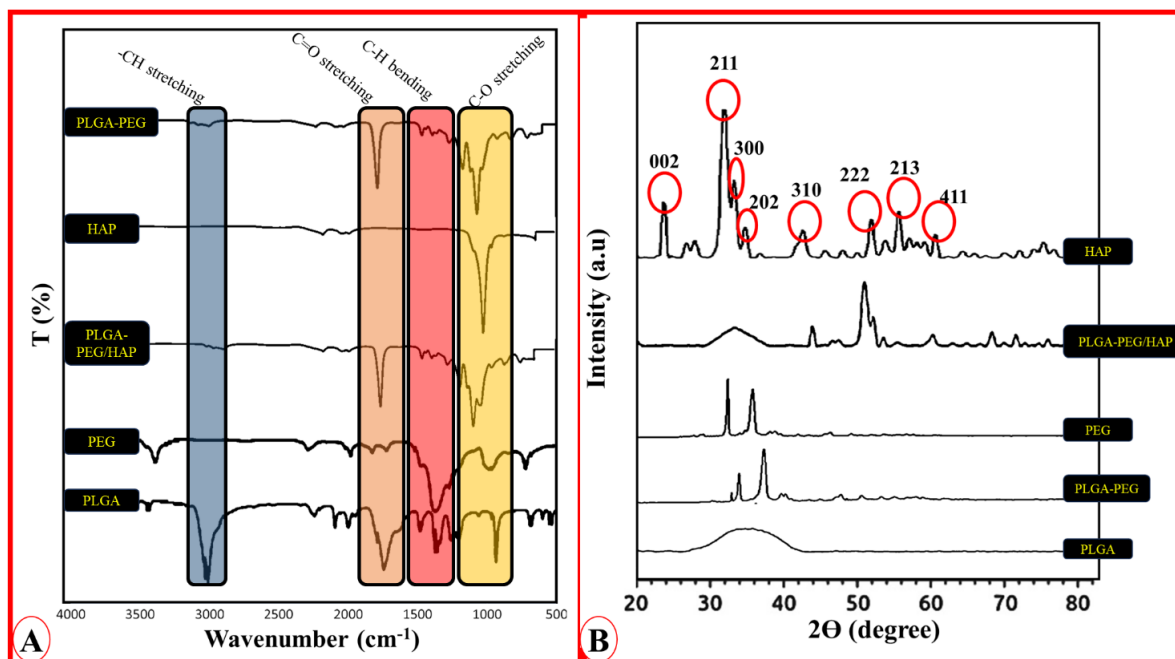


**Figure 1:** (A) FTIR spectra of and (B) XRD pattern of PLGA, PEG, HAP, PLGA-PEG, PLGA-PEG/HAP.

#### 3.3. SEM Analysis

In the SEM micrographs (Figure 2), a comprehensive examination was conducted on PLGA, HAP, and the composite film system involving PLGA-PEG and HAP. Remarkably, the utilization of an amorphous manifestation of PLGA-PEG was pursued, culminating in films that exhibited a notable cohesiveness in their structural makeup. Evident in the observations was a considerably gradual film formation process, distinct from the expeditious crystalline PLGA counterpart. This variance notably influenced the dispersion profile of hydroxyapatite within the polymer matrix. Noteworthy clusters of HAP were

perceptible within the SEM micrograph of the PLGA-PEG/HAP composite. However, a visual appraisal of the film's surface led to the discernment of a more uniformly distributed surface. The precise management of surface material attributes holds pivotal importance in dictating the efficacy of cell adhesion. Pertinent factors impacting the efficacy of biomaterial surfaces encompass attributes such as wettability and surface topography. Significantly, surface roughness has emerged as a pivotal facet influencing cellular adhesion dynamics. It has been suggested that certain textured configurations exhibit enhanced cellular behavior when compared to

conventional films. This interplay of surface roughness, in tandem with the surface's wettability and chemical composition, collectively orchestrates and modifies cellular affinity towards the substrate. While a meticulous quantification of surface roughness was not undertaken within this investigation, it is noteworthy that the scrutinized films exhibit a surface characterized by nuanced

roughness and embellished with hydroxyapatite attributes. This material is widely renowned for its inherent wettability, biocompatibility, and osteoconductive qualities. Consequently, the films at hand demonstrate tangible potential for biomedical applications, particularly in the realm of bone-regenerative pursuits (31,34–36).

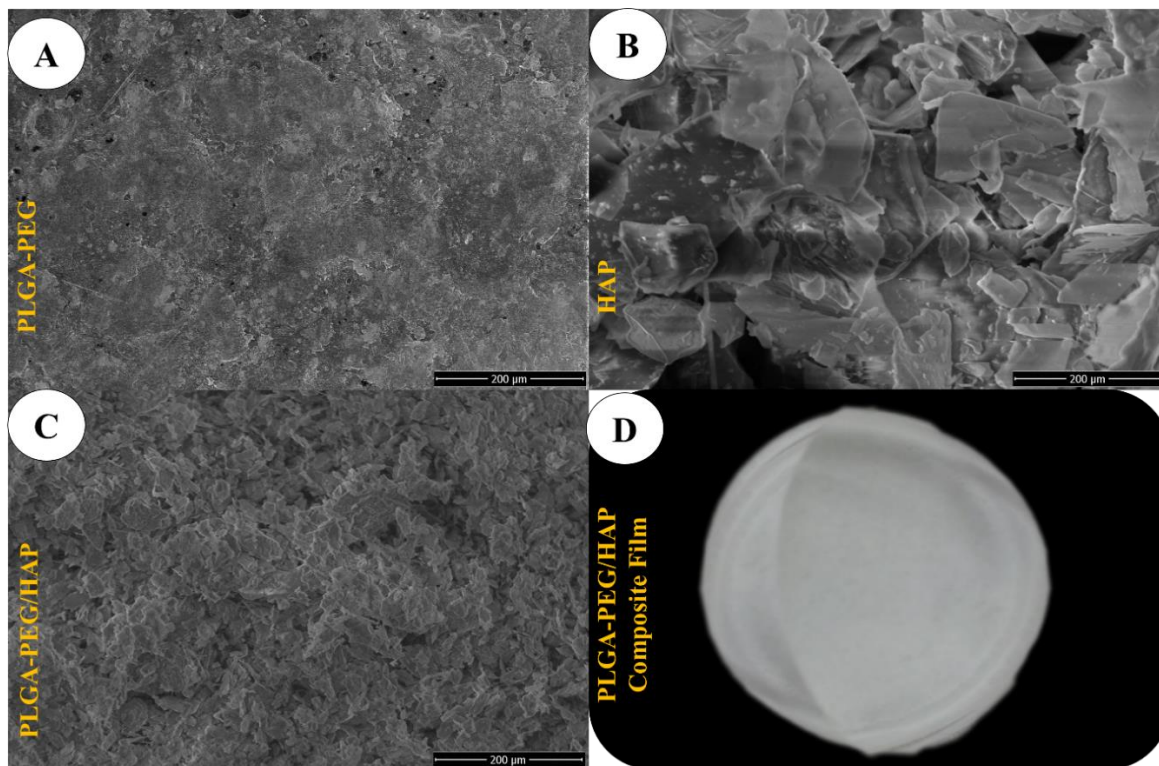


**Figure 2:** SEM micrographs of the surface of PLGA-PEG, HAP and PLGA-PEG/HAP composite film (Scale bar: 200  $\mu\text{m}$ ) and the image of PLGA-PEG/HAP composite film.

### 3.4. TGA and DSC Analysis

Figure 3 (B) illustrates the DSC profiles of HAP, PLGA-PEG, and PLGA-PEG/HAP composite film specimens. The determination of glass transition temperature ( $T_g$ ) for PEG polymers has exhibited variability across literature sources, with certain studies acknowledging the absence of  $T_g$  for PEG polymers with low molecular weights (37). However, prevailing research generally suggests a  $T_g$  value below 35  $^{\circ}\text{C}$  for PEG (38,39). Conversely, a well-established  $T_g$  range of 50–55  $^{\circ}\text{C}$  has been attributed to PLGA 50:50 polymer (40–42). Consequently, the distinct TGA and DSC plots for the PLGA and PEG polymers employed in this investigation were omitted. Notably, the HAP sample displayed no discernible  $T_g$  or distinctive thermal point throughout the temperature ramp until 100  $^{\circ}\text{C}$ . For the PLGA-PEG composite, a  $T_g$  within the range of 37–40  $^{\circ}\text{C}$  was ascertained. These findings, in accordance with previous inquiries, align with the notion that the

incorporation of PEG diminishes the  $T_g$  of the polymer blend (38,41,43). The scrutiny of the DSC profile for the PLGA-PEG/HAP composite film evinced negligible distinctions compared to the DSC profile of PLGA-PEG samples. This observation implies that the HAP sample, which lacks any apparent temperature-related characteristics upon temperature elevation to 100  $^{\circ}\text{C}$ , does not exert any influence on the thermal attributes of the PLGA-PEG blend (44). Thus, it can be inferred that the introduction of HAP into the PLGA-PEG blend exerts no alteration on the thermal traits of the composite. Moreover, a crystallization peak at approximately 72  $^{\circ}\text{C}$  was conspicuous in the DSC patterns of both PLGA-PEG and PLGA-PEG/HAP composite films, produced through a simple methodology encompassing mixing, sonication, and casting-drying stages. Thus, it can be posited that the impact of PEG and HAP content on the of the composite films parallels at the  $T_g$  crystallization temperature (43,45).

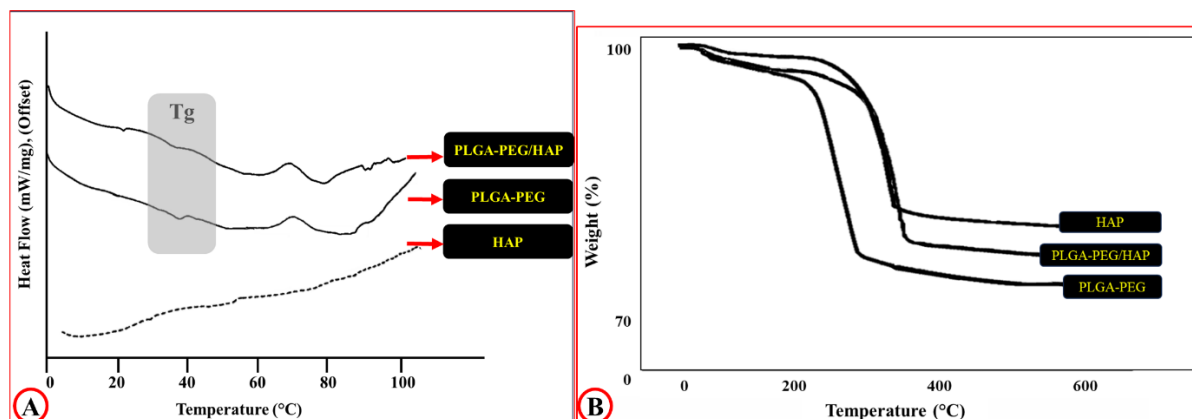


**Figure 3:** (A) TGA curves of and (B) DSC graph of HAP, PLGA-PEG, and PLGA-PEG/HAP.

Figure 3. (A), and Table 1. demonstrate the TGA curves and numerical data of HAP, PLGA-PEG, and PLGA-PEG/HAP samples, respectively. All specimens experienced mass loss in two different temperature zones (Region-I and Region-II). The moisture-induced mass loss values of HAP, PLGA-PEG, and PLGA-PEG/HAP samples at the first 100 degrees were determined as 0.64, 1.29, and 1.02(%), respectively. The total mass loss (%) in these two regions,

i.e. total degradation (%), was lowest in the HAP sample and highest in the PLGA-PEG sample. This is an indication that ceramic materials have a higher thermal stability than polymeric materials. In addition, the mass loss in the PLGA-PEG/HAP sample was higher than in the HAP sample and lower than in the PLGA-PEG sample. Thus, it may be said that the thermal stability of the PLGA-PEG polymer system with the addition of HAP increases (46,47).

**Table 1:** The results of TGA analysis of HAP, PLGA-PEG, and PLGA-PEG/HAP.

		HAP	PLGA-PEG	PLGA-PEG/HAP
(A); Region-I (B); Region-II	Temperature Range (°C)	(A) 25-194 (B) 194-611	(A) 25-224 (B) 224-528	(A) 25-205 (B) 200-610
	Degradation Amount (%)	(A) 2.68 (B) 2.64	(A) 3.73 (B) 6.70	(A) 3.08 (B) 5.33
	Maximum Degradation Rate (%/min)	(A) 0.28 (B) 0.08	(A) 0.69 (B) 0.96	(A) 0.42 (B) 0.58
	Maximum Degradation Temperature (°C)	(A) 46 (B) 450	(A) 182 (B) 451	(A) 168 (B) 450
Total Degradation (%)		5.96	11.72	9.43
Remaining (%)		94.04	88.28	90.57

### 3.5. Cell proliferation Study

The results of cell attachment and proliferation after DAPI staining on PLGA-PEG (control) and PLGA-PEG/HAP composite films are shown in Figure 4. For the cell proliferation assay, the cell amount of the PLGA-PEG/HAP composite group was 1.8 times higher than that of the control group, PLGA-PEG, on

day 7 of culture, showing a significant improvement in statistical analysis ( $P < 0.05$ ). In particular, fewer cells proliferated in the PLGA-PEG composite film on day 7. It was concluded that HAP in the polymeric composite film was effective in the attachment and proliferation of chondrocytes (11,48-51).

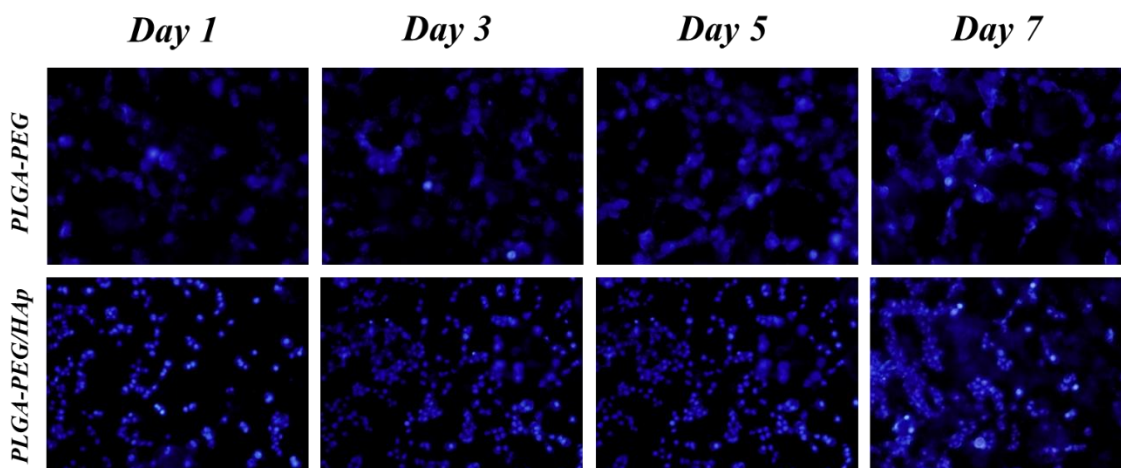


**Figure 4:** Cell line study fluorescence DAPI micrographs of 40x.

After incubation of fibroblast NIH/3T3 cells on composite films for 24 h, the behavior of cells was directly observed by fluorescence microscopy. The increase in the number of cells was clearly observed at the end of the 1<sup>st</sup>, 3<sup>rd</sup>, 5<sup>th</sup>, and 7<sup>th</sup> days, especially on the PLGA-PGE/HAP composite film. In a similar study, tissue engineered poly (lactide-co-glycolide)/polyethylene glycol (PLGA-PEG) nanofiber scaffolds were designed by electrospun technique for the treatment of spinal cord injuries. In vitro-vivo studies were performed on induced mouse embryonic fibroblasts (MEFs) reprogrammed into neural stem cells (iNSCs) using PLGA-PEG nanofibers. No difference was observed in iNSC cell viability at day 7 in PLGA and PLGA-PEG groups. Cell adhesion rates, cell proliferation and cell number on PLGA-PEG scaffolds increased steadily from day 1 to day 9 of incubation. Hoechst33342 cell nuclear staining of the sections was performed to determine the iNSCs in the PLGA-PEG scaffolds. No differences were observed in the cells within the scaffold. Hoechst staining showed core quality in the PLGA-PEG nanofiber scaffold. Nuclear staining showed that the cell population growing on the PLGA-PEG scaffold was larger than on the PLGA scaffold (52). In another previous study, PLGA and nano-hydroxyapatite (nHA)/PLGA composite scaffolds were designed as a predictive preclinical tool to study prostate cancer (mPC) and reduce the gap that exists with conventional 2D cultures. 2D and 3D cell distribution was observed using core fluorescence imaging on (nHA)/PLGA composite scaffolds. Cells were stained with Dio (green-hFOB 1.19) and Dil (red-PC-3). At the end of day 7, it was observed that hFOB: PC-3 cells were present in 2D cells. In addition, PC-3 cells were also observed equivalently. In 3D culture medium, (nHA)/PLGA scaffold colonized both hFOB 1.19 and PC-3 cells. However, more PC-3 cells were observed in the 4 mg (nHA)/PLGA scaffold group. The addition of nHA to the composite scaffolds corresponded to increased cell viability. As a result of this study, fluorescence imaging showed that PC-3 proliferated to a greater extent, and qualitatively this was more pronounced in scaffolds with higher nHA content (53).

#### 4. CONCLUSION

This investigation successfully undertook the preparation of PLGA-PEG/HAP composite films employing a simplified fabrication methodology. The inclusion of HAP within the polymer matrix has garnered significant attention in the field of tissue engineering. XRD patterns exhibited distinctive crystalline features, affirming the quality of the resultant samples. FTIR analysis revealed salient spectral bands, notably the broad signals in the aromatic region spanning 1600 cm<sup>-1</sup> to 1400 cm<sup>-1</sup>, signifying the amalgamation of HAP and the polymer substrate. SEM micrographs depicted surface uniformity in the samples, attributed to the amorphous nature of the polymer. This amorphous nature retards matrix formation, thereby promoting efficient filler dispersion. Further enhancement was achieved through sonication, accentuating filler distribution within the polymeric matrix. Consequently, the production methodology's potential for ensuring

reproducibility in terms of surface morphology and chemical composition becomes evident, presenting prospects for medical applications. TGA disclosed a maximum material loss of around ~9.5% in the PLGA-PEG/HAP composite film. This outcome validates the feasibility of autoclave sterilization for applications necessitating sterile substrates. In the DSC curve, a discrete yet broad transition within the 25-40 °C temperature range indicated the composite material's glass transition region. Integrating cellular assays and DAPI staining demonstrated the composite film's propensity for promoting cell adhesion in tissue engineering scenarios, while concurrently exhibiting minimal cytotoxic effects. Anticipated forthcoming research endeavors encompassing comprehensive biocompatibility assessments, degradation kinetics, and in vivo animal experimentation will provide a more nuanced understanding, substantiating the applicability of these composite films within the domain of bone tissue engineering.

#### 5. CONFLICT OF INTEREST

The authors declare no potential conflict of interest.

#### 6. REFERENCES

1. Ozder MN, Ciftci F, Rencuzogullari O, Arisan ED, Ustündag CB. In situ synthesis and cell line studies of nano-hydroxyapatite/graphene oxide composite materials for bone support applications. *Ceram Int* [Internet]. 2023 May 1;49(9):14791-803. Available from: [<URL>](#).
2. Yuan B, Chen H, Zhao R, Deng X, Chen G, Yang X, et al. Construction of a magnesium hydroxide/graphene oxide/hydroxyapatite composite coating on Mg-Ca-Zn-Ag alloy to inhibit bacterial infection and promote bone regeneration. *Bioact Mater* [Internet]. 2022 Dec 1;18:354-67. Available from: [<URL>](#).
3. Taylor EC, Fitzpatrick CE, Thompson SE, Justice SB. Acute Traumatic Spinal Cord Injury. *Adv Emerg Nurs J* [Internet]. 2022 Oct 1;44(4):272-80. Available from: [<URL>](#).
4. Serafin A, Rubio MC, Carsi M, Ortiz-Serna P, Sanchis MJ, Garg AK, et al. Electroconductive PEDOT nanoparticle integrated scaffolds for spinal cord tissue repair. *Biomater Res* [Internet]. 2022 Nov 22;26(1):63. Available from: [<URL>](#).
5. Ma Y, Chen Q, Li W, Su H, Li S, Zhu Y, et al. Spinal cord conduits for spinal cord injury regeneration. *Eng Regen* [Internet]. 2023 Mar 1;4(1):68-80. Available from: [<URL>](#).
6. Pourkhodad S, Hosseinkazemi H, Bonakdar S, Nekounam H. Biomimetic engineered approaches for neural tissue engineering: Spinal cord injury. *J Biomed Mater Res Part B Appl Biomater* [Internet]. 2023 Mar 10;111(3):701-16. Available from: [<URL>](#).
7. Wang M, Xu P, Lei B. Engineering multifunctional bioactive citrate-based biomaterials for tissue engineering. *Bioact Mater* [Internet]. 2023 Jan;19:511-37. Available from: [<URL>](#).
8. Sun F, Sun X, Wang H, Li C, Zhao Y, Tian J, et al. Application of 3D-Printed, PLGA-Based Scaffolds in Bone Tissue Engineering. *Int J Mol Sci* [Internet]. 2022 May 23;23(10):5831. Available from: [<URL>](#).

9. Makadia HK, Siegel SJ. Poly Lactic-co-Glycolic Acid (PLGA) as Biodegradable Controlled Drug Delivery Carrier. *Polymers (Basel)* [Internet]. 2011 Aug 26;3(3):1377–97. Available from: [<URL>](#).
10. Wang Z, Cui K, Costabel U, Zhang X. Nanotechnology-facilitated vaccine development during the coronavirus disease 2019 (COVID-19) pandemic. *Exploration* [Internet]. 2022 Oct 21;2(5):20210082. Available from: [<URL>](#).
11. Wei J, Yan Y, Gao J, Li Y, Wang R, Wang J, et al. 3D-printed hydroxyapatite microspheres reinforced PLGA scaffolds for bone regeneration. *Biomater Adv* [Internet]. 2022 Feb;133:112618. Available from: [<URL>](#).
12. Shabani Z, Rahbarghazi R, Karimipour M, Ghadiri T, Salehi R, Sadigh-Eteghad S, et al. Transplantation of bioengineered Reelin-loaded PLGA/PEG micelles can accelerate neural tissue regeneration in photothrombotic stroke model of mouse. *Bioeng Transl Med* [Internet]. 2022 Jan 29;7(1):e10264. Available from: [<URL>](#).
13. Lin C-C, Anseth KS. PEG Hydrogels for the Controlled Release of Biomolecules in Regenerative Medicine. *Pharm Res* [Internet]. 2009 Mar 18;26(3):631–43. Available from: [<URL>](#).
14. Mikhail AS, Ranger JJ, Liu L, Longenecker R, Thompson DB, Sheardown HD, et al. Rapid and Efficient Assembly of Functional Silicone Surfaces Protected by PEG: Cell Adhesion to Peptide-Modified PDMS. *J Biomater Sci Polym Ed* [Internet]. 2010 Jan 2;21(6–7):821–42. Available from: [<URL>](#).
15. Wang P, Wang H, Ma K, Wang S, Yang C, Mu N, et al. Novel cytokine-loaded PCL-PEG scaffold composites for spinal cord injury repair. *RSC Adv* [Internet]. 2020;10(11):6306–14. Available from: [<URL>](#).
16. Xu L, Wang Y-Y, Huang J, Chen C-Y, Wang Z-X, Xie H. Silver nanoparticles: Synthesis, medical applications and biosafety. *Theranostics* [Internet]. 2020;10(20):8996–9031. Available from: [<URL>](#).
17. Ielo I, Calabrese G, De Luca G, Conoci S. Recent Advances in Hydroxyapatite-Based Biocomposites for Bone Tissue Regeneration in Orthopedics. *Int J Mol Sci* [Internet]. 2022 Aug 27;23(17):9721. Available from: [<URL>](#).
18. Jianfei H, Fuke W, Guiran Y, Xinyu L, Di J, Dejian L. Application advantages of hydroxyapatite surface modification as a bone scaffold for tissue engineering. *Chinese J Tissue Eng Res* [Internet]. 2022 Apr 8;26(10):1610–4. Available from: [<URL>](#).
19. Aminatun, Suciati T, Sari YW, Sari M, Alamsyah KA, Purnamasari W, et al. Biopolymer-based polycaprolactone-hydroxyapatite scaffolds for bone tissue engineering. *Int J Polym Mater Polym Biomater* [Internet]. 2023 Mar 24;72(5):376–85. Available from: [<URL>](#).
20. Fiume E, Magnaterra G, Rahdar A, Verné E, Baino F. Hydroxyapatite for Biomedical Applications: A Short Overview. *Ceramics* [Internet]. 2021 Sep 28;4(4):542–63. Available from: [<URL>](#).
21. Farag MM. Recent trends on biomaterials for tissue regeneration applications: review. *J Mater Sci* [Internet]. 2023 Jan 1;58(2):527–58. Available from: [<URL>](#).
22. Scaffaro R, Lopresti F, Maio A, Botta L, Rigogliuso S, Ghersi G. Electrospun PCL/GO-g-PEG structures: Processing-morphology-properties relationships. *Compos Part A Appl Sci Manuf* [Internet]. 2017 Jan;92:97–107. Available from: [<URL>](#).
23. Yavuz E, Erdem R, Küçüksayan E, Akarsu E, Akarsu M. Preparation and Characterization of Polyethylene Glycol Functional Hydroxyapatite/Polycaprolactone Electrospun Biomembranes for Bone Tissue Engineering Applications. *Fibers Polym* [Internet]. 2021 May 27;22(5):1274–84. Available from: [<URL>](#).
24. dos Santos VI, Merlini C, Aragones Á, Cesca K, Fredel MC. In vitro evaluation of bilayer membranes of PLGA/hydroxyapatite/ $\beta$ -tricalcium phosphate for guided bone regeneration. *Mater Sci Eng C* [Internet]. 2020 Jul;112:110849. Available from: [<URL>](#).
25. Álvarez-Suarez AS, López-Maldonado EA, Graeve OA, Martínez-Pallares F, Gómez-Pineda LE, Oropeza-Guzmán MT, et al. Fabrication of porous polymeric structures using a simple sonication technique for tissue engineering. *J Polym Eng* [Internet]. 2017 Nov 27;37(9):943–51. Available from: [<URL>](#).
26. Liu X, Ma Y, Chen M, Ji J, Zhu Y, Zhu Q, et al. Ba/Mg co-doped hydroxyapatite/PLGA composites enhance X-ray imaging and bone defect regeneration. *J Mater Chem B* [Internet]. 2021;9(33):6691–702. Available from: [<URL>](#).
27. Liao S, Watari F, Zhu Y, Uo M, Akasaka T, Wang W, et al. The degradation of the three layered nano-carbonated hydroxyapatite/collagen/PLGA composite membrane in vitro. *Dent Mater* [Internet]. 2007 Sep;23(9):1120–8. Available from: [<URL>](#).
28. Lee JB, Lee SH, Yu SM, Park J-C, Choi JB, Kim JK. PLGA scaffold incorporated with hydroxyapatite for cartilage regeneration. *Surf Coatings Technol* [Internet]. 2008 Aug;202(22–23):5757–61. Available from: [<URL>](#).
29. Qian J, Xu W, Yong X, Jin X, Zhang W. Fabrication and in vitro biocompatibility of biomorphic PLGA/nHA composite scaffolds for bone tissue engineering. *Mater Sci Eng C* [Internet]. 2014 Mar;36:95–101. Available from: [<URL>](#).
30. Yelten-Yilmaz A, Yilmaz S. Wet chemical precipitation synthesis of hydroxyapatite (HA) powders. *Ceram Int* [Internet]. 2018 Jun;44(8):9703–10. Available from: [<URL>](#).
31. Hassan M, Sulaiman M, Yuvaraju PD, Galiwango E, Rehman I ur, Al-Marzouqi AH, et al. Biomimetic PLGA/Strontium-Zinc Nano Hydroxyapatite Composite Scaffolds for Bone Regeneration. *J Funct Biomater* [Internet]. 2022 Jan 28;13(1):13. Available from: [<URL>](#).
32. Yuan B, Zhang Y, Wang Q, Ren G, Wang Y, Zhou S, et al. Thermosensitive vancomycin@PLGA-PEG-PLGA/HA hydrogel as an all-in-one treatment for osteomyelitis. *Int J Pharm* [Internet]. 2022 Nov;627:122225. Available from: [<URL>](#).
33. Liyun J, Chengdong X, Lixin J, Lijuan X. Degradation behavior of hydroxyapatite/poly(lactic-co-glycolic) acid nanocomposite in simulated body fluid. *Mater Res Bull* [Internet]. 2013 Oct;48(10):4186–90. Available from: [<URL>](#).
34. Chang P-C, Luo H-T, Lin Z-J, Tai W-C, Chang C-H, Chang Y-C, et al. Preclinical evaluation of a 3D-printed hydroxyapatite/poly(lactic-co-glycolic acid) scaffold for ridge augmentation. *J Formos Med Assoc* [Internet]. 2021 Apr;120(4):1100–7. Available from: [<URL>](#).
35. Jiang L, Li Y, Xiong C, Su S. Preparation and characterization of a novel degradable nano-

hydroxyapatite/poly(lactic- co -glycolic) composite reinforced with bamboo fiber. Mater Sci Eng C [Internet]. 2017 Jun;75:1014–8. Available from: [<URL>](#).

36. Selvaraju S, Ramalingam S, Rao JR. Inorganic apatite nanomaterial: Modified surface phenomena and its role in developing collagen based polymeric bio-composite (Coll-PLGA/HAp) for biological applications. Colloids Surfaces B Biointerfaces [Internet]. 2018 Dec;172:734–42. Available from: [<URL>](#).

37. Zhu KJ, Xiangzhou L, Shilin Y. Preparation, characterization, and properties of polylactide (PLA)–poly(ethylene glycol) (PEG) copolymers: A potential drug carrier. J Appl Polym Sci [Internet]. 1990 Jan 5;39(1):1–9. Available from: [<URL>](#).

38. Pişkin E, Kaitian X, Denkbaş EB, Küçükyavuz Z. Novel PDLLA/PEG copolymer micelles as drug carriers. J Biomater Sci Polym Ed [Internet]. 1996 Jan 2;7(4):359–73. Available from: [<URL>](#).

39. Zheng F, Wang C, Huang K, Li J. Surface Adsorption in PEG/Hydroxyapatite and PEG/Dickite Composite Phase Change Materials. Energy & Fuels [Internet]. 2021 Jul 1;35(13):10850–9. Available from: [<URL>](#).

40. Xu XF. Preparation and *In Vitro* Degradation of PLGA/HA Composite Fiber Scaffolds by Electrospinning. Adv Mater Res [Internet]. 2012 Nov;591–593:982–8. Available from: [<URL>](#).

41. Vega E, Egea, Calpena, Espina, García. Role of hydroxypropyl-β-cyclodextrin on freeze-dried and gamma-irradiated PLGA and PLGA&ndash;PEG diblock copolymer nanospheres for ophthalmic flurbiprofen delivery. Int J Nanomedicine [Internet]. 2012 Mar;2012(7):1357–71. Available from: [<URL>](#).

42. Park J-W, Hwang J-U, Back J-H, Jang S-W, Kim H-J, Kim P-S, et al. High strength PLGA/Hydroxyapatite composites with tunable surface structure using PLGA direct grafting method for orthopedic implants. Compos Part B Eng [Internet]. 2019 Dec;178:107449. Available from: [<URL>](#).

43. Sheth M, Kumar RA, Dave V, Gross RA, McCarthy SP. Biodegradable polymer blends of poly(lactic acid) and poly(ethylene glycol). J Appl Polym Sci [Internet]. 1997 Nov 21;66(8):1495–505. Available from: [<URL>](#).

44. Nedaipour F, Bagheri H, Mohammadi S. "Polylactic acid-polyethylene glycol-hydroxyapatite composite" an efficient composition for interference screws. Nanocomposites [Internet]. 2020 Jul 2;6(3):99–110. Available from: [<URL>](#).

45. Ferri J, Gisbert I, García-Sanoguera D, Reig M, Balart R. The effect of beta-tricalcium phosphate on mechanical and thermal performances of poly(lactic acid). J Compos

Mater [Internet]. 2016 Dec 28;50(30):4189–98. Available from: [<URL>](#).

46. Tukulula M, Hayeshi R, Fonteh P, Meyer D, Ndamase A, Madziva MT, et al. Curdlan-Conjugated PLGA Nanoparticles Possess Macrophage Stimulant Activity and Drug Delivery Capabilities. Pharm Res [Internet]. 2015 Feb 28;32:2713–6. Available from: [<URL>](#).

47. Cañas-Gutiérrez A, Toro L, Fornaguera C, Borrós S, Osorio M, Castro-Herazo C, et al. Biomineralization in Three-Dimensional Scaffolds Based on Bacterial Nanocellulose for Bone Tissue Engineering: Feature Characterization and Stem Cell Differentiation. Polymers (Basel) [Internet]. 2023 Apr 24;15(9):2012. Available from: [<URL>](#).

48. Yang X, Li Y, He W, Huang Q, Zhang R, Feng Q. Hydroxyapatite/collagen coating on PLGA electrospun fibers for osteogenic differentiation of bone marrow mesenchymal stem cells. J Biomed Mater Res Part A [Internet]. 2018 Nov 5;106(11):2863–70. Available from: [<URL>](#).

49. Zhao Z, Ma X, Ma J, Kang J, Zhang Y, Guo Y. Sustained release of naringin from silk-fibroin-nanohydroxyapatite scaffold for the enhancement of bone regeneration. Mater Today Bio [Internet]. 2022 Jan;13:100206. Available from: [<URL>](#).

50. Espitia-Quiroz LC, Fernández-Orjuela AL, Anaya-Sampayo LM, Acosta-Gómez AP, Sequeda-Castañeda LG, Gutiérrez-Prieto SJ, et al. Viability and Adhesion of Periodontal Ligament Fibroblasts on a Hydroxyapatite Scaffold Combined with Collagen, Poly(lactic Acid–Polyglycolic Acid Copolymer and Platelet-Rich Fibrin: A Preclinical Pilot Study. Dent J [Internet]. 2022 Sep 6;10(9):167. Available from: [<URL>](#).

51. Shahabi S, Najafi F, Majdabadi A, Hooshmand T, Haghbin Nazarpak M, Karimi B, et al. Effect of Gamma Irradiation on Structural and Biological Properties of a PLGA-PEG-Hydroxyapatite Composite. Sci World J [Internet]. 2014;2014:420616. Available from: [<URL>](#).

52. Liu C, Huang Y, Pang M, Yang Y, Li S, Liu L, et al. Tissue-Engineered Regeneration of Completely Transected Spinal Cord Using Induced Neural Stem Cells and Gelatin-Electrospun Poly (Lactide-Co-Glycolide)/Polyethylene Glycol Scaffolds. Sensebé L, editor. PLoS One [Internet]. 2015 Mar 24;10(3):e0117709. Available from: [<URL>](#).

53. Dozzo A, Chullipalliyalil K, McAuliffe M, O'Driscoll CM, Ryan KB. Nano-Hydroxyapatite/PLGA Mixed Scaffolds as a Tool for Drug Development and to Study Metastatic Prostate Cancer in the Bone. Pharmaceutics [Internet]. 2023 Jan 11;15(1):242. Available from: [<URL>](#).

